

**The *in vitro* differentiation of prostate epithelial  
cells and gonadal adipocytes from  
mouse embryonic stem cells**

**Badwi Bob Boumelhem**

*A thesis submitted in fulfilment of the requirements of the degree of Doctor of  
Philosophy.*

*School of Medical Sciences*

*Discipline of Physiology*

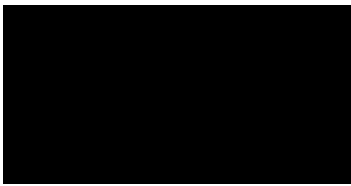
*University of Sydney*

**2017**

This page has intentionally been left blank.

## **Declaration**

I certify that the intellectual content of this thesis is the product of my own work and that all the assistance received in preparing this thesis and sources have been acknowledged. This thesis has not been submitted for any degree or other purposes.



Badwi Bob Boumelhem

## **Acknowledgements**

First and foremost, my deepest gratitude to my supervisors Associate Professor Stuart Fraser and Associate Professor Stephen Assinder. Thank you both so much for your patience, guidance and support over the past five years. I deeply appreciate everything the both of you have provided me with. I could not have asked for better mentors.

I would also like to acknowledge my colleagues from the Blood Cell Development and Andrology Research Group laboratories. Mr Jia Hao Yeo and Dr Kurt Brigden in particular, whom have been with me from the start of my journey. Thank you both for the support, the ideas, the rants, the laughs and the coffee runs. To the Honours students, past and present, thank you.

I also acknowledge the technical assistance provided by Dr. Angeles Sanchez-Perez, Dr. Louise Cole and Miss Janine Street. Thank you to Dr. Elizabeth New and Dr Jacek Kolanowski for their collaboration and technical expertise in the realm of chemistry. I would also like to acknowledge Professor Margot Day and Dr. Michael Morris for providing feedback and advice upon starting my postgraduate degree.



To my brothers, Mr Shadi Obeid and Mr Gabriel Abi-Saab, thank you both for supporting me, especially during times of frustration. The both of you were happy to hear me rave about my work, even if it went over your head. Thank you.

To my parents, your unwavering love and support has carried me this far. I truly hope I made the both of you proud. Love always.

*"A scientist without imagination is a butcher with dull knives and a worn-out scale."*

-Khalil Gibran

## **Publications arising from this thesis**

Wu, A., Kolanowski, J.L., Boumelhem, B.B., Yang, K., Lee, R., Kaur, A., Fraser, S.T., New, E.J., Rendina. (2017). A Carborane-Containing Fluorophore as a Stain of Cellular Lipid Droplets. *Chemistry, An Asian Journal*, 12(14), 1704-1708.

Boumelhem, B.B, Assinder, S.J., Bell-Anderson, K.S., Fraser, S.T. (2017). Flow cytometric single cell analysis reveals heterogeneity between adipose depots. *Adipocyte*, 6(2), 112-123.

## **Abstracts arising from this thesis**

**Boumelhem, B.B**, Assinder, S.J, Fraser, S.T. (April 2013). *In vitro* differentiation of mouse embryonic stem cells as a model of prostate organogenesis and tumorigenesis. 10-minute oral presentation at the Cancer Research Network conference, University of Sydney, Australia.

**Boumelhem, B.B**, Assinder SJ, Fraser, S.T. (September 2014). Macrophage colony stimulating factor receptor: A potential cell surface marker for prostate organogenesis. Poster presentation at the Sydney Cancer Conference, University of Sydney, Australia.

**Boumelhem, B.B**, Assinder, S.J, Fraser, S.T. (November 2014). Prostate in a dish: An *in vitro* model of prostate organogenesis using mouse embryonic stem cells. Poster presentation at the Australian Society for Stem Cell Research at Lorne, Melbourne, Australia.

**Boumelhem, B.B**, Assinder, S.J, Fraser, S.T. (March 2015) Same same but different: Distinguishing white and brown adipose tissue using flow cytometry. Poster presentation at the NSW Cell and Developmental Biology Meeting at UNSW, Randwick, Australia.

**Boumelhem, B.B**, Assinder, S.J, Fraser, S.T. (June 2015). Towards a model of prostate organogenesis: The differentiation of mouse embryonic stem cells into cells of the prostate. Poster presentation at the International Society for Stem Cell Research at Stockholm, Sweden.

**Boumelhem, B.B**, Assinder, S.J, Fraser ST. (March 2016). Pregnant mice have increased mitochondrial function and CD36 surface expression in adipocytes at the single cell level. Poster presentation at the NSW Cell and Developmental Biology Meeting at UNSW, Randwick, Australia.

**Boumelhem, B.B**, Bell-Anderson, K.S, Assinder, S.J, Fraser, S.T. (September 2016). Mitochondrial heterogeneity in adipose tissue. Poster presentation at the AussieMit conference at the Kolling Institute, Sydney, Australia.

**Boumelhem, B.B**, Assinder, S.J, Fraser, S.T. (March 2017). Endoderm culture conditions unexpectedly lead to adipocyte differentiation in mouse ES cells. Poster presentation at the NSW Cell and Developmental Biology meeting at UNSW, Randwick, Australia.

## Co-author contribution to published works

Parts of this thesis are based on selected peer-reviewed and submitted manuscripts. Below are descriptions of co-author contributions to published work.

Wu, A., Kolanowski, J.L., Boumelhem, B.B., Yang, K., Lee, R., Kaur, A., Fraser, S.T., New, E.J., Rendina. (2017). A Carborane-Containing Fluorophore as a Stain of Cellular Lipid Droplets. *Chemistry, An Asian Journal*, 12(14), 1704-1708.

A.W: designed the study, collected data, interpreted data, manuscript writing and editing

J.L.K: designed the study, collected data, interpreted data, manuscript writing and editing

**B.B.B**: manuscript writing, flow cytometric analyses and confocal imaging

K.Y: manuscript writing and editing

R.L: manuscript writing and editing

A.K: manuscript writing and editing

S.T.F: manuscript writing and editing, intellectual input

E.J.N: designed the study, intellectual input, manuscript writing and editing

L.M.R: designed the study, intellectual input, manuscript writing and editing

Boumelhem, B.B, Assinder, S.J., Bell-Anderson, K.S., Fraser, S.T. (2017). Flow cytometric single cell analysis reveals heterogeneity between adipose depots. *Adipocyte*, 6(2), 112-123.

B.B.B: manuscript writing and editing, intellectual input, flow cytometric analyses

K.S.B: manuscript editing, intellectual input

S.J.A: manuscript writing and editing, intellectual input

S.T.F: manuscript writing and editing, intellectual input

## Co-author signatures

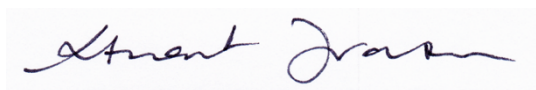
The corresponding authors listed below certify that the authors have contributed to publications and/or manuscripts in submission as outlined on the previous page and that agree to use those publications in submission in this thesis.

Elizabeth New

Elizabeth New

A handwritten signature in black ink, appearing to read 'Elizabeth New', with a horizontal line underneath.

Louis Rendina

A handwritten signature in black ink, appearing to read 'Louis Rendina', with a horizontal line underneath.

Stuart T. Fraser

## Abstract

Mouse embryonic stem (ES) cells are pluripotent, undifferentiated cells that can differentiate into any cell of the three germ layers: the ectoderm, the mesoderm and the endoderm. Mammalian development is challenging to study due to the *in utero* gestation and small size of early embryos. Mouse ES cells overcome this hurdle by recapitulating *in vivo* organogenesis in an *in vitro* setting.

There are currently no *in vitro* models of prostate development from mouse ES cells. The prostate is an endoderm derived exocrine organ that functions to provide the seminal constituents for sperm. The initial aim of this study was to differentiate mouse ES cells into mature, prostatic epithelial cells *in vitro* in stepwise manner. The prostate is derived from the urogenital sinus which in turn is derived from the endoderm. The endoderm and urothelium have been generated from mouse ES cells *in vitro* with the addition of Activin-A and all-trans retinoic acid respectively. It was hypothesised that treatment of mouse ES cell-derived urothelial cells with dihydrotestosterone (DHT), TGF $\beta$ 1 and FGF10 would induce prostate epithelial cell differentiation. Gene expression of homeobox protein *Nkx3.1* and prostate marker probasin (*Pbsn*) were identified in day 16 and day 22 differentiated cultures treated with the aforementioned growth factors. Additionally, day 22 cultures treated with DHT, TGF $\beta$ 1 and FGF10 developed cyst-like acinus structures with a lumen.



In conjunction with prostate epithelial cell differentiation, adipocyte-like cells were unexpectedly generated. Brown and white adipocytes are thought to arise from the mesoderm germ layer. Mouse ES cell culture conditions used to generate prostate epithelial cells were primed for endoderm specification. The question was then asked if the adipocytes generated were indicative of a particular adipose depot and if the endoderm could be a source of adipocytes. In order to identify the adipocyte-like cells differentiated *in vitro*, a method was developed to characterise brown, subcutaneous and visceral white adipocytes by flow cytometry. Multi-parametric flow cytometric analyses of adipocytes stained with Nile Red, MitoTracker Deep Red, Nile Blue, fatty acid translocase CD36 and laminin receptor integrins  $\alpha 6$  and  $\beta 1$  established adipocyte heterogeneity at the single cell level. Comparisons in dye uptake and surface protein expression between adipocytes revealed a code that was applied to the adipocyte-like cells differentiated under endoderm culture conditions. Adipocytes generated in mouse ES cell cultures treated with DHT, TGF $\beta$ 1 and FGF10 matched the profile of gonadal adipocytes.

Here, I report the first protocol describing prostate epithelial cell differentiation from mouse ES cells. As mouse ES cells can be genetically modified, the development of prostate epithelial cells may serve as an alternative approach for the study of prostate disease *in vitro*. The generation of adipocytes from mouse ES cells under endoderm conditions prompted the development of a

flow cytometric method to characterise adipocyte heterogeneity at the single cell level. The method can potentially be used for the diagnosis of a range of metabolic disorders stemming from obesity such as diabetes. Contrary to reports of a mesoderm origin of adipocytes, a possible endoderm origin of gonadal adipocytes is hypothesised, the adipose depot closest to the prostate. The development of the prostate in conjunction with gonadal adipocytes has yet to be reported.

# Table of Contents

<b>Declaration.....</b>	<b>ii</b>
<b>Acknowledgements .....</b>	<b>iii</b>
<b>Publications arising from this thesis.....</b>	<b>v</b>
<b>Abstracts arising from this thesis .....</b>	<b>vi</b>
<b>Co-author contribution to published works.....</b>	<b>viii</b>
<b>Co-author signatures .....</b>	<b>x</b>
<b>Abstract .....</b>	<b>xxi</b>
<b>List of Figures .....</b>	<b>xxv</b>
<b>List of Tables.....</b>	<b>xxv</b>
<b>List of Abbreviations.....</b>	<b>xxvi</b>
<b>Chapter 1: Introduction.....</b>	<b>1</b>
<b>1.1 The prostate is an endoderm-derived exocrine gland .....</b>	<b>1</b>
1.1.1 Anatomy of the prostate in mice .....	1
1.1.2 Histology of the mouse prostate .....	3
1.1.2.1 Epithelial cells of the prostate.....	3
1.1.2.2 Stromal cells of the prostate.....	4
1.1.3 Physiology of the prostate.....	6
1.1.4 Prostate disease in the ageing man.....	7
1.1.4.1 The TRAMP mouse model of prostate cancer .....	8
1.1.5 Development of the prostate <i>in vivo</i> .....	9
1.1.5.1 Development of the prostate begins with the mesendoderm.....	9
1.1.5.2 Prostate epithelial cells arise from the endoderm .....	13
1.1.5.3 The hindgut endoderm gives rise to the urogenital sinus .....	14
1.1.5.4 Branching morphogenesis of prostate epithelial cells is dependent upon paracrine signalling from the urogenital mesenchyme .....	14
1.1.6 Androgens regulate prostate development.....	15
1.1.6.1 Growth factors that are important in prostate organogenesis.....	16
1.1.7 Prostate development at the molecular level .....	17
1.1.7.1 Homeobox protein Nkx3.1.....	17
1.1.7.2 Probasin .....	17
<b>1.2 Embryonic stem cells as an <i>in vitro</i> model of development .....</b>	<b>20</b>
1.2.5.3 Differentiation of ES cells into the endoderm .....	24
1.2.5.4 Differentiation of prostate epithelial cell from mouse ES cells.....	26
1.3 Aims and hypotheses.....	27
<b>Chapter 2: Materials and Methods .....</b>	<b>28</b>
<b>2.1 Materials.....</b>	<b>28</b>
<b>2.2 Reagents.....</b>	<b>28</b>
<b>2.3 Cell culture.....</b>	<b>34</b>
2.3.1 Maintenance of mouse embryonic stem (ES) cells .....	34

2.3.2	Passaging of mouse ES cells.....	34
<b>2.4</b>	<b>Reverse-transcriptase polymerase chain reaction (RT-PCR) analysis.....</b>	<b>35</b>
<b>2.5</b>	<b>Animals.....</b>	<b>41</b>
2.5.1	Dissection and excision of tissue from mice.....	41
2.5.1.1	Genitourinary organs.....	42
2.5.1.2	Adipose tissue.....	42
2.5.1.2.1	Brown adipose tissue.....	42
2.5.1.2.2	White adipose tissue .....	43
2.5.1.3	Femoral and caudal vertebrae marrow .....	43
<b>2.6</b>	<b>Flow cytometry .....</b>	<b>46</b>
2.6.1	Generation of single cell suspensions from undifferentiated mouse ES cells and D5 embryoid bodies. ....	46
2.6.2	Generation of single cell suspensions from primary tissue. ....	47
2.6.2.1	Adipose tissue.....	47
2.6.2.2	Bone marrow .....	48
2.6.3	Sample preparation for flow cytometry.....	50
2.6.3.1	Controls used for flow cytometric analyses .....	50
2.6.3.1.1	Undifferentiated mouse ES cells .....	50
2.6.3.1.2	Primary tissue .....	50
2.6.3.2	Staining of cells with fluorescently-conjugated antibodies or fluorescent probes.....	51
2.6.3.3	Instrument settings .....	55
2.6.3.4	Compensation.....	55
2.6.3.5	Data analysis .....	55
<b>2.7</b>	<b>Imaging.....</b>	<b>57</b>
2.7.1	Light microscopy .....	57
2.7.2	Confocal microscopy .....	57
<b>2.8</b>	<b>Statistical analyses.....</b>	<b>57</b>
 <b>Chapter 3: The differentiation of mouse embryonic stem cells into prostate epithelial cells.....58</b>		
<b>3.1</b>	<b>Introduction .....</b>	<b>58</b>
3.1.1	Hypothesis:.....	59
3.1.2	Aims: .....	59
<b>3.2</b>	<b>Methods.....</b>	<b>62</b>
3.2.1	Differentiation of mouse ES cells into endoderm. ....	62
3.2.2	Differentiation of endoderm to urothelium. ....	62
3.2.3	Differentiation of urothelial cells to prostate epithelial cells: .....	63
3.2.4	Reverse-transcriptase polymerase chain reaction (RT-PCR) analysis.....	63
3.2.5	Flow cytometric analyses .....	63
3.2.5.1	Analysis of endoderm markers c-Kit and CXCR4 by flow cytometry .....	63
3.2.5.2	Analysis of colony stimulating factor 1 receptor (CSF-1R) by flow cytometry.....	64
3.2.6	Phase contrast imaging of undifferentiated mouse ES cells and differentiated cultures. ....	65
<b>3.3</b>	<b>Results.....</b>	<b>66</b>

3.3.1 Pluripotency markers <i>Oct4</i> and <i>Nanog</i> are detected in undifferentiated mouse ES cells.....	66
3.3.2 Activin-A and Wnt-3A promotes endoderm differentiation from mouse ES cells.....	68
3.3.3 Retinoic acid promotes differentiation of mouse ES cell-derived endoderm into urothelium.....	72
3.3.4 DHT, TGF $\beta$ 1 and FGF10 drives the differentiation of prostate epithelial cells from mouse ES cell-derived urothelial cells.....	76
3.3.4.1 Prostate epithelial cell specific marker <i>Nkx3.1</i> is detected in day 16 cultures treated with DHT, TGF $\beta$ 1 and FGF10.....	76
3.3.4.2 Development of acinus-like structures in DHT, TGF $\beta$ 1 and FGF10 treated mouse ES cell cultures.....	79
3.3.5 Colony-stimulating factor 1 receptor (CSF-1R) is expressed on few cells in the developing urogenital sinus.....	85
<b>3.4 Discussion.....</b>	<b>89</b>
3.4.1 Mouse ES cells as a model of prostate organogenesis.....	89
3.4.1.1 DHT, FGF10 and TGF $\beta$ 1 induce differentiation of prostate epithelial cells from mouse ES cell-derived urothelial cells.....	89
3.4.1.2 Homeobox protein <i>Nkx3.1</i> is restricted to epithelial cells of the prostate and bulbourethral glands.....	91
3.4.1.3 Probasin expression confirms the differentiation of prostatic epithelial cells.....	91
3.4.1.4 Androgen receptor is not solely expressed in the organs of the male reproductive tract.....	92
3.4.1.5 Evaluation of colony stimulating factor 1 receptor (CSF-1R) as a marker of prostate development.....	92
3.4.1.6 Applications for prostate epithelial cell differentiation from mouse ES cells.....	93
3.4.2 Conclusions.....	94
<b>Chapter 4: Endoderm culture conditions unexpectedly drive differentiation of adipocyte-like cells from mouse ES cells <i>in vitro</i>.....</b>	<b>95</b>
<b>4.1 Introduction.....</b>	<b>95</b>
4.1.1 Developmental origins of adipocytes.....	95
4.1.2 Morphology of brown and white adipocytes.....	96
4.1.3 Aims.....	96
<b>4.2 Methods:.....</b>	<b>98</b>
4.2.1 Cell culture.....	98
4.2.2 Oil Red O staining.....	98
4.2.3 Nile Red staining.....	98
4.2.4 Imaging.....	99
4.2.5 Measurement of lipid droplets.....	99
4.2.6 Statistical analyses.....	99
<b>4.3 Results.....</b>	<b>100</b>
4.3.1 Detection of adipocyte-like cells derived from mouse ES cells in endoderm conditions.....	100

4.3.1.1 Adipocyte-like cells derived from mouse ES cells first appear at day 12 of differentiation in endoderm culture conditions. ....	100
4.3.1.2 Mouse ES cells treated with DHT, TGF $\beta$ 1 and FGF10 have the largest adipocyte-like cells. ....	102
4.3.2 Adipocyte-like cells derived from mouse ES cells resemble 3T3-L1-derived adipocytes and isolated primary adipocytes. ....	105
4.3.4 Lipophilic dyes Oil Red O and Nile Red stain adipocyte-like cells derived from mouse ES cells. ....	107
<b>4.4 Discussion</b> .....	<b>110</b>
4.4.1 Adipocytes arise from mouse ES cells under endodermal culture conditions. ....	110
4.4.2 Comparisons between mouse ES cell-derived adipocytes differentiated from the mesoderm, neural crest and endoderm culture conditions. ....	111
4.4.3 Conclusion.....	112
<b>Chapter 5: Development of a flow cytometric method to characterise probe uptake in adipocytes at the single cell level.</b> .....	<b>113</b>
<b>5.1 Introduction</b> .....	<b>113</b>
5.1.1 There is a need for flow cytometric analyses of mature adipocytes. ....	114
5.1.2 The stromal vascular fraction (SVF) of brown and white adipose tissue. ....	115
<b>5.2 Methods</b> .....	<b>117</b>
5.2.1 Flow cytometry of adipose tissue. ....	117
5.2.1.1 Flow cytometric analysis of the SVF and buoyant adipocyte fraction. ....	117
5.2.3 Fluorescent imaging.....	118
5.2.3.1 FLoiD microscopy of whole mount adipose tissue.....	118
5.2.3.2 Confocal microscopy of adipocytes from the buoyant fraction .....	118
5.2.4 Statistical analyses.....	119
<b>5.3 Results</b> .....	<b>122</b>
5.3.1 Cells from buoyant adipose fraction have a distinct size and granularity profile compared to the SVF. ....	122
5.3.2 Lipophilic probes stain cells from the buoyant adipocyte fraction. ....	124
5.3.3 Nile Red uptake is proportional to adipocyte size and granularity. ....	128
5.3.4 Cells from the SVF do not take up Nile Red. ....	130
5.3.5 The buoyant adipocyte fraction of brown and white adipose tissue lack cell surface protein expression of haematopoietic markers. ....	132
5.3.6 Mitochondrial membrane potential dye MitoTracker Deep Red does not effectively differentiate between brown, subcutaneous and visceral white adipocytes.....	136
5.3.7 Carborane coumarin and phenyl coumarin co-localise with Nile Red. ....	141
<b>5.4 Discussion</b> .....	<b>146</b>
5.4.1 Flow cytometry is underutilised in the study of adipocyte biology.....	146
5.4.2 The utility of Nile Red as a neutral lipid dye for flow cytometric analyses of adipocytes. ....	146
5.4.3 Mitochondrial membrane potential distinguishes adipocytes. ....	147
5.4.4 Diagnostic application for Nile Red staining of adipocytes .....	148
5.4.5 Conclusion.....	149

<b>Chapter 6: Nile Blue is a cell permeable sensor of intracellular free fatty acids in live cells.</b>	<b>150</b>
<b>6.1 Introduction</b>	<b>150</b>
6.1.1 Chemical properties of Nile Red and Nile Blue	150
6.1.2 Nile Blue is a benzophenoxazine dye that detects phospholipids and free fatty acids	151
6.1.3 Fatty acid metabolism	152
<b>6.2 Methods</b>	<b>155</b>
6.2.1 Spectrofluorometric analyses of Nile Red and Nile Blue	155
6.2.2 Flow cytometry	155
6.2.2.1 Adipose tissue, skeletal muscle and liver tissue	155
6.2.3 Statistical analyses	156
<b>6.3 Results</b>	<b>157</b>
6.3.1 Spectrofluorometric analyses of Nile Blue and Nile Red	157
6.3.1.1 The presence of oleate and linoleate but not palmitate results in increasing Nile Blue fluorescence	157
6.3.1.2 The presence of oleate and linoleate but not palmitate results in increasing Nile Red fluorescence	157
6.3.1.3 Nile Blue fluorescence is greater than Nile Red in the presence of free fatty acids in solution	160
6.3.2 Hepatocytes and adipocytes have the greatest uptake of Nile Blue	162
6.3.3 Nile Red and Nile Blue uptake distinguishes adipocyte populations in brown and white adipocytes	165
<b>6.4 Discussion</b>	<b>169</b>
6.4.1 Nile Blue detects oleate and linoleate	169
6.4.2 Advantages in flow cytometric analyses of Nile Red and Nile Blue uptake	170
6.4.3 Nile Red and Nile Blue uptake characterises the maturation process of adipocytes	170
6.4.4 Modelling fatty acid metabolism in live cells with Nile Red and Nile Blue	171
6.4.4.1 Nile Red and Nile Blue as a diagnostic tool in fatty acid metabolism disorders	172
6.4.5 Conclusions	174
<b>Chapter 7: Characterisation of adipocytes from different adipose depots according to cell surface protein expression.</b>	<b>175</b>
<b>7.1 Introduction</b>	<b>175</b>
7.1.1 Heterogeneity of adipose tissue	175
7.1.1.1 Differences in the extracellular matrix between adipose depots	176
7.1.2 Surface protein expression of CD137 and CD40 reportedly characterise beige adipocytes	177
<b>7.2 Methods</b>	<b>179</b>
7.2.1 Flow cytometry of brown, subcutaneous and visceral white adipocytes	179
7.2.1.1 Flow cytometry of marrow adipocytes	179
7.2.2 Statistical analyses	179
<b>7.3 Results</b>	<b>180</b>

7.3.1 Adipocytes do not display immunoreactivity to a range of fluorescently-conjugated antibodies. ....	180
7.3.2 Immunoreactivity of fatty acid translocase CD36 differs between brown and white adipose depots. ....	182
7.3.3 Immunoreactivity of laminin receptor proteins $\alpha 6$ and $\beta 1$ integrin distinguishes brown and gonadal white adipocytes. ....	185
7.3.4 Subcutaneous inguinal adipocytes do not display immunoreactivity for “beige” adipocytes markers CD40 or CD137. ....	188
7.3.5 Marrow adipocytes are a distinct type of adipocyte. ....	191
<b>7.4 Discussion</b> .....	<b>193</b>
7.4.1 Fatty acid translocase has discrete roles in brown and white adipose tissue. ....	193
7.4.2 Changes in the extracellular matrix of adipose tissue disrupts homeostasis .....	195
7.4.3 BReaking BEige: Challenging CD40 and CD137 as specific markers of beige adipocytes. ....	196
7.4.4 Marrow adipocytes are distinct from white and brown adipocytes .....	197
7.4.5 Adipocyte heterogeneity in obese and diabetic mice .....	199
7.4.6 Conclusion. ....	199
<b>Chapter 8: Endoderm-derived adipocytes from mouse ES cells resemble gonadal adipocytes.</b> .....	<b>200</b>
<b>8.1 Introduction</b> .....	<b>200</b>
<b>8.2 Methods</b> .....	<b>201</b>
8.2.1 Serum starvation of undifferentiated mouse ES cells .....	201
8.2.2 Imaging of undifferentiated mouse ES cells stained with Nile Blue .....	201
8.2.3 Flow cytometric analyses .....	201
8.2.3.1 Undifferentiated mouse ES cells .....	201
8.2.3.2 Endoderm-derived adipocyte-like cells .....	202
8.2.4 Statistical analyses .....	202
<b>8.3 Results</b> .....	<b>203</b>
8.3.1 Modelling free fatty acid uptake with undifferentiated mouse ES cells ...	203
8.3.1.1 Visualising Nile Blue uptake in fatty acid treated mouse ES cells. ....	203
8.3.1.2 Undifferentiated mouse ES cells treated with oleate have the greatest Nile Blue uptake. ....	205
8.3.1.2 Serum starved undifferentiated mouse ES cells have increased uptake of Nile Blue. ....	207
8.3.2 Assessing probe uptake and surface protein expression of adipocyte markers in adipocyte-like cells differentiated from mouse ES cells. ....	211
8.3.2.1 Adipocyte-like cells differentiated from mouse ES cells treated with DHT, FGF10 and TGF $\beta$ 1 have greater Nile Red fluorescence. ....	211
8.3.2.2 Endoderm-derived adipocytes have a similar profile to gonadal adipocytes. ....	213
<b>8.4 Discussion</b> .....	<b>216</b>
8.4.1 Questioning the embryological origin of gonadal adipocytes. ....	216
8.4.2 Utility of a code to characterise adipocytes from brown and white adipose depots. ....	217



8.4.3 Applying the code to identify mesoderm and neural crest derived adipocytes.....	217
8.4.4 Sorting adipocytes derived from mouse ES cell cultures.....	218
8.4.5 Conclusion.....	218
<b>Chapter 9 General discussion.....</b>	<b>220</b>
9.1 Opening remarks .....	220
9.2 Recapitulation of the early developmental processes in prostate epithelial cell determination and differentiation from mouse ES cells.....	221
9.3 Applications for prostate epithelial cell differentiation from mouse ES cells .....	225
9.3.1 Prostate organoids derived from human iPS cells .....	225
9.3.2 Replacement of animal models .....	226
9.3.3 Modelling prostate oncogenesis <i>in vitro</i> with mouse ES cells .....	227
9.3.4 Prostate-on-a-chip. Characterisation of cell types differentiated under conditions promoting prostate epithelial cell differentiation.....	229
9.4 An endodermal origin of gonadal adipocytes .....	231
9.4.1 Do adipocytes support the normal development of the prostate? .....	235
9.5 Obesity is a multi-faceted disease and is a risk factor for multiple cancers	236
9.5.1 Peri-prostatic adipose tissue facilitates prostate cancer metastasis .....	237
9.5.2 Obese women have a higher risk of developing breast cancer. ....	238
9.5.3 What about carcinomas from cell types other than the prostate? .....	238
9.6 Flow cytometry as a diagnostic tool for pathophysiological conditions in humans. ....	241
9.6.1 Lipotoxicity is a serious metabolic syndrome.....	241
9.7 Future endeavours .....	244
9.7.1 Do adipocytes support the development of other endoderm-derived cell types? .....	244
9.8 Concluding remarks.....	245
<b>Chapter 10. References.....</b>	<b>246</b>
<b>Appendices.....</b>	<b>271</b>
Appendix I: The mesendoderm: A wellspring of cell lineages for regenerative medicine.....	271
Appendix II: Macrophage colony stimulating factor receptor: A potential cell surface marker for prostate oncogenesis.....	337
Appendix III: A new carborane-containing fluorophore as a stain of cellular lipid droplets.....	338
Appendix IV: Flow cytometric single cell analysis reveals heterogeneity between adipose depots.....	344
Appendix V: Table 8.1: Comparisons in Nile Blue fluorescence between ethanol, palmitate, linoleate and oleate treated mouse ES cells starved of serum over 12 hours.....	359
Table 8.2: Comparisons in Nile Red fluorescence between ethanol, palmitate, linoleate and oleate treated mouse ES cells starved of serum over 12 hours.....	360
Appendix VI: Making blood: The haematopoietic niche throughout ontogeny.....	361

## List of Figures

Figure 1.1: Anatomy of the prostate in mice and men .....	2
Figure 1.2: Histology of the prostate gland.....	5
Figure 1.3: The mesendoderm is a bi-potential progenitor that gives rise to cell types from both the mesoderm and endoderm germ layers. ....	12
Figure 1.4: The developmental stages of prostate organogenesis in the mouse. ....	19
Figure 1.5: Embryonic and induced pluripotent stem cells are capable of differentiating into all cell types of the body. ....	23
Figure 2.1: Generation of single cell suspensions from BAT, subcutaneous and visceral WAT depots and separation of the adipocytes from the SVF. ....	45
Figure 3.1: Proposed method of differentiation prostate epithelial cells from mouse ES cell <i>in vitro</i> .....	61
Figure 3.2: Undifferentiated mouse ES cells express pluripotency markers <i>Oct4</i> and <i>Nanog</i> .....	67
Figure 3.3: Activin-A and Wnt-3A promote the differentiation of mouse ES cells into endoderm.....	70
Figure 3.4: Mesoderm surface protein markers Flk-1 and PDGFR $\alpha$ are not expressed on day 5 embryoid bodies cultured under endoderm conditions. ....	71
Figure 3.5: Retinoic acid induces a cobblestone-like phenotype in mouse ES cell-derived endoderm cultures.....	74
Figure 3.6: Expression of uroplakin detected in day 12 mouse ES cell cultures treated with retinoic acid. ....	75
Figure 3.7: Day 16 differentiated mouse ES cell cultures treated with DHT, TGF $\beta$ 1 and FGF10 express prostate epithelial cell markers <i>Nkx3.1</i> and <i>Svs2</i> . ....	78
Figure 3.8: The formation of acinus-like structures in day 22 mouse ES cell cultures treated with DHT, TGF $\beta$ 1 and FGF10. ....	81
Figure 3.9: Prostate epithelial cell markers <i>Pbsn</i> and <i>Nkx3.1</i> are expressed in day 22 differentiated cultures treated with DHT, TGF $\beta$ 1 and FGF10. ....	82
Figure 3.10: Urothelial cell markers <i>Upk1b</i> and <i>Upk2</i> are expressed in day 22 differentiated cultures treated with DHT, TGF $\beta$ 1 and FGF10. ....	83
Figure 3.11: Colony-stimulating factor 1 receptor (CSF-1R) is expressed on few cells in the developing urogenital tract. ....	87
Figure 3.12: <i>Csf-1R</i> is expressed on day 22 differentiated mouse ES cell cultures and adult mouse prostate tissue. ....	88
Figure 4.1: Adipocyte-like cells are first identified at day 12 of differentiation in endoderm culture conditions. ....	101

Figure 4.2: Adipocyte-like cells differentiate from mouse ES cells under endodermal culture conditions. ....	103
Figure 4.3: Adipocyte-like cells derived from mouse ES cell treated with DHT, TGF $\beta$ 1 and FGF10 are larger compared to endoderm base medium and vehicle control. ....	104
Figure 4.4: Adipocyte-like cells derived from mouse ES cells resemble adipocytes from the 3T3-L1 cell line and primary adipocytes. ....	106
Figure 4.5: Oil Red O stains the lipid droplets in the mouse ES cell derived adipocyte-like cells. ....	108
Figure 4.6: Nile Red stains the lipid droplet within the mouse ES cell derived adipocyte-like cells. ....	109
Figure 5.1: Morphological characteristics of white and brown adipocytes. ....	116
Figure 5.2: Flow cytometric analysis of cells from the SVF and buoyant adipocyte fraction of adipose depots demonstrate significant differences in their size and granularity. ....	123
Figure 5.3: Lipophilic probes LipidTox Green and Nile Red stain cells in the supernatant fraction of BAT, subcutaneous inguinal and visceral gonadal WAT. ....	126
Figure 5.4: Frequency of uptake and mean fluorescence intensity is greatest in Nile Red stained cells. ....	127
Figure 5.5: Nile red fluorescence is greatest amongst the largest, most granular cells in the supernatant fraction. ....	129
Figure 5.6: Cells in Region 3 of the SVF do not exhibit Nile Red fluorescence. ....	131
Figure 5.7: Cells of the buoyant adipocyte fraction of brown adipose tissue do not express markers of the stromal vascular fraction. ....	133
Figure 5.8: Cells of the buoyant adipocyte fraction of subcutaneous inguinal adipose tissue do not express markers of the stromal vascular fraction. ....	134
Figure 5.9: Cells of the buoyant adipocyte fraction of visceral gonadal adipose tissue do not express markers of the stromal vascular fraction. ....	135
Figure 5.10: Confocal imaging of live, intact, brown and white adipocytes stained with Nile Red and MitoTracker Deep Red. ....	138
Figure 5.11: Nile Red <sup>High</sup> adipocytes have high levels of MitoTracker Deep Red. ....	139
Figure 5.12: No differences observed in MitoTracker Deep Red uptake between brown and white adipose depots. ....	140
Figure 5.13: Fluorescent microscopy reveals co-localisation of Nile Red and coumarin dyes in brown and white adipose tissue. ....	141

Figure 5.14: Confocal microscopy reveals co-localisation of Nile Red and coumarin dyes in brown and white adipocytes. ....	144
Figure 5.15: Flow cytometric analysis reveal co-localisation of Nile Red and coumarin probes in brown and white adipocytes. ....	145
Figure 6.1: Chemical structure of Nile Blue and Nile Red. ....	151
Figure 6.2: Exchange of lipids between adipose tissue, liver tissue and skeletal muscle following dietary fat intake. ....	153
Figure 6.3: Free fatty acid uptake measured by Nile Blue may distinguish between brown and white adipocytes. ....	154
Figure 6.4: Nile Blue fluorescence is greatest in the presence of oleate and linoleate. ....	159
Figure 6.5: Nile Red detects tri-oleate and non-esterified fatty acids. ....	161
Figure 6.6: Single cell suspensions from metabolically active tissues take up Nile Red and Nile Blue. ....	163
Figure 6.7: Adipocytes have greater Nile Red uptake than hepatocytes and myocytes. ....	164
Figure 6.8: Uptake of Nile Red and Nile Blue in adipocytes reveals distinct populations. ....	167
Figure 6.9: Brown and white adipocyte heterogeneity according to Nile Red and Nile Blue uptake. ....	168
Figure 7.1: Proposed assessment of cell surface protein markers and extracellular matrix proteins in white and brown adipocytes. ....	178
Figure 7.2: Nile Red <sup>High</sup> adipocytes exhibit either CD36 <sup>Low</sup> or CD36 <sup>High</sup> immunoreactivity. ....	183
Figure 7.3: Nile Red <sup>High</sup> brown adipocytes have the least levels of CD36 immunoreactivity. ....	184
Figure 7.4: Surface protein expression of $\beta$ 1 integrin distinguishes brown and visceral gonadal white adipocytes. ....	186
Figure 7.5: Surface protein expression of $\alpha$ 6 integrin distinguishes brown and gonadal white adipocytes. ....	187
Figure 7.6: Reported beige adipocyte specific markers CD40 or CD137 are not expressed on subcutaneous inguinal adipocytes. ....	190
Figure 7.7: Marrow adipocytes have a distinct cell surface phenotype. ....	192
Figure 7.8: Characterisation of brown and white adipocytes according to probe uptake and surface protein expression. ....	198
Figure 8.1: Nile Blue intensely stains the vesicles within the cytoplasm in fatty acid treated undifferentiated mouse ES cells. ....	204
Figure 8.2: Undifferentiated mouse ES cells treated with oleate have the greatest Nile Blue staining. ....	206

Figure 8.3: Serum starved undifferentiated mouse ES cells have increased uptake of Nile Blue. ....	210
Figure 8.4: Nile Red fluorescence is greatest in the buoyant fraction of mouse ES cells treated with DHT, FGF10 and TGF $\beta$ 1.....	212
Figure 8.5: The buoyant fraction of day 22 differentiated mouse ES cells treated with DHT, FGF10 and TGF $\beta$ 1 .....	214
Figure 8.6: Day 22 differentiated adipocytes from mouse ES cells treated with DHT, TGF $\beta$ 1 and FGF10 resemble gonadal adipocytes. ....	215
Figure 9.1: Epithelial and stromal cells of the prostate and markers used to identify them.....	224
Figure 9.2: Modelling prostate development and prostate cancer progression using mouse ES cells. ....	230
Figure 9.3: Proposed germ layer origins of brown, subcutaneous and visceral white adipocytes. ....	234
Figure 9.4: Changes in adipose tissue function and structure in obese individuals.....	240
Figure 9.5: Clinical application of flow cytometric analyses of adipose tissue. ....	243

## List of Tables

Table 1.1 Tissues that arise from the different regions of the endoderm .....	26
Table 2.1. List of consumables used in this study .....	29
Table 2.2. List of reagents used in this study .....	30
Table 2.3. Composition of the reagents used in this study.....	32
Table 2.4: Composition of buffers used in this study. ....	32
Table 2.5: Composition of cell culture media used in this study. ....	33
Table 2.6. Components required for conversion of RNA to cDNA. ....	37
Table 2.7. Components for RT-PCR reactions. ....	38
Table 2.8. Sequences of primers used for RT-PCR analyses in this study. ....	39
Table 2.9. Conditions used to dissociate undifferentiated mouse ES cells, embryoid bodies and primary tissue into single cells. ....	49
Table 2.10: Controls used for flow cytometric analyses in this study. ....	51
Table 2.11. List of fluorescently conjugated antibodies used in this study. ....	52
Table 2.12. List of probes used in this study. ....	54
Table 2.13. Parameters measured by each channel on the flow cytometer.....	56
Table 2.14. The settings used to measure fluorescence on undifferentiated mouse ES cells. ....	56
Table 2.15. The settings used to measure fluorescence on single cells generated from primary tissue. ....	56
Table 3.1: Summary of transcripts detected in the RNA of undifferentiated mouse ES cells, differentiated mouse ES cells and adult ventral prostate tissue. ....	84
Table 5.1: Characteristics of undifferentiated mouse ES cells, prostate epithelial cells, white adipocytes and brown adipocytes.....	114
Table 5.2: Fluorophore conjugated monoclonal antibodies used in this chapter. ....	120
Table 5.3: The fluorescent probes used in this chapter. ....	121
Table 7.1: A list of fluorescently-conjugated monoclonal antibodies used to screen for surface protein expression in brown, white and marrow adipocytes.....	181

## List of Abbreviations

Name	Abbreviation
1-Thioglycerol	MTG
Albumin from bovine serum	BSA
Allophycocyanin	APC
All-trans Retinoic Acid	RA
Brown adipose tissue	BAT
Cytokeratin	CK
Dihydrotestosterone	DHT
Dimethyl Suphoxide	DMSO
Dulbecco Modified Eagle Medium	DMEM
Embryonic day	(E)
Embryoid body	EB
Embryonic stem	ES
Epithelial Cell Adhesion Molecule	EpCAM
Epicardial white adipose tissue	WAT:EC
Ethylenediaminetetraacetic acid	EDTA
Extracellular matrix	ECM
Fibroblast Growth Factor	FGF
Fluorescence-activated cell sorting buffer	FACS buffer
Fluorescein isothiocyanate	FITC
Foetal Bovine Serum	FBS
Gonadal white adipose tissue	WAT:GON
Inguinal white adipose tissue	WAT:ING
Inner Cell Mass	ICM
Iscoves Modified Dulbecco Medium	IMDM
Leukaemia Inhibitory Factor	LIF
Mesenteric white adipose tissue	WAT:MES
Non-alcoholic Fatty Liver Disease	NAFLD

Paraformaldehyde	PFA
Pencillin Streptomycin	PEN/STREP
Peri-renal white adipose tissue	WAT:PR
Phosphate Buffered Saline	PBS
Phycoerythrin	PE
Prostatic Intraepithelial Neoplasia	PIN
Prostate Specific Antigen	PSA
Reverse Transcriptase Polymerase Chain Reaction	RT-PCR
Transgenic Adenocarcinoma of the Mouse Prostate	TRAMP
Transforming growth factor	TGF
Tris-Acetate-EDTA	TAE
Urogenital sinus	UGS
White adipose tissue	WAT



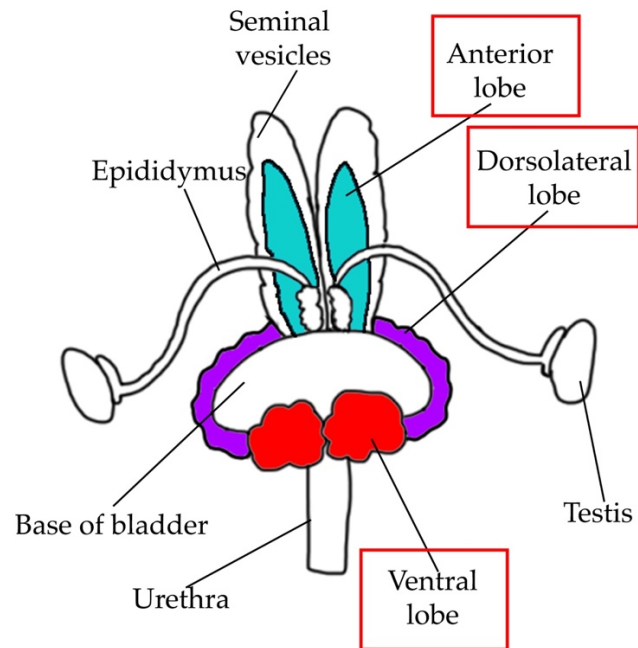
## **Chapter 1: Introduction**

### **1.1 The prostate is an endoderm-derived exocrine gland**

#### **1.1.1 Anatomy of the prostate in mice**

The prostate is an exocrine gland of the reproductive tract of a number of male mammals and provides components of seminal fluid (Cunha et al., 2004b). The prostate gland in adult mice consists of three lobes situated around the urethra and defined by their anatomical location: the ventral, dorsolateral and anterior prostate (Figure 1.1A) (Kusama, Enami, & Kano, 1989; Marker, 2003a). The ventral lobe wraps around the urethra whereas the dorsolateral lobes are located at the base of the seminal vesicles (Figure 1.1A). The anterior prostate lobes (or coagulating glands) are attached to the seminal vesicles (Figure 1.1A). Contrary to mice, the prostate in male humans comprises of a singular organ with four defined zones: the central, transitional, peripheral and periurethral zones (Figure 1.1B) (McNeal, 1981).

### A) Mouse prostate



### B) Human prostate

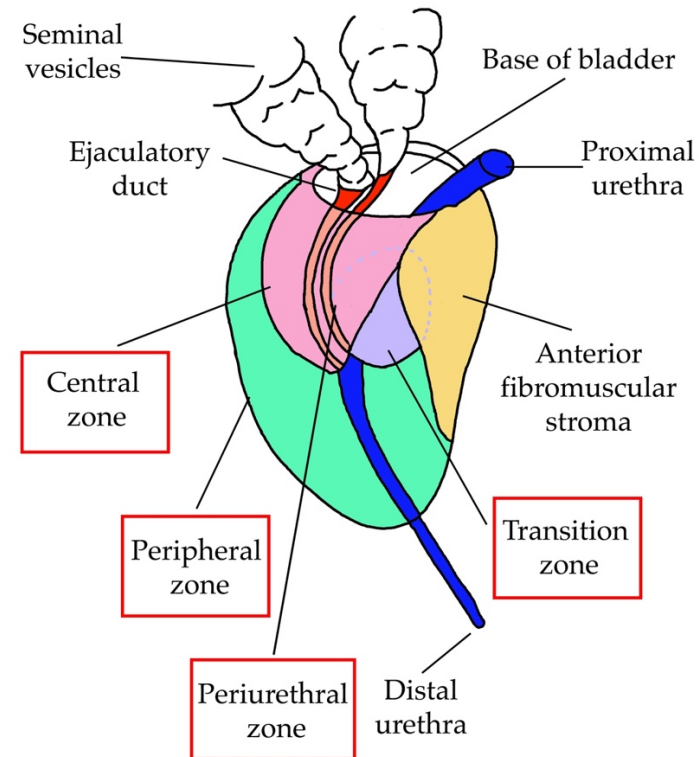


**Figure 1.1: Anatomy of the prostate in mice and men.**

(A) The mouse prostate is composed of three lobes: the anterior lobe (turquoise), the dorsolateral lobe (purple) and the ventral lobe (red).

(B) The human prostate consists of four distinct zones: the central zone (pink), the peripheral zone (green), the transition zone (purple) and the periurethral zone (situated next to the urethra, uncoloured).

### **1.1.2 Histology of the mouse prostate**

Each lobe contains a distinct pattern of branching (Marker et al, 2003a). All prostatic lobes contain columnar luminal and cuboidal basal epithelial cells that are arranged to form the secretory acini (Figure 1.2) (Marker et al., 2003a; Thomson & Marker, 2006). The ventral lobe contains large acini while the dorsolateral lobes are composed of smaller acini (Marker et al., 2003a; Thomson & Marker, 2006). The acini of the anterior lobe is described as complex with papillary patterns (Marker et al., 2003a; Thomson & Marker, 2006).

#### **1.1.2.1 Epithelial cells of the prostate**

The secretory luminal layer of glandular epithelium is composed of tall columnar epithelial cells which are supported by a basal layer of cuboidal epithelial cells (Figure 1.2) (Sherwood et al., 1990; Wang et al., 2001). The luminal layer consists of androgen-dependent cells and is most commonly characterised by cytokeratins (CK) 8 and 18 expression (Sherwood et al., 1990; Sherwood et al., 1991). The basal layer consists of androgen-independent cells and is characterised by CK5 and 14 expression (Sherwood et al., 1990; Sherwood et al., 1991). An intermediate epithelial cell type has been identified that expressed both luminal and basal CKs as well as CK19 (Xue et al., 1998; Wang et al., 2001). Neuroendocrine cells are a sparse population of androgen-independent epithelial cells situated between the basal and luminal layers (Figure 1.2) (van Steenbrugge et al., 1995). Neuroendocrine cells are identified by chromogranin-

A and synaptophysin expression and lack expression of androgen receptor (Krijnen et al., 1993).

#### **1.1.2.2 Stromal cells of the prostate**

Situated opposite to the basal lamina is the fibromuscular stroma (Figure 1.2). The stroma is composed of smooth muscle actin, blood vessels and an extracellular matrix rich in collagen fibres (Figure 1.2) (Barron & Rowley, 2012). Additionally, the stromal compartment contains endothelial cells, fibroblasts and several immune cells (Figure 1.2). The stroma of the prostate gland was once thought to be a passive structure (cited in: Tuxhorn et al., 2001). However, the dynamic environment influences epithelial cell differentiation, migration and attachment as well as promote tissue repair in response to injury (Tuxhorn et al., 2001). Alterations in normal prostate homeostasis such as infiltration of the stroma by carcinoma cells lead to a reactive stroma (expanded in 1.1.3) (Tuxhorn et al., 2001).

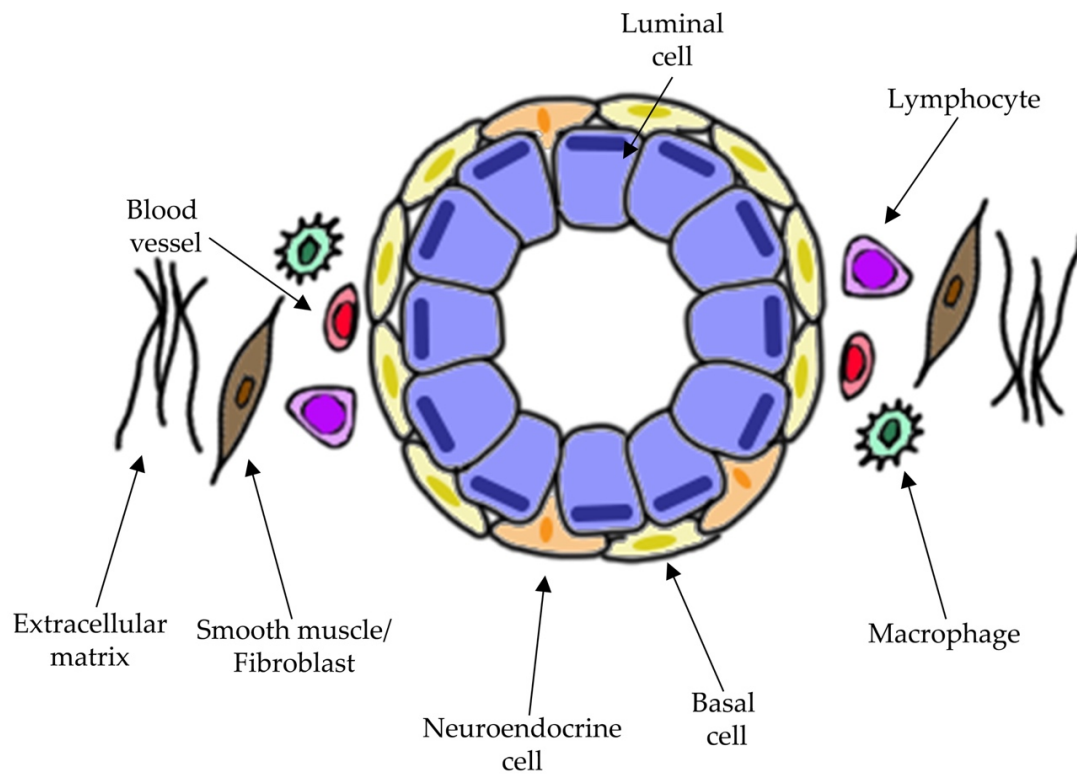


**Figure 1.2: Histology of the prostate gland.**

The prostate consists of cuboidal basal and columnar luminal epithelial cells that form the secretory acini. Neuroendocrine cells are sparse and situated between basal and luminal epithelial cells. The stroma surrounding the epithelial cells consists of smooth muscle, fibroblasts, macrophages, blood vessels, inflammatory cells and extracellular matrix components.

### **1.1.3 Physiology of the prostate**

The prostate is essential for the successful reproduction in mammalian species (Hayward & Cunha, 2000). Men without a prostate have impaired fertility (Hayward & Cunha, 2000). The prostate provides the components of seminal fluid which functions to soften, coagulate and gelatinise semen (Cunha et al., 1987). Secretory proteins in the seminal fluid coat spermatozoa (Aumüller & Seitz, 1990). The major secretory proteins released in the human prostate gland are prostate-specific antigen (PSA), prostate-secreted acid phosphatase (PAP) and prostatic secretory protein of 94 aa (PSP94) (Lee et al., 1986; Lilja & Abrahamsson, 1988). PSA is the most well-known prostatic secretory protein in humans which functions to dissolve seminal coagulum (Lee et al., 1986; Hayward & Cunha, 2000). PSA is produced by the columnar epithelial cells of the prostate and secreted into the ductal lumina (Hayward & Cunha, 2000). Under physiological conditions, PSA does not cross the epithelial basement membrane (Hayward & Cunha, 2000). However, under pathophysiological conditions such as inflammation and cancer, PSA can leak into the stroma leading to elevated serum levels of PSA (Hayward & Cunha, 2000; reviewed in: Velonas et al., 2013).

PSA and PAP are not secreted from the prostate in rodents (Fujimoto et al. 2006). Instead, prostatein, cystatin-related protein, PSP94, probasin and seminal vesicle secretory protein (Svs2) are abundant in the ventral and dorsal and lateral lobe of the mouse prostate (Cunha et al., 1987; Fujimoto et al., 2006). Transgenic mouse models

of prostate cancer are generated by expressing the SV40 antigen under a probasin promoter (detailed in 1.1.4.1).

#### **1.1.4 Prostate disease in the ageing man.**

Every four minutes, prostate cancer claims the life of a man (Assinder & Bhoopalan, 2017). Prostate cancer is the most common male malignancy in Western societies and the second most common cause of male cancer-related death (Haas et al., 2008). Benign prostatic hypertrophy (BPH) is characterised as non-malignant growth of the adult prostate by similar processes that occur during prostate development in the embryo (McNeal, 1978; McNeal, 1983). BPH is not a precursor to prostate cancer (Chokkalingam et al., 2003). BPH arises in the transition zone of the prostate in men, whereas the peripheral zone of the prostate is the origin of prostate cancer (Shappell et al., 2004) . In the mouse, prostate cancer is thought to begin with prostatic hyperplasia (Shappell et al., 2004; Ittmann et al., 2013).

Prostatic intraepithelial neoplasia (PIN) is the proliferation of atypical cells within the glands (Grabowska et al., 2014). In humans, low grade PIN may be dormant, however, high grade PIN is associated with progression to carcinoma (Bostwick et al., 1995; Bostwick et al., 2004). Similarly, mice can develop PIN (reviewed in: Shappell et al., 2004; Ittman et al., 2013). Lesions in mouse PIN distort the fibromuscular sheath, disrupting smooth muscle actin and laminin (Park et al., 2002).

Disease progression of high grade PIN into prostate carcinoma is defined by the presence of epithelial migration into the stroma (Humphrey et al., 2011). The majority of cases are adenocarcinomas, whilst small cell (neuroendocrine) carcinomas and sarcomatoid carcinomas are rare (Humphrey et al., 2011). Adenocarcinomas are graded according to levels of disorganisation (normal to very abnormal) using the Gleason pattern scale (Humphrey et al., 2011). Neuroendocrine and sarcomatoid carcinomas, which tend to be on the very abnormal end, are normally androgen insensitive and do not respond well to chemotherapy (Wang et al., 2009).

Unlike humans, mice develop all phenotypes of prostate cancer (adenocarcinomas, small cell carcinomas and sarcomatoid carcinomas) (reviewed in: Ittmann et al., 2013). Prostate cancer in the mouse can also be classified as invasive or microinvasive carcinoma (reviewed in: Grabowska et al., 2014; Ittmann et al., 2013). Both categories are associated with changes in the stroma in which there is proliferation beyond the prostatic ducts (invasive) or outside the basal layer and basement membrane (microinvasive) (Grabowska et al., 2014; Ittmann et al., 2013).

#### **1.1.4.1 The TRAMP mouse model of prostate cancer**

The first transgenic mouse model of prostate cancer was the transgenic adenocarcinoma mouse prostate (TRAMP) model (Greenberg et al., 1995). The TRAMP model was generated by fusing the promoter region of probasin to the early region of Simian Virus 40 (Greenberg et al., 1995). TRAMP mice exhibit rapid



development of prostatic intraepithelial neoplasia (PIN) and eventual progression to adenocarcinomas in the dorsolateral lobe (Shibata et al., 1996). The generation of adenocarcinomas in TRAMP mice is similar to adenocarcinomas in the peripheral zone of the human prostate (Greenberg et al., 1995). Whilst the TRAMP mouse model does not cover the entirety of the human disease, it has been useful in validating genes involved in prostate cancer progression and implementing therapeutic strategies for the treatment of prostate disease (Irshad et al., 2013; Harper et al., 2007; Raina et al., 2007; Kumar et al., 2007).

#### **1.1.5 Development of the prostate *in vivo***

The prostate is derived from the urogenital sinus, which constitutes an endodermally derived epithelial layer that is surrounded by a mesodermally derived mesenchymal layer (Thomson & Marker, 2006). The mesendoderm then, marks the beginning of prostate development.

##### **1.1.5.1 Development of the prostate begins with the mesendoderm**

The mesendoderm is a progenitor to the endoderm and mesoderm and has been identified in the African claw-frog *Xenopus laevis*, zebrafish and mammals (Nieuwkoop, 1997; Agius et al., 2000; Rodaway & Patient, 2001; Nelson et al., 2014). The mesendoderm progenitor was discovered by fate mapping individual cells in early embryos that led to cell types arising from both the mesoderm and endoderm (Nieuwkoop, 1997; Rodaway & Patient, 2001). With the exception of ectoderm-

derived tissues, the mesendoderm is responsible for the development of much of the body.

Epithelial tissues derived from the endoderm consist of a mesoderm component to support structural integrity and provide signals for normal organogenesis (Haynes, 1984; Walker, Hall, Hurst, & White, 1990; Lammert, Cleaver, & Melton, 2001; Goldman et al., 2014; Ribatti & Santoiemma, 2014; reviewed in: Boumelhem et al., 2017). Conversely, mesoderm derivatives such as blood, skeletal muscle and endothelium do not contain endoderm components (Willey et al., 2006, Buckingham et al., 2003; De Val & Black, 2009; Tirziu & Simons, 2009). The cell types that arise from the mesendoderm are outlined below (Figure 1.6).

The mesendoderm is regulated by Nodal signalling (Agius et al., 2000). Nodal belongs to the TGF $\beta$  family of signalling molecules (D'Amour et al., 2005). Nodal signalling is required for the specification and patterning of the primary body axes (left-right symmetry) during gastrulation (Shen, 2007; Schier & Shen, 1999). Nodal ligands bind to type I and type II serine-threonine kinase receptors and activate the Smad2/Smad3 branch of the TGF $\beta$  signalling pathway (Shen, 2007; Schier & Shen, 1999). Unique to the Nodal signalling pathway are the co-receptors of the EGF-CFC family of proteins (Shen, 2007). The EGF-CFC family of proteins are essential for Nodal signalling (Shen, 2007). Downstream of Nodal signalling is the transcriptional regulator Eomesdermin (*Eomes*), which induces expression of T-box transcription factor Brachyury (*Bry/T*),

Mix-Like 1 (*Mixl1*) and Goosecoid (*Gsc*) (Agius et al., 2000; Costello et al., 2011; Costello et al., 2015). Mice embryos deficient for *Mixl1* and *Bry/T* have an enlarged primitive streak and exhibit defective endoderm and mesoderm patterning (Hart et al., 2002; Beddington, Rashbass, & Wilson, 1992).

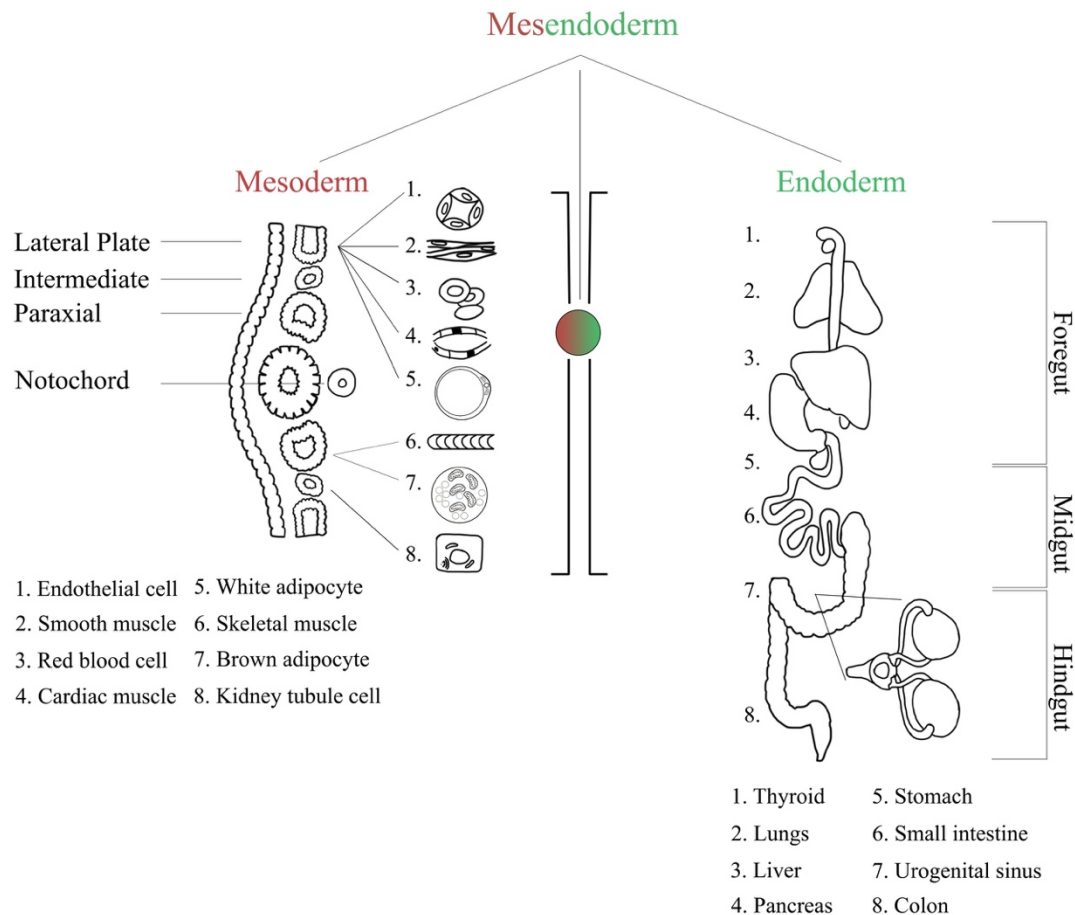


**Figure 1.3: The mesendoderm is a bi-potential progenitor that gives rise to cell types from both the mesoderm and endoderm germ layers.**

The mesoderm (red) gives rise to support structures in the body such as vessels, connective tissue, blood and muscle. Derivatives of the lateral plate mesoderm include: endothelial cells, smooth muscle cells, red blood cells, cardiac muscle and white adipocytes. Derivatives of the intermediate mesoderm include skeletal muscle and brown adipocytes. Derivatives of the paraxial mesoderm include the kidney tubule cell. The endoderm (green) gives rise to the epithelial cells which line the major tubes in the body. Derivatives of the foregut endoderm include: the thyroid, the lungs, the liver and the pancreas. Derivatives of the midgut endoderm include the stomach and small intestine. Derivatives of the hindgut endoderm include the urogenital sinus (including organs of the genitourinary tract) and the colon. Figure adapted from Boumelhem et al., 2017.

#### 1.1.5.2 Prostate epithelial cells arise from the endoderm

The endoderm is the source for the three major internal tracts: the respiratory, gastrointestinal and urogenital tracts (Figure 1.3) (Grapin-Botton, 2008). In mammals, development of definitive endoderm begins at gastrulation (embryonic day (E) 6.5) (Zorn & Wells, 2009). Endoderm precursors migrate from the epiblast to the anterior primitive streak and become embedded into the visceral endoderm (Tam & Behringer, 1997). Movement of the definitive endoderm is facilitated by an epithelial-to-mesenchymal transition (Blanco et al., 2007).

Activin and Nodal-related proteins were shown to be crucial for endoderm formation as inhibition leads to improper formation in the *Xenopus* embryo (Thisse, Wright, & Thisse, 2000; Agius et al., 2000; Grapin-Botton, 2008). Like Nodal, Activin also belongs to the TGF $\beta$  family of signalling molecules (D'Amour et al., 2005). In explant studies, loss of TGF $\beta$  signalling in the endoderm increased expression of mesoderm and ectoderm markers (Henry, Brivanlou, & Kessler, 1996). Canonical Wnt signalling pathways activate Nodal expression during embryogenesis (Grapin-Botton, 2008). Specification of definitive endoderm requires both Wnt signalling and Nodal expression as mouse embryos lacking *Nodal* fail to form a primitive streak (Conlon et al., 1994).

#### **1.1.5.3 The hindgut endoderm gives rise to the urogenital sinus**

The endoderm can be divided into three regions: the foregut, midgut and hindgut endoderm (Figure 1.4). The hindgut endoderm ends as a caudal expansion called the cloaca (Gupta et al., 2014). The cloaca is a transitory endoderm-derived cavity that subdivides into the urogenital sinus (UGS) and the anal canal (Gupta et al., 2014). The urogenital sinus (UGS) is an endoderm-derived structure that arises between E12.5-E13.5 of development in the mouse and approximately during the 7<sup>th</sup> week of gestation in humans (cited in: Marker et al., 2003a; reviewed in: Cao et al., 2008). Determination of prostate development begins at E13.5 (Figure 1.4). Urogenital tissues such as the bladder and the prostate rely on paracrine signalling between the urogenital mesenchyme and epithelium for normal growth (Cunha et al., 1983; Tanaka et al., 2010; Li et al., 2008). The urothelium that lines the bladder forms an impervious membrane to prevent the toxic components of urine leaking onto underlying tissues (Moll et al., 1995; Kątnik-Prastowska, Lis, & Matejuk, 2014). The integrity of the membrane is dependent upon the uroplakin proteins (*Upk1a*, *Upk1b*, *Upk2*, *Upk3*) (Moll et al., 1995; Wu et al., 2009). Uroplakins are the first identifiable markers for urothelial cell differentiation *in vivo* (Moll et al., 1995).

#### **1.1.5.4 Branching morphogenesis of prostate epithelial cells is dependent upon paracrine signalling from the urogenital mesenchyme**

Initial budding of the prostate epithelial cells occurs at E16.5 (Sugimura, Cunha, & Donjacour, 1986). Androgen receptor signalling from the urogenital mesenchyme

stimulates epithelial cell budding (Thomson & Marker, 2006). Branching morphogenesis of the epithelial ducts is critical for normal prostate development (Thomson & Marker, 2006). Branching morphogenesis occurs when the budding epithelial ducts elongate and branch into the urogenital mesenchyme (Thomson & Marker, 2006). Developmental cues from the urogenital mesenchyme are critical for prostate ductal morphogenesis, growth and differentiation (Prins & Putz, 2008). If the urogenital sinus or urogenital mesenchyme are grown separately in explant cultures, no differentiation of prostatic epithelial buds occurs (Cunha et al, 1983). Further, explants of urogenital mesenchyme cultured with epithelium from embryonic or bladder tissue are sufficient to induce prostatic duct formation (Cunha et al., 1987). Implantation of human ES cells with urogenital mesenchyme into the kidney capsule of immunodeficient SCID mice prompt the formation of tumours with human prostatic tissue (Taylor et al., 2006).

#### **1.1.6 Androgens regulate prostate development**

Androgens are pivotal in forming the identity of the prostate (Cunha et al., 2004b). In particular, dihydrotestosterone (DHT), the more potent metabolite of testosterone, acts to stimulate outgrowth of the ductal epithelial buds during branching morphogenesis (Marker et al., 2003a). Branching of the epithelial buds is reliant upon androgen receptor expression on the urogenital mesenchyme, signifying the importance of paracrine signalling (Marker et al., 2003a). Androgens also regulate prostate specific genes probasin (*Pbsn*) and homeobox gene *Nkx3.1* (Pritchard &

Nelson, 2008; Marker et al., 2003a). Probasin is a marker of prostate differentiation and androgen receptor activity (Johnson et al., 2000). Probasin is often targeted to generate prostate cancer models in the mouse and rat (Johnson et al., 2000; Parisotto et al., 2013; Sharma et al., 1999).

#### **1.1.6.1 Growth factors that are important in prostate organogenesis**

The transforming growth factor (TGF) superfamily of cytokines are important in mediating the interaction between stromal cells and epithelium during development of the prostate (Li et al., 2008). In particular, TGF $\beta$  is correlated with epithelial prostate differentiation from the bladder (Li et al., 2008). Bladder urothelial cells cultured on the urogenital mesenchyme isolated from a TGF $\beta$  conditional knockout mouse retained a bladder epithelial cell phenotype (Li et al., 2008). Conversely, bladder urothelial cells cultured on the urogenital mesenchyme of a control mouse yielded prostatic cell differentiation (Li et al., 2008). A summary outlining the timeline of development and gene expression of the prostate relevant for this study are outlined in Figure 1.4

Paracrine signalling of fibroblast growth factor (FGF) 10 is also integral for the development of the prostate (Thomson & Cunha, 1999). Expression of *FGF10* in the prostate is greatest during the earliest stages of organ development (during neonatal growth) but is low in the adult stages of development (Thomson & Cunha, 1999). Supplementation of *ex vivo* prostate organ cultures with FGF10 lead to the



development of prostate rudiments (Thomson & Cunha, 1999). Testosterone did not have exhibit a synergistic role with FGF10 in co-cultures (Thomson & Cunha, 1999). Thus, FGF10 is a key regulator of epithelial growth in the prostate.

### **1.1.7 Prostate development at the molecular level**

#### **1.1.7.1 Homeobox protein *Nkx3.1***

Homeodomain transcription factor *Nkx3.1* was the first identified molecular marker of prostate epithelium and is expressed at E15.5 in the UGS following androgen stimulation (Prins & Putz, 2008; Marker et al., 2003a). As branching morphogenesis takes place, expression of *Nkx3.1* is restricted to the epithelial cells of the embryonic prostate buds at E17.5 (Prins & Putz, 2008). Ablation of *Nkx3.1* causes abnormal prostate ductal morphogenesis (Abate-Shen et al., 2008). Additionally, *Nkx3.1* is not expressed on ductal urogenital tissues such as the seminal vesicles, the bladder or the urethra (Abate-Shen et al., 2008). In humans, *NKX3.1* expression has been detected in the testes, urethral epithelium and prostatic epithelium (Abate-Shen et al., 2008). Loss of *NKX3.1* expression in the human prostate has been associated with prostate cancer progression (Bowen et al., 2000).

#### **1.1.7.2 Probasin**

Probasin is a prostate-specific, androgen regulated protein in rodents (Matuo et al., 1982). Probasin is a marker of prostate differentiation and androgen receptor activity and is often targeted to generate prostate cancer models in the mouse and rat (Johnson

et al., 2000; Parisotto et al., 2013; Sharma et al., 1999). Expression of probasin is first detected around E17.5 as prostatic lobes undergo branching morphogenesis and remains expressed in the epithelium of terminally differentiated prostatic epithelial cells (Johnson et al., 2000; Parisotto et al., 2013; Sharma et al., 1999).

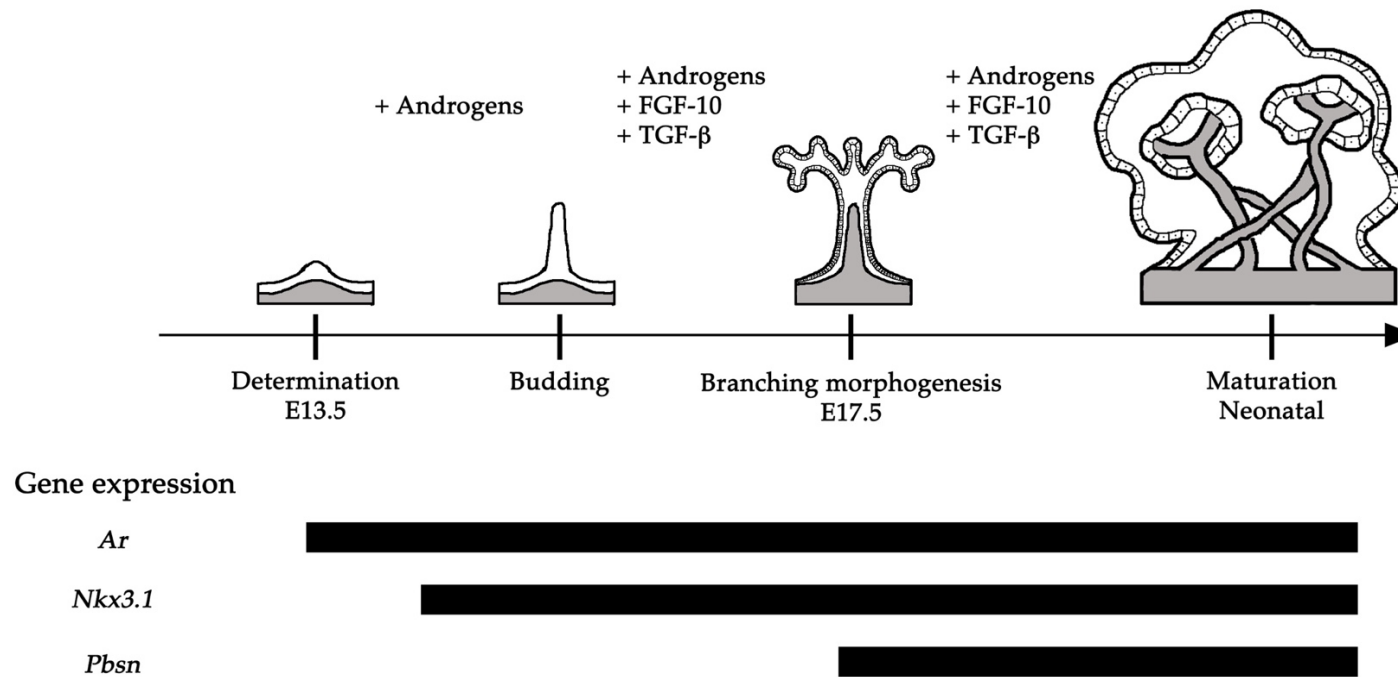


**Figure 1.4: The developmental stages of prostate organogenesis in the mouse.**

Development of the prostate *in vivo* can be classified into four distinct stages. Androgen signalling from the mesenchyme (grey) leads to prostate determination at E13.5 of development in the mouse. Expression of mouse androgen receptor is first observed at E13.5. Budding of the ductal tips occurs between E13.5 and E17.5. Branching morphogenesis of the prostate occurs at E17.5 and is essential for proper prostate formation and separation into the three lobes (dorsolateral, ventral and anterior). Homeobox domain factor *Nkx3.1* is expressed at E15.5 and remains expressed in the epithelial cells of the prostate. Expression of prostate specific marker *Probasin* is first observed at E17.5 and also remains expressed throughout the life of the mouse. Maturation of the prostatic lobes in mice occurs after birth. Androgens, FGF-10 and TGF $\beta$  promote the commitment, development and maturation of prostatic epithelial cells.

## 1.2 Embryonic stem cells as an *in vitro* model of development

The blastocyst develops at E3.5 of embryogenesis (Tam & Behringer, 1997). The blastocyst is composed of an outer layer of trophoblast cells which give rise to the extra-embryonic placenta and an inner cell population called the inner cell mass (ICM) (Tam & Behringer, 1997; Vazin et al, 2009). At E4.0, the embryo is implanted into the uterine wall of the mother and undergoes drastic structural changes (Tam & Behringer, 1997). Between E4.5-E6.5, the embryo develops into an elongated structure which consists of the ectoplacental cone, the extraembryonic ectoderm, the epiblast a layer of visceral endoderm (Tam & Behringer, 1997). Gastrulation commences at E6.5 with the formation of the primitive streak as epiblast cells ingress to form the mesoderm and endoderm (Tam & Behringer, 1997). Epiblast cells in the proximity of the distal primitive streak are exposed to high concentrations of Nodal signalling factors. This results in their development to definitive endoderm (Lawson, Meneses, & Pedersen, 1991; Kwon, Viotti, & Hadjantonakis, 2008). Conversely, epiblast cells at the proximal end of the primitive streak are exposed to high levels of bone morphogenic protein (BMP), which leads to mesoderm generation (Lawson et al., 1991; Parameswaran & Tam, 1995). Epiblast cells that do not ingress form the ectoderm and together with the mesoderm and endoderm, constitute the three primary germ layers of the body (Tam & Behringer, 1997).

The ectoderm forms the external layer of the skin and the peripheral nervous system; the mesoderm contributes to bone, blood, ligaments, tendons, lymph nodes, cardiac

tissue, connective tissue, kidney tubule cells, vessels and muscle tissue (smooth and skeletal); and the endoderm generates the epithelial tissues of the respiratory, gastrointestinal and genitourinary tracts (Bronner-Fraser et al., 1995; Keller, 2005a; Grapin-Botton, 2008).

Embryonic stem (ES) cells are derived from the inner cell mass (ICM) of the blastocyst and are capable of generating cell types from the ectoderm, the mesoderm and the endoderm (Evans & Kaufman, 1981; Martin et al., 1981; Thomson et al., 1998). Embryonic stem cells are generated by isolating and plating the ICM onto a supportive layer of non-proliferative feeder cells (Evans & Kaufman, 1981; Martin et al., 1981; Vazin et al., 2009). The resulting outgrowth of cells are dissociated and replated onto fresh feeder layers before use as stem cells (Figure 1.5) (Evans & Kaufman, 1981; Martin et al., 1981; Vazin et al., 2009).

In 2006, Takahashi and Yamanaka generated pluripotent stem cells from adult fibroblasts. Induction of Oct4, Sox2, c-Myc and Klf4 into adult fibroblasts led to reprogramming into pluripotent stem cells (dubbed induced pluripotent stem (iPS) cells) (Figure 1.5B) (Takahashi & Yamanaka, 2006). The reprogrammed fibroblasts displayed characteristics of embryonic stem cells and subcutaneous transplantation of iPS cells into nude mice resulted in tumours containing tissues from all three germ layers (Takahashi & Yamanaka, 2006). Implantation of iPS cells into the blastocysts resulted in contribution towards mouse embryonic development (Takahashi &

Yamanaka, 2006). The generation of iPS cells from a few factors was a new milestone in developmental biology.

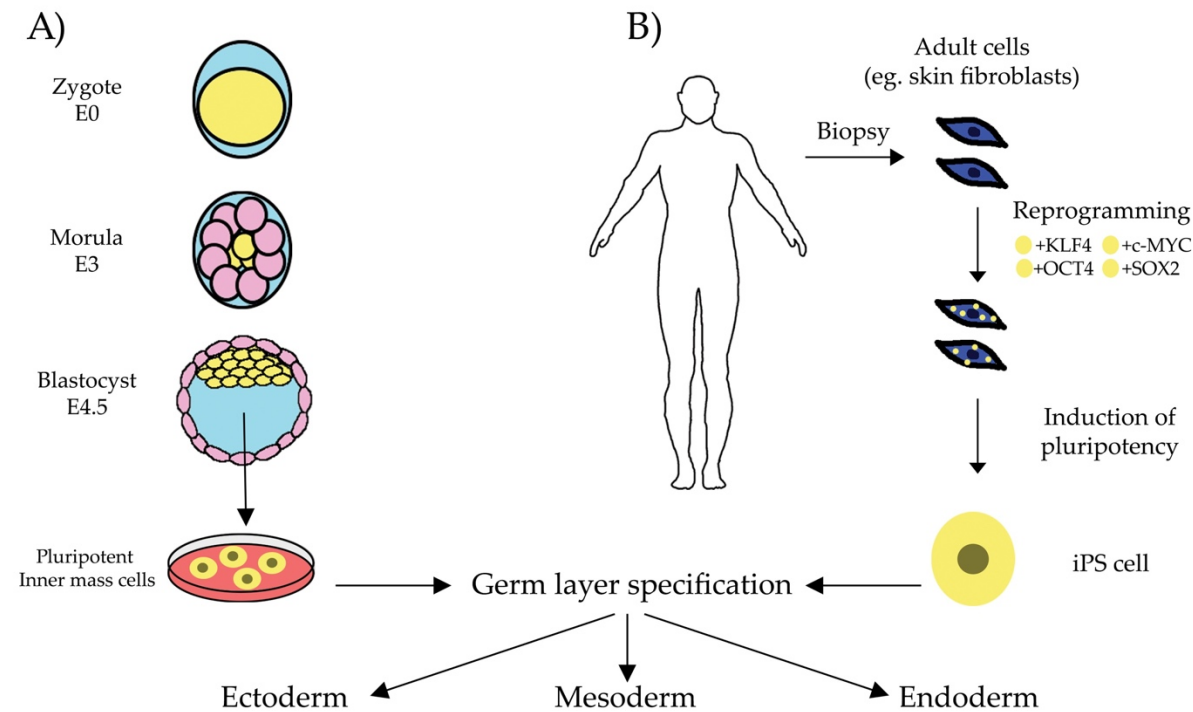


**Figure 1.5: Embryonic and induced pluripotent stem cells are capable of differentiating into all cell types of the body.**

(A) Embryonic stem (ES) cells are derived from the inner cell mass of the blastocyst. Isolated ES cells are plated on non-proliferative feeder cells. The resulting outgrowth of cells are dissociated and re-plated onto fresh feeder layers prior to germ layer specification. (B) Induced pluripotent stem (iPS) cells are generated from adult cells (such as skin fibroblasts) obtained from a biopsy. Adult cells are reprogrammed into pluripotent stem cells with the inductions of KLF4, c-MYC, OCT4 and SOX2 *in vitro*.

### 1.2.5.3 Differentiation of ES cells into the endoderm

The use of mouse ES cell reporter lines have contributed in generating, isolating and characterising endoderm populations. ES cell lines with the green fluorescent protein (GFP) cDNA targeted to *Bry/T* have revealed endoderm generation from brachyury positive populations (Kubo et al., 2004). Changes in serum concentration to differentiating ES cells also affects endoderm differentiation (Kubo et al., 2004). Using the GFP-Bry/T ES cell line, serum-free cultures prolonged the expression of *Sox17* and *FoxA2* and reduced expression of *Bry/T* (Kubo et al., 2004). Furthermore, Activin-A promotes endoderm differentiation in a dose-dependent manner (Kubo et al., 2004). Greater than 50% of the GFP-Bry/T ES cells treated with high dose Activin-A (100 ng.mL<sup>-1</sup>) expressed endoderm marker *FoxA2* (Kubo et al., 2004).

Activin-A binds to the same receptors as Nodal, triggering the signalling cascade to mimic Nodal activity *in vitro* (de Caestecker, 2004). Low levels of Activin promote mesoderm differentiation while high levels of Activin promote endoderm formation in ES cells (Kubo et al., 2004; Ogawa et al., 2007). The molecular response of ES cells to Activin mimic *in vivo* gastrulation (Kubo et al., 2004; Ogawa et al., 2007). Mesendoderm markers *Mixl1* and *Bry/T* are expressed on day 2 of ES cell differentiation (Loebel et al., 2003). Definitive endoderm is confirmed by expression of *Sox17*, *FoxA2* and *Cxcr4* (Keller, 2005a; D'Amour et al., 2005; Murry & Keller, 2008; Loebel et al., 2003).



Identification of the mesendoderm progenitors in mouse ES cell differentiation highlights the utility of ES cells as models of *in vivo* development. The combination of mesendoderm marker *Gsc* and endoderm marker *Sox17* in the reporter ES cell line ES-*Gsc<sup>gfp</sup>Sox17<sup>CD25</sup>* has distinguished between definitive, anterior visceral and visceral endodermal lineages (Yasunaga et al., 2005). Definitive endoderm is characterised by *Gsc<sup>+</sup>Sox17<sup>+</sup>* expressing cells in differentiated ES cell cultures (Yasunaga et al., 2005). Expression of *Cxcr4* further distinguishes definitive endoderm from visceral endoderm (McGrath et al., 1999). ES cells as well as visceral endoderm do not express *Cxcr4* (Yasunaga et al., 2005; McGrath et al., 1999). Thus, *Cxcr4* can be used to isolate definitive endoderm from differentiated mouse ES cell cultures.

In the GFP-Bry/T ES cell line, CD4 cDNA was targeted to the *FoxA2* locus to monitor endoderm development from the primitive streak (Gadue et al., 2006; Gadue et al., 2009). High concentrations of Activin-A promoted a CD4-*FoxA2<sup>High</sup>GFP-Bry/T<sup>+</sup>* population indicative of definitive endoderm formation (Gadue et al., 2006). Signalling through the TGF $\beta$  Nodal pathways by Activin-A was required for the commitment of primitive streak-like cells into definitive endoderm (Gadue et al., 2006). Endodermal cell types differentiated from mouse and human ES and iPS cells are listed in Table 1.1.

**Table 1.1 Endoderm derived cell types successfully differentiated from mouse and human ES and iPS cells.**

Region	Cell type	Reference
Foregut endoderm	Thyroid epithelial cells	Ma et al., 2015
	Lung epithelial cells	Ghaedi, Niklason, & Williams, 2015; Si-Tayeb et al., 2010
	Hepatocytes	
	Pancreatic $\beta$ -cells	Mallanna & Duncan, 2013; D'Amour et al., 2005; Murtaugh, 2006; Nostro et al., 2015
Midgut endoderm	Enterocytes	Noguchi et al., 2015
	Small intestine epithelial cells	Cramer et al., 2015
Hindgut endoderm	Large intestine epithelial cells	Cramer et al., 2015
	Bladder urothelial cells	Osborn et al., 2014; Mauney et al., 2010

#### **1.2.5.4 Differentiation of prostate epithelial cell from mouse ES cells.**

There are no *in vitro* models of prostate development from embryogenesis. Studying the early developmental processes of prostate organogenesis is challenging due to the small size of early embryos. The development of an *in vitro* model of prostate organogenesis using mouse ES cells could reveal the earliest signalling processes in prostate epithelial cell commitment and differentiation.

### 1.3 Aims and hypotheses

There are no reported *in vitro* models of prostate epithelial cell differentiation from mouse ES cells. This study aimed to differentiate mature, functional epithelial cells of the prostate from mouse ES cells *in vitro*. The development of this model could serve to replace foetal tissue. The prostate is derived from the urogenital sinus (UGS), which in turn is derived from the endoderm germ layer. Induction of endoderm differentiation from mouse ES cells is achieved with the addition of Activin-A and Wnt-3a in cell cultures. Urothelial cell specification is achieved with treatment of retinoic acid on endoderm cells. Paracrine signalling of DHT, TGF $\beta$ 1 and FGF10 from the urogenital mesenchyme are critical for the budding of prostatic epithelium *in vivo*. Subsequently, it was hypothesised that DHT, TGF $\beta$ 1 and FGF10 would drive prostate cell differentiation from mouse ES cell-derived urothelial cells. Confirmation of epithelial prostatic cells was to be confirmed by identification of prostate specific genes *Pbsn* and *Nkx3.1*.

The development of a system to differentiate prostate epithelial cells from mouse ES cells will reduce the need for foetal tissue. If prostate epithelial cell differentiation is successful, the study could go on to model prostate carcinogenesis by over expressing known oncogenes critical for prostate cancer progression such as *Nkx3.1* and *PTEN* in mouse ES cells.

## **Chapter 2: Materials and Methods**

### **2.1 Materials**

The consumables used for the experiments detailed in this study are listed in Table 2.1.

### **2.2 Reagents**

The reagents used for the experiments detailed in this thesis are listed in Table 2.2. Tables 2.3-5 display the composition of reagents, buffers and cell culture media used in this study.

**Table 2.1. List of consumables used in this study.**

<b>Product</b>	<b>Cat. Number</b>	<b>Company, Location</b>
0.2 mL flat cap PCR tubes	TWI0201	Bio-Rad (Gladesville, NSW, Australia)
1.5 mL Eppendorf tubes	T9661	Eppendorf (Hamburg, Germany)
1 mL Insulin syringe with needle	SS*10M2713A	Terumo (Macquarie Park, NSW, Australia)
20G x 1.5" Needle	NN*2038R	Terumo (Macquarie Park, NSW, Australia)
24mm x 24mm Cover glass	GCC2424	ProSciTech (Kirwan, QLD, Australia)
23G x 1" Needle	NN*2325R	Terumo (Macquarie Park, NSW, Australia)
26G x 1.5"	NN*2613R	Terumo (Macquarie Park, NSW, Australia)
35mm petri dish	627102	Greiner bio-one (Kremsmünster, Austria)
5 mL Stripette	4487	Sigma Aldrich (Castle Hill, NSW, Australia)
6-well cell culture plate	657160	Greiner bio-one (Kremsmünster, Austria)
15 mL Corning® Centrifuge tube	CLS430791	Sigma Aldrich (Castle Hill, NSW, Australia)
50 mL Corning® Centrifuge tube	CLS430897	Sigma Aldrich (Castle Hill, NSW, Australia)
Dissecting forceps + scissors	E118A/E140	Australian Entomological Supplies (Murwillumbah, NSW, Australia)
Eppendorf® Micropestle	Z317314	Sigma Aldrich (Castle Hill, NSW, Australia)
Razor blades	L055	ProSciTech (Kirwan, QLD, Australia)
Round bottom 5 mL, 75 x 12mm tubes	55.1759	Sarstedt (Nümbrecht, Germany)
Safe-lock Tubes 0.5 mL	T8911	Eppendorf (Hamburg, Germany)
Sterile 10 mL Disposable syringe	DSL010MLL	Livingstone (Rosebery, NSW, Australia)

**Table 2.2. List of reagents used in this study**

<b>Product</b>	<b>Cat. Number</b>	<b>Company, Location</b>
1-Thioglycerol (MTG)	M6145	Sigma (Castle Hill, NSW, Australia)
5x DNA Loading Buffer Blue	BIO-37045	BioLine (Eveleigh, NSW, Australia)
Agarose	BIO-41026	BioLine (Eveleigh, NSW, Australia)
Albumin from bovine serum	A9647-50G	Sigma (Castle Hill, NSW, Australia)
AmpliTaq Gold® 360 Master Mix	4398881	Applied Biosystems (Foster Hill, CA, USA)
Cell Dissociation Buffer (Enzyme-free, PBS based)	13151-014	Gibco (North Ryde, NSW, Australia)
Chloroform, anhydrous, >99%	372978-1L	Sigma (Castle Hill, NSW, Australia)
Collagenase Type II	LS004176	Worthington (Lakewood, NJ, USA)
DEPC treated H <sub>2</sub> O	AM9916	ThermoFisher Scientific (North Ryde, NSW, Australia)
Dimethyl sulphoxide (DMSO)	122650	Sigma (Castle Hill, NSW, Australia)
Dulbecco Modified Eagle Medium (1X)	11995-065	Gibco (North Ryde, NSW, Australia)
Ethanol	E7023-500mL	Sigma (Castle Hill, NSW, Australia)
Ethidium bromide	E1510	Sigma (Castle Hill, NSW, Australia)
Ethylenediaminetetraacetic acid (EDTA)	EDS	Sigma (Castle Hill, NSW, Australia)
Foetal Bovine Serum (FBS) (Sterile)	SFBS-F	Bovogen (Keilor East, VIC, Australia)
Formalin solution	HT50-1-1	Sigma (Castle Hill, NSW, Australia)
Glutamax (100X)	19140-122	Gibco (North Ryde, NSW, Australia)
Glutaraldehyde	C001	ProSciTech (Kirwan, QLD, Australia)
High Capacity RNA-to-cDNA Kit	4387406	ThermoFisher Scientific (North Ryde, NSW, Australia)
HyperLadder™ 100bp	BIO-33029	Bioline (Eveleigh, NSW, Australia)

Iscoves Modified Dulbecco Medium	12440061	Gibco (North Ryde, NSW, Australia)
Knockout Serum Replacement	10828-028	Gibco (North Ryde, NSW, Australia)
MilliQ H <sub>2</sub> O	CDUFBI001	Merck Millipore (Bayswater, VIC, Australia)
Penicillin Streptomycin (PEN/STREP)	15140122	Gibco (North Ryde, NSW, Australia)
Phosphate Buffered Saline (PBS)	09-2051-100	Astral Scientific (Sydney, NSW, Australia)
Recombinant Leukaemia Inhibitory Factor (LIF) -mouse	01-A1140-0010	ORF Genetic Isokine™ (Kopavogur, Iceland)
All-Trans Retinoic acid	R2625-50mg	Sigma (Castle Hill, NSW, Australia)
Reverse Osmosis H <sub>2</sub> O	TANKPE030	Merck Miliipore (Bayswater, VIC, Australia)
Sodium Pyruvate	11360-070	Gibco (North Ryde, NSW, Australia)
Trizma Base	T1503-1Kg	Sigma (Castle Hill, NSW, Australia)
TRIzol® Reagent	15596018	Life Technologies (North Ryde, NSW, Australia)
TrypLE® Express	12605-010	Gibco (North Ryde, NSW, Australia)
Ultrapure Water with 0.1% Gelatin	ES-006-B	Merck Millipore (Bayswater, VIC, Australia)

**Table 2.3. Composition of the reagents used in this study**

Name	Composition
0.1% (w/v) Type II Collagenase	1 mg of Type II Collagenase per mL of FACS buffer
0.5 M EDTA (pH 8.0)	29.225 g EDTA 200 mL MilliQ water Adjusted to pH 8.0 with concentrated NaOH.
Ascorbic Acid	5mg of Ascorbic acid dissolved per mL of MilliQ water.
Paraformaldehyde	4% (w/v) of paraformaldehyde powder dissolved in PBS. The solution was boiled at 60°C until the powder dissolved completely.

**Table 2.4: Composition of buffers used in this study.**

Name	Composition
Fluorescence-activated cell sorting (FACS) buffer	Phosphate Buffered Saline + 0.5% FBS (v/v)
10x Tris-Acetate-EDTA Running Buffer (10x TAE Buffer)	48.4 g Tris base 11.42 glacial acetic acid 20 mL 0.5 M EDTA



**Table 2.5: Composition of cell culture media used in this study.**

Name	Composition
Mouse ES cell maintenance media	DMEM supplemented to volume with: 20% (v/v) FBS 2 mM Glutamax™ 1 mM Sodium Pyruvate 50,000 U/mL Penicillin 50 mg/mL Streptomycin 150 µm 1-Thioglycerol
Endoderm differentiation media	IMDM supplemented to volume with: 20%(v/v) Knockout Serum Replacement 1 mM Glutamax™ 2.5 mM Sodium ascorbate 50,000 U/mL Penicillin 50 mg/mL Streptomycin 450 µm 1-Thioglycerol

## **2.3 Cell culture**

Reagents used for cell culture were warmed to 37°C before use. Cell culture was performed under sterile conditions in a laminar flow tissue culture hood (Edwards Instruments, Narellan, NSW, Australia).

### **2.3.1 Maintenance of mouse embryonic stem (ES) cells**

The mouse embryonic stem (ES) cell line used in this study was obtained from the embryos of wild-type 129SV/J mice (Kuo et al., 2001). Mouse ES cells were plated on gelatin-coated 6-well plates in the absence of a feeder layer. Mouse ES cells were maintained in Dulbecco Modified Eagle Medium supplemented with 20% (V/V) foetal calf serum, 2 mM Glutamax, 1 mM sodium pyruvate, 50,000 U.mL<sup>-1</sup> penicillin, 50 mg.mL<sup>-1</sup>, streptomycin and 150 µm of 1-thioglycerol (mouse ES cell maintenance media). Addition of 100 units.mL<sup>-1</sup> leukaemia inhibitory factor (LIF) inhibited the differentiation of stem cells and maintained undifferentiated status. Mouse ES cells were passaged every two days.

### **2.3.2 Passaging of mouse ES cells**

Prior to passaging of mouse ES cells, 1 mL of gelatin was added to a 6-well plate and let to sit for 10 min at room temperature before discarded. The mouse ES cell maintenance media was aspirated and cells washed with 1 mL PBS. PBS was removed and 500 µL of TrypLE® Express added. The 6-well plate was placed into the incubator at 37°C to initiate dissociation. Afterwards, 1.5 mL of

mouse ES cell maintenance media was added to quench the TrypLE® Express and mouse ES cells transferred into a 15 mL Corning tube. The mouse ES cells were centrifuged at  $240 \times g$  for 5 minutes. The supernatant was discarded and  $100 \text{ units.mL}^{-1}$  LIF was added to the mouse ES cells. The mouse ES cells were re-suspended in 6 mL of mouse ES cell maintenance media and plated onto three wells of a gelatinised 6-well plate.

#### **2.4 Reverse-transcriptase polymerase chain reaction (RT-PCR) analysis**

Cells at each stage of the differentiation protocol (undifferentiated mES; endoderm; urothelial cell and prostate cell) were washed twice with 2 mL of PBS and harvested with the addition of 1 mL of cell dissociation buffer. Cells were incubated at  $37^{\circ}\text{C}$  for 10 minutes to initiate dissociation. Following, the cells were resuspended and centrifuged at  $240 \times g$  for 5 minutes and supernatant discarded. The pellet was then resuspended in 1 mL of Trizol and transferred into a 1.7 mL Eppendorf tube.

For positive controls, mouse bladder and dorsolateral prostate tissue were washed with PBS and re-suspended in 1 mL of Trizol reagent. The tissues were homogenised by carefully grinding them with a micropestle. Once the tissue was homogenised, it was left to incubate for 5 minutes at  $22^{\circ}\text{C}$  then transferred into a 1.7 mL Eppendorf tube and stored at  $-80^{\circ}\text{C}$  until needed.

Samples stored at -80°C were left to equilibrate to room temperature before proceeding. RNA isolated following Trizol extraction was performed according to manufacturer's instructions. Following precipitation of RNA, the pellet was washed twice with 1 mL ice-cold 75% ethanol. The 1.7 mL Eppendorf tube was briefly vortexed and centrifuged at 7500g for 5 minutes at 4°C. The supernatant was discarded and the tube was left to air-dry. The RNA pellet was resuspended in 50 µL of RNase/DNase free water and incubated at 60°C for 10 minutes. RNA purity was determined by the 1:2:1 ratio of absorbance at 280 nm, 260 nm and 230 nm measured on a NanoDrop ND1000 spectrophotometer.

Reverse transcription of RNA samples was performed using the RNA-to-cDNA Kit according to manufacturer's instructions. Volume and RNA concentrations of reactions are given in Table 2.6. Reaction mixes were prepared in 0.2 mL thin walled, domed cap PCR tubes.

**Table 2.6. Components required for reverse transcription of RNA.**

Kit component	Component volume	
	+RT	-RT (control)
2X RT Buffer (includes a mix of: dNTPs, random octamers and oligo dT-16.	10 $\mu$ L	10 $\mu$ L
20X Enzyme Mix	1 $\mu$ L	N/A
RNA Sample	4 $\mu$ L (total 1 $\mu$ g RNA)	4 $\mu$ L (total 1 $\mu$ g RNA)
DEPC-water	Up to 20 $\mu$ L	Up to 20 $\mu$ L
Total per reaction	20 $\mu$ L	20 $\mu$ L

PCR tubes were briefly centrifuged and incubated at 37°C for 60 minutes, followed by 95°C for 5 minutes using a Bio-Rad T100 thermal cycler (Gladesville, NSW, Australia).

One  $\mu$ g of cDNA was mixed with universal components of Amplitaq Gold® 360 Master Mix as per manufacturer's instructions (Table 2.7). Reactions were made to a total volume of 20  $\mu$ L in thin walled 0.2 mL domed cap PCR tubes. To each mix, gene specific forward and reverse primers were added. Sequences were obtained from the Nucleotide database provided by the National Centre for Biotechnology Information (NCBI). Primer sequences were generated using Primer3 software. All forward and reverse primers were designed across intron-exon boundaries except for *Nkx3.1*, *FoxA2* and *Upk1b*. The melting

temperature of the primers was 60°C. Forward and reverse primers were re-suspended in RNase/DNase free water to a final concentration of 100 µmol.L<sup>-1</sup>. Stock concentrations were further diluted to 10 µmol.L<sup>-1</sup> prior to PCR reaction set up. Primer sequences are provided in Table 2.8.

Both no RT and no template controls were included. The reaction mixes were briefly centrifuged prior to reaction protocol of 1 cycle at 95°C for 10 min; 45 cycles of 30 sec at 95°C, 30 sec at 65°C and 1 minute at 72°C; followed by 1 cycle at 72°C for 7 min. For nested primer sequences, PCR products were diluted in RNase/DNase free water in a ratio of 1:10. One µL of the diluted PCR product was then used to generate amplified PCR reactions using nested primer sequences (Table 2.8).

**Table 2.7. Components for RT-PCR reactions.**

Component	Volume (20 µL reaction)	Final concentration
Amplitaq® Gold 360 Master Mix	10 µL	N/A
10 µM forward primer	2 µL	0.4 µM
10 µM reverse primer	2 µL	0.4 µM
cDNA	1 µL	1 µg/reaction
DPEC water	5 µL	N/A

**Table 2.8. Sequences of primers used for RT-PCR analyses in this study.**

Sequences were obtained from the Nucleotide database provided by the National Centre for Biotechnology Information (NCBI reference). Primer sequences were generated using Primer3 software (<http://primer3.ut.ee/>). All forward and reverse primers were designed across intron-exon boundaries except for *Nkx3.1*, *FoxA2* and *Upk1b*. The melting temperature of the primers was 70°C.

Gene	Forward (3' to 5')	Reverse (5' to 3')	Predicted amplicon size (bp)	NCBI reference
<i>β-actin</i>	CCTCTATGCCAACACAGTGC	CCTGCTTGCTGATCCACATC	120	NM_007393.3
<i>Oct4</i>	CACGAGTGGAAAGCAACTCA	AGATGGTGGTCTGGCTGAAC	246	NM_013633.3
<i>Nanog</i>	AAGTACCTCAGCCTCCAGCA	GTGCTGAGCCCTTCTGAATC	163	NM_028016.2
<i>FoxA2</i>	CTACACACACGCCAAACCTC	GGCACCTTGAGAAAGCAGTC	201	NM_010446
<i>Upk1a</i>	ATCAATGAAGATGGCTGCCG	GACCCTCCCTGTGATGTTGA	151	NM_026815.2
<i>Upk1b</i>	TCCGTCAGACTGGCAGAAAT	GTCCAGGTTGAGAGGCTCTT	118	NM_178924.4
<i>Upk2</i>	AGCCTGTTAATTGCCTTGCC	TGTCACCTGATATGCGCTGA	195	NM_009476.2
<i>mAR</i>	TAAGTCGCTGTACCCCCAAC	GAAATGGGGTCAGGGATTTT	450	NM_013476
<i>Csf-1R</i>	GACCTGCTCCACTTCTCCAG	GATGTCCCTAGCCAGTCCAA	300	NM_001037859.2
<i>Nkx3.1</i>	CTACCCATTACCCACACCT	TTTTCTGTAGAGCCGGGGT	150	NM_010921.3
<i>Nkx3.1</i> (Nested)	CTGGTAGAAACGTGGCCTGT	CCGGGGTTTGCTAACTGATT	115	NM_010921.3
<i>Pbsn</i>	TGCACAGTATGAAGGGAGCA	ACAGTTGTCCGTGTCCATGA	229	NM_017471.2
<i>Svs2</i>	CCACACCAGGGAGTGTTCTT	CTCCACTTCTGACTGCCCTC	150	NM_017390
<i>Svs2</i> (Nested)	CCCTGTGACCTCTGCTTTTC	GAGTGGATTTCTGCCTGCT	115	NM_017390
<i>Msmb</i>	GCATCACCTGTGAGCTTTGA	ATAGTGGTCCTGTGCCAAGG	150	NM_020597.3

Amplicons generated from RT-PCR were analysed by agarose gel submarine electrophoresis. Ten  $\mu\text{L}$  of samples were mixed with 2  $\mu\text{L}$  of DNA loading buffer (containing 30% (v/v) glycerol, 0.25% (w/v) bromophenol blue and 0.25% (w/v) xylene cyanol FF) and loaded onto a 2% (w/v) agarose/Tris acetate EDTA (pH 8.0) (TAE) buffer gel containing 0.1% (w/v) ethidium bromide. Five  $\mu\text{L}$  of the HyperLadder™ 50bp was included on each gel. Loaded samples were separated at 100 V for 1 hour and products were visualised under an ultra-violet transilluminator (Bio-Rad, North Ryde, NSW, Australia). The amplicon was sized with reference to HyperLadder™.



## **2.5 Animals**

Quackenbush Swiss mice were purchased from the Animal Resources Centre (Canning Vale, WA, Australia) and housed in filter top cages at the animal house facilities of the Medical Foundation Building (University of Sydney, NSW, Australia). Mice were kept under a 12-hour day and night cycle at constant temperature (21-22°C) and provided food and water *ad libitum*. Male mice were housed individually while female mice were housed in groups. The welfare of the animals in the housing area and experiments conducted were in accordance with the Australian Code of Practice and the University of Sydney Ethics Committee (763) for the use of animals in research. Tissue collected for these experiments were part of the University of Sydney tissue-sharing scheme.

### **2.5.1 Dissection and excision of tissue from mice**

Mice were euthanised by cervical dislocation according to the University of Sydney Animal Ethics Committee approval. Dissection equipment used is listed in Table 2.1. Prior to dissection, the mouse was sprayed with 80% ethanol to manage the fur.

### **2.5.1.1 Genitourinary organs**

The genitourinary organs examined in this study were the bladder and the prostate. A midline incision was made to the ventral side of the abdomen to expose the abdominal cavity. The abdominal cavity was then opened to reveal the internal organs of the mouse.

The bladder is a balloon-like organ that is distinct from the surrounding genitourinary organs. The prostate is situated between the bladder and the urethra of the mouse. While gently pinching the bladder (as it can burst when full of fluid), an incision was made as caudal as possible. The bladder was then removed along with the prostate glands.

### **2.5.1.2 Adipose tissue**

The anatomical location of all adipose depots was demonstrated by Dr. Kim Bell-Anderson (School of Life and Environmental Sciences, University of Sydney, Australia).

#### **2.5.1.2.1 Brown adipose tissue**

The mouse was placed dorsal side up to expose the interscapular region. The skin was pinched gently between the scapula and an incision was made. The fur and skin were removed to expose the interscapular fat pad where brown adipose tissue (BAT) is located (Figure 2.1A). The fat pad was excised, turned

over and the BAT separated from the subcutaneous interscapular white adipose tissue (WAT).

#### **2.5.1.2.2 White adipose tissue**

The mouse was placed in a supine position. The skin was gently pinched around the abdomen and a midline incision was made. The exposed abdominal cavity was cut open to reveal the internal organs. WAT was then dissected from five different anatomical locations. Subcutaneous WAT was excised from the inguinal adipose depot located just above the femur (inguinal; WAT:ING) (Figure 2.1B). Visceral WAT was excised from adipose depots situated around the reproductive tract (gonadal; WAT:GON), the kidneys (peri-renal; WAT:PR), the intestines (mesenteric; WAT:MES) and the heart (epicardial; WAT:EC) (Figure 2.1C-F).

#### **2.5.1.3 Femoral and caudal vertebrae marrow**

The mouse was placed in a supine position. A midline incision was made and extended to the genito-femoral junction in the pelvic region. The fur and skin were removed to expose the quadriceps muscle that was separated from the bone via bilateral incision. The femur was removed by cutting the bone at the hip joint followed by the knee joint. A cut was made at both ends of the femur to expose the marrow. The marrow was flushed using a 23G needle attached to a 5 mL syringe containing 3 mL of ES maintenance medium.

The caudal vertebra (tail) of the mouse was removed by snipping at the base of the tail. Four incisions were made around the opening to allow for the removal of the skin surrounding the tail by forceps. Individual vertebrae were sliced by a razor blade and then sliced again in half to expose the marrow before flushing.

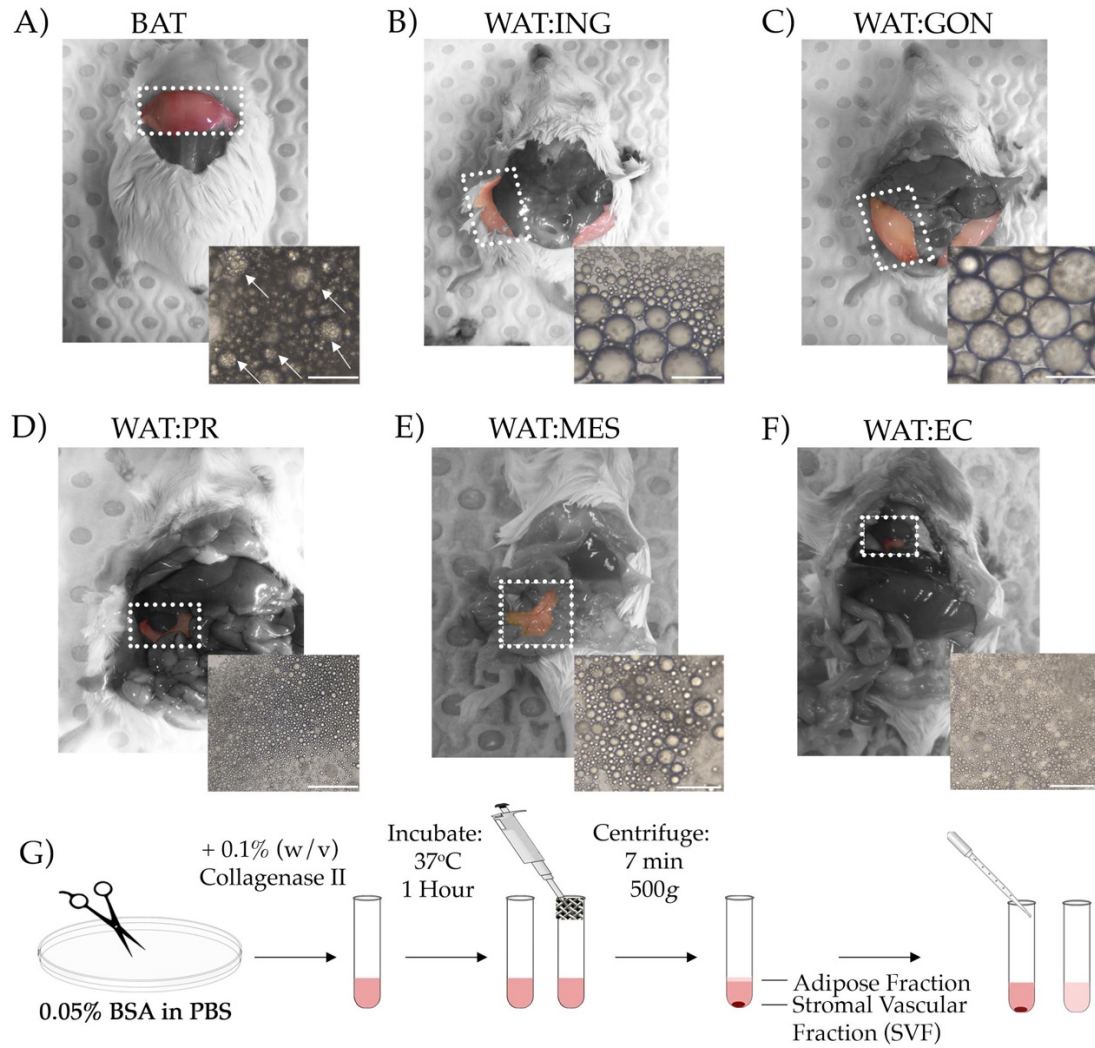


**Figure 2.1: Generation of single cell suspensions from BAT, subcutaneous and visceral WAT depots and separation of the adipocytes from the SVF.**

Adipose tissue (dotted white box) from (A) interscapular brown (BAT), (B) subcutaneous inguinal (WAT:ING), (C) visceral gonadal (WAT:GON), (D) peri-renal (WAT:PR), (E) mesenteric (WAT:MES), and (F) epicardial (WAT:EC) depots were dissected out and further prepared for the generation of single cell suspensions as outlined (G). Inset photomicrographs (A-F) of adipocytes in the buoyant cell fraction viewed under phase contrast. Arrowheads indicate multi-locular adipocytes liberated from BAT. Scale bar = 50  $\mu\text{m}$ . Figure adapted from Boumelhem et al., 2017.

## **2.6 Flow cytometry**

### **2.6.1 Generation of single cell suspensions from undifferentiated mouse ES cells and D5 embryoid bodies.**

Confluent undifferentiated mouse ES cells were washed twice with 1 mL PBS followed by addition of 1 mL Cell Dissociation Buffer. Undifferentiated mouse ES cells were placed in the incubator at 37°C for 10 minutes to initiate dissociation of the cells. An equal volume of FACS buffer was then added to inactivate the Cell Dissociation Buffer. Mouse ES cells were pipetted repeatedly, transferred to a 15 mL Corning tube and centrifuged for 5 minutes at 240 x g. The supernatant was removed and the cells re-suspended in 1 mL of FACS buffer, ready for staining.

Mouse ES cells plated in low-adhesive culture dishes will form aggregates termed embryoid bodies (EB). For mouse ES cell differentiation cultures, day 5 EBs were transferred into a 15 mL Corning tube and allowed to settle by gravity. After the EBs had sunk to the bottom (~10 min), the supernatant was removed and the cells washed with 2 mL of PBS. Once the EBs had sunk to the bottom, the PBS was aspirated and 1 mL Cell Dissociation Buffer was added. The EBs were placed in the incubator at 37°C for 10 minutes with gentle shaking every three minutes. Following, an equal volume of FACS buffer was added and the EBs centrifuged for 5 minutes at 240 x g. The supernatant was

removed and the cells re-suspended in 1 mL of FACS buffer, ready to be stained.

## **2.6.2 Generation of single cell suspensions from primary tissue.**

For dissociation of primary tissue into single cells, Type II Collagenase was used. The methodology for breaking down the tissues used in this study is outlined below.

### **2.6.2.1 Adipose tissue**

Brown and white adipose tissues (2.5.1.1) were minced into 1-3mm<sup>3</sup> pieces in FACS buffer and digested with 3-5 mL of 0.1% (w/v) Collagenase Type II for 1 hour at 37°C with vigorous shaking every 15 minutes (Figure 2.1G). Digested adipose tissue was dispersed further with repeated pipetting followed by filtration through a 350 µm polystyrene mesh. An equal volume of FACS buffer was added to the filtered single cell suspension to inactivate collagenase and then centrifuged for 7 minutes at 500g. Centrifugation pellets the stromal vascular fraction (SVF) while the buoyant adipocytes float at the surface of the suspension. The supernatant fraction containing adipocytes was transferred to a separate 15 mL Corning tube whilst the SVF was re-suspended in 1 mL of FACS buffer prior to staining (Figure 2.1G).

#### **2.6.2.2 Bone marrow**

Marrow from the femur and caudal vertebrae (2.5.1.3) was gently flushed using a 23G needle attached to a 5 mL syringe containing 3 mL of ES maintenance media. Bones were flushed until translucent. The flushed marrow was gently re-suspended multiple times using the same syringe and needle followed by centrifugation for 5 minutes at 500g. The supernatant was transferred into a separate 15 mL Corning tube for marrow adipocyte analysis. The pellet was re-suspended in 1 mL of FACS buffer prior to staining. Table 2.4 summarises the conditions used to dissociate cells and primary tissue into single cells.



**Table 2.9. Conditions used to dissociate undifferentiated mouse ES cells, embryoid bodies and primary tissue into single cells.**

<b>Cell type</b>	<b>Mechanical dissociation</b>	<b>Chemical reagent</b>	<b>Incubation 37°C (min)</b>	<b>Agitation (intervals)</b>	<b>Filtration</b>
Mouse ES cells	N/A	Cell Dissociation Buffer	10	N/A	N/A
Embryoid bodies	N/A	Cell Dissociation Buffer	10	3 min	N/A
Primary tissue	Minced into 1-3mm <sup>3</sup> pieces	0.1% (w/v) Collagenase Type II	60	15 min	~350µm polystyrene mesh
Marrow	Flushed using a 23G needle attached to a 5 mL syringe.	N/A	N/A	N/A	N/A

## **2.6.3 Sample preparation for flow cytometry**

### **2.6.3.1 Controls used for flow cytometric analyses**

The types of controls used for flow cytometric analyses are presented in Table 2.10.

#### **2.6.3.1.1 Undifferentiated mouse ES cells**

For mouse ES cells, the following single colour controls were used: phycoerythrin (PE) conjugated anti-mouse epithelial cell adhesion marker (EpCAM), and allophycocyanin (APC) conjugated anti-mouse epithelial cadhesion marker (ECad) antibody. The isotype controls used were PE-conjugated rat IgG2a antibody and APC-conjugated rat IgG1 antibody.

#### **2.6.3.1.2 Primary tissue**

For single cells dissociated from primary tissue, flushed femoral marrow was used to establish single colour controls. The single colour controls included: PE conjugated anti-mouse CD45, fluorescein isothiocyanate (FITC)-conjugated anti-mouse Ter119 and APC conjugated F4/80. The isotype controls used for all tissue types were PE-conjugated rat IgG2b antibody, FITC-conjugated rat IgG2b antibody and APC-conjugated rat IgG2a antibody.

**Table 2.10: Controls used for flow cytometric analyses in this study.**

Control	Purpose
No stain/Unstained	Measure auto fluorescence caused by dead or dying cells.
Isotype	Measure background signal that is normally the result of immunoglobulins binding non-specifically to Fc receptors.
Single colour	To set the voltage of a given channel and to correct spectral overlap.
Fluorescence minus one	Contains all the fluorochromes in a given cocktail, minus the fluorochrome being analysed.

#### **2.6.3.2 Staining of cells with fluorescently-conjugated antibodies or fluorescent probes**

Cocktails of FITC-conjugated, PE-conjugated and APC-conjugated antibodies were prepared to a working concentration outlined in Table 2.11. Cocktails of fluorescent dyes or probes were prepared to a working concentration outlined in Table 2.12. The cocktail mix (100  $\mu$ L) was then pipetted onto single cell suspensions (100  $\mu$ L). The cells were then incubated at 4°C for 45 minutes in the dark. Following incubation, the cells were washed with 1 mL of FACS buffer to wash any unbound cells and centrifuged for 5 minutes at 240g. The supernatant was removed and the cells re-suspended in 400  $\mu$ L of FACS buffer with propidium iodide (PI, 1:1000 dilution). The re-suspended cells were transferred into round-bottom tubes, ready for flow cytometric analysis.

**Table 2.11. List of fluorescently conjugated antibodies used in this study.**

Antigen	Clone	Concentration	Fluorophore	Company, location
$\alpha$ 2-integrin	DX5	3.25 $\mu\text{g.mL}^{-1}$	APC	BioLegend
$\alpha$ 4-integrin	R1-2	1.3 $\mu\text{g.mL}^{-1}$	FITC	eBioscience
$\alpha$ 5-integrin	eBioHMa5-1	3.25 $\mu\text{g.mL}^{-1}$	APC	eBioscience
$\alpha$ 6-integrin	GoH3	3.25 $\mu\text{g.mL}^{-1}$	APC	BioLegend
$\alpha$ 7-integrin	3C12	3.25 $\mu\text{g.mL}^{-1}$	APC	Miltenyi Biotec
$\alpha$ L-integrin	M17/4	1.3 $\mu\text{g.mL}^{-1}$	APC	BioLegend
$\beta$ 1-integrin	HM $\alpha$ 1-1	3.25 $\mu\text{g.mL}^{-1}$	FITC	BioLegend
$\beta$ 3-integrin	2C9.G3	3.25 $\mu\text{g.mL}^{-1}$	FITC	eBioscience
$\beta$ 4-integrin	346-11A	3.25 $\mu\text{g.mL}^{-1}$	FITC	AbD Serotec
$\beta$ 7-integrin	FIB504	3.25 $\mu\text{g.mL}^{-1}$	FITC	eBioscience
c-Kit	2B8	3.25 $\mu\text{g.mL}^{-1}$	APC	BioLegend
CD3 $\epsilon$	145-2C11	6.5 $\mu\text{g.mL}^{-1}$	FITC	eBioscience
CD4	GK1.5	3.25 $\mu\text{g.mL}^{-1}$	APC	eBioscience
CD11b	M1/70	3.25 $\mu\text{g.mL}^{-1}$	APC	eBioscience
CD19	eBio1D3	3.25 $\mu\text{g.mL}^{-1}$	FITC	eBioscience
CD31	390	3.25 $\mu\text{g.mL}^{-1}$	FITC	eBioscience
CD34	RAM34	3.25 $\mu\text{g.mL}^{-1}$	FITC	eBioscience
CD36	72-1	1.3 $\mu\text{g.mL}^{-1}$	APC	eBioscience
CD40	1C10	3.25 $\mu\text{g.mL}^{-1}$	APC	eBioscience
CD41	MWReg30	3.25 $\mu\text{g.mL}^{-1}$	APC	BD Bioscience

CD45	30-F11	1.3 µg.mL <sup>-1</sup>	APC	eBioscience
CD47	miap301	6.5 µg.mL <sup>-1</sup>	FITC	eBioscience
CD48	HM48-1	1.3 µg.mL <sup>-1</sup>	APC	eBioscience
CD71	R17217	3.25 µg.mL <sup>-1</sup>	FITC	eBioscience
CD133	315-2C11	3.25 µg.mL <sup>-1</sup>	APC	BioLegend
CD137 (4-1BB)	17B5	3.25 µg.mL <sup>-1</sup>	APC	BioLegend
CD144	BV13	3.25 µg.mL <sup>-1</sup>	APC	eBioscience
Csf-1R	12-3A3-1B10	1.3 µg.mL <sup>-1</sup>	PE	eBioscience
CXCR4	2B11	1.3 µg.mL <sup>-1</sup>	PE	eBioscience
E-Cadherin	DECMA-1	3.25 µg.mL <sup>-1</sup>	APC	BioLegend
EpCAM	G8.8	3.25 µg.mL <sup>-1</sup>	PE, APC	BioLegend
F4/80	BM8	1.3 µg.mL <sup>-1</sup>	APC	eBioscience
Flk-1	Avas12a1	1.3 µg.mL <sup>-1</sup>	APC	eBioscience
Gr-1	Rb6-8C5	3.25 µg.mL <sup>-1</sup>	FITC	eBioscience
I-CAM-1	HA58	3.25 µg.mL <sup>-1</sup>	APC	eBioscience
Rat IgG1 κ	DECMA-1	1.3 µg.mL <sup>-1</sup>	APC, FITC, PE	Biolegend
Rat IgG2a κ	eBR2a	1.3 µg.mL <sup>-1</sup>	APC, FITC, PE	eBioscience
Rat IgG2b κ	eB149/10H5	1.3 µg.mL <sup>-1</sup>	APC, FITC, PE	eBioscience
Ter119	TER-119	1.3 µg.mL <sup>-1</sup>	APC, FITC, PE	BioLegend
V-CAM-1	429	1.3 µg.mL <sup>-1</sup>	APC	eBioscience

**Table 2.12. List of probes used in this study.**

Probe/dye	Catalogue number	Concentration	Company, location
Carborane coumarin	N/A	0.5 $\mu$ M	School of Chemistry, University of Sydney, Australia
DRAQ5	62251	5 $\mu$ M	Thermo Fisher Scientific (North Ryde, NSW, Australia)
LipidTox® Green	H34475	1X solution	Life Technologies
LipidTox® Red	H34476	1X solution	Life Technologies
MitoTracker® Deep Red	M22426	0.2 $\mu$ M	Life Technologies
Nile Blue	N0766	0.25 $\mu$ M	Sigma
Nile Red	N3013	0.1 $\mu$ M	Sigma
Phenyl coumarin	N/A	0.5 $\mu$ M	School of Chemistry, University of Sydney, Australia
Oil Red O	OREDO	N/A	POCD Scientific

### **2.6.3.3 Instrument settings**

Flow cytometry for cell surface protein expression and probe uptake was examined using a FACSCalibur 4-color flow cytometer (Becton Dickinson, San Jose, CA, USA) and data collected using CellQuest software. Table 2.13 highlights the channels used by the flow cytometer and the parameter being measured. Table 2.13 also outlines the settings used for undifferentiated mouse ES cells and D5 EBs. Table 2.14 outlines the settings used for single cells dissociated from primary tissue. All parameters were measured on the log setting. For undifferentiated mouse ES cells, size and granularity (FSC-H and SSC-H respectively) were measured using linear settings.

### **2.6.3.4 Compensation**

While fluorescent-conjugated antibodies have a narrow spectrum, probes may have spectral overlap between channels. Single colour controls can be used to correct spectral overlap by ensuring fluorescence is only observed in a single channel. Table 2.15 displays the settings used to compensate samples.

### **2.6.3.5 Data analysis**

Flow cytometric data was analysed using the FlowJo software package (Version X.0.7, TreeStar, Ashland, OR, USA).

**Table 2.13. The settings used to measure fluorescence on undifferentiated mouse ES cells.**

Channel	Parameter	Voltage	Amp Gain	Mode
FSC	Forward scatter (size)	E00	2.45	Linear
SSC	Side scatter (granularity)	425	2.90	Linear
FL-1	FITC-conjugated antibodies	525	1.00	Logarithmic
FL-2	PE-conjugated antibodies	480	1.00	Logarithmic
FL-3	Propidium Iodide	600	1.00	Logarithmic
FL-4	APC-conjugated antibodies	750	1.00	Logarithmic

**Table 2.14. The settings used to measure fluorescence on single cells generated from primary tissue.**

Channel	Voltage	Amp Gain	Mode
FSC	E00	9.99	Logarithmic
SSC	400	9.99	Logarithmic
FL-1	650	1.00	Logarithmic
FL-2	650	1.00	Logarithmic
FL-3	800	1.00	Logarithmic
FL-4	750	1.00	Logarithmic

**Table 2.15. Settings used to correct spectral overlap of fluorescently-conjugated antibodies and probes.**

	FL-1	FL-2	FL-3	FL-4
FL-1		22%	N/A	N/A
FL-2	18%		0%	N/A
FL-3	N/A	27.5%		0%
FL-4	N/A	N/A	0%	



## **2.7 Imaging**

### **2.7.1 Light microscopy**

Light microscopy was performed on an Axiovert35 (Zeiss, Germany) microscopy under 20x and 32x magnification (ACROSTIMA 20x and 30x objective, NA: 0.40 and NA: 0.30 respectively) and imaged using ZEN 2011 imaging software (Zeiss).

### **2.7.2 Confocal microscopy**

Confocal images were taken with a Leica SPEII (Leica, Germany) equipped with four solid-state lasers (405nm, 488nm, 532nm and 625nm). Images were taken using an oil-immersed Leica ACS Apochromat 63x objective coupled to the Leica Application Suite – Advanced Fluorescence Software.

## **2.8 Statistical analyses**

All data presented as mean  $\pm$  SEM. Graphpad Prism® (Version 7.0a) was used to generate graphs and determine statistical significance. Where relevant, two-tailed Student's *t*-test was used to compare between two groups. A two-tailed one-way ANOVA with Tukey's *posthoc* analysis was used to compare more than two groups. A two-tailed two-way ANOVA with Tukey's multiple comparison test was used to compare two variables between several groups. A *P* value less than 0.05 was deemed significant.

## Chapter 3: The differentiation of mouse embryonic stem cells into prostate epithelial cells.

### 3.1 Introduction

The prostate is an exocrine gland derived from the urogenital sinus, which in turn is derived from the endoderm (Marker et al., 2003b). Development of the endoderm, urogenital sinus and the prostate *in vivo* is detailed in 1.1.4. There are no *in vitro* models of prostate epithelial cell differentiation from mouse ES cells. Mouse ES cells are capable of differentiating into all cell types from the three germ layers: the ectoderm, the endoderm and the mesoderm by mimicking processes critical for *in vivo* development (Keller, 2005b). Paracrine signalling from the urogenital mesenchyme is critical for prostate epithelial cell development (outlined in 1.2.2). Androgen receptor, TGF $\beta$ 1 and FGF10 signalling can be replicated *in vitro* to recapitulate the developmental cues required for normal development. A proposed timeline of prostate epithelial cell differentiation from mouse ES cells is depicted in Figure 3.1.

### **3.1.1 Hypothesis:**

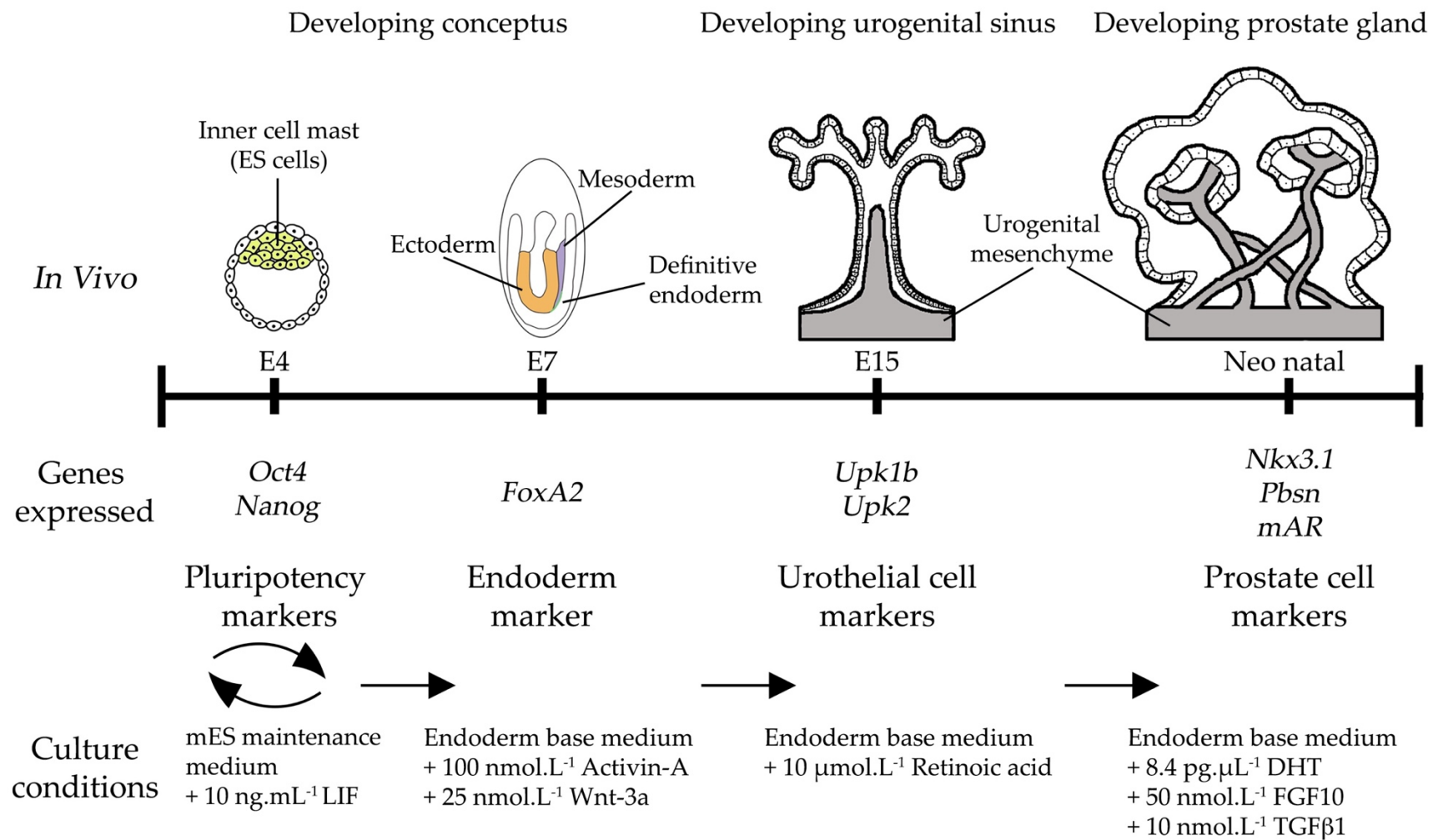
Treatment of mouse ES cells *in vitro* with factors known to be important for *in vivo* prostate development in a stepwise manner (with intermediate stages of differentiation identified) will result in the differentiation of prostate epithelial cell types. Thus, the treatment of urothelial cells derived from mouse ES cells with dihydrotestosterone (DHT), TGF $\beta$ 1 and FGF10 would be sufficient to drive differentiation into prostate epithelial cells.

### **3.1.2 Aims:**

- 1) To recapitulate the developmental processes in prostate organogenesis *in vitro* using mouse ES cells.
- 2) To drive differentiation of mouse ES cells into prostatic glandular epithelial cells with factors reported to be critical for *in vivo* prostate organogenesis.

**Figure 3.1: Proposed method of differentiation prostate epithelial cells from mouse ES cell *in vitro*.**

Pluripotency markers *Oct4* and *Nanog* are expressed on undifferentiated mouse ES cells. The presence of leukemia inhibitory factor (LIF) in mouse ES cell cultures prevents spontaneous differentiation of mouse ES cells into cells from the three germ layers: the endoderm (green), the ectoderm (orange) and the mesoderm (purple). Endoderm (*FoxA2* expression) induction from mouse ES cells is achieved by removal of LIF and addition of Activin-A and Wnt-3A in cell cultures. Urothelial cell (*Upk1b* and *Upk2* expression) differentiation is driven by retinoic acid. Finally, the proposed method to induce prostate epithelial cell differentiation is by treatment of mouse ES cell derived-urothelial cells with DHT, TGFβ1 and FGF10. Gene expression of *Nkx3.1*, *Svs2* and *Pbsn* will confirm the generation of prostate epithelial cells.



## **3.2 Methods**

### **3.2.1 Differentiation of mouse ES cells into endoderm.**

The maintenance of mouse ES cells is outlined in **2.4.1**. For differentiation of mouse ES cells,  $1.5 \times 10^4$  cells.mL<sup>-1</sup> were plated on 30 mm petri dishes in the absence of LIF and kept in an incubator set to 37°C and 5% CO<sub>2</sub>. Mouse ES cells will form aggregates termed embryoid bodies (EB). To induce endoderm differentiation, 100 nM of Activin-A and 25 nM of Wnt-3A were added to EB cultures for 5 days after the removal of LIF. Media was changed every two days. Endoderm differentiation was confirmed by detection of *FoxA2* gene expression and surface protein expression of CXCR4 and c-Kit by RT-PCR and flow cytometry respectively as described below.

### **3.2.2 Differentiation of endoderm to urothelium.**

Following endoderm differentiation, day 5 embryoid bodies (EBs) were plated on gelatin coated 6-well plates to form a monolayer. Endoderm cultures were treated with 10 μmol.L<sup>-1</sup> retinoic acid for 5 days to induce urothelial cell differentiation. Urothelial cell generation was confirmed by the expression of *Upk1b* and *Upk2* by RT-PCR as described below.

### **3.2.3 Differentiation of urothelial cells to prostate epithelial cells:**

Dihydrotestosterone (DHT), TGF $\beta$ 1 and FGF10, factors crucial for normal prostate development *in vivo*, were added to urothelial cultures for 12 days. Differentiated prostate epithelial cells were confirmed by gene expression of *Nkx3.1*, probasin (*Pbsn*) and *Svs2*. Androgen receptor (*AR*) was also evaluated by RT-PCR as described below.

### **3.2.4 Reverse-transcriptase polymerase chain reaction (RT-PCR) analysis**

Generation of RNA, reverse transcription into cDNA and the steps to generate RT-PCR reactions are outline in **2.4**. The conditions and primer sets used are outlined in Tables 2.6-8.

### **3.2.5 Flow cytometric analyses**

#### **3.2.5.1 Analysis of endoderm markers c-Kit and CXCR4 by flow cytometry**

Undifferentiated mouse ES cells and D5 EBs treated with endoderm media alone or endoderm media with Activin-A and Wnt-3A were generated into single cells as described in **2.6.1** and Table 2.9. APC-conjugated c-Kit (BioLegend) and PE-conjugated CXCR4 (eBioscience) endoderm surface markers were made to 1 mL at a final concentration of 1.3  $\mu\text{g.mL}^{-1}$  and 3.25  $\mu\text{g.mL}^{-1}$  respectively. Single cells were stained with 100  $\mu\text{L}$  of the antibody mix and incubated at 4°C for 45 min and protected from light. No stain controls, isotype controls and single stain controls were also prepared (outlined in **2.6.3**,

Table 2.10). Undifferentiated mouse ES cells were stained with PE-conjugated EpCAM and APC-conjugated E-Cad for single stain controls. All samples were stained with PE-conjugated rat IgG2a and APC-conjugated rat IgG1 for isotype controls. Following incubation, cells were washed with 1 mL of FACS buffer and centrifuged for 5 min at 240 x g. The supernatant was discarded and the cells resuspended in 400  $\mu$ L of FACS buffer containing 0.01% propidium iodide. The cells were then transferred to round-bottom tubes for flow cytometric analyses.

#### **3.2.5.2 Analysis of colony stimulating factor 1 receptor (CSF-1R) by flow cytometry.**

Timed matings between female and stud male mice were performed by Chelsea Pilgrim (Blood Cell Development laboratory, University of Sydney, NSW, Australia). Pregnant mice were left to gestate until E18.5. The developing urogenital tract was dissected as reported by Staack and colleagues (2003). Prostate tissue was also extracted from new-born, pubertal and adult mice and dissociated into single cell suspensions as outlined in 2.6.2 and Table 2.9. APC-conjugated EpCAM (BioLegend) and PE-conjugated CSF-1R (eBioscience) endoderm surface markers were made to 1 mL at a final concentration of 3.25  $\mu$ g.mL<sup>-1</sup> and 1.3  $\mu$ g.mL<sup>-1</sup> respectively. Single cell suspensions were stained as outlined above in 3.2.5.1.



Flow cytometry was performed on a FACSCalibur 4-colour flow cytometer (Becton Dickinson, San Jose, CA, USA) and data collected using CellQuest software. The parameters and settings used are described in 2.6.3.3 and Table 2.13-2.14. Cell size and granularity was measured using the forward and side scatter channel respectively. Surface protein expression c-Kit and CXCR4 was detected using the FL-4 and FL-2 channels respectively. Gates identifying positively labelled regions was determined by the single stain control.

### **3.2.6. Phase contrast imaging of undifferentiated mouse ES cells and differentiated cultures.**

Light microscopy was conducted at all points of the differentiation time line (D0, undifferentiated mouse ES cells; D5 endoderm; D10-12 urothelial cells; D22 prostate epithelial cells) using an Axiovert35 (Zeiss, Germany) microscope under 20x magnification. Images were taken using ZEN 2011 imaging software. Scale bars represent 50  $\mu\text{m}$ .

### 3.3 Results

#### 3.3.1 Pluripotency markers *Oct4* and *Nanog* are detected in undifferentiated mouse ES cells.

Undifferentiated mouse ES cells were maintained in a pluripotent state by the addition of leukaemia inhibitory factor (LIF) in media (Figure 3.2A). The pluripotency state of undifferentiated mouse ES cells was confirmed by the production of amplicons corresponding to the expected sizes for pluripotency markers *Oct4* and *Nanog* in mRNA (246bp and 163bp respectively) (Figure 3.2B). No amplicons were detected in the No RT and NTC lanes, indicating no amplification of genomic DNA (Figure 3.2B).

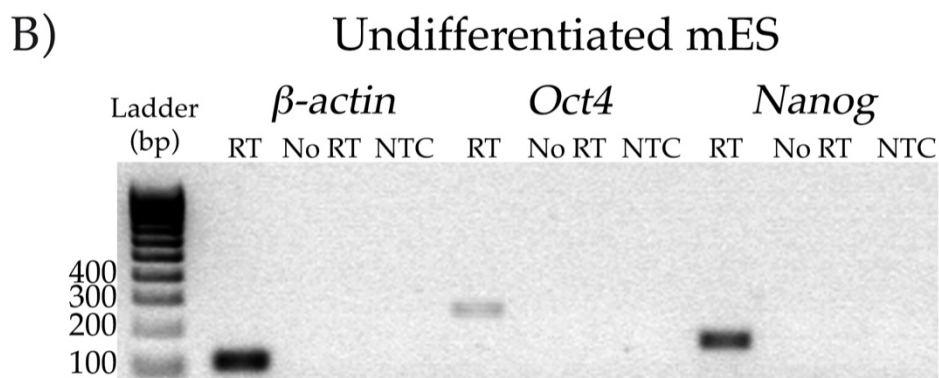
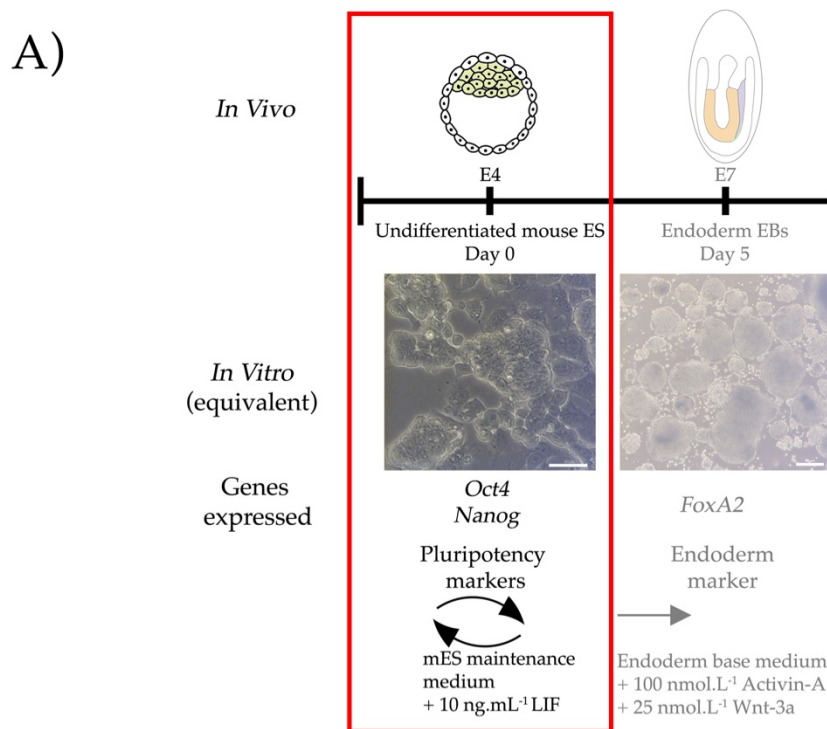


**Figure 3.2: Undifferentiated mouse ES cells express pluripotency markers *Oct4* and *Nanog*.**

(A) Graphical representation of mouse *in vivo* development mimicked by *in vitro* differentiation of mouse ES cells.

(B) Total RNA was harvested from undifferentiated mouse ES cells and gene expression of pluripotency markers *Oct4* and *Nanog* examined. Predicted amplicon sizes for *Oct4* and *Nanog* were 246bp and 163bp respectively.  $\beta$ -actin (predicted amplicon size of 120bp) was run alongside as an internal control as well as No RT and NTC controls.

### 3.3.2 Activin-A and Wnt-3A promotes endoderm differentiation from mouse ES cells.

Mouse ES cells were plated on non-adhesive petri dishes to form embryoid bodies (EB) and treated with Activin-A and Wnt-3A for 5 days (Figure 3.1). Definitive endoderm molecular marker *FoxA2* and surface protein markers c-Kit and CXCR4 were not detected on undifferentiated mouse ES cells (Figure 3.3i-ii). An amplicon of predicted size for *FoxA2* (201bp) was generated by RT-PCR from total RNA of cells harvested from day 5 cultures treated with endoderm media alone or endoderm media with Activin-A and Wnt-3A (Figure 3.3i). No amplicons were detected in the No RT and NTC lanes for all samples. Surface protein expression of c-Kit and CXCR4 was significantly greater in day 5 EBs treated with Activin-A and Wnt-3A ( $28\% \pm 2\%$ ) compared to day 5 EBs treated with endoderm media alone ( $10\% \pm 2\%$ ) ( $P < 0.0001$ ) (Figure 3.3ii).

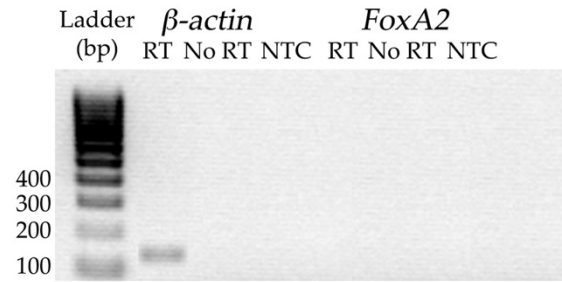
Mesoderm surface protein markers Flk-1 and platelet derived growth factor  $\alpha$  (PDGFR $\alpha$ ) were also assessed on undifferentiated mouse ES cells and day 5 embryoid bodies treated with or without Activin-A and Wnt-3A (Figure 3.4). Mesoderm cell populations were not detected in undifferentiated mouse ES cells and day 5 embryoid bodies (Figure 3.4).

**Figure 3.3: Activin-A and Wnt-3A promote the differentiation of mouse ES cells into endoderm.**

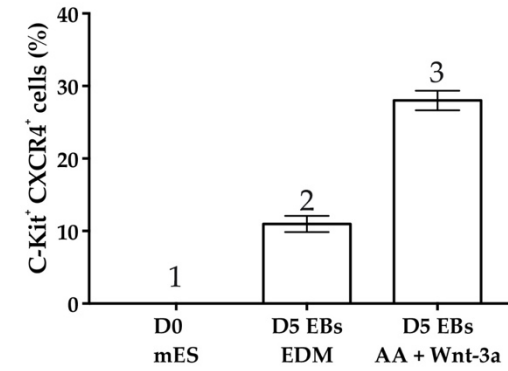
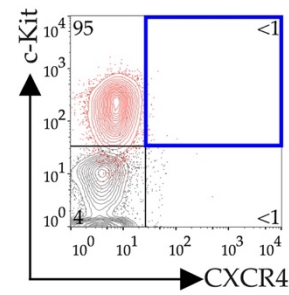
Total RNA was extracted from (i) undifferentiated mouse ES cells, day 5 embryoid bodies (EB) treated with endoderm media alone and day 5 EBs treated with Activin-A (AA) and Wnt-3A and gene expression of definitive endoderm marker *FoxA2* examined (predicted amplicon size of 201bp). The house-keeping gene  *$\beta$ -actin* was used as an internal control (predicted amplicon size of 120bp). (ii) Representative flow cytometric plot assessing surface protein expression of endoderm markers c-Kit and CXCR4. (iii) Comparisons in the frequency of cells expressing c-Kit and CXCR4 (blue box) between undifferentiated mouse ES cells and day 5 EBs with or without Activin-A and Wnt-3A. Data presented as mean  $\pm$  SEM (n = 5). Significance of c-Kit<sup>+</sup> CXCR4<sup>+</sup> expression between groups was determined by a two-tailed, one-way ANOVA and *post hoc* analysis by Tukey's HSD. Groups not sharing a numeral are significantly different from each other.

i)

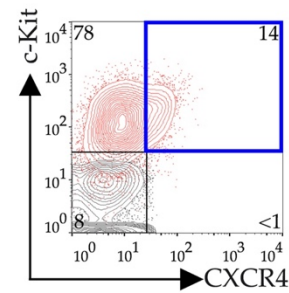
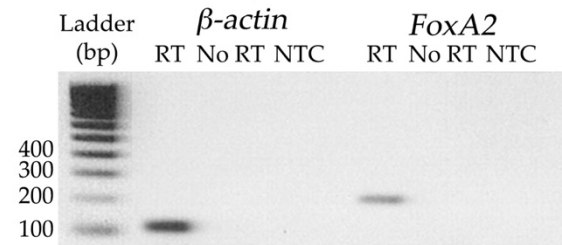
### Undifferentiated mES



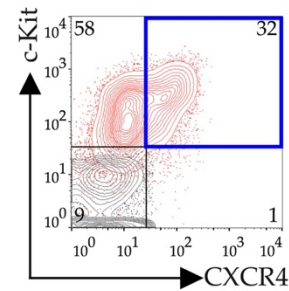
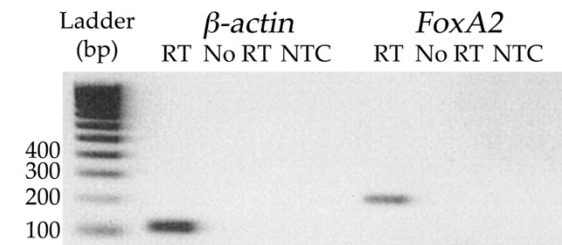
ii)



### Day 5 EBs + EDM



### Day 5 EBs + Activin-A + Wnt-3a



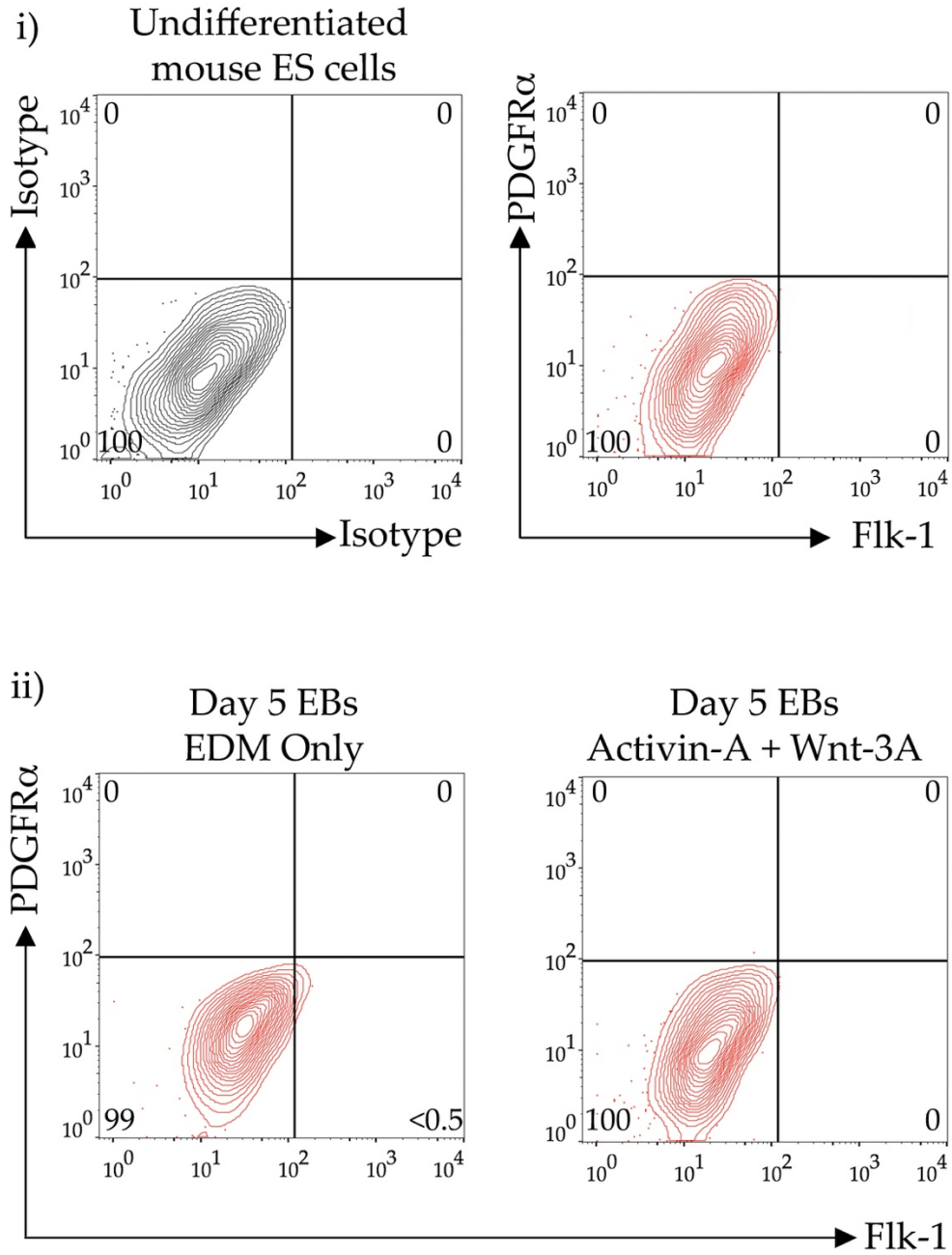


**Figure 3.4: Mesoderm surface protein markers Flk-1 and PDGFR $\alpha$  are not expressed on day 5 embryoid bodies cultured under endoderm conditions.**

Representative flow cytometric plot of Flk-1 and PDGFR $\alpha$  surface protein expression on (i) undifferentiated mouse ES cells and (ii) day 5 embryoid bodies treated with endoderm media alone (EDM) or Activin-A and Wnt-3A.

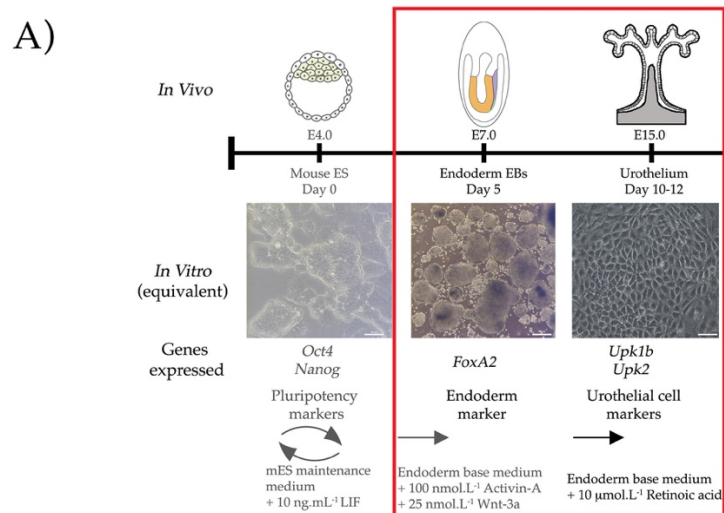
### **3.3.3 Retinoic acid promotes differentiation of mouse ES cell-derived endoderm into urothelium.**

Day 5 EBs were then plated on gelatin coated dishes to form a monolayer as described in the protocol by (Mauney et al., 2010) (Figure 3.5A). Day 5 EBs were treated with 10  $\mu\text{mol.L}^{-1}$  retinoic acid for 7 days to induce urothelial cell differentiation (Figure 3.5A). The cell morphology in cultures treated with retinoic acid consistently displayed a cobblestone-like phenotype (Figure 3.5B, red box). A glandular-like structure was identified in the retinoic acid treated cultures at day 12 of differentiation (Figure 3.5B, red arrow). Conversely, the cell morphology in cultures treated with endoderm media alone or ethanol (vehicle) resembled neuron-like projections (Figure 3.5B, yellow arrows).

Amplicons of predicted sizes for *Upk1b* (118bp) and *Upk2* (195bp) were not detected in the RNA of cells harvested from undifferentiated mouse ES cells or day 12 differentiated cultures treated with endoderm media only (Figure 3.6i-ii). Day 12 differentiated cultures treated with retinoic acid however, produced an amplicon of predicted sizes for *Upk1b* and *Upk2* (Figure 3.6iii). Amplicons of the same size were generated from the RNA of mouse bladder tissue (positive control) (Figure 3.6iv). No amplicons were generated for pluripotency markers *Oct4* and *Nanog* and endoderm marker *FoxA2* in day 12 differentiated cultures (Figure 3.6ii-iii). No amplicons were detected in the No RT and No template



control lanes. For *Upk1a* (151bp), a faint band was detected only in the RNA of bladder tissue (Figure 3.6iv).



## B) Day 12 differentiated cultures

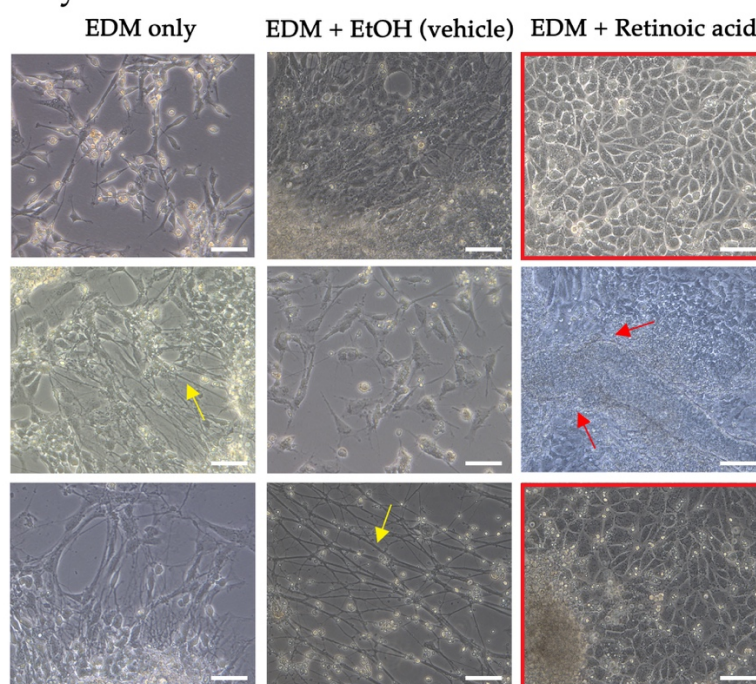


**Figure 3.5: Retinoic acid induces a cobblestone-like phenotype in mouse ES cell-derived endoderm cultures.**

(A) Timeline of urothelial cell differentiation following endoderm specification from mouse ES cells. (B) Representative bright-field micrographs of day 12 differentiated mouse ES cell cultures treated with endoderm media alone (EDM), endoderm media and ethanol (EtOH – vehicle) or endoderm media and retinoic acid. The yellow arrows signify neuron-like cells. The red boxed region highlights the cobblestone-like cells and the red arrows indicate epithelium-like structures. Scale bars represent 20 μm.

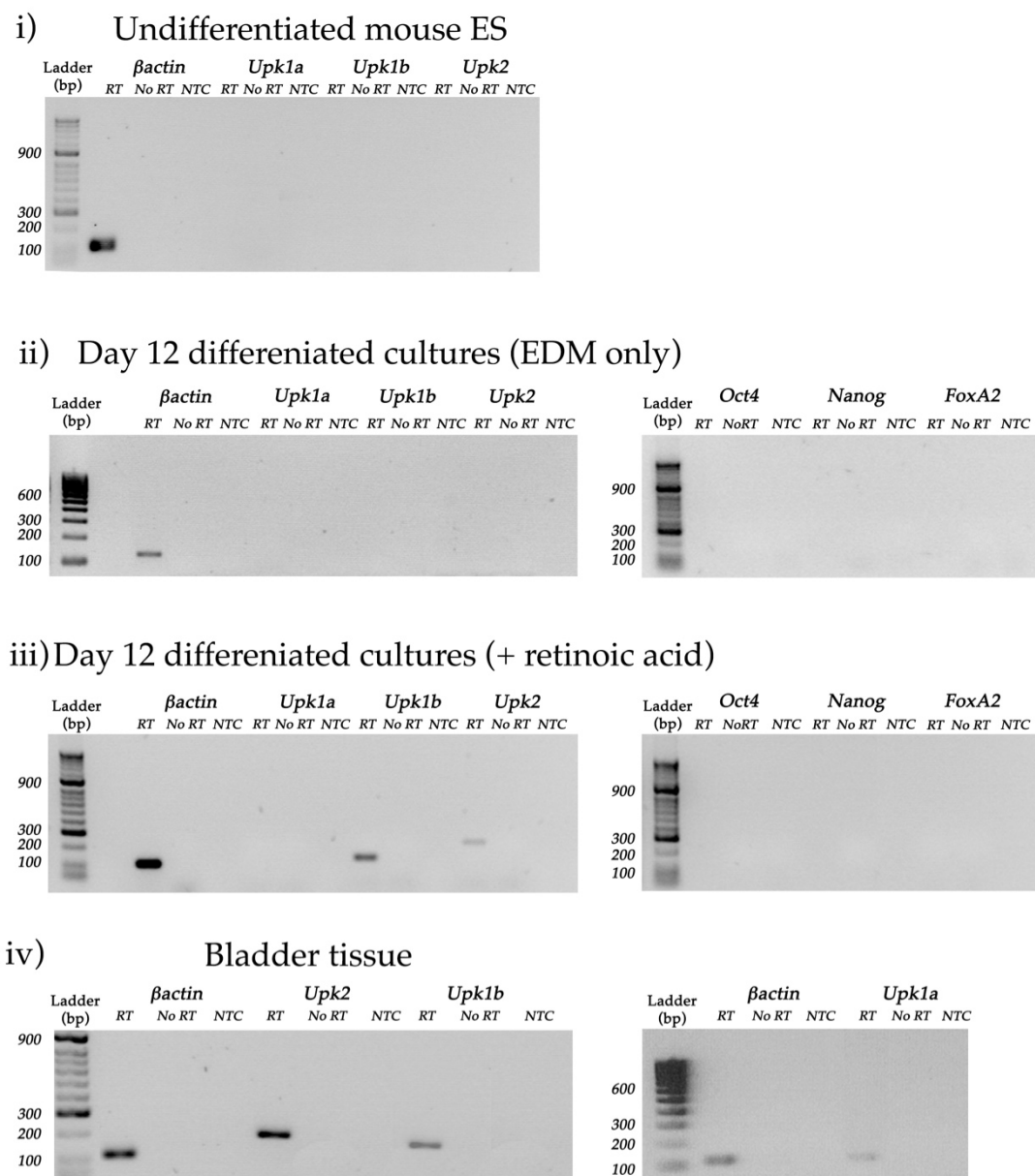


**Figure 3.6: Expression of uroplakin detected in day 12 mouse ES cell cultures treated with retinoic acid.**

Total RNA was harvested from (i) undifferentiated mouse ES cells, (ii) day 12 cultures treated with endoderm media alone or (iii) 10  $\mu\text{mol.L}^{-1}$  retinoic acid and (iv) mouse bladder tissue (positive control) and gene expression for urothelial cell markers *Upk1a*, *Upk1b* and *Upk2* examined. Predicted amplicon sizes for *Upk1a*, *Upk1b* and *Upk2* are 151bp, 118bp and 195bp respectively.  *$\beta$ -actin* (predicted amplicon size of 120bp) was run alongside as an internal control as well as No RT and NTC controls.

### **3.3.4 DHT, TGF $\beta$ 1 and FGF10 drives the differentiation of prostate epithelial cells from mouse ES cell-derived urothelial cells.**

#### **3.3.4.1 Prostate epithelial cell specific marker *Nkx3.1* is detected in day 16 cultures treated with DHT, TGF $\beta$ 1 and FGF10.**

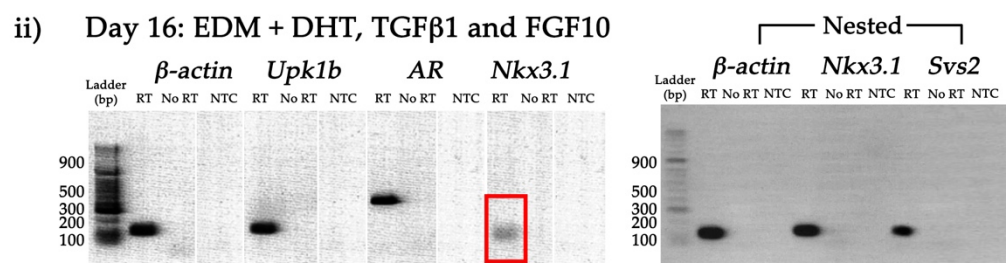
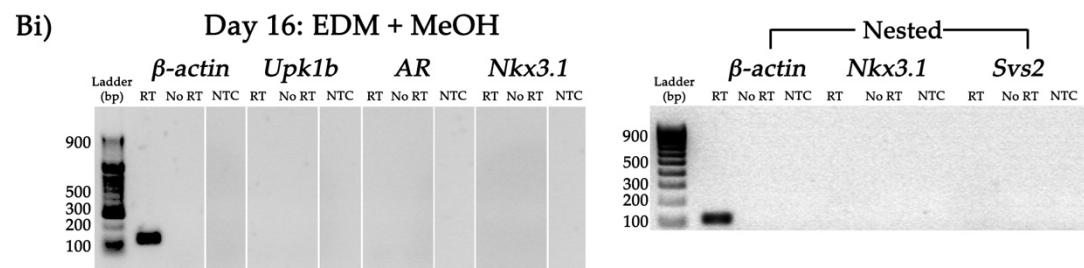
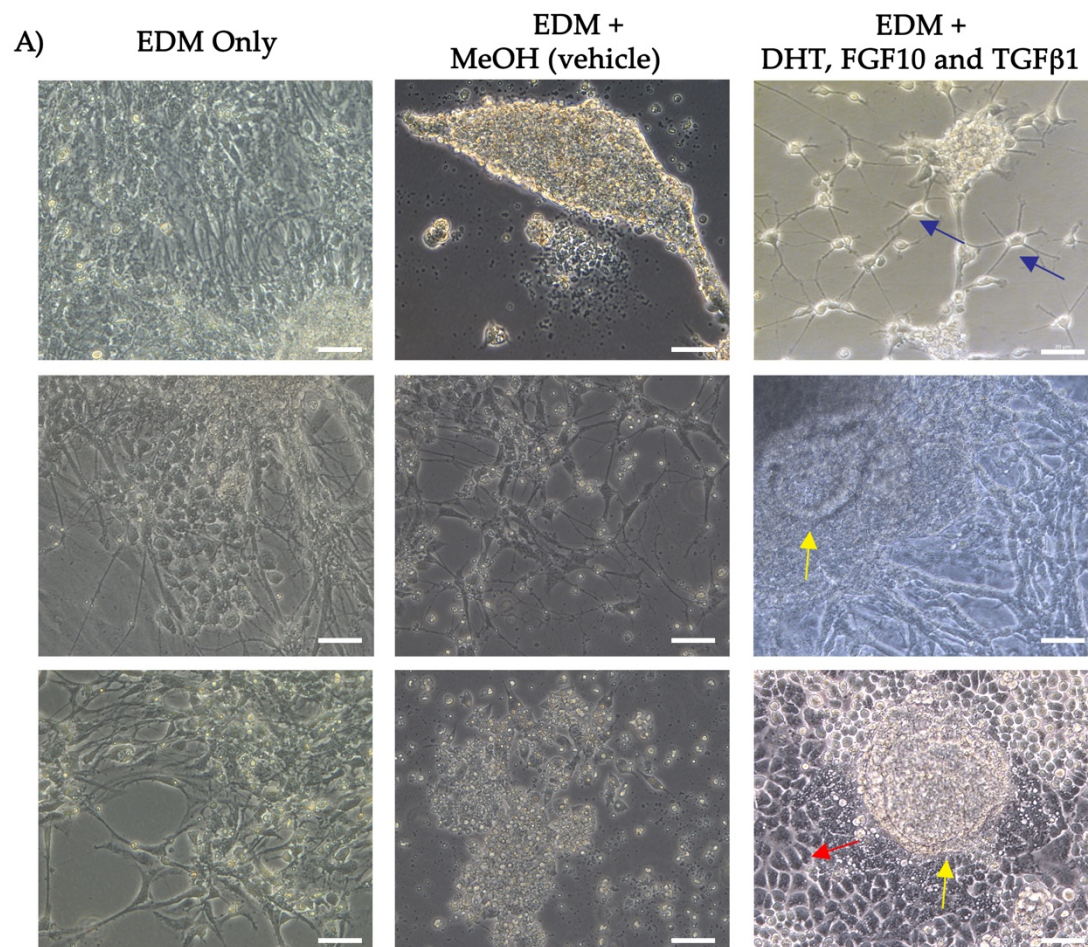
Differentiated urothelial cells were then treated with DHT, TGF $\beta$ 1 and FGF10 for the remainder of the differentiation protocol (Figure 3.1). At day 16 of differentiation, cultures treated with DHT, TGF $\beta$ 1 and FGF10 consisted of neuroendocrine-like cells, cobblestone-like cells and cyst-like structures (Figure 3.7A, blue, red and yellow arrows respectively). Day 16 differentiated cultures treated with endoderm media alone displayed a neuron-like phenotype while cultures treated with endoderm media and methanol (vehicle) displayed elongated cells (Figure 3.7A).

Amplicons of predicted sizes for *Upk1b* (118bp), mouse androgen receptor (*AR*) (400bp) and *Nkx3.1* (195bp) were only detected in day 16 differentiated cultures treated with DHT, TGF $\beta$ 1 and FGF10 (Figure 3.7Bi). As the amplicon for *Nkx3.1* was faint, a nested PCR approach was used to determine expression (Figure 3.7Bii). Furthermore, a nested primer set for *Svs2* was also assessed in day 16 differentiated cultures. An amplicon of predicted size for *Svs2* (115bp) was detected in DHT, TGF $\beta$ 1 and FGF10 treated cultures (Figure 3.7Bii). No amplicons were detected in the No RT and no template control lanes.

**Figure 3.7: Day 16 differentiated mouse ES cell cultures treated with DHT, TGF $\beta$ 1 and FGF10 express prostate epithelial cell markers *Nkx3.1* and *Svs2*.**

(A) Representative bright-field images of day 16 differentiated mouse ES cultures treated with endoderm media (EDM) only, EDM and methanol (MeOH – vehicle) or EDM and DHT, TGF $\beta$ 1 and FGF10 (n=5 for each condition). Blue arrows indicate neuroendocrine-like cells. Red arrow indicates cobblestone-like cells. Yellow arrows indicate cyst-like structures. Scale bars represent 20  $\mu$ m.

(B) Total RNA was harvested from day 16 differentiated mouse ES cells treated with (i) EDM and methanol or (ii) EDM and DHT, TGF $\beta$ 1 and FGF10, and gene expression of *Upk1b* (118bp), mouse androgen receptor (*AR*, 400bp), *Nkx3.1* (195bp) examined. Nested primers for *Nkx3.1* (115bp) and *Svs2* (115bp) were used to enhance detection.  *$\beta$ -actin* (predicted amplicon size of 120bp) was run alongside as an internal control as well as No RT and NTC controls.





### **3.3.4.2 Development of acinus-like structures in DHT, TGFβ1 and FGF10 treated mouse ES cell cultures.**

By day 22 of differentiation, mouse ES cell cultures treated with DHT, TGFβ1 and FGF10 underwent pronounced morphological changes (Figure 3.8). Glandular, acinus-like structures with a developing lumen was identified in day 22 cultures treated with DHT, TGFβ1 and FGF10 (Figure 3.8). Control cultures treated with endoderm medium alone or endoderm medium with methanol (vehicle) exhibited an elongated, neuron-like morphology (Figure 3.8).

To confirm the differentiation of prostatic luminal epithelial cells from mouse ES cells, gene expression of androgen receptor (*AR*), probasin (*Pbsn*), *Nkx3.1*, *Svs2* and *Msmb* was examined in day 22 differentiated cultures (Figure 3.9). An amplicon of predicted size for androgen receptor (450bp) was detected by RT-PCR from total RNA of cells harvested from day 22 differentiated cultures (Figure 3.9A-Ci). An amplicon of predicted size for *Pbsn* (229bp) was identified in the RNA of day 22 differentiated cultures treated with DHT, TGFβ1 and FGF10 (Figure 3.9Ci). For *Nkx3.1*, no amplicons of predicted sizes were initially detected (Figure 3.9A-Ci). However, when nested primers for *Nkx3.1* and *Svs2* were used, amplicons of predicted size for *Nkx3.1* (115bp) and *Svs2* (115bp) were detected in day 22 differentiated cultures treated with DHT, TGFβ1 and FGF10 (Figure 3.9Cii). Amplicons of the same size were generated from the

RNA of mouse prostate tissue (positive control (Figure 3.9D). No amplicons were detected in the No RT and No template control lanes.

Gene expression of urothelial markers and pluripotency markers was then examined in day 22 differentiated cultures and adult mouse ventral prostate tissue (Figure 3.10). No amplicons for uroplakin proteins were identified in day 22 differentiated cultures treated with endoderm base medium alone or endoderm base medium with methanol (Figure 3.10A-B). Amplicons of predicted size for *Upk1b* (118bp) and *Upk2* (195bp) were generated in day 22 cultures treated with DHT, TGF $\beta$ 1 and FGF10 (Figure 3.10C). Amplicons of the same size for *Upk1b* and predicted size for *Upk1a* (151bp) were generated in the RNA of mouse prostate tissue (Figure 3.10Di). An amplicon of predicted size for *Oct4* (163bp) was detected in day 22 differentiated cultures (Figure 3.10A-C). Pluripotency markers were not expressed in the cDNA of mouse prostate tissue (Figure 3.10D). No amplicons were detected in the No RT and NTC lanes.

Table 3.4 summarises the detection of amplicons identifying landmark lineages throughout mouse ES cell differentiation.



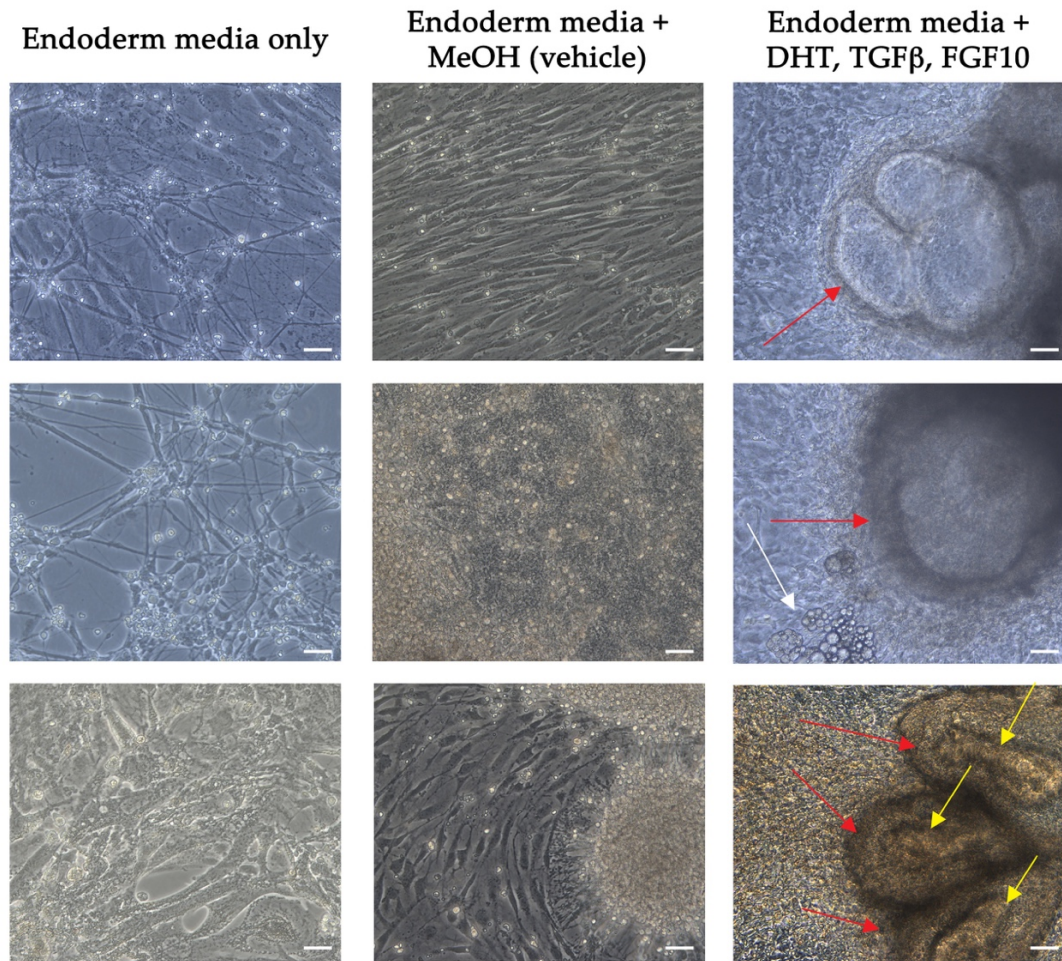


**Figure 3.8: The formation of acinus-like structures in day 22 mouse ES cell cultures treated with DHT, TGF $\beta$ 1 and FGF10.**

Representative bright-field images of day 22 differentiated mouse ES cultures treated with endoderm media (EDM) only, EDM plus methanol (MeOH – vehicle) or EDM plus DHT, TGF $\beta$ 1 and FGF10 (n=5 for each condition). Red arrow indicates acinus-like structures. White arrow indicates adipocyte-like cells. Yellow arrow indicates lumen-like structure. Scale bars represent 20  $\mu$ m.

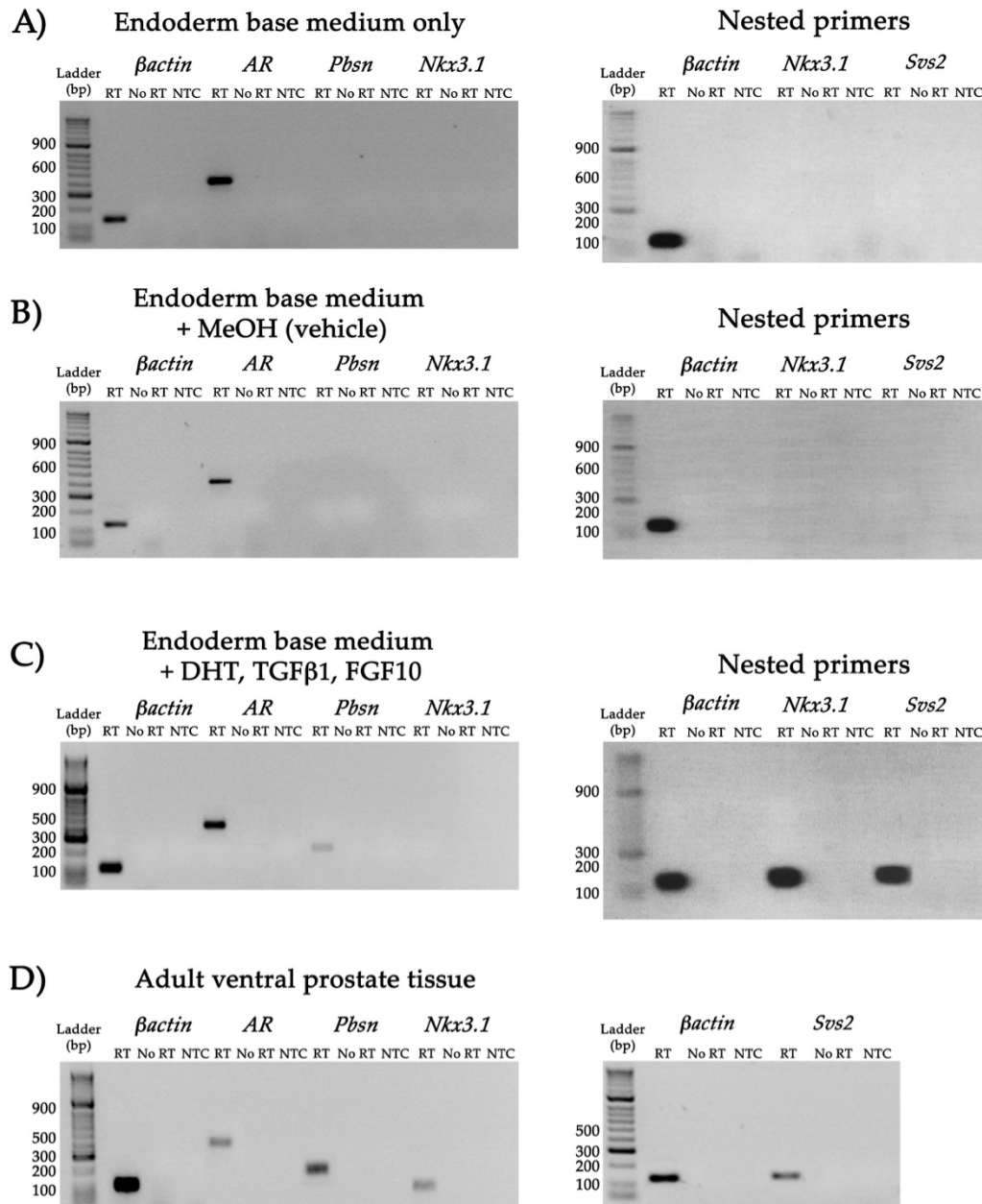
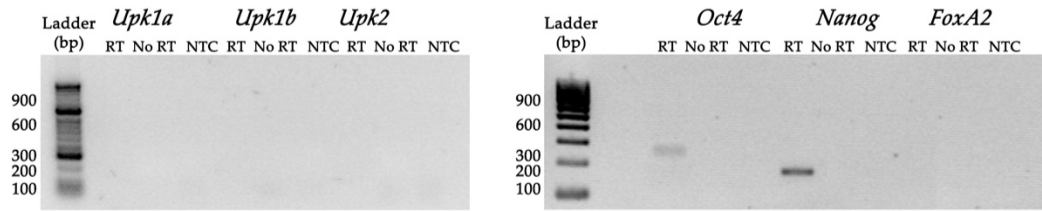


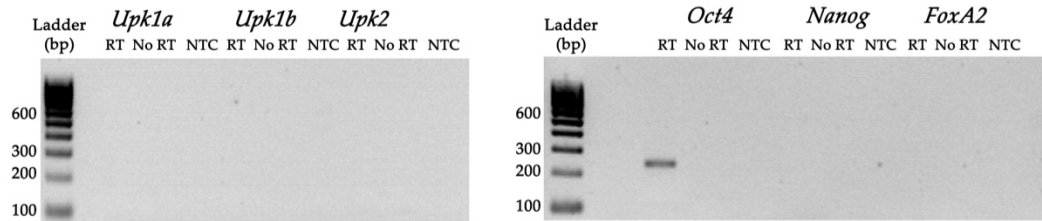
**Figure 3.9: Prostate epithelial cell markers *Pbsn* and *Nkx3.1* are expressed in day 22 differentiated cultures treated with DHT, TGFβ1 and FGF10.**

Total RNA was harvested from day 22 differentiated mouse ES cell cultures treated with (A) endoderm base medium alone, (B) endoderm base medium with methanol (MeOH, vehicle), (C) endoderm base medium with DHT, TGFβ1 and FGF10 and (D) adult mouse ventral prostate tissue (positive control) and gene expression for prostate epithelial cell markers examined. Predicted amplicon sizes for *Nkx3.1*, *Pbsn* and *AR* were 150bp, 229bp and 450bp respectively. Predicted amplicon sizes for nested *Nkx3.1* and *Svs2* are 115bp for each transcript. *β-actin* (predicted amplicon size of 120bp) was run alongside as an internal control as well as No RT and NTC controls.

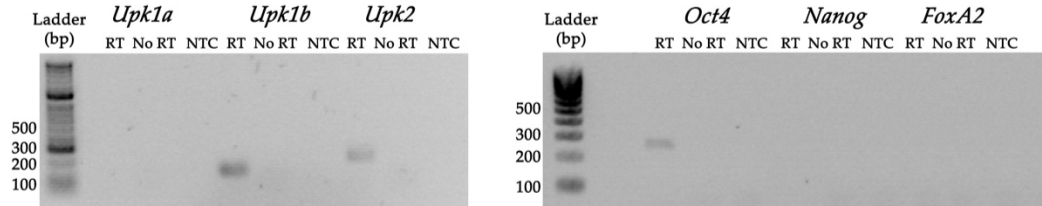
**A) Endoderm base medium only**



**B) Endoderm base medium + MeOH (vehicle)**



**C) Endoderm base medium + DHT, TGFβ1, FGF10**



**D) Adult ventral prostate tissue**

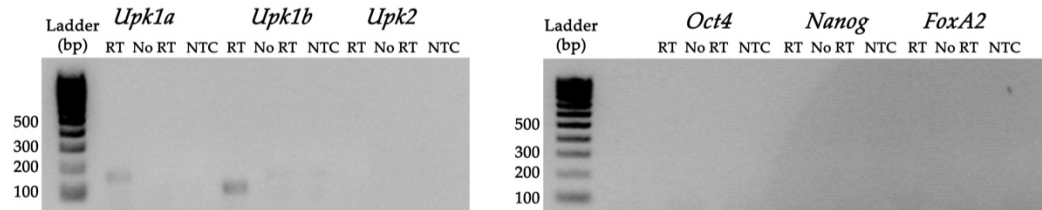


**Figure 3.10: Urothelial cell markers *Upk1b* and *Upk2* are expressed in day 22 differentiated cultures treated with DHT, TGFβ1 and FGF10.**

Total RNA was harvested from day 22 differentiated mouse ES cell cultures treated with (A) endoderm base medium alone, (B) endoderm base medium with methanol (MeOH, vehicle), (C) endoderm base medium with DHT, TGFβ1 and FGF10 and (D) adult mouse ventral prostate tissue and gene expression for (i) urothelial cell and (ii) pluripotency markers examined. Predicted amplicon sizes for *Upk1a*, *Upk1b*, *Upk2*, *Oct4*, *Nanog* and *FoxA2* are 150bp, 118bp, 195bp, 246bp, 163bp and 201bp respectively. *β-actin* (predicted amplicon size of 120bp) was run alongside as an internal control as well as No RT and NTC controls.

**Table 3.1: Summary of transcripts detected in the RNA of undifferentiated mouse ES cells, differentiated mouse ES cells and adult ventral prostate tissue.**

Cell type  Amplicon	Mouse ES cells	Day 5 Embryoid bodies		Day 12 Differentiated cultures		Day 16 Differentiated cultures		Day 22 Differentiated cultures			Adult ventral prostate tissue
		-AA -Wnt3A	+AA +Wnt3A	+EtOH (vehicle	+RA	+MeOH (vehicle)	+DHT +FGF10 +TGFβ1	+Base medium	+MeOH (vehicle)	+DHT +FGF10 +TGFβ1	
<i>β-actin</i>	+	+	+	+	+	+	+	+	+	+	+
<i>Oct4</i>	+	-	-	-	-	-	-	+	+	+	-
<i>Nanog</i>	+	-		-	-	-	-	+	-	-	-
<i>FoxA2</i>	-	+	+	-	-	-	-	-	-	-	-
<i>Upk1a</i>	-		-	-	-	-	-	-	-	-	+
<i>Upk1b</i>	-	-	-	-	+	-	+	-	-	+	+
<i>Upk2</i>	-	-	-	-	+	-	-	-	-	-	-
<i>mAR</i>	-	-	-	-	-	-	+	+	+	+	+
<i>Nkx3.1</i>	-	-	-	-	-	-	+	-	-	+	+
<i>Svs2</i>	-	-	-	-	-	-	+	-	-	+	+
<i>Pbsn</i>	-	-	-	-	-	-	-	-	-	+	+

### **3.3.5 Colony-stimulating factor 1 receptor (CSF-1R) is expressed on few cells in the developing urogenital sinus.**

Ide and colleagues (2002) published a report demonstrating immunohistochemical staining of mouse prostate tissue with CSF-1R (Ide et al., 2002). Staining was abundant in the developing (E17.5) urogenital tract but diminished by 8 weeks of development (Ide et al., 2002). Thus, to determine whether CSF-1R was a viable marker for developing prostate epithelial cells from differentiated mouse ES cells, surface protein expression was analysed on day 16 differentiated mouse ES cell cultures, developing prostate tissue from E18.5 embryos, newborn mice and 8-day-old mice and developed prostate tissue from pubertal and adult mice (Figure 3.11).

Epithelial cell adhesion molecule (EpCAM) was used in conjunction with CSF-1R to determine epithelial cell expression of CSF-1R (Figure 3.11). Surface protein expression of CSF-1R and EpCAM was not detected in day 16 differentiated mouse ES cell cultures (Figure 3.11). In the developing urogenital tract, 1% of the cell population exhibited CSF-1R immunoreactivity (Figure 3.11). Developing and developed prostate tissue had fewer than 1% of cells displaying CSF-1R surface protein expression (Figure 3.11).

As CSF-1R was not detected on day 16 differentiated mouse ES cell cultures by flow cytometry, gene expression of *Csf-1R* was assessed (Figure 3.12). An amplicon of predicted size for *Csf-1R* (150bp) was detected in the RNA of day 16 mouse ES cell cultures treated with or without DHT, TGF $\beta$ 1 and FGF10 as well as adult mouse prostate tissue (Figure 3.12).

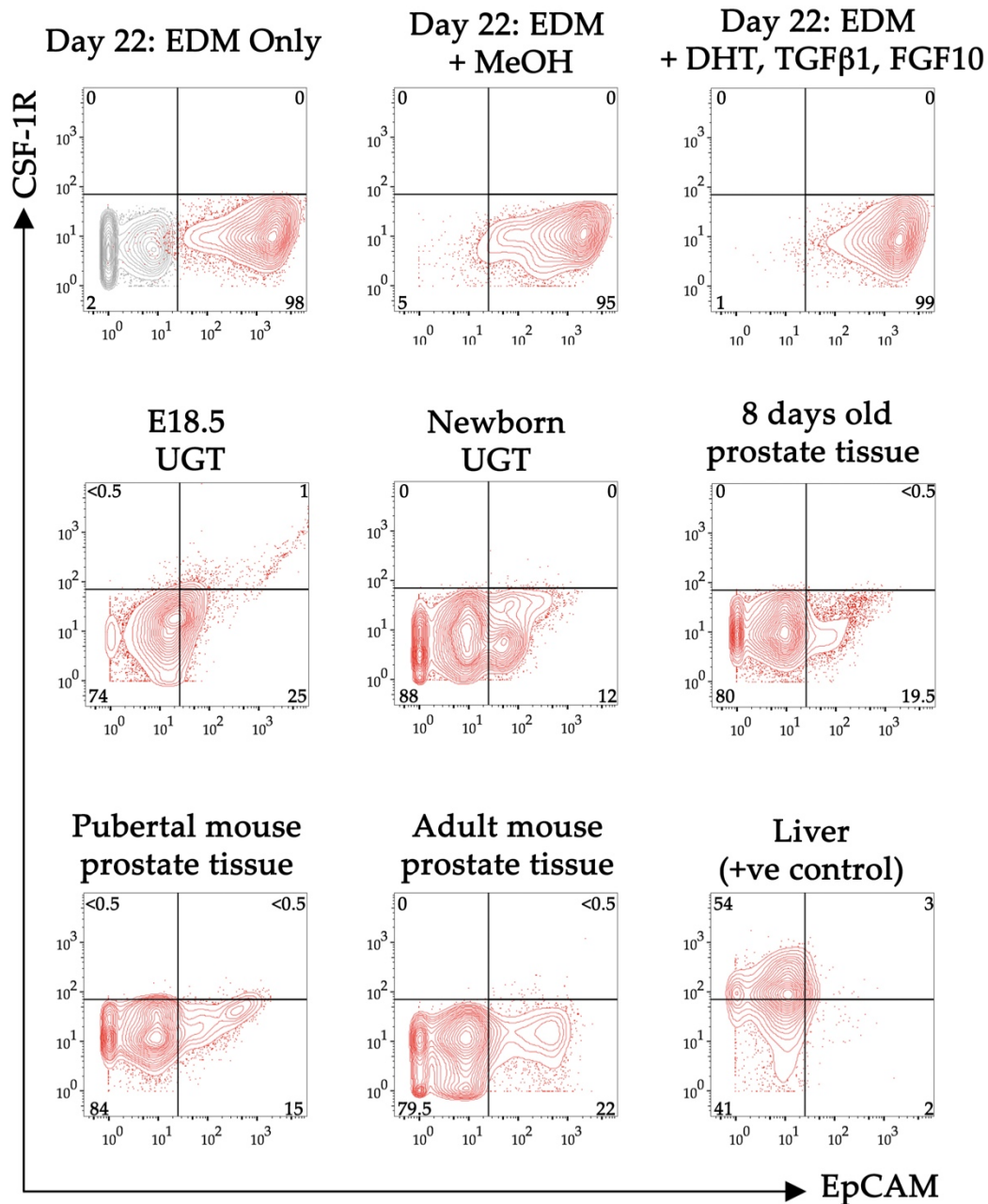


**Figure 3.11: Colony-stimulating factor 1 receptor (CSF-1R) is expressed on few cells in the developing urogenital tract.**

Representative flow cytometric plot of CSF-1R and epithelial cell adhesion molecule (EpCAM) surface protein expression on: day 22 differentiated mouse ES cells treated with endoderm media (EDM) only; EDM and methanol (MeOH – vehicle); EDM and DHT, TGFβ1 and FGF10; developing urogenital tract (UGT) from E18.5 embryos and newborn mice; ventral prostatic tissue from pubertal and adult mice and liver tissue (positive control for CSF-1R). Grey contour plot represents the isotype control while the blue contour plot represents the stained sample.



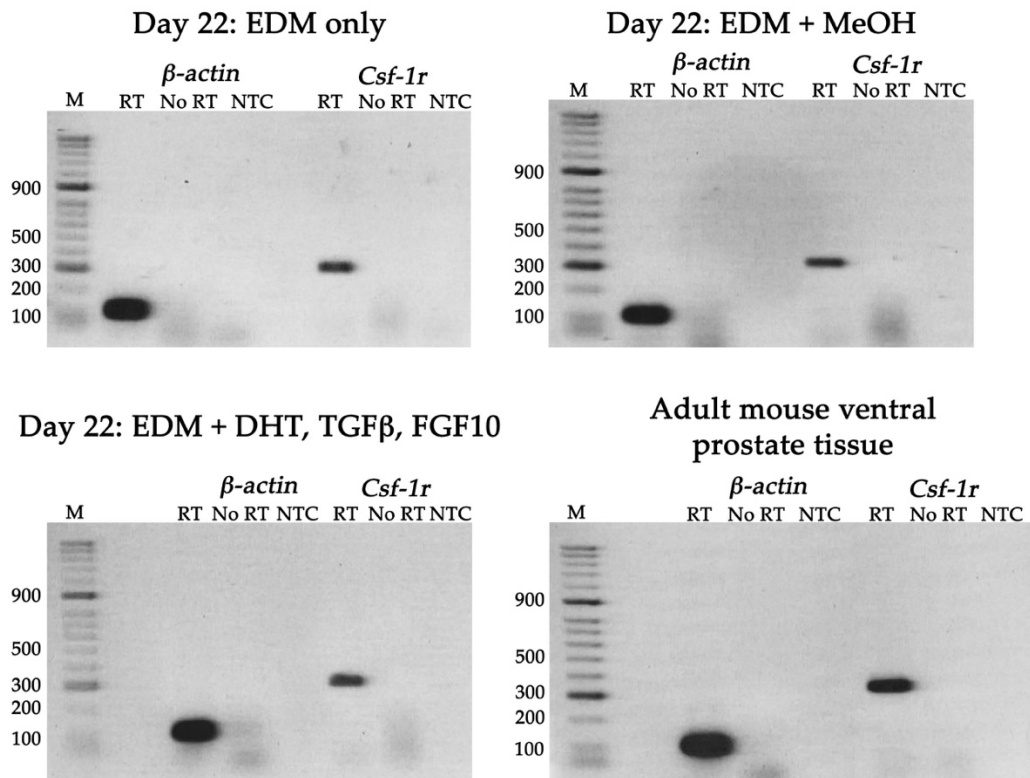


**Figure 3.12: *Csf-1R* is expressed on day 22 differentiated mouse ES cell cultures and adult mouse prostate tissue.**

Total RNA was harvested from day 22 differentiated mouse ES cell cultures treated with endoderm base medium (EDM) alone, EDM and methanol (MeOH, vehicle), EDM with DHT, TGFβ1 and FGF10 and adult mouse ventral prostate tissue and gene expression for *Csf-1R* (300bp) examined. *β-actin* (predicted amplicon size of 120bp) was run alongside as an internal control as well as No RT and NTC controls.



### **3.4 Discussion**

#### **3.4.1 Mouse ES cells as a model of prostate organogenesis**

Presented here is the first report of differentiating prostate epithelial cells from mouse ES cells. Studying the signalling processes during prostate development is challenging due to the small size of early embryos and accessibility of tissue. Many studies rely on *ex vivo* culture explants or transplantation of prostate epithelium into the kidney capsule of immunodeficient mice (Cunha et al., 1983; Cunha et al., 1987; Cunha et al., 2004; Taylor et al., 2006). As androgen signalling is critical for prostate development, it was hypothesised that treatment of mouse ES cell-derived urothelial cells with DHT, TGF $\beta$ 1 and FGF10 would drive differentiation towards prostatic epithelium. Mouse ES cell cultures treated with the aforementioned growth factors led to the development of cyst-like, acinus structures with a developing lumen, reminiscent of developing glandular prostatic epithelium.

##### **3.4.1.1 DHT, FGF10 and TGF $\beta$ 1 induce differentiation of prostate epithelial cells from mouse ES cell-derived urothelial cells.**

Mouse ES cells were differentiated along the endoderm lineage towards the urothelium and then further specified towards the prostate to recapitulate *in vivo* prostate development. Definitive endoderm differentiation was induced by Activin-A and Wnt-3A as described previously (D'Amour et al., 2005). Surface protein expression of endoderm markers c-Kit and CXCR4 in day 5 differentiated embryoid bodies reflected similar levels of expression achieved by Mfopou *et al.* (2014) and

Christadoulou *et al.* (2011). However, mouse ES cells can undergo spontaneous differentiation through paracrine and autocrine signalling (Davey & Zandstra, 2006; Roh *et al.*, 2017). Mesoderm markers Flk-1 and PDGFR $\alpha$  were not detected in differentiated mouse ES cell cultures indicating limited mesoderm differentiation. Serum-free conditions are also used to differentiate ES cells into neuronal cell types however, retinoic acid is required at the onset of ES cell differentiation to induce ectoderm differentiation (Kim *et al.*, 2009; Engberg *et al.*, 2010; Kawasaki *et al.*, 2000; Schulz *et al.*, 2004; Soprano *et al.*, 2007). Therefore, there was confidence that mouse ES cells treated with Activin-A and Wnt-3A were differentiating into definitive endoderm.

Retinoic acid induced urothelial cell differentiation from mouse ES cell-derived definitive endoderm as described in (Mauney *et al.*, 2010; Kang, Kim, & Han, 2014; Osborn *et al.*, 2014; Oottamasathien *et al.*, 2007). Retinoic acid is the main derivative of Vitamin A and plays roles in embryogenesis and cell differentiation (Soprano *et al.*, 2007). Terminal differentiation of urothelial cells is determined by uroplakin expression (Moll *et al.*, 1995). Uroplakins are specialised membrane proteins crucial for plaque formation on the apical surface of urothelium (Moll *et al.*, 1995). Expression of uroplakin proteins on mouse ES cell-derived endoderm cells treated with retinoic acid confirmed urothelial cell specification. Retinoic acid also plays a role in prostate epithelial cell specification (Bryant *et al.*, 2014). In the developing prostate, retinoic acid increases prostate epithelial cell budding (Bryant *et al.*, 2014). Here, retinoic acid

may be priming urothelial cells to differentiate into prostatic epithelium.

#### **3.4.1.2 Homeobox protein *Nkx3.1* is restricted to epithelial cells of the prostate and bulbourethral glands.**

Homeobox protein *Nkx3.1* is detected at E15.5 in the urogenital sinus of mice and marks the onset of prostate epithelial cell differentiation (Bhatia-Gaur et al., 1999). Gene expression of *Nkx3.1* is restricted to the endoderm derived epithelial cells of the prostate and bulbourethral gland (Abate-Shen et al., 2008). Wolffian duct derivatives such as the seminal vesicles, ductus deferens, ampullary gland and epididymis develop do not exhibit *Nkx3.1* gene expression (Abate-Shen et al., 2008; Dutta et al., 2016). Here, detection of *Nkx3.1* in differentiated mouse ES cell cultures confirmed the presence of differentiated prostatic epithelial cells or bulbourethral epithelial cells and not cells from other male sex accessory tissues.

#### **3.4.1.3 Probasin expression confirms the differentiation of prostatic epithelial cells.**

To distinguish between epithelial cells from the prostate and the bulbourethral gland, gene expression of probasin was assessed. Probasin is an androgen-regulated, prostate-specific protein found in all lobes of the prostate gland in rodents (Johnson et al., 2000). Expression of probasin is first detected around E17.5 as prostatic lobes undergo branching morphogenesis and remains expressed in the epithelium of terminally differentiated prostatic epithelial cells (Johnson et al., 2000; Abbott et al., 2003).

#### **3.4.1.4 Androgen receptor is not solely expressed in the organs of the male reproductive tract.**

Expression of mouse androgen receptor (*AR*) is not restricted to the prostate (Crocoll et al., 1998). During mouse embryogenesis, *AR* mRNA is first detected at E12.5 in the mesonephric mesenchyme, prior to embryonic hormone production (Crocoll et al., 1998). Expression of *AR* is found in the developing reproductive system of both male and female embryos (Crocoll et al., 1998). Mouse *AR* is strongly expressed in the urogenital mesenchyme surrounding the UGS, but is absent in the epithelial buds from which the prostate develops (Crocoll et al., 1998; Johnson et al., 2000). Rising levels of androgens during E14.5 to E17.5 act directly on the urogenital mesenchyme to induce prostate organogenesis (Cunha et al., 1973). Thus, it could be possible that detection of *AR* in differentiated mouse ES cell cultures was indicative of the urogenital mesenchyme, a crucial component for normal prostate organogenesis. Expression of *AR* has also been detected in the adrenal gland, pituitary gland, the liver, the bladder, the gastrointestinal tract as well as on adipocytes (de Winter et al., 1991; Crocoll et al., 1998; Dieudonne et al., 1998).

#### **3.4.1.5 Evaluation of colony stimulating factor 1 receptor (CSF-1R) as a marker of prostate development.**

CSF-1R was chosen as a candidate marker for the identification of prostate epithelial cell differentiation from mouse ES cells at the single cell level. Ide and colleagues (2002) characterised CSF-1R expression in the developing prostate by

immunohistochemistry with staining localised on the basal epithelial cells of the prostate (Ide et al., 2002). Expression of CSF-1R was absent in mature prostatic tissue but present in prostatic tissue isolated from transgenic adenocarcinoma of the mouse prostate (TRAMP) (Ide et al., 2002). Here, surface protein expression of CSF-1R was detected on few cells in the urogenital sinus of E17.5 embryos at the single cell level. Gene expression of *Csf-1r* was also evaluated using the primer sets detailed by Ide *et al.* (2002) (Ide et al., 2002). Since *Csf-1r* was detected in differentiated mouse ES cells from all culture conditions, it was concluded that CSF-1R was not a suitable marker for prostate cell differentiation from mouse ES cells.

#### **3.4.1.6 Applications for prostate epithelial cell differentiation from mouse ES cells.**

So, what can the differentiated prostate epithelial cells be used for? Differentiation of endoderm derivatives such as pancreatic  $\beta$ -cells and hepatocytes propose a possible therapeutic approach for the treatment of diabetes and cirrhosis respectively (Jiang et al., 2007; Liu & Lee, 2012; Yoshida et al., 2011; Little et al., 2007). Prostate cell transplantation is unnecessary and ineffective in the case of androgen receptor insensitivity syndrome (Li et al., 2005). Instead, mouse ES cell differentiation of the prostate can be used to model changes in genotype and subsequent phenotype during progression of prostate oncogenesis. Many of the processes and signalling for *in vivo* development of the prostate are reactivated in oncogenesis (Schaeffer et al., 2008; Abate-Shen et al., 2008; Gingrich et al., 1996). Prostate-specific regulatory genes critical for normal prostate organogenesis such as *Nkx3.1* and *Pbsn* also play roles in prostate

carcinogenesis (Abate-Shen et al., 2008; Greenberg et al., 1994). Gene editing tools such as CRISPR can be utilised to over-express or knock out *Nkx3.1* from mouse ES cells and examine how prostate epithelial cells differentiate.

### 3.4.2 Conclusions

In this chapter, the protocol successfully induced prostate epithelial cell differentiation in a stage dependent manner. Definitive endoderm was generated as demonstrated by c-Kit and CXCR4 surface protein expression and *FoxA2* gene expression. Urothelial cell differentiation was induced with retinoic acid and confirmed through *Upk1b* and *Upk2* gene expression. Finally, treatment of mouse ES cell-derived urothelial cells with DHT, FGF10 and TGF $\beta$ 1 led to the apparent differentiation of prostatic luminal epithelial cell as confirmed by gene expression of *Nkx3.1*, *Svs2* and *Pbsn*.

Alongside prostate epithelial cell differentiation, adipocyte-like cells were unexpectedly generated (Figure 3.8, white arrow). The development of adipocyte-like cells from conditions designed to promote endoderm differentiation has not been reported. The focus of the subsequent chapters in this study will be the characterisation of the differentiated adipocyte-like cells.

## **Chapter 4: Endoderm culture conditions unexpectedly drive differentiation of adipocyte-like cells from mouse ES cells *in vitro*.**

### **4.1 Introduction**

In Chapter 3, mouse ES cells were differentiated into prostate epithelial cells *in vitro* in a stepwise manner. Mouse ES cells treated with DHT, TGF $\beta$ 1 and FGF10 developed cyst-like, acinus structures resembling prostate epithelial cells. Detection of prostate epithelial cell-specific genes *Nkx3.1* and *Pbsn* confirmed successful of prostatic epithelial cells. Unexpectedly, cell types containing lipid droplets were also observed in differentiated cultures (Figure 3.8). The differentiation of adipocyte-like cells is unexpected as they have not been reported to develop from mouse ES cells under conditions designed to promote endoderm differentiation.

#### **4.1.1 Developmental origins of adipocytes**

The two main classes of adipose tissue are brown and white adipose tissue (BAT and WAT respectively). WAT can be further divided into subcutaneous and visceral adipose depots. Brown and white adipocytes were originally thought to be from the same mesodermal precursor (Berry et al., 2013). However, lineage tracing studies identified brown adipocytes stemming from myogenic factor-5 (*Myf5*)-expressing precursors, a gene thought to be exclusive to the myogenic lineage (Seale et al., 2008). Brown adipocytes develop before white adipocytes as precursors can be distinguished

around E11.5 of gestation and morphologically distinct at E14.5 in the mouse (Chabowska-Kita & Kozak, 2016). Conversely, visceral white adipocytes reportedly stem from the lateral plate mesoderm (Feng et al., 2013). Wilms' tumour (*Wt1*) expressing precursors have been proposed a source for visceral but not subcutaneous white adipocytes (Chau et al., 2014). Visceral white adipocytes have been identified from *Wt1* precursors at E14.5 (Chau et al., 2014).

#### **4.1.2 Morphology of brown and white adipocytes**

Brown and white adipocytes are morphologically distinct. Brown adipocytes contain a central nucleus, multi-locular lipid droplets and high numbers of mitochondria (Cannon & Nedergaard, 2004). Conversely, white adipocytes contain a central unilocular lipid droplet (stored as neutral lipids) that occupies up to 95% of the cell volume (Lee, Wu, & Fried, 2013). The nucleus and mitochondria are eccentrically located.

#### **4.1.3 Aims**

Although prostate epithelial cells were differentiated from mouse ES cells, current ES cell differentiation protocols do not result in 100% of the final cell type desired (Zhu & Huangfu, 2013). In Chapter 3, spindle-like cells, neuron-like cells and epithelial cells were identified in cultures (Figure 3.8). The most striking cell type observed however, was lipid-droplet containing cells in close proximity to the acinus structures (Figure 3.8). Here, the aim was to characterise the lipid-droplet containing cells by



morphology and lipophilic dye uptake to determine whether the differentiated cells are adipocytes.

## **4.2 Methods:**

### **4.2.1 Cell culture**

The conditions used for mouse ES cell differentiation are outlined in 3.2.1-3.2.3. Fibroblast cell line 3T3-L1-derived adipocytes were provided by Dr. Andrew Hoy (Lipid Metabolism Laboratory, University of Sydney, Australia) and cultured as described by Zebisch *et al.* (2012).

### **4.2.2 Oil Red O staining**

Oil Red O was reconstituted according to manufacturer's instructions. Differentiated mouse ES cells were fixed in 10% formalin for 10 minutes. Following fixation, differentiated mouse ES cells were washed with 60% isopropanol. Oil Red O was then added for 15 minutes, discarded and cells rinsed with 60% isopropanol followed by distilled water. Oil Red O stained cells were viewed under light microscopy.

### **4.2.3 Nile Red staining**

Nile Red was dissolved in DMSO to a stock concentration of 10 mmol.L<sup>-1</sup> as previously described (Schaedlich et al., 2010). The stock concentration was diluted to a working solution of 100 µmol.L<sup>-1</sup> in DMSO. Nile Red was added to differentiated mouse ES cell cultures at a final concentration of 100 nmol.L<sup>-1</sup> in FACS buffer for 10 minutes at room temperature. Cells were then washed with PBS and viewed under epifluorescence microscopy.

#### **4.2.4 Imaging**

Light and epifluorescent microscopy was performed on an Axiovert35 (Zeiss, Germany) microscopy under 20x and 32x magnification (ACROSTIMA 20x and 30x objective, NA: 0.40 and NA: 0.30 respectively) equipped with a mercury lamp (Zeiss, Germany). Nile Red was excited at 510 nm using the Zeiss Axiovert Microscope Filter Slider (Zeiss, Germany). Images were taken using the ZEN 2011 imaging software (Zeiss, Germany).

#### **4.2.5 Measurement of lipid droplets**

Quantification of cells with lipid droplets and measurement of lipid droplet area was performed using Image J software (NIH, USA). To ensure there was no bias in measurements, cells containing lipid droplets that only intersected a 5x5 grid were included for analyses. Lipid droplet size was determined by measuring the diameter at two points. Measurements were normalised to cell area ( $\mu\text{m}^2$ ).

#### **4.2.6 Statistical analyses**

Data presented as mean  $\pm$  SEM. Differences in lipid droplet number and area between culture conditions were determined using a two-tailed, one-way ANOVA and pairwise *post-hoc* comparison by Tukey's HSD test. A *P* value less than 0.05 was deemed significant.

## **4.3 Results**

### **4.3.1 Detection of adipocyte-like cells derived from mouse ES cells in endoderm conditions.**

In Chapter 3, prostatic epithelial cells were differentiated from mouse ES cells in a stepwise manner using chemically defined serum-free medium (3.2.3). In conjunction to the development of acinus structures, cells that resembled adipocytes were also identified (Figure 3.8).

#### **4.3.1.1 Adipocyte-like cells derived from mouse ES cells first appear at day 12 of differentiation in endoderm culture conditions.**

Mouse ES cell cultures were imaged between day 8 and day 22 of differentiation to determine when the adipocyte-like cells appeared (Figure 4.1). No adipocyte-like cells were identified at day 8 of differentiation (Figure 4.1). Clusters of circular, lipid-containing cells were first identified at day 12 of differentiation in all conditions and persisted until the end time point of day 22 (Figure 4.1, yellow arrows). Additionally, adipocyte-like cells were interspersed with spindle-like cells and identified within the neuron-like projections in the control conditions (Figure 4.1). By day 22 of differentiation, adipocyte-like cells were identified in specific clusters and close to acinus structures in the EDM with DHT, TGF $\beta$ 1 and FGF10 treatment group.

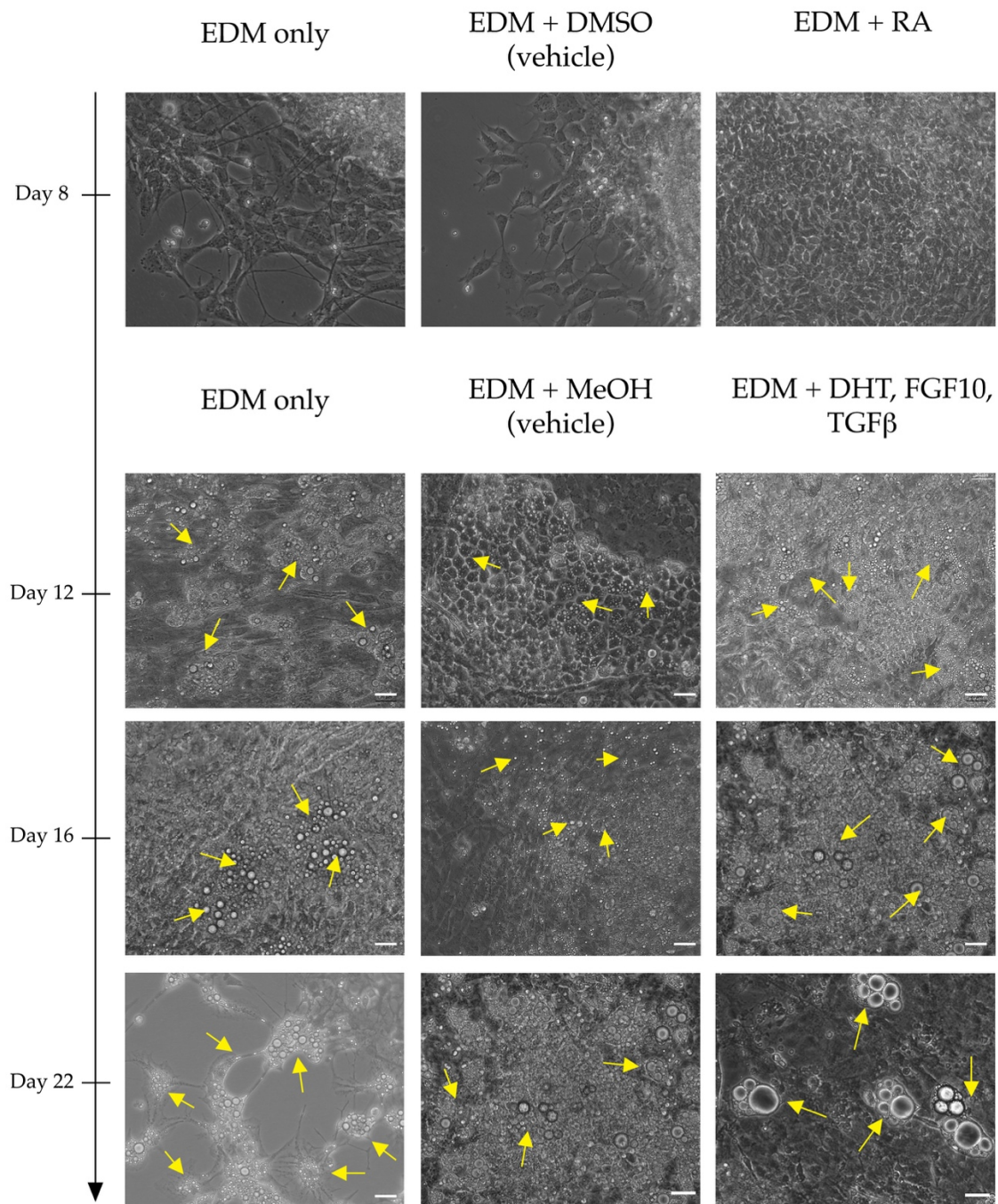


**Figure 4.1: Adipocyte-like cells are first identified at day 12 of differentiation in endoderm culture conditions.**

Representative bright-field images of differentiated mouse ES cells treated with endoderm base medium (EDM) alone (left), EDM with DMSO (vehicle) or EDM with retinoic acid (RA) at day 8 of differentiation and EDM with methanol (MeOH) or DHT, FGF10 and TGFβ1 at days 12, 16 and 22 of differentiation. Yellow arrows indicate adipocyte-like cells containing lipid droplets. Scale bars represent 20 μm.

#### **4.3.1.2 Mouse ES cells treated with DHT, TGF $\beta$ 1 and FGF10 have the largest adipocyte-like cells.**

To determine whether there were differences in the adipocyte-like cells between endoderm conditions, the quantity and size of the lipid droplets were compared (Figure 4.2,4.3). Cells containing lipid droplets that intersected a 5x5 grid were used for analyses. The quantity and size of the lipid droplets were normalised to cell area (Figure 4.2,4.3). No differences were observed in the amount of lipid droplets per cell area (Figure 4.3i). Conversely, adipocyte-like cells derived from mouse ES cells treated with DHT, TGF $\beta$ 1 and FGF10 were larger compared to endoderm base medium ( $P < 0.0001$ ) and the vehicle control ( $P < 0.0001$ ) (Figure 4.3ii).

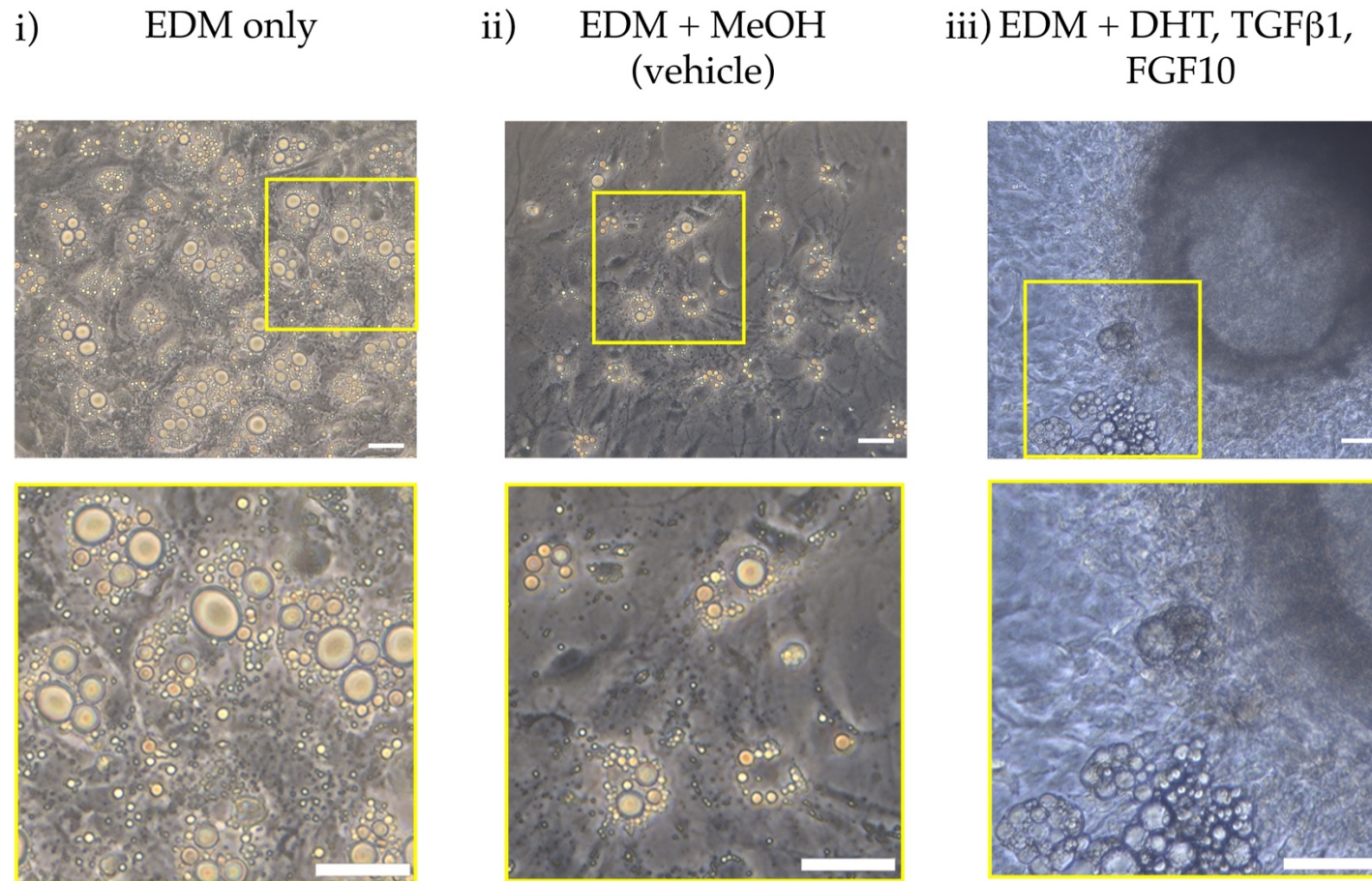


**Figure 4.2: Adipocyte-like cells differentiate from mouse ES cells under endodermal culture conditions.**

Representative bright-field images of differentiated mouse ES cells treated with (i) endoderm base medium (EDM) alone, (ii) EDM with methanol (MeOH) and (iii) EDM with DHT, FGF10 and TGFβ1 at day 22 of differentiation. Yellow boxed region indicates digital magnification of boxed area. Scale bars represent 20 μm.



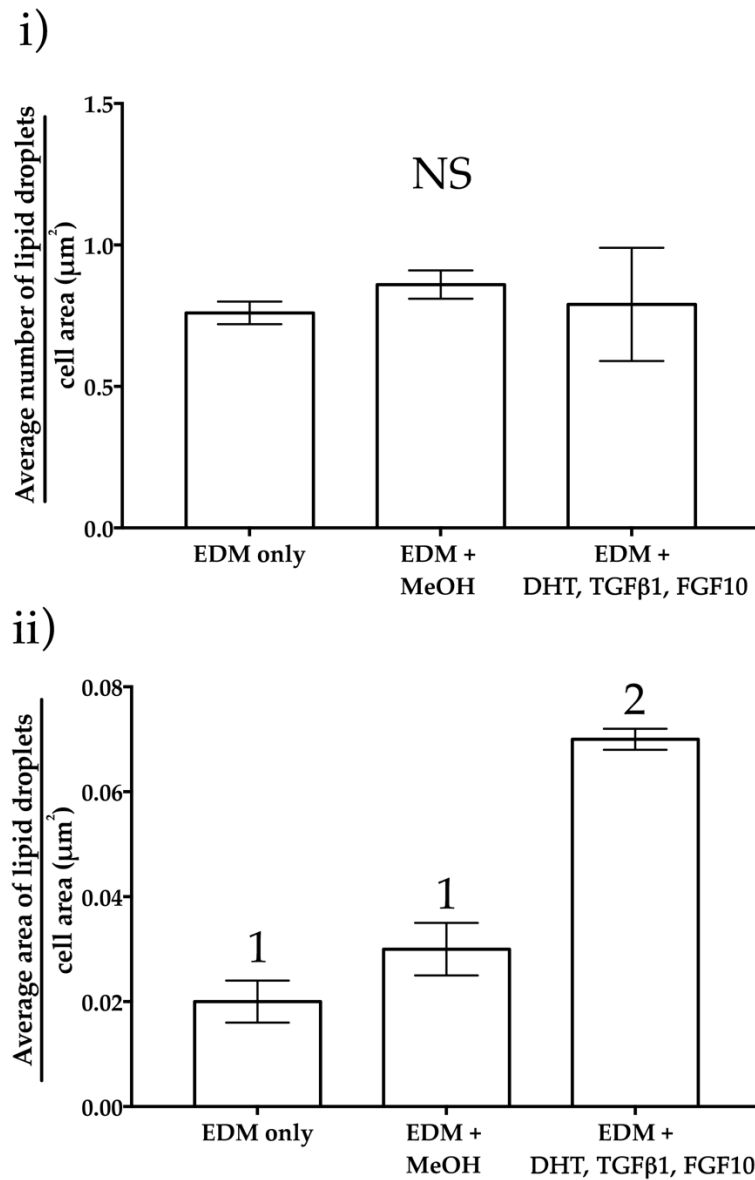


**Figure 4.3: Adipocyte-like cells derived from mouse ES cell treated with DHT, TGFβ1 and FGF10 are larger compared to endoderm base medium and vehicle control.**

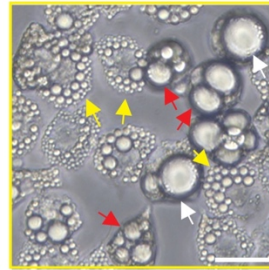
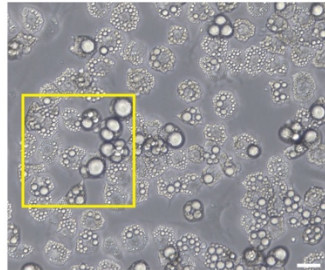
Comparisons in the (i) quantity and (ii) area of lipid droplets from adipocyte-like cells derived from endoderm base medium (EDM) only, EDM plus methanol (MeOH), and EDM plus DHT, TGFβ1 and FGF10. Lipid droplet number and area were measured on cells that intersected a 5x5 grid across 10 fields of view. At least 25 cells containing lipid droplets were measured and normalised to cell area (µm<sup>2</sup>). Data presented as mean ± SEM (n=3). Differences in lipid droplet number and area between culture conditions were determined using a two-tailed, one-way ANOVA and pairwise *post-hoc* comparison by Tukey's HSD test. Groups not sharing a numeral are significantly different from each other. NS = not significantly different from each other.



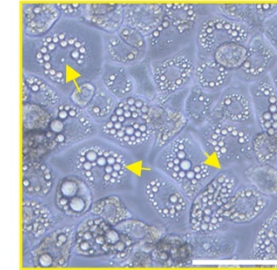
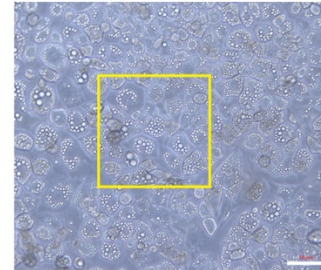
### **4.3.2 Adipocyte-like cells derived from mouse ES cells resemble 3T3-L1-derived adipocytes and isolated primary adipocytes.**

The morphology of the adipocyte-like cells differentiated from mouse ES cells were then compared to adipocytes derived from the 3T3-L1 fibroblast cell line and primary brown and white adipocytes (Figure 4.4). The adipocyte-like cells derived from mouse ES cells had clusters of lipid droplets similar to those in the 3T3-L1 cell line (Figure 4.4i-ii, yellow arrows). Further, the adipocyte-like cells derived from mouse ES cells contained multi-locular (red arrows) and unilocular (white arrows) lipid droplets that resemble brown and white adipocytes respectively (Figure 4.4iii-iv). The close resemblance in phenotype to an established adipocyte cell line as well as primary adipocytes reinforced the possibility that the differentiated cells are adipocytes.

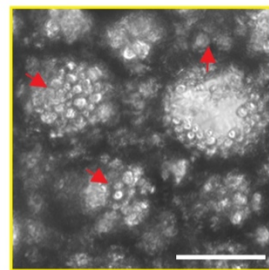
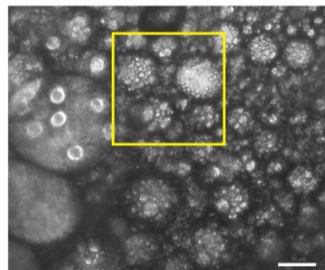
i) Mouse ES derived adipocyte-like cells



ii) 3T3-L1 Adipocytes



iii) Primary brown adipocytes



iv) Primary white adipocytes

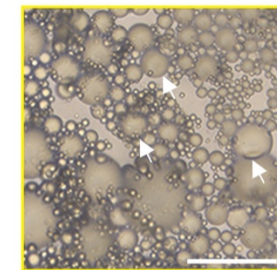
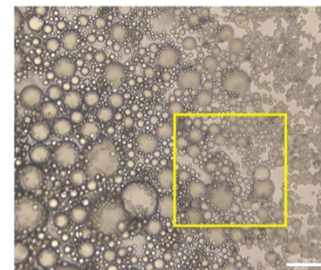


**Figure 4.4: Adipocyte-like cells derived from mouse ES cells resemble adipocytes from the 3T3-L1 cell line and primary adipocytes.**

Representative bright-field images of (i) endoderm derived adipocyte-like cells, (ii) 3T3-L1 derived adipocytes, (iii) primary brown and (iv) white adipocytes. Yellow boxed region is the digital magnification of the boxed region. Yellow arrows indicate similarities to adipocytes from 3T3-L1 cells. Red arrows indicate multi-locular lipid droplets. White arrows indicate unilocular lipid droplets. Scale bars represent 20  $\mu\text{m}$ .

#### **4.3.4 Lipophilic dyes Oil Red O and Nile Red stain adipocyte-like cells derived from mouse ES cells.**

To confirm the adipocyte-like cells contained lipids, lipophilic dyes Oil Red O and Nile Red were used for staining. Oil Red O has been used to stain adipocytes differentiated from mouse ES cell cultures (Dani et al., 1997; Billon et al., 2007; Cuaranta-Monroy et al., 2015). Here, Oil Red O intensely stained the lipid droplets in the adipocyte-like cells derived from mouse ES cells in all culture conditions (Figure 4.5i-iii). Upon enhancing the field of view, cells without lipid droplets were not stained with Oil Red O (Figure 4.5i-iii).

Nile Red is a fluorescent lipophilic dye that stains neutral lipids (Smith, 1908; Smith, 1911; Fowler & Greenspan, 1985). Nile Red has been used to stain 3T3-L1-derived adipocytes as well as SGBS-derived pre-adipocytes (Aldridge et al., 2013; Kim et al., 2015; Doan-Xuan et al., 2013). Nile Red is advantageous over Oil Red O as staining can be applied to live cells. Similar to Oil Red O, Nile Red only stained the lipid droplets in the adipocyte-like cells in all culture conditions (Figure 4.6i-iii). Cells that did not contain lipid droplets exhibited no Nile Red staining. Nile Red also distinguished the smaller lipid droplets more clearly than Oil Red O (Figure 4.6ii-iii).

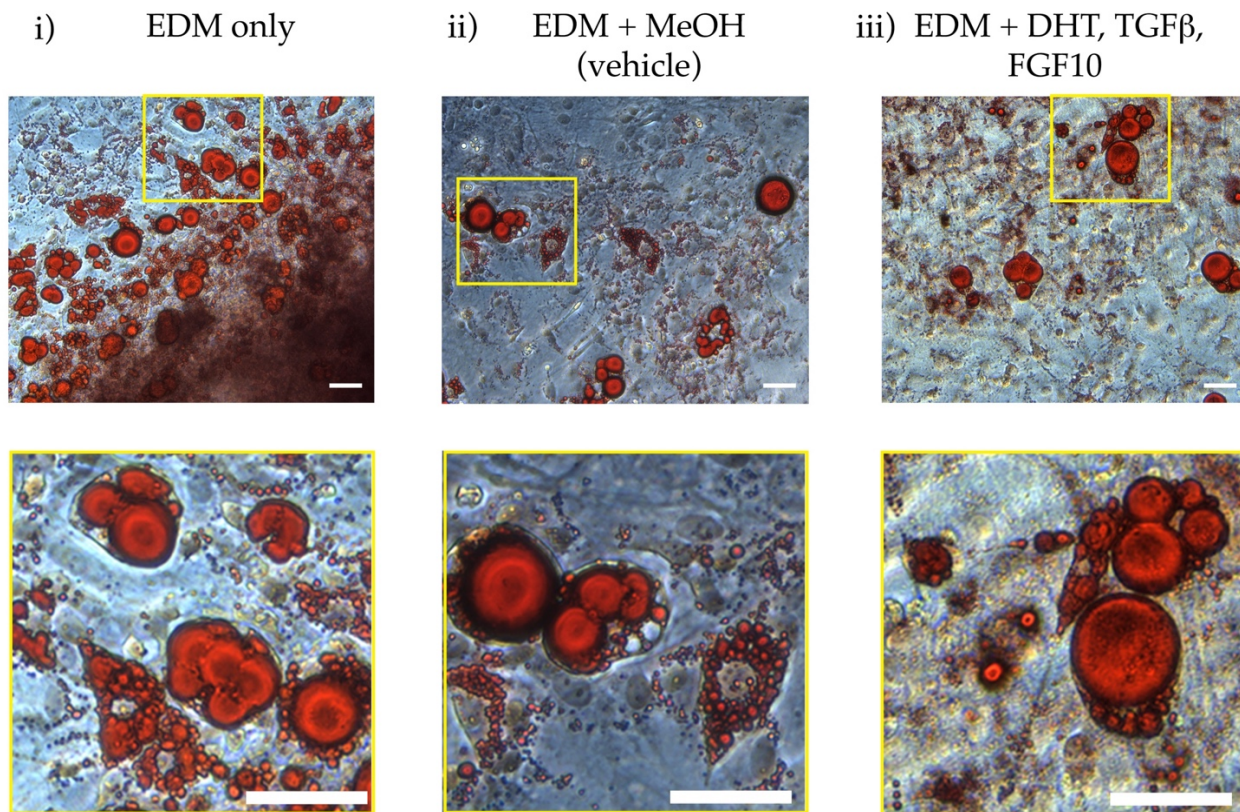
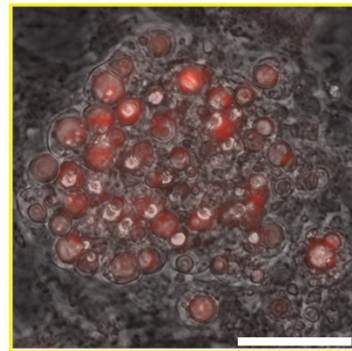
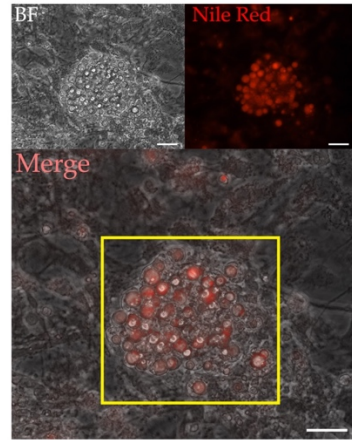


**Figure 4.5: Oil Red O stains the lipid droplets in the mouse ES cell derived adipocyte-like cells.**

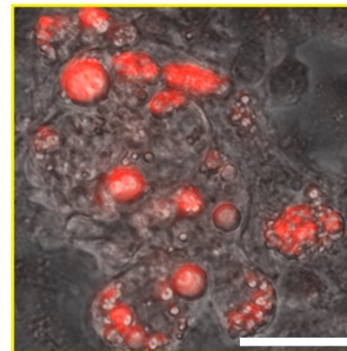
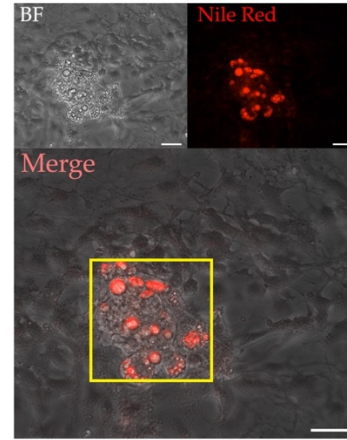
Representative bright-field images of Oil Red O stained differentiated mouse ES cells treated with (i) endoderm base medium (EDM) alone, (ii) EDM plus methanol (MeOH) and (iii) EDM plus DHT, FGF10 and TGF $\beta$ 1 at day 22 of differentiation. Yellow boxed region is the digital magnification of the boxed region. Scale bars represent 20  $\mu$ m.



i) EDM only



ii) EDM + MeOH  
(vehicle)



iii) EDM + DHT, FGF10,  
TGF $\beta$

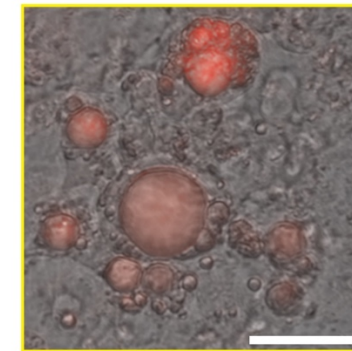
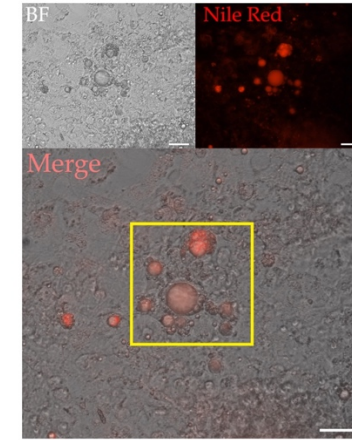


**Figure 4.6: Nile Red stains the lipid droplet within the mouse ES cell derived adipocyte-like cells.**

Representative bright-field (BF) and epifluorescent images of Nile Red stained differentiated mouse ES cells treated with (i) endoderm base medium (EDM) alone, (ii) EDM plus methanol (MeOH) and (iii) EDM plus DHT, TGF $\beta$ 1 and FGF10 at day 22 of differentiation. Yellow boxed region is the digital magnification of the boxed region. Scale bars represent 20  $\mu$ m.

## 4.4 Discussion

### 4.4.1 Adipocytes arise from mouse ES cells under endodermal culture conditions.

Presented here is the first report of adipocyte-like cells differentiated from mouse ES cells under conditions designed to promote endoderm differentiation. Adipocytes are derived from the mesoderm and in some cases the neural crest (Sanchez-Gurmaches & Guertin, 2014; Billon et al., 2007). Extensive interrogation of the literature failed to find reports of an endoderm origin of adipocytes. Adipocytes are classed as brown or white adipocytes (reviewed in: (Berry et al., 2013). Brown adipocytes stem from the paraxial mesoderm at E11.5 (Gesta, Tseng, & Kahn, 2007). White adipocytes are divided into subcutaneous and visceral depots and are derived from the lateral plate mesoderm (Chau & Hastie, 2014; Chau et al., 2014; Björntorp & Östman, 1971). The lateral plate mesoderm also gives rise to cardiac tissue, red blood cells, endothelial cells and smooth muscle (Grubb, 2006). Beating patches (indicative of cardiomyocyte differentiation), endothelial sheets and haematopoietic cells were not observed in the mouse ES cell cultures described in Chapter 3 and Chapter 4. Furthermore, as reported in Chapter 3, no Flk-1 or PDGFR $\alpha$  expression was detected under these culture conditions. Taken together, the adipocyte-like cells were not likely to be generated from the mesoderm.

Adipocytes are not the only cell type to contain lipid droplets. Endoderm-derived hepatocytes and enterocytes are involved in lipid metabolism and secrete triglycerides into circulation in the form of very-low density lipoprotein (Enjoji, Kohjima, &

Nakamuta, 2016; Nguyen et al., 2008; Hussain, 2014). Hepatocytes and enterocytes are fore- and midgut endoderm derivatives respectively (reviewed in: Grapin-Botton, 2008). The culture conditions described here were designed to induce hindgut endoderm as demonstrated in Chapter 3. Furthermore, hepatocytes and enterocytes are columnar epithelial cells with a central nucleus and connected by tight junctions (Grubb, 2006). Conversely, white adipocytes are circular cells with a unilocular lipid droplet that occupies up to 90% of the cell and an eccentrically located nucleus (Lee et al., 2013). Brown adipocytes have smaller lipid droplets surrounded by abundant amounts of mitochondria (Cannon & Nedergaard, 2004). The cells containing lipid droplets in the differentiated mouse ES cell cultures were clustered together and circular in morphology. Intense staining with lipophilic dyes Oil Red O and Nile Red reinforced the adipocyte-like morphology. Thus, the lipid-droplet containing cells are more similar to adipocytes than enterocytes or hepatocytes. Future studies will aim to confirm adipocyte differentiation at the molecular level by gene expression analyses of brown adipocyte marker *Ucp1* and white adipocyte markers *Fabp4*, *Leptin* and *Adiponectin*.

#### **4.4.2 Comparisons between mouse ES cell-derived adipocytes differentiated from the mesoderm, neural crest and endoderm culture conditions.**

Differentiation of mesoderm-derived and neural-crest derived adipocytes from mouse ES cells has been reported (Cuaranta-Monroy et al., 2015; Billon et al., 2007). The adipocytes derived from the neural-crest have been postulated to give rise to

cephalic white adipose tissue found in the face (Billon et al., 2007). Conversely, mesoderm-derived adipocytes have been likened to subcutaneous white adipocytes (Cuaranta-Monroy et al., 2015). The differentiated adipocyte-like cells can be labelled and traced through cell lineage and fate mapping to determine which adipose depot they ultimately form. A similar approach could be used to reveal a possible endoderm origin of adipocytes.

#### **4.4.3 Conclusion**

Apparent adipocytes, cell types typically associated with the mesoderm germ layer, were generated in endoderm culture conditions in which prostate epithelial cells were differentiated. The morphology of the adipocyte-like cell closely resembles 3T3-L1 derived adipocytes as well as adipocyte isolated from primary sources. This is the first report of adipocytes differentiated from mouse ES cells under endoderm culture conditions. To determine whether the adipocytes are representative of a specific adipose depot, a flow cytometric method to assess adipocytes is required and will be the focus of the following chapters.



## Chapter 5: Development of a flow cytometric method to characterise probe uptake in adipocytes at the single cell level.

### 5.1 Introduction

In Chapter 4, adipocyte-like cells differentiated *in vitro* from mouse ES cells resembled the morphology of white and brown adipocytes. Molecular markers of white adipocytes (*Fabp4*, *Ppar $\gamma$*  and *Adiponectin*) do not distinguish adipocytes from white adipose depots (Tang et al., 2008; Birsoy et al., 2011). Proteomic analyses by mass spectrometry have identified differences between brown and gonadal adipocytes (Forner et al., 2009). However, optimisation for the analysis of a single analyte by mass spectrometry is a time consuming and costly process. Furthermore, lipids must be extracted from biological samples resulting in the destruction of the cells (Kofeler et al., (2012). Flow cytometry is a powerful analytical tool that can sort live cells based on cell size, granularity, surface protein expression and dye uptake as outlined in Table 5.1.

**Table 5.1: Characteristics of undifferentiated mouse ES cells, prostate epithelial cells, white adipocytes and brown adipocytes.**

	<b>Mouse ES cell</b>	<b>Prostate epithelial cell</b>	<b>White adipocyte</b>	<b>Brown adipocyte</b>
<b>Size</b>	Small	Intermediate	Large	Small - intermediate
<b>Granularity</b>	Low	High	High	High
<b>Nucleus:Cytoplasm</b>	Large	Small	Small	Intermediate
<b>Shape</b>	Cuboidal	Cuboidal/columnar	Round	Round/elliptical
<b>Lipid content</b>	?	?	Unilocular lipid droplet	Multi-locular lipid droplets
<b>Mitochondria</b>	Many	Many	Few	Many
<b>Surface protein expression</b>	EpCAM eCad PECAM	EpCAM eCad	??	??

### **5.1.1 There is a need for flow cytometric analyses of mature adipocytes.**

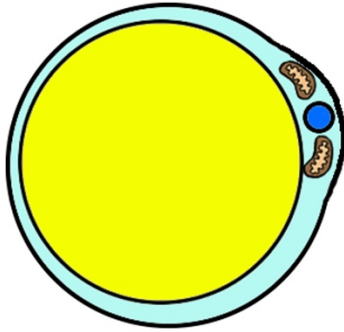
For mature adipocytes, flow cytometry has been used to assess; lipid accumulation in adipocytes; adipocytes derived *in vitro* from myeloid and bone marrow progenitors and adipocytes isolated from a single adipose depot (Lee, 2004; Majka et al., 2010; Crossno et al., 2006; Majka et al., 2014; Durandt et al., 2016; Festy et al., 2005). Reports characterising live, mature adipocytes from multiple adipose depots at the single cell level are limited. One complication in analysing adipocytes at the single cell level is contamination from the stromal vascular fraction (SVF) (Majka et al., 2014).

### **5.1.2 The stromal vascular fraction (SVF) of brown and white adipose tissue.**

Brown and white adipose tissues are comprised of more than just adipocytes. The SVF of adipose tissues consists of a subset of endothelial cells, macrophages, immune cells, pre-adipocytes and multipotent stem cells (Cawthorn, Scheller, & MacDougald, 2012). Isolation of the SVF from adipose tissue is routine (Han et al., 2015). Thus far, flow cytometry of adipose tissue is primarily focussed on pre-adipocytes of the SVF (Cho et al., 2014; Zhu et al., 2014; Zhu et al., 2013; Grant et al., 2013; Brake & Smith, 2008). Whilst the SVF may give an indication of the composition of cells within an adipose depot, the adipocytes are ignored or discarded.

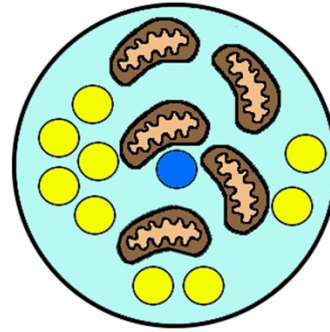
The aim here was to determine whether a method can be developed to analyse adipocytes at the single cell level by flow cytometry. If a method could be developed, then adipocytes could be assessed according to size, granularity and probe uptake. One of the defining traits of brown and white adipocytes is the number of lipid droplets and mitochondria they contain (Figure 5.1). Based off lipid droplet content and mitochondria number, the question was asked whether these two parameters could distinguish brown and white adipocytes.

White adipocyte



- Single lipid droplet
- Eccentrically located mitochondria

Brown adipocyte



- Multi-locular lipid droplets
- Mitochondria laden

**Figure 5.1: Morphological characteristics of white and brown adipocytes.**

White adipocytes contain a unilocular lipid droplet which occupies up to 90% of the cell. White adipocytes have few mitochondria that are located eccentrically. Brown adipocytes contain multi-locular lipids droplets and are rich in mitochondria.

## **5.2 Methods**

### **5.2.1 Flow cytometry of adipose tissue.**

Dissection and dissociation of adipose tissue for flow cytometric analyses is outlined in **2.5.1.2** and Figure 2.1. Preparation of the buoyant adipocyte fraction and SVF for flow cytometric analyses is outlined in **2.6.3**.

#### **5.2.1.1 Flow cytometric analysis of the SVF and buoyant adipocyte fraction.**

Antibody and fluorescent dye cocktails used in this chapter were prepared to a working concentration outlined in Table 5.1 and 5.2. Staining of the buoyant adipocyte fraction and the SVF with fluorescently-conjugated antibodies or fluorescent dyes is outlined in **2.6.3.2**. For cells from the buoyant fraction, 200  $\mu$ L of buoyant adipocytes were taken from the top layer of the supernatant fraction following centrifugation and transferred into a round-bottom tube containing 200  $\mu$ L of FACS buffer with 0.02% PI.

Flow cytometry was performed on a FACSCalibur 4-colour flow cytometer (Becton Dickinson, San Jose, CA, USA) and data collected using CellQuest software. The parameters and settings used are described in **2.6.3.3**, Table **2.13** and Table **2.15**. Cell size and granularity was measured using the forward and side scatter channels respectively. Immunoreactivity and lipophilic probe uptake were analysed on live cells as determined by a lack of PI uptake. Gates identifying positively labelled cells were determined by the single antibody controls outlined in **2.6.3.1.2** and Table **2.10**.

Compounds 5 and 7 (Carborane coumarin and phenyl coumarin respectively) are lipophilic probes developed by the New Lab (Faculty of Chemistry, University of Sydney, Australia). Both coumarin probes are excited by the UV laser line (410-470nm). A Gallios flow cytometer (Beckman Coulter, Brea, CA, USA) was used to measure fluorescence of carborane and phenyl coumarin.

### **5.2.3 Fluorescent imaging**

#### **5.2.3.1 FLoiD microscopy of whole mount adipose tissue**

Brown, subcutaneous inguinal and visceral gonadal adipose tissue was minced into 1-3 mm<sup>3</sup> pieces, stained for Nile Red, Carborane coumarin or Phenyl coumarin and plated onto a 12-well plate. Whole mount imaging was performed on an EVOS FLoiD Cell Imaging System (ThermoFisher Scientific, North Ryde, Australia). Nile Red was excited using the green fluorescent laser (488nm) while Carborane and Phenyl coumarin were excited using the blue fluorescent laser (390nm). Images were taken with at a 20x objective.

#### **5.2.3.2 Confocal microscopy of adipocytes from the buoyant fraction**

Single cell suspensions of brown and visceral gonadal adipocytes were stained for Nile Red and Carborane coumarin, Phenyl coumarin or MitoTracker Deep Red, pipetted onto a glass slide and a 24x24 mm cover slip placed on top. The cover slip was sealed with nail polish and the slide protected from light until imaging. Nile Red was excited by the 532nm laser, carborane coumarin and phenyl coumarin were

excited by the 405nm laser and MitoTracker Deep Red was excited by the 625nm laser.

All confocal images were taken on a single plane using a Leica SPEII as outlined in

2.7.2. Scale bars represent 50  $\mu\text{m}$ .

#### **5.2.4 Statistical analyses**

Statistical analyses were performed on GraphPad Prism®. All data represented as mean  $\pm$  SEM. Differences between two groups were determined by a two-tailed, Student's *t*-test. Differences between more than two groups were determined by a two-tailed, one-way ANOVA with Tukey's *post-hoc* analysis.

**Table 5.2: Fluorophore conjugated monoclonal antibodies used in this chapter.**

Listed here are the antibodies, the cell types they identify, their clone/source, the fluorophore they are conjugated to and the working concentration used.

<b>Antigen</b>	<b>Detects:</b>	<b>Clone/Source</b>	<b>Source</b>	<b>Fluorophore</b>	<b>Concentration</b>
CD3ε	T-cell (Aniansson et al., 1999)	145-2C11	eBioscience	FITC	6.5 µg.mL <sup>-1</sup>
CD34	Endothelial (Mund et al., 2012)	RAM34	eBioscience	FITC	3.25 µg.mL <sup>-1</sup>
CD45	Pan-haematopoietic (van Lochem et al., 2004)	30-F11	eBioscience	APC	1.3 µg.mL <sup>-1</sup>
F4/80	Macrophage (Gonçalves & Mosser, 2001)	BM8	eBioscience	APC	1.3 µg.mL <sup>-1</sup>
Ter119	Erythroid (Kina et al., 2000)	TER-119	BioLegend	APC, FITC, PE	1.3 µg.mL <sup>-1</sup>
Rat IgG1 κ		RTK2071	BioLegend	APC, FITC, PE	1.3 µg.mL <sup>-1</sup>
Rat IgG2a κ		eBR2a	eBioscience	APC, FITC, PE	1.3 µg.mL <sup>-1</sup>
Rat IgG2b κ		eB149/10H5	eBioscience	APC, FITC, PE	1.3 µg.mL <sup>-1</sup>



**Table 5.3: The fluorescent probes used in this chapter.**

Listed below are the fluorescent probes, the final concentration used and their source.

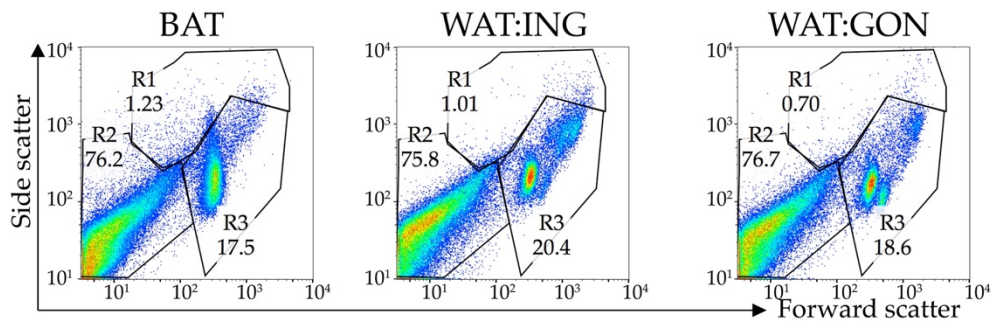
<b>Probe</b>	<b>Detects:</b>	<b>Catalogue No:</b>	<b>Source</b>	<b>Concentration</b>
Oil Red O	Lipids (Mehlem et al., 2013)	OREDO	POCD Scientific	N/A
LipidTox® Red	Phospholipidosis (Grandl & Schmitz, 2010)	H34476	Life Technologies	1X solution
LipidTox® Green	Neutral lipids (Grandl & Schmitz, 2010)	H34475	Life Technologies	1X solution
Nile Red	Neutral lipids (Smith, 1911)	N3013	Sigma	0.1 $\mu\text{mol.L}^{-1}$
MitoTracker Deep Red	Mitochondrial membrane potential (Cottet-Rousselle, Ronot, Leverve, & Mayol, 2011)	M22426	Life Technologies	0.1 $\mu\text{mol.L}^{-1}$
Compound 5 (Carborane coumarin)	Neutral lipids (Wu et al., 2017)	N/A	School of Chemistry, University of Sydney, Australia	0.5 $\mu\text{mol.L}^{-1}$
Compound 7 (Phenyl coumarin)	Neutral lipids (Wu et al., 2017)	N/A	School of Chemistry, University of Sydney, Australia	0.5 $\mu\text{mol.L}^{-1}$
DRAQ5	Nuclei (Smith et al., 1999)	62251	ThermoFisher Scientific	5 $\mu\text{mol.L}^{-1}$

## 5.3 Results

### 5.3.1 Cells from buoyant adipose fraction have a distinct size and granularity profile compared to the SVF.

To accommodate the large variability in the size and granularity of cells, forward (size) and side (granularity) scatter parameters were expressed on a logarithmic scale (Figure 5.2A-B). The size and granularity profiles of the SVF and supernatant fraction from BAT, subcutaneous inguinal WAT and visceral gonadal WAT were gated into three populations (R1-R3) (Figure 5.2A-B). The large, granular cells gated in Region 1 were greatest amongst the buoyant fraction of all adipose depots assayed ( $P < 0.05$  for all adipose depots) (Figure 5.2, R1). Cells from Region 2 were present in both the buoyant fraction and the SVF, however the frequency of cells in Region 2 was greater amongst the buoyant fraction ( $P < 0.005$  for all adipose depots) (Figure 5.2, R2). The cells gated in Region 3 were distinct for the SVF of the adipose depots assayed ( $P < 0.005$  for all adipose depots) (Figure 5.3, R3).

### A) Stromal vascular fraction



### B) Buoyant adipocyte fraction

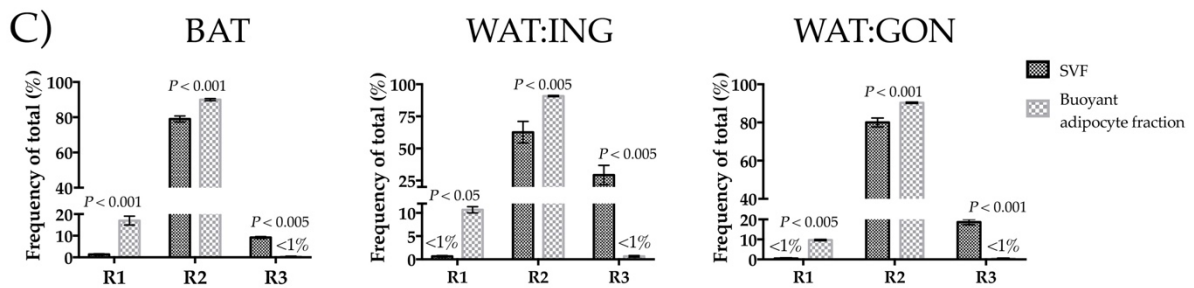
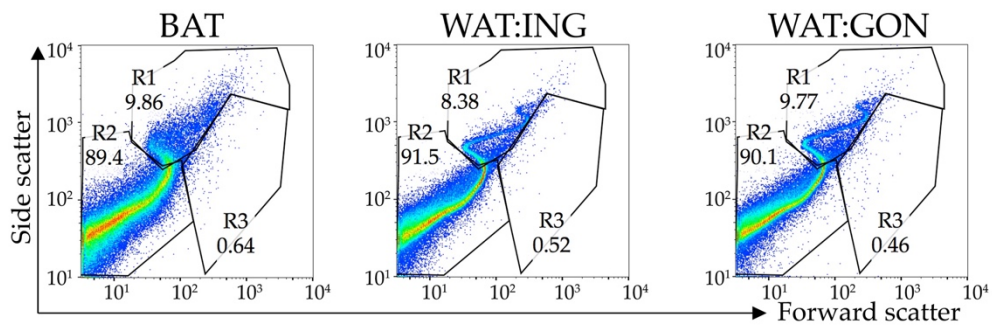


**Figure 5.2: Flow cytometric analysis of cells from the SVF and buoyant adipocyte fraction of adipose depots demonstrate significant differences in their size and granularity.**

Representative flow cytometric plots of forward (size) and side (granularity) scatter of the (A) SVF and (B) buoyant adipocyte fraction of brown (BAT), subcutaneous inguinal (WAT:ING) and visceral gonadal (WAT:GON) adipose depots. Identical gates (R1-R3) of distinct cell populations (according to forward and side scatter) were applied. (C) The mean ( $\pm$  SEM,  $n=5$ ) proportion of the total number of cells analysed for each distinct region were compared. Significant differences between each gated region from the SVF and buoyant adipocyte fraction were determined by a two tailed Student's *t*-test.

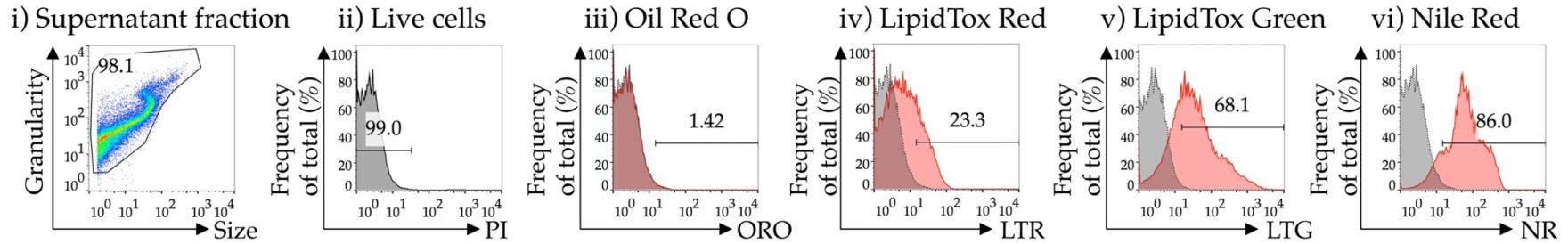
### **5.3.2 Lipophilic probes stain cells from the buoyant adipocyte fraction.**

To confirm whether the cells from the buoyant fraction were adipocytes, a range of lipophilic probes were tested (Figure 5.3). Irrespective of the adipose depot assayed, Oil Red O staining was not detected by fluorescence analysis (Figure 5.3A-Ciii). Cells stained with LipidTox Red displayed low fluorescence intensities (Figure 5.3A-Civ). Fluorescence of LipidTox Green and Nile Red was observed across all adipose depots (Figure 5.3A-Cv-vi). A greater proportion of cells from the buoyant fraction took up Nile Red compared to LipidTox Green ( $P < 0.001$ ) (Figure 5.4Ai-iii). Further, Nile Red had a greater mean fluorescence intensity (MFI) compared to all other lipophilic dyes assayed and was therefore chosen as the lipophilic probe for further use in this study ( $P < 0.0001$ ) (Figure 5.4Bi-iii).

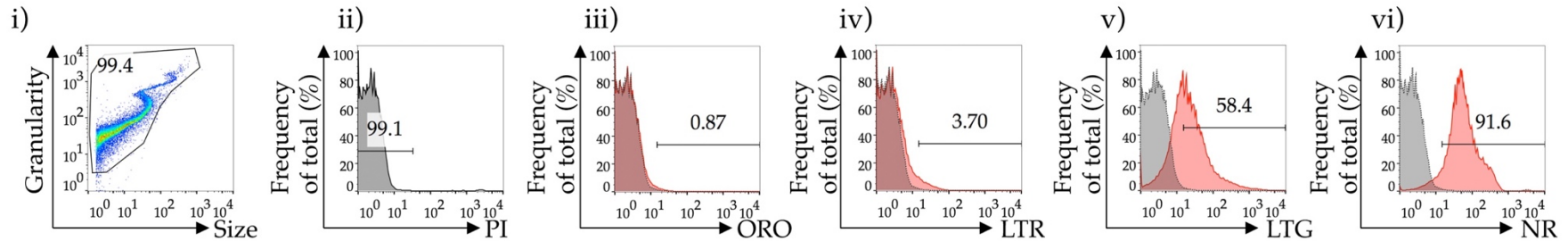
**Figure 5.3: Lipophilic probes LipidTox Green and Nile Red stain cells in the supernatant fraction of BAT, subcutaneous inguinal and visceral gonadal WAT.**

Representative flow cytometric plot comparing lipophilic probe uptake in the buoyant fraction of (Ai) brown (BAT), (Bi) subcutaneous inguinal (WAT:ING) and (Ci) visceral gonadal (WAT:GON) adipocytes (shaded in red). (ii) Live cells were gated according to lack of propidium iodide uptake, and (iii) Oil Red O (ORO), (iv) LipidTox Red (LTR), (v) LipidTox Green (LTG) and (vi) Nile Red (NR) fluorescence measured. Uptake of lipophilic dyes expressed as a percentage of the total number of cells (frequency of total (%)). Grey shaded plots represent the no-dye (negative) control.

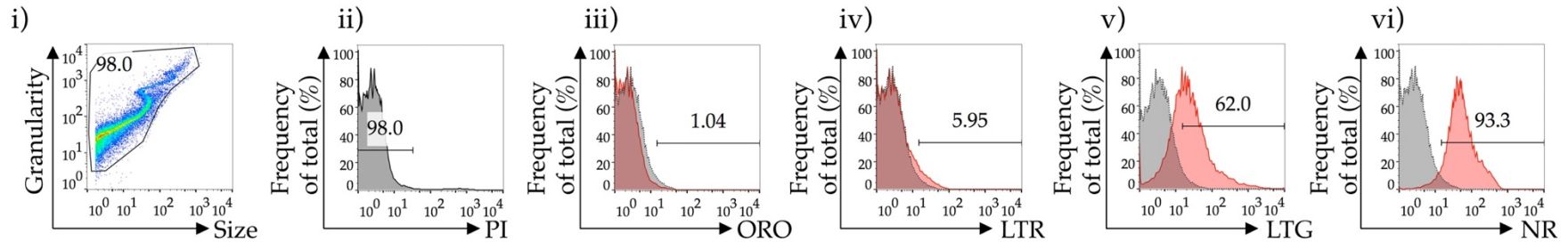
## A) Brown adipose tissue



## B) Subcutaneous white adipose tissue



## C) Visceral white adipose tissue



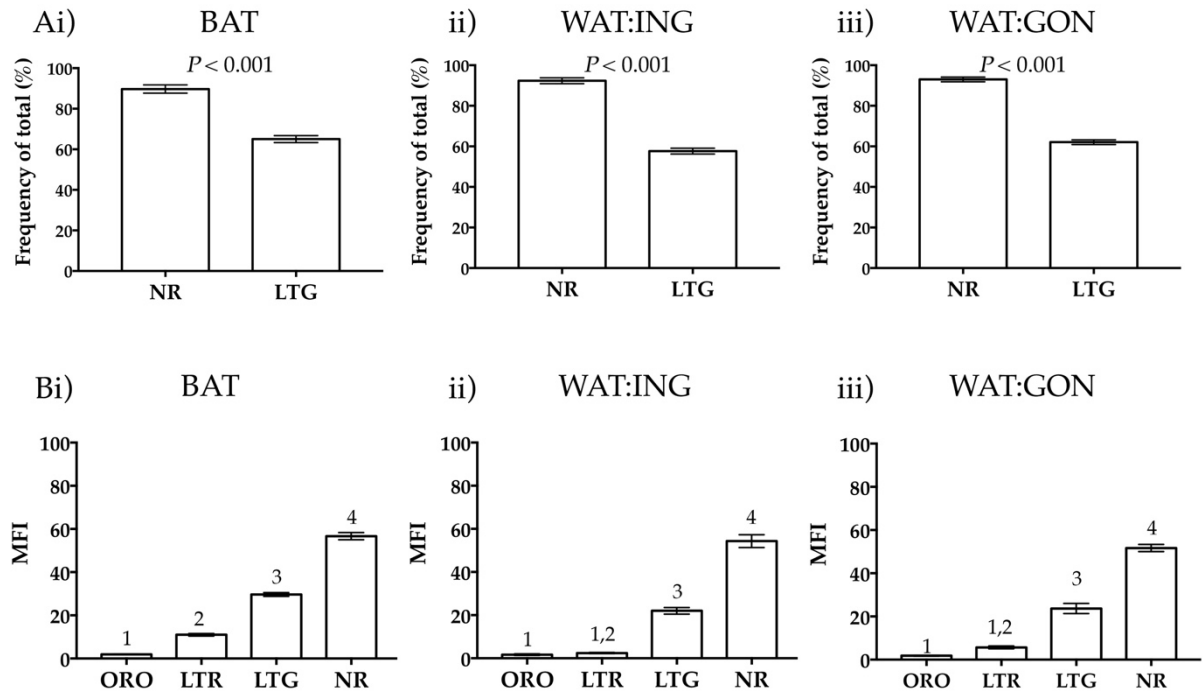


**Figure 5.4: Frequency of uptake and mean fluorescence intensity is greatest in Nile Red stained cells.**

(A) Proportion of cells taking up Nile Red and LipidTox Green in the buoyant fraction of (i) brown (BAT), (ii) subcutaneous inguinal (WAT:ING) and (iii) visceral gonadal (WAT:GON) adipocytes. Data presented as mean  $\pm$  SEM ( $n=3$ ). Differences in the frequency of Nile Red and LipidTox Green uptake across adipose depots was determined by a two tailed, Student's *t*-test.

(B) Comparisons of the mean fluorescence intensity (MFI) between Oil Red O, LipidTox Red, LipidTox Green and Nile Red between (i) BAT, (ii) WAT:ING and (iii) WAT:GON adipocytes. Data presented as mean  $\pm$  SEM ( $n=3$ ). Differences in the mean fluorescence intensity of lipophilic probes across the buoyant fraction of brown and white adipocytes were determined by two-tailed, one-way ANOVA and pairwise *post-hoc* analysis by Tukey's HSD test. Groups not sharing a numeral are significantly different from each other ( $P < 0.0001$ ).

### 5.3.3 Nile Red uptake is proportional to adipocyte size and granularity.

Uptake of Nile Red was then analysed according to cell size and granularity. The size and granularity scatter plot of the buoyant fraction was divided into three regions and Nile Red fluorescence measured (Figure. 5.5A- R1, R2, R3). The largest, most granular cells in Region 1 exhibited the greatest fluorescence of Nile Red (Figure. 5.5Bi). Region 1 was termed Nile Red<sup>High</sup>. Cells in Region 2 (Nile Red<sup>Mid</sup>) had less Nile Red fluorescence than cells in Region 3 but greater than cells in Region 1 (Nile Red<sup>Low</sup>) (Figure 5.5C-Di). The mean fluorescence intensity was consistently higher in Region 1 compared to Regions 2 and 3 (Figure 5.5E).

To confirm that the adipocytes in the buoyant fraction were intact and contained a nucleus, uptake of nuclei probe DRAQ5 and cell membrane marker wheat germ agglutinin (WGA) was measured. Nile Red<sup>Mid</sup> and Nile Red<sup>High</sup> cells exhibited greater than 90% uptake for DRAQ5 and WGA (Figure 5.5B,Cii-iii). Nile Red<sup>Low</sup> cells exhibited greater than 70% DRAQ5 and WGA uptake (Figure 5.5Dii-iii).



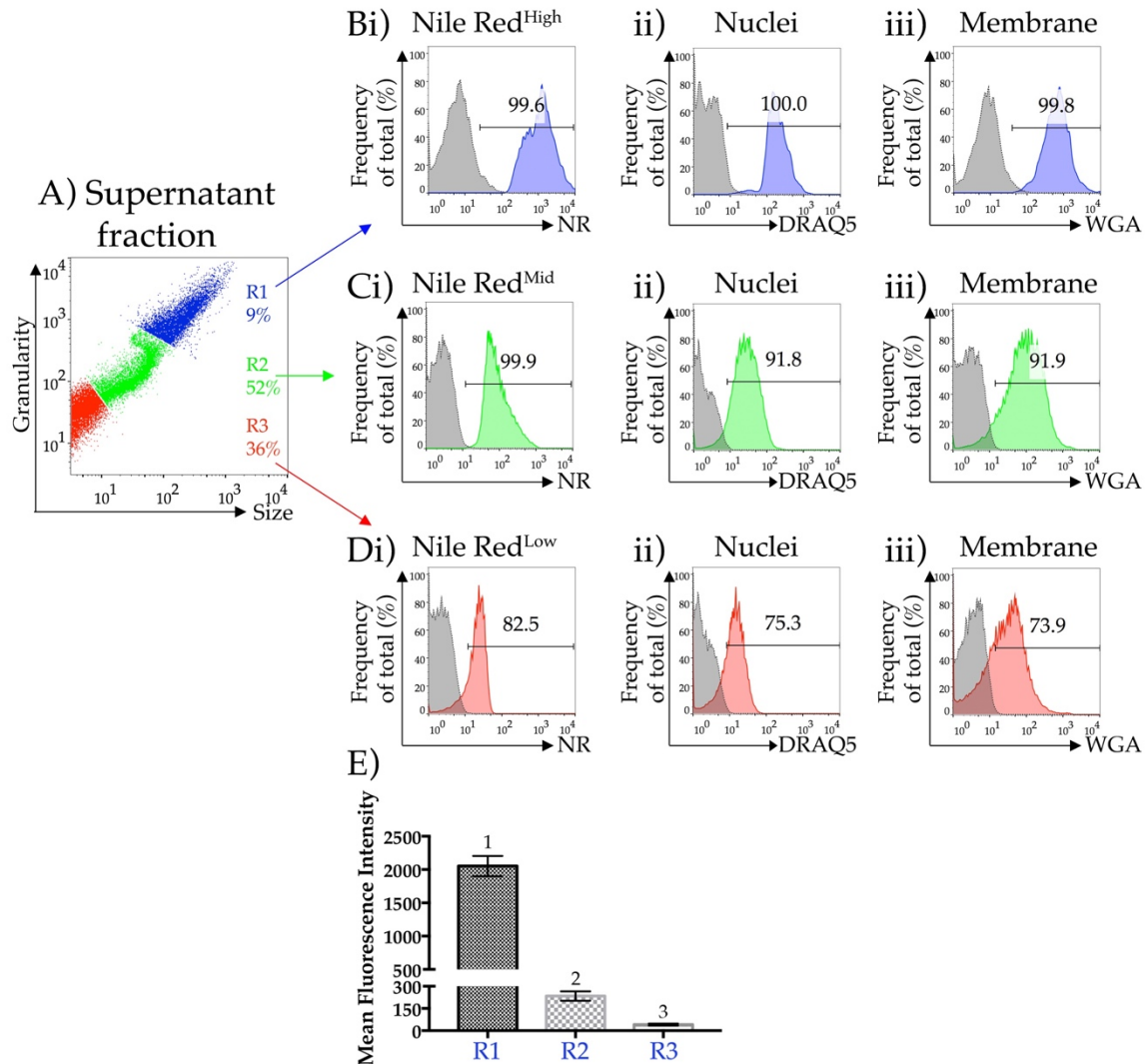


**Figure 5.5: Nile red fluorescence is greatest amongst the largest, most granular cells in the supernatant fraction.**

(A) Representative forward and side scatter plot of the buoyant fraction of brown adipose tissue. The size and granularity of the supernatant fraction from brown adipocytes was divided into three regions (R1 (red), R2 (green) and R3 (blue)). Live cells were gated and analysed for (i) Nile Red, (ii) DRAQ5 and (iii) wheat germ agglutinin (WGA) uptake in (B) R1 (Nile Red<sup>High</sup>), (C) R2 (Nile Red<sup>Mid</sup>) and (D) R3 (Nile Red<sup>Low</sup>) gated cells. (E) Comparisons of the mean fluorescence intensity (MFI) of Nile Red between R1, R2 and R3. Data presented as mean  $\pm$  SEM ( $n = 6$ ). Differences in the MFI of Nile Red between R1, R2 and R3 were determined by two-tailed, one way ANOVA and pairwise *post-hoc* comparison by Tukey's HSD test. Groups not sharing a numeral are significantly different from each other ( $P < 0.0001$ ).

#### **5.3.4 Cells from the SVF do not take up Nile Red.**

Nile Red was used to stain cells of the SVF to determine whether uptake was present.

Nile Red uptake was observed in Region 1 (R1) and Region 2 (R2) of the SVF (Figure 5.6). As Region 1 and Region 2 are also present in the buoyant fraction containing

adipocytes, the cells in those regions could be remnants from the separation process.

Region 3, which is distinct in the SVF and absent in the buoyant fraction, did not exhibit Nile Red uptake (Figure 5.6).

## Stromal vascular fraction

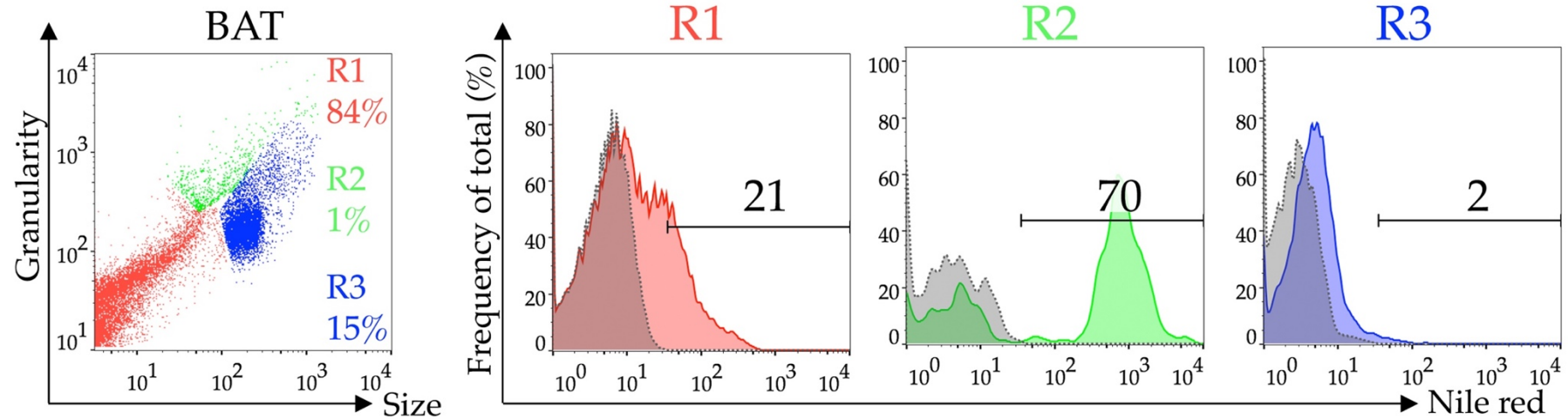


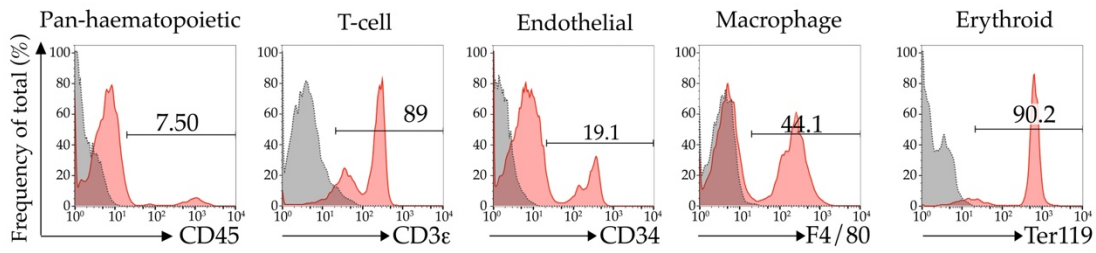
**Figure 5.6: Cells in Region 3 of the SVF do not exhibit Nile Red fluorescence.**

Representative flow cytometric plot of the SVF of brown adipose tissue stained with Nile Red. Cell populations were gated according to size and granularity and Nile Red uptake measured in Region 1 (red shaded plot), Region 2 (green shaded plot) and Region 3 (blue shaded plot). Nile Red uptake measured as a proportion to the total number of cells (frequency of max (%)). The grey plots represent the no-dye (negative) control.

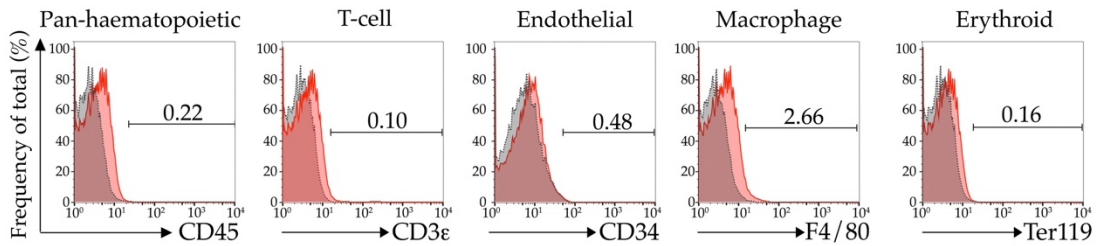
### **5.3.5 The buoyant adipocyte fraction of brown and white adipose tissue lack cell surface protein expression of haematopoietic markers.**

The SVF and buoyant adipocyte fraction were assessed using a panel of fluorescently conjugated antibodies identifying surface protein expression of haematopoietic cell (CD45), T-cell (CD3 $\epsilon$ ), endothelial cell (CD34), macrophage (F4/80) and erythroid cell (Ter119) populations (Figure 5.9-5.11). In all adipose depots assayed, only cells of the SVF exhibited surface expression for CD45, CD3 $\epsilon$ , CD34, F4/80 and Ter119 (Figure 5.7-9A). No immunoreactivity for these haematopoietic and vascular cell types were detected in the buoyant adipocyte fraction for all adipose depots (Figure 5.7-9B).

A) Brown adipose tissue: Stromal vascular fraction



B) Brown adipose tissue: Buoyant adipocyte fraction



C)

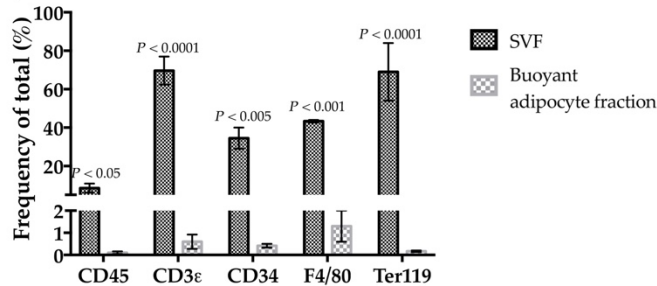
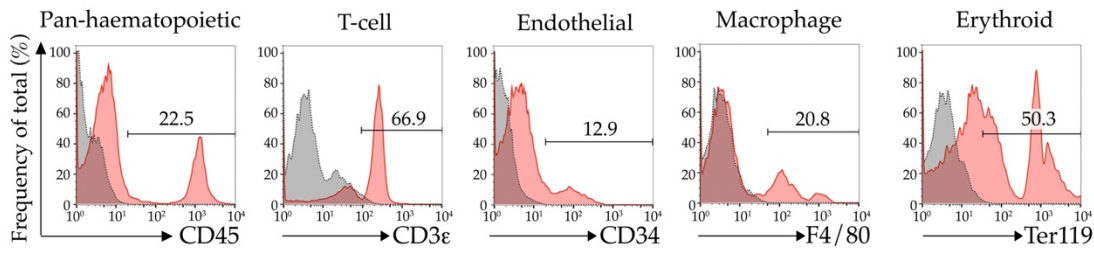


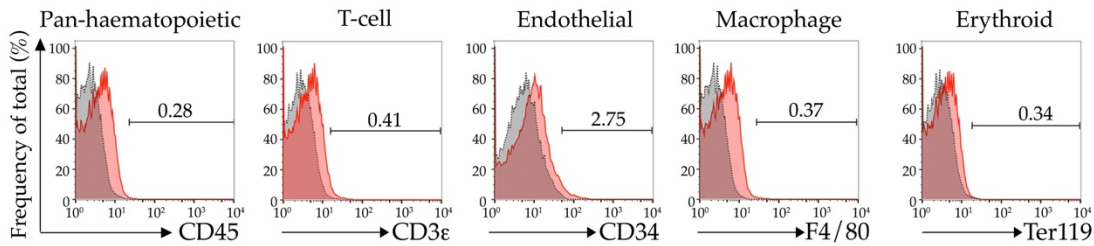
**Figure 5.7: Cells of the buoyant adipocyte fraction of brown adipose tissue do not express markers of the stromal vascular fraction.**

Representative histogram plots of the total number of cells (frequency of total (%)) exhibiting immunoreactivity for CD45, CD3ε, CD34, F4/80 and Ter119 in the (A) SVF and (B) buoyant fraction of brown adipose tissue (BAT). Red shaded plots indicate the antibody-stained sample while the grey plots indicate the no-antibody (negative) control. (C) Comparison of the frequency of cells expressing CD45, CD3ε CD34, F4/80 and Ter119 between the SVF and buoyant fraction of BAT. Data presented as mean  $\pm$  SEM (n=3). Differences in surface protein expression of examined markers between the SVF and buoyant fraction were determined by two-tailed, Student's *t*-test.

A) Subcutaneous white adipose tissue: Stromal vascular fraction



B) Subcutaneous white adipose tissue: Buoyant adipocyte fraction



C)

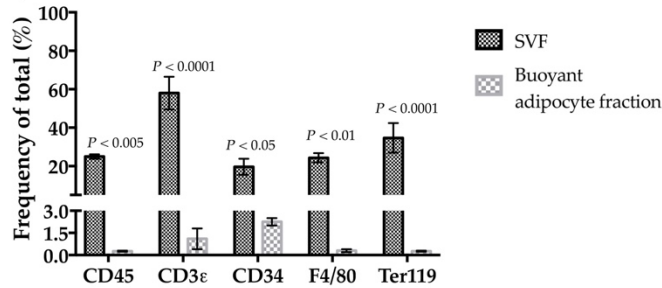
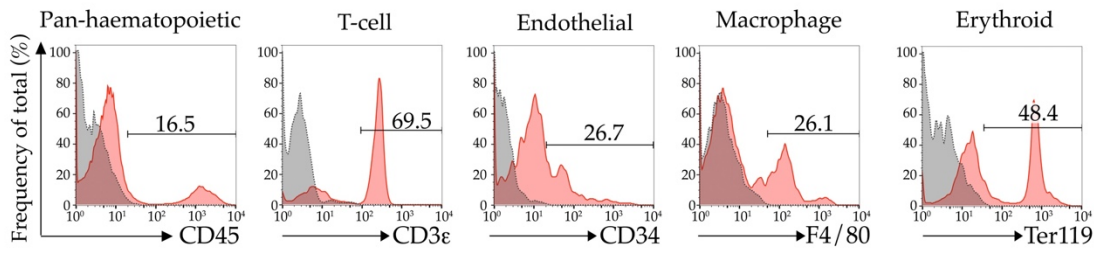


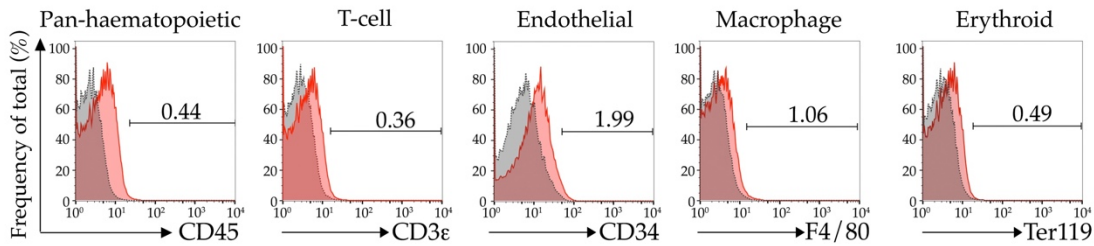
**Figure 5.8: Cells of the buoyant adipocyte fraction of subcutaneous inguinal adipose tissue do not express markers of the stromal vascular fraction.**

Representative histogram plots of the total number of cells (frequency of total (%)) exhibiting immunoreactivity for CD45, CD3ε, CD34, F4/80 and Ter119 in the (A) SVF and (B) buoyant fraction of subcutaneous inguinal adipose tissue (WAT:ING). Red shaded plots indicate the antibody-stained sample while the grey plots indicate the no-antibody (negative) control. (C) Comparison of the frequency of cells expressing CD45, CD3ε, CD34, F4/80 and Ter119 between the SVF and buoyant fraction of WAT:ING. Data presented as mean  $\pm$  SEM (n=3). Differences in surface protein expression of examined markers between the SVF and buoyant fraction were determined by two-tailed, Student's *t*-test.

A) Visceral white adipose tissue: Stromal vascular fraction



B) Visceral white adipose tissue: Buoyant adipocyte fraction



C)

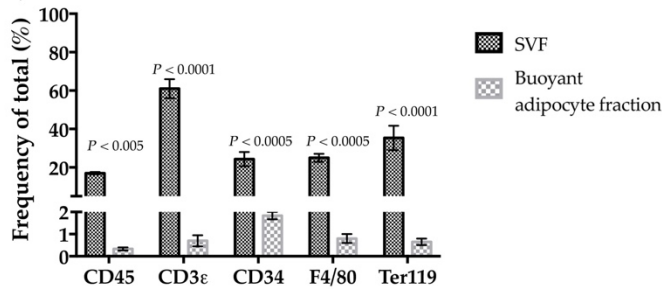


**Figure 5.9: Cells of the buoyant adipocyte fraction of visceral gonadal adipose tissue do not express markers of the stromal vascular fraction.**

Representative histogram plots of the total number of cells (frequency of total (%)) exhibiting immunoreactivity for CD45, CD3ε, CD34, F4/80 and Ter119 in the (A) SVF and (B) buoyant fraction of visceral gonadal adipose tissue (WAT:GON). Red shaded plots indicate the antibody-stained sample while the grey plots indicate the no-antibody (negative) control. (C) Comparison of the frequency of cells expressing CD45, CD3ε, CD34, F4/80 and Ter119 between the SVF and buoyant fraction of WAT:GON. Data presented as mean  $\pm$  SEM (n=3). Differences in surface protein expression of examined markers between the SVF and buoyant fraction were determined by two-tailed, Student's *t*-test.

### **5.3.6 Mitochondrial membrane potential dye MitoTracker Deep Red does not effectively differentiate between brown, subcutaneous and visceral white adipocytes.**

Although Nile Red uptake was able to distinguish between adipocytes and the SVF, uptake of Nile Red did not discriminate between brown, subcutaneous inguinal and visceral gonadal adipocytes. Due to the high numbers of mitochondria in brown adipocytes, Nile Red was combined with MitoTracker Deep Red to determine if there were any differences between brown and white adipocytes. Brown, subcutaneous inguinal and visceral gonadal adipocytes were stained with Nile Red and MitoTracker Deep Red and imaged under confocal microscopy before flow cytometric analyses were performed (Figure 5.10).

Multi-locular brown and unilocular white adipocytes were identified by Nile Red (red) uptake (Figure 5.10). MitoTracker Deep Red (cyan) signal was seen localised within the cytoplasm of brown and white adipocytes (Figure 5.10). Co-localisation of MitoTracker and Nile Red is presented as an intense white signal (Figure 5.10). Prior to this study, confocal imaging of live brown and white adipocytes stained with Nile Red and MitoTracker Deep Red had not been described (Boumelhem et al., 2017).

Nile Red and MitoTracker Deep Red uptake was then compared between brown, subcutaneous and visceral adipocytes by flow cytometry (Figure 5.11). As Nile Red fluorescence was proportional to adipocyte size, the largest, most granular adipocytes



were chosen for subsequent flow cytometric analyses (Figure 5.5, 5.11). MitoTracker Deep Red uptake was divided into MitoTracker<sup>Low</sup> (light blue box) and MitoTracker<sup>High</sup> (dark blue box) populations (Figure 5.11). Adipocytes from all adipose depots assayed were predominantly MitoTracker<sup>High</sup> (Figure 5.11). Regardless of the adipose depot assayed, there were no differences in MitoTracker Deep Red uptake between adipose depots (Figure 5.12).

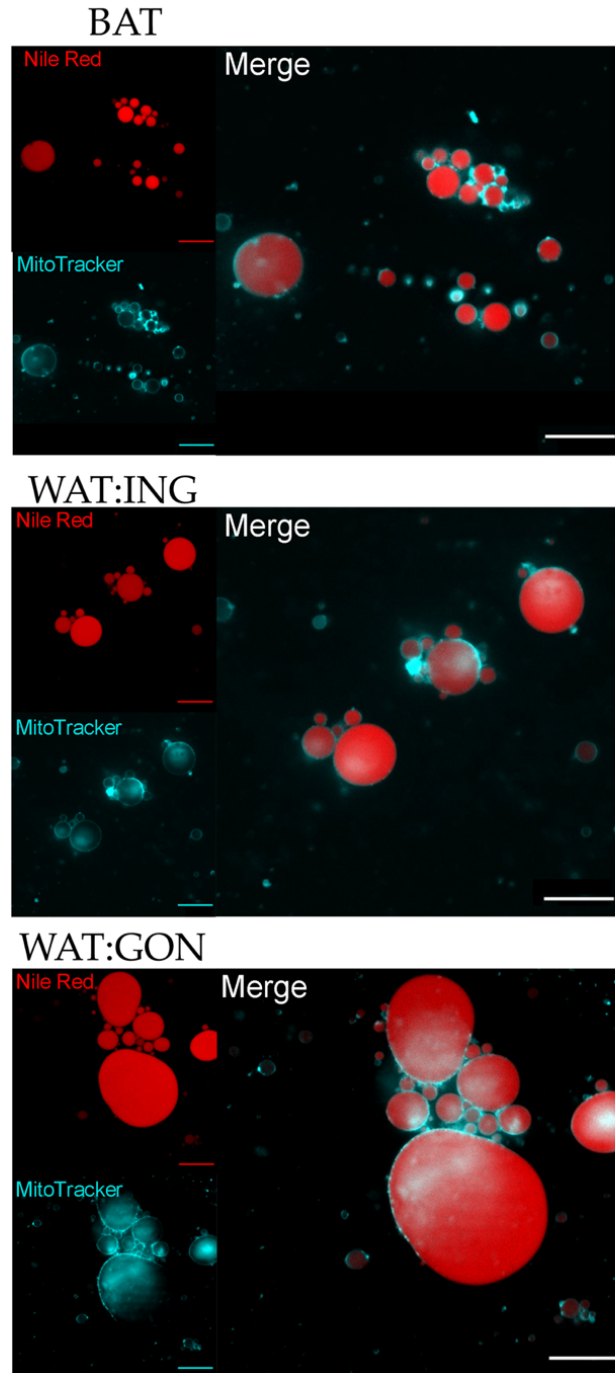


**Figure 5.10: Confocal imaging of live, intact, brown and white adipocytes stained with Nile Red and MitoTracker Deep Red.**

Confocal images of brown (BAT) (left), subcutaneous inguinal (WAT:ING) (centre) and visceral gonadal (WAT:GON) (right) adipocytes stained with MitoTracker Deep Red (cyan) and Nile Red (red). Images were taken on a single plane using a Leica SPEII equipped with an oil-immersed Leica ACS Apochromat 63x objective. WGA was excited by the 488 nm laser; Nile Red was excited by the 532 nm laser and MitoTracker Deep Red was excited by the 625nm laser. Scale bars represent 20  $\mu\text{m}$ .

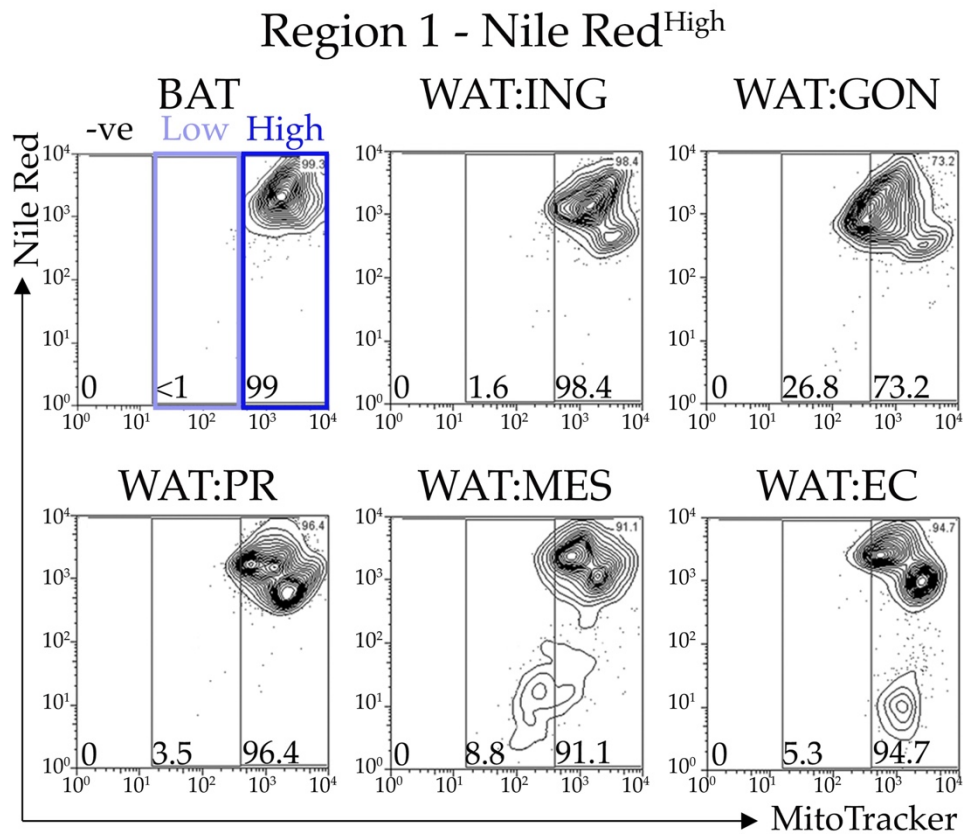


**Figure 5.11: Nile Red<sup>High</sup> adipocytes have high levels of MitoTracker Deep Red.**

Representative flow cytometric plot of Nile Red<sup>High</sup> gated brown (BAT), subcutaneous inguinal (WAT:ING) and visceral gonadal (WAT:GON), peri-renal (WAT:PR), mesenteric (WAT:MES) and epicardial (WAT:EC) adipocytes stained with Nile Red and MitoTracker Deep Red. Uptake of Nile Red<sup>High</sup> and MitoTracker Deep Red was divided into MitoTracker<sup>Low</sup> (light blue box) and MitoTracker<sup>High</sup> (dark blue box) populations for subsequent analyses. Figure adapted from Boumelhem et al., 2017.

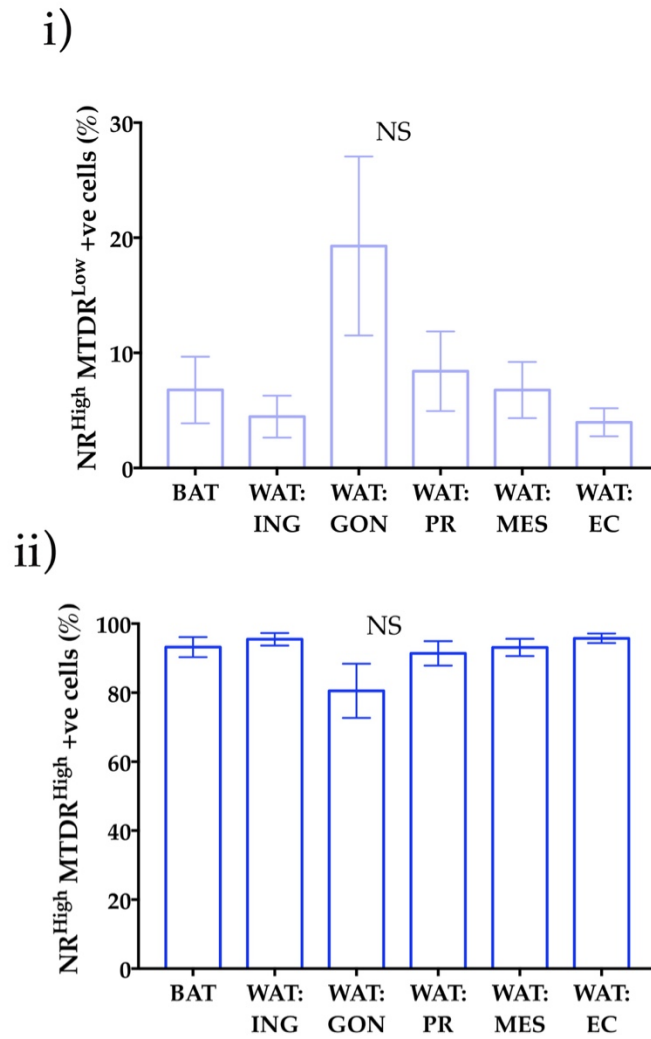


**Figure 5.12: No differences observed in MitoTracker Deep Red uptake between brown and white adipose depots.**

Comparisons of the frequency of (i) Nile Red<sup>High</sup> MitoTracker<sup>Low</sup> positive and (ii) Nile Red<sup>High</sup> MitoTracker<sup>High</sup> cells between brown (BAT), subcutaneous inguinal (WAT:ING) and visceral gonadal (WAT:GON), peri-renal (WAT:PR), mesenteric (WAT:MES) and epicardial (WAT:EC) adipocytes. Data presented as mean  $\pm$  SEM (n=6 for all groups). Differences in Nile Red and MitoTracker Deep Red uptake between adipose depots were determined by two-tailed, one-way ANOVA and pairwise *post hoc* comparison by Tukey's HSD test. Groups not sharing a numeral are significantly different from each other. Figure adapted from Boumelhem et al., 2017.

### **5.3.7 Carborane coumarin and phenyl coumarin co-localise with Nile Red.**

In collaboration with the New Research Group (Faculty of Chemistry, University of Sydney, Australia), uptake of probes carborane coumarin and phenyl coumarin were assessed in brown and white adipocytes. Carborane coumarin and phenyl coumarin are the only lipophilic dyes that are excited by the UV laser line (410 nm – 470 nm).

Whole mount imaging of brown, subcutaneous inguinal and visceral gonadal white adipose tissue revealed intense fluorescence of carborane and phenyl coumarin in adipose tissues (Figure 5.13). In small brown adipocytes, only carborane coumarin uptake was observed (Figure 5.13). Co-localisation of carborane coumarin and phenyl coumarin with Nile Red was also detected in brown and white adipose tissue indicated by purple colouring (Figure 5.13). Nucleic acid stain YoYo-1 was readily observed on adipocytes at the periphery of the tissue (Figure 5.13). Co-localisation of Nile Red, the coumarin probes and YoYo-1 is presented as a white or light purple colouring (Figure 5.13). Nile Red staining was predominant on the membrane of adipocytes (Figure 5.13).

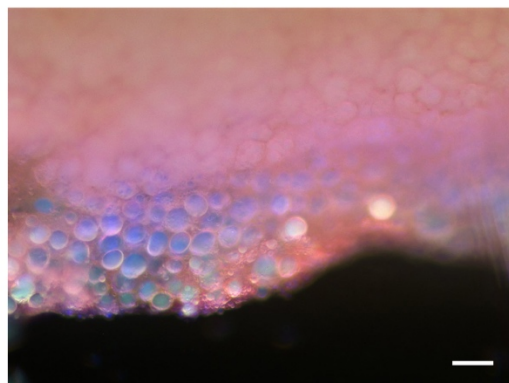
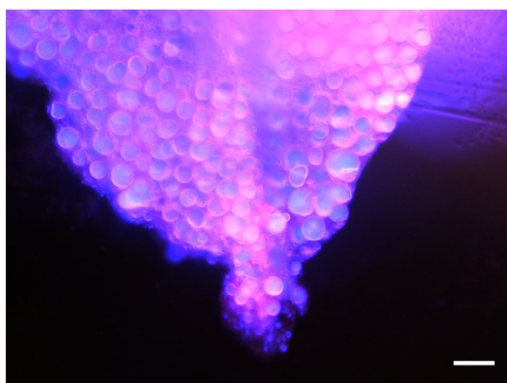
Single cell suspensions of brown and visceral gonadal adipocytes stained with Nile Red and either carborane or phenyl coumarin were then visualised by confocal microscopy (Figure 5.14). Confocal microscopy revealed co-localisation of Nile Red and coumarin probe fluorescence amongst the adipocytes (Figure 5.14A-B). Co-localisation analysis performed on Image J by the New Research Group revealed a

deeper staining of lipid droplets by carborane coumarin when compared to phenyl coumarin (Wu et al., 2017).

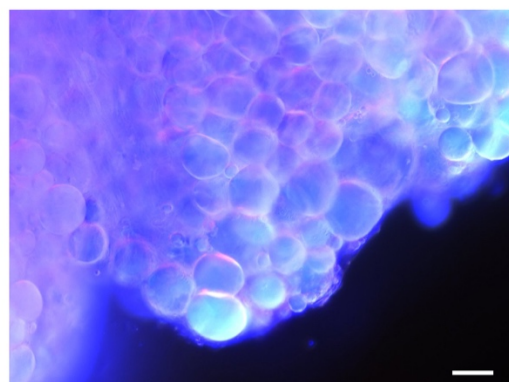
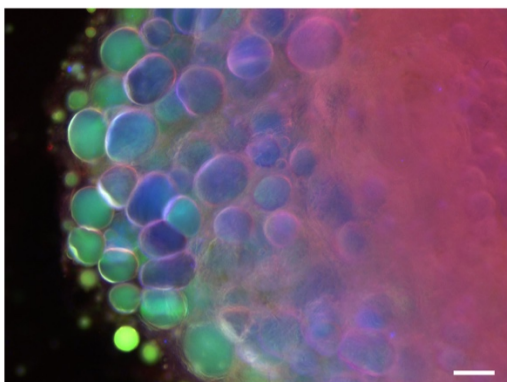
Flow cytometric analyses performed here revealed that only cells stained with Nile Red were stained with either carborane and phenyl coumarin (Figure 5.15). Irrespective of the adipose depot assayed, all adipocytes from the supernatant fraction exhibited equal fluorescence of Nile Red and the coumarin probes (Figure 5.15A-B). However, fluorescence intensity of carborane coumarin was greater than phenyl coumarin (Figure 5.15A-B).

## BAT

- i) Nile Red + Carborane coumarin + YoYo-1    ii) Nile Red + Phenyl coumarin + YoYo-1



## WAT:ING



## WAT:GON

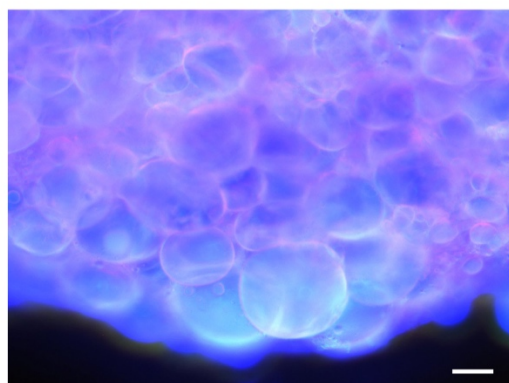
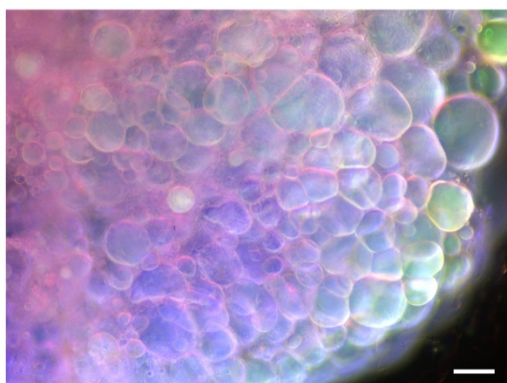


**Figure 5.13: Fluorescent microscopy reveals co-localisation of Nile Red and coumarin dyes in brown and white adipose tissue.**

Representative whole mount fluorescent microscopy images of brown (BAT), subcutaneous inguinal (WAT:ING) and visceral gonadal (WAT:GON) white adipose tissue stained with Nile Red (red), YoYo-1 Iodide (green) and (i) carborane coumarin (blue) or (ii) phenyl coumarin (blue). Images were taken at 20x objective using an EVOS FLoiD Cell Imaging System. Scale bars represent 50  $\mu\text{m}$ .

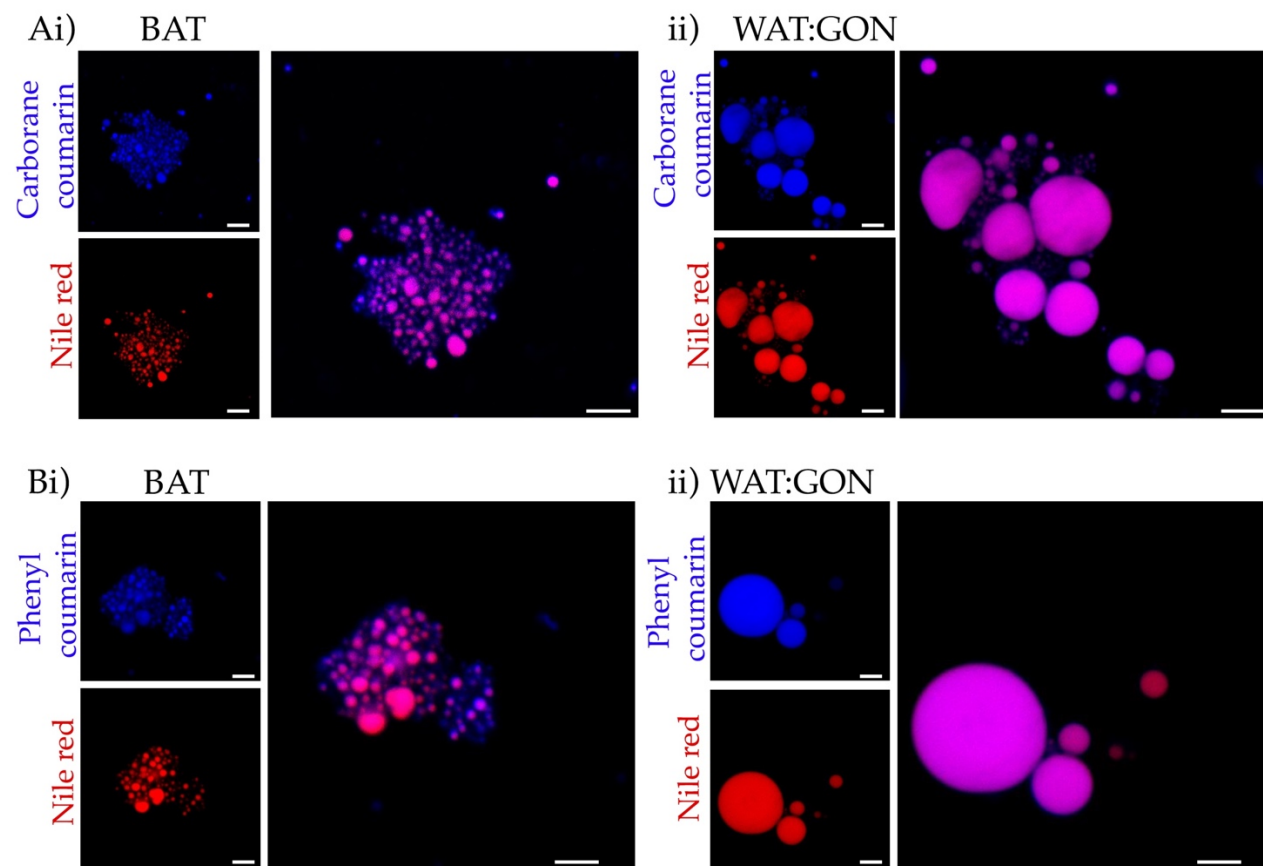


**Figure 5.14: Confocal microscopy reveals co-localisation of Nile Red and coumarin dyes in brown and white adipocytes.**

Representative confocal microscopy images of buoyant adipocytes from (i) brown (BAT) and (ii) visceral gonadal adipose depots stained with Nile Red (red) and (A) carborane coumarin (blue) or (B) phenyl coumarin (blue). Images were taken on a single plane at 63x objective using a Leica SPEII confocal microscope. Scale bars represent 20 μm



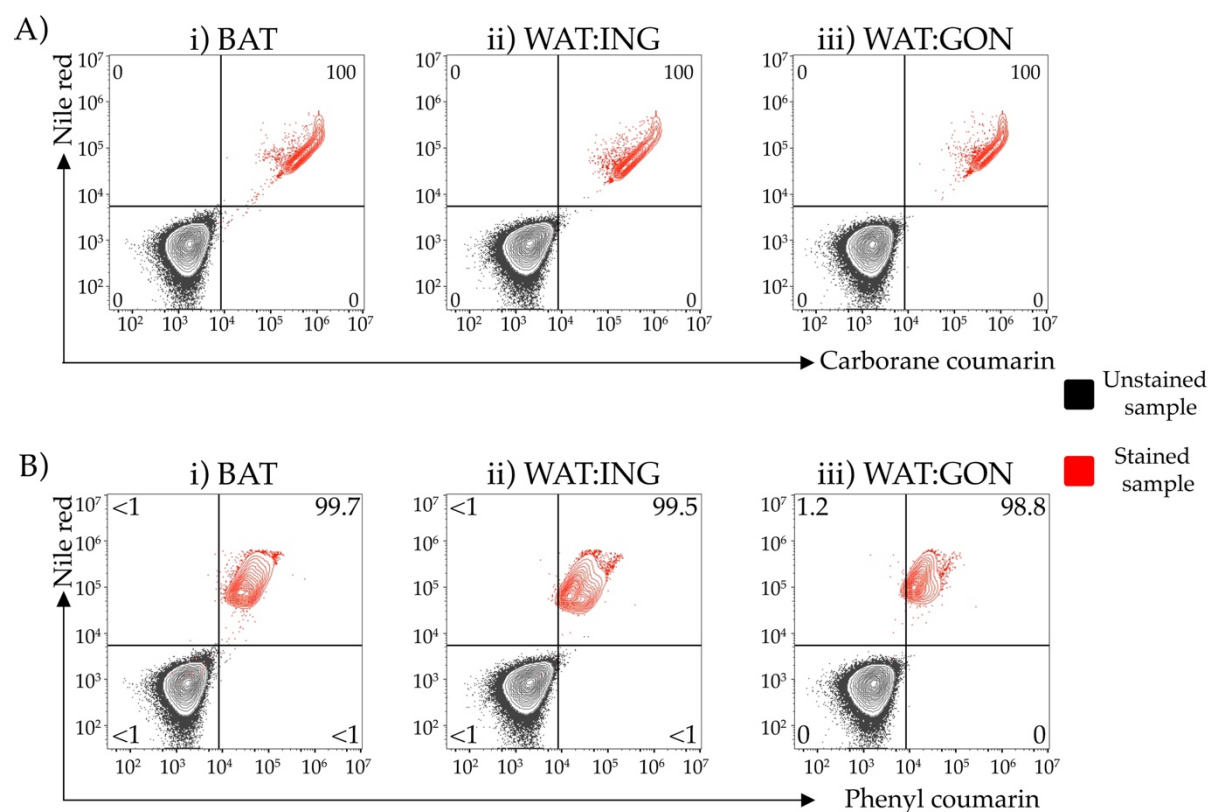


**Figure 5.15: Flow cytometric analysis reveal co-localisation of Nile Red and coumarin probes in brown and white adipocytes.**

(A) Representative flow cytometric plot of the buoyant fraction of (i) brown (BAT), (ii) subcutaneous inguinal (WAT:ING) and (iii) visceral gonadal (WAT:GON) adipose tissue stained with Nile Red, carborane coumarin and (B) phenyl coumarin. The black contour plot represents the no stain control while the red contour plot represents stained sample.

## **5.4 Discussion**

### **5.4.1 Flow cytometry is underutilised in the study of adipocyte biology.**

There is a lack of a reliable method to analyse adipocytes at the single cell level. While flow cytometric analyses of the stromal vascular fraction (SVF) is routine, analyses of mature adipocytes from the buoyant fraction of adipose tissue are largely unreported (Majka et al., 2014; Durandt et al., 2016; Festy et al., 2005). The SVF is not an accurate representation of adipose tissue as a whole. Previous flow cytometric analyses on adipocytes have reported lipid accumulation in adipocytes; adipocytes derived *in vitro* from myeloid and bone marrow progenitors and adipocytes isolated from a single adipose depot (Lee, 2004; Festy et al., 2005; Majka et al., 2010; Crossno et al., 2006; Majka et al., 2014; Durandt et al., 2016). Here, a robust, simple method to analyse live, viable and intact brown and white adipocytes at the single cell level was demonstrated. Flow cytometry was applied to assess differences in adipocyte size, granularity, lipophilic and mitochondrial membrane potential probe uptake.

### **5.4.2 The utility of Nile Red as a neutral lipid dye for flow cytometric analyses of adipocytes.**

Neutral lipid dye Nile Red has been used to selectively stain lipid droplets in aortic smooth muscle, macrophages, Leydig cells and adipocytes derived from stem cell cultures (Greenspan, Mayer, & Fowler, 1985; Rumin, 2015; Gocze & Freeman, 1994; Schaedlich et al., 2010). Prior to this study, Nile Red had not been used to analyse isolated adipocytes by flow cytometry (Friedman, 2015). Nile Red effectively

discriminated between adipocytes and the SVF. Furthermore, Nile Red fluorescence was proportional to adipocyte size. Since Nile Red fluorescence increased with adipocyte size and granularity, Nile Red may be an indicator for adipocyte maturation. Adipose tissue contains adipocytes of different sizes, which vary according to adipose depot and the stage of maturation (Sinnott-Smith et al., 1992; Jo et al., 2009). Flow cytometry has been used to characterise adipogenesis from mesenchymal stromal cell-derived adipocytes (Aldridge et al., 2013). A report published by Aldridge *et al.* (2013) demonstrated an increase in cell granularity and Nile Red fluorescence by flow cytometry over the course adipocyte differentiation from mesenchymal stromal cells (Aldridge et al., 2013).

An alternative to Nile Red are coumarin-based lipophilic probes. Coumarin-based probes are the only lipophilic probes that are excited by the UV laser line (410 nm – 470 nm). This offers advantages for multi-parametric flow cytometry of adipocytes. Coumarin-based probes could replace Nile Red, opening a channel for the addition of a fluorescently-conjugated antibody of interest.

#### **5.4.3 Mitochondrial membrane potential distinguishes adipocytes.**

Mitochondria in adipose tissue is crucial for lipolysis and fatty acid synthesis and oxidation (De Pauw et al., 2009; Boudina & Graham, 2014). In WAT, mitochondria serve to maintain adipogenesis, lipogenesis and lipolysis (Boudina & Graham, 2014). Conversely, mitochondria in BAT oxidise free fatty acids to generate heat by the action

uncoupling protein-1 (UCP1) (Cannon & Nedergaard, 2004). Since brown adipocytes are rich in mitochondria, they were anticipated to be distinct from white adipocytes according to mitochondrial membrane potential dye MitoTracker Deep Red uptake. However, mitochondrial membrane potential was greatest in epicardial adipocytes. Although classified as a visceral adipose depot, epicardial adipose tissue is suggested to be essential for normal cardiac function (Marchington, Mattacks, & Pond, 1989; Sacks et al., 2013; Rabkin, 2007). Compared to other adipose depots, epicardial adipose tissue has the greatest capacity for free fatty acid release (Marchington et al., 1989). Due to the close proximity to the heart, epicardial adipose tissue provides free fatty acids to fuel myocardial contraction as well as buffer excess free fatty acids (Bjørndal et al., 2011; Gaborit et al., 2011). Expression of *UCP1* is present in high levels in epicardial adipose tissue, particularly in neonates suggesting similarities to brown adipose tissue (Sacks et al., 2013; Ojha et al., 2016). However, mitochondrial components involved with thermogenesis (including *UCP1*) are downregulated in infant humans (Ojha et al., 2016).

#### **5.4.4 Diagnostic application for Nile Red staining of adipocytes**

Adipose tissue remodelling occurs with obesity, diabetes, ageing, calorie restriction and cancers (cited in: Parlee et al., 2014). Adipocyte size has also been proposed to affect lipid metabolism and could be an indicator for the development of Type II diabetes (Varlamov et al., 2010). Smaller adipocytes are more sensitive to insulin than larger adipocytes (Varlamov et al., 2010; Smith et al., 1971; Jacobsson et al., 1972;

Olefsky et al., 1976). Additionally, reduced mitochondrial function in adipose tissue has been linked to obesity and type II diabetes (Bournat & Brown, 2010; reviewed in: Cedikova et al., 2016). Based on Nile Red and MitoTracker Deep Red uptake, cell size and granularity, the method presented could be applied to examine and characterise adipocytes from obese or diabetic mice and humans. The flow cytometric method could be used to quantify the ratio of small to large adipocytes as an indirect measure of adipogenesis in obese or diabetic mice.

#### **5.4.5 Conclusion**

A method to distinguish adipocytes based on adipocyte size, granularity, Nile Red and MitoTracker Deep Red uptake was presented. Nile Red fluorescence intensity was also proportional to the size and granularity of adipocytes. Although the flow cytometric method effectively distinguished between isolated adipocytes and the SVF, Nile Red uptake did not differ between brown, subcutaneous and visceral white adipocytes. Membrane potential measured by MitoTracker Deep Red distinguished epicardial adipocytes from all adipose depots examined. The next parameter to be examined by the developed flow cytometric method is Nile Blue. Nile Blue is the precursor to Nile Red and stains free fatty acids. In the following chapter, free fatty acid dye Nile Blue is characterised and uptake assessed in adipocytes.

## **Chapter 6: Nile Blue is a cell permeable sensor of intracellular free fatty acids in live cells.**

### **6.1 Introduction**

In Chapter 5, a flow cytometric method was presented that can analyse adipocytes at the single cell level. Nile Red effectively stained adipocytes and uptake correlated with cell size and granularity but was not sufficient in distinguishing adipocytes from brown and white adipose depots. Subsequently, Nile Red was combined with mitochondrial potential probe MitoTracker Deep Red to determine whether there were differences between brown, subcutaneous and visceral adipocytes. Together, Nile Red and MitoTracker Deep Red did not effectively discriminate adipocyte populations from different adipose depots. A further parameter to be assessed in conjunction with Nile Red is free fatty acid uptake. Commercially available free fatty acid dyes such as the BODIPY dye series share the same spectra as Nile Red. Nile Blue, is a far-red fluorescent dye which can be used in conjunction with Nile Red to assess free fatty acid uptake.

#### **6.1.1 Chemical properties of Nile Red and Nile Blue**

Nile Blue was first synthesised in 1896 by German researchers Möhlau and Uhlmann (cited in: Martinez & Henary, 2016). Nile Blue and Nile Red belong to the benzophenoxazine family (Martinez & Henary, 2016). They are both heterocyclic

molecules with a 6-membered ring and two double bonds (Martinez & Henary, 2016). Nile Blue is a cationic molecule with a charged iminium group (Figure 6.1) (Martinez & Henary, 2016). Nile Red is a neutral molecule with a carbonyl group instead of an iminium group (Figure 6.1) (Martinez & Henary, 2016). The oxazone component of Nile Red was first extracted by boiling Nile Blue with sulfuric acid (Smith, 1911). Nile Red is soluble in lipids and stains neutral lipids red by diffusion (Dunnigan et al., 1968).

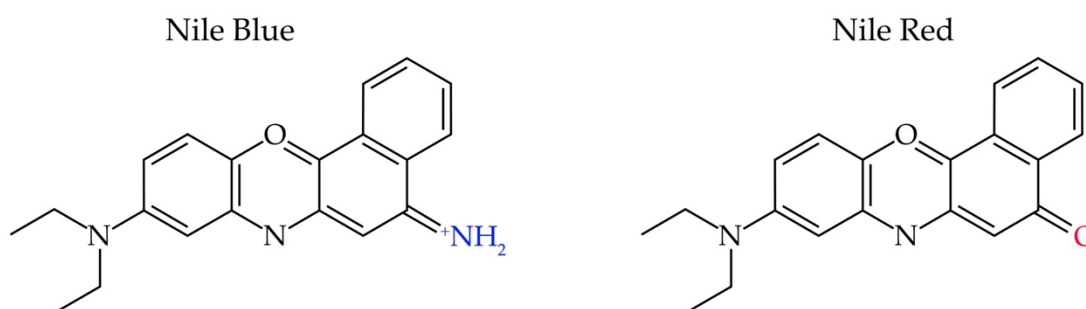


**Figure 6.1: Chemical structure of Nile Blue and Nile Red.**

### **6.1.2 Nile Blue is a benzophenoxazine dye that detects phospholipids and free fatty acids.**

The first reported use of Nile Blue was in 1908. Professor James Lorrain Smith reported Nile Blue staining of cardiac, liver and pancreatic sections (Smith, 1908). Fat globules containing neutral lipids stained red while fat globules containing fatty acids stained a deep blue (Smith, 1908; Smith, 1911). The deep blue staining of fatty acids is due to blue oxazine base forming a soap-like compound with the fatty acids (Smith, 1911).

When Nile Blue is reconstituted in water, the oxazine base oxidises to oxazone (Smith, 1911). The oxidation process can be hastened by boiling the solution with sulfuric acid, which can then be extracted using xylol (Smith, 1911). The extracted oxazone base becomes Nile Red (Smith, 1911).

### **6.1.3 Fatty acid metabolism**

Triglycerides are the most abundant source for energy in mammals (Berg, Tymoczko, & Stryer, 2002; reviewed in: Frayn, Arner, & Yki-Järvinen, 2006). Triglycerides are esters with a glycerol backbone and three fatty acids (Berg et al., 2002). Fatty acids are chains of carbon atoms with a methyl ( $-\text{CH}_3$ ) group at one end and a carboxylic acid group ( $-\text{COOH}$ ) at the other end (Berg et al., 2002). Triglycerides can be hydrolysed into free fatty acids to be released into circulation (Berg et al., 2002). The three main organs which regulate triglyceride hydrolysis are adipose tissue, skeletal muscle and the liver (reviewed in: Frayn et al., 2006). In adipose tissue, free fatty acids may be re-esterified into triglycerides by glyceroneogenesis (Reshef et al., 2003).

After meal consumption, triglycerides bound to chylomicrons are transported into tissues expressing the enzyme lipoprotein lipase (LPL) (Berg et al., 2002; Goldberg, Eckel, & Abumrad, 2008). The leftover chylomicron-bound triglycerides are taken up by the liver by hepatic lipase (HL) (Cooper, 1997; Goldberg et al., 2008). Hydrolysis of stored triglycerides is due to the actions of hormone-sensitive lipase (HSL), which releases non-esterified fatty acids (NEFA) into the plasma (Berg et al., 2002). Albumin-



bound NEFA is taken up by skeletal muscle and the liver (Berg et al., 2002; Frayn et al., 2006). The liver releases hydrolysed triglycerides in the form of very-low density lipoprotein while skeletal muscle (and cardiac tissue) consume fatty acids for oxidation (Berg et al., 2002; Frayn et al., 2006). Figure 6.2 outlines fatty acid translocation between adipose tissue, skeletal muscle and the liver.

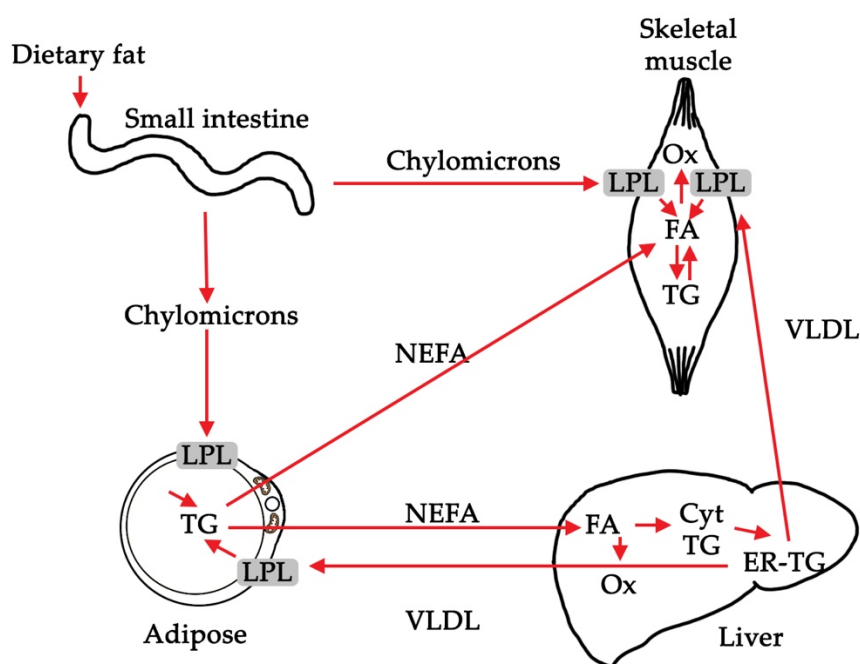


**Figure 6.2: Exchange of lipids between adipose tissue, liver tissue and skeletal muscle following dietary fat intake.** FA, fatty acid; LPL, lipoprotein lipase; TG, triglyceride; Cyt TG, cytosolic triglyceride; ER, endoplasmic reticulum; VLDL, very low-density lipoprotein; NEFA, non-esterified fatty acids.

Nile Blue was first used for histochemical staining of pancreatic, cardiac and hepatic sections (Smith, 1908; Smith, 1911; Cain, 1947). However, specificity of Nile Blue to free fatty acids by spectrofluorometry has not been reported. To date,

spectrofluorimetric analyses of Nile Blue have only been conducted in *Eremothecium ashbyii* fungal filaments for the quantification of lipids (Vijayalakshmi et al., 2003). The question was asked whether Nile Blue could detect free fatty acids in adipocytes, myocytes and hepatocytes at the single cell level. Furthermore, the question was asked whether Nile Blue could be used as a parameter in characterising adipocytes from brown, subcutaneous and visceral adipose depots (Figure 6.3).

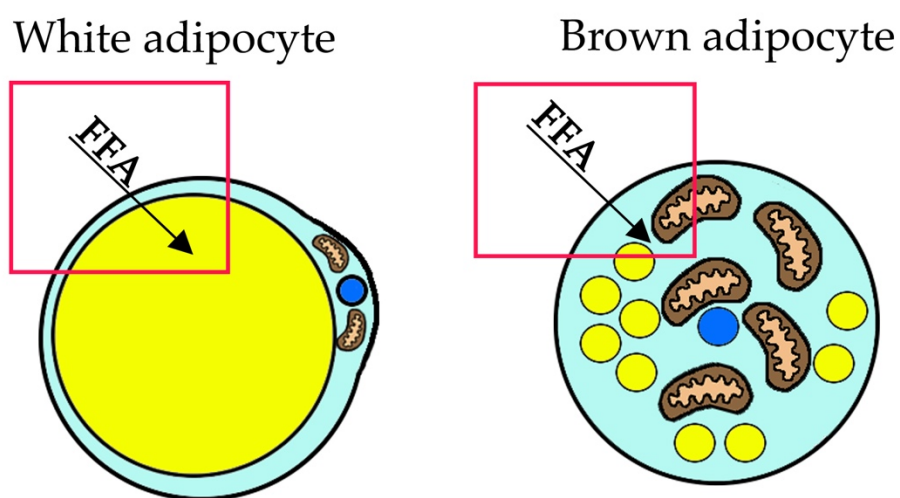


**Figure 6.3: Free fatty acid uptake measured by Nile Blue may distinguish between brown and white adipocytes.**

## **6.2 Methods**

### **6.2.1 Spectrofluorometric analyses of Nile Red and Nile Blue**

Spectrofluorometric analyses were conducted using a Cary Eclipse Fluorescence Spectrophotometer (Agilent Technologies, Santa Clara, California, USA) with the assistance of Dr. Jacek Kolanowski. Palmitate (P9767, Sigma Aldrich), linoleate (L1376, Sigma Aldrich) and oleate (O1008, Sigma Aldrich) were reconstituted in ethanol to a stock concentration of 100 mmol.L<sup>-1</sup>. Nile Blue was dissolved in water to a stock concentration of 10 mmol.L<sup>-1</sup>. The final concentration of Nile Blue used to stain free fatty acids for spectrofluorometric analysis was 1 µmol.L<sup>-1</sup>.

Lipids were pipetted into a cuvette containing 1 µmol.L<sup>-1</sup> Nile Blue or Nile Red in PBS. The cuvette was sealed and inverted up to 15 times to mix the solution. Nile Blue was excited at 630 nm and emission measured between 650 to 750 nm. Nile Red was excited at 500 nm and emission measured between 520 to 750 nm. Data was recorded using the Cary Eclipse software package.

### **6.2.2 Flow cytometry**

#### **6.2.2.1 Adipose tissue, skeletal muscle and liver tissue**

Dissection and dissociation of adipose tissue for flow cytometric analyses is outlined in 2.6.1. and Figure 2.1. Preparation of the buoyant adipocyte fraction for flow cytometric analyses is outlined in 2.6.3 and 5.2.1.1. Skeletal muscle tissue was dissected from the quadriceps by bilateral incision. Skeletal muscle and liver tissue

were dissociated into single cell suspensions in the same manner as adipose tissue (outlined in 2.5.1.2, Table 2.9, Figure 2.1). The buoyant fraction of each tissue was stained with FACS buffer containing 100 nmol.L<sup>-1</sup> of Nile Red and Nile Blue as described in 4.2.2.

### 6.2.3 Statistical analyses

All data presented as mean  $\pm$  SEM. Statistical analyses were performed on GraphPad Prism®. Comparisons between Nile Red and Nile Blue fluorescence in the presence of lipids was determined by a two-tailed, Student's *t*-test. Differences in Nile Red and Nile Blue uptake in adipocytes, hepatocytes and myocytes were determined by a two-tailed, one-way ANOVA with Tukey's *post-hoc* analysis. For all statistical tests, a *P* value < 0.05 was deemed significant.

## **6.3 Results**

### **6.3.1 Spectrofluorometric analyses of Nile Blue and Nile Red**

#### **6.3.1.1 The presence of oleate and linoleate but not palmitate results in increasing Nile Blue fluorescence.**

As there are no reports characterising Nile Blue by spectrofluorometry, fluorescence of Nile Blue in the presence of fatty acids was measured by spectrofluorometry. Nile Blue exhibited some background fluorescence in PBS but did not auto-fluoresce in the presence of ethanol (Figure 6.4Aii). No fluorescence was detected in Nile Blue with palmitate (Figure 6.4Aii). Conversely, fluorescence was greatest in the presence of Nile Blue with oleate or linoleate (Figure 6.4Aii). Furthermore, fluorescence increased linearly with increasing concentrations of palmitate and linoleate (Figure 6.4Aiii). Fluorescence was comparable between oleate and linoleate at all concentrations tested but fluorescence was greater compared to palmitate (Figure 6.4Aiii).

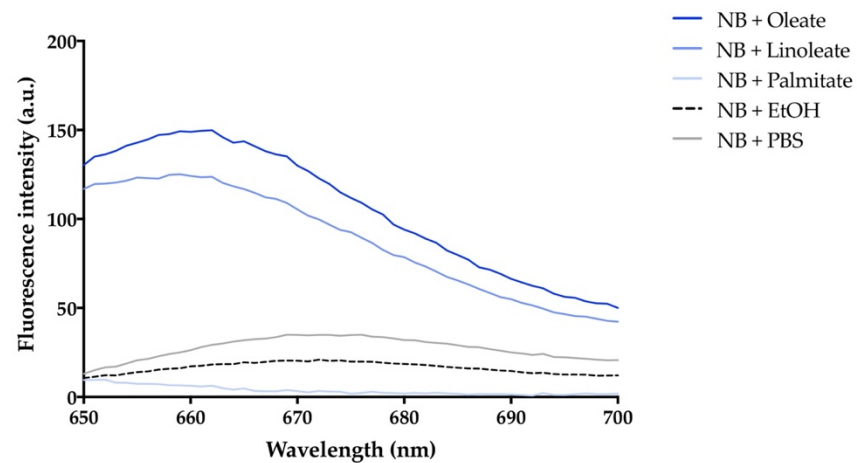
#### **6.3.1.2 The presence of oleate and linoleate but not palmitate results in increasing Nile Red fluorescence.**

Nile Red fluorescence was also measured in the presence of fatty acids. Similarly, Nile Red exhibited no fluorescence in the presence of ethanol (Figure 6.4Bii). Fluorescence intensity of Nile Red was greatest in the presence of linoleate and oleate compared to palmitate (Figure 6.4Bii-iii). Nile Red fluorescence increased with increasing concentrations of linoleate and oleate, but not palmitate (Figure 6.4Biii).

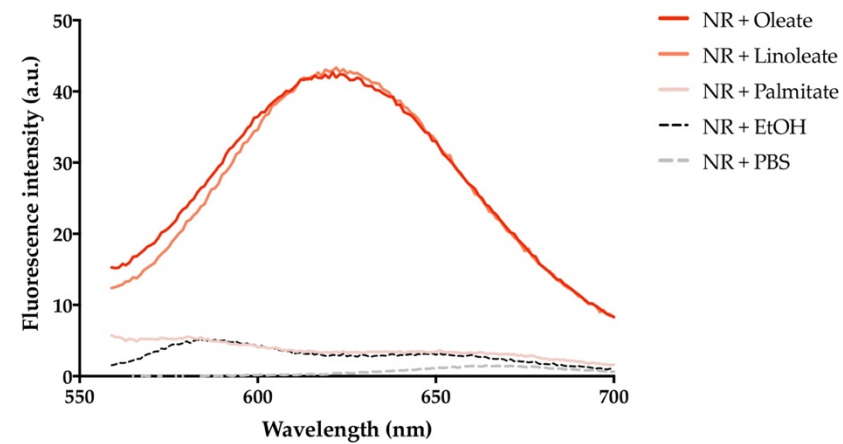
**Figure 6.4: The presence of oleate and linoleate but not palmitate results in increasing Nile Blue fluorescence.**

Representative fluorescence intensity (a.u.) of (Ai) Nile Blue and (Bi) Nile Red in the presence of ethanol, PBS, palmitate, linoleate and oleate. Fluorescence of Nile Blue was measured between 640 nm to 750 nm. Fluorescence of Nile Red was measured between 560 nm to 700 nm. Fold change in fluorescence intensity of (Aii) Nile Blue and (Bii) Nile Red in the presence of 100  $\mu\text{mol.L}^{-1}$ , 200  $\mu\text{mol.L}^{-1}$  and 300  $\mu\text{mol.L}^{-1}$  palmitate, linoleate and oleate. Data presented as mean  $\pm$  SEM (n=3). Differences in the fold change of Nile Blue and Nile Red fluorescence in the presence of increasing concentration of fatty acids was determined by a two-tailed, one-way ANOVA with Tukey's *post hoc* analysis. Groups not sharing a numeral are significantly different from each other. Differences in Nile Blue and Nile Red fluorescence between fatty acids was determined by a two-tailed, two-way ANOVA with Tukey's comparison test. Groups not sharing a symbol (#) are significantly different from each other.

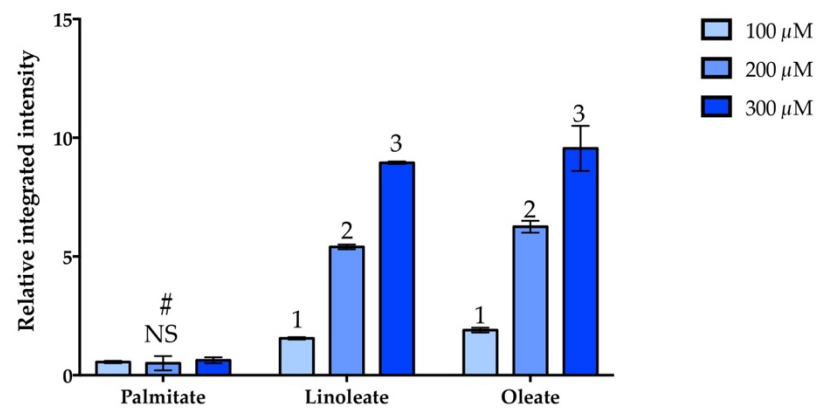
Ai)



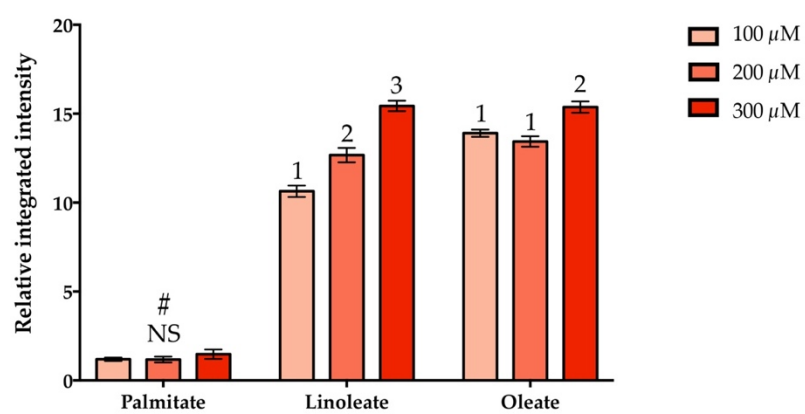
ii)



Bi)



ii)



### **6.3.1.3 Nile Blue fluorescence is greater than Nile Red in the presence of free fatty acids in solution.**

The fluorescence intensity of Nile Blue and Nile Red were compared in the presence of different fatty acids in solution. Nile Blue displayed greater fluorescence in the presence of linoleate, oleate, 1- $\alpha$ -phosphatidylcholine, tri-oleate and non-esterified fatty acids (NEFA) than Nile Red (Figure 6.5i). However, when fluorescence intensity was normalised to background fluorescence, Nile Red had greater fluorescence intensity in the presence of tri-oleate and NEFA compared to Nile Blue (Figure 6.5ii).



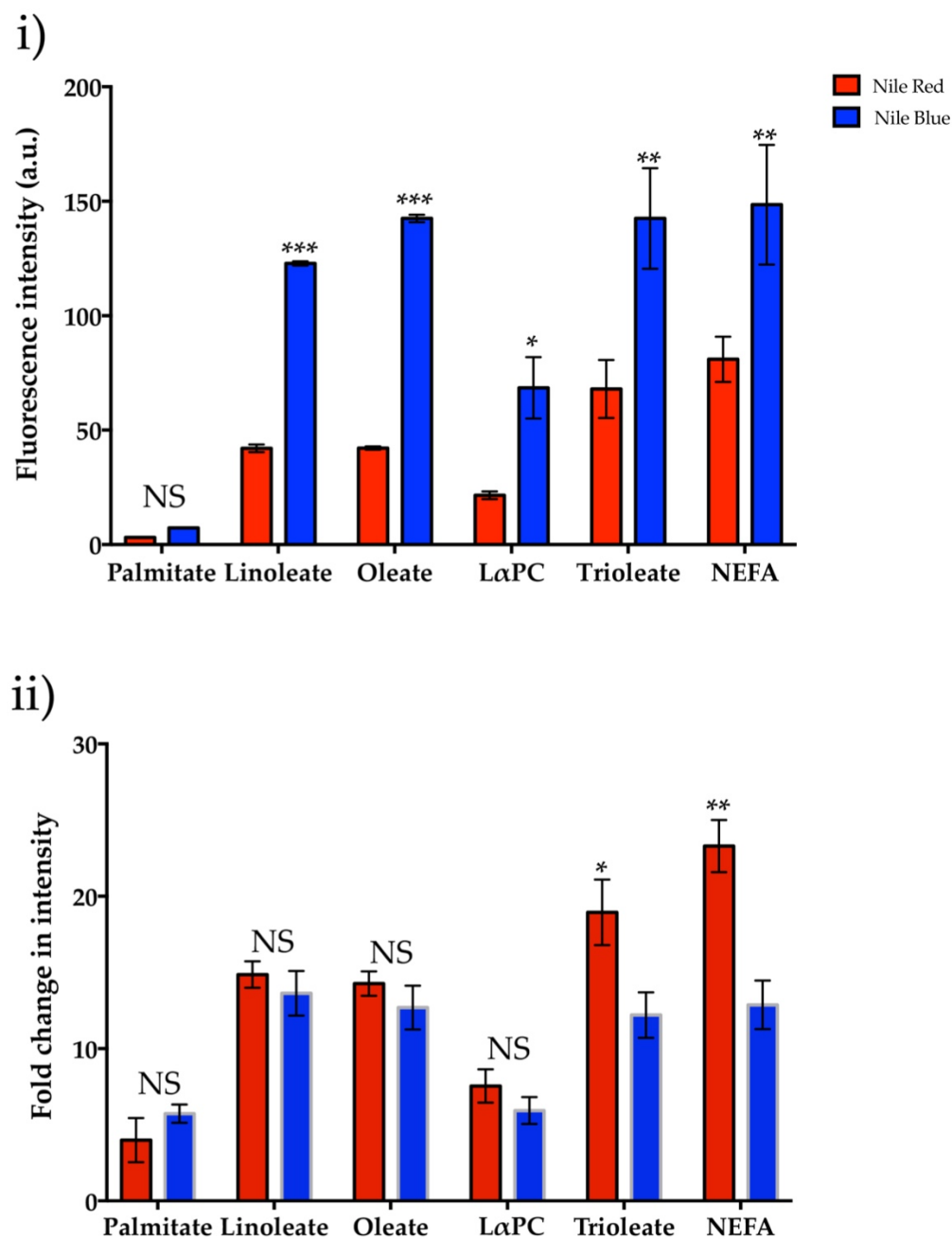


**Figure 6.5: Nile Red detects tri-oleate and non-esterified fatty acids.**

Comparisons in the (i) raw and (ii) integrated fluorescence intensity (a.u.) of Nile Red and Nile Blue in the presence of palmitate, linoleate, oleate, 1- $\alpha$ -phosphatidyl choline (L $\alpha$ PC), tri-oleate and non-esterified fatty acids (NEFA). Differences between Nile Red and Nile Blue fluorescence in the presence of fatty acids was determined by a two-tailed Student's t-test. \* =  $P < 0.05$ , \*\* =  $P < 0.01$ , \*\*\* =  $P < 0.001$ , NS = not significantly different.

### **6.3.2 Hepatocytes and adipocytes have the greatest uptake of Nile Blue**

In Chapter 5, a method was developed to analyse Nile Red uptake in single cell suspensions of adipocytes. Here, the buoyant fraction of dissociated liver tissue, skeletal muscle and brown and white adipose tissue was analysed for Nile Red and Nile Blue uptake (Figure 6.6i). Nile Red and Nile Blue fluorescence was observed in all cell types (Figure 6.6ii-iii). Brown and white adipocytes had significantly greater uptake of Nile Red compared to hepatocytes ( $P < 0.0001$ ) and myocytes ( $P < 0.0005$ ) (Figure 6.6ii, 6.7i). Nile Blue uptake was equivalent between hepatocytes and brown and white adipocytes (Figure 6.6iii, 6.7ii). Myocytes displayed lower uptake of Nile Blue compared to hepatocytes ( $P < 0.0001$ ), brown ( $P < 0.005$ ) and white ( $P < 0.001$ ) adipocytes (Figure 6.6iii, 6.7ii).

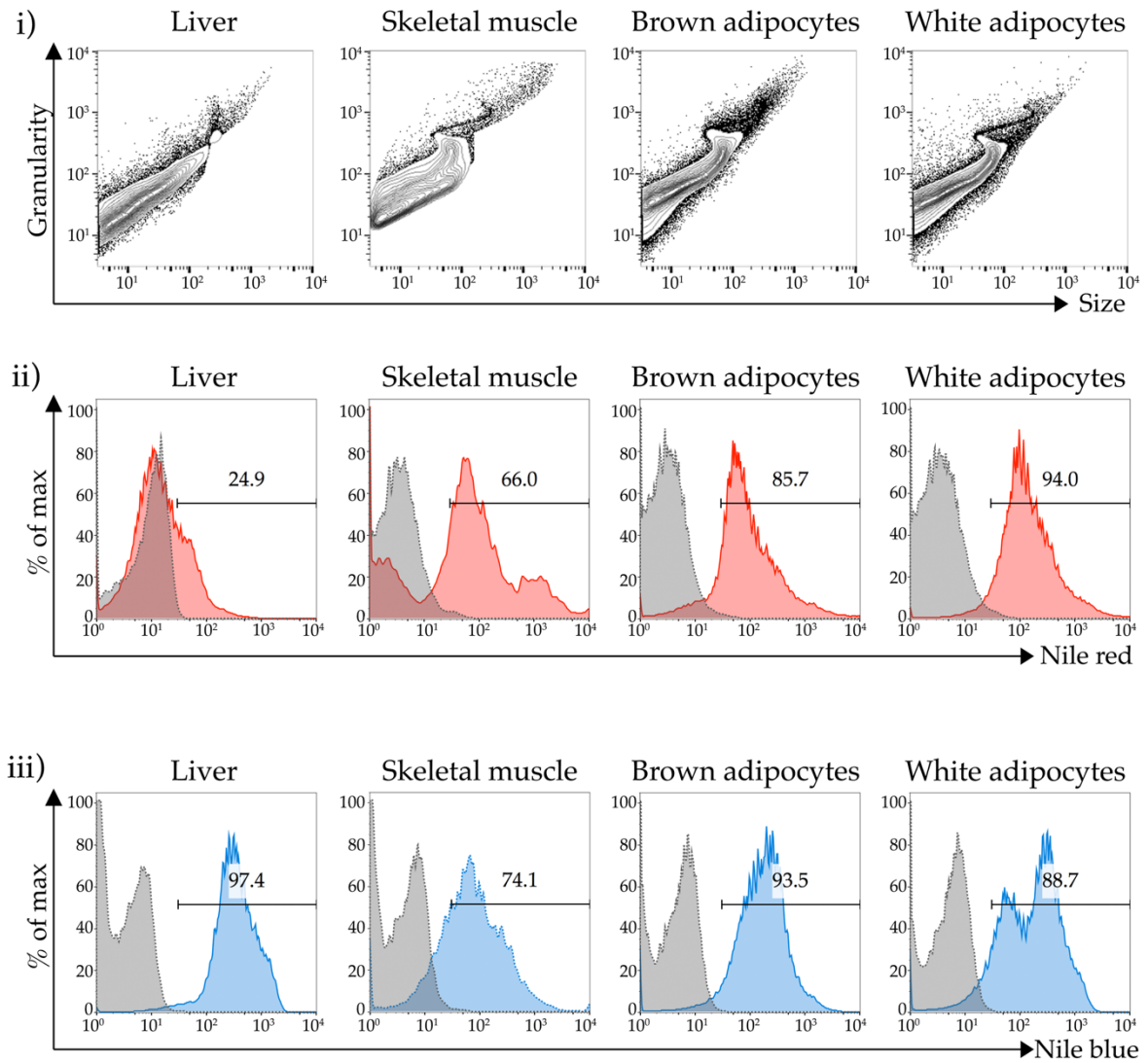


**Figure 6.6: Single cell suspensions from metabolically active tissues take up Nile Red and Nile Blue.** Representative flow cytometric plot of the (i) forward (size) and side scatter (granularity) of the buoyant fraction of dissociated liver tissue, skeletal muscle and brown and white adipose tissue. Live cells were gated and fluorescence of (ii) Nile Blue (blue shaded plot) and (iii) Nile Red (red shaded plot) measured. Uptake of Nile Blue and Nile Red expressed as a percentage of the total number of cells (% of max). Grey shaded plots represent the no-dye control.

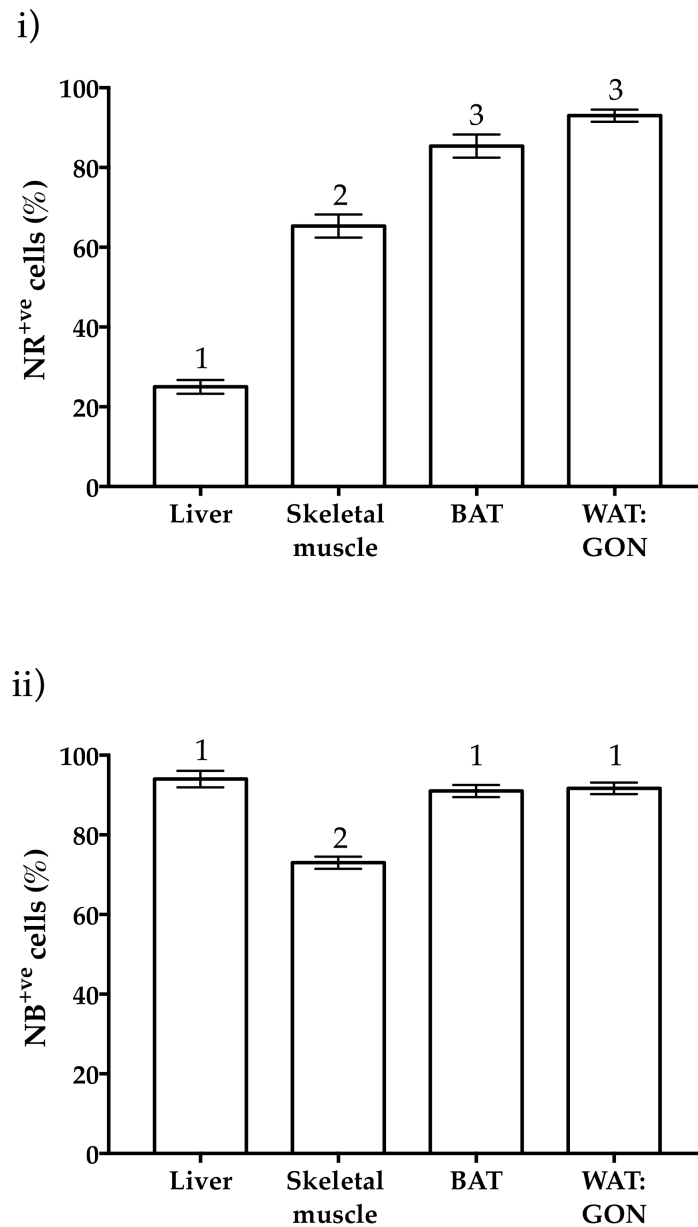


**Figure 6.7: Adipocytes have greater Nile Red uptake than hepatocytes and myocytes.**

Comparisons in the frequency of (i) Nile Blue<sup>+</sup>ve and (ii) Nile Red<sup>+</sup>ve cells between the buoyant fraction of dissociated liver tissue, skeletal muscle and brown and white adipose tissue (BAT and WAT respectively). Data presented as mean  $\pm$  SEM (n=3 for all groups). Differences in the frequency of Nile Blue and Nile Red positive cells between cell types were determined by two-tailed, one-way ANOVA and pairwise *post-hoc* comparison by Tukey's HSD test. Groups not sharing a numeral are significantly different from each other.

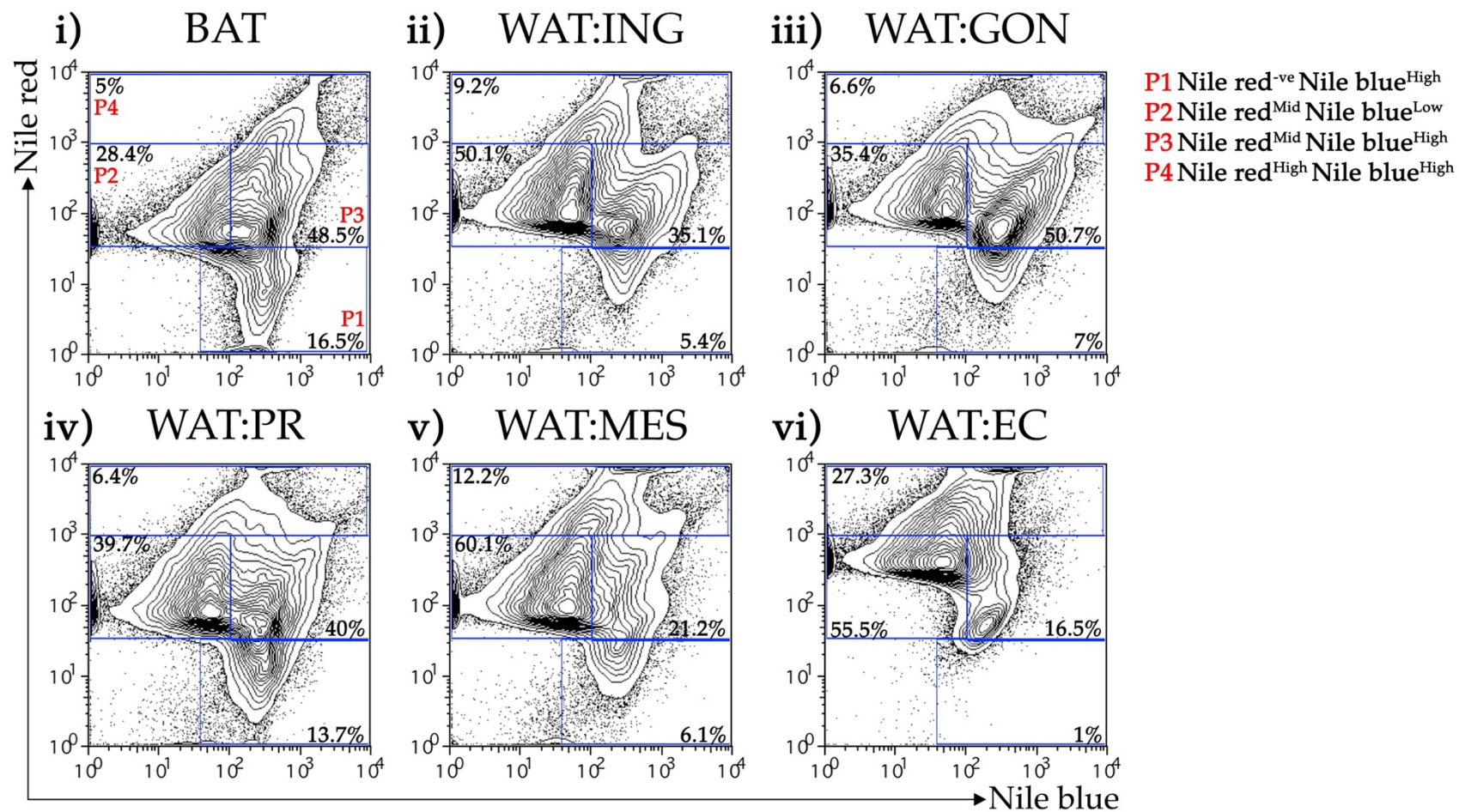
### **6.3.3 Nile Red and Nile Blue uptake distinguishes adipocyte populations in brown and white adipocytes.**

Confident that Nile Blue was detecting free fatty acids, adipocytes from six different depots were stained with Nile Red and Nile Blue and uptake measured (Figure 6.8). Uptake of Nile Red and Nile Blue revealed four distinct cell populations according to fluorescence intensity (Figure 6.8). The populations were defined as: Nile Red<sup>-ve</sup> Nile Blue<sup>High</sup> (P1), Nile Red<sup>Mid</sup> Nile Blue<sup>Low</sup> (P2), Nile Red<sup>Mid</sup> Nile Blue<sup>High</sup> (P3) and Nile Red<sup>High</sup> Nile Blue<sup>High</sup> (P4) (Figure 6.8).

Brown adipocytes had the greatest number of cells that were Nile Red<sup>-ve</sup> Nile Blue<sup>High</sup> (P1,  $P < 0.005$ ) (Figure 6.9i). Mesenteric and epicardial adipocytes had more Nile Red<sup>Mid</sup> Nile Blue<sup>Low</sup> (P2) cells compared to brown ( $P < 0.008$ ,  $P < 0.004$  respectively) and gonadal ( $P < 0.05$ ,  $P < 0.006$  respectively) adipocytes (Figure 6.9ii). Epicardial and mesenteric adipocytes had the least number of cells that were Nile Red<sup>Mid</sup> Nile Blue<sup>High</sup> (P3,  $P < 0.05$ ) (Figure 6.9iii). Conversely, epicardial adipocytes had the most Nile Red<sup>High</sup> Nile Blue<sup>High</sup> (P4) cells compared to brown ( $P < 0.01$ ) and gonadal ( $P < 0.05$ ) adipocytes (Figure 6.9iv).

**Figure 6.8: Uptake of Nile Red and Nile Blue in adipocytes reveals distinct populations.**

Representative flow cytometric plot of Nile Red and Nile Blue uptake in (i) brown (BAT), (ii) subcutaneous inguinal (WAT:ING) and visceral (iii) gonadal (WAT:GON), (iv) peri-renal (WAT:PR), (v) mesenteric (WAT:MES) and (vi) epicardial (WAT:EC) adipocytes. Cell populations (P1-P4) were gated according to Nile Red and Nile Blue fluorescence. P1 represents the Nile Red<sup>-ve</sup> Nile Blue<sup>High</sup> population; P2 represents the Nile Red<sup>Mid</sup> Nile Blue<sup>Low</sup> population; P3 represents the Nile Red<sup>Mid</sup> Nile Blue<sup>High</sup> population and P4 represents the Nile Red<sup>High</sup> Nile Blue<sup>High</sup> population.



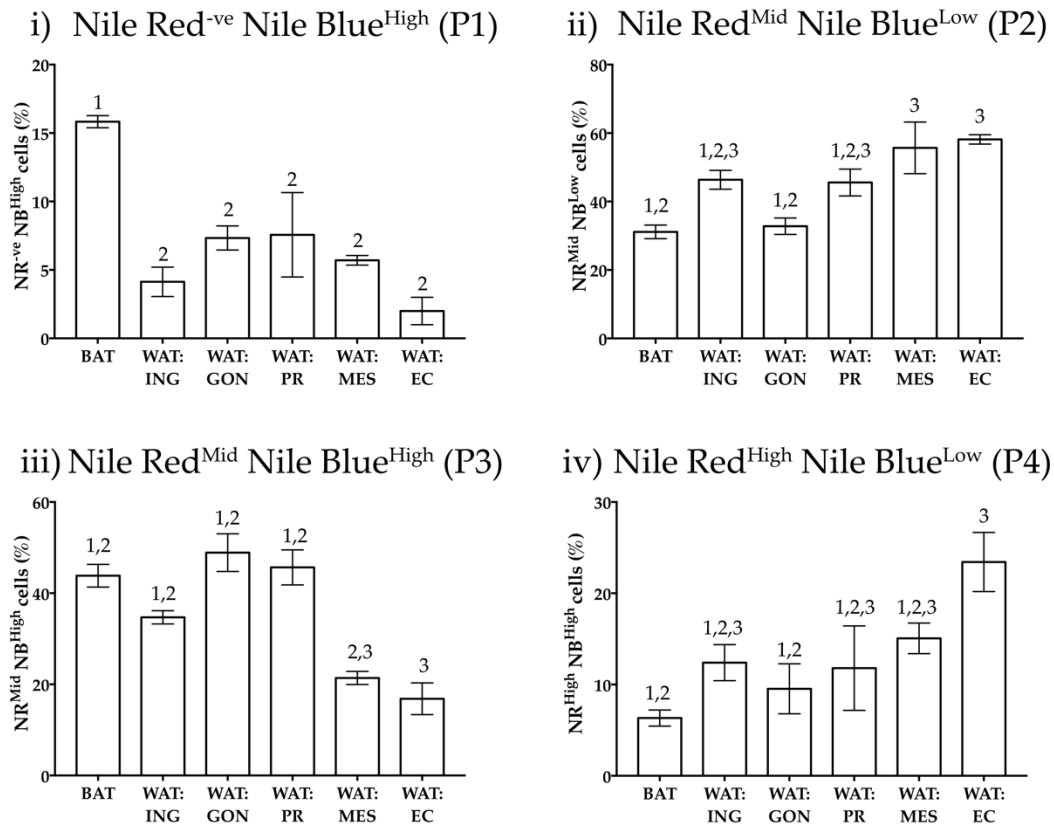


**Figure 6.9: Brown and white adipocyte heterogeneity according to Nile Red and Nile Blue uptake.**

Comparisons between each adipose depot according to frequency of cells in (i) Nile Red<sup>-ve</sup> Nile Blue<sup>High</sup> (P1), (ii) Nile Red<sup>Mid</sup> Nile Blue<sup>Low</sup> (P2), (iii) Nile Red<sup>Mid</sup> Nile Blue<sup>High</sup> (P3) and (iv) Nile Red<sup>High</sup> Nile Blue<sup>High</sup> (P4). Data presented as mean  $\pm$  SEM (n=5). Differences in cell frequency between adipose depots were determined by two-tailed, one-way ANOVA and pairwise *post-hoc* comparison by Tukey's HSD test. Groups not sharing a numeral are significantly different from each other.



## **6.4 Discussion**

Nile Blue was synthesised over a century ago and has been met with criticism regarding its utility (cited in: Cain, 1947). German researchers Kaufmann and Lehmann and French researcher Lison concluded that Nile Blue was a non-specific lipophilic dye and was of no histological value (cited in: Cain, 1947). Despite the criticisms raised against Nile Blue, Cain (1947) demonstrated utility of Nile Blue in distinguishing between neutral lipids and fatty acids (Cain, 1947). The findings presented in this chapter support the findings reported by Cain (1947) and highlight the utility of Nile Blue as an intracellular sensor of free fatty acids.

### **6.4.1 Nile Blue detects oleate and linoleate**

A spectrofluorometric approach was analysed to provide insight into the photochemical properties and utility of Nile Blue. Early reports of Nile Blue described an intense blue staining for phospholipids such as lecithin and an intense red staining for triglycerides and cholesterol esters (Smith, 1911; Cain, 1947; Dunnigan et al., 1968). Staining of palmitic, oleic and linoleic acid was described to be purple, further supporting the observations made in this study (Cain, 1947; Dunnigan et al., 1968).

#### **6.4.2 Advantages in flow cytometric analyses of Nile Red and Nile Blue uptake**

While spectrofluorometric assays are useful in the rapid screening of different fatty acids in a cell free system, flow cytometry can quantify changes in dye uptake at the single cell level. As the fluorescence spectra for Nile Blue and Nile Red do not overlap, they can be combined to stain for free fatty acids and neutral lipids respectively in single cells. Cells do not require fixation prior to staining with Nile Red and Nile Blue (Greenspan et al., 1985). Although current methodologies for measuring and identifying fatty acids such as mass spectrometry are sensitive and specific, they are complex, time consuming and costly. Flow cytometric analyses of Nile Red and Nile Blue could be utilised as a precursor to mass spectrometry to determine whether samples containing a combination of neutral lipids or fatty acids differ prior further analysis by mass spectrometry.

#### **6.4.3 Nile Red and Nile Blue uptake characterises the maturation process of adipocytes**

Adipose tissue contains adipocytes of different sizes, which vary according to adipose depot and the stage of maturation (Jo et al., 2009). In Chapter 5, Nile Red uptake was proposed as an indicator of adipocyte maturation as uptake was proportional to cell size and granularity. Uptake of Nile Red and Nile Blue provides further evidence of adipocyte maturation. Doan-Xuan and colleagues (2013) used laser scanning cytometry to assess Nile Red and Nile Blue fluorescence on the pre-adipocyte cell line SGBS (Doan-Xuan et al., 2013). Differentiated adipocytes exhibited greater Nile Red

fluorescence whilst pre-adipocytes had greater Nile Blue fluorescence (Doan-Xuan et al., 2013). In conjunction with the findings reported by Doan-Xuan and colleagues (2013), the method presented here may describe the maturation of adipocytes as they progress from maturing (Nile Blue only) to mature adipocytes (Nile Red and Nile Blue). Live cell fluorescent imaging can also be utilised to measure Nile Red and Nile Blue uptake in cultured primary adipocytes as they undergo adipogenesis.

#### **6.4.4 Modelling fatty acid metabolism in live cells with Nile Red and Nile Blue**

Triglyceride levels in the liver are low under physiological conditions (Kawano & Cohen, 2013; Frayn et al., 2006). In times of excess food consumption, the liver begins to accumulate triglycerides in a condition termed non-alcoholic fatty liver disorder (NAFLD) (Kawano & Cohen, 2013). The low uptake of Nile Red and high uptake of Nile Blue reported here may be indicative of triglyceride clearance in the liver.

Nile Red and Nile Blue uptake in myocytes could represent the adipocytes stored within the muscle fibre (intramyocellular adipocytes) or the adipocytes interspersed with the muscle fibres. Intramyocellular adipocytes are posited to be an energy source for extended periods of exercise (Frayn et al., 2006). In a clinical setting, Nile Red and Nile Blue could be utilised to assess changes in lipid metabolism in Duchennes muscular dystrophy. For instance, there is a decrease in the ratio of phospholipids to triglycerides in Duchennes muscular dystrophy (Pearce et al., 1981). Thus, the ratio of Nile Blue to Nile Red could be used as a screening tool for muscular dystrophy.

Additionally, histopathological analysis of sections acquired from muscle biopsies revealed an increase in the amount of fat accumulation in the diseased muscle (Bell & Conen, 1968). Indeed, patients diagnosed with Duchennes muscular dystrophy present with an increase in fatty acid infiltration in the pelvic, thigh and gluteal muscles (Kim et al, 2013; Li et al, 2015). One possibility in increased adipocyte deposition in muscle may be due to differentiation of mesenchymal stem cells into adipocytes (Sienkiewicz et al, 2015). However, the mechanism behind adipocyte infiltration remains largely unexplored.

#### **6.4.4.1 Nile Red and Nile Blue as a diagnostic tool in fatty acid metabolism disorders**

Approximately 70% of obese individuals with type II diabetes are diagnosed with NAFLD (Targher et al., 2007). The hallmark of NAFLD is an increase in intrahepatic triglyceride accumulation, traditionally assessed by liver biopsies (Kawano & Cohen, 2013), (Fabbrini & Magkos, 2015). NAFLD encompasses steatosis, non-alcoholic steatohepatitis and cirrhosis and is recognised as the leading cause for liver dysfunction in individuals who do not consume alcohol (Kawano & Cohen, 2013).

Nile Red and Nile Blue could be used clinically as a diagnostic tool for the development and progression of NAFLD. In mice, NAFLD induced steatosis can be induced by feeding mice a high fat and high carbohydrate diet (Clapper et al., 2013; Kirsch et al., 2003; Fengler et al., 2015; Schultz et al., 2015). An assay can be designed to measure the balance between Nile Red and Nile Blue uptake in hepatocytes from

mice fed different diets. In this study, the hepatocytes of adult, wild-type mice fed a normal chow diet had low uptake of Nile Red and high uptake of Nile Blue. Accumulation of triglycerides, as depicted in NAFLD can be measured by the increased uptake of Nile Red and decreased uptake of Nile Blue.

#### **6.4.5 Conclusions**

Nile Red and Nile Blue are useful lipophilic probes that can be applied to measure differences in lipid metabolism. Nile Red preferentially detects neutral lipids while Nile Blue detects fatty acids oleate and linoleate. As the fluorescence spectrum of Nile Red and Nile Blue do not overlap, they can be combined for staining at the single cell level as demonstrated by flow cytometric analyses. However, uptake of Nile Red and Nile Blue was not sufficient in distinguishing differences between adipose depots. In the following chapter, Nile Red is combined with cell surface protein markers to determine whether there are differences between brown and white adipocytes.

## **Chapter 7: Characterisation of adipocytes from different adipose depots according to cell surface protein expression.**

### **7.1 Introduction**

In Chapter 5, a method was developed to characterise buoyant adipocytes from dissociated adipose tissue using cell size, granularity and Nile Red uptake. Nile Red was combined with mitochondrial probe MitoTracker Deep Red and free fatty acid dye Nile Blue (Chapter 6) to determine whether adipocyte heterogeneity existed at the single cell level. However, neither probe was able to sufficiently distinguish adipocytes from brown, subcutaneous and visceral adipose depots. Here, Nile Red is assessed in combination with a panel of surface protein markers to determine if there are any differences between brown and white adipocytes (Figure 7.1).

#### **7.1.1 Heterogeneity of adipose tissue.**

Adipose tissue is considered a metabolically active endocrine organ. However, each distinct adipose depot differs in metabolic, hormonal and physiological profiles (reviewed in: Kwok, Lam, & Xu, 2016). Reflecting this is the report that the proteins involved in ATP generation and the metabolism of glucose, lipid and free fatty acids differ between adipose depots (Bjørndal et al., 2011; Sackmann-Sala et al., 2011). Visceral adipose depots have greater levels of glucose and lipid metabolism compared to subcutaneous adipose depots (Bjørndal et al., 2011; Lee et al., 2013). Subcutaneous adipose tissue however, has greater levels of leptin expression and is more efficient in

taking up free fatty acids from circulation compared to visceral adipose depots (Coelho, Oliveira, & Fernandes, 2013; White & Tchoukalova, 2014). Brown adipocytes fuel non-shivering thermogenesis through uncoupling protein-1 (Nedergaard and Canon, 2014). Mass spectrometric analyses have identified greater amounts of phospholipids and free fatty acids in brown adipocytes compared to subcutaneous and visceral white adipocytes (Hoene et al., 2014). Conversely, white adipocytes contain more triglycerides than brown adipocytes (Hoene et al., 2014).

#### **7.1.1.1 Differences in the extracellular matrix between adipose depots.**

An integral component of adipose tissue is the extracellular matrix (ECM) that encompasses it (Mariman & Wang, 2010; Pellegrinelli et al., 2016). The ECM of adipose tissue is dynamic, responding to biochemical cues and mechanical force (Craft et al., 2015). The ECM also regulates adipocyte expansion (Pellegrinelli et al., 2016). Collagen IV is one of the major components of the ECM of adipocytes (Craft et al., 2015).

Proteomic studies have labelled 12 types of collagens in primary rodent adipocytes (Mariman & Wang, 2010). Interestingly, there are differences in the expression of the subunits of collagen differ across species (rodents and humans) and adipose depots (subcutaneous and visceral WAT) (Mariman & Wang, 2010). Subunits of collagen type II, XI and XXIII are absent in human visceral WAT (Mariman & Wang, 2010). Fibronectin, laminin and thrombospondin-1 have been identified in human subcutaneous WAT, rodent primary adipocytes and 3T3-L1 pre-adipocytes (Mariman



& Wang, 2010). Subcutaneous WAT has greater protein expression of collagen type I than visceral WAT (Pellegrinelli et al., 2016). Collagen fibres form networks with fibronectin and laminin, which allow integrins to dock into the membrane of adipocytes (Bonnans, Chou, & Werb, 2014). Integrins are composed of alpha and beta subunits (Barczyk, Carracedo, & Gullberg, 2010). During adipogenesis, alpha integrin expression shifts from  $\alpha 5$  to  $\alpha 6$  while  $\beta 1$  integrin is upregulated in mature adipocytes (Farnier et al., 2003; Liu et al., 2005; Noro et al., 2013). The integrin complex  $\alpha 6\beta 1$  recognises laminin receptor and is expressed at greater levels in subcutaneous WAT compared to visceral WAT (Mori et al., 2014). Compared to white adipose tissue however, little is known about the extracellular matrix composition of brown adipose tissue (Pope et al., 2016).

#### **7.1.2 Surface protein expression of CD137 and CD40 reportedly characterise beige adipocytes.**

Recently, Wu *et al.* (2012) reported CD137 (4-1BB) and CD40 as beige adipocyte specific surface markers found within subcutaneous inguinal adipocytes (Wu et al., 2012). The terms brite (**brown in white**) and beige are often used interchangeably to classify a third class of adipocytes (Cinti, 2012; Harms & Seale, 2013). Brite adipocytes refer to a population of brown adipocytes residing within a white adipose tissue depot (Rosenwald & Wolfrum, 2014). In response to cold stimuli or  $\beta 3$ -adrenergic stimulation, white adipocytes may undergo a 'browning' process which converts white adipocytes into brown-like adipocytes (Park, Kim, & Bae, 2014; Harms & Seale,

2013). The subsequent beige adipocyte is considered a distinct class of adipocytes (Wu et al., 2012). The subcutaneous inguinal adipose depot is predisposed to 'browning' in response to cold stimuli whilst visceral adipose depots like gonadal are resistant (Harms & Seale, 2013).

Since MitoTracker Deep Red and Nile Blue were not sufficient in distinguishing brown and white adipocytes, the aim here was to assess a panel of cell surface protein markers to determine if there were any differences between brown and white adipocytes. This work (together with the findings from Chapter 5), made up the majority of a recently published manuscript (Appendix 3) (Boumelhem et al., 2017).

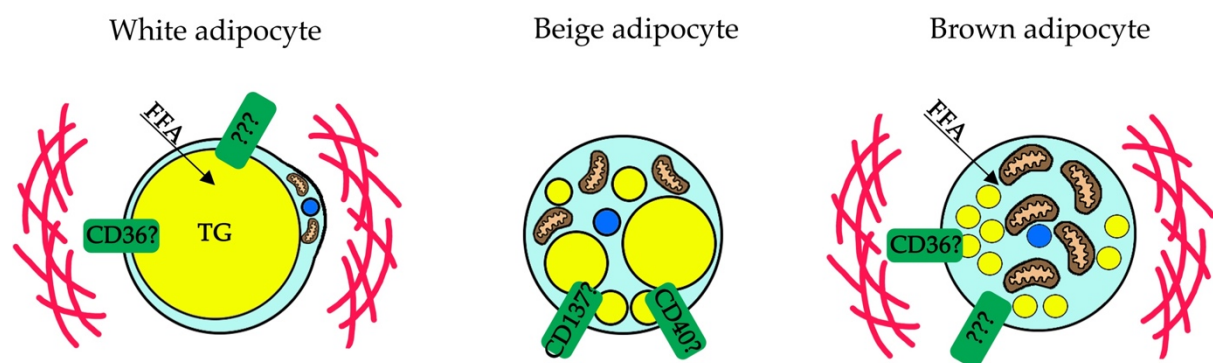


**Figure 7.1: Proposed assessment of cell surface protein markers and extracellular matrix proteins in white, beige and brown adipocytes.**

## **7.2 Methods**

### **7.2.1 Flow cytometry of brown, subcutaneous and visceral white adipocytes**

Dissection and dissociation of adipose tissue for flow cytometric analyses is outlined in 2.5.1.2 and Figure 2.1. Preparation of the buoyant adipocyte fraction for flow cytometric analyses is outlined in 2.6.3 and 5.2.1.1.

#### **7.2.1.1 Flow cytometry of marrow adipocytes**

Flow cytometric analyses of marrow adipocytes was performed on flushed caudal vertebrae (tail) marrow. The tail was removed by snipping at the base. Four incisions were made around the opening to allow for the removal of the skin surrounding the tail with forceps. Individual vertebrae were sliced by a razor blade and then sliced again in half to expose the marrow. The marrow was flushed using a 23G needle attached to a 5 mL syringe containing 3 mL of ES maintenance medium. Staining of marrow adipocytes performed in the same manner as brown and white adipocytes (2.6.3 and 5.2.1.1).

#### **7.2.2 Statistical analyses**

Statistical analyses were performed on GraphPad Prism®. All data represented as mean  $\pm$  SEM. Where relevant, two-tailed Student's *t*-test was used to compare between two groups. A two-tailed one-way ANOVA with Tukey's *posthoc* analysis was used to compare more than two groups.

## 7.3 Results

### 7.3.1 Adipocytes do not display immunoreactivity to a range of fluorescently-conjugated antibodies.

In Chapter 5, cell surface protein expression of haematopoietic markers was not detected on the buoyant fraction containing adipocytes (Figure 5.7-9). In Chapters 6 and 7, mitochondrial membrane potential probe MitoTracker Deep Red and fatty acid dye Nile Blue did not clearly discriminate adipocytes from multiple adipose depots. In search of candidate markers to distinguish adipocytes, a panel of surface protein markers were selected based from the literature as well online database searches. Here, a panel of surface protein markers were assessed on brown, white and marrow adipocytes (Table 7.1). Surface protein markers identifying adhesion molecules including integrins  $\alpha 2$ ,  $\alpha 4$ ,  $\alpha 5$ ,  $\alpha 7$ ,  $\beta 3$ ,  $\beta 4$ ,  $\beta 7$ ; epithelial markers E-Cadherin and Epithelial Cell Adhesion Molecule; CD133 and Intracellular Adhesion Molecule 1 were not detected on brown, white or marrow adipocytes (Table 7.1). Conversely,  $\alpha 6$  integrin,  $\beta 1$  integrin and fatty acid translocase CD36 displayed immunoreactivity. Thus, those markers were chosen for further evaluation in brown, subcutaneous and visceral white adipocytes. A complete list of all the antibodies assayed in this study is presented in Table 7.1.

**Table 7.1: A list of fluorescently-conjugated monoclonal antibodies used to screen for surface protein expression in brown and white adipocytes.**

<b>Antibody</b>	<b>BAT</b>	<b>WAT:ING</b>	<b>WAT:GON</b>	<b>WAT:PR</b>	<b>WAT:MES</b>	<b>WAT:EC</b>
$\alpha$ 2-integrin	-	-	-	-	-	-
$\alpha$ 4-integrin	-	-	-	-	-	-
$\alpha$ 5-integrin	-	-	-	-	-	-
$\alpha$ 6-integrin	+	+	+	+	+	+
$\alpha$ 7-integrin	-	-	-	-	-	-
$\alpha$ L-integrin	-	-	-	-	-	-
$\beta$ 1-integrin	+	+	+	+	+	+
$\beta$ 3-integrin	-	-	-	-	-	-
$\beta$ 4-integrin	-	-	-	-	-	-
$\beta$ 7-integrin	-	-	-	-	-	-
c-Kit	-	-	-	-	-	-
CD3 $\epsilon$	-	-	-	-	-	-
CD4	-	-	-	-	-	-
CD11b	-	-	-	-	-	-
CD19	-	-	-	-	-	-
CD31	-	-	-	-	-	-
CD34	-	-	-	-	-	-
CD36	+	+	+	+	+	+
CD41	-	-	-	-	-	-
CD45	-	-	-	-	-	-
CD47	-	-	-	-	-	-
CD48	-	-	-	-	-	-
CD61	-	-	-	-	-	-
CD62P	-	-	-	-	-	-
CD71	-	-	-	-	-	-
CD133	-	-	-	-	-	-
CD144	-	-	-	-	-	-
Csf-1R	-	-	-	-	-	-
CXCR4	-	-	-	-	-	-
E-Cadherin	-	-	-	-	-	-
EpCAM	-	-	-	-	-	-
F4/80	-	-	-	-	-	-
Flk-1	-	-	-	-	-	-
I-CAM1	-	-	-	-	-	-
PDGFR $\alpha$	-	-	-	-	-	-
Sca-1	-	-	-	-	-	-
Ter119	-	-	-	-	-	-
V-Cam1	-	-	-	-	-	-

### **7.3.2 Immunoreactivity of fatty acid translocase CD36 differs between brown and white adipose depots.**

Fatty acid translocase CD36 was chosen as a candidate surface marker of adipocytes. CD36 is a multi-ligand receptor that shuttles fatty acids into cells (Qiao et al., 2008). CD36 surface protein expression has been reported on human adipocytes obtained from lipoaspirates (Festy et al., 2005). However, no comparisons have apparently been made in surface protein expression of CD36 between brown, subcutaneous and visceral white adipose depots (Boumelhem et al., 2017).

CD36 immunoreactivity was assessed according to Nile Red uptake in brown and white adipocytes (Figure 7.1). Surface protein expression of CD36 was gated according to CD36<sup>Low</sup> (light green) and CD36<sup>High</sup> (dark green) populations (Figure 7.2, 7.3). CD36<sup>High</sup> positive cells were prevalent in the Nile Red<sup>High</sup> gated adipocytes (Figure 7.2). Amongst the Nile Red<sup>High</sup> population, brown adipocytes had significantly more surface CD36<sup>Low</sup> positive cells compared to epicardial adipocytes ( $P < 0.005$ ) (Figure 7.3i). In contrast, brown adipocytes had less CD36<sup>High</sup> positive cells compared to inguinal, gonadal and epicardial adipocytes ( $P < 0.01$  for all groups) (Figure 7.3ii).

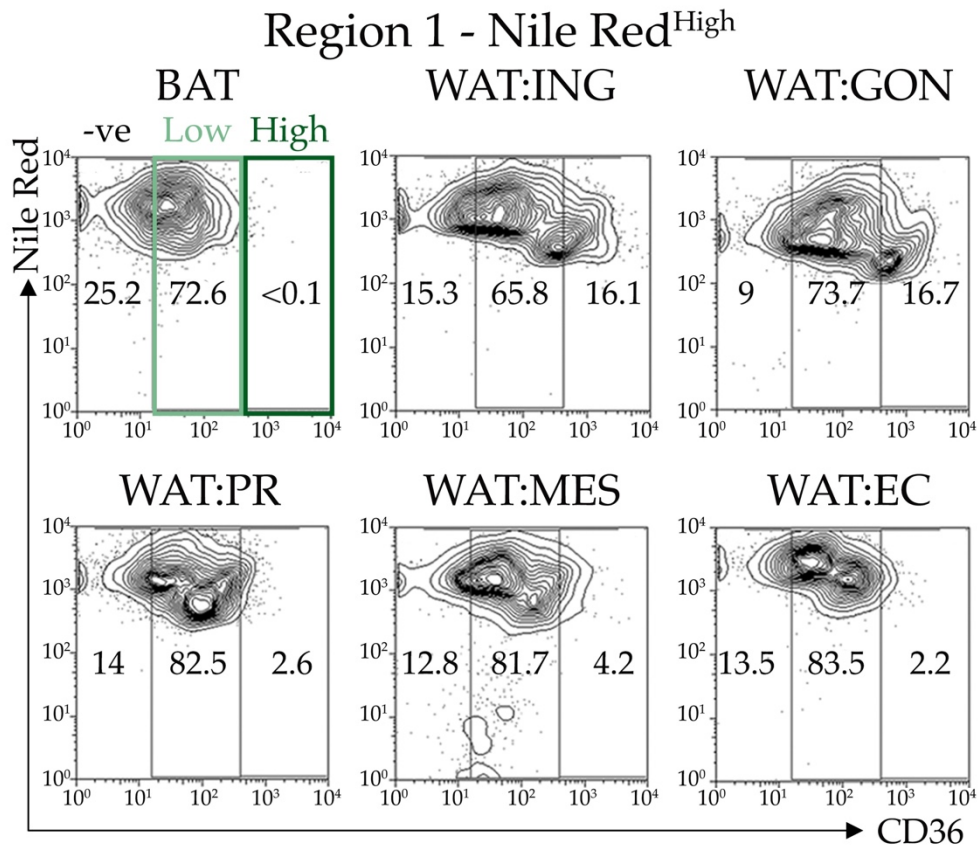
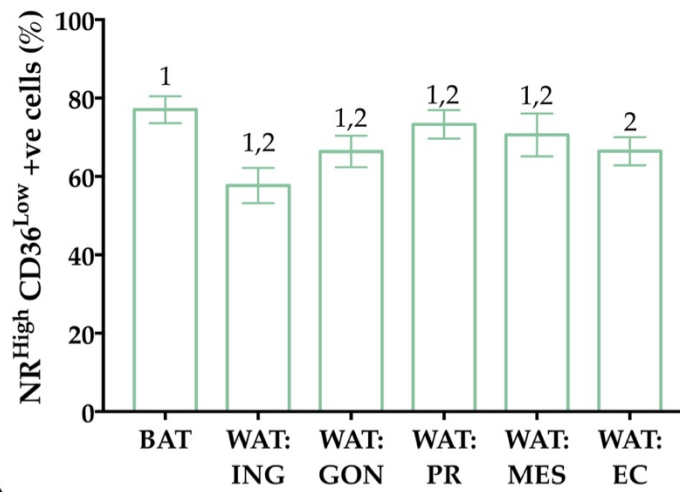


**Figure 7.2: CD36 expression distinguishes BAT from WAT.**

Representative flow cytometric plot of Nile Red<sup>High</sup> brown (BAT), subcutaneous inguinal (WAT:ING) and visceral gonadal (WAT:GON), peri-renal (WAT:PR), mesenteric (WAT:MES) and epicardial (WAT:EC) adipocytes stained with Nile Red and CD36. CD36 immunoreactivity was divided into CD36<sup>Low</sup> (light green box) and CD36<sup>High</sup> (dark green box) populations for subsequent analyses. Figure adapted from Boumelhem et al., 2017.

i)



ii)

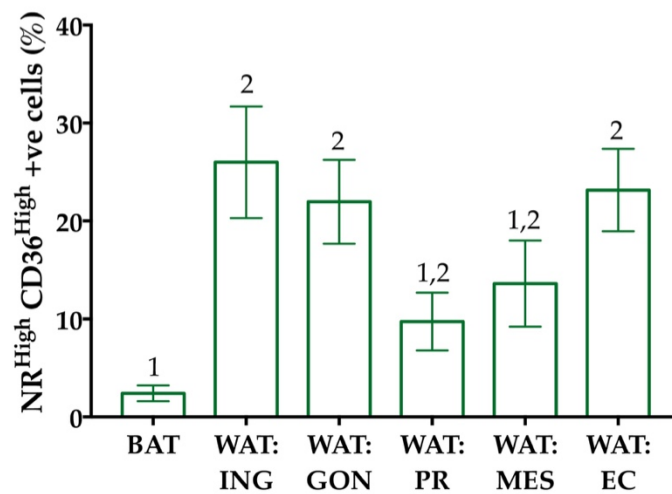


**Figure 7.3: CD36 expression distinguishes BAT from WAT.**

Comparisons of the frequency of (i) Nile Red<sup>High</sup> CD36<sup>Low</sup> positive and (ii) Nile Red<sup>High</sup> CD36<sup>High</sup> positive cells between brown (BAT), subcutaneous inguinal (WAT:ING) and visceral gonadal (WAT:GON), peri-renal (WAT:PR), mesenteric (WAT:MES) and epicardial (WAT:EC) adipocytes. Data presented as mean  $\pm$  SEM (n=6 for all groups). Differences in Nile Red uptake and CD36 immunoreactivity between adipose depots were determined by two-tailed, one-way ANOVA and pairwise *post hoc* comparison by Tukey's HSD test. Groups not sharing a numeral are significantly different from each other. Figure adapted from Boumelhem et al., 2017.



### **7.3.3 Immunoreactivity of laminin receptor proteins $\alpha 6$ and $\beta 1$ integrin distinguishes brown and gonadal white adipocytes.**

CD36 was the first surface protein marker to be detected on the buoyant fraction containing adipocytes. Following, surface protein expression of laminin receptor integrins  $\alpha 6$  and  $\beta 1$  were assessed on Nile Red stained adipocytes.  $\beta 1$  integrin immunoreactivity was greatest in brown ( $P < 0.0001$ ) and gonadal ( $P < 0.0003$ ) adipocytes compared to subcutaneous inguinal and visceral peri-renal, mesenteric and epicardial adipocytes. (Figure 7.4) Brown and gonadal adipocytes exhibited  $75\% \pm 5\%$  and  $60\% \pm 3\%$  of  $\beta 1$  integrin surface protein expression respectively (Figure 7.4). Similarly,  $\alpha 6$  integrin surface protein expression was also greatest in brown and gonadal adipocytes compared to all adipocytes examined ( $P < 0.01$ ) (Figure 7.5). Brown adipocytes displayed  $50\% \pm 6\%$  of  $\alpha 6$  integrin surface protein expression while gonadal adipocytes displayed  $55\% \pm 2\%$  (Figure 7.5). No differences were observed between subcutaneous inguinal, visceral peri-renal and epicardial adipocytes in  $\beta 1$  integrin and  $\alpha 6$  integrin surface protein expression.

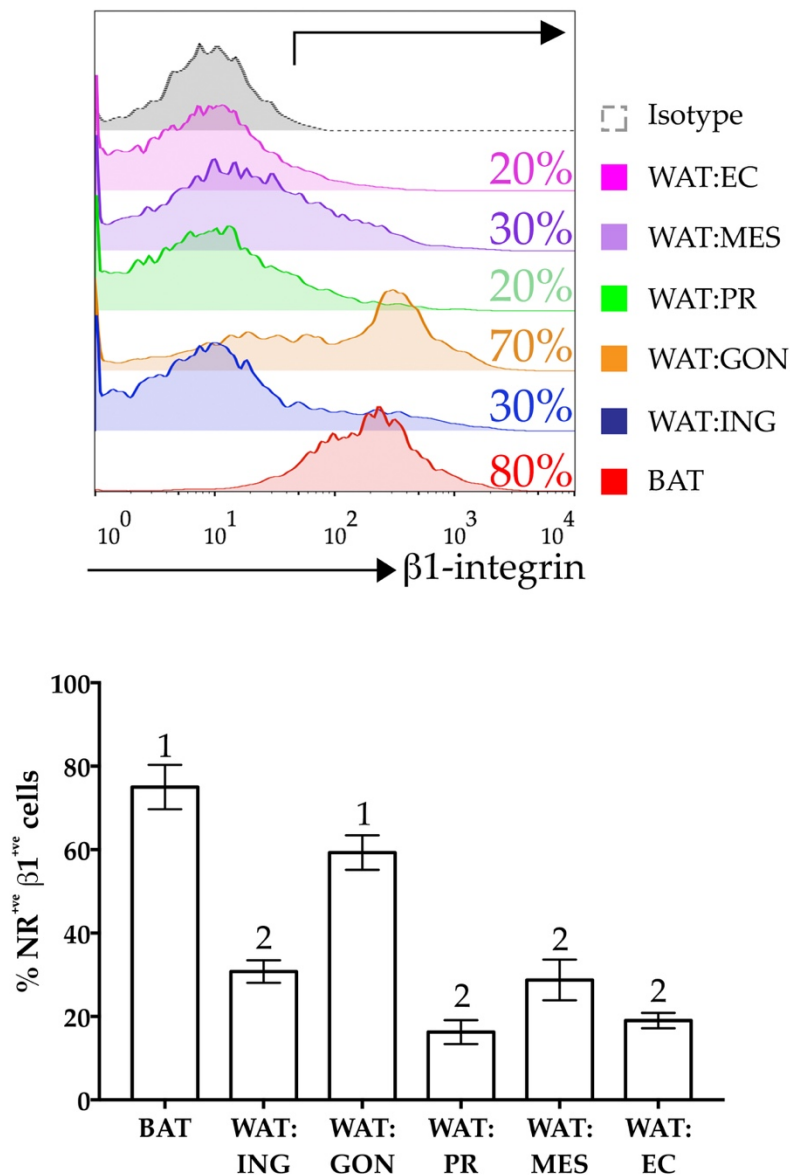


**Figure 7.4: Surface protein expression of  $\beta 1$  integrin distinguishes brown and visceral gonadal white adipocytes.**

(i) Representative histogram plot of Nile Red<sup>+</sup>ve  $\beta 1$  integrin<sup>+</sup>ve cells in brown (BAT), subcutaneous inguinal (WAT:ING) and visceral gonadal (WAT:GON), peri-renal (WAT:PR), mesenteric (WAT:MES) and epicardial (WAT:EC) adipocytes. (ii) Comparisons in the frequency of Nile Red<sup>+</sup>ve  $\beta 1$  integrin<sup>+</sup>ve cells between brown and white adipocytes. Data presented as mean  $\pm$  SEM (n=4). Differences between brown and white adipocytes was determined by a two-tailed, one-way ANOVA and Tukey's pairwise *post hoc* analysis.  $P < 0.05$  was deemed significant. Groups not sharing a numeral are significantly different.

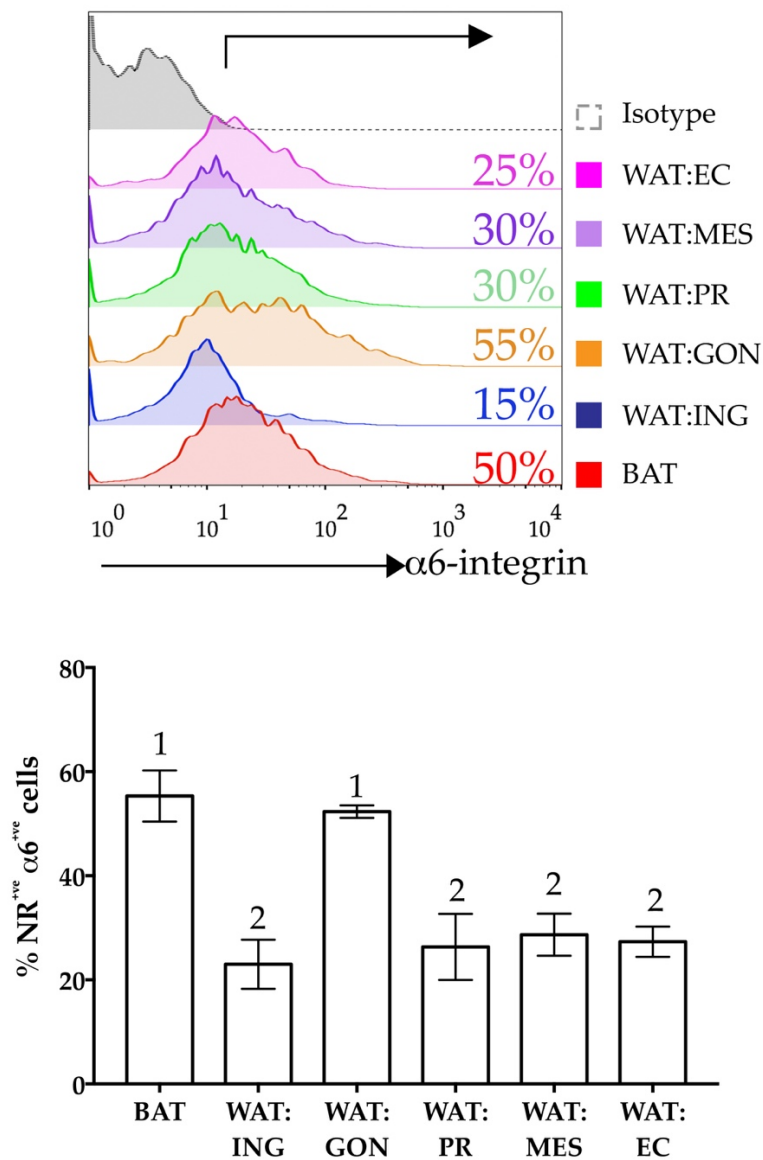


**Figure 7.5: Surface protein expression of  $\alpha 6$  integrin distinguishes brown and gonadal white adipocytes.**

(i) Representative histogram plot of Nile Red<sup>+</sup>  $\alpha 6$  integrin<sup>+</sup> cells in brown (BAT), subcutaneous inguinal (WAT:ING) and visceral gonadal (WAT:GON), peri-renal (WAT:PR), mesenteric (WAT:MES) and epicardial (WAT:EC) adipocytes. (ii) Comparisons in the frequency of Nile Red<sup>+</sup>  $\alpha 6$  integrin<sup>+</sup> cells between brown and white adipocytes. Data presented as mean  $\pm$  SEM (n=4). Differences between brown and white adipocytes was determined by a two-tailed, one-way ANOVA and Tukey's pairwise *post hoc* analysis.  $P < 0.05$  was deemed significant. Groups not sharing a numeral are significantly different.

### **7.3.4 Subcutaneous inguinal adipocytes do not display immunoreactivity for “beige” adipocytes markers CD40 or CD137.**

Wu *et al.* (2012) reported CD137 and CD40 as specific markers for beige adipocytes in subcutaneous inguinal adipose tissue (Wu et al., 2012). To determine whether beige adipocytes reside within the buoyant fraction of subcutaneous inguinal adipose tissue, Nile Red was combined with either CD137 or CD40 and surface protein expression measured. Inguinal lymph nodes exhibited immunoreactivity to both CD137 and CD40, confirming antibody specificity to immune cells (Figure 7.6A).

Initial assessment of CD137 and CD40 immunoreactivity on subcutaneous inguinal adipose tissue from outbred QS mice revealed no surface protein expression. As the expected findings were not obtained, the mouse strain was confirmed with the original publication and then analyses performed with CD137 and CD40 (Wu et al., 2013). Subcutaneous inguinal adipose tissue was isolated from inbred 129/SV mice and CD137 and CD40 immunoreactivity examined. Live, viable, Nile Red stained subcutaneous inguinal and brown adipocytes did not exhibit CD137 or CD40 immunoreactivity (n=3) (Figure 7.6B).

CD45 is expressed on all haematopoietic cells except erythrocytes and platelets (Nakano et al., 1990). The SVF of subcutaneous inguinal adipocytes were assessed for CD45 and CD137 or CD40 immunoreactivity. The SVF of subcutaneous inguinal adipocytes had few cells with surface protein expression of CD137 (Figure 7.6C).

Additionally, the cells that were positive for CD137 were also positive CD45 (Figure 7.5C). Surface protein expression of CD40 was also observed in the SVF of subcutaneous inguinal adipocytes (Figure 7.6C). However, all CD40 positive cells exhibited surface protein expression for CD45 (Figure 7.6C).

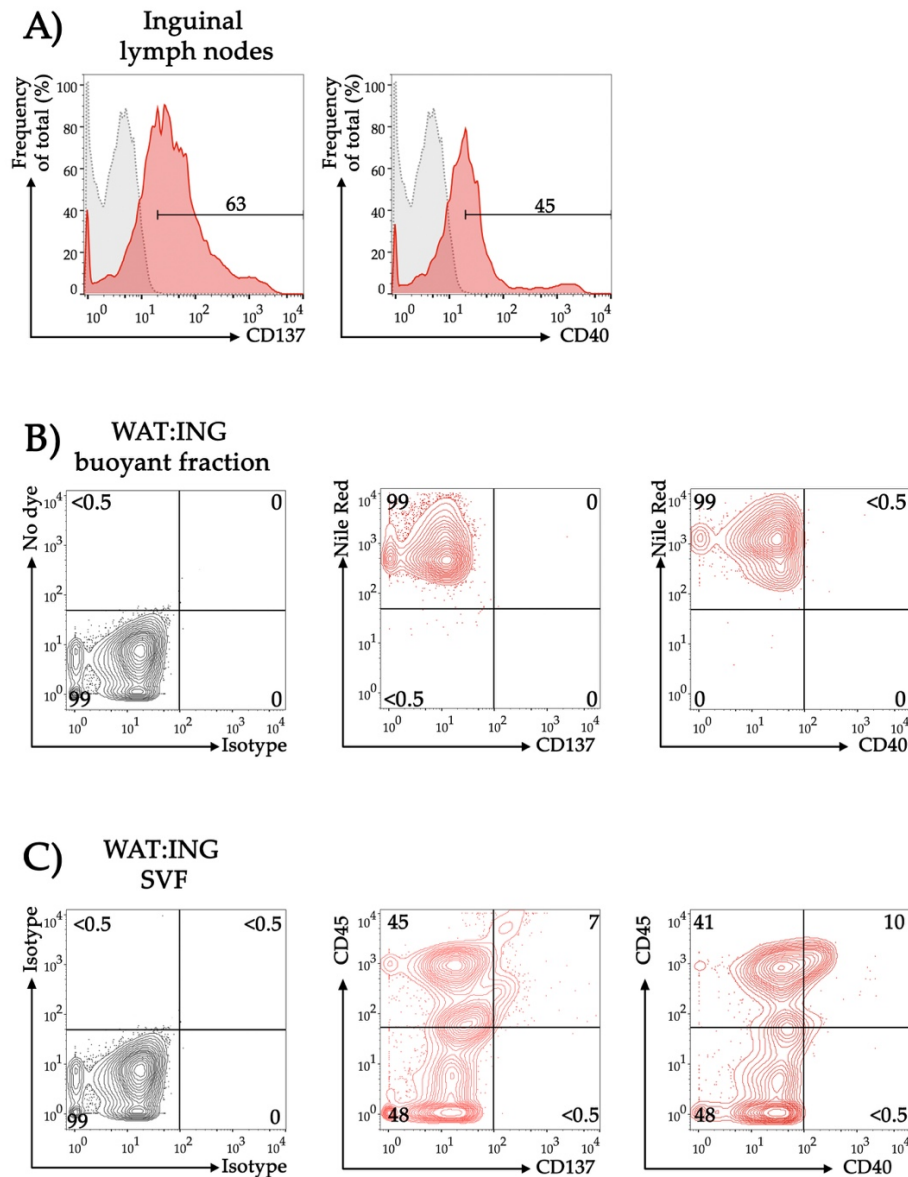


**Figure 7.6: Reported beige adipocyte specific markers CD40 or CD137 are not expressed on subcutaneous inguinal adipocytes.**

(A) Representative histogram plot of isolated inguinal lymph nodes stained with anti-CD137 antibody or anti-CD40 antibody. Grey shaded plot indicates the isotype control. Red shaded plot indicates the stained sample. (B) Representative flow cytometric plot of the buoyant fraction of dissociated subcutaneous inguinal adipose tissue (WAT:ING) stained with Nile Red and anti-CD137 antibody or anti-CD40 antibody. (C) Representative flow cytometric plot of the stromal vascular fraction (SVF) of WAT:ING stained with anti-CD45 antibody and anti-CD137 antibody or anti-CD40 antibody. Samples from (A) – (C) acquired from 129/SV male mice (n=4). Gates determining positive cell surface protein expression were set according to the isotype control.

### **7.3.5 Marrow adipocytes are a distinct type of adipocyte.**

Marrow adipose tissue is recognised as an independent adipose organ with origins and functions distinct from both WAT and BAT (Scheller et al., 2014). At this point, six parameters were identified that characterised brown and white adipocytes: Nile Red, Nile Blue, MitoTracker Deep Red, CD36 and  $\alpha 6$  and  $\beta 1$  integrins. Here, marrow adipocytes were isolated and the aforementioned markers examined. Strikingly, Nile Red<sup>+</sup> marrow adipocytes lacked surface protein expression of  $\alpha 6$  integrin and  $\beta 1$  integrin (Figure 7.7). Surface protein expression of CD36 was detected in  $5\% \pm 2\%$  of Nile Red positive marrow adipocytes. (Figure 7.7). Uptake of Nile Blue and MitoTracker Deep Red was detected on  $20\% \pm 4\%$  and  $87\% \pm 7\%$  of marrow adipocytes respectively (Figure 7.7).

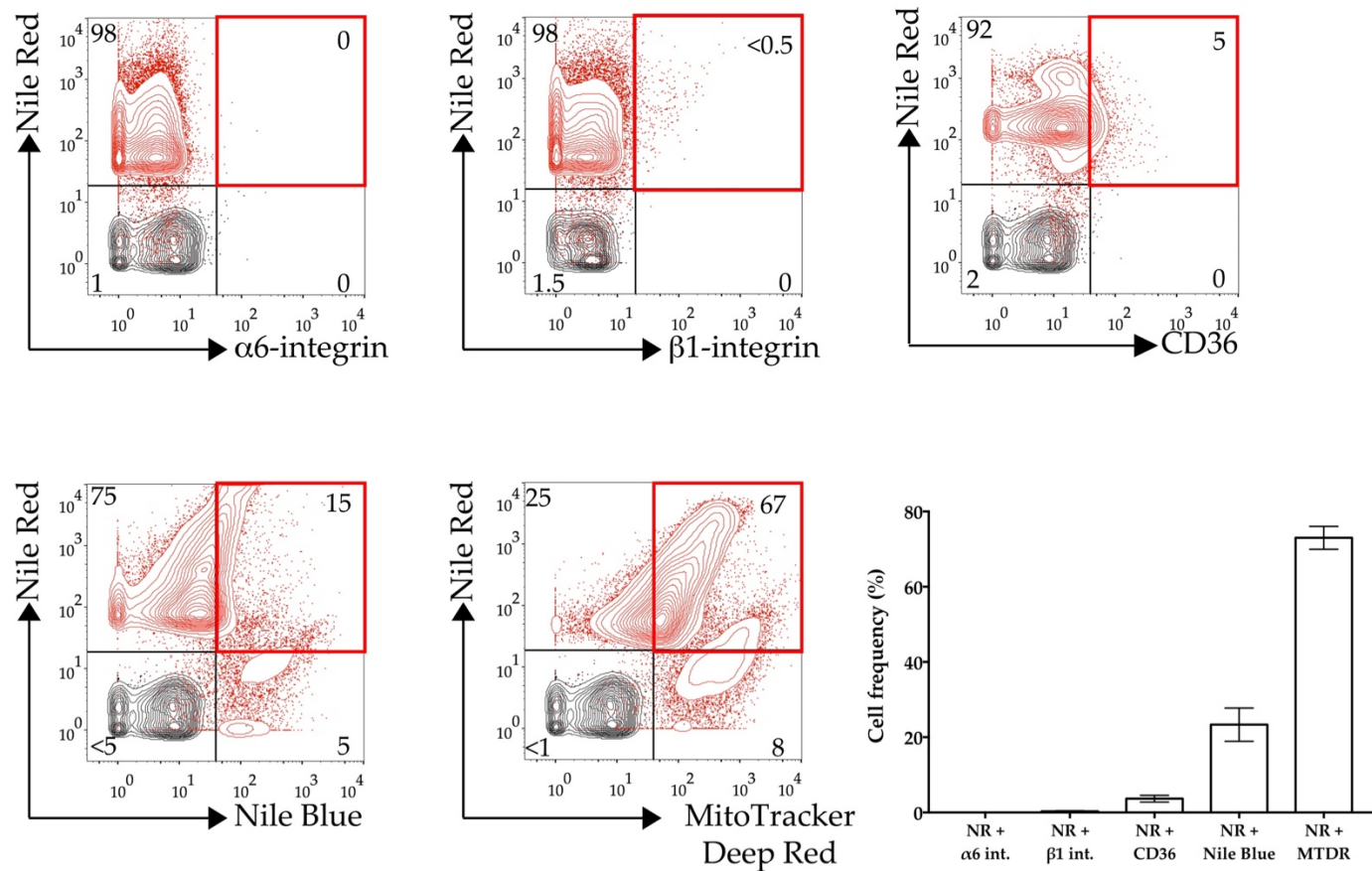


**Figure 7.7: Marrow adipocytes have a distinct cell surface phenotype.**

(i) Representative flow cytometric plot of marrow adipocytes stained with Nile Red and MitoTracker. The Nile Red<sup>+</sup> MitoTracker<sup>+</sup> population was gated (red box) and frequency measured. (ii) The frequency of Nile Red<sup>+</sup> and Nile Blue<sup>+</sup>, CD36<sup>+</sup>,  $\beta 1$ -integrin<sup>+</sup> and  $\alpha 6$ -integrin<sup>+</sup> cells in marrow adipocytes. Black dotted line represents the isotype control. Red shaded plot indicated the stained sample. Frequency of cells expressed as mean  $\pm$  SEM (n=3).



## 7.4 Discussion

The growing rate of obesity worldwide has prompted a new outlook on the role of adipose tissues from distinct adipose depots. Visceral WAT is linked to an increased risk of developing metabolic disorders while subcutaneous WAT is implicated as a protective adipose depot (Porter et al., 2009; Seale et al., 2011; Wajchenberg et al., 2000; Donohoe et al., 2011). One of the limitations in assessing adipocytes is the lack of a method to characterise them at the single cell level. Here, a method to distinguish adipocytes from brown, subcutaneous and visceral WAT depots at the single cell level is reported (Boumelhem et al., 2017).

### 7.4.1 Fatty acid translocase has discrete roles in brown and white adipose tissue.

Fatty acid translocase CD36 belongs to the scavenger receptor family of transmembrane glycoproteins (Febbraio, Hajjar, & Silverstein, 2001). CD36 facilitates the uptake of fatty acids and lipoproteins by accelerating intracellular esterification into triglycerides (Jay et al., 2013). CD36 is also a receptor for oxidised lipoproteins, thrombospondin and collagen (Febbraio et al., 2001). Mice deficient for *CD36* have increased serum triglyceride levels due to impaired fatty acid uptake (Goudriaan et al., 2005; Cai et al., 2012; Putri et al., 2015). The heart and skeletal muscle compensate for the lack of fatty acid uptake by increasing uptake of glucose, which leads to decreased serum glucose levels (Putri et al., 2015).

As reservoirs of adipose tissue surrounding the heart are scarce in rodents, CD36 serves to fuel myocardial contraction by supplying fatty acids for mitochondrial oxidation (Cherian, Lopaschuk, & Carvalho, 2012). The role of CD36 has been posited to prevent cardiac lipotoxicity by reducing free fatty acid levels in the heart (Burgeiro et al., 2016). Obese individuals with coronary artery disease have impaired fatty acid metabolism, contributing to cardiac arrhythmias (Burgeiro et al., 2016; Payne, Kohr, & Tune, 2012). The data presented here suggests that the metabolic functions of epicardial adipocytes are tightly regulated, evident by the high levels of Nile Blue, MitoTracker Deep Red and CD36.

In response to cold exposure, CD36 accelerates fatty acid uptake in BAT to contribute to heat production (Putri et al., 2015). Following cold exposure, *CD36<sup>-/-</sup>* mice have distinct hypothermia due to depletion of triglycerides and fatty acids in BAT (Putri et al., 2015). Mice void of *CD36* also have impaired uptake of the lipid co-enzyme Q (Anderson et al., 2015). Co-enzyme Q functions as a transporter of electrons in the mitochondrial transport chain (reviewed in: Crane et al., 2001). CD36 specifically facilitates co-enzyme Q uptake in BAT (Anderson et al., 2015). Here, the mice were maintained under thermoneutral conditions. To further characterise CD36 immunoreactivity in BAT (and WAT depots), mice could be subjected to the cold to induce thermogenesis. Changes in CD36 immunoreactivity following thermogenesis in brown adipocytes could be measured using the method developed.

Nullizygous *CD36* mice have less adiposity due to reduced uptake of fatty acids in adipose tissue (Vroegrijk et al., 2013). Gonadal adipose tissue in particular exhibited a larger pool of pre-adipocytes compared to subcutaneous and visceral mesenteric adipose depots (Vroegrijk et al., 2013). *CD36* may serve as a regulatory mechanism to inhibit adipose tissue hypertrophy (Christiaens et al., 2012; Bonen et al., 2006). A follow up assessment on *CD36* immunoreactivity in gonadal adipose tissue from newborn and pubertal mice can be applied here to examine changes in *CD36* with age.

#### **7.4.2 Changes in the extracellular matrix of adipose tissue disrupts homeostasis**

The remodelling of adipose tissue leads to an expansion of adipose mass, primarily through the increase in the size (hypertrophy) and number (hyperplasia) of adipocytes (Pellegrinelli et al., 2016). To accommodate the increase in adipose mass, the extracellular matrix (ECM) undergoes structural changes (Pellegrinelli et al., 2016). Obesity disrupts the homeostatic mechanisms that regulate normal tissue expansion and causes metabolic dysfunction. Obesity-induced metabolic disorders manifest in the form of insulin resistance (and type II diabetes), reduced secretion of adipokines and abnormal adipogenesis (Pellegrinelli et al., 2016). Further problems ensue as obesity leads to excess infiltration of adipose tissue by inflammatory macrophages as well as the ECM components collagen VI and thrombospondin (Spencer et al., 2011). One could hypothesise that  $\alpha 6\beta 1$  integrin and *CD36* surface protein expression would increase in subcutaneous and visceral adipose depots in obese individuals as they have the largest capacity for growth.

### **7.4.3 BReaking BEige: Challenging CD40 and CD137 as specific markers of beige adipocytes.**

The findings reported by Wu *et al.* (2012) cannot be replicated. CD137 belongs to the tumour necrosis factor (TNF) receptor superfamily of proteins (Alfaro et al., 2015; Kim et al., 2011). Expression of CD137 is abundant in immune cells including activated T cells and macrophages (Alfaro et al., 2015). Flow cytometric analyses with CD137 are routinely used to screen for activated T cells (Maerten et al., 2004; Bacher & Scheffold, 2013; Litjens et al., 2013; Alfaro et al., 2015; Kroon et al., 2016). Recently, CD137 was detected in the inguinal lymph nodes in response to tumour irradiation (Kroon et al., 2016). The inguinal lymph nodes surround the inguinal adipose tissue, the site where beige adipocytes are often sourced (Park et al., 2014; Garcia, Roemmich, & Claycombe, 2016). CD40 is also a member of the TNF receptor superfamily and is expressed on a range of cells including haematopoietic cells, B cells, monocytes, dendritic cells and macrophages (Hasbold et al., 1994; Fiumara & Younes, 2001).

The inguinal lymph nodes are embedded in inguinal adipose tissue (Harrell, Iritani, & Ruddell, 2008; Kim et al., 2008). Wu *et al.* (2013) did not describe the removal of the inguinal lymph nodes prior to analyses (Wu et al., 2012). Further, the flow cytometric analyses are centred on cultured inguinal SVF cells (Wu et al., 2012). If the inguinal lymph nodes were not removed prior to culturing, then it is possible that the expansion and differentiation of the contaminating inguinal lymph nodes would generate a false positive for CD137 and CD40 immunoreactivity. In support of this

argument, Alfaro and colleagues (2015) reported CD137 immunoreactivity of cultured lymphocytes (Alfaro et al., 2015). Here, CD137 immunoreactivity was detected on the inguinal lymph nodes and cells expressing CD45. Thus, the findings presented in this chapter suggest that CD137 and CD40 are not specific markers for beige adipocytes.

#### **7.4.4 Marrow adipocytes are distinct from white and brown adipocytes**

The unique haematopoietic microenvironment of marrow adipocytes may serve to explain the distinct cell surface phenotype (reviewed in: Al-Drees et al., 2015, Appendix IV). The integrin  $\alpha 6 \beta 1$  anchors haematopoietic cells to the basal lamina which influences maturation of eosinophils and the proliferation of macrophages and T cells (Tourkin et al., 2009, Shaw, Messier, & Mercurio, 1990; Shimizu et al. 1990). The absence of integrin  $\alpha 6 \beta 1$  integrin in marrow adipocytes could serve as a homeostatic mechanism to ensure adipocytes do not bind to the basal lamina, disrupting critical processes that influence haematopoiesis.

In the bone marrow, CD36 is expressed on endothelial cells, macrophages, platelets and dendritic cells and has been implicated in malaria, neurotoxicity and several cancers including breast and prostate (Cunha-Rodrigues et al., 2007; Zhou et al., 2011; Gusky et al., 2016; Herroon et al., 2013). Recently, CD36 surface protein expression was upregulated in marrow adipocytes co-cultured with acute, monocytic leukaemia cells (Tabe et al., 2017). Marrow adipocytes are thought to supply fatty acids to the tumour microenvironment via CD36 (Tabe et al., 2017; Herroon et al., 2013; Gusky et

al., 2016). Similar to  $\alpha 6 \beta 1$  integrin expression, a lack of CD36 on marrow adipocytes in healthy mice may serve as a homeostatic mechanism to prevent fatty acid accumulation in the bone marrow compartment. Characterisation of brown, white and marrow adipocytes according to the parameters used in this study is presented in Figure 7.9.

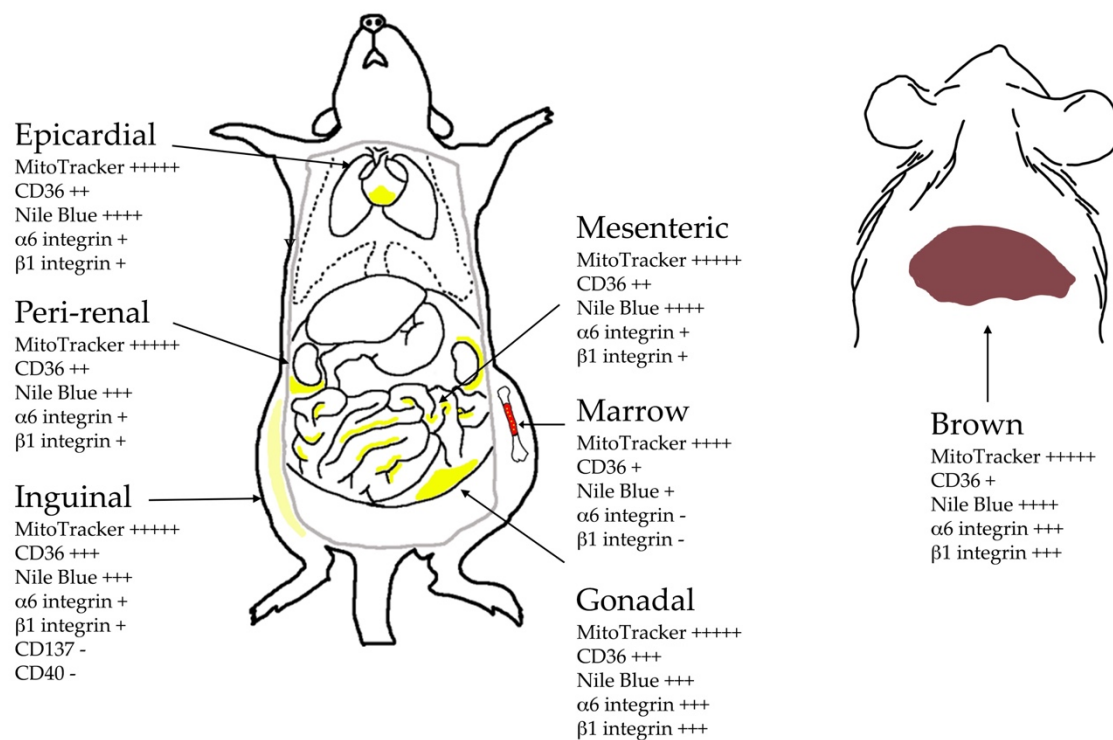


**Figure 7.9: Characterisation of brown and white adipocytes according to probe uptake and surface protein expression.**

Nile Red stained brown and white adipocytes were assessed for uptake of MitoTracker Deep Red, Nile Blue as well as immunoreactivity of CD36, and  $\beta 1$  and  $\alpha 6$  integrins by flow cytometry. Frequency of dye uptake or antibody immunoreactivity in brown and white adipocytes represented as + (denotes <10%), ++ (denotes 10-20%), +++ (denotes 20-50%) and +++++ (denotes >50%).

#### **7.4.5 Adipocyte heterogeneity in obese and diabetic mice**

Obese and diabetic individuals have pronounced adipose tissue remodelling and upregulation of *CD36* expression in subcutaneous and visceral WAT (Bonen et al., 2006). Additionally, reduced mitochondrial function in adipose tissue has been linked to obesity and type II diabetes (Bournat & Brown, 2010; reviewed in: Cedikova et al., 2016). The flow cytometric method presented in this study can be utilised to characterise brown and white adipocytes from obese mice (*Ob/Ob*). Nile Red fluorescence would hypothetically be greater in the adipocytes from obese mice compared to their wild-type counterparts. Since obesity leads to remodelling of adipose tissue, surface protein expression of integrin markers  $\alpha 6\beta 1$  could be elevated. Conversely, mitochondrial membrane potential probe MitoTracker may exhibit reduced fluorescence in the adipocytes from obese mice. Comparisons of brown and white adipocytes from obese mice have not been characterised at the single cell level.

#### **7.4.6 Conclusion**

A description of adipose tissue heterogeneity at the single cell level is reported (Boumelhem et al., 2017). In the following chapter, the parameters used to distinguish adipocytes across brown and white adipose depots will be assessed on adipocytes derived from mouse ES cells under endoderm culture conditions.

## **Chapter 8: Endoderm-derived adipocytes from mouse ES cells resemble gonadal adipocytes.**

### **8.1 Introduction**

The generation of adipocyte-like cells alongside prostatic epithelial cells from mouse ES cells was an unexpected finding in this study (Chapters 3 and 4). To determine whether the differentiated adipocyte-like cells were indicative of adipocytes that represented those isolated from any specific adipose depot, a flow cytometric method was developed to characterise adipocytes at the single cell level (Chapter 5, 6 and 7). Adipocyte heterogeneity was profiled based on probe (Nile Red, Nile Blue and MitoTracker Deep Red) uptake and surface protein expression (CD36 and  $\beta 1$  and  $\alpha 6$  integrin). The aim here was to assess the parameters used to distinguish adipocytes at the single cell level on the adipocytes derived from mouse ES cells under conditions designed to promote endoderm differentiation.



## **8.2 Methods**

### **8.2.1 Serum starvation of undifferentiated mouse ES cells**

Undifferentiated mouse ES cells were plated on gelatin coated 6-well plates in ES maintenance medium without foetal calf serum. Undifferentiated mouse ES cells were serum-starved for 0.5, 1, 2, 6 and 12 hours before treating with 0.1% (v/v) ethanol or 300  $\mu\text{mol.L}^{-1}$  of palmitate, linoleate or oleate for 15 minutes prior to imaging or flow cytometric analyses.

### **8.2.2 Imaging of undifferentiated mouse ES cells stained with Nile Blue**

Following lipid treatment of mouse ES cells, the media was aspirated and washed twice with PBS. The mouse ES cells were incubated with 100  $\text{nmol.L}^{-1}$  of Nile Blue for 10 minutes at 4°C. Nile Blue stained mouse ES cells were imaged using an Olympus FluoView 1000 Spectral-based Laser Scanning Confocal Microscope configured to an Olympus IX81 equipped with a red helium neon gas laser (635 nm).

### **8.2.3 Flow cytometric analyses**

#### **8.2.3.1 Undifferentiated mouse ES cells**

Treated and untreated mouse ES cells were dissociated into single cells using cell dissociation buffer as outlined in 2.6.1. Single cell suspensions of mouse ES cells were incubated with 100  $\text{nmol.L}^{-1}$  Nile Red and Nile Blue solution for 15 minutes at 4°C. No stain controls and single stain controls were also prepared as outlined in 2.6.3.1.1.

### 8.2.3.2 Endoderm-derived adipocyte-like cells

Day 22 differentiated mouse ES cells were dissociated into single cell suspensions as outlined in 2.6.1. Cells from the buoyant fraction were taken for flow cytometric analyses and stained with Nile Red and MitoTracker Deep Red, Nile Blue, CD36,  $\beta 1$  integrin or  $\alpha 6$  integrin in the steps outlined in 2.6.3.2.

### 8.2.4 Statistical analyses

All data presented as mean  $\pm$  SEM. Differences in the uptake of Nile Red and parameters used to distinguish adipocytes (MitoTracker Deep Red, Nile Blue, CD36,  $\alpha 6$  integrin and  $\beta 1$  integrin) was determined by a two-tailed, one way ANOVA and *post hoc* analysis by Tukey's comparison test. A *P* value less than 0.05 was deemed significant. Graphical visualisation of brown and white adipocyte heterogeneity in an unbiased manner was generated using HeatMap Generator (available from: <https://github.com/Bohdan-Khomtchouk/HeatmapGenerator>) (Khomtchouk, Van Booven, & Wahlestedt, 2014).

## **8.3 Results**

### **8.3.1 Modelling free fatty acid uptake with undifferentiated mouse ES cells**

#### **8.3.1.1 Visualising Nile Blue uptake in fatty acid treated mouse ES cells**

Prior to flow cytometric analyses with adipocyte derived from mouse ES cells under endoderm culture conditions, Nile Blue and Nile Red fluorescence was measured in undifferentiated mouse ES cells. The aim here was two-fold: to corroborate the findings presented in Chapter 6 and compare uptake of Nile Red and Nile Blue between undifferentiated mouse ES cells and day 22 differentiated mouse ES cells. Undifferentiated mouse ES cells were treated with palmitate, linoleate or oleate and either visualised by confocal microscopy or fluorescence measured at the single cell level by flow cytometry. Nile Blue stained the phospholipid membrane of mouse ES cells in all conditions (Figure 8.1). Mouse ES cells treated with palmitate, oleate and linoleate had punctate staining within the cytosol compared to the ethanol treated mouse ES cells (Figure 8.1).

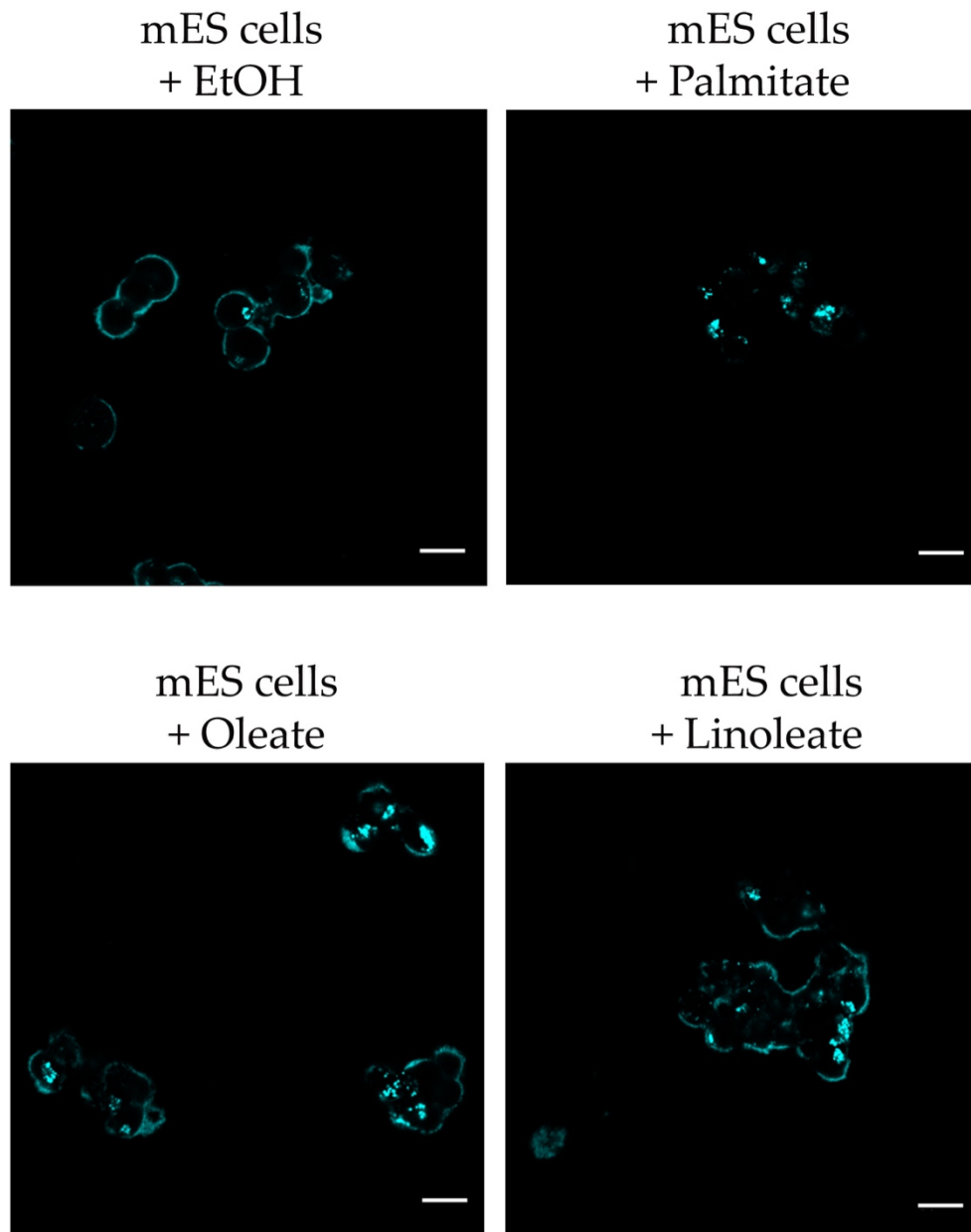


**Figure 8.1: Nile Blue intensely stains the vesicles within the cytoplasm in fatty acid treated undifferentiated mouse ES cells.**

Undifferentiated mouse ES cells were treated with ethanol, palmitate, linoleate and oleate for 15 minutes, washed with PBS and then stained with Nile Blue. Confocal images of Nile Blue stained mouse ES cells were taken using an Olympus FluoView 1000 equipped with a red helium neon gas laser. Nile Blue was excited at 620nm. Images were taken at 40x objective. Scale bars represent 20  $\mu\text{m}$ .

### **8.3.1.2 Undifferentiated mouse ES cells treated with oleate have the greatest Nile Blue uptake.**

Mouse ES cells were then treated with free fatty acids to determine how Nile Blue fluorescence would be affected. Untreated mouse ES cells exhibited high levels of Nile Blue fluorescence, but low levels of Nile Red fluorescence (Figure 6.2Ai). Palmitate and linoleate treated mouse ES cells had significantly greater Nile Red fluorescence compared to oleate ( $P < 0.01$  and  $P < 0.02$  respectively), but comparable to ethanol treated mouse ES cells (Figure 6.2Aii, Bi). Nile Blue fluorescence however, was greatest in oleate treated mouse ES cells compared to palmitate ( $P < 0.0001$ ), linoleate ( $P < 0.0005$ ) and ethanol ( $P < 0.0001$ ) treated mouse ES cells (Figure 6.2Aiii, Bii).

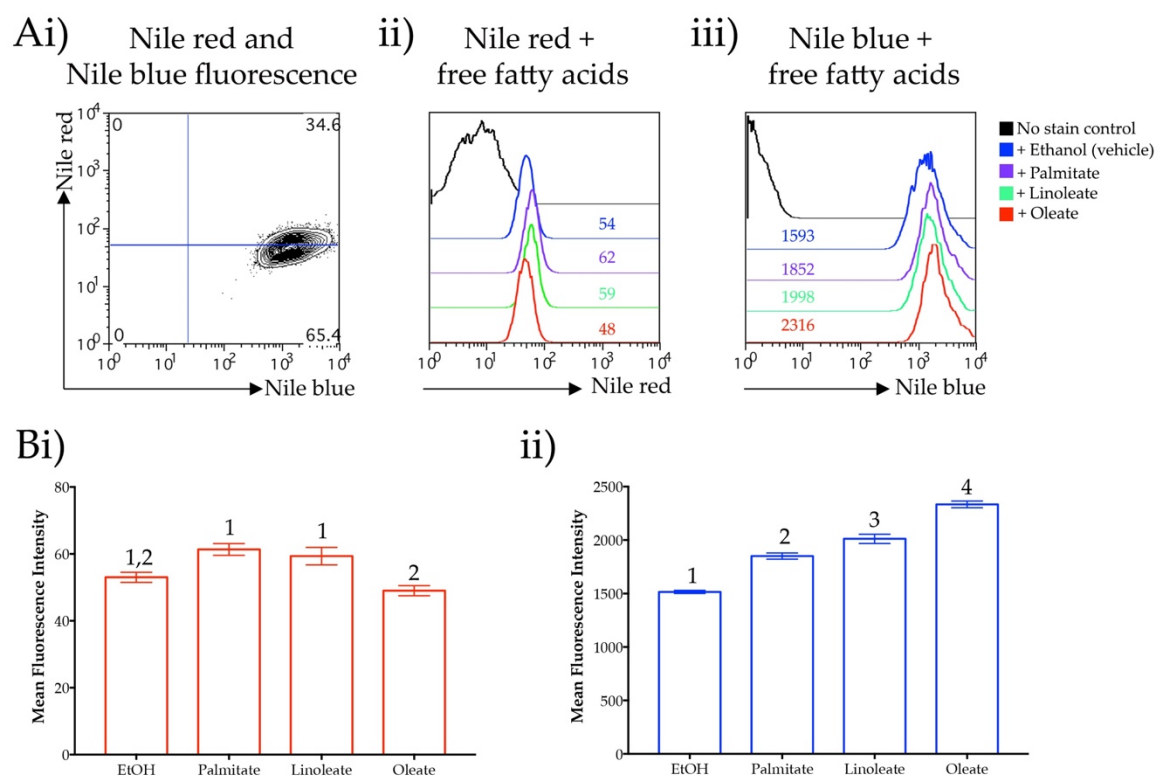


**Figure 8.2: Undifferentiated mouse ES cells treated with oleate have the greatest Nile Blue staining.**

(Ai) Representative flow cytometric plot of mouse ES cells stained with Nile Red and Nile Blue. Mean fluorescence intensity of (ii) Nile Red and (iii) Nile Blue in the presence of ethanol (blue), palmitate (purple), linoleate (green) and oleate (red). (B) Comparisons in the mean fluorescence intensity of (i) Nile Red and (ii) Nile Blue of mouse ES cells in the presence of fatty acids. Data presented as mean  $\pm$  SEM (n=3). Significance in the mean fluorescence intensity between mouse ES cells treated with fatty acids was determined by a two-tailed, one-way ANOVA with Tukey's *post hoc* analysis. Groups not sharing a numeral are significantly different from each other.

### **8.3.1.2 Serum starved undifferentiated mouse ES cells have increased uptake of Nile Blue.**

Mouse ES cells were subjected to serum starvation over the course of 12 hours to strip them of cytokines, growth factors and lipids. Subsequently, Nile Red and Nile Blue uptake was measured at selected time points (Figure 8.3i). There was no difference in Nile Red and Nile Blue fluorescence between less than 1 minute serum starved and 2 hours of serum starved mouse ES cells (Figure 8.3ii). Compared to baseline, Nile Blue fluorescence significantly increased at 6 and 12 hours of serum starvation ( $P < 0.005$  and  $P < 0.0001$  respectively) (Figure 8.3ii). Nile Red fluorescence significantly decreased from 6 and 12 hours of serum starvation compared to 2 hours of serum starvation ( $P < 0.01$  and  $P < 0.001$  respectively) (Figure 8.3ii).

Serum starved mouse ES cells were then treated with fatty acids (Figure 8.3ii). There was a significant increase in Nile Blue fluorescence after 6 hours of serum-starvation in all fatty acid treated cultures (Figure 8.3ii). Nile Red fluorescence decreased between 2 and 6 hours of serum-starvation in all conditions, but was not significantly different from the baseline (Figure 8.3ii).

At 6 hours of serum starvation, Nile Blue fluorescence increased from  $1900 \pm 70$  a.u. to  $3700 \pm 270$  a.u. ( $P < 0.0001$ ) in palmitate treated mouse ES cells (Figure 8.3ii). There was no change in Nile Blue fluorescence between 6 and 12 hours of serum starvation

(Figure 8.3ii). Nile Red fluorescence decreased from  $85 \pm 5$  a.u. to  $48 \pm 1$  a.u between 1 hour and 12 hours of serum starvation ( $P < 0.0001$ ) (Figure 8.3ii).

Linoleate treated mouse ES cells displayed an increase in Nile Blue fluorescence from  $1800 \pm 80$  a.u. to  $3200 \pm 190$  a.u. ( $P < 0.0001$ ) after 6 hours of serum starvation (Figure 8.3ii). Nile Blue fluorescence elevated to  $3600 \pm 300$  a.u. at 12 hours of serum starvation ( $P < 0.0001$ ) (Figure 8.3ii). Nile Red fluorescence decreased from  $73 \pm 2$  a.u. to  $48 \pm 2$  a.u. between 1 hour and 12 hours of serum starvation ( $P < 0.0001$ ) (Figure 8.3ii).

Serum starved mouse ES cells treated with oleate exhibited an increase in Nile Blue fluorescence from  $2300 \pm 104$  a.u. to  $3900 \pm 123$  a.u. ( $P < 0.0001$ ) at 6 hours of serum starvation (Figure 8.3ii). Nile Blue fluorescence increased further to  $4610 \pm 400$  a.u. at 12 hours of serum starvation ( $P < 0.0001$ ) (Figure 8.3ii). Nile Red fluorescence decreased from  $55 \pm 2$  a.u. to  $32 \pm 4$  a.u. between 1 hour and 12 hours of serum starvation ( $P < 0.0001$ ) (Figure 8.3ii).

Serum starved mouse ES cells exhibited an increase in Nile Blue fluorescence in the presence of oleate compared to ethanol and palmitate (Appendix IV, Table 8.1). After 6 hours of serum starvation, Nile Blue fluorescence was significantly greater in oleate treated mouse ES cell cultures compared to linoleate treated cultures (Appendix IV, Table 8.1). Nile Red fluorescence on the other hand, was reduced in oleate treated,



serum starved mouse ES cells compared to ethanol, palmitate and linoleate treatment  
(Appendix IV, Table 8.2).

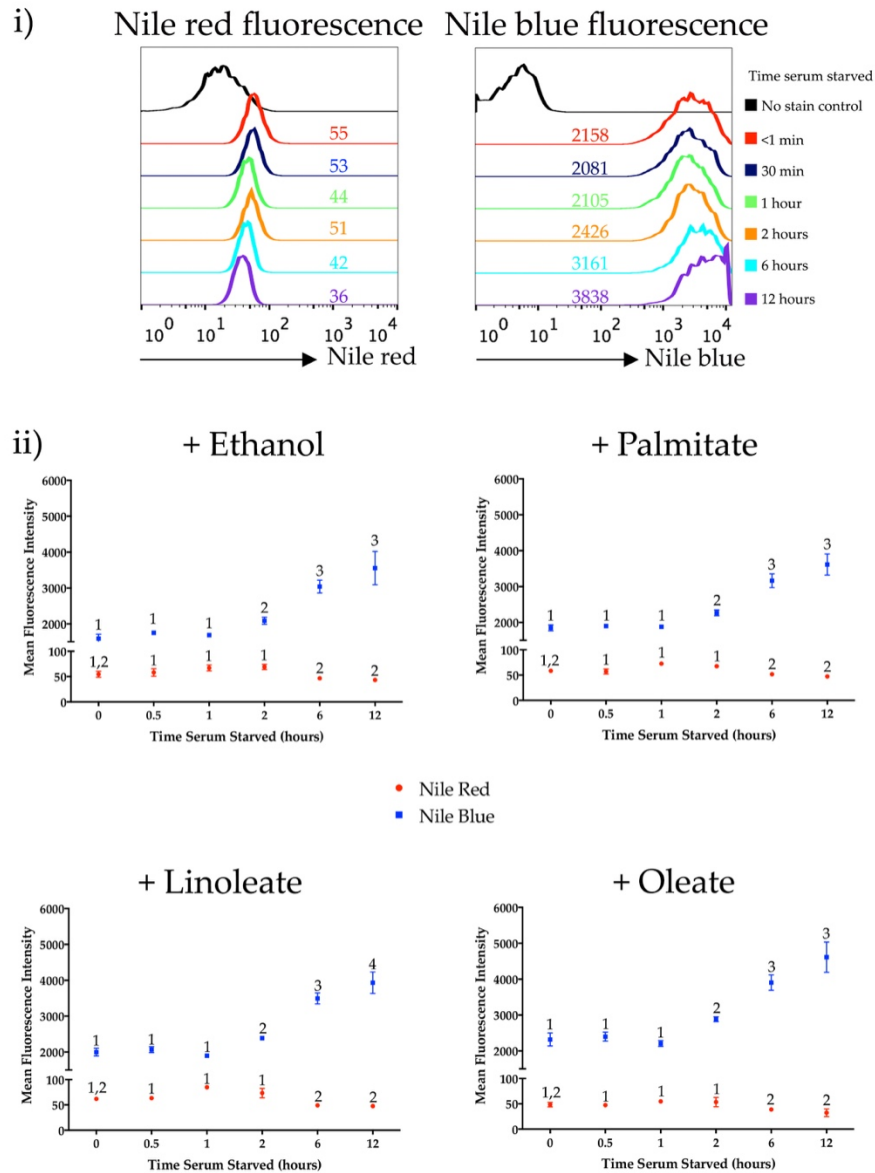


**Figure 8.3: Serum starved undifferentiated mouse ES cells have increased uptake of Nile Blue.**

Mean fluorescence intensity of (i) Nile Red and Nile Blue in undifferentiated mouse ES cells starved of serum for less than one minute (red), 30 minutes (blue), 1 hour (green), 2 hours (orange), 6 hours (cyan) and 12 hours (purple). (ii) Changes in mean fluorescence intensity of Nile Blue (blue) and Nile Red (red) over time in serum starved mouse ES cell treated with ethanol, palmitate, linoleate and oleate. Data presented as mean  $\pm$  SEM (n=3). Significance in Nile Blue and Nile Red fluorescence over time was determined by a two-tailed, one-way ANOVA with Tukey's pairwise *post hoc* analysis. Groups not sharing a numeral are significantly different from each other.

### **8.3.2 Assessing probe uptake and surface protein expression of adipocyte markers in adipocyte-like cells differentiated from mouse ES cells.**

#### **8.3.2.1 Adipocyte-like cells differentiated from mouse ES cells treated with DHT, FGF10 and TGF $\beta$ 1 have greater Nile Red fluorescence.**

In Chapter 4, measurements were made to determine whether differences existed in the adipocyte-like cells treated with endoderm differentiation medium alone, methanol (vehicle control) or prostate epithelial cell differentiation medium (DHT, FGF10 and TGF $\beta$ 1). The lipid droplets in the adipocyte-like cells derived from the prostate epithelial cell differentiation medium occupied a greater cell area (Figure 4.2). Here, Nile Red uptake was compared between the adipocyte-like cells differentiated from each condition at the single cell level. There was no difference in the number of cells exhibiting Nile Red uptake (Figure 8.4i). However, Nile Red fluorescence intensity in the adipocyte-like cells derived from the prostate epithelial cell differentiation medium was greater compared to control conditions ( $810 \pm 90$  a.u.  $P < 0.01$ ) (Figure 8.4).

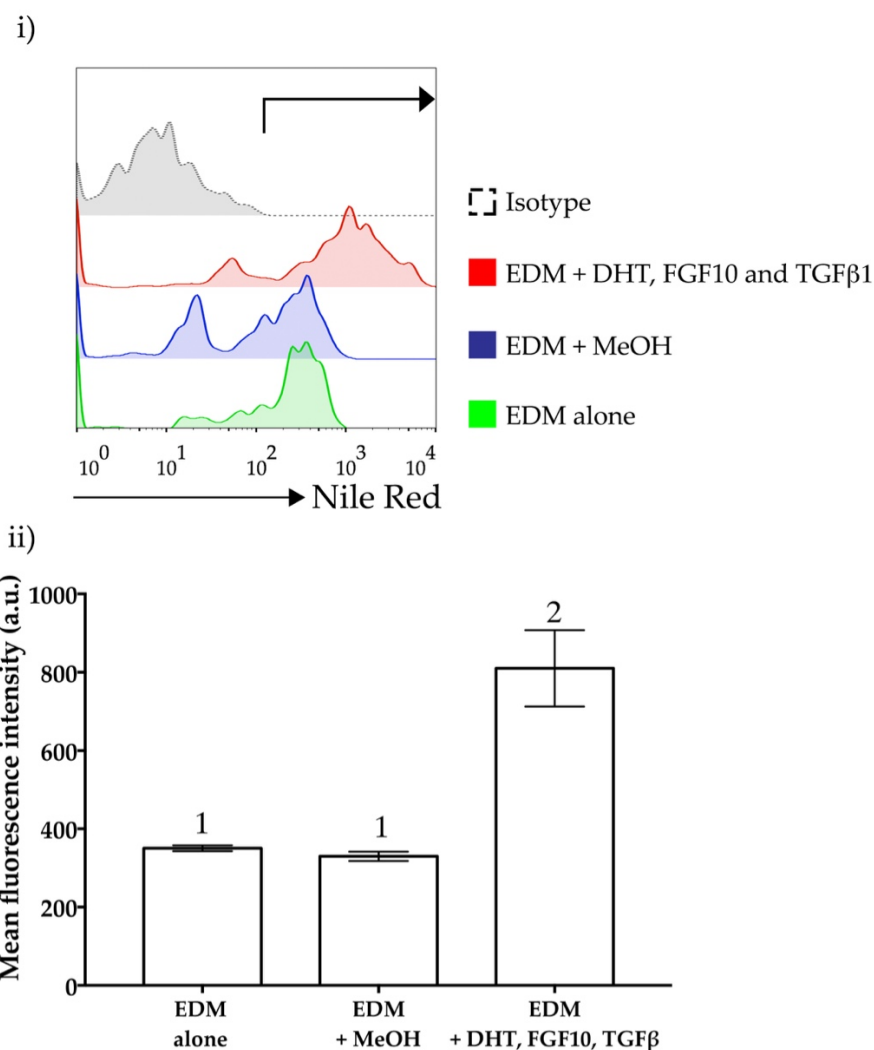


**Figure 8.4: Nile Red fluorescence is greatest in the buoyant fraction of mouse ES cells treated with DHT, FGF10 and TGF $\beta$ 1.**

(i) Representative histogram plot of Nile Red fluorescence in the buoyant fraction of day 22 differentiated mouse ES cells in endoderm media alone (EDM, green), EDM with methanol (MeOH, vehicle, blue) and EDM with DHT, FGF10 and TGF $\beta$ 1 (red). (ii) Comparisons in the mean fluorescence intensity (MFI) of Nile Red in day 22 differentiated mouse ES cells treated with EDM alone, EDM with MeOH or EDM with DHT, FGF10 and TGF $\beta$ 1. Data presented as mean  $\pm$  SEM ( $n = 4$ ). Significant differences between the MFI of Nile Red between groups was determined by a two-tailed, one way ANOVA with Tukey's *post hoc* analysis. Groups not sharing a numeral are significantly different from each other.

### **8.3.2.2 Endoderm-derived adipocytes have a similar profile to gonadal adipocytes.**

Finally, the adipocyte-like cells differentiated were examined for Nile Red uptake and the markers used to distinguish brown and white adipocytes. Nile Red<sup>+</sup> cells were gated in the buoyant fraction of dissociated day 22 differentiated mouse ES cell cultures and frequency of surface protein expression (or dye uptake) measured (Figure 8.5). Adipocyte-like cells derived from conditions promoting prostate epithelial cell differentiation had more Nile Blue and MitoTracker Deep Red uptake and CD36 surface protein expression compared to control conditions (Figure 8.5).

An unbiased approach was then used to compare brown, subcutaneous, visceral, marrow and endoderm-derived adipocytes according to the parameters described in this study. A heatmap was generated that compared frequency of surface protein expression or dye uptake across all adipocytes. The adipocyte heterogeneity heatmap revealed marrow adipocytes to be distinct from all other adipocytes (Figure 8.6). Brown, subcutaneous inguinal and visceral epicardial adipocytes have a distinct profile compared to visceral peri-renal and mesenteric adipocytes (Figure 8.6). The adipocyte-like cells differentiated from mouse ES cells under control conditions (base endoderm media alone and methanol) did not match the profile of brown, subcutaneous or visceral adipocytes (Figure 8.6). However, the adipocyte-like cells generated from prostate epithelial cell differentiation media closely resembled the profile of gonadal adipocytes (Figure 8.6).

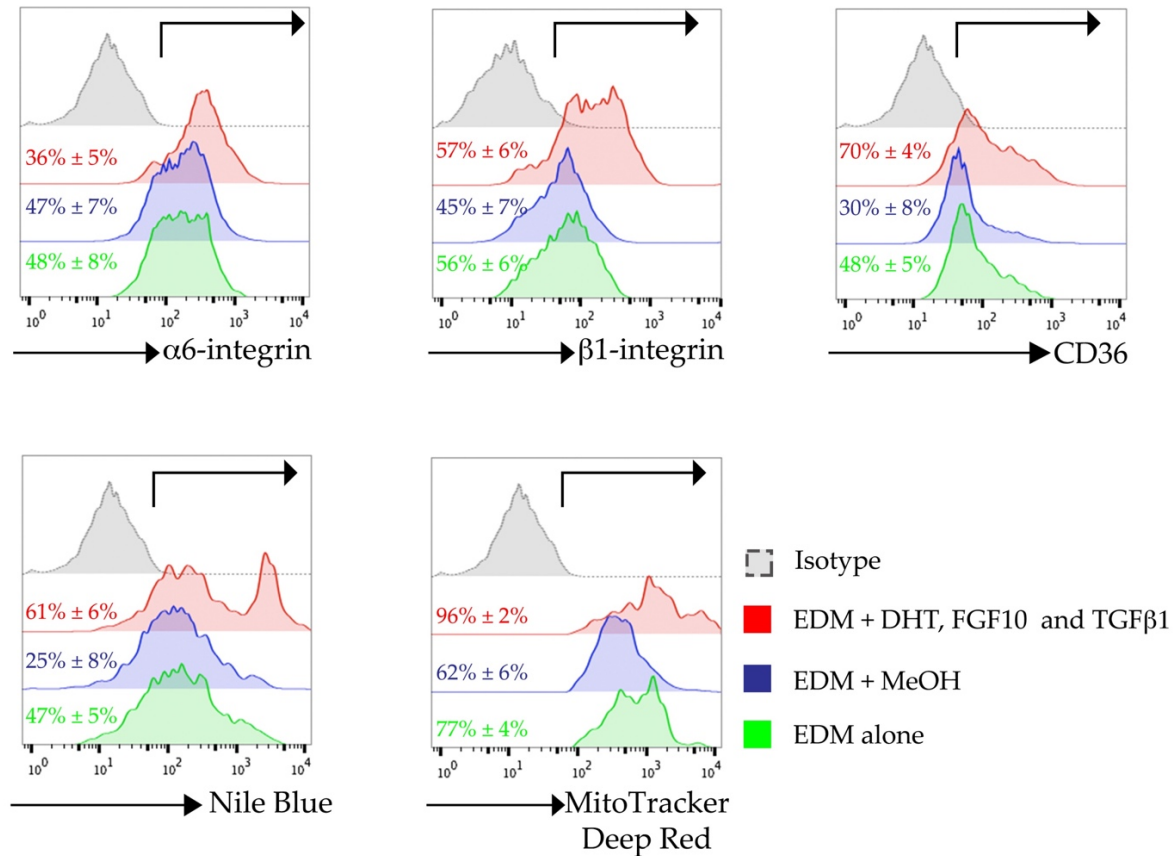


**Figure 8.5: The buoyant fraction of day 22 differentiated mouse ES cells treated with DHT, FGF10 and TGFβ1.**

Representative histogram plot of  $\alpha 6$  integrin<sup>+</sup>,  $\beta 1$  integrin<sup>+</sup>, CD36, Nile Blue (NB) and MitoTracker Deep Red (MTDR) positive cells in day 22 differentiated mouse ES cells treated with endoderm media alone (EDM, green), EDM with methanol (MeOH, vehicle, blue) and EDM with DHT, FGF10 and TGFβ1 (red). Frequency of surface protein expression or dye uptake is presented as mean  $\pm$  SEM (n = 4).

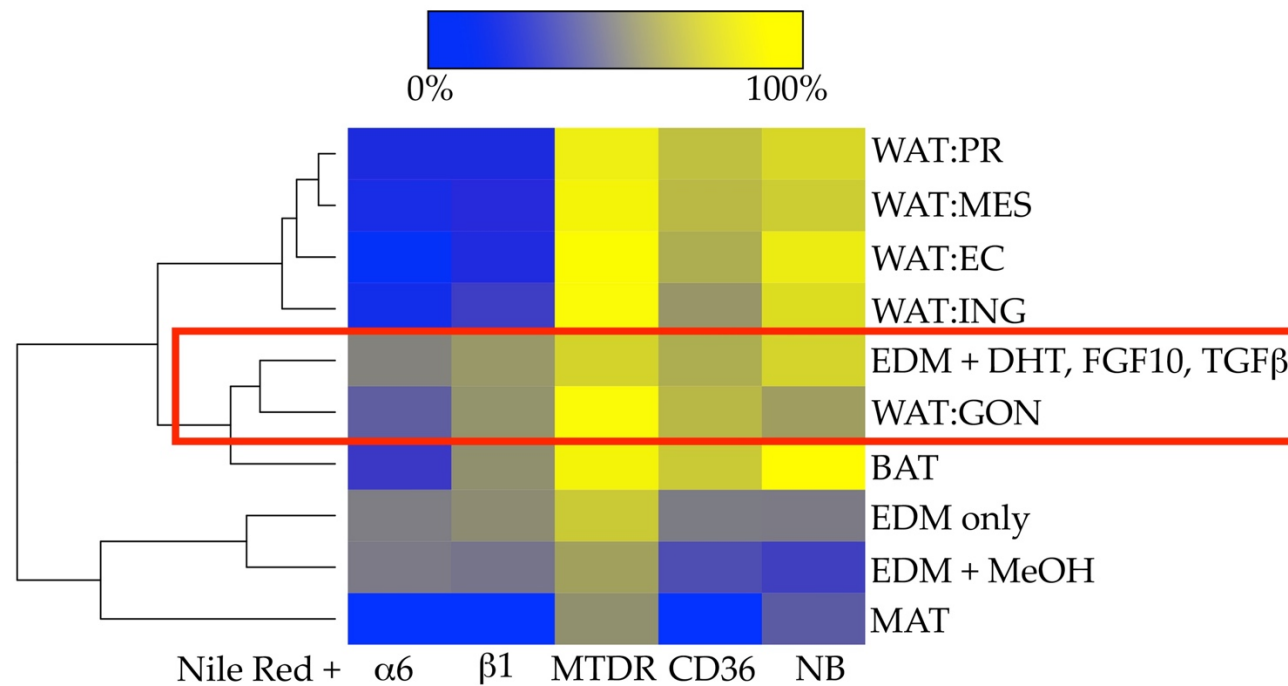


**Figure 8.6: Day 22 differentiated adipocytes from mouse ES cells treated with DHT, TGFβ1 and FGF10 resemble gonadal adipocytes.**

Comparisons in the frequency of Nile Red<sup>+</sup> cells labelled with Nile Blue, MitoTracker Deep Red, CD36, α6 integrin and β1 integrin between brown (BAT), subcutaneous inguinal (WAT:ING), visceral gonadal (WAT:GON), peri-renal (WAT:PR), mesenteric (WAT:MES), epicardial (WAT:EC), marrow (MAT) and mouse ES cell-derived adipocytes depicted in a heatmap. Blue indicates low levels of surface protein expression while yellow indicates high levels. Heatmap generated using Heatmap Generator (Khomtchouk et al., 2014).

## 8.4 Discussion

### 8.4.1 Questioning the embryological origin of gonadal adipocytes.

The bulk of this study served to answer whether the adipocyte-like cells differentiated from mouse ES cells were representative of adipocytes from a particular adipose depot. Due to the close proximity of gonadal adipose tissue to the prostate, the hypothesis was that the adipocytes derived from mouse ES cell cultures treated with DHT, TGF $\beta$ 1 and FGF10 would be characteristic of gonadal adipocytes. Based on Nile Red uptake with 5 independent parameters, adipocytes derived from mouse ES cells treated with DHT, TGF $\beta$ 1 and FGF10 exhibited a profile similar to gonadal adipocytes. These findings raise the possibility of an endoderm origin for gonadal adipocytes.

Do adipocytes support the growth and development of endoderm derivatives such as the prostate? The relationship between peri-prostatic adipose tissue and prostate cancer is well founded (Laurent et al., 2016; Freedland et al., 2004; Parikesit et al., 2016; Hsing et al., 2007). The increase in secretion of pro-inflammatory cytokines from adipocytes favours the growth of prostate cancer cells (Parikesit et al., 2016; Hsing et al., 2007). Outside of prostate cancer, there is a lack of understanding on the role of adipocytes on the development of the prostate. To date, only one group has reported the effect of adipocytes on prostate organogenesis (Tokuda et al., 1999). Isolated dorsal prostatic cells cultured with mature adipocytes had promoted the differentiation and proliferation of acinus-like structures *in vitro* (Tokuda et al., 1999).



#### **8.4.2 Utility of a code to characterise adipocytes from brown and white adipose depots.**

The heat map generated to characterise adipocyte heterogeneity provides an interesting avenue to assess differences in brown and white adipocyte cell biology. Collectively, the code can be summarised into three sections: adipocyte morphology (laminin receptor  $\alpha 6\beta 1$  integrin), metabolism (fatty acid translocase CD36 and free fatty acid dye Nile Blue) and mitochondrial membrane potential (MitoTracker Deep Red). Aside from identifying adipocytes from multiple sources, the adipocyte heterogeneity code can be applied to assess changes to adipocytes in pathophysiological situations such as obesity and diabetes. Data visualisation tools such as SPADE and viSNE cluster cell populations based on phenotypic similarity (Leelatian, Diggins, & Irish, 2015). Both modes of data visualisation are alternative unbiased approaches that can also be used to assess adipocyte heterogeneity. Future studies could compare adipocyte heterogeneity according to SPADE or viSNE analyses.

#### **8.4.3 Applying the code to identify mesoderm and neural crest derived adipocytes.**

In Chapter 4, the idea was put forward to compare adipocytes differentiated from mouse ES cells under neural crest or mesoderm culture conditions. In a similar manner that was presented in this chapter, the code can be used to determine which adipocytes neural crest-derived or mesoderm-derived adipocytes resemble. Neural crest derived adipocytes are proposed to give rise to cephalic adipose tissue in the

skull (Billon et al., 2007). Cuaranta-Monroy and colleagues (2014) describe the differentiation of adipocytes from mouse ES cells under mesoderm culture conditions have a similar gene expression identity to subcutaneous adipocytes (Cuaranta-Monroy et al., 2014). The code developed in this study could be used in conjunction to support the findings presented by Cuaranta-Monroy and colleagues (2014).

#### **8.4.4 Sorting adipocytes derived from mouse ES cell cultures.**

An extension of flow cytometry is cell sorting. Based on immunoreactivity (and dye uptake), cells can be isolated, grown in culture or used for gene expression analyses. The adipocytes differentiated from mouse ES cells described here can be sorted according to Nile Red uptake. The sorted adipocytes can be grown *in vitro* whereby modelling adipogenesis of endoderm-derived adipocytes can be achieved. Furthermore, gene expression analyses can be performed on the sorted endoderm-derived adipocytes to reveal heterogeneity at the molecular level. Alternatively, to confirm the possibility of endoderm-derived adipocytes, definitive endoderm can be sorted from mouse ES cells according to CXCR4<sup>+</sup> and c-Kit<sup>+</sup> surface protein expression and treated with the growth factors used to differentiate prostate epithelial cells.

#### **8.4.5 Conclusion**

An unbiased analysis of the data collected throughout this study revealed a code that characterised adipocyte heterogeneity at the single cell level. The code revealed a resemblance between gonadal adipocytes and adipocytes differentiated from mouse

ES cell under conditions that promote prostate epithelial cell differentiation. The findings presented demonstrate a possible endoderm origin of gonadal adipocytes and a supportive role of adipocytes in prostate organogenesis.

## Chapter 9 General discussion

### 9.1 Opening remarks

The study presented aimed at differentiating prostate epithelial cells from mouse embryonic stem cells. By mimicking the signalling factors critical for *in vivo* prostate organogenesis, prostate luminal epithelial cells were successfully differentiated from mouse ES cells as determined by gene expression of *Nkx3.1* and *Svs2*. Generation of prostate epithelial cells from mouse ES cells serve as an *in vitro* model of prostate development from embryogenesis. Due to the small size of early embryos and accessibility to developing prostatic tissue, modelling the early stages of prostate development is challenging. Thus, mouse ES cell-derived prostate epithelial cells could be used here to characterise the early stages of prostate development. The successful differentiation of prostate epithelial cells from mouse ES cells provides a new approach to model prostate disease progression and possible drug screening capabilities.

Alongside prostate epithelial cell differentiation, adipocyte-like cells were detected. Since adipocytes typically arise from the mesoderm germ layer, the differentiation of adipocyte-like cells from endoderm culture conditions was an unexpected finding in this study. The study then set out to determine whether the adipocyte-like cells were representative of a specific adipose depot. By characterising adipocytes from brown, subcutaneous and visceral white adipose depots at the single cell level, the adipocytes

differentiated alongside prostate epithelial cells closely resembled gonadal adipocytes. Together, the findings suggest a possible synergistic interaction between adipocytes and prostate cell development and question the embryological origin of gonadal adipocytes. Here, I will describe the utility of differentiating prostate epithelial cells from mouse ES cells and evaluate the embryological origins of gonadal adipocytes.

## **9.2 Recapitulation of the early developmental processes in prostate epithelial cell determination and differentiation from mouse ES cells.**

The prostate develops from the urogenital sinus in mice at E17.5 (Marker et al., 2003b). Androgen receptor signalling from the urogenital mesenchyme prompts the budding of epithelial cells of the prostate (Marker et al., 2003b; Prins & Putz, 2008). The earliest known marker for prostate development is the homeobox gene *Nkx3.1* at E15.5, prior to ductal formation (Bhatia-Gaur et al., 1999). Additionally, *Nkx3.1* is not expressed on ductal urogenital tissues such as the seminal vesicle, the bladder or the urethra (Bhatia-Gaur et al., 1999; Abate-Shen et al., 2008; Dutta et al., 2016).

The molecular mechanisms mediating the inductive processes between the urogenital mesenchyme and urogenital epithelium are poorly defined (Shen & Abate-Shen, 2010). Currently, there are two models that describe the role of androgens in prostate development (Costello & Corcoran, 2012). The andromedin model describes a ligand binding to androgen receptor (AR) to mediate prostate formation (Costello &

Corcoran, 2012). FGF10 was considered an andromedin since it can induce growth and development of the prostate, but FGF10 does not bind to androgen receptor (Costello & Corcoran, 2012; Lu et al., 1999; Huang et al., 2005)

The alternative model is the smooth muscle hypothesis that proposes androgen receptor signalling has indirect effects on prostate epithelial cell differentiation by regulating the differentiation of a smooth muscle layer (Costello & Corcoran, 2012).

The smooth muscle theory suggests that a layer of smooth muscle mediates the inductive capacity of the urogenital mesenchyme (Costello & Corcoran, 2012).

However, budding of prostatic epithelial cells occurs before the development of the smooth muscle layer, indicating induction is independent of the smooth muscle layer (Thomson et al., 2002; Costello & Corcoran, 2012). Smooth muscle arises from the mesoderm germ layer (Majesky, 2007). Here, mouse ES cell cultures were directed towards definitive endoderm differentiation.

The stepwise differentiation of prostate epithelial cells from mouse ES cells presented in this study supports the andromedin hypothesis. Endoderm differentiation was induced with the addition of Activin-A and confirmed by c-Kit and CXCR4 surface protein expression. Furthermore, mesoderm markers Flk-1 and PDGFR $\alpha$  were not expressed on Activin-A treated mouse ES cells. Mouse ES cell-derived endoderm treated with retinoic acid led to urothelial cell specification.

The strongest evidence for prostate epithelial cell differentiation was the detection of prostate specific genes *Nkx3.1*, *Svs2* and *Pbsn* in day 16 and day 22 of differentiated cultures treated with DHT, TGF $\beta$ 1 and FGF10 respectively (herein prostate differentiation medium). Future studies would confirm the differentiation of luminal or basal epithelial cells by immunohistochemical staining with CK8 and CK18 or CK5 and CK14 respectively (Figure 9.1) (Sherwood et al., 1990; Sherwood et al., 1991). Intermediate prostate epithelial cells can be characterised by luminal and basal CKs as well as CK19 (Xue et al., 1998; Wang et al., 2001). Additionally, cell types that resembled neuroendocrine cells were identified. Immunohistochemical staining with chromogranin-A or synaptophysin could confirm the differentiation of neuroendocrine cells (Figure 9.1) (Krijnen et al., 1993).

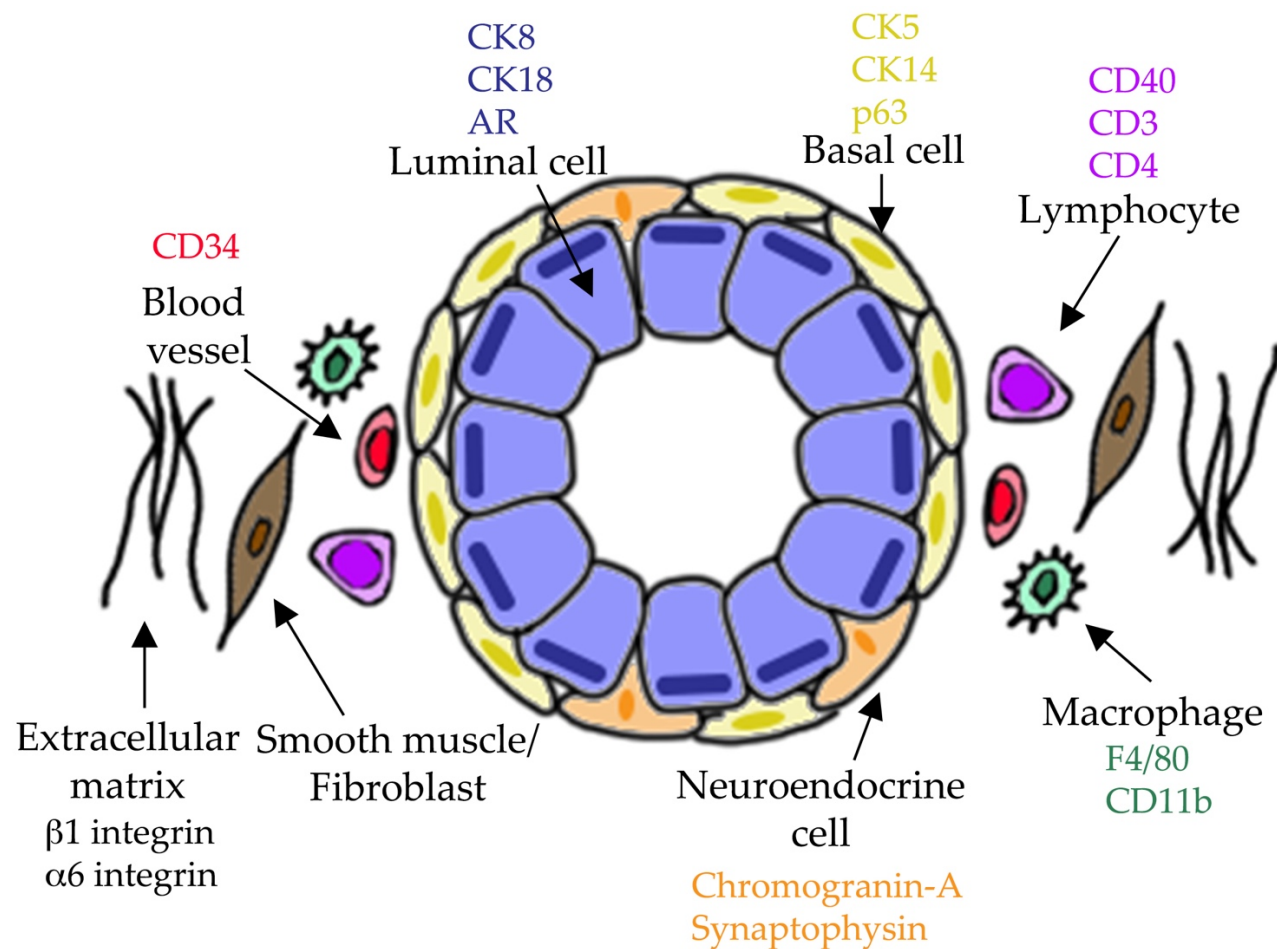


**Figure 9.1: Epithelial and stromal cells of the prostate and markers used to identify them.**

Secretory acinus of the prostate includes the luminal (blue) and basal (yellow) epithelial cells. Neuroendocrine (orange) cells are rare epithelial cells found interspersed with basal and luminal epithelial cell types. Stromal cells of the prostate include lymphocytes (purple), macrophages (green), smooth muscle (brown), blood vessels (red) and the extracellular matrix (black).



### **9.3 Applications for prostate epithelial cell differentiation from mouse ES cells**

#### **9.3.1 Prostate organoids derived from human iPS cells**

Prior to the onset of this study, there had only been one previous report on the differentiation of prostatic tissue from ES cells (Taylor et al., 2006). Taylor and colleagues (2006) grafted human ES cells with explants of urogenital mesenchyme into the renal capsule of immunodeficient SCID mice (Taylor et al., 2006). The resulting tumour was sectioned and stained for androgen receptor, P63 and luminal cytokeratins 8 and 18 (CK8 and CK18) (Taylor et al., 2006). Here, mouse ES cell differentiation into prostate luminal epithelial cells was achieved without tissue grafting, co-culture or culture on 3D matrigels.

As the focus of the study shifted towards identifying and characterising the adipocytes generated from mouse ES cells under endoderm culture conditions, Calderon-Gierszal and Prins (2015) reported the differentiation of prostatic organoids from human ES cells (Calderon-Gierszal and Prins, 2015). Human ES cells were differentiated into definitive endoderm and then cultured the cells with FGF10, WNT-10B, testosterone, EGF, Noggin, R-Spondin1 and all-trans retinoic acid to induce prostate organoid formation (Calderon-Gierszal and Prins, 2015). Presence of prostate luminal cell differentiation was determined by immunohistochemistry of CK8, CK18, androgen receptor and Nkx3.1 (Calderon-Gierszal and Prins, 2015). The differentiated prostate organoids were then treated with endocrine disruptor Bisphenol-A to assess morphological changes to branched structures (Calderon-Gierszal and Prins, 2015).

Bisphenol-A led to a perturbed number of branching structures, suggesting that *in utero* exposure to Bisphenol-A may disrupt prostate organogenesis (Calderon-Gierszal and Prins, 2015).

ES cells can be utilised for drug screening and toxicity assessment (Calderon-Gierszal and Prins, 2015). One of the advantages of mouse ES cells is the rapid assessment and high throughput screening of small molecules (reviewed in: Pouton & Haynes, 2007; Lou, 2011). An extension of the protocol described in this study is assessing the efficacy and toxicity of prostate cancer drugs on mouse ES cell-derived prostate epithelial cells.

### **9.3.2 Replacement of animal models**

The *in vitro* model of prostate epithelial cell differentiation presented here also presents benefits from an animal ethics standpoint. The model is completely animal free. This system will dramatically reduce the number of animals being used to develop models of prostate development and animals being tested for prostate cancer treatment. As mouse ES cells can be maintained almost indefinitely, it is plausible to accrue near infinite numbers of various cell types, otherwise impossible to achieve without dissecting large numbers of animals.

### 9.3.3 Modelling prostate oncogenesis *in vitro* with mouse ES cells

Differentiation of other endoderm derivatives such as pancreatic  $\beta$  cells and hepatocytes propose a possible therapeutic approach for the treatment of diabetes and cirrhosis respectively (Jiang et al., 2007; Liu & Lee, 2012; Yoshida et al., 2011; Little et al., 2007). Prostate cell transplantation is unnecessary, but mouse ES cell differentiation of the prostate can be used to model changes in genotype and subsequent phenotype during progression of prostate oncogenesis. Many of the processes and signalling for *in vivo* development of the prostate are reactivated in oncogenesis (Schaeffer et al., 2008; Abate-Shen et al., 2008; Gingrich et al., 1996).

Androgen dependent, prostate-specific regulatory genes critical for embryonic prostate development such as *Nkx3.1* and *Pbsn* also play roles in prostate carcinogenesis (Schaeffer et al., 2008; Abate-Shen et al., 2008; Greenberg et al., 1994). Loss of function of *Nkx3.1* in mice leads to impaired ductal morphogenesis and abnormal differentiation of prostate epithelial luminal cells (Bhatia-Gaur et al., 1999; Abate-Shen et al., 2008; Wang et al., 2009; Dutta et al., 2016). In humans, expression of *NKX3.1* is reduced in non-invasive and early stage prostate cancer (Abate-Shen et al., 2008). A prominent phenotype of *Nkx3.1* nullizygous mice is the histological appearance of prostate epithelial hyperplasia, a similar phenotype to prostate intraepithelial neoplasia (PIN) observed in human prostate cancer (Bhatia-Gaur et al., 1999; Abdulkadir et al., 2002; Abate-Shen et al., 2008). Notably, the stroma is reduced, the basal epithelial cell layer is perturbed and markers of epithelial cell differentiation

are expressed heterogeneously (Kim et al., 2002). Although mice void of *Nkx3.1* are predisposed to develop PIN, they do not develop invasive carcinoma (Abate-Shen et al., 2008).

Tissue recombinant systems utilising prostatic tissue from *Nkx3.1*<sup>-/-</sup> mice have characterised the histopathological alterations in PIN (Kim et al., 2002). Modelling the development of PIN and invasive carcinoma with mouse ES cells can be achieved with gene editing tools such as the CRISPR/Cas9 system. The CRISPR/Cas9 system can be used to replace and remove up to 10 genes (Le Cong et al., 2013). If *Nkx3.1* is knocked out of mouse ES cells, the differentiation of prostate epithelial cells (or lack thereof) using the protocol described in this study can be monitored (Figure 9.2). Since *Nkx3.1* is critical for prostate development, deletion of *Nkx3.1* may prevent prostate epithelial cell differentiation, regardless of culture conditions.

*Pten* is a tumour suppressor associated with many cancers including human prostate cancer (Cairns et al., 1997). *Pten* is essential for embryogenesis as *Pten* nullizygous mice die *in utero* (Di Cristofano et al., 1998; Podsypanina et al., 1999). Heterozygotes however, display a range of phenotypes in multiple tissues (Di Cristofano et al., 1998; Podsypanina et al., 1999). Specifically, the prostate becomes enlarged and hyperplastic which suggests *Pten* is a regulator of prostate cancer initiation progression (Di Cristofano et al., 1998; Podsypanina et al., 1999). Loss of *Pten* with other tumour suppressors such as *p27* and *Nkx3.1* lead to more aggressive phenotypes (Guo, Zhang,

& Garraway, 2012; Abate-Shen et al., 2003). Prostate tissue from mice void of *Pten* and either *p27* and *Nkx3.1* had multifocal lesions indicative of high grade PIN and adenocarcinoma (Guo et al., 2012; Abate-Shen et al., 2003). Future studies could aim to assess deletion of *Nkx3.1* as well as *Pten* in mouse ES cells to assess changes in genotype and subsequent phenotype during prostate epithelial cell differentiation.

#### **9.3.4 Prostate-on-a-chip. Characterisation of cell types differentiated under conditions promoting prostate epithelial cell differentiation.**

In this study, flow cytometry was utilised to characterise cell types according to size, granularity, probe uptake and surface protein expression. Although prostate epithelial cells were differentiated from mouse ES cells, ES cell populations do not contain 100% of the desired cell type. Could flow cytometry be utilised to distinguish the different cell types generated? In particular, could the different epithelial cells of the prostate as well as cells from the stroma be identified from differentiated mouse ES cell cultures? The markers used to commonly identify prostatic epithelial and stromal cells are outlined in Figure 9.1. Here, the adipocytes generated alongside prostate epithelial cells resembled gonadal adipocytes.

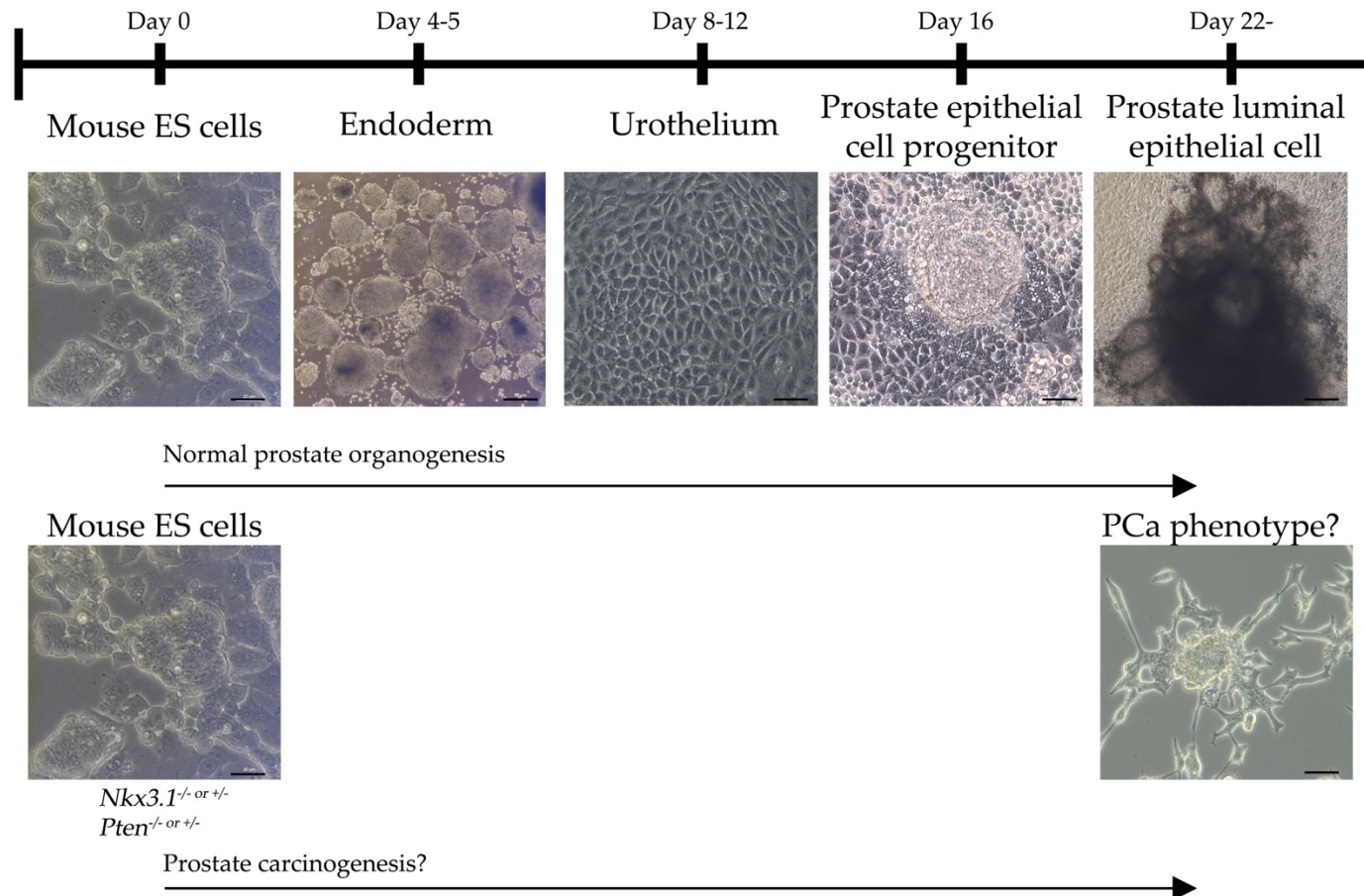


**Figure 9.2: Modelling prostate development and prostate cancer progression using mouse ES cells.**

Mouse ES cells were directed towards prostate epithelial cell differentiation in a stage dependent manner *in vitro*. Gene editing tools such as CRISPR/Cas9 can be implemented to knockout or overexpress genes critical for prostate epithelial cell development such as *Nkx3.1* or prostate oncogenesis such as *PTEN* and subsequent phenotype analysed. Prostate cancer (PCa) image taken from PCa cell line LnCAP. Scale bars represent 20  $\mu$ m.

#### 9.4 An endodermal origin of gonadal adipocytes

There has been no consideration of a possible endoderm source of adipocytes. According to surface protein expression and probe fluorescence, the mouse ES cell-derived adipocytes from prostate differentiation medium closely resembled gonadal adipocytes. While fate-mapping and lineage tracing studies have identified the origins of brown adipocytes, the embryological origins of subcutaneous and visceral white adipocytes remains ambiguous (Sanchez-Gurmaches & Guertin, 2014).

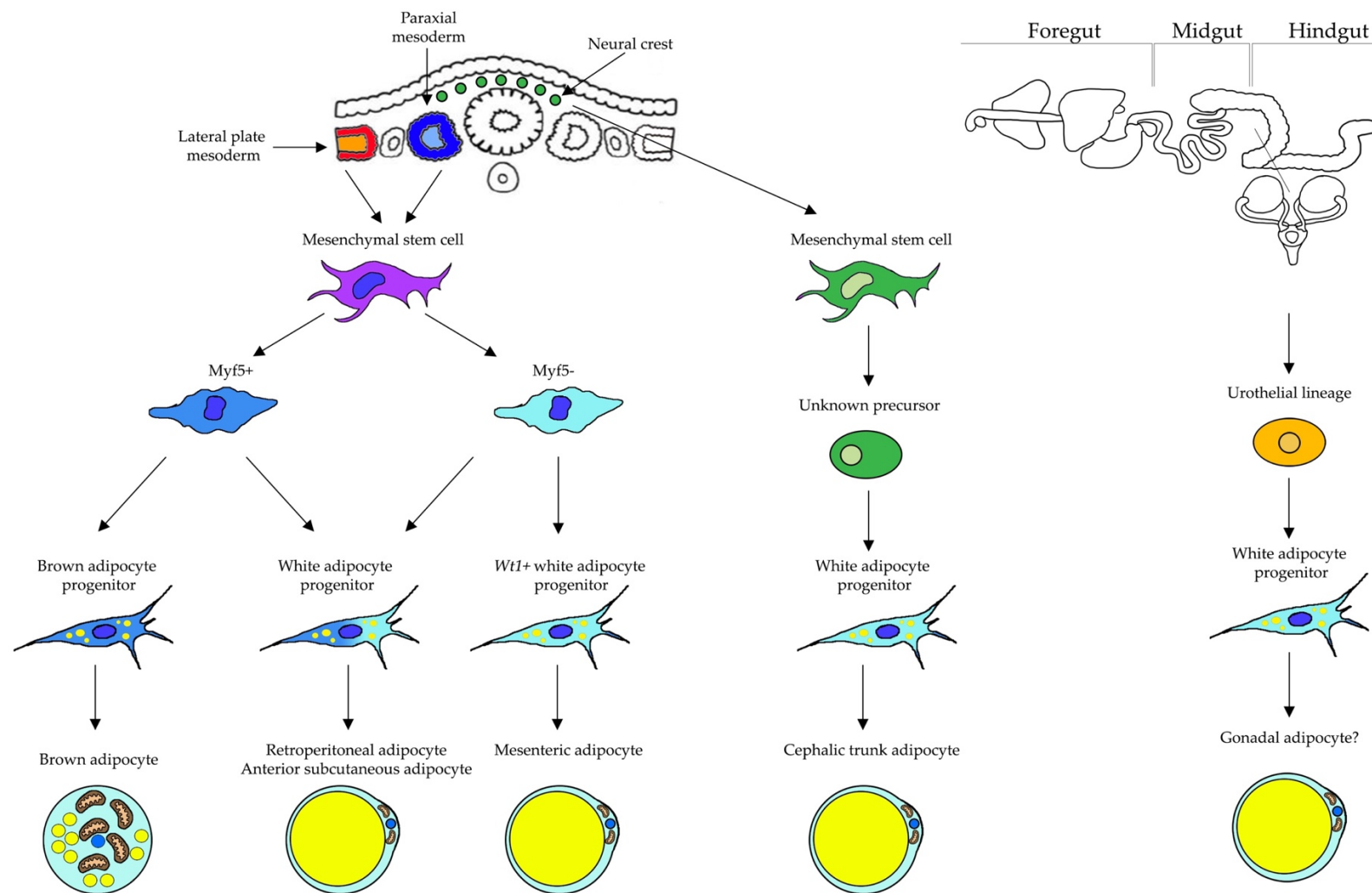
The origin of brown adipocytes has been identified as sharing the same lineage as skeletal muscle (Berry et al., 2013). Myogenic factor 5 (*Myf5*) progenitors give rise to brown adipocytes and a subset of retroperitoneal and anterior subcutaneous white adipocytes (Figure 9.3) (Sanchez-Gurmaches & Guertin, 2014). Recently, Shao *et al* (2017) used a Cre-Lox system targeting zinc finger protein 423 (*Zfp423*) to assess deletion of *Zfp423* on fetal development of adipose tissue (Shao et al., 2017). The *Zfp423*<sup>-/-</sup> mice had arrested terminal development of subcutaneous inguinal adipose tissue, suggesting the importance of *Zfp423* in commitment of subcutaneous adipose tissue (Shao et al., 2017). For visceral white adipocytes, mesenteric adipocytes have been traced to mesothelium-derived Wilms' tumour 1 (*Wt1*) progenitors (Figure 9.3) (Chau et al., 2014). Gonadal adipocytes are also thought to arise from *Wt1* progenitors (Chau et al., 2014). However, the study presented proposes otherwise (Chau et al., 2014). To ascertain whether gonadal adipocytes do arise from an endodermal origin, mouse ES cells transfected with a fluorescent reporter protein (such as mCherry) for

definitive endoderm (such as CXCR4 or Sox17) can be sorted by FACS to enrich for endoderm differentiation. Following, the protocol described in this study for differentiating prostate epithelial cells can be implemented to determine whether adipocytes differentiate alongside prostate epithelial cells.



**Figure 9.3: Proposed germ layer origins of brown, subcutaneous and visceral white adipocytes.**

Brown adipocytes arise from the paraxial mesoderm while white adipocytes arise from the lateral plate mesoderm. Mesenchymal stem cells produce *Myf5*<sup>+</sup> and *Myf5*<sup>-</sup> progenitors that in turn give rise to brown and white adipocytes respectively. Retroperitoneal and anterior subcutaneous WAT arise from a pool of *Myf5*<sup>+</sup> and *Myf5*<sup>-</sup> progenitors. Visceral mesenteric white adipocytes arise from *Myf5*<sup>-</sup> *Wt1*<sup>+</sup> progenitors. Mesenchymal stem cells from the neural crest give rise to an unknown progenitor cell that leads to cephalic white adipocyte differentiation. As adipocytes differentiated in mouse ES cell cultures in conjunction to prostate epithelial cells were similar to gonadal adipocytes, a possible hindgut endoderm origin of gonadal adipocytes is proposed.



#### 9.4.1 Do adipocytes support the normal development of the prostate?

Interactions between peri-prostatic adipose tissue and the prostate are well documented in the case of prostate cancer (expanded in 9.5.1) (Lughezzani et al., 2011; Irani et al., 2003; Rundle et al., 2013; Park et al., 2014). However, the role of adipose tissue in the development of the prostate is largely unexplored (Tokuda et al., 1999). Explant co-cultures of dorsal prostatic tissue with gonadal white adipocytes prompted organisation of epithelial cells into more acinus-like structures (Tokuda et al., 1999). *In vivo* adipocytes are found in the periphery of the prostate and histological sections of the prostate have identified adipocytes within the stroma of the prostate (Tokuda et al., 1999). Proliferation of prostate epithelial cells from adipocytes were suggested by Tokuda and colleagues (1999) to be due to the actions of adipokines like insulin growth factor, adiponin and leptin (Tokuda et al., 1999).

While prostate epithelial cells are derived from the endoderm, adipocytes typically arise from the mesoderm (Cunha et al., 2004b; Sanchez-Gurmaches & Guertin, 2014). The mesendoderm then, is the common ancestor shared by both cell types. Could adipocytes differentiate along-side prostate epithelial cells to facilitate and promote ductal morphogenesis? Adipocytes arise before prostate epithelial cells at E14 (Wang et al., 2013; Berry et al., 2013). Indeed, explant studies have demonstrated the growth and differentiation of the urogenital sinus cultured with the urogenital mesenchyme (Cunha et al., 1986; Cunha, Cooke, & Kurita, 2004a). In the absence of the urogenital mesenchyme, adipocytes may be playing a supportive role for prostate development.

### **9.5 Obesity is a multi-faceted disease and is a risk factor for multiple cancers**

The increasing rate of obesity has reached alarming levels. Hypertrophy (increase in adipocyte size) and hyperplasia (increase in adipocyte number) progress throughout obese individuals. Obesity is a serious health problem that has been linked to the development of coronary artery disease, hypertension and diabetes (Criqui et al., 1982; Hubert et al., 1983; Mokdad et al., 2003). Obesity has also been associated with several cancers including prostate, breast, liver and colon cancer (Bray et al., 2002). Several studies have reported obesity as a risk factor for prostate cancer and progression into high-grade disease (Lughezzani et al., 2011; Irani et al., 2003; Rundle et al., 2013; Park et al., 2014).

Mechanisms thought to promote prostate cancer in obese individuals are alterations in testosterone levels and secretion of adipokines (adipocyte hormones) (Taylor et al., 2015). Obese men have low levels of testosterone and increased levels of estradiol (Schneider et al., 1979). Increased secretion of the adipokine leptin causes testosterone levels to decrease (Soderberg et al., 2001). Leptin has also been linked to supporting tumour growth through the promotion of angiogenesis (Ando et al., 2014; reviewed in: Dutta et al., 2012). Conversely, levels of the anti-tumour adipokine adiponectin are reduced (Gao et al., 2014). Thus, a vicious feedback loop is generated as increased accumulation of adipose tissue leads to decreased testosterone levels.

Obesity-induced metabolic disorders manifest in the form of insulin resistance (and type II diabetes), reduced secretion of adipokines and abnormal adipogenesis (Pellegrinelli et al., 2016). The onset of obesity leads to cellular and structural changes in adipose tissue (Mariman & Wang, 2010). Fasting free fatty acid (FFA) and glycerol levels increase, which is thought to promote insulin resistance (Greenberg et al., 2006). The remodelling of adipose tissue leads to an expansion of adipose mass through the increase in the size (hypertrophy) and number (hyperplasia) of adipocytes (Pellegrinelli et al., 2016). To accommodate the increase in adipose mass, the extracellular matrix (ECM) undergoes structural changes (Pellegrinelli et al., 2016). The enlargement of adipocytes within WAT depot disrupts the homeostatic mechanisms that regulate normal tissue expansion and causes metabolic dysfunction. Further problems ensue as obesity leads to excess infiltration of adipose tissue by inflammatory macrophages as well as the ECM components collagen VI and thrombospondin (Spencer et al., 2011).

#### **9.5.1 Peri-prostatic adipose tissue facilitates prostate cancer metastasis**

The relationship between peri-prostatic adipose tissue and prostate cancer is well founded (Laurent et al., 2016; Freedland et al., 2016; Parikesit et al., 2016; Hsing et al., 2007). The increase in secretion of pro-inflammatory cytokines from adipocytes favours the growth of prostate cancer cells (Parikesit et al., 2016; Hsing et al., 2007). Co-cultures of androgen-dependent (LNCaP) prostate cancer cell line with mature

peri-prostatic adipocytes *in vitro* leads to significant proliferative ability (Kaneko et al., 2010). Conversely, androgen-independent (PC3 and DU145) prostate cancer cell lines cultured with mature peri-prostatic adipocytes have variable changes (Kaneko et al., 2010). Recently, Laurent and colleagues (2016) proposed that secretion of chemokine CCL7 from peri-prostatic adipocytes facilitates the migration of prostatic cancer cells (Laurent et al., 2016). When the CCL7 axis is inhibited, there is no pronounced migration of prostatic cancer cells (Laurent et al., 2016)

### **9.5.2 Obese women have a higher risk of developing breast cancer.**

Breast cancer shares similarities with prostate cancer as both develop in tissues which require gonadal steroids for normal development (Risbridger, Davis, & Birrell, 2010). In contrast to prostate tissue, the most abundant stromal cells in human breast tissue are adipocytes (Fletcher et al., 2017). While the interactions between adipose tissue and breast cancer progression are yet to be characterised, co-cultures of human breast cancer cell line MCF-7 with 3T3-L1 derived adipocytes and pre-adipocytes from breast tissue promote cancer cell proliferation and migration (Balaban et al., 2017). The cancer cells stimulate the lipolysis of the triglycerides stored within adipocytes, which in turn fuel cancer progression (Balaban et al., 2017).

### **9.5.3 What about carcinomas from cell types other than the prostate?**

Epidemiological studies have estimated obesity to be linked to approximately 20% of all cancer cases (reviewed in: De Pergola & Silvestris, 2013). Hepatocellular carcinoma

is the second most common cause of cancer death worldwide (Henry & Caldwell, 2015). Excess weight gain leads to ectopic deposition of lipids in the liver which leads to triglyceride accumulation (Targher et al., 2007). Left unchecked, non-alcoholic fatty liver disease (NAFLD) progresses towards cirrhosis and is considered a risk factor for hepatocellular carcinoma (Reeves, Zaki, & Day, 2016).

The expansion of adipocyte size in obesity hinders secretion of adiponectin (Reeves et al., 2016). Adiponectin promotes insulin sensitivity, fatty acid oxidation and suppresses lipogenesis (Reeves et al., 2016). Infiltration by macrophages contributes to the inflammatory state (Figure 9.4) (Reeves et al., 2016). Lipolysis liberates fatty acids which contribute to triglyceride accumulation in visceral adipose depots with reduced insulin sensitivity (Figure 9.4) (Reeves et al., 2016). As the capacity for mitochondrial oxidation of fatty acids crosses threshold, reactive oxygen species lead to damage to liver tissue (Reeves et al., 2016). Thus, a vicious cycle manifests in the presence of ongoing inflammation, promoting an environment for hepatocellular carcinoma.

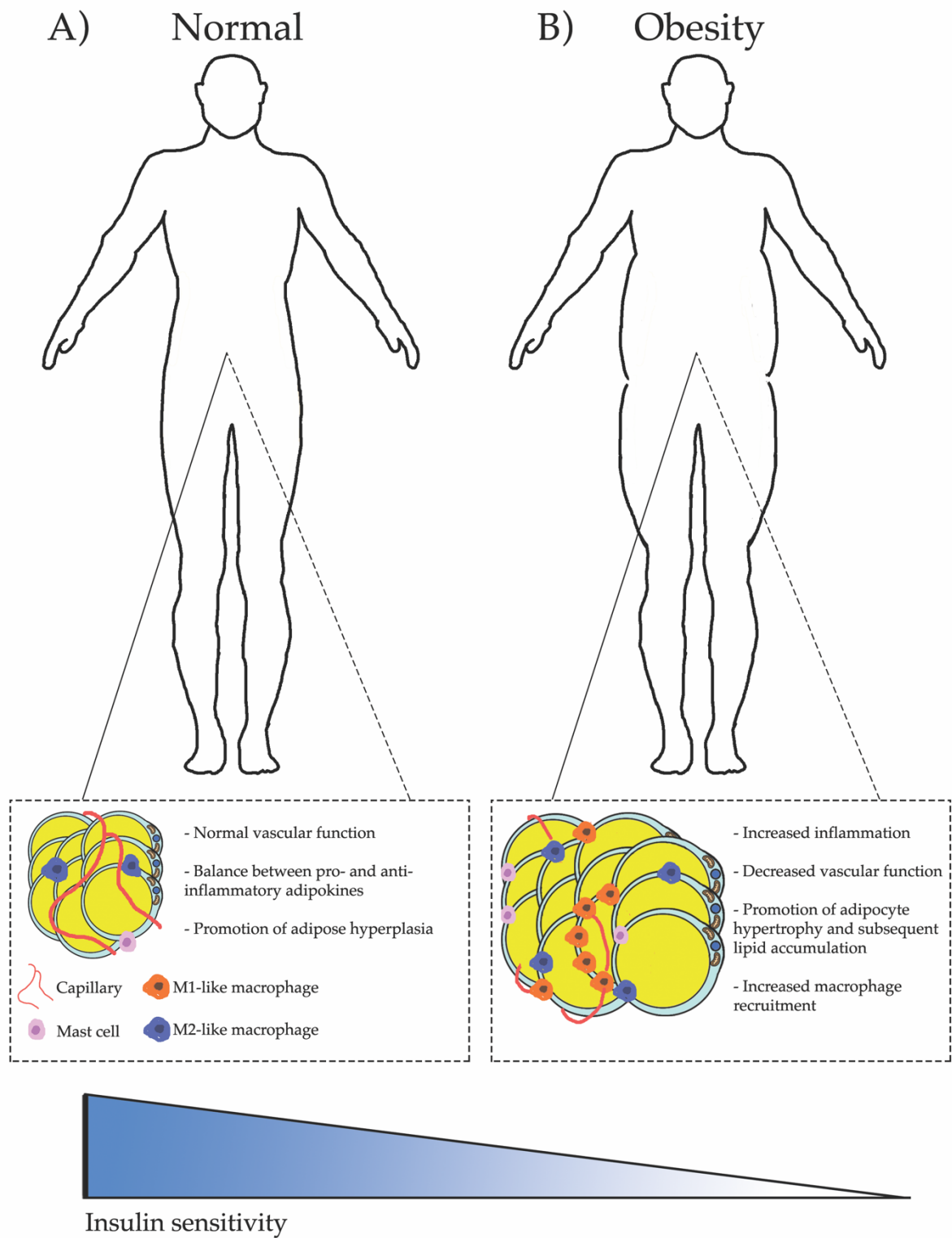


**Figure 9.4** Changes in adipose tissue function and structure in obese individuals



## **9.6 Flow cytometry as a diagnostic tool for pathophysiological conditions in humans.**

Flow cytometry is a useful tool for analysing heterogeneous cell populations based on size, granularity and surface protein immunoreactivity (Brown et al., 2000). In a haematological setting, flow cytometry is routinely used to phenotype leukemias and lymphomas (Liu et al., 2015; Adachi et al., 2015). Flow cytometry has also been valuable in monitoring immune cell number in HIV patients (Saag et al., 1996; Mellors et al., 1996). Throughout this study, the utility of flow cytometry in the study of adipocyte biology has been presented. Flow cytometric analyses of adipocytes can discriminate between adipocytes from multiple adipose depots and characterise adipocytes according to Nile Red uptake and surface protein immunoreactivity.

### **9.6.1 Lipotoxicity is a serious metabolic syndrome**

Under physiological conditions, triglyceride levels in non-adipose tissues is low (Engin, 2017). Pathophysiological conditions, such as obesity, leads to excess circulating lipids as the adipocytes have diminished capacity to store triglycerides (Engin, 2017). Failure in packaging lipids leads to ectopic deposition on non-adipose tissues such as the liver (NAFLD), skeletal muscle and the heart (Reeves et al., 2016; Engin, 2017; Duncan, 2008). Alterations in lipid metabolism and composition may pose as a phenotype overlooked in skeletal and cardiac muscle myopathies (Engin, 2017). Nile Red, Nile Blue and fatty acid translocase CD36 can be implemented here

for benchtop flow cytometric analyses identifying changes to lipid metabolism and composition.

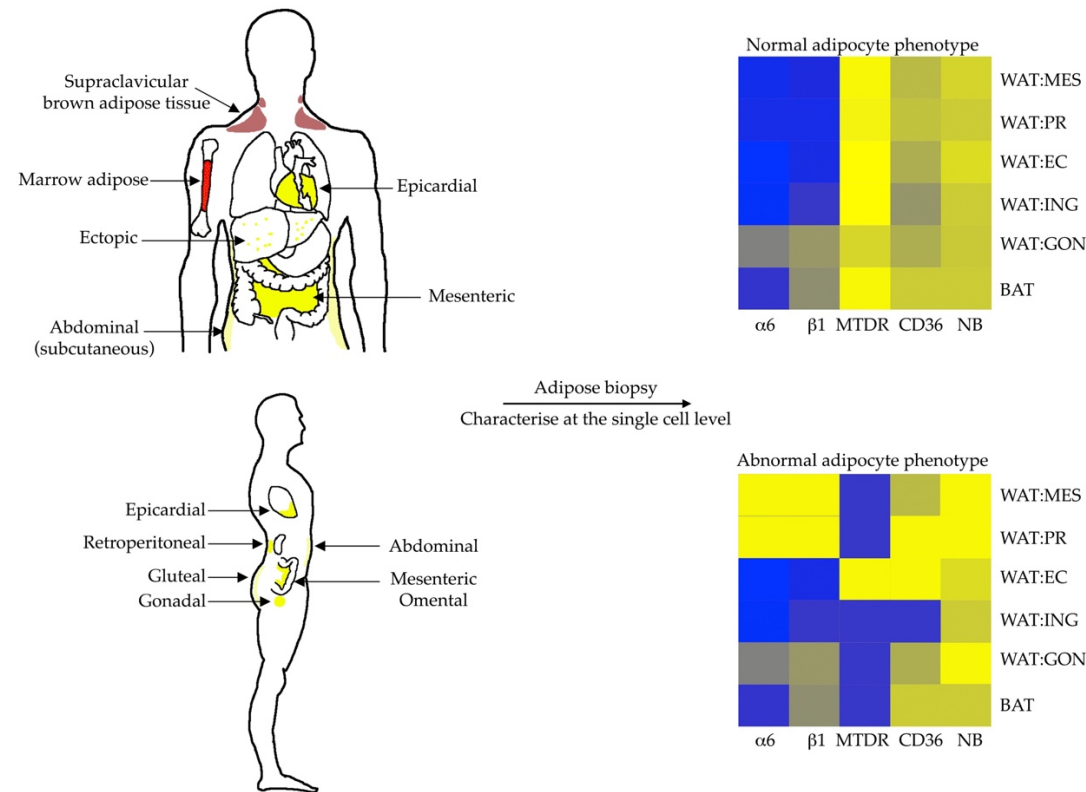


**Figure 9.5: Hypothetical clinical application of flow cytometric analyses of adipose tissue.**

In humans, brown adipose tissue is located in the supraclavicular region. Visceral white adipose tissue depots include epicardial, mesenteric, omental, retroperitoneal, peri-renal, gonadal and ectopic deposits on the liver and heart. Subcutaneous white adipose tissue is located around the abdomen and gluteal regions. As described in this study, adipocytes from multiple depots can be characterised from healthy individuals and compared to adipocytes from obese or diabetic individuals. The 'normal adipocyte phenotype' is based off data collected in this study. The 'abnormal adipocyte phenotype' is a hypothetical mock up based off reported changes in adipose tissue function in obesity.

## 9.7 Future endeavours

In this study, a method was developed to analyse adipocytes at the single cell level. The method was utilised to assess sexual dimorphism in adipocytes as well changes to adipocyte biology during pregnancy (Appendix III) (Boumelhem et al., 2017). Furthermore, the method refuted the findings reported by Wu *et al.* (2012) in which beige adipocyte markers CD137 (4-1BB) and CD40 were not expressed on inguinal adipocytes. Subsequently, a code to identify adipocyte heterogeneity in healthy, wild-type adult mice was revealed. The next step would be to determine how the code changes in brown, subcutaneous and visceral white adipocytes from obese and diabetic mice. To model obesity in mice, a high-fat diet can be used to induce obesity (and lipotoxicity) or genetically with *Ob/Ob* nullizygous mice. Ultimately, the method can be applied to adipocytes extracted from adipose depots in humans. A code developed for human adipocytes may be useful as a diagnostic tool.

### 9.7.1 Do adipocytes support the development of other endoderm-derived cell types?

In this study, the adipocytes differentiated in conjunction to mouse ES cell-derived prostate epithelial cells closely resembled gonadal adipocytes. While prostate epithelial cell differentiation may be supported by adipocytes, what then of other endoderm derived cell types such as hepatocytes, pancreatic  $\beta$ -cells or enterocytes? Those endoderm cell types are all implicated in obesity-induced metabolic disorder in the case of lipotoxicity. There are however no reports on the role of adipocytes for normal organogenesis of endoderm derivatives. The culture conditions implemented

in this study can be modified to promote hepatocyte, pancreatic  $\beta$ -cell, enterocyte or other endoderm derivatives as previously reported (Mallanna & Duncan, 2013; Hannan et al., 2013; Goldman et al., 2014; D'Amour et al., 2005; Ozawa et al., 2015). Differentiating ES cell cultures can be assessed for the generation of adipocytes and characterised by the code developed in this study. The proposed undertaking could shed light on an unreported role for adipocytes during embryogenesis.

### **9.8 Concluding remarks**

For the first time, a method to differentiate prostate epithelial cells from mouse ES cells in a stepwise manner is reported. Successful differentiation of prostate epithelial cells also resulted in the generation of adipocytes, a cell type conventionally associated with the mesoderm germ layer. A method was developed to characterise brown and white adipocytes at the single cell level and applied to the adipocytes differentiated in endoderm culture conditions. Profiling of the mouse ES cell-derived adipocytes revealed striking similarities to gonadal adipocytes. The study presented here challenges the origins of gonadal adipocytes and poses a supportive role of adipocytes in the development of the prostate.

## Chapter 10. References

- Abate-Shen, C., Banach-Petrosky, W. A., Sun, X., Economides, K. D., Desai, N., Gregg, J. P., et al. (2003). Nkx3.1; Pten mutant mice develop invasive prostate adenocarcinoma and lymph node metastases. *Cancer Research*, 63(14), 3886–3890.
- Abate-Shen, C., Shen, M. M., & Gelmann, E. (2008). Integrating differentiation and cancer: the Nkx3.1 homeobox gene in prostate organogenesis and carcinogenesis. *Differentiation; Research in Biological Diversity*, 76(6), 717–727.  
<http://doi.org/10.1111/j.1432-0436.2008.00292.x>
- Abdulkadir, S. A., Magee, J. A., Peters, T. J., Kaleem, Z., Naughton, C. K., Humphrey, P. A., & Milbrandt, J. (2002). Conditional loss of nkx3.1 in adult mice induces prostatic intraepithelial neoplasia. *Molecular and Cellular Biology*, 22(5), 1495–1503. <http://doi.org/10.1128/MCB.22.5.1495-1503.2002>
- Adachi, Y., Hino, T., Ohsawa, M., Ueki, K., Murao, T., Li, M., et al. (2015). A case of CD10-negative angioimmunoblastic T cell lymphoma with leukemic change and increased plasma cells mimicking plasma cell leukemia: A case report. *Oncology Letters*. <http://doi.org/10.3892/ol.2015.3490>
- Agius, E., Oelgeschläger, M., Wessely, O., Kemp, C., & De Robertis, E. M. (2000). Endodermal Nodal-related signals and mesoderm induction in *Xenopus*. *Development*, 127(6), 1173–1183.
- Al-Drees, M. A., Yeo, J. H., Boumelhem, B. B., Antas, V. I., Brigden, K. W. L., Colonne, C. K., & Fraser, S. T. (2015). Making blood: The haematopoietic niche throughout ontogeny. *Stem Cells International*, 2015(10), 1–14.  
<http://doi.org/10.1038/nmeth.2938>
- Aldridge, A., Kouroupis, D., Churchman, S., English, A., Ingham, E., & Jones, E. (2013). Assay validation for the assessment of adipogenesis of multipotential stromal cells. *Journal of Cytotherapy*, 15(1), 89–101.  
<http://doi.org/10.1016/j.jcyt.2012.07.001>
- Alfaro, C., Echeveste, J. I., Rodriguez-Ruiz, M. E., Solorzano, J. L., Perez-Gracia, J. L., Idoate, M. A., et al. (2015). Functional expression of CD137 (4-1BB) on T helper follicular cells. *OncoImmunology*, 4(12), e1054597.  
<http://doi.org/10.1080/2162402X.2015.1054597>
- Anderson, C. M., Kazantzis, M., Wang, J., Venkatraman, S., Goncalves, R. L. S., Quinlan, C. L., et al. (2015). Dependence of brown adipose tissue function on cd36-mediated coenzyme q uptake. *Cell Reports*, 10(4), 505–515.  
<http://doi.org/10.1016/j.celrep.2014.12.048>
- Aniansson Zdolsek, H., Ernerudh, J., Holt, P. G., Nilsson, J., & Björkstén, B. (1999). Expression of the T-cell markers CD3, CD4 and CD8 in healthy and atopic children during the first 18 months of life. *International Archives of Allergy and Immunology*, 119(1), 6–12.
- Assinder, S. J., & Bhoopalan, V. (2017). A promising future for prostate cancer Diagnostics. *Diagnostics (Basel, Switzerland)*, 7(1), 6.

- <http://doi.org/10.3390/diagnostics7010006>
- Aumüller, G., & Seitz, J. (1990). Protein secretion and secretory processes in male accessory sex glands. *International Review of Cytology*, 121, 127–231.
- B Boumelhem, B., J Assinder, S., Hammans, C., P Tanudisastro, M., T M Le, D., Brigden, K., & T Fraser, S. (Eds.). (2017). The mesendoderm: A wellspring of cell lineages for regenerative medicine. In *Frontiers in Stem Cell and Regenerative Medicine Research* (pp. 36–100). Bentham Science Publishers.  
<http://doi.org/10.2174/9781681084350117040004>
- Bacher, P., & Scheffold, A. (2013). Flow-cytometric analysis of rare antigen-specific T cells. *Cytometry. Part a : the Journal of the International Society for Analytical Cytology*, 83(8), 692–701. <http://doi.org/10.1002/cyto.a.22317>
- Balaban, S., Shearer, R. F., Lee, L. S., van Geldermalsen, M., Schreuder, M., Shtein, H. C., et al. (2017). Adipocyte lipolysis links obesity to breast cancer growth: adipocyte-derived fatty acids drive breast cancer cell proliferation and migration. *Cancer & Metabolism*, 5(1), 1. <http://doi.org/10.1186/s40170-016-0163-7>
- Barczyk, M., Carracedo, S., & Gullberg, D. (2010). Integrins. *Cell and Tissue Research*, 339(1), 269–280. <http://doi.org/10.1007/s00441-009-0834-6>
- Barron, D. A., & Rowley, D. R. (2012). The reactive stroma microenvironment and prostate cancer progression. *Endocrine Related Cancer*, 19(6), R187–R204. <http://doi.org/10.1530/ERC-12-0085>
- Beddington, R. S., Rashbass, P., & Wilson, V. (1992). Brachyury--a gene affecting mouse gastrulation and early organogenesis. *Development (Cambridge, England). Supplement*, 157–165.
- Berg, J. M., Tymoczko, J. L., & Stryer, L. (2002). Biochemistry, Fifth Edition. W. H. Freeman.
- Bell, C.D., & Conen, P.E. (1968). Histopathological changes in Duchenne Muscular Dystrophy. *Journal of the Neurological Sciences*, 7(3), 529–544. [http://doi.org/10.1016/0022-510X\(68\)90058-0](http://doi.org/10.1016/0022-510X(68)90058-0)
- Berry, D. C., Stenesen, D., Zeve, D., & Graff, J. M. (2013). The developmental origins of adipose tissue. *Development*, 140(19), 3939–3949. <http://doi.org/10.1242/dev.080549>
- Bhatia-Gaur, R., Donjacour, A. A., Sciavolino, P. J., Kim, M., Desai, N., Young, P., et al. (1999). Roles for Nkx3.1 in prostate development and cancer. *Genes & Development*, 13(8), 966–977.
- Billon, N., Iannarelli, P., Monteiro, M. C., Glavieux-Pardanaud, C., Richardson, W. D., Kessaris, N., et al. (2007). The generation of adipocytes by the neural crest. *Development*, 134(12), 2283–2292. <http://doi.org/10.1242/dev.002642>
- Birsoy, K., Berry, R., Wang, T., Ceyhan, O., Tavazoie, S., Friedman, J. M., & Rodeheffer, M. S. (2011). Analysis of gene networks in white adipose tissue development reveals a role for ETS2 in adipogenesis. *Development*, 138(21), 4709–4719. <http://doi.org/10.1242/dev.067710>
- Björntorp, P., & Östman, J. (1971). Human adipose tissue dynamics and regulation (Vol. 5, pp. 277–327). Elsevier. <http://doi.org/10.1016/B978-0-12-027305-8.50027-8>

- Bjørndal, B., Burri, L., Staalesen, V., Skorve, J., & Berge, R. K. (2011). Different adipose depots: Their role in the development of metabolic syndrome and mitochondrial response to hypolipidemic agents. *Journal of Obesity*, 2011(1), 1–15. <http://doi.org/10.1016/j.bbalip.2005.02.011>
- Blanco, M. J., Barrallo-Gimeno, A., Acloque, H., Reyes, A. E., Tada, M., Allende, M. L., et al. (2007). Snail1a and Snail1b cooperate in the anterior migration of the axial mesendoderm in the zebrafish embryo. *Development*, 134(22), 4073–4081. <http://doi.org/10.1242/dev.006858>
- Bonen, A., Tandon, N. N., Glatz, J. F. C., Luiken, J. J. F. P., & Heigenhauser, G. J. F. (2006). The fatty acid transporter FAT/CD36 is upregulated in subcutaneous and visceral adipose tissues in human obesity and type 2 diabetes. *International Journal of Obesity* (2005), 30(6), 877–883. <http://doi.org/10.1038/sj.ijo.0803212>
- Bonnans, C., Chou, J., & Werb, Z. (2014). Remodelling the extracellular matrix in development and disease. *Nature Reviews Molecular Cell Biology*, 15(12), 786–801. <http://doi.org/10.1038/nrm3904>
- Boudina, S., & Graham, T. E. (2014). Mitochondrial function/dysfunction in white adipose tissue. *Experimental Physiology*, 99(9), 1168–1178. <http://doi.org/10.1113/expphysiol.2014.081414>
- Boumelhem, B. B., Assinder, S. J., Bell-Anderson, K. S., & Fraser, S. T. (2017). Flow cytometric single cell analysis reveals heterogeneity between adipose depots. *Adipocyte*, 6(2), 112–123. <http://doi.org/10.1080/21623945.2017.1319536>
- Bournat, J. C., & Brown, C. W. (2010). Mitochondrial dysfunction in obesity. *Current Opinion in Endocrinology, Diabetes and Obesity*, 17(5), 446–452. <http://doi.org/10.1097/MED.0b013e32833c3026>
- Brake, D. K., & Smith, C. W. (2008). Flow cytometry on the stromal-vascular fraction of white adipose tissue. *Methods in Molecular Biology (Clifton, N.J.)*, 456, 221–229. [http://doi.org/10.1007/978-1-59745-245-8\\_16](http://doi.org/10.1007/978-1-59745-245-8_16)
- Bryant, S. L., Francis, J. C., Lokody, I. B., Wang, H., Risbridger, G. P., Loveland, K. L., & Swain, A. (2014). Sex specific retinoic acid signaling is required for the initiation of urogenital sinus bud development. *Developmental Biology*, 395(2), 209–217. <http://doi.org/10.1016/j.ydbio.2014.09.016>
- Buckingham, M., Bajard, L., Chang, T., Daubas, P., Hadchouel, J., Meilhac, S., et al. (2003). The formation of skeletal muscle: from somite to limb. *Journal of Anatomy*, 202(1), 59–68. <http://doi.org/10.1046/j.1469-7580.2003.00139.x>
- Burgeiro, A., Fuhrmann, A., Cherian, S., Espinoza, D., Jarak, I., Carvalho, R. A., et al. (2016). Glucose uptake and lipid metabolism are impaired in epicardial adipose tissue from heart failure patients with or without diabetes. *AJP: Endocrinology and Metabolism*, 310(7), E550–E564. <http://doi.org/10.1152/ajpendo.00384.2015>
- Cai, L., Wang, Z., Ji, A., Meyer, J. M., & van der Westhuyzen, D. R. (2012). Scavenger receptor CD36 expression contributes to adipose tissue inflammation and cell death in diet-induced obesity. *PLoS ONE*, 7(5), e36785. <http://doi.org/10.1371/journal.pone.0036785>
- Cain, A. J. (1947). The use of Nile blue in the examination of lipoids. *Journal of Cell*



- Science*, 33-88(3), 383–392.
- Cairns, P., Okami, K., Halachmi, S., Halachmi, N., Esteller, M., Herman, J. G., et al. (1997). Frequent inactivation of PTEN/MMAC1 in primary prostate cancer. *Cancer Research*, 57(22), 4997–5000.
- Calderon-Gierszal, E. L., & Prins, G. S. (2015). Directed differentiation of human embryonic stem cells into prostate organoids in vitro and its perturbation by low-dose bisphenol A exposure. *PLoS ONE*, 10(7), e0133238. <http://doi.org/10.1371/journal.pone.0133238>
- Cannon, B., & Nedergaard, J. (2004). Brown adipose tissue: function and physiological significance. *Physiological Reviews*, 84(1), 277–359. <http://doi.org/10.1152/physrev.00015.2003>
- Cao, M., Liu, B., Cunha, G., & Baskin, L. (2008). Urothelium patterns bladder smooth muscle location. *Pediatric Research*, 64(4), 352–357. <http://doi.org/10.1203/PDR.0b013e318180e4c9>
- Cawthorn, W. P., Scheller, E. L., & MacDougald, O. A. (2012). Adipose tissue stem cells meet preadipocyte commitment: going back to the future. *The Journal of Lipid Research*, 53(2), 227–246. <http://doi.org/10.1194/jlr.R021089>
- Cedikova, M., K., Dvorakova, J., Pitule, P., Grundmanova, M., Babuska, V., et al. (2016). Mitochondria in white, brown, and beige adipocytes. *Stem Cells International*, 2016(4, part 1), 1–11. <http://doi.org/10.1155/2016/6067349>
- Chabowska-Kita, A., & Kozak, L. P. (2016). The critical period for brown adipocyte development: Genetic and environmental influences. *Obesity*, 24(2), 283–290. <http://doi.org/10.1002/oby.21376>
- Chau, Y.-Y., & Hastie, N. (2014). Wt1, the mesothelium and the origins and heterogeneity of visceral fat progenitors. *Adipocyte*, 4(3), 217–221. <http://doi.org/10.4161/21623945.2014.985009>
- Chau, Y.-Y., Bandiera, R., Serrels, A., Martínez-Estrada, O. M., Qing, W., Lee, M., et al. (2014). Visceral and subcutaneous fat have different origins and evidence supports a mesothelial source. *Nature Cell Biology*, 16(4), 367–375. <http://doi.org/10.1038/ncb2922>
- Cherian, S., Lopaschuk, G. D., & Carvalho, E. (2012). Cellular cross-talk between epicardial adipose tissue and myocardium in relation to the pathogenesis of cardiovascular disease. *AJP: Endocrinology and Metabolism*, 303(8), E937–E949. <http://doi.org/10.1152/ajpendo.00061.2012>
- Chkourko Gusky, H., Diedrich, J., MacDougald, O. A., & Podgorski, I. (2016). Omentum and bone marrow: how adipocyte-rich organs create tumour microenvironments conducive for metastatic progression. *Obesity Reviews*, 17(11), 1015–1029. <http://doi.org/10.1111/obr.12450>
- Cho, K. W., Morris, D. L., & Lumeng, C. N. (2014). Flow cytometry analyses of adipose tissue macrophages. In *Methods of Adipose Tissue Biology, Part A* (Vol. 537, pp. 297–314). Elsevier. <http://doi.org/10.1016/B978-0-12-411619-1.00016-1>
- Christiaens, V., Van Hul, M., Lijnen, H. R., & Scroyen, I. (2012). CD36 promotes adipocyte differentiation and adipogenesis. *Biochimica Et Biophysica Acta (BBA)* -

- General Subjects*, 1820(7), 949–956. <http://doi.org/10.1016/j.bbagen.2012.04.001>
- Christodoulou, C., Longmire, T. A., Shen, S. S., Bourdon, A., Sommer, C. A., Gadue, P., et al. (2011). Mouse ES and iPS cells can form similar definitive endoderm despite differences in imprinted genes. *Journal of Clinical Investigation*, 121(6), 2313–2325. <http://doi.org/10.1172/JCI43853>
- Cinti, S. (2012). The adipose organ at a glance. *Disease Models & Mechanisms*, 5(5), 588–594. <http://doi.org/10.1242/dmm.009662>
- Clapper, J. R., Hendricks, M. D., Gu, G., Wittmer, C., Dolman, C. S., Herich, J., et al. (2013). Diet-induced mouse model of fatty liver disease and nonalcoholic steatohepatitis reflecting clinical disease progression and methods of assessment. *American Journal of Physiology - Gastrointestinal and Liver Physiology*, 305(7), G483–G495. <http://doi.org/10.1152/ajpgi.00079.2013>
- Coelho, M., Oliveira, T., & Fernandes, R. (2013). State of the art paper Biochemistry of adipose tissue: an endocrine organ. *Archives of Medical Science*, 2(2), 191–200. <http://doi.org/10.5114/aoms.2013.33181>
- Conlon, F. L., Lyons, K. M., Takaesu, N., Barth, K. S., Kispert, A., Herrmann, B., & Robertson, E. J. (1994). A primary requirement for nodal in the formation and maintenance of the primitive streak in the mouse. *Development*, 120(7), 1919–1928.
- Cooper, A. D. (1997). Hepatic uptake of chylomicron remnants. *The Journal of Lipid Research*, 38(11), 2173–2192.
- Costello, A. J., & Corcoran, N. M. (2012). Development, applied, and surgical anatomy of the prostate. In *Prostate Cancer: A Comprehensive Perspective* (pp. 3–17). London: Springer London. [http://doi.org/10.1007/978-1-4471-2864-9\\_1](http://doi.org/10.1007/978-1-4471-2864-9_1)
- Costello, I., Nowotschin, S., Sun, X., Mould, A. W., Hadjantonakis, A.-K., Bikoff, E. K., & Robertson, E. J. (2015). Lhx1 functions together with Otx2, Foxa2, and Ldb1 to govern anterior mesendoderm, node, and midline development. *Genes & Development*, 29(20), 2108–2122. <http://doi.org/10.1101/gad.268979.115>
- Costello, I., Pimeisl, I.-M., Dräger, S., Bikoff, E. K., Robertson, E. J., & Arnold, S. J. (2011). The T-box transcription factor Eomesodermin acts upstream of Mesp1 to specify cardiac mesoderm during mouse gastrulation. *Nature Cell Biology*, 13(9), 1084–1091. <http://doi.org/10.1038/ncb2304>
- Cottet-Rousselle, C., Ronot, X., Leverve, X., & Mayol, J.-F. (2011). Cytometric assessment of mitochondria using fluorescent probes. *Cytometry Part A*, 79A(6), 405–425. <http://doi.org/10.1002/cyto.a.21061>
- Craft, C. S. (2014). MAGP1, the extracellular matrix, and metabolism. *Adipocyte*, 4(1), 60–64. <http://doi.org/10.4161/adip.32209>
- Cramer, J. M., Thompson, T., Geskin, A., LaFramboise, W., & Lagasse, E. (2015). Distinct human stem cell populations in small and large intestine. *PLoS ONE*, 10(3), e0118792. <http://doi.org/10.1371/journal.pone.0118792>
- Crane, F. L. (2001). Biochemical functions of coenzyme Q 10. *Journal of the American College of Nutrition*, 20(6), 591–598. <http://doi.org/10.1080/07315724.2001.10719063>
- Crocoll, A., Zhu, C. C., Cato, A. C., & Blum, M. (1998). Expression of androgen receptor mRNA during mouse embryogenesis. *Mechanisms of Development*, 72(1–

- 2), 175–178.
- Crossno, J. T., Majka, S. M., Grazia, T., Gill, R. G., & Klemm, D. J. (2006). Rosiglitazone promotes development of a novel adipocyte population from bone marrow–derived circulating progenitor cells. *Journal of Clinical Investigation*, 116(12), 3220–3228. <http://doi.org/10.1172/JCI28510>
- Cuaranta-Monroy, I., Simandi, Z., & Nagy, L. (2015). Differentiation of adipocytes in monolayer from mouse embryonic stem cells. In *Embryonic Stem Cell Protocols* (Vol. 1341, pp. 407–415). New York, NY: Springer New York. [http://doi.org/10.1007/7651\\_2015\\_219](http://doi.org/10.1007/7651_2015_219)
- Cuaranta-Monroy, I., Simandi, Z., Kolostyak, Z., Doan-Xuan, Q. M., Poliska, S., Horvath, A., et al. (2014). Highly efficient differentiation of embryonic stem cells into adipocytes by ascorbic acid. *Stem Cell Research*, 13(1), 88–97. <http://doi.org/10.1016/j.scr.2014.04.015>
- Cunha, G. R., Cooke, P. S., & Kurita, T. (2004a). Role of stromal-epithelial interactions in hormonal responses. *Archives of Histology and Cytology*, 67(5), 417–434. <http://doi.org/10.1679/aohc.67.417>
- Cunha, G. R., Donjacour, A. A., Cooke, P. S., Mee, S., Bigsby, R. M., Higgins, S. J., & Sugimura, Y. (1987). The endocrinology and developmental biology of the prostate. *Endocrine Reviews*, 8(3), 338–362. <http://doi.org/10.1210/edrv-8-3-338>
- Cunha, G. R., Riche, W., Thomson, A., Marker, P. C., Risbridger, G., Hayward, S. W., et al. (2004b). Hormonal, cellular, and molecular regulation of normal and neoplastic prostatic development. *The Journal of Steroid Biochemistry and Molecular Biology*, 92(4), 221–236. <http://doi.org/10.1016/j.jsbmb.2004.10.017>
- Cunha-Rodrigues, M., Portugal, S., Febbraio, M., & Mota, M. M. (2007). Bone marrow chimeric mice reveal a dual role for CD36 in Plasmodium berghei ANKA infection. *Malaria Journal*, 6(1), 32. <http://doi.org/10.1186/1475-2875-6-32>
- D'Amour, K. A., Agulnick, A. D., Eliazar, S., Kelly, O. G., Kroon, E., & Baetge, E. E. (2005). Efficient differentiation of human embryonic stem cells to definitive endoderm. *Nature Biotechnology*, 23(12), 1534–1541. <http://doi.org/10.1038/nbt1163>
- Dani, C., Smith, A. G., Dessolin, S., Leroy, P., Staccini, L., Villageois, P., et al. (1997). Differentiation of embryonic stem cells into adipocytes in vitro. *Journal of Cell Science*, 110 ( Pt 11), 1279–1285.
- Davey, R. E., & Zandstra, P. W. (2006). Spatial organization of embryonic stem cell responsiveness to autocrine gp130 ligands reveals an autoregulatory stem cell niche. *Stem Cells*, 24(11), 2538–2548. <http://doi.org/10.1634/stemcells.2006-0216>
- de Caestecker, M. (2004). The transforming growth factor-beta superfamily of receptors. *Cytokine & Growth Factor Reviews*, 15(1), 1–11.
- De Pauw, A., Tejerina, S., Raes, M., Keijer, J., & Arnould, T. (2009). Mitochondrial (dys)function in adipocyte (de)differentiation and systemic metabolic alterations. *The American Journal of Pathology*, 175(3), 927–939. <http://doi.org/10.2353/ajpath.2009.081155>
- De Pergola, G., & Silvestris, F. (2013). Obesity as a major risk factor for cancer. *Journal of Obesity*, 2013(8), 291546–11. <http://doi.org/10.1155/2013/291546>

- De Val, S., & Black, B. L. (2009). Transcriptional control of endothelial cell development. *Developmental Cell*, 16(2), 180–195. <http://doi.org/10.1016/j.devcel.2009.01.014>
- Di Cristofano, A., Pesce, B., Cordon-Cardo, C., & Pandolfi, P. P. (1998). Pten is essential for embryonic development and tumour suppression. *Nature Genetics*, 19(4), 348–355. <http://doi.org/10.1038/1235>
- Dieudonne, M. N., Pecquery, R., Boumediene, A., Leneuve, M. C., & Giudicelli, Y. (1998). Androgen receptors in human preadipocytes and adipocytes: regional specificities and regulation by sex steroids. *The American Journal of Physiology*, 274(6 Pt 1), C1645–52.
- Doan-Xuan, Q. M., Sarvari, A. K., Fischer-Posovszky, P., Wabitsch, M., Balajthy, Z., Fesus, L., & Bacso, Z. (2013). High content analysis of differentiation and cell death in human adipocytes. *Cytometry. Part a : the Journal of the International Society for Analytical Cytology*, 83(10), 933–943. <http://doi.org/10.1002/cyto.a.22333>
- Donohoe, C. L., Doyle, S. L., & Reynolds, J. V. (2011). Visceral adiposity, insulin resistance and cancer risk. *Diabetology & Metabolic Syndrome*, 3(1), 12. <http://doi.org/10.1186/1758-5996-3-12>
- Duncan, J. G. (2008). Lipotoxicity: what is the fate of fatty acids? *The Journal of Lipid Research*, 49(7), 1375–1376. <http://doi.org/10.1194/jlr.E800010-JLR200>
- Durandt, C., van Vollenstee, F. A., Dessels, C., Kallmeyer, K., de Villiers, D., Murdoch, C., et al. (2016). Novel flow cytometric approach for the detection of adipocyte sub-populations during adipogenesis. *The Journal of Lipid Research*. <http://doi.org/10.1194/jlr.D065664>
- Dutta, A., Le Magnen, C., Mitrofanova, A., Ouyang, X., Califano, A., & Abate-Shen, C. (2016). Identification of an NKX3.1-G9a-UTY transcriptional regulatory network that controls prostate differentiation. *Science*, 352(6293), 1576–1580. <http://doi.org/10.1126/science.aad9512>
- Engberg, N., Kahn, M., Petersen, D. R., Hansson, M., & Serup, P. (2010). Retinoic acid synthesis promotes development of neural progenitors from mouse embryonic stem cells by suppressing endogenous, wnt-dependent nodal signaling. *Stem Cells*, 28(9), 1498–1509. <http://doi.org/10.1002/stem.479>
- Engin, A. B. (2017). What Is Lipotoxicity? In *Obesity and Lipotoxicity* (Vol. 960, pp. 197–220). Cham: Springer, Cham. [http://doi.org/10.1007/978-3-319-48382-5\\_8](http://doi.org/10.1007/978-3-319-48382-5_8)
- Enjoji, M., Kohjima, M., & Nakamuta, M. (2016). Lipid Metabolism and the Liver. In *The Liver in Systemic Diseases* (Vol. 22, pp. 105–122). Tokyo: Springer Japan. [http://doi.org/10.1007/978-4-431-55790-6\\_6](http://doi.org/10.1007/978-4-431-55790-6_6)
- Evans, M. J., & Kaufman, M. H. (1981). Establishment in culture of pluripotential cells from mouse embryos. *Nature*, 292(5819), 154–6. <http://doi.org/10.1038/292154a0>
- Fabbrini, E., & Magkos, F. (2015). Hepatic steatosis as a marker of metabolic dysfunction. *Nutrients*, 7(6), 4995–5019. <http://doi.org/10.3390/nu7064995>
- Farnier, C., Krief, S., Blache, M., Diot-Dupuy, F., Mory, G., Ferre, P., & Bazin, R. (2003). Adipocyte functions are modulated by cell size change: potential

- involvement of an integrin/ERK signalling pathway. *International Journal of Obesity*, 27(10), 1178–1186. <http://doi.org/10.1038/sj.ijo.0802399>
- Febbraio, M., Hajjar, D. P., & Silverstein, R. L. (2001). CD36: a class B scavenger receptor involved in angiogenesis, atherosclerosis, inflammation, and lipid metabolism. *Journal of Clinical Investigation*, 108(6), 785–791. <http://doi.org/10.1172/JCI14006>
- Fengler, V. H. I., Haybäck, J., Lackner, C., & Sargsyan, K. (2015). P0962 : Manifestation of diet-associated NAFLD/AFLD in different mouse strains. *Journal of Hepatology*, 62, S706–S707. [http://doi.org/10.1016/S0168-8278\(15\)31163-6](http://doi.org/10.1016/S0168-8278(15)31163-6)
- Festy, F., Hoareau, L., Bes-Houtmann, S., Péquin, A.-M., Gonthier, M.-P., Munstun, A., et al. (2005). Surface protein expression between human adipose tissue-derived stromal cells and mature adipocytes. *Histochemistry and Cell Biology*, 124(2), 113–121. <http://doi.org/10.1007/s00418-005-0014-z>
- Fiumara, P., & Younes, A. (2001). CD40 ligand (CD154) and tumour necrosis factor-related apoptosis inducing ligand (Apo-2L) in haematological malignancies. *British Journal of Haematology*, 113(2), 265–274. <http://doi.org/10.1046/j.1365-2141.2001.02593.x>
- Fletcher, S. J., Sacca, P. A., Pistone-Creydt, M., Coló, F. A., Serra, M. F., Santino, F. E., et al. (2017). Human breast adipose tissue: characterization of factors that change during tumor progression in human breast cancer. *Journal of Experimental & Clinical Cancer Research : CR*, 36(1), 26. <http://doi.org/10.1186/s13046-017-0494-4>
- Forner, F., Kumar, C., Lubber, C. A., Fromme, T., Klingenspor, M., & Mann, M. (2009). Proteome differences between brown and white fat mitochondria reveal specialized metabolic functions. *Cell Metabolism*, 10(4), 324–335. <http://doi.org/10.1016/j.cmet.2009.08.014>
- Fowler, S. D., & Greenspan, P. (1985). Application of Nile red, a fluorescent hydrophobic probe, for the detection of neutral lipid deposits in tissue sections: comparison with oil red O. *The Journal of Histochemistry and Cytochemistry : Official Journal of the Histochemistry Society*, 33(8), 833–836. <http://doi.org/10.1177/33.8.4020099>
- Frayn, K. N., Arner, P., & Yki-Järvinen, H. (2006). Fatty acid metabolism in adipose tissue, muscle and liver in health and disease. *Essays in Biochemistry*, 42, 89–103. <http://doi.org/10.1042/bse0420089>
- Freedland, S. J., Humphreys, E. B., Mangold, L. A., Eisenberger, M., Dorey, F. J., Walsh, P. C., & Partin, A. W. (2005). Risk of prostate cancer-specific mortality following biochemical recurrence after radical prostatectomy. *Jama*, 294(4), 433–439. <http://doi.org/10.1001/jama.294.4.433>
- Friedman, J. E. (2015). Obesity and gestational diabetes mellitus pathways for programming in mouse, monkey, and man—where do we go next? The 2014 norbert freinkel award lecture. *Diabetes Care*, 38(8), 1402–1411. <http://doi.org/10.2337/dc15-0628>
- Fujimoto, N., Akimoto, Y., Suzuki, T., Kitamura, S., & Ohta, S. (2006). Identification of prostatic-secreted proteins in mice by mass spectrometric analysis and

- evaluation of lobe-specific and androgen-dependent mRNA expression. *The Journal of Endocrinology*, 190(3), 793–803. <http://doi.org/10.1677/joe.1.06733>
- Gaborit, B., Sengenès, C., Ancel, P., Jacquier, A., & Dutour, A. (2011). Role of epicardial adipose tissue in health and disease: A matter of fat? (Vol. 67, pp. 1051–1082). Hoboken, NJ, USA: John Wiley & Sons, Inc. <http://doi.org/10.1002/cphy.c160034>
- Gadue, P., Gouon-Evans, V., Cheng, X., Wandzioch, E., Zaret, K. S., Grompe, M., et al. (2009). Generation of monoclonal antibodies specific for cell surface molecules expressed on early mouse endoderm. *Stem Cells*, 27(9), 2103–2113. <http://doi.org/10.1002/stem.147>
- Gadue, P., Huber, T. L., Paddison, P. J., & Keller, G. M. (2006). Wnt and TGF-beta signaling are required for the induction of an in vitro model of primitive streak formation using embryonic stem cells. *Pnas*, 103(45), 16806–16811. <http://doi.org/10.1073/pnas.0603916103>
- Garcia, R. A., Roemmich, J. N., & Claycombe, K. J. (2016). Evaluation of markers of beige adipocytes in white adipose tissue of the mouse. *Nutrition & Metabolism*, 13(1), 24. <http://doi.org/10.1186/s12986-016-0081-2>
- Gesta, S., Tseng, Y.-H., & Kahn, C. R. (2007). Developmental origin of fat: tracking obesity to its source. *Cell*, 131(2), 242–256. <http://doi.org/10.1016/j.cell.2007.10.004>
- Ghaedi, M., Niklason, L. E., & Williams, J. (2015). Development of lung epithelium from induced pluripotent stem cells. *Current Transplantation Reports*, 2(1), 81–89. <http://doi.org/10.1007/s40472-014-0039-0>
- Gingrich, J. R., Barrios, R. J., Morton, R. A., Boyce, B. F., DeMayo, F. J., Finegold, M. J., et al. (1996). Metastatic prostate cancer in a transgenic mouse. *Cancer Research*, 56(18), 4096–4102.
- Gocze, P. M., & Freeman, D. A. (1994). Factors underlying the variability of lipid droplet fluorescence in MA-10 Leydig tumor cells. *Cytometry Part A*, 17(2), 151–158. <http://doi.org/10.1002/cyto.990170207>
- Goldberg, I. J., Eckel, R. H., & Abumrad, N. A. (2008). Regulation of fatty acid uptake into tissues: lipoprotein lipase- and CD36-mediated pathways. *The Journal of Lipid Research*, 50(Supplement), S86–S90. <http://doi.org/10.1194/jlr.R800085-JLR200>
- Goldman, O., Han, S., Hamou, W., de Villeroche, V. J., Uzan, G., Lickert, H., & Gouon-Evans, V. (2014). Endoderm generates endothelial cells during liver development. *Stem Cell Reports*, 3(4), 556–565. <http://doi.org/10.1016/j.stemcr.2014.08.009>
- Gonçalves, R., & Mosser, D. M. (2001). The isolation and characterization of murine macrophages (Vol. 168, pp. 14.1.1–14.1.16). Hoboken, NJ, USA: John Wiley & Sons, Inc. <http://doi.org/10.1002/0471142735.im1401s111>
- Goudriaan, J. R., Boer, den, M. A. M., Rensen, P. C. N., Febbraio, M., Kuipers, F., Romijn, J. A., et al. (2005). CD36 deficiency in mice impairs lipoprotein lipase-mediated triglyceride clearance. *The Journal of Lipid Research*, 46(10), 2175–2181. <http://doi.org/10.1194/jlr.M500112-JLR200>

- Grabowska, M. M., DeGraff, D. J., Yu, X., Jin, R. J., Chen, Z., Borowsky, A. D., & Matusik, R. J. (2014). Mouse models of prostate cancer: picking the best model for the question. *Cancer and Metastasis Reviews*, 33(2-3), 377–397. <http://doi.org/10.1007/s10555-013-9487-8>
- Grandl, M., & Schmitz, G. (2010). Fluorescent high-content imaging allows the discrimination and quantitation of E-LDL-induced lipid droplets and Ox-LDL-generated phospholipidosis in human macrophages. *Cytometry. Part a : the Journal of the International Society for Analytical Cytology*, 77(3), 231–242. <http://doi.org/10.1002/cyto.a.20828>
- Grapin-Botton, A. (2008). Endoderm specification. *StemBook*. <http://doi.org/10.3824/stembook.1.30.1>
- Greenberg, N. M., DeMayo, F. J., Sheppard, P. C., Barrios, R., Lebovitz, R., Finegold, M., et al. (1994). The rat probasin gene promoter directs hormonally and developmentally regulated expression of a heterologous gene specifically to the prostate in transgenic mice. *Molecular Endocrinology (Baltimore, Md.)*, 8(2), 230–239. <http://doi.org/10.1210/mend.8.2.8170479>
- Greenspan, P., Mayer, E. P., & Fowler, S. D. (1985). Nile red: a selective fluorescent stain for intracellular lipid droplets. *The Journal of Cell Biology*, 100(3), 965–973.
- Grubb, B. J. (2006). Developmental Biology, Eighth Edition. Scott F. Gilbert, editor. *Integrative and Comparative Biology*, 46(5), 652–653. <http://doi.org/10.1093/icb/icl011>
- Guo, C., Zhang, B., & Garraway, I. P. (2012). Methods in Molecular Biology. (S. R. Singh, Ed.) (Vol. 879, pp. 315–326). Totowa, NJ: Humana Press. [http://doi.org/10.1007/978-1-61779-815-3\\_18](http://doi.org/10.1007/978-1-61779-815-3_18)
- Gupta, A., Bischoff, A., Peña, A., Runck, L. A., & Guasch, G. (2014). The great divide: septation and malformation of the cloaca, and its implications for surgeons. *Pediatric Surgery International*, 30(11), 1089–1095. <http://doi.org/10.1007/s00383-014-3593-8>
- Haas, G. P., Delongchamps, N., Brawley, O. W., Wang, C. Y., & la Roza, de, G. (2008). The worldwide epidemiology of prostate cancer: perspectives from autopsy studies. *The Canadian Journal of Urology*, 15(1), 3866–3871.
- Hannan, N. R. F., Segeritz, C.-P., Touboul, T., & Vallier, L. (2013). Production of hepatocyte-like cells from human pluripotent stem cells. *Nature Protocols*, 8(2), 430–437.
- Harms, M., & Seale, P. (2013). Brown and beige fat: development, function and therapeutic potential. *Nature Publishing Group*, 19(10), 1252–1263. <http://doi.org/10.1038/nm.3361>
- Harrell, M. I., Iritani, B. M., & Ruddell, A. (2008). Lymph node mapping in the mouse. *Journal of Immunological Methods*, 332(1-2), 170–174. <http://doi.org/10.1016/j.jim.2007.11.012>
- Hart, A. H., Hartley, L., Sourris, K., Stadler, E. S., Li, R., Stanley, E. G., et al. (2002). Mixl1 is required for axial mesendoderm morphogenesis and patterning in the murine embryo. *Development*, 129(15), 3597–3608.

- Hasbold, J., Johnson-Léger, C., Atkins, C. J., Clark, E. A., & Klaus, G. G. (1994). Properties of mouse CD40: cellular distribution of CD40 and B cell activation by monoclonal anti-mouse CD40 antibodies. *European Journal of Immunology*, 24(8), 1835–1842. <http://doi.org/10.1002/eji.1830240817>
- Haynes, B. F. (1984). Phenotypic characterization and ontogeny of mesodermal-derived and endocrine epithelial components of the human thymic microenvironment. *Journal of Experimental Medicine*, 159(4), 1149–1168. <http://doi.org/10.1084/jem.159.4.1149>
- Hayward, S. W., & Cunha, G. R. (2000). The prostate: development and physiology. *Radiologic Clinics of North America*, 38(1), 1–14.
- Henry, G. L., Brivanlou, I. H., & Kessler, D. S. (1996). TGF-beta signals and a pattern in *Xenopus laevis* endodermal development. *Development*, 122(3), 1007–15.
- Henry, Z. H., & Caldwell, S. H. (2015). Obesity and hepatocellular carcinoma: A complex relationship. *Gastroenterology*, 149(1), 18–20. <http://doi.org/10.1053/j.gastro.2015.05.024>
- Herroon, M. K., Rajagurubandara, E., Hardaway, A. L., Powell, K., Turchick, A., Feldmann, D., & Podgorski, I. (2013). Bone marrow adipocytes promote tumor growth in bone via FABP4-dependent mechanisms. *Oncotarget*, 4(11), 2108–2123. <http://doi.org/10.18632/oncotarget.1482>
- Hoene, M., Li, J., Häring, H.-U., Weigert, C., Xu, G., & Lehmann, R. (2014). The lipid profile of brown adipose tissue is sex-specific in mice. *Biochimica Et Biophysica Acta*, 1842(10), 1563–1570. <http://doi.org/10.1016/j.bbalip.2014.08.003>
- Hsing, A. W., Sakoda, L. C., & Chua, S. (2007). Obesity, metabolic syndrome, and prostate cancer. *The American Journal of Clinical Nutrition*, 86(3), s843–57.
- Huang, L., Pu, Y., Alam, S., Birch, L., & Prins, G. S. (2005). The role of Fgf10 signaling in branching morphogenesis and gene expression of the rat prostate gland: lobe-specific suppression by neonatal estrogens. *Developmental Biology*, 278(2), 396–414. <http://doi.org/10.1016/j.ydbio.2004.11.020>
- Hussain, M. M. (2014). Intestinal lipid absorption and lipoprotein formation. *Current Opinion in Lipidology*, 25(3), 200–206. <http://doi.org/10.1097/MOL.0000000000000084>
- Ide, H., Seligson, D. B., Memarzadeh, S., Xin, L., Horvath, S., Dubey, P., et al. (2002). Expression of colony-stimulating factor 1 receptor during prostate development and prostate cancer progression. *Pnas*, 99(22), 14404–14409. <http://doi.org/10.1073/pnas.222537099>
- Ittmann, M., Huang, J., Radaelli, E., Martin, P., Signoretti, S., Sullivan, R., et al. (2013). Animal models of human prostate cancer: The consensus report of the New York meeting of the mouse models of human cancers consortium prostate pathology committee. *Cancer Research*, 73(9), 2718–2736. <http://doi.org/10.1158/0008-5472.CAN-12-4213>
- Jacobsson, B., Holm, G., Björntorp, P., & Smith, U. (1976). Influence of cell size on the effects of insulin and noradrenaline on human adipose tissue. *Diabetologia*, 12(1), 69–72.



- Jiang, J., Au, M., Lu, K., Eshpeter, A., Korbitt, G., Fisk, G., & Majumdar, A. S. (2007). Generation of insulin-producing islet-like clusters from human embryonic stem cells. *Stem Cells*, 25(8), 1940–1953. <http://doi.org/10.1634/stemcells.2006-0761>
- Jo, J., Gavrilova, O., Pack, S., Jou, W., Mullen, S., Sumner, A. E., et al. (2009). Hypertrophy and/or hyperplasia: Dynamics of adipose tissue growth. *PLoS Computational Biology*, 5(3), e1000324. <http://doi.org/10.1371/journal.pcbi.1000324.s002>
- Johnson, S., & Rabinovitch, P. (2001). Ex vivo imaging of excised tissue using vital dyes and confocal microscopy (Vol. 584, pp. 5–20). Hoboken, NJ, USA: John Wiley & Sons, Inc. <http://doi.org/10.1002/0471142956.cy0939s61>
- Kang, M., Kim, H., & Han, Y.-M. (2014). Generation of bladder urothelium from human pluripotent stem cells under chemically defined serum- and feeder-free system. *International Journal of Molecular Sciences*, 15(5), 7139–7157. <http://doi.org/10.3390/ijms15057139>
- Kawano, Y., & Cohen, D. E. (2013). Mechanisms of hepatic triglyceride accumulation in non-alcoholic fatty liver disease. *Journal of Gastroenterology*, 48(4), 434–441. <http://doi.org/10.1007/s00535-013-0758-5>
- Kawasaki, H., Mizuseki, K., Nishikawa, S., Kaneko, S., Kuwana, Y., Nakanishi, S., et al. (2000). Induction of midbrain dopaminergic neurons from ES cells by stromal cell-derived inducing activity. *Neuron*, 28(1), 31–40.
- Katnik-Prastowska, I., Lis, J., & Matejuk, A. (2014). Glycosylation of uroplakins. Implications for bladder physiopathology. *Glycoconjugate Journal*, 31(9), 623–636. <http://doi.org/10.1007/s10719-014-9564-4>
- Keller, G. (2005a). Embryonic stem cell differentiation: emergence of a new era in biology and medicine. *Genes & Development*, 19(10), 1129–1155. <http://doi.org/10.1101/gad.1303605>
- Keller, G. (2005b). Embryonic stem cell differentiation: emergence of a new era in biology and medicine. *Genes & Development*, 19(10), 1129–1155. <http://doi.org/10.1101/gad.1303605>
- Khomtchouk, B. B., Van Booven, D. J., & Wahlestedt, C. (2014). HeatmapGenerator: high performance RNAseq and microarray visualization software suite to examine differential gene expression levels using an R and C++ hybrid computational pipeline. *Source Code for Biology and Medicine*, 9(1), 30. <http://doi.org/10.1186/s13029-014-0030-2>
- Kim, C. S., Lee, S. C., Kim, Y. M., Kim, B. S., Choi, H. S., Kawada, T., et al. (2008). Visceral fat accumulation induced by a high-fat diet causes the atrophy of mesenteric lymph nodes in obese mice. *Obesity (Silver Spring, Md.)*, 16(6), 1261–1269. <http://doi.org/10.1038/oby.2008.55>
- Kim, C.-S., Kim, J. G., Lee, B.-J., Choi, M.-S., Choi, H.-S., Kawada, T., et al. (2011). Deficiency for costimulatory receptor 4-1BB protects against obesity-induced inflammation and metabolic disorders. *Diabetes*, 60(12), 3159–3168. <http://doi.org/10.2337/db10-1805>
- Kim, H.Y., Merrow, A.C., Shiraj, S., Wong, B.L., Horn, P.S., & Laor, T. (2013).

- Analysis of fatty infiltration and inflammation of the pelvic and thigh muscles in boys with Duchenne muscular dystrophy (DMD): grading of disease involvement on MR imaging and correlation with clinical assessments. *Pediatric Radiology*, 43(10), 1327-1335.  
<http://doi.org/10.1007/s00247-013-2696-z>
- Kim, J. I., Huh, J. Y., Sohn, J. H., Choe, S. S., Lee, Y. S., Lim, C. Y., et al. (2015). Lipid-overloaded enlarged adipocytes provoke insulin resistance independent of inflammation. *Molecular and Cellular Biology*, 35(10), 1686–1699.  
<http://doi.org/10.1128/MCB.01321-14>
- Kim, M. J., Bhatia-Gaur, R., Banach-Petrosky, W. A., Desai, N., Wang, Y., Hayward, S. W., et al. (2002). Nkx3.1 mutant mice recapitulate early stages of prostate carcinogenesis. *Cancer Research*, 62(11), 2999–3004.  
<http://doi.org/10.1101/gad.819500>
- Kim, M., Habiba, A., Doherty, J. M., Mills, J. C., Mercer, R. W., & Huettner, J. E. (2009). Regulation of mouse embryonic stem cell neural differentiation by retinoic acid. *Developmental Biology*, 328(2), 456–471.  
<http://doi.org/10.1016/j.ydbio.2009.02.001>
- Kina, T., Ikuta, K., Takayama, E., Wada, K., Majumdar, A. S., Weissman, I. L., & Katsura, Y. (2000). The monoclonal antibody TER-119 recognizes a molecule associated with glycophorin A and specifically marks the late stages of murine erythroid lineage. *British Journal of Haematology*, 109(2), 280–287.
- Kirsch, R., Clarkson, V., Shephard, E. G., Marais, D. A., Jaffer, M. A., Woodburne, V. E., et al. (2003). Rodent nutritional model of non-alcoholic steatohepatitis: Species, strain and sex difference studies. *Journal of Gastroenterology and Hepatology*, 18(11), 1272–1282. <http://doi.org/10.1046/j.1440-1746.2003.03198.x>
- Köfeler, H.C., Fauland, A., Rechberger, G. N., & Trötz Müller, M. (2012). Mass Spectrometry Based Lipidomics: An Overview of Technological Platforms. *Metabolites*, 2(1), 19-38.
- Krijnen, J. L., Janssen, P. J., Ruizeveld de Winter, J. A., van Krimpen, H., Schröder, F. H., & van der Kwast, T. H. (1993). Do neuroendocrine cells in human prostate cancer express androgen receptor? *Histochemistry*, 100(5), 393–398.
- Kroon, P., Gadiot, J., Peeters, M., Gasparini, A., Deken, M. A., Yagita, H., et al. (2016). Concomitant targeting of programmed death-1 (PD-1) and CD137 improves the efficacy of radiotherapy in a mouse model of human BRAFV600-mutant melanoma. *Cancer Immunology, Immunotherapy : CII*, 65(6), 753–763.  
<http://doi.org/10.1007/s00262-016-1843-4>
- Kubo, A., Shinozaki, K., Shannon, J. M., Kouskoff, V., Kennedy, M., Woo, S., et al. (2004). Development of definitive endoderm from embryonic stem cells in culture. *Development*, 131(7), 1651–1662. <http://doi.org/10.1242/dev.01044>
- Kuo, Y. M., Zhou, B., Cosco, D., & Gitschier, J. (2001). The copper transporter CTR1 provides an essential function in mammalian embryonic development. *Pnas*, 98(12), 6836–6841. <http://doi.org/10.1073/pnas.111057298>
- Kusama, Y., Enami, J., & Kano, Y. (1989). Growth and morphogenesis of mouse

- prostate epithelial cells in collagen gel matrix culture. *Cell Biology International Reports*, 13(6), 569–575.
- Kwok, K. H. M., Lam, K. S. L., & Xu, A. (2016). Heterogeneity of white adipose tissue: molecular basis and clinical implications. *Experimental & Molecular Medicine*, 48(3), e215. <http://doi.org/10.1038/emm.2016.5>
- Kwon, G. S., Viotti, M., & Hadjantonakis, A.-K. (2008). The endoderm of the mouse embryo arises by dynamic widespread intercalation of embryonic and extraembryonic lineages. *Developmental Cell*, 15(4), 509–520. <http://doi.org/10.1016/j.devcel.2008.07.017>
- Lammert, E., Cleaver, O., & Melton, D. (2001). Induction of pancreatic differentiation by signals from blood vessels. *Science*, 294(5542), 564–567. <http://doi.org/10.1126/science.1064344>
- Laurent, V., Guérard, A., Mazerolles, C., Le Gonidec, S., Toulet, A., Nieto, L., et al. (2016). Periprostatic adipocytes act as a driving force for prostate cancer progression in obesity. *Nature Communications*, 7, 10230. <http://doi.org/10.1038/ncomms10230>
- Lawson, K. A., Meneses, J. J., & Pedersen, R. A. (1991). Clonal analysis of epiblast fate during germ layer formation in the mouse embryo. *Development*, 113(3), 891–911.
- Le Cong, Ran, F. A., Cox, D., Lin, S., Barretto, R., Habib, N., et al. (2013). Multiplex Genome Engineering Using CRISPR/Cas Systems. *Science*, 339(6121), 819–823. <http://doi.org/10.1126/science.1231143>
- Lee, C., Tsai, Y., Sensibar, J., Oliver, L., & Grayhack, J. T. (1986). Two-dimensional characterization of prostatic acid phosphatase, prostatic specific antigen and prostate binding protein in expressed prostatic fluid. *The Prostate*, 9(2), 135–146. <http://doi.org/10.1002/pros.2990090204>
- Lee, M.-J., Wu, Y., & Fried, S. K. (2013). Adipose tissue heterogeneity: Implication of depot differences in adipose tissue for obesity complications. *Molecular Aspects of Medicine*, 34(1), 1–11. <http://doi.org/10.1016/j.mam.2012.10.001>
- Lee, Y. H. (2004). Simple flow cytometric method used to assess lipid accumulation in fat cells. *The Journal of Lipid Research*, 45(6), 1162–1167. <http://doi.org/10.1194/jlr.D300028-JLR200>
- Leelatian, N., Diggins, K. E., & Irish, J. M. (2015). Characterizing phenotypes and signaling networks of single human cells by mass cytometry. In *Embryonic Stem Cell Protocols* (Vol. 1346, pp. 99–113). New York, NY: Springer New York. [http://doi.org/10.1007/978-1-4939-2987-0\\_8](http://doi.org/10.1007/978-1-4939-2987-0_8)
- Li, W., Cavasotto, C. N., Cardozo, T., Ha, S., Dang, T., Taneja, S. S., et al. (2005). Androgen receptor mutations identified in prostate cancer and androgen insensitivity syndrome display aberrant ART-27 coactivator function. *Molecular Endocrinology (Baltimore, Md.)*, 19(9), 2273–2282. <http://doi.org/10.1210/me.2005-0134>
- Li, W., Zheng, Y., Zhang, W., Wang, Z., Xiao, J., & Yuan, Y. (2015). Progression and variation of fatty infiltration of the thigh muscles in Duchenne muscular

- dystrophy, a muscle magnetic resonance imaging study. *Neuromuscular Disorders*, 25(5), 375–380.  
<http://dx.doi.org/10.1016/j.nmd.2015.01.003>
- Lilja, H., & Abrahamsson, P. A. (1988). Three predominant proteins secreted by the human prostate gland. *The Prostate*, 12(1), 29–38.
- Litjens, N. H. R., de Wit, E. A., Baan, C. C., & Betjes, M. G. H. (2013). Activation-induced CD137 is a fast assay for identification and multi-parameter flow cytometric analysis of alloreactive T cells. *Clinical and Experimental Immunology*, 174(1), 179–191. <http://doi.org/10.1111/cei.12152>
- Little, M. H., Brennan, J., Georgas, K., Davies, J. A., Davidson, D. R., Baldock, R. A., et al. (2007). A high-resolution anatomical ontology of the developing murine genitourinary tract. *Gene Expression Patterns*, 7(6), 680–699.  
<http://doi.org/10.1016/j.modgep.2007.03.002>
- Liu, J., DeYoung, S. M., Zhang, M., Zhang, M., Cheng, A., & Saltiel, A. R. (2005). Changes in integrin expression during adipocyte differentiation. *Cell Metabolism*, 2(3), 165–177. <http://doi.org/10.1016/j.cmet.2005.08.006>
- Liu, Q., Wang, M., Hu, Y., Xing, H., Chen, X., Zhang, Y., & Zhu, P. (2015). Significance of CD71 expression by flow cytometry in diagnosis of acute leukemia. *Leukemia & Lymphoma*, 55(4), 892–898.  
<http://doi.org/10.3109/10428194.2013.819100>
- Liu, S.-H., & Lee, L.-T. (2012). Efficient differentiation of mouse embryonic stem cells into insulin-producing cells. *Experimental Diabetes Research*, 2012(5819), 1–5.  
<http://doi.org/10.1007/s00125-004-1458-8>
- Loebel, D. A. F., Watson, C. M., De Young, R. A., & Tam, P. P. L. (2003). Lineage choice and differentiation in mouse embryos and embryonic stem cells. *Developmental Biology*, 264(1), 1–14.
- Lu, W., Luo, Y., Kan, M., & McKeehan, W. L. (1999). Fibroblast growth factor-10. A second candidate stromal to epithelial cell andromedin in prostate. *The Journal of Biological Chemistry*, 274(18), 12827–12834.
- Maerten, P., Geboes, K., De Hertogh, G., Shen, C., Cadot, P., Bullens, D. M. A., et al. (2004). Functional expression of 4-1BB (CD137) in the inflammatory tissue in Crohn's disease. *Clinical Immunology (Orlando, Fla.)*, 112(3), 239–246.  
<http://doi.org/10.1016/j.clim.2004.04.009>
- Majesky, M. W. (2007). Developmental basis of vascular smooth muscle diversity. *Arteriosclerosis, Thrombosis, and Vascular Biology*, 27(6), 1248–1258.  
<http://doi.org/10.1161/ATVBAHA.107.141069>
- Majka, S. M., Miller, H. L., Helm, K. M., Acosta, A. S., Childs, C. R., Kong, R., & Klemm, D. J. (2014). Analysis and isolation of adipocytes by flow cytometry. *Methods of Adipose Tissue Biology, Part A* (1st ed., Vol. 537, pp. 281–296). Elsevier Inc. <http://doi.org/10.1016/B978-0-12-411619-1.00015-X>
- Mallanna, S. K., & Duncan, S. A. (2013). Differentiation of hepatocytes from pluripotent stem cells. *Current Protocols in Stem Cell Biology*, 26, Unit 1G.4.–1G.4.13. <http://doi.org/10.1002/9780470151808.sc01g04s26>

- Marchington, J. M., Mattacks, C. A., & Pond, C. M. (1989). Adipose tissue in the mammalian heart and pericardium: Structure, foetal development and biochemical properties. *Comparative Biochemistry and Physiology Part B: Comparative Biochemistry*, 94(2), 225–232. [http://doi.org/10.1016/0305-0491\(89\)90337-4](http://doi.org/10.1016/0305-0491(89)90337-4)
- Mariman, E. C. M., & Wang, P. (2010). Adipocyte extracellular matrix composition, dynamics and role in obesity. *Cellular and Molecular Life Sciences*, 67(8), 1277–1292. <http://doi.org/10.1007/s00018-010-0263-4>
- Marker, P. C., Donjacour, A. A., Dahiya, R., & Cunha, G. R. (2003a). Hormonal, cellular, and molecular control of prostatic development. *Developmental Biology*, 253(2), 165–174. [http://doi.org/10.1016/S0012-1606\(02\)00031-3](http://doi.org/10.1016/S0012-1606(02)00031-3)
- Marker, P. C., Donjacour, A. A., Dahiya, R., & Cunha, G. R. (2003b). Hormonal, cellular, and molecular control of prostatic development. *Developmental Biology*, 253(2), 165–174. [http://doi.org/10.1016/S0012-1606\(02\)00031-3](http://doi.org/10.1016/S0012-1606(02)00031-3)
- Martinez, V., & Henary, M. (2016). Nile Red and Nile Blue: Applications and syntheses of structural analogues. *Chemistry - a European Journal*, 22(39), 13764–13782. <http://doi.org/10.1002/chem.201601570>
- Matuo, Y., Nishi, N., Negi, T., Tanaka, Y., & Wada, F. (1982). Isolation and characterization of androgen-dependent non-histone chromosomal protein from dorsolateral prostate of rats. *Biochemical and Biophysical Research Communications*, 109(2), 334–340.
- Mauney, J. R., Ramachandran, A., Yu, R. N., Daley, G. Q., Adam, R. M., & Estrada, C. R. (2010). All-trans retinoic acid directs urothelial specification of murine embryonic stem cells via gata4/6 signaling mechanisms. *PLoS ONE*, 5(7), e11513. <http://doi.org/10.1371/journal.pone.0011513.s005>
- McGrath, K. E., Koniski, A. D., Maltby, K. M., McGann, J. K., & Palis, J. (1999). Embryonic expression and function of the chemokine SDF-1 and its receptor, CXCR4. *Developmental Biology*, 213(2), 442–456. <http://doi.org/10.1006/dbio.1999.9405>
- McNeal, J. E. (1978). Origin and evolution of benign prostatic enlargement. *Investigative Urology*, 15(4), 340–345.
- McNeal, J. E. (1981). The zonal anatomy of the prostate. *The Prostate*, 2(1), 35–49.
- McNeal, J. E., Redwine, E. A., Freiha, F. S., & Stamey, T. A. (1988). Zonal distribution of prostatic adenocarcinoma: correlation with histologic pattern and direction of spread. *The American Journal of Surgical Pathology*, 12(12), 897.
- Mehlem, A., Hagberg, C. E., Muhl, L., Eriksson, U., & Falkevall, A. (2013). Imaging of neutral lipids by oil red O for analyzing the metabolic status in health and disease. *Nature Protocols*, 8(6), 1149–1154. <http://doi.org/10.1038/nprot.2013.055>
- Mfopou, J. K., Geeraerts, M., Dejene, R., Van Langenhoven, S., Aberkane, A., Van Grunsven, L. A., & Bouwens, L. (2014). Efficient definitive endoderm induction from mouse embryonic stem cell adherent cultures: a rapid screening model for differentiation studies. *Stem Cell Research*, 12(1), 166–177. <http://doi.org/10.1016/j.scr.2013.10.004>

- Moll, R., Wu, X. R., Lin, J. H., & Sun, T. T. (1995). Uroplakins, specific membrane proteins of urothelial umbrella cells, as histological markers of metastatic transitional cell carcinomas. *The American Journal of Pathology*, 147(5), 1383–1397.
- Mori, S., Kiuchi, S., Ouchi, A., Hase, T., & Murase, T. (2014). Characteristic expression of extracellular matrix in subcutaneous adipose tissue development and adipogenesis; comparison with visceral adipose tissue. *International Journal of Biological Sciences*, 10(8), 825–833. <http://doi.org/10.7150/ijbs.8672>
- Mund, J. A., Estes, M. L., Yoder, M. C., Ingram, D. A., & Case, J. (2012). Flow cytometric identification and functional characterization of immature and mature circulating endothelial cells. *Arteriosclerosis, Thrombosis, and Vascular Biology*, 32(4), 1045–1053. <http://doi.org/10.1161/ATVBAHA.111.244210>
- Murry, C. E., & Keller, G. (2008). Differentiation of embryonic stem cells to clinically relevant populations: lessons from embryonic development. *Cell*, 132(4), 661–680. <http://doi.org/10.1016/j.cell.2008.02.008>
- Murtaugh, L. C. (2006). Pancreas and beta-cell development: from the actual to the possible. *Development*, 134(3), 427–438. <http://doi.org/10.1242/dev.02770>
- Nakano, A., Harada, T., Morikawa, S., & Kato, Y. (1990). Expression of leukocyte common antigen (CD45) on various human leukemia/lymphoma cell lines. *Pathology International*, 40(2), 107–115. <http://doi.org/10.1111/j.1440-1827.1990.tb01549.x>
- Nelson, A. C., Cutty, S. J., Niini, M., Stemple, D. L., Flicek, P., Houart, C., et al. (2014). Global identification of Smad2 and Eomesodermin targets in zebrafish identifies a conserved transcriptional network in mesendoderm and a novel role for Eomesodermin in repression of ectodermal gene expression. *BMC Biology*, 12, 81. <http://doi.org/10.1186/s12915-014-0081-5>
- Nguyen, P., Leray, V., Diez, M., Serisier, S., Bloc'h, J. L., Siliart, B., & Dumon, H. (2008). Liver lipid metabolism. *Journal of Animal Physiology and Animal Nutrition*, 92(3), 272–283. <http://doi.org/10.1111/j.1439-0396.2007.00752.x>
- Nieuwkoop, P. D. (1997). Short historical survey of pattern formation in the endomesoderm and the neural anlage in the vertebrates: the role of vertical and planar inductive actions. *Cellular and Molecular Life Sciences*, 53(4), 305–318.
- Noguchi, T.-A. K., Ninomiya, N., Sekine, M., Komazaki, S., Wang, P.-C., Asashima, M., & Kurisaki, A. (2015). Generation of stomach tissue from mouse embryonic stem cells. *Nature Cell Biology*, 17(8), 984–993. <http://doi.org/10.1038/ncb3200>
- Noordzij, M. A., van Steenbrugge, G. J., van der Kwast, T. H., & Schröder, F. H. (1995). Neuroendocrine cells in the normal, hyperplastic and neoplastic prostate. *Urological Research*, 22(6), 333–341.
- Noro, A., Sillat, T., Virtanen, I., Ingerpuu, S., Bäck, N., Konttinen, Y. T., & Korhonen, M. (2013). Laminin production and basement membrane deposition by mesenchymal stem cells upon adipogenic differentiation. *The Journal of Histochemistry and Cytochemistry : Official Journal of the Histochemistry Society*, 61(10), 719–730. <http://doi.org/10.1369/0022155413502055>
- Nostro, M. C., Sarangi, F., Yang, C., Holland, A., Elefanty, A. G., Stanley, E. G., et al.

- (2015). Efficient generation of NKX6-1+ pancreatic progenitors from multiple human pluripotent stem cell lines. *Stem Cell Reports*, 4(4), 591–604. <http://doi.org/10.1016/j.stemcr.2015.02.017>
- Ogawa, K., Saito, A., Matsui, H., Suzuki, H., Ohtsuka, S., Shimosato, D., et al. (2007). Activin-Nodal signaling is involved in propagation of mouse embryonic stem cells. *Journal of Cell Science*, 120(Pt 1), 55–65. <http://doi.org/10.1242/jcs.03296>
- Ojha, S., Fainberg, H. P., Wilson, V., Pelella, G., Castellanos, M., May, S. T., et al. (2016). Gene pathway development in human epicardial adipose tissue during early life. *JCI Insight*, 1(13), e87460. <http://doi.org/10.1172/jci.insight.87460>
- Olefsky, J. M. (1976). The effects of spontaneous obesity on insulin binding, glucose transport, and glucose oxidation of isolated rat adipocytes. *Journal of Clinical Investigation*, 57(4), 842–851. <http://doi.org/10.1172/JCI108360>
- Ottamasathien, S. S., Wang, Y. Y., Williams, K. K., Franco, O. E. O., Wills, M. L. M., Thomas, J. C. J., et al. (2007). Directed differentiation of embryonic stem cells into bladder tissue. *Developmental Biology*, 304(2), 11–11. <http://doi.org/10.1016/j.ydbio.2007.01.010>
- Osborn, S. L., Thangappan, R., Luria, A., Lee, J. H., Nolte, J., & Kurzrock, E. A. (2014). Induction of human embryonic and induced pluripotent stem cells into urothelium. *Stem Cells Translational Medicine*, 3(5), 610–619. <http://doi.org/10.5966/sctm.2013-0131>
- Ozawa, T., Takayama, K., Okamoto, R., Negoro, R., Sakurai, F., Tachibana, M., et al. (2015). Generation of enterocyte-like cells from human induced pluripotent stem cells for drug absorption and metabolism studies in human small intestine. *Scientific Reports*, 5(1), 16479. <http://doi.org/10.1038/srep16479>
- Parameswaran, M., & Tam, P. P. (1995). Regionalisation of cell fate and morphogenetic movement of the mesoderm during mouse gastrulation. *Developmental Genetics*, 17(1), 16–28. <http://doi.org/10.1002/dvg.1020170104>
- Parikesit, D., Mochtar, C. A., Umbas, R., & Hamid, A. R. A. H. (2016). The impact of obesity towards prostate diseases. *Prostate International*, 4(1), 1–6. <http://doi.org/10.1016/j.pnrl.2015.08.001>
- Parisotto, M., & Metzger, D. (2013). Genetically engineered mouse models of prostate cancer. *Molecular Oncology*, 7(2), 190–205. <http://doi.org/10.1016/j.molonc.2013.02.005>
- Park, A., Kim, W. K., & Bae, K.-H. (2014). Distinction of white, beige and brown adipocytes derived from mesenchymal stem cells. *World Journal of Stem Cells*, 6(1), 33–42. <http://doi.org/10.4252/wjsc.v6.i1.33>
- Parlee, S. D., Lentz, S. I., Mori, H., & MacDougald, O. A. (2014). Quantifying size and number of adipocytes in adipose tissue. *Methods in Enzymology*, 537, 93–122. <http://doi.org/10.1016/B978-0-12-411619-1.00006-9>
- Payne, G. A., Kohr, M. C., & Tune, J. D. (2012). Epicardial perivascular adipose tissue as a therapeutic target in obesity-related coronary artery disease. *British Journal of Pharmacology*, 165(3), 659–669. <http://doi.org/10.1111/j.1476-5381.2011.01370.x>
- Pearce, P. H., Johnsen, R. D., Wysocki, S. J., & Kakulas, B. A. (1981). Muscle lipids in

- Duchenne Muscular Dystrophy. *Australian Journal of Experimental Biology and Medical Science*, 59(1), 77–90.
- Pellegrinelli, V., Carobbio, S., & Vidal-Puig, A. (2016). Adipose tissue plasticity: how fat depots respond differently to pathophysiological cues. *Diabetologia*, 59(6), 1075–1088. <http://doi.org/10.1007/s00125-016-3933-4>
- Podsypanina, K., Ellenson, L. H., Nemes, A., Gu, J., Tamura, M., Yamada, K. M., et al. (1999). Mutation of Pten/Mmac1 in mice causes neoplasia in multiple organ systems. *Pnas*, 96(4), 1563–1568.
- Pope, B. D., Warren, C. R., Parker, K. K., & Cowan, C. A. (2016). microenvironmental control of adipocyte fate and function. *Trends in Cell Biology*, 26(10), 745–755. <http://doi.org/10.1016/j.tcb.2016.05.005>
- Porter, S. A., Massaro, J. M., Hoffmann, U., Vasan, R. S., O'Donnel, C. J., & Fox, C. S. (2009). Abdominal subcutaneous adipose tissue: a protective fat depot? *Diabetes Care*, 32(6), 1068–1075. <http://doi.org/10.2337/dc08-2280>
- Pouton, C. W., & Haynes, J. M. (2007). Embryonic stem cells as a source of models for drug discovery. *Nature Reviews Drug Discovery*.
- Prins, G. S., & Putz, O. (2008). Molecular signaling pathways that regulate prostate gland development. *Differentiation; Research in Biological Diversity*, 76(6), 641–659. <http://doi.org/10.1111/j.1432-0436.2008.00277.x>
- Pritchard, C. C., & Nelson, P. S. (2008). Gene expression profiling in the developing prostate. *Differentiation; Research in Biological Diversity*, 76(6), 624–640. <http://doi.org/10.1111/j.1432-0436.2008.00274.x>
- Putri, M., Syamsunarno, M. R. A. A., Iso, T., Yamaguchi, A., Hanaoka, H., Sunaga, H., et al. (2015). CD36 is indispensable for thermogenesis under conditions of fasting and cold stress. *Biochemical and Biophysical Research Communications*, 457(4), 520–525. <http://doi.org/10.1016/j.bbrc.2014.12.124>
- Qiao, L., Zou, C., Shao, P., Schaack, J., Johnson, P. F., & Shao, J. (2008). Transcriptional regulation of fatty acid translocase/CD36 expression by CCAAT/enhancer-binding protein alpha. *The Journal of Biological Chemistry*, 283(14), 8788–8795. <http://doi.org/10.1074/jbc.M800055200>
- Rabkin, S. W. (2007). Epicardial fat: properties, function and relationship to obesity. *Obesity Reviews*, 8(3), 253–261. <http://doi.org/10.1111/j.1467-789X.2006.00293.x>
- Reeves, H. L., Zaki, M. Y. W., & Day, C. P. (2016). Hepatocellular carcinoma in obesity, type 2 diabetes, and NAFLD. *Digestive Diseases and Sciences*, 61(5), 1234–1245. <http://doi.org/10.1007/s10620-016-4085-6>
- Reshef, L., Olswang, Y., Cassuto, H., Blum, B., Croniger, C. M., Kalhan, S. C., et al. (2003). Glyceroneogenesis and the triglyceride/fatty acid cycle. *The Journal of Biological Chemistry*, 278(33), 30413–30416. <http://doi.org/10.1074/jbc.R300017200>
- Ribatti, D., & Santoiemma, M. (2014). Epithelial-mesenchymal interactions: a fundamental Developmental Biology mechanism. *The International Journal of Developmental Biology*, 58(5), 303–306. <http://doi.org/10.1387/ijdb.140143dr>
- Risbridger, G. P., Davis, I. D., & Birrell, S. N. (2010). Breast and prostate cancer: more similar than different. *Nature Reviews*, 10(3), 205–12.



- <http://doi.org/10.1038/nrc2795>
- Rodaway, A., & Patient, R. (2001). Mesendoderm. an ancient germ layer? *Cell*, 105(2), 169–172.
- Roh, H. C., Tsai, L. T.-Y., Lyubetskaya, A., Tenen, D., Kumari, M., & Rosen, E. D. (2017). Simultaneous Transcriptional and Epigenomic Profiling from Specific Cell Types within Heterogeneous Tissues In Vivo. *Cell Reports*, 18(4), 1048–1061. <http://doi.org/10.1016/j.celrep.2016.12.087>
- Rosenwald, M., & Wolfrum, C. (2014). The origin and definition of brite versus white and classical brown adipocytes. *Adipocyte*, 3(1), 4–9. <http://doi.org/10.4161/adip.26232>
- Ruizeveld de Winter, J. A., Trapman, J., Vermey, M., Mulder, E., Zegers, N. D., & van der Kwast, T. H. (1991). Androgen receptor expression in human tissues: an immunohistochemical study. *The Journal of Histochemistry and Cytochemistry : Official Journal of the Histochemistry Society*, 39(7), 927–936. <http://doi.org/10.1177/39.7.1865110>
- Rumin, J. (2015). The use of fluorescent Nile red and BODIPY for lipid measurement in microalgae. *Biotechnology for Biofuels*, 8:42. <http://doi.org/10.1186/s13068-015-0220-4>
- Sackmann-Sala, L., Berryman, D. E., Munn, R. D., Lubbers, E. R., & Kopchick, J. J. (2011). Heterogeneity among white adipose tissue depots in male C57BL/6J mice. *Obesity*, 20(1), 101–111. <http://doi.org/10.1038/oby.2011.235>
- Sacks, H. S., Fain, J. N., Bahouth, S. W., Ojha, S., Frontini, A., Budge, H., et al. (2013). Adult epicardial fat exhibits beige features. *The Journal of Clinical Endocrinology & Metabolism*, 98(9), E1448–E1455. <http://doi.org/10.1210/jc.2013-1265>
- Sanchez-Gurmaches, J., & Guertin, D. A. (2014). Adipocytes arise from multiple lineages that are heterogeneously and dynamically distributed. *Nature Communications*, 5, 4099. <http://doi.org/10.1038/ncomms5099>
- Schaedlich, K., Knelangen, J. M., Navarrete Santos, A., Fischer, B., & Navarrete Santos, A. (2010). A simple method to sort ESC-derived adipocytes. *Cytometry Part A*, 77A(10), 990–995. <http://doi.org/10.1002/cyto.a.20953>
- Schaeffer, E. M., Marchionni, L., Huang, Z., Simons, B., Blackman, A., Yu, W., et al. (2008). Androgen-induced programs for prostate epithelial growth and invasion arise in embryogenesis and are reactivated in cancer. *Oncogene*, 27(57), 7180–7191. <http://doi.org/10.1038/onc.2008.327>
- Scheller, E. L., & Rosen, C. J. (2014). What's the matter with MAT? Marrow adipose tissue, metabolism, and skeletal health. *Annals of the New York Academy of Sciences*, 1311(1), 14–30. <http://doi.org/10.1111/nyas.12327>
- Schier F.A., & Shen, M.M. (1999). Nodal signalling in vertebrate development. *Nature*, 403(6768), 385–389. <http://doi.org/10.1038/35000126>
- Schultz, A., Barbosa-da-Silva, S., Aguila, M. B., & Mandarin-de-Lacerda, C. A. (2015). Differences and similarities in hepatic lipogenesis, gluconeogenesis and oxidative imbalance in mice fed diets rich in fructose or sucrose. *Food & Function*,

- 6(5), 1684–1691. <http://doi.org/10.1039/C5FO00251F>
- Schulz, T. C., Noggle, S. A., Palmarini, G. M., Weiler, D. A., Lyons, I. G., Pensa, K. A., et al. (2004). Differentiation of human embryonic stem cells to dopaminergic neurons in serum-free suspension culture. *Stem Cells*, 22(7), 1218–1238. <http://doi.org/10.1634/stemcells.2004-0114>
- Seale, P., Conroe, H. M., Estall, J., Kajimura, S., Frontini, A., Ishibashi, J., et al. (2011). Prdm16 determines the thermogenic program of subcutaneous white adipose tissue in mice. *Journal of Clinical Investigation*, 121(1), 96–105. <http://doi.org/10.1172/JCI44271>
- Shao, M., Hepler, C., Vishvanath, L., MacPherson, K. A., Busbuso, N. C., & Gupta, R. K. (2017). Fetal development of subcutaneous white adipose tissue is dependent on Zfp423. *Molecular Metabolism*, 6(1), 111–124. <http://doi.org/10.1016/j.molmet.2016.11.009>
- Shappell, S. B., Thomas, G. V., Roberts, R. L., Herbert, R., Ittmann, M. M., Rubin, M. A., et al. (2004). Prostate pathology of genetically engineered mice: definitions and classification. The consensus report from the Bar Harbor meeting of the Mouse Models of Human Cancer Consortium Prostate Pathology Committee. (Vol. 64, pp. 2270–2305). Presented at the Cancer research.
- Sharma, P., & Schreiber-Agus, N. (1999). Mouse models of prostate cancer. *Oncogene*, 18(38), 5349–5355. <http://doi.org/10.1038/sj.onc.1203037>
- Shaw, L. M., Messier, J. M., & Mercurio, A. M. (1990). The activation dependent adhesion of macrophages to laminin involves cytoskeletal anchoring and phosphorylation of the alpha 6 beta 1 integrin. *The Journal of Cell Biology*, 110(6), 2167–2174. <http://doi.org/10.1083/jcb.110.6.2167>
- Shen, M. M., & Abate-Shen, C. (2010). Molecular genetics of prostate cancer: new prospects for old challenges. *Genes & Development*, 24(18), 1967–2000. <http://doi.org/10.1101/gad.1965810>
- Shen, M.M. (2007). Nodal signaling: developmental roles and regulation. *Development*, 134(6), 1023–1034. <http://doi.org/10.1242/dev.000166>
- Sherwood, E. R., Berg, L. A., Mitchell, N. J., McNeal, J. E., Kozlowski, J. M., & Lee, C. (1990). Differential cytokeratin expression in normal, hyperplastic and malignant epithelial cells from human prostate. *Juro*, 143(1), 167–171.
- Sherwood, E. R., Theyer, G., Steiner, G., Berg, L. A., Kozlowski, J. M., & Lee, C. (1991). Differential expression of specific cytokeratin polypeptides in the basal and luminal epithelia of the human prostate. *The Prostate*, 18(4), 303–314.
- Shimizu, Y., Van Seventer, G. A., Horgan, K. J., & Shaw, S. (1990). Costimulation of proliferative responses of resting CD4+ T cells by the interaction of VLA-4 and VLA-5 with fibronectin or VLA-6 with laminin. *Journal of Immunology (Baltimore, Md. : 1950)*, 145(1), 59–67.
- Si-Tayeb, K., Noto, F. K., Nagaoka, M., Li, J., Battle, M. A., Duris, C., et al. (2010). Highly efficient generation of human hepatocyte-like cells from induced pluripotent stem cells. *Hepatology*, 51(1), 297–305.

- <http://doi.org/10.1002/hep.23354>
- Smith, J. L. (1908). On the simultaneous staining of neutral fat and fatty acid by oxazine dyes. *The Journal of Pathology and Bacteriology*, 12(1), 1–4.  
<http://doi.org/10.1002/path.1700120103>
- Smith, J. L. (1911). The staining of fat by Nile-blue sulphate. *Journal of Pathology and Bacteriology*, 15, 53–55.
- Smith, P. J., Wiltshire, M., Davies, S., Patterson, L. H., & Hoy, T. (1999). A novel cell permeant and far red-fluorescing DNA probe, DRAQ5, for blood cell discrimination by flow cytometry. *Journal of Immunological Methods*, 229(1-2), 131–139.
- Smith, U. (1972). Studies of human adipose tissue in culture. I. Incorporation of glucose and release of glycerol. *The Anatomical Record*, 172(4), 597–602.  
<http://doi.org/10.1002/ar.1091720401>
- Soprano, D. R., Teets, B. W., & Soprano, K. J. (2007). Role of retinoic acid in the differentiation of embryonal carcinoma and embryonic stem cells. *Vitamins and Hormones*, 75, 69–95. [http://doi.org/10.1016/S0083-6729\(06\)75003-8](http://doi.org/10.1016/S0083-6729(06)75003-8)
- Spencer, M., Unal, R., Zhu, B., Rasouli, N., McGehee, R. E., Jr., Peterson, C. A., & Kern, P. A. (2011). Adipose tissue extracellular matrix and vascular abnormalities in obesity and insulin resistance. *Journal of Clinical Endocrinology & Metabolism*, 96(12), E1990–E1998. <http://doi.org/10.1210/jc.2011-1567>
- Staack, A., Donjacour, A. A., Brody, J., Cunha, G. R., & Carroll, P. (2003). Mouse urogenital development: a practical approach. *Differentiation; Research in Biological Diversity*, 71(7), 402–413. <http://doi.org/10.1046/j.1432-0436.2003.7107004.x>
- Sugimura, Y., Cunha, G. R., & Donjacour, A. A. (1986). Morphogenesis of ductal networks in the mouse prostate. *Biology of Reproduction*, 34(5), 961–971.
- Tabe, Y., Yamamoto, S., Saitoh, K., Sekihara, K., Monma, N., Ikeo, K., et al. (2017). Bone marrow adipocytes facilitate fatty acid oxidation activating AMPK and a transcriptional network supporting survival of acute monocytic leukemia cells. *Cancer Research*, 77(6), 1453–1464. <http://doi.org/10.1158/0008-5472.CAN-16-1645>
- Takahashi, K., & Yamanaka, S. (2006). Induction of pluripotent stem cells from mouse embryonic and adult fibroblast cultures by defined factors. *Cell*, 126(4), 663–676. <http://doi.org/10.1016/j.cell.2006.07.024>
- Tam, P. P. L., & Behringer, R. R. (1997). Mouse gastrulation: the formation of a mammalian body plan. *Mechanisms of Development*, 68(1-2), 3–25.  
[http://doi.org/10.1016/S0925-4773\(97\)00123-8](http://doi.org/10.1016/S0925-4773(97)00123-8)
- Tanaka, S. T., Ishii, K., Demarco, R. T., Pope, J. C., Brock, J. W., & Hayward, S. W. (2010). Endodermal origin of bladder trigone inferred from mesenchymal-epithelial interaction. *Juro*, 183(1), 386–391.  
<http://doi.org/10.1016/j.juro.2009.08.107>
- Tang, W., Zeve, D., Suh, J. M., Bosnakovski, D., Kyba, M., Hammer, R. E., et al. (2008). White fat progenitor cells reside in the adipose vasculature. *Science*, 322(5901), 583–586. <http://doi.org/10.1126/science.1156232>

- Targher, G., Bertolini, L., Padovani, R., Rodella, S., Tessari, R., Zenari, L., et al. (2007). Prevalence of nonalcoholic fatty liver disease and its association with cardiovascular disease among type 2 diabetic patients. *Diabetes Care*, 30(5), 1212–1218. <http://doi.org/10.2337/dc06-2247>
- Taylor, R. A., Cowin, P. A., Cunha, G. R., Pera, M., Trounson, A. O., Pedersen, J., & Risbridger, G. P. (2006). Formation of human prostate tissue from embryonic stem cells. *Nature Methods*, 3(3), 179–181. <http://doi.org/10.1038/nmeth855>
- Thisse, B., Wright, C. V., & Thisse, C. (2000). Activin- and Nodal-related factors control antero-posterior patterning of the zebrafish embryo. *Nature*, 403(6768), 425–428. <http://doi.org/10.1038/35000200>
- Thomson, A. A., & Cunha, G. R. (1999). Prostatic growth and development are regulated by FGF10. *Development*, 126(16), 3693–3701.
- Thomson, A. A., & Marker, P. C. (2006). Branching morphogenesis in the prostate gland and seminal vesicles. *Differentiation; Research in Biological Diversity*, 74(7), 382–392. <http://doi.org/10.1111/j.1432-0436.2006.00101.x>
- Thomson, A. A., Timms, B. G., Barton, L., Cunha, G. R., & Grace, O. C. (2002). The role of smooth muscle in regulating prostatic induction. *Development*, 129(8), 1905–1912.
- Thomson, J. A., Itskovitz-Eldor, J., Shapiro, S. S., Waknitz, M. A., Swiergiel, J. J., Marshall, V. S., & Jones, J. M. (1998). Embryonic stem cell lines derived from human blastocysts. *Science*, 282(5391), 1145–1147. <http://doi.org/10.1126/science.282.5391.1145>
- Tirziu, D., & Simons, M. (2009). Endothelium as master regulator of organ development and growth. *Vascular Pharmacology*, 50(1-2), 1–7. <http://doi.org/10.1016/j.vph.2008.08.003>
- Tokuda, Y., Toda, S., Masaki, Z., & Sugihara, H. (1999). Proliferation and differentiation of rat dorsal prostatic epithelial cells in collagen gel matrix culture, focusing upon effects of adipocytes. *International Journal of Urology : Official Journal of the Japanese Urological Association*, 6(10), 509–519.
- Tourkin, A., Anderson, T., Leroy, E. C., & Hoffman, S. (2009). Eosinophil adhesion and maturation is modulated by laminin. *Cell Adhesion and Communication*, 1(2), 161–176. <http://doi.org/10.3109/15419069309095692>
- Tuxhorn, J. A., Ayala, G. E., & Rowley, D. R. (2001). Reactive stroma in prostate cancer progression. *Juro*, 166(6), 2472–2483.
- van Lochem, E. G., van der Velden, V. H. J., Wind, H. K., Marvelde, te, J. G., Westerdaal, N. A. C., & van Dongen, J. J. M. (2004). Immunophenotypic differentiation patterns of normal hematopoiesis in human bone marrow: Reference patterns for age-related changes and disease-induced shifts. *Cytometry Part A*, 60B(1), 1–13. <http://doi.org/10.1002/cyto.b.20008>
- Varlamov, O., Somwar, R., Cornea, A., Kievit, P., Grove, K. L., & Roberts, C. T. (2010). Single-cell analysis of insulin-regulated fatty acid uptake in adipocytes. *AJP: Endocrinology and Metabolism*, 299(3), E486–E496. <http://doi.org/10.1152/ajpendo.00330.2010>

- Velonas, V. M., Woo, H. H., Remedios, dos, C. G., & Assinder, S. J. (2013). Current status of biomarkers for prostate cancer. *International Journal of Molecular Sciences*, 14(6), 11034–11060. <http://doi.org/10.3390/ijms140611034>
- Vijayalakshmi, S., Karthika, T. N., Mishra, A. K., & Chandra, T. S. (2003). Spectrofluorimetric method for the estimation of total lipids in *Eremothecium ashbyii* fungal filaments using Nile blue and avoiding interference of autofluorescent riboflavin. *Journal of Microbiological Methods*, 55(1), 99–103.
- Vroegrijk, I. O. C. M., Klinken, J. B., Diepen, J. A., Berg, den, S. A. A., Febbraio, M., Steinbusch, L. K. M., et al. (2013). CD36 is important for adipocyte recruitment and affects lipolysis. *Obesity*, 21(10), 2037–2045. <http://doi.org/10.1002/oby.20354>
- Wajchenberg, B. L., Giannella-Neto, D., da Silva, M. E., & Santos, R. F. (2002). Depot-specific hormonal characteristics of subcutaneous and visceral adipose tissue and their relation to the metabolic syndrome. *Hormone and Metabolic Research = Hormon- Und Stoffwechselforschung = Hormones Et Metabolisme*, 34(11-12), 616–621. <http://doi.org/10.1055/s-2002-38256>
- Walker, H. K., Hall, W. D., Hurst, J. W., & White, J. M. (1990). An overview of the genitourinary system. In: Walker HK, Hall WD, Hurst JW, editors. *Clinical Methods: The History, Physical, and Laboratory Examinations*. 3<sup>rd</sup> edition. Boston: Butterworths; 1990. Chapter 180. Available from: <https://www.ncbi.nlm.nih.gov/books/NBK290/>
- Wang, Q. A., Tao, C., Gupta, R. K., & Scherer, P. E. (2013). Tracking adipogenesis during white adipose tissue development, expansion and regeneration. *Nature Medicine*, 19(10), 1338–1344. <http://doi.org/10.1038/nm.3324>
- Wang, X., Julio, M. K.-D., Economides, K. D., Walker, D., Yu, H., Halili, M. V., et al. (2009). A luminal epithelial stem cell that is a cell of origin for prostate cancer. *Nature*, 461(7263), 495–500. <http://doi.org/10.1038/nature08361>
- Wang, Y., Hayward, S., Cao, M., Thayer, K., & Cunha, G. (2001). Cell differentiation lineage in the prostate. *Differentiation; Research in Biological Diversity*, 68(4-5), 270–279.
- White, U. A., & Tchoukalova, Y. D. (2014). Sex dimorphism and depot differences in adipose tissue function. *Biochimica Et Biophysica Acta*, 1842(3), 377–392. <http://doi.org/10.1016/j.bbadis.2013.05.006>
- Willey, S., Ayuso-Sacido, A., Zhang, H. L., Fraser, S. T., Sahr, K. E., Adlam, M. J., et al. (2006). Acceleration of mesoderm development and expansion of hematopoietic progenitors in differentiating ES cells by the mouse mix-like homeodomain transcription factor. *Blood*, 107(8), 3122–3130. <http://doi.org/10.1182/blood-2005-104120>
- Wu, A., Kolanowski, J. L., Boumelhem, B. B., Yang, K., Lee, R., Kaur, A., et al. (2017). A carborane-containing fluorophore as a stain of cellular lipid droplets. *Chemistry, an Asian Journal*, 1, 328. <http://doi.org/10.1002/asia.201700423>
- Wu, J., Boström, P., Sparks, L. M., Ye, L., Choi, J. H., Giang, A.-H., et al. (2012). Beige adipocytes are a distinct type of thermogenic fat cell in mouse and human. *Cell*, 150(2), 366–376. <http://doi.org/10.1016/j.cell.2012.05.016>

- Wu, J., Cohen, P., & Spiegelman, B. M. (2013). Adaptive thermogenesis in adipocytes: Is beige the new brown? *Genes & Development*, 27(3), 234–250.  
<http://doi.org/10.1101/gad.211649.112>
- Wu, X.-R., Kong, X.-P., Pellicer, A., Kreibich, G., & Sun, T.-T. (2009). Uroplakins in urothelial biology, function, and disease. *Kidney International*, 75(11), 1153–1165.  
<http://doi.org/10.1038/ki.2009.73>
- Xu, S., Jay, A., Brunaldi, K., Huang, N., & Hamilton, J. A. (2013). CD36 enhances fatty acid uptake by increasing the rate of intracellular esterification but not transport across the plasma membrane. *Biochemistry*, 52(41), 7254–7261.  
<http://doi.org/10.1021/bi400914c>
- Xue, Y., Smedts, F., Debruyne, F. M. J., la Rosette, de, J. J. M. C. H., & Schalken, J. A. (1998). Identification of intermediate cell types by keratin expression in the developing human prostate. *The Prostate*, 34(4), 292–301.  
[http://doi.org/10.1002/\(SICI\)1097-0045\(19980301\)34:4<292::AID-PROS7>3.0.CO;2-J](http://doi.org/10.1002/(SICI)1097-0045(19980301)34:4<292::AID-PROS7>3.0.CO;2-J)
- Yasunaga, M., Tada, S., Torikai-Nishikawa, S., Nakano, Y., Okada, M., Jakt, L. M., et al. (2005). Induction and monitoring of definitive and visceral endoderm differentiation of mouse ES cells. *Nature Biotechnology*, 23(12), 1542–1550.  
<http://doi.org/10.1038/nbt1167>
- Yi-jia Lou, X.-G. L. (2011). Embryonic stem cell application in drug discovery. *Acta Pharmacologica Sinica*, 32(2), 152–159. <http://doi.org/10.1038/aps.2010.194>
- Yoshida, T., Takayama, K., Kondoh, M., Sakurai, F., Tani, H., Sakamoto, N., et al. (2011). Use of human hepatocyte-like cells derived from induced pluripotent stem cells as a model for hepatocytes in hepatitis C virus infection. *Biochemical and Biophysical Research Communications*, 416(1-2), 119–124.  
<http://doi.org/10.1016/j.bbrc.2011.11.007>
- Zebisch, K., Voigt, V., Wabitsch, M., & Brandsch, M. (2012). Protocol for effective differentiation of 3T3-L1 cells to adipocytes. *Analytical Biochemistry*, 425(1), 88–90.  
<http://doi.org/10.1016/j.ab.2012.03.005>
- Zhou, P., Qian, L., Gallo, E. F., Deeb, R. S., Anrather, J., Gross, S. S., & Iadecola, C. (2011). The scavenger receptor CD36 contributes to the neurotoxicity of bone marrow-derived monocytes through peroxynitrite production. *Neurobiology of Disease*, 42(3), 292–299.
- Zhu, Z., & Huangfu, D. (2013). Human pluripotent stem cells: an emerging model in developmental biology. *Development*, 140(4), 705–717.  
<http://doi.org/10.1242/dev.086165>
- Zorn, A. M., & Wells, J. M. (2009). Vertebrate endoderm development and organ formation. *Annual Review of Cell and Developmental Biology*, 25(1), 221–251.  
<http://doi.org/10.1146/annurev.cellbio.042308.113344>

## **Appendices**

**Appendix I: The mesendoderm: A wellspring of cell lineages for regenerative medicine.**

## CHAPTER 10

# The Mesendoderm: A Wellspring of Cell Lineages for Regenerative Medicine

Badwi B. Boumelhem<sup>1</sup>, Stephen J. Assinder<sup>1,3</sup>, Christoph Hammans<sup>1</sup>, Marietta P. Tanudisastro<sup>1</sup>, Damien T. M. Le<sup>1</sup>, Kurt W. L. Brigden<sup>1</sup> and Stuart T. Fraser<sup>1,2,3,\*</sup>

<sup>1</sup> *Disciplines of Physiology and Anatomy & Histology*

<sup>2</sup> *School of Medical Science, University of Sydney, Camperdown, New South Wales, Australia*  
*Bosch Institute*

<sup>3</sup> *University of Sydney, Camperdown, New South Wales, Australia*

**Abstract:** Regenerative medicine is centred around the premise that progenitor populations can be engineered to give rise to mature cell lineages forming a complex tissue architecture which in turn produces functional organs. The potency of the starting progenitor population is therefore a critical consideration. The mesendoderm is a rare population of cells present in the embryo only at gastrulation. This bipotent population gives rise to the mesoderm and the definitive endoderm and all mature cell types derived from these germ layers. Mesodermal progenitors generate cardiac, smooth and skeletal muscle, as well as the blood and vascular lineages, bone and connective tissue cells. The endoderm is the source of numerous cell lineages with potential utility for regenerative medicine including hepatocytes, pancreatic lineages and the epithelial cells of the respiratory, gastrointestinal and reproductive tracts. The development of numerous organs is dependent upon mesoderm-derived lineages interacting with endodermal-derived cell types. The kidney, adrenal gland, pancreas and genito-urinary tract development all require interactions between mesodermal and endodermal derivative cell types. Here, we describe the unique genetic programmes that lead to mesendoderm formation, the pathways leading to mesoderm and endoderm specification and examples where mature cell types from both germ layers interact to support their mutual development. We will also show how these programmes are being

---

\* **Corresponding author Stuart T. Fraser:** Disciplines of Physiology and Anatomy & Histology, School of Medical Science, University of Sydney, Camperdown, New South Wales, Australia; Tel: +612 9036 3313; Fax: +612 9036 3316; E-mail: [stuart.fraser@sydney.edu.au](mailto:stuart.fraser@sydney.edu.au)



harnessed to direct the differentiation of pluripotent cells *in vitro* into mesendoderm-derived cells and tissues which can be used to improve the quality of human life. Finally, we will discuss considerations for combining stem cell differentiation with tissue engineering through 3D bioprinting modalities.

**Keywords:** 3D bioprinting, Embryonic development, Embryonic stem cells (ESC), Endoderm, Germ layer specification, Induced pluripotent stem cells (iPSC), Mesendoderm, Mesoderm, Regenerative medicine, Tissue engineering.

## INTRODUCTION

The complex adult mammalian body is derived from three simple structures early in embryogenesis termed the germ layers. These are: the ectoderm, which forms the skin and central nervous system; the endoderm which gives rise to the epithelial tissues of the viscera such as the respiratory, gastrointestinal and genitourinary tracts; and the mesoderm, which forms all of the connective tissue, blood, vessels and muscle tissues. These three germ layers, can be first distinguished at the developmental stage termed gastrulation. However, it has been proposed for some time that the mesoderm and endoderm arise from a single cell type with the potential to form both lineages. This cell type, termed the mesendoderm, can be identified in simpler animal models such as the frog embryo, and an equivalent cell type can be generated from mammalian pluripotent stem cells in culture. The mesendoderm is, in the end, responsible for the formation of essentially vast amounts of the body except for the brain, skin (derived from the ectoderm) and other tissues derived from a structure arising later in embryogenesis termed the neural crest.

All of the epithelial tissues contain mesoderm-derived lineages. For example, the gastro-intestinal epithelial tissue has a mesoderm-derived connective tissue component essential in maintaining structural integrity. Indeed, it is now clear that, in many organs, extensive cross-talk must take place between endoderm-derived tissues and mesodermal-derived structures during embryogenesis of organogenesis to proceed. The developing pancreas and liver (endoderm) require signals from underlying blood vessels (mesoderm) to form [1, 2]. Removal of the blood vessels leads to a loss of appropriate signals and failure of pancreatic

development. In contrast, most mesoderm-derived organs lack epithelial structures. For example, the heart, skeletal muscle and bone marrow do not contain endoderm-derived cell types (Table 1).

**Table 1. Organs and cells derived from the mesendoderm.**

<b>Organ</b>	<b>Endoderm-derived Lineages</b>	<b>Mesoderm-derived Lineages</b>
<b>Salivary gland</b>	serous, mucosal and seromucosal epithelial cells	connective tissue fibroblasts, macrophages endothelial cells, adipose cells
<b>Trachea</b>	Goblet cells columnar epithelial cells	tracheal cartilage, lymphoid cells, macrophages
<b>Lungs</b>	Type I and II alveolar cells Clara/club cells, Goblet cells	endothelial cells alveolar macrophages
<b>Stomach</b>	surface mucous cells mucous neck cells entero-endocrine cells chief cells, parietal cells	smooth muscle, adipocytes, endothelial cells fibroblasts, lymphoid cells
<b>Liver</b>	hepatocyte cholangiocyte	sinusoidal endothelial cell Kupffer cell, hepatic stellate cell
<b>Gastrointestinal tract</b>	gastric epithelium glands (pyloric, cardiac, fundus)	mesenteric connective tissue fibroblasts smooth muscle, endothelial cells, lymphoid cells
<b>Pancreas</b>	acinar cells, centroacinar cells pancreatic $\alpha$ , $\beta$ and $\delta$ cells	capillary endothelial cells connective tissue fibroblasts
<b>Kidney</b>	tubular epithelial cells	glomerular endothelial cells, mesangial cells podocytes, capsular stromal fibroblast
<b>Prostate</b>	cuboidal epithelial cells columnar epithelial cells	prostatic stroma fibroblasts, smooth muscle connective tissue
<b>Urinary bladder</b>	urothelium	smooth muscle, hematopoietic cells, endothelial cells
<b>Bone</b>		osteocytes, osteoblasts, chondrocytes, endothelial cells, hematopoietic cells, adipocytes
<b>Thymus</b>	cortical thymic epithelial cells medullary thymic epithelial cells	thymocytes (developing T lymphocytes) dendritic cells, thymic macrophages
<b>Spleen</b>		capsule stromal fibroblasts, erythrocytes lymphocytes, sinusoidal endothelium macrophages
<b>Gonads</b>		Leydig cells, Sertoli cells, follicular cells thecal cells

Understanding the biology underpinning mesendoderm development offers us insight in the formation of a vast amount of the human body. Defining the molecular processes that control mesendoderm formation and differentiation, as well as the formation of other similar bi-potent populations in the embryo, can be of great benefit to regenerative medicine. In particular, the *ex vivo* generation of functional mini-organs or organoids exhibiting appropriate morphology and tissue architecture and derived from a patient's own stem cells offers enormous potential for individuals with many pathological conditions. Successful 3D bioprinting and differentiation of stem cells into functional tissue equivalents as insulin-producing pancreatic islets, clusters of functional hepatocytes, lung or mini-kidney tissue will have a profound effect on a vast cohort of patients, most of whom are waiting for matching organ donors. However, an understanding of the embryological processes required in the formation of these tissues is required before we can proceed to generating new tissues *in vitro*. This chapter aims to inform the reader of the developmental processes taking place to form and differentiate the mesendoderm and to demonstrate how this basic biological knowledge can be applied to regenerative medicine *via* induced pluripotent stem cells, tissue engineering and 3D bioprinting.

### **The Germ Layers**

In contrast to the formation of bi-laminar organisms such as jellyfish, mammalian embryogenesis requires the formation of three distinct three germ layers; ectoderm, endoderm and mesoderm. It is these three layers of cells that give rise to all of the different cell lineages in the adult human body. The ectoderm gives rise to the external layer of the skin and the central nervous system. The endoderm forms all of the major epithelial cell lineages giving rise to the different tracts of the body such as the respiratory, gastrointestinal and genitourinary systems. All of these systems must form tube-like structures with tight junctions forming between cells to seal the external environment from the internal body and yet still allow transport (of oxygen and nutrients from food) or secretion and excretion (of carbon dioxide, urine, faeces, sperm *etc.*). In complex animals, such as mammals, a third germ layer exists which forms all of the supportive structures between the external skin, central nervous systems and internal epithelial organs. Supportive structures such as the skeletal system, the integumentary system, blood and

lymphatic vessels, heart, smooth and skeletal muscle and blood are all derived from the mesoderm.

### The Mesendoderm

Investigations into the origins of the endoderm and mesoderm led to the concept that a bi-potent progenitor cell exists early in development capable of giving rise to each germ layer. This cell type has been termed “the mesendoderm”. Evidence for the existence of the mesendoderm has been collecting for decades [3]. When individual cells in early embryos were labelled and the fate of these cells explored, it was observed that some labelled single cells gave rise to cell types arising from both the mesoderm and the endoderm. In the developing nematode *C.elegans* at the 4 cell stage of development there is a single mesendodermal blastomere that, during the subsequent cleavage stage, will give rise to two daughter blastomeres: one a mesodermal progenitor and the other an endodermal progenitor [4]. Origins of the mesendoderm population were identified by removing cells fated to become ectoderm or endoderm, and then culturing both tissues in close proximity, resulting in the formation of cells of a mesodermal origin [5]. Studies on the nematodes and zebrafish have revealed a bi-potent cell type that is able to generate both mesoderm and endoderm. The tissues that are generated from the mesendoderm are shown in Fig. (1).

The existence of a bi-potent mesendodermal progenitor was supported by studies showing shared gene expression profiles in candidate mesendodermal cells across multiple species. The soluble factor Nodal (and related factors) was consistently identified as a key regulator of mesendoderm development in species as far ranging as the African clawed frog *Xenopus*, zebrafish and the mouse [6]. Binding of Nodal to its receptor activated phosphorylation of the Smad pathway inducing gene expression. Amongst the downstream targets of Nodal signalling is the transcriptional regulator Eomesodermin (*Eomes*) [7]. Eomesodermin then functions in multiple ways to focus differentiation along the mesendoderm lineages. Eomesodermin inhibits ectoderm differentiation [8]. Eomesodermin also induces expression of a range of transcription factors critical to mesendoderm development including Brachyury (*Bry/T*), Mix-like 1 (*Mix11*) and Goosecoid (*Gsc*). These form transcriptional complexes that regulate mesendoderm

differentiation. Lhx1, another downstream target of Eomesodermin also partners with other transcriptional regulators that play critical roles in mesendoderm development [9]. A grossly simplified model of mesendoderm formation is presented in Fig. (2).

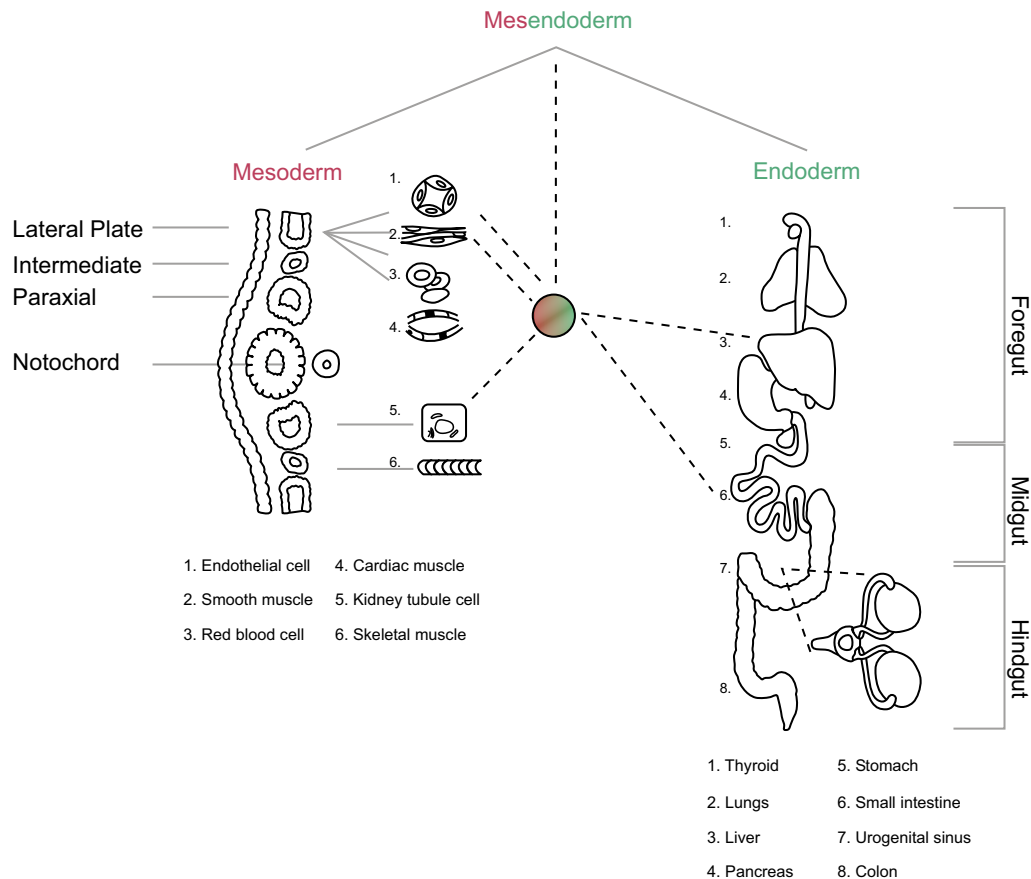


**Fig. (1).** Derivatives of the mesendoderm. The mesendoderm gives rise to cell types from both the mesoderm (red) and endoderm (green) germ layers. Mesoderm derivatives include: endothelial cells, smooth muscle cells, red blood cells and cardiac cells from the lateral plate mesoderm; kidney tubule cells from intermediate mesoderm and skeletal muscle from the paraxial mesoderm. Endoderm derivatives include: the thyroid, lungs, liver and pancreas from the foregut endoderm; stomach and small intestine from the midgut endoderm and urogenital sinus and colon from the hindgut endoderm.

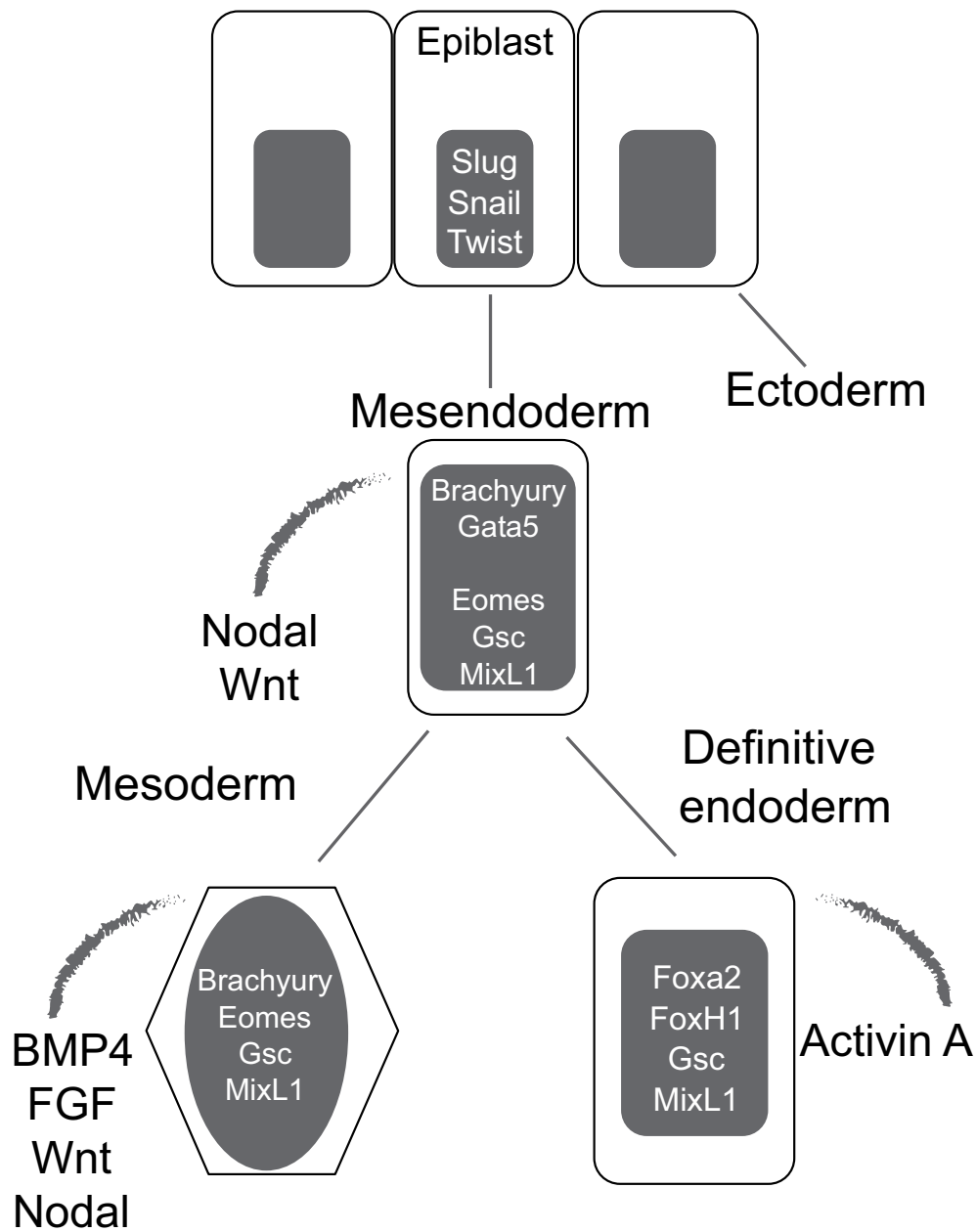


**Fig. (2).** A simplified model of mesendoderm formation. Rounded rectangular cells represent E-cadherin<sup>+</sup> epithelial cells. Gradients of critical soluble morphogenic and growth factors are shown next to each developmental stage. Transcription factors playing critical roles in each lineage are shown within the schematic nucleus.

## Mesoderm Differentiation

Eomesodermin can induce expression of genes which play critical roles in mesoderm development [7]. In particular, cardiac and head mesoderm is derived from *Eomes*-expressing progenitors [10]. Other transcriptional regulators expressed in the mesendoderm develop more restricted roles in the mesoderm including Brachyury that becomes restricted to the axial mesoderm responsible for notochord formation. The soluble factor Bone morphogenetic factor-4 (Bmp4) is an essential requirement for mesoderm development across many species [11]. Genetic ablation of the gene encoding Bmp4 in the mouse leads to early embryonic lethality with many embryos failing to proceed through gastrulation or form mesodermal cells [12]. A combination of soluble factor signalling through Bmp4, and transcriptional regulator complexes (including Brachyury, Mixl1, eomesodermin and goosecoid) lead to expression of mesoderm-specific transcription factors such as *Mesp1* and commit the progenitor cells which have received these signals to become mesodermal cells. Specification of mesoderm into more committed progenitors requires a range of different soluble factors generating a gradient of cell signalling according to cellular location within the developing embryo. This gradient of signalling in turn initiates differentiation transcriptional programmes leading the specification of distinct types of mesoderm progenitors. This is a gross simplification of a truly complex system, however it serves to offer us a model for mimicking early embryological events *in vitro* to generate cell types that may be of use for regenerative medicine.

## Endoderm Specification

The endoderm gives rise to the epithelial lining of the three major internal tubes: the respiratory, gastrointestinal and genitourinary tracts, as well as the organs that branch off them (Fig. 1). Development of definitive endoderm (DE) in mammals begins at gastrulation, when endoderm precursors migrate from the epiblast to the anterior primitive streak followed by implantation into the visceral endoderm (VE). This movement is facilitated by an epithelial-to-mesenchymal transition (EMT) which is dependent upon the expression of genes *Snail* and *Slug*, both of which momentarily suppress E-cadherin [13]. In *Xenopus* and zebrafish, migration of endodermal precursors is dependent upon mesoderm-derived

Sdf1/Cxcl12b, which acts on endoderm expressing Cxcr4 [14]. Observations in Zebrafish models suggest that there is a feedback check on differentiation of cells and its neighbouring environment [15]. Inhibition of the Activin A receptor and Nodal-related proteins in *Xenopus* embryo provided the first insight into the underlying mechanisms of endoderm formation in vertebrates [13]. Activin and nodal are part of the TGF- $\beta$  family. Findings from explant studies suggested that the inhibition of TGF- $\beta$  signalling in the endoderm lead to increased expression of mesodermal and ectodermal markers at the cost of endoderm marker expression. The separation of the three embryonic germ layers is in part, due to TGF- $\beta$  signalling [16]. Nodal signalling, a subclass of the TGF- $\beta$  superfamily has been shown to induce formation of mesoderm and endoderm in vertebrates [17]. Ligands that belong to the TGF- $\beta$  family (including Activin A and Nodal) operate through the homologous intracellular mediators Smad2 and Smad3 [18]. Mutations of the *Nodal* allele led to the loss of endoderm differentiation in embryos due to reductions in gene expression of *Smad2* and *Smad3* [18]. Overexpression of Activin A or Nodal-related factors in *Xenopus* and zebrafish however, confirmed mesodermal and endodermal cell fates required a gradient of nodal and activin-related signals [6, 19]. Cells furthest from the source of Nodal express mesodermal genes, due to the exposure of low concentration of Nodal [20, 21]. The canonical Wnt signalling pathway activates Nodal expression during embryogenesis [13]. Specification of DE requires both Wnt signalling and Nodal expression as mouse embryos lacking *Nodal* fail to form a primitive streak [22]. *Wnt3*<sup>-/-</sup> mice do not form a primitive streak or mesoderm highlighting its importance in germ layer formation [23]. *Wnt3* expression during gastrulation is found in the posterior visceral endoderm shortly before mesendodermal cells begin migrating into the primitive streak [24]. Wnt3 has been shown to induce Nodal (and *vice versa*) through feedback signalling which demonstrates the ability of the canonical Wnt pathway to directly enhance endoderm generation in mammals [23].

In the vast network of endodermal transcription factors, there are two key families: the GATA family and the FoxA family of Forkhead transcription factors. Members of both gene families are downstream targets of Nodal, however, the direct mechanisms regulating them are still poorly understood. *Gata4*, *Gata5* and



*Gata6* play roles in endoderm development [25]. *Gata4*<sup>-/-</sup> and *Gata6*<sup>-/-</sup> embryos exhibit reduced development of both the visceral endoderm and the definitive endoderm however *Gata5*<sup>-/-</sup> mice did not show any endoderm defects [26 - 28]. Inactivation of members of the FoxA family of Forkhead genes results in a reduction but not a cessation of endoderm generation [29]. *FoxA2* is required for the formation of the foregut, but not the mid- or hindgut [30]. Members of the GATA and Forkhead families are proposed to synergistically form a complex stimulating endoderm gene transcription [13, 31, 32]. Downstream factors stemming from the Nodal pathway Sox17 and MixL1 have also been shown to play a part in endoderm generation [33]. In the developing mouse embryo, *Sox17* expression appears in the DE between 7.5-8.5 days post coitus (dpc). *Sox17*<sup>-/-</sup> mice show a reduction in DE formation with a failure of midgut expansion and elevated levels of apoptosis in the foregut [34]. These findings suggest that Sox17 plays a role in maintaining endoderm integrity. *Mixer* has been shown to regulate *Sox17* and other endodermal genes through feedback loops involving members of the GATA family [35]. *Mixl1*<sup>-/-</sup> mouse embryos exhibit reduced DE generation and deformities in the hindgut development [36]. *Mixl1*-overexpression in *Xenopus* induced surplus formation of the endoderm with an increase in Nodal expression [37]. These findings suggest that *Mixl1* is part of a feedback loop regulating Nodal.

### ***In vitro* Models of Mesendoderm Formation**

Dissecting the molecular pathways regulating the formation of the cells, tissues and organs derived from the mesendoderm has been conducted in a number of animal models. Simpler organisms such as the nematode *C.elegans* have proven useful. Externally fertilising species such as the African clawed frog *Xenopus* and zebrafish have also been useful as individual cells in the early embryo can be labelled and their derivative cell types assessed for retention of the label. The development of null mutant mouse strains proved a boon for understanding the specific roles of genes in mesendoderm development. In many cases, the genes ablated have proven essential for embryonic survival and the null mutant embryos have died *in utero*. The intra-uterine development of the mouse embryo has also proven to be a hurdle for analyzing developmental processes.

***Embryonic Stem (ES) Cell Differentiation as in vitro Model of Mesendoderm Development***

A number of research groups have capitalized on the ability of embryonic stem (ES) cells to remain pluripotent under controlled cell culture conditions to recapitulate developmental processes and events *in vitro* [38]. For mouse ES cells this typically requires administration of leukemia inhibitory factor (LIF) to culture medium. Once LIF is removed, mouse ES cells will spontaneously differentiate according to the signals the ES cells receive from the cell culture environment. Embryonic stem (ES) cells are derived from the inner cell mass of the blastocyst and are extremely useful pluripotent, undifferentiated cells that have the capability to generate any cell type in the body. ES cells can also be used as an *in vitro* model of embryogenesis. This is particularly useful as mammalian development is challenging to study due to the *in utero* gestation and small size of early embryos. ES cell cultures can be scaled up, genetically modified, exposed to chemically defined media and directed along specific differentiation pathways. Some strategies used for generating and isolating mesendoderm, endoderm and mesoderm progenitors during pluripotent stem cell *in vitro* differentiation are presented in Fig. (3).

ES cells derived from the mouse or humans have been used to identify critical stages and processes in mesendoderm development. Upon withdrawal of any agents maintaining self-renewal, ES cells will begin to spontaneously differentiate *in vitro*. The direction of differentiation will depend upon the signals present in the cell culture system. Soluble growth factors, morphogens, cytokines and chemokines can all induce differentiation. These factors, as well as components of the media, exogenously added additives (vitamins, salts, lipids) or inhibitors can all be included to drive differentiation along specific lineages, or to improve the yield of specific cell types. The surface on which the ES cells differentiate can also influence differentiation. Different extracellular matrix components such as fibronectin, laminin or vitronectin activate distinct integrin proteins and transduce different signalling into the ES cell cultures. Stiffness of the matrix on which cells are growing also influences differentiation [39]. The addition of fetal calf serum drives ES differentiation away from ectodermal lineages towards mesendoderm. In serum-free, chemically-defined systems, the addition of soluble Nodal directs

ES cell differentiation towards mesendoderm [40]. Once ES cells have been differentiated out of their self-renewing state, genes specific for the mesendoderm lineage will be expressed. These genes can be used as indicators of mesendoderm differentiation either in mRNA readout systems or as tags which can be utilized to enrich and purify mesendoderm from all other cells in the differentiation culture.

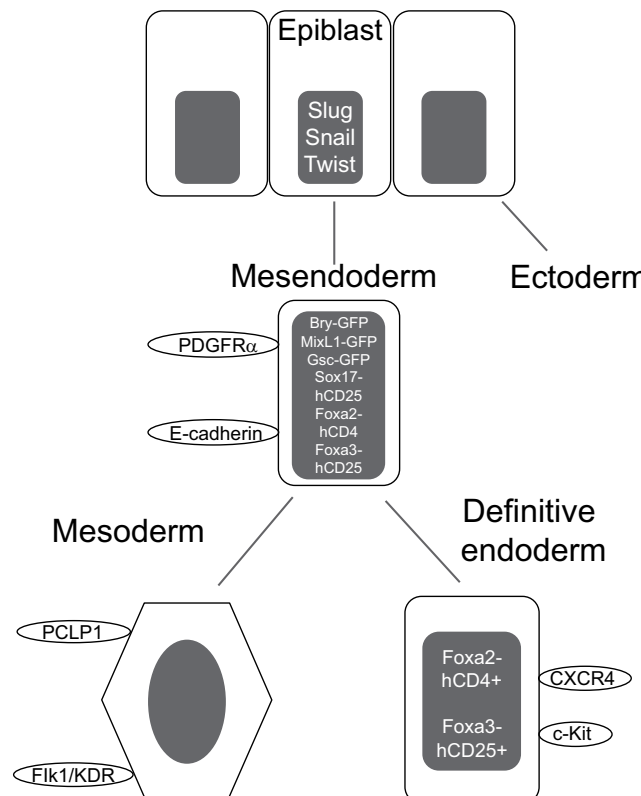


**Fig. (3).** Differentiating cultures of pluripotent stem cells such as ES and iPS cells can be purified at distinct steps of differentiation using a broad range of methodologies. Lineage- or stage-dependent surface markers are indicated here including PDGFR $\alpha$  and E-cadherin for mesendoderm. Reporter transgenes (represented within the nucleus of each cell type) can be used if coupled to a fluorescent protein such as GFP (green fluorescent protein) or used to drive a surface protein such as human CD4 (hCD4) or human CD25 (hCD25) on the cell surface. Fluorescently conjugated monoclonal antibodies against these human cell surface proteins can then be used to distinguish mouse cells at different stages of differentiation allowing for purification, transcriptome analysis or re-culture.

A number of systems have been developed using the promoter regions of mesendoderm-specific genes such as Brachyury (*T*), goosecoid (*Gsc*) or Mixl1 to

drive fluorescent protein expression thus indicating successful differentiation into the mesendoderm. The regulatory elements driving T, Gsc and Mixl1 have all been used to drive green fluorescent protein (GFP) expression in ES differentiation cultures. When cells expressing GFP are purified using fluorescence-activated cell sorting (FACS) they were found to express high levels of mesendoderm genes (Fig. 3). Combining this with cell surface protein expression can help improve the purity of mesendoderm differentiation. Tada and colleagues found that Gsc-GFP<sup>+</sup> cells express the epithelial (E)-cadherin and the platelet-derived growth factor receptor alpha chain and that FACS can be used to purify this population [41]. Similar approaches can be used in the differentiation of human ES (hES) cell cultures to obtain useful quantities of purified mesendodermal cells which can then be used in tissue engineering or 3D printing. Other groups have used mesendodermal regulatory elements to drive expression of human surface proteins on mouse cells. Species-specific fluorescent antibodies against these non-functional human surface proteins (CD4 or CD25) can then detect surface expression of these molecules and be used to monitor mesendoderm development or purify these cells by FACS [42].

Mesendodermal cells derived *in vitro* from ES cultures can then be differentiated into mesodermal cells or endoderm-derived lineages. For example, Bry-GFP<sup>+</sup> cells purified by FACS have been used to differentiate mesodermal lineages such as hematopoietic and endothelial lineages as well as endodermal lineages including pancreatic and hepatic lineages [43 - 45]. Modulating mesendoderm regulators in ES differentiation cultures can improve the yield of desired cell types. Activation of inducible *Mixl1* gene accelerated generation of mesodermal and endodermal cell types [46].

Following differentiation from mesendoderm, cell-surface markers can identify mesodermal progenitors. Mesodermal cells lack epithelial surface proteins during epithelial-mesenchymal transition. The vascular endothelial growth factor-2, also known as Flk1 or KDR (in humans) is expressed on the surface of lateral plate mesodermal cells fated to become blood or blood vessel progenitors [47]. Therefore mesodermal differentiation to the E-cadherin<sup>-</sup> Flk1<sup>+</sup> stage allows for enrichment of lateral plate mesoderm. The hematopoietic committed Flk1<sup>+</sup> population could be further enriched according to  $\alpha$ 4-integrin or podocalyxin

expression [48, 49]. Vascular and cardiac mesodermal progenitors derived from ES differentiation cultures can also be purified using a different combination of surface markers. Endodermal progenitors can also be identified from ES differentiation cultures. A combination of surface expression of CXCR4 and c-Kit has proven to be an effective means for assessing endodermal differentiation *in vitro*. In the context of embryonic stem (ES) and induced pluripotent stem (iPS) cell cultures, feedback from the differentiating mesoderm influences the formation and expansion of endodermal precursors. Depending on the feedback provided by the mesoderm, endodermal precursors may differentiate within a heterogeneous culture or die *in vitro* [13]. Together, this highlights the importance of mesoderm-endoderm interactions and the development of the later during gastrulation. This will be expanded upon in this chapter.

### ***Induced Pluripotent Stem Cells as a Novel Source of Mesendodermal Progenitors for Regenerative Medicine***

While ES cells have been used extensively since the early 1980s, their use for regenerative medicine was limited to helping define appropriate differentiation conditions to generate cell types useful for regenerative therapies. The utility of pluripotent stem cells for regenerative medicine changed dramatically when, in 2006, Shinya Yamanaka and colleagues reported the generation of induced pluripotent stem (iPS) cells from terminally differentiated adult fibroblasts. This revolution led to the widespread and routine production of iPS cell lines from a range of species including humans [50]. Induced pluripotent stem cells exhibit very similar properties to ES cells including pluripotency, teratoma formation and the ability to differentiate into a broad range of cell types upon receiving the appropriate signals *in vitro*. Similar to ES cells, iPS can also be potentially used for therapies, disease models or drug screening. One advantage they have over ES is that they can be made readily from adult cells, avoiding the ethically challenging aspects of ES cell biology. Patient-specific iPS have been generated in which the genetic lesion underpinning the pathology the patients experience has then been repaired [51 - 53]. Since the discovery of iPS cells, groups have made great strides in publishing cellular models outlining a vast multitude of conditions and potential therapies. Here, we will show the current standings of differentiation of mature cell types and how these can be implemented for regenerative medicine.

## Modelling Interactions Between Endoderm- and Mesoderm-derived Cell Types Using Pluripotent Stem Cells

As shown in Table 1, many endoderm-derived tissues and organs have a significant mesoderm-derived component. To form physiologically and medically relevant cell types, tissues or organs for regenerative medicine, an understanding of how the mesendoderm gives rise to these complex biological structures is required. Here, we will describe medically important organ systems that are being mimicked *in vitro* to generate useful 3D structures for regenerative medical interventions.

### *Differentiation of Pancreatic $\beta$ -cells as a Treatment for Diabetes*

The pancreas is often described as two organs with distinct endocrine and exocrine components [54]. The exocrine acinar cells are responsible for the production of digestive enzymes whereas the endocrine cells of the islets of Langerhans regulate blood sugar levels [54]. The insulin-producing cell type of the islet of Langerhans is the  $\beta$ -cell. Autoimmune destruction of the  $\beta$ -cell leads to type-1 diabetes [55]. Type-2 diabetes manifests as resistance to insulin in the peripheral tissues [55]. Collectively, diabetes affects 300 million people worldwide [56]. One of the biggest limitations in curing type-1 diabetes is finding a renewable source of functional  $\beta$ -cells. Generation of mature, functional  $\beta$ -cells from embryonic and induced pluripotent stem cells has raised the exciting possibility for a near-limitless source of  $\beta$ -cells for transplantation [38].

The pancreas is an endodermal organ at the posterior foregut level [57]. The sites of pancreatic induction occur precisely where the endodermal epithelium contacts the mesodermal endothelium of major blood vessels [1]. Pancreatic progenitors are found at E8.5 in the mouse with expression of homeodomain transcription factor *Pdx1* [54]. Pancreatic buds will then form from  $Pdx1^+$  cells [58]. Culturing endodermal cells with the dorsal aortae induces expression of insulin and *Pdx1*, where expression was found adjacent to the endothelium, highlighting the importance of endothelial cells in pancreatic cell induction [1]. While *Pdx1* is the first indicator of pancreatic generation, it is not solely limited to the pancreas [38]. It is also found in other foregut endodermal tissues such as the stomach and

duodenum [38]. Commitment of pancreatic cell differentiation occurs with co-expression of *Pdx1* with transcription factor *Ptf1a* [59]. Secretion of Fibroblast growth factor 10 (FGF10) from the mesenchyme expands *Pdx1*<sup>+</sup>/*Ptf1a*<sup>+</sup> cell number [38]. Genetic lineage tracing studies have found that *Pdx1*<sup>+</sup>/*Ptf1a*<sup>+</sup> progenitor cells give rise to all mature pancreatic cells [59, 60]. Furthermore, ablation or mutation of *Pdx1* and/or *Ptf1a* has resulted in blunted pancreatic growth and differentiation [59]. There have been few studies that examine human embryonic pancreas development, however, the similarities between rodent and human pancreatic organogenesis is evidently clear [61]. Understanding the embryology of pancreatic development has paved the way for differentiation of pancreatic cells from stem cells.

Equipped with this knowledge, researchers have been able to generate mature, functional  $\beta$ -cells *in vitro* from ES and iPS cells. The protocol established by D'Amour and colleagues has been the most routinely used, however, modifications have been made. Briefly, DE was induced by Activin-A. Pancreatic fate was then specified through retinoic acid and FGF10 signalling [62]. Maturation of  $\beta$ -cells included supplementation with IGF-1, HGF, and extendin-1 [62]. Confirmation of the differentiated cell types was sequential, with induction of FOXA2<sup>+</sup>, CXCR4<sup>+</sup>, SOX17<sup>+</sup> endoderm, generation of PDX1<sup>+</sup>/PDF1a<sup>+</sup> pancreatic progenitors and development of NGN3<sup>+</sup>/NKX2.2<sup>+</sup> endocrine cells [38]. Production of insulin secreting cells was determined by the expression of C-peptide, which is released when proinsulin is converted to insulin [38].

Transplantation of  $\beta$ -cells for the purpose of curative purposes has had mixed results. One of the biggest hurdles is the maturation of  $\beta$ -cells to produce insulin prior to or following transplantation. In streptozocin-induced diabetic mice, Jiang and colleagues transplanted glucose-responsive stem cell derived  $\beta$ -cells that reversed the hyperglycemic state of 30% of mice. Graft analysis showed the recipient mice expressed human C-peptide and PDX1 [63]. Addressing the issue of the amount of  $\beta$ -cells derived from stem cells, Pagliuca and colleagues were able to generate hundreds of millions of insulin-producing  $\beta$ -cells *in vitro*. Following transplantation, the differentiated  $\beta$ -cells were able to secrete human insulin in a glucose-regulated manner [56].

## **Developing New Systems for Regenerative Medical Intervention During Liver Disease**

The liver is a multi-purpose organ that serves roles in metabolic, endocrine and exocrine functions [64]. These functions largely serve to restore homeostasis through detoxification, metabolism of dietary compounds, regulation of glucose and control of blood homeostasis [64]. The primary cell type of the liver is the hepatocyte [65]. Hepatocytes and biliary epithelial cells (cholangyocytes) are endodermal derivatives supported by mesodermal-derived stromal cells, endothelial cells, Kupffer cells and blood vessels [65].

The embryological origin of the liver begins at day 8 of gestation (E8.0), located in the foregut endoderm [65]. At E9.0, the embryonic liver forms a thickened epithelium, making it morphologically distinguishable [66]. The next stage of hepatogenesis is the formation of the liver bud. This occurs at E9.5 when endodermal hepatoblasts (hepatocyte progenitors) shed from the epithelium and occupy the mesodermal septum transversum mesenchyme (STM) [66]. The STM gives rise to the mesodermal cell types of the liver including: macrophages, stromal fibroblasts, sinusoidal endothelial cells and stellate cells [67]. At E10.5-E11.0 of development, haematopoietic progenitors migrate from the yolk sac, aorta-gonad-mesonephros and placenta to the foetal liver, which becomes one of the major sites of blood production [68]. This is supplemented as the liver becomes vascularised and populated by haematopoietic cells between E10.0-E15.0 [64].

Endothelial cells which reside between the epithelium and STM aid in the migration of hepatoblasts into the stroma [69]. Hepatoblasts are bi-potential as they can differentiate into cholangyocytes and hepatocytes depending on their location in the developing liver. Hepatoblasts in the portal vein will differentiate into cholangyocytes that will line the lumen whereas hepatoblasts in the parenchyma will differentiate into hepatocytes [64]. Maturation and function of these cells begins at E13.0 and continues after birth [69]. In all, hepatogenesis demonstrates the sequence of tissue interactions between the endoderm and mesoderm.



Hepatoblast specification and regulation of liver morphogenesis are dependent upon vascular endothelial growth factor receptor 2 (KDR) [70]. Prior to hepatic specification, KDR<sup>+</sup> cells are located in the endoderm at E8.0 with expression waning throughout hepatogenesis [70]. KDR<sup>-/-</sup> mouse embryos lacked the development of endothelial cells, which in turn, instruct liver development [2]. Endothelial cells have also been shown to aid in hepatocyte and cholangiocyte specification through Wnt and Notch pathways [71]. While KDR expressing endothelial cells were believed to be restricted to the mesodermal lineage, Goldman and colleagues revealed the bi-potency of KDR<sup>+</sup> cells using human and mouse embryonic stem cells (2). Endodermal cells lack KDR expression, however, when cultured in media supporting differentiation of hepatic cells, two populations arise; KDR<sup>+</sup> hepatic progenitors and KDR<sup>-</sup> hepatic cells [2]. The KDR<sup>+</sup> hepatic progenitors serve to stimulate differentiation and maturation of the KDR<sup>-</sup> hepatic cells, which further enforces the interaction between the mesoderm and endoderm [70].

Understanding the development of the hepatic niche *in vivo* paved the way for researchers to recapitulate the development of the liver *in vitro* using stem cells. Differentiation of hepatocytes from stem cells begins at the endoderm. Generating DE from stem cells is routine with the addition of Activin-A and Wnt3A [72]. Next, supplementation with FGF-2 and BMP-4 initiates hepatic induction [73]. Hepatoblast maturation and expansion requires the addition of hepatic growth factor, FGF4, Oncostatin M and Dexamethasone in cultures [64]. Differentiated hepatic-like cells look and function like hepatocytes. These functions include: secretion of albumin, storage of glycogen, expression of hepatic enzymes and metabolism of drugs [74].

Chronic liver diseases such as cirrhosis and hepatitis affect millions worldwide [75]. Transplantation is the only curative means for chronic liver diseases [75]. Other means of restoration are needed. One such possibility is the transplantation of hepatocytes, which could delay the progression of the disease and act as a conduit for patients awaiting a liver transplant [76]. Despite the success of hepatic-like cell differentiation from stem cells, their implantation and integration into mice with various liver injury models have shown only a modest rescue of function. Their inability to repopulate diseased livers *in vivo* may be attributed to

stem cells that have not fully matured into hepatocytes [70]. Success was seen in hepatectomised mouse given a bioartificial liver coupled with mES cell-derived hepatocytes [77]. Liver- function and overall survival improved compared to mice that did not receive the mES-derived hepatocytes [77]. While the use of stem cell derived hepatocytes for regenerative purposes is still being refined, they have been a useful source for modelling liver diseases. Yoshida and colleagues demonstrated the prowess of induced pluripotent stem cells at modelling the hepatitis C virus, which can be expanded upon for potential drug treatments [78].

### **Endodermal and Mesodermal Derivative Lineages in Treatment for Disease of the Genitourinary Tract**

Interactions between the mesoderm and endoderm-derivative cell lineages can be observed in the genitourinary tract. Derivatives that comprise the mesodermal germ layer here include: the nephron, ureter, renal pelvis, glomerular endothelial and mesangial cells, renal interstitial cells, adventitial fibroblasts and ureteral and bladder smooth muscle [78]. Endodermal derivatives include the luminal and basal epithelial cells of the bladder, urethra and prostate [78]. These mesodermal cell types originate from a narrow strip of tissue located bilateral of the embryonic midline termed the intermediate mesoderm [79]. Preceding the formation of the kidney and ureter is the mesoderm-derived nephric duct. During the development of the nephric duct, the surrounding intermediate mesoderm undergoes a mesenchymal-to-epithelial (MET) transformation [80]. This inductive process results in the generation of mature nephrons.

### **Development of the Bi-potential Gonad and Reproductive Tracts**

The intermediate mesoderm gives rise to the urogenital system (kidneys, gonads and associated ducts). The reproductive tract develops as a sexually bi-potential structure, in close association with the urinary tract, for the first 7 weeks of human development [81], (Fig. 1). The intermediate mesoderm extends to form bilateral nephrogenic chords during the second week of development in the human. These chords will eventually become bilateral urogenital ridges around 5 weeks when development of gonadal tissue starts with the indifferent gonadal phase. At this stage the mesothelium toward the middle of the mesonephros thickens to form the

gonadal urogenital ridges. Primary sex chords (epithelial digitations) form and extend into the mesenchyme and remain as undifferentiated gonadal ridges that are invaded by migrating primordial germ cells during week 6 of gestation (see later). Three weeks of gestation heralds the formation of the pronephros, a primitive kidney, which is continuous caudally with the mesonephros (Wolffian duct). Around 4 weeks this caudal end meets and fuses with an endoderm lined sinus at the caudal end of the gut tube called the cloaca. The region anterior to the fusion point will become the bladder and pelvic urethra of the neonate. The posterior portion of the cloaca forms the urogenital sinus and the anorectal canal. The cranial region of the Wolffian duct regresses to form a lumened duct that will persist in the male and form the efferent ducts, epididymides and vasa deferentia.

At around 6 weeks of gestation, focal infolding of the intermediate mesoderm-derived coelomic epithelium, lateral to the mesonephric ducts occurs to generate the paramesonephric ducts [82]. These ducts are the precursors of the uterus, uterine ducts, cervix and upper portion of the vagina in the female. Hence by the end of week six of gestation the foetus possesses two genital ridges, each on the medial surface of a pair of patent mesonephric (Wolffian) ducts and collectively called the urogenital ridges. Lateral to each urogenital ridge is a paramesonephric (Müllerian) duct. The metanephros, mesonephric ducts and paramesonephric ducts all join to the bi-potential urogenital sinus. Up to this point, both male and female foetuses are indistinguishable. Sex determination and sexual differentiation occurs after seven weeks of gestation, and once the gonadal ridges have been populated with migrating primordial germ cells [83]. This chapter will not deal with sexual differentiation, the reader is directed to recent reviews [84, 85].

### **Development of Kidney Organoids from Human Embryonic and Induced Pluripotent Stem Cells as a Model of Kidney Development**

Kidney transplants are the most common form of organ transplantation worldwide. There is a clear need for new medical interventions for the treatment of renal disease. The formation of the kidney is a highly complex process however; recapitulation of renal organogenesis *in vitro* offers great hope to alleviate the challenges experienced by patients with renal failure. Development

of the mammalian kidney is a product of the reciprocal interactions between the endodermal uretic bud and mesodermal mesenchyme [80]. Derivatives of the uretic bud give rise to the renal collecting ducts, epithelial lining of the renal calyces and the urothelial lining of the ureter [80]. Conversely, the mesenchyme undergoes a mesenchyme-to-epithelial transition and leads to the differentiation of the nephron segments, including: the glomerulus, proximal and distal tubules and the loops of Henle [80]. Differentiation of embryonic and induced pluripotent stem cells into renal lineages has been successful [86 - 89]. Vigneau and colleagues utilized the Bry-GFP mouse ES cell line to obtain renal progenitor cells [91]. ES cells were differentiated to generate Bry-GFP<sup>+</sup> cells that were then purified by fluorescence-activated cell sorting (FACS). Bry-GFP<sup>+</sup> progenitors could form renal progenitors expressing marker genes such Cadherin-11 and Wt1. Upon transplantation into live neonatal kidneys, these cells could integrate into the renal tubules [90].

Takasato and colleagues have recently reported the successful induction of both the uretic epithelium and metanephric mesenchyme *in vitro* [92]. Their system has also been extended for induction of kidney formation in organoid cultures [91]. Briefly, treatment of human ES and iPS cells with FGF9 and retinoic acid promotes differentiation of the uretic epithelium with exposed Wnt signalling aiding in the differentiation of the metanephric mesenchyme [91]. Indeed, differentiation of both cells types have been made possible by replicating the signalling and temporo-spatial development of the kidney *in vivo*. Generation of kidney organoids have given rise to the exciting possibility of testing models of kidney diseases and the ability to screen drugs for toxicity for cellular therapy.

### **The Urogenital Sinus and Accompanying Organs**

The urogenital sinus originates initially as a sub-compartment of the cloaca; a transient endoderm-derived cavity, located at the posterior end of the gut [92]. Cross talk between the mesenchyme and epithelium are critical for the development of urogenital tissues. Secretion of *Sonic hedgehog* (Shh) from the endoderm is key to patterning and separation of the cloaca [92]. Failure of the cloaca to separate during foetal development has severe clinical consequences and is thought to underlie the pathogenesis of a wide range of urogenital

malformations [80].

The genitourinary tract (GUT) encompasses the entirety of the genital ridge as well as the organs that filter waste and fluid from the blood: the kidneys, ureters, bladder and the urethra. The kidneys also control blood pressure through the secretion of hormones, angiotensin and aldosterone [93]. The passage of urine from its production by the nephron and elimination by the urethra highlights the most critical function of the GUT [94]. The tract is susceptible to malfunctions at any point, which may impair the complete emptying of the bladder. Issues involving the bladder are currently remedied by surgically replacing the bladder wall with either intestinal or stomach tissue [95]. However, the transplantation leads to eventual salt imbalances, infection, stones and in some cases, cancer [96]. Ideally, the replacement of the bladder wall should be comprised of a bioengineered scaffold augmented with stem cells that promote cell growth, proliferation and survival.

Kidney diseases result in the degradation of the microstructural components, which lead to an obstruction in the passage of urine [94]. The accumulation of urine along the tract leads to infection and scarring and eventual failure [97]. The diseases that fall under this category include: urinary tract infections, glomerulonephritis, polycystic kidney disease, haemolytic uremic syndrome and hydronephrosis [97]. The male genital tract comprises of the bladder, urethra, prostate, seminal vesicles, gonads, penis and testes [94]. Physiologically, they produce and transport sperm, secrete sex hormones and facilitate erections. Complications in the tract may lead to infertility and erectile dysfunction [95]. Correlations of the genital tract with the urinary tract lead to clashes in diagnosis, which also complicates matters. Here, stem cells can be used to model the development of the male genital tract, including the prostate. This would provide insight into the mechanisms that underpin normal growth which are lacking, and applied into a cell/scaffold graft to alleviate impairments of the genital tract.

### **Differentiation of Urothelium from Mouse, Human and Adult Stem Cells.**

The urothelium of the bladder is unique as it lines the luminal surface and acts as a near impermeable membrane [98]. This tissue is composed of basal,

intermediate and superficial cells, which express unique structural proteins called uroplakins (UPK) [99]. Assembly of the four subtypes of UPK (UPK1a, UPK1b, UPK2 and UPK3) results in plaque formation on the luminal surface [98]. Presence of UPK is a marker of urothelial differentiation. Of all the cell types that have been differentiated from ES and iPS cells, studies looking into the differentiation of urothelial cells are limited. Differentiation of urothelium from human ES and iPS cells as well as mouse ES cells has been reported [98, 100, 101]. In mouse ES cells, GATA4 signalling has been shown to drive urothelial differentiation, however, in human ES cells; GATA4 signalling was shown to be minimal [98, 101].

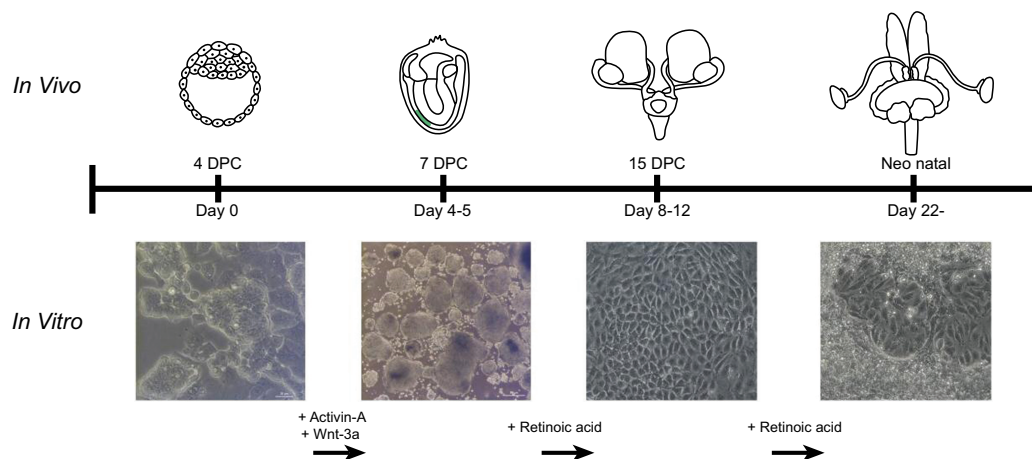


**Fig. (4).** Timeline of *in vivo* development of the urogenital sinus and *in vitro* differentiation of urothelium mouse embryonic stem cells. The inner cell mass of the blastocyst (*in vivo*, 4 days post coitus (DPC)) gives rise to all three germ layers: the ectoderm, the mesoderm and the endoderm (*in vivo*, 7 DPC, green). Mimicking this *in vitro* with mouse embryonic stem cells, cultures treated with Activin-A and Wnt-3a lead to definitive endoderm induction (*in vitro* Day 4-5). Development of the urogenital sinus continues from 15 DPC (*in vivo*) and matures after birth (neonatal). Differentiation of definitive endoderm into urothelium requires treatment with retinoic acid (*in vitro*, D8-12, D22-onwards).

As the bladder is of endodermal origin, the first step in the generation of urothelium (and all endodermal cell types) is the temporal differentiation of ES and iPS cells into DE with Activin A [72]. Following induction of DE, the above groups supplemented their cultures with retinoic acid and urothelial-specific medium for differentiation of urothelium in mouse and human ES and iPS cells respectively (Fig. 4) [98, 101]. Confirmation of urothelium was determined by

expression of the UPK proteins *via* immunohistochemical, real time RT-PCR and flow cytometric analyses [98, 101]. Despite the limited number of studies aiming to differentiate urothelium from ES and iPS cells, the above methodologies have shown that is possible to do so without the need for matrices or co-cultures. For tissue regenerative purposes, the next step would be to augment scaffolds with differentiated urothelial cells to repair damaged tissue.

### **Primordial Germ Cell Development**

Many of the processes of early specification and migration in the human are assumed similar to those in other mammalian models including the mouse [102]. Primordial germ cells (PGC) in mice originate from proximal epiblast cells to form a cluster of precursor PGCs in the incipient allantois in extra-embryonic mesoderm at approximately E7.25 [103, 104]. Following specification, their numbers expand as they start to migrate to and through the developing gut endoderm, into and through the mesentery to colonise the gonadal ridges [102]. Precursor PGCs are specified in the epiblast prior to gastrulation through bone morphogenic protein (BMP) signalling between the extra-embryonic ectoderm and visceral endoderm [83]. Mice lacking BMP2, BMP4, BMP8b or SMAD mediators of BMP receptor signalling all exhibit reduced induction and proliferation of early PGCs along with defective mesoderm formation and allantois development [105, 106]. Evidences show that it is extra-embryonic ectoderm derived BMPs acting on BMP receptors expressed by visceral endoderm that results in the formation of PGCs in a dose dependent manner [107]. In addition to inducing a founding population of PGCs in the mouse, BMPs are also important for PGC migration to, and proliferation at the genital ridge [108]. As well as gradients of stimulatory BMPs, the induction of epiblast cells to PGCs is also dependent on gradients of inhibitory factors [109]. BMPs subsequently induce expression of *Prdm1* that encodes the protein BLIMP1, a key regulator of PGC specification [110]. BLIMP1 acts to repress progression to the mesodermal somatic lineage [110, 111] and to promote epigenetic reprogramming of early PGCs [109].

***In vitro* Generation of PGCs and Regenerative Medicine**

Early PGCs can undergo de-differentiation into pluripotent germ cells when treated with FGF and LIF in culture due to suppression of *Prdm1* expression and BLIMP1 synthesis [112, 113]. This knowledge of BLIMP1 and its interactions with other key factors, PRDM14 and AP2g, that act to suppress mesodermal genes [109], have helped establish that the majority of epiblast cells from whole explants are all able to be directed to a PGC fate in the presence of BMP4 *in vitro* [114]. These PGCs can further differentiate to gametes that are able to produce viable offspring [115]. Hayashi and colleagues also demonstrated that PGCs could be derived from embryonic stem cells under specific culture regimen. Furthermore, iPSCs derived from somatic cells can be induced to form PGCs provides an exciting prospect in regenerative medicine [109].

As well as providing a model for the study of the molecular regulation of germ cell differentiation, it also has potential for a source of unlimited numbers of gametes for treatment of infertility, including transplantation. This is particularly pertinent to induced infertility in cancer patients following certain treatments (*e.g.* gametotoxic chemotherapies, whole body and gonad radiation therapies). Advancements in treatment protocols has resulted in increasing numbers of cancer survivors and hence significant subsequent morbidities due to resulting infertility [116]. This has led to clinical recommendations that sperm and egg banking to preserve fertility be considered prior to treatment [117]. Whilst this is an option for adolescent and adult patients, it is not an option for pre-pubertal patients. One potential future is the transplantation of germ stem cells isolated from the pre-pubertal gonad or of PGCs/germ stem cells derived in culture from iPSCs [115].

In the male, spermatogonial stem cells collected prior to chemotherapy might be transplanted back to the testis at a later appropriate date. Whilst this has been trialled in humans, no follow-up reports of long-term maintenance, which includes live births and fertility in these subjects is apparent [118, 119]. However, such successful outcome measures have been achieved in other mammals, including non-human primates [120, 121].



**Adipogenesis and Differentiation of Adipocytes from Stem Cells.**

Adipose tissue arises concurrently with the developing kidneys, urogenital sinus and primordial germ cells.

Mammals have two types of adipose tissue, white (WAT) and brown (BAT). Both WAT and BAT serve distinct roles in energy metabolism with WAT storing energy in the form of triglycerides while BAT expends energy as heat [122]. Lineage tracing studies have shown that BAT originates from myogenic factor 5 (Myf5)-expressing progenitors, compared to the non-Myf5 lineage progenitors that give rise to WAT [123]. WAT can be further subdivided into subcutaneous and visceral WAT, with visceral shown to have implications in metabolic dysfunction such as obesity [124].

Adipose tissue is currently thought to be derived from the mesoderm germ layer [122]. Characterisation of adipocyte differentiation has been described in two phases, determination and terminal phase [125]. The determination phase results in the conversion of a stem cell into a pre-adipocyte, the details of which remain largely unexplored [126]. The terminal phase of differentiation describes the maturation of pre-adipocytes using adipocyte cell lines 3T3-L1 and 3T3-F44a [125, 127]. These cell lines are useful as they are restricted into differentiating into other cell types and culturing primary adipocytes are difficult to maintain [125, 128].

Another model that can be utilised to detail adipogenesis is adipocytes derived from ESC and iPSCs. While ESCs and iPSCs recreate the key steps that occur during development *in vivo*, replicating the signalling events required for adipocyte differentiation *in vitro* is difficult [128]. It is useful then, to initiate differentiation into the adipocytes using growth factors known to terminally differentiate adipocytes [128]. Transcriptional regulation of adipocyte differentiation is largely due to peroxisome proliferator-activated receptor  $\gamma$ 2 (PPAR $\gamma$ 2) [128]. Therefore, differentiation of WAT from ESCs and iPSCs routinely use PPAR $\gamma$ 2 agonist such as rosiglitazone along with adipogenic factors insulin and dexamethasone [128, 126]. Further inclusion of all-trans retinoic acid aids in the differentiation of adipocytes *in vitro* [129, 126].

The above process describes the differentiation of adipocytes that resemble WAT phenotypically and functionally. Conversely, differentiation of brown-like adipocytes from ESCs and iPSCs has only recently been achieved [130 - 132, 128]. For differentiation of BAT, a combination of PPAR $\gamma$ 2, CCAAT/enhancer-binding protein  $\beta$  (CEPB $\beta$ ) and PR domain containing 16 (PRDM16) can be used [128]. Lee and Cowan (2014) describe the addition of lentiviruses of the above transcription factors for a high yield of brown adipocyte differentiation from human pluripotent stem cells [128]. Alternatively, addition of reported brown adipocyte inducer BMP7 can be added in cultures along with KIT ligand, tyrosine kinase 3 ligand, interleukin-6 and vascular endothelial growth factor [133, 132]. Confirmation of brown adipocyte differentiation from ESCs and iPSCs is expression of BAT specific genes *UCP1* and *PRDM16* and functional assays inducing thermogenesis from  $\beta$ -adrenergic receptor stimulation [132].

### **Mesendoderm and Tissue Engineering for Regenerative Medicine**

We have described the developmental processes regulating the formation of organs derived from the mesendoderm. While pluripotent stem cells offer tremendous hope for regenerative medicine, many of the differentiation protocols developed thus far have been lacking the architectural and three-dimensional (3D) signals that are essential for proper organogenesis *in vivo*. A revolution in engineering, 3D printing, is now being applied to modelling embryonic processes from stem cells to obtain material for transplantation that is more appropriate in tissue and organ architecture than previously considered feasible. Here, we will discuss the application of 3D printing to the formation of mesendoderm-derived tissues with some insight from our own experiences.

### ***Introduction to 3D Printing***

There are few technological innovations that have been received with as much as enthusiasm and excitement as 3D printing. The prospect of printing into the third dimension has captivated the imaginations of scientists and laypeople alike. The rapid development and decreasing cost of this technology has meant that the promise this technology has offered is now becoming a reality. 3D printing is the process of manufacturing a customised three-dimensional object. 3D printing,

otherwise known as additive manufacturing, was first developed by the engineer and scientist, Charles Hull. In the 1980s, Hull sought to improve the lengthy and error-prone process of producing plastic prototypes from photopolymers. In 1983, Hull produced the first 3D-printed object, a small plastic cup [134]. In 1986, Hull obtained the patent for *stereolithography* (one 3D printing technique which is outlined below), followed by a number of others on 3D printing technology [135]. 3D printing has since undergone extensive development and expansion so that a number of variations of the technology are now available for applications that range from commercial prototyping to medical implants, the food industry and weapon production in the defence forces [135].

To understand the digital workflow which gives rise to a 3D printed object, the different stages of the printing process have been detailed below and are represented in Fig. (5). The process of printing an object begins with a CAD (computer aided design) file. CAD is a commonplace method of developing a digital representation of a 3D objects and can be readily performed by a number of different available software [135]. Once a CAD file has been developed, the CAD model is converted into another file type known as .STL (standard tessellation language). STL files store information about each surface of the object in the form of vertices' coordinates. The .STL file is interpreted by the printer, which then performs another conversion to a G-file. The G-file is a deconstruction of the object into two-dimensional cross-sections which are then printed layer by layer on top of each other [135].

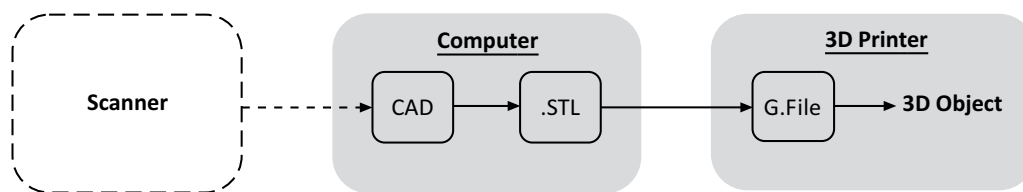


**Fig. (5).** Illustration showing the digital files and conversions involved in producing a 3D printed object. Note that the 3D CAD object may be based on a newly developed design or a scan of an existing object.

### **3D Printing Technologies**

There is currently a number of available 3D printing techniques, six of which have been briefly explained below. It should be noted that while the following

techniques use quite different technical approaches, the underlying principle of 3D printing (or additive manufacturing) remains the same. Each printer produces a specific 2D cross-sectional shape before shifting the existing layers and adding a subsequent 2D shape on top or below. Repeated additions of cross-sections finally result in the 3D object.

Stereolithography involves the hardening of a photopolymerizing liquid resin as UV light is beamed at a bath of resin. The beam is projected onto the base of the bath in the shape of a desired 2D cross-section. After the photopolymer is cross-linked, the cross-section is lifted by a stage and the next 2D layer can be solidified at the interface between the resin and UV light. This was the technique first described and patented by Charles Hull in 1986 [135]. Inkjet printing refers to the traditional method of printing ink onto paper in 2 dimensions. Two different techniques can be used for 3D inkjet printing as outlined include “drop on demand” and “continuous flow” printing. The principle of a drop on demand (DOD) inkjet printer is that pulses of voltage and pressure at the paper and ink interface direct the ink droplet to the desired place in the 2D plane. However, through reasonably simple modifications, this technique has been adapted to print in 3D. The adapted method works by printing ‘binding’ liquids in a way that binds a layer of powder (substrate particles 50 - 100  $\mu\text{m}$  diameter) into a specific 2D shape. A stage is then lowered after printing each layer, a further layer of particles is added on, and the next 2D cross-section can be added. This method of printing is not confined to use with photopolymerizing materials, so allows a greater diversity of substrates that can be bound by the printed liquid [135]. Continuous inkjet printing uses electrically charged plates as well as patterns of pressure waves in the printer head to direct droplets of ink to the desired site on the 2D paper. Once again, with reasonably simple modifications, the printer can also position droplets of liquids other than ink onto the 2D plane, which can then be lowered to print subsequent 2D cross sections from the STL file. Successive stage lowering and addition of cross-sections then produces the desired 3D construct. The benefit of this technique is that any liquid with appropriate viscosity can be printed.

Selective laser sintering operates under the same basic process as 3D Inkjet printing. Layers of particles are hardened into 2D cross sections before lowering a

stage. However rather than using a binding liquid to bind the particles, the substrate particles are melted by a CO<sub>2</sub> laser before amalgamating and solidifying in the shape of the desired cross-section [135]. Fused Deposition Modelling (FDM) is perhaps the most widely used 3D printing technique when considering personal use and commercial prototype production. Fused deposition modelling involves depositing a melted thermoplastic filament onto a 2D plane over a stage. The plastic filament is rolled into a heating unit and then extruded through a nozzle. The printer head is then guided in two dimensions by belts to produce the specified 2D cross-section. Upon completion of this cross-section, the stage is lowered and a further cross-section is deposited based on the STL file. A limitation of this method is that it must use thermoplastic materials such as polycarbonate and polystyrene. Furthermore, heterogeneity in the plastic substrate and the way that the STL file is sliced into a printer path introduces defects in the model [135]. Pressure Based Extrusion (PBE) functions similarly to fused deposition modelling (FDM). A printer head can be manipulated in two dimensions to extrude 2D cross-sectional shapes, while a platform may be raised and lowered in order to print successive cross-sections. However PBE varies from FDM in that the extruded material originates from a syringe or reservoir that is emptied by creating a pressure gradient. This gives the printer a wider range of available printing substrates, as any fluid with appropriate viscosity can be extruded. One such printer is the Fab@Home Model 3.0 which is described in the section below [135]. Laminated Object Manufacturing of 3D printing cuts 2D layers out of sheets of materials such as paper, plastic or metal. Each cross-section is cut using a laser, knife or welder and fused onto the sections below by heating before the stage is lowered and the next sheet of material is added over the top [135].

Note that all of these 3D printing techniques have specific advantages and limitations that make them suitable for use in different fields and applications. Considerations which must be undertaken before choosing a printing method in a research setting include: the ability to print with different materials (discussed in the next chapter), the resolution, shapes and sizes that can be achieved by each printer as well as the cost, which may range from hundreds of dollars for a

desktop printer, to a cost in excess of US\$250,000 for industrial type printers [135].

### ***3D Printing of Biomaterials in Tissue Engineering***

Biomaterials were mainly used as coatings to support the transplantation of medical devices into patients. However, in recent times, the focus has shifted to using biomaterials as the main components of implantable scaffolds for regenerative medicine applications [136]. This is due the ability of biomaterials to promote the viability, proliferation and differentiation of cells. The increased interest in creating biomaterial scaffolds appears to coincide with the development of 3D printing [137]. As described above, various 3D printing processes have been developed and refined over the years. Consequently, due to advances in cell biology, engineering and biomaterials science, more biomaterials with different properties have also been fabricated [138]. This has allowed for the production of tissue-engineered scaffolds for a wide range of applications including restoration of anatomical defects, reconstruction of complex organs and tissues, as well as scaffolds for stem cell differentiation [138]. However, challenges still remain in perfecting the structure of tissue-engineered scaffolds so that they are able to reflect the intricate architecture of human extracellular matrices as this will optimise and guide the proliferation, differentiation and function of cells towards specific tissue types [137]. This is important because the ultimate goal of 3D bioprinting is to produce scaffolds with anatomically and physiologically similar properties to specific tissues and organs for use in regenerative medicine [137].

Although the printing processes are important in developing and manipulating the architecture of these scaffolds, factors such as the biomaterial and cell source also have to be considered. Therefore, this section will provide an overview of the general criteria that can be used to select biomaterials and cells for 3D bioprinting, as well as the various modifications that can be applied to aid in the generation of specific tissue-engineered scaffolds. Furthermore, this section will also discuss the tests that can be employed to analyse the properties of the scaffold and observe the progressive development of the included cells to determine the overall success of the final product.

### ***Selecting the Biomaterial for 3D Bioprinting***

3D bioprinting offers the potential of a tissue engineering approach that is even more comprehensive and widely relevant than that of scaffolding [139]. Bioprinting involves the printing of ‘bioinks’, which comprise live cells with a fluid that acts as an extracellular matrix, most commonly a hydrogel and may also include biochemical factors, proteins or drugs [140]. The rationale of this technique is that by bioprinting cells as part of an architecture, they will readily differentiate to the range of cells which make up a functional tissue [139]. The biological nature of the bioinks imposes a number of limitations on the printing process. So far, 3D inkjet continuous printing and pressure-based extrusion (PBE) have been most successfully applied to this printing approach. This technique may be particularly useful in soft tissues such as the cardiovascular system. This approach has had limited clinical relevance but recent research has revealed that this is a promising field. Challenges which need to be overcome include low cell survival after printing, a lack of well-directed cell differentiation protocols, insufficient vascularisation and the creation of matrices through which metabolites will diffuse [140]. When selecting suitable biomaterials for 3D bioprinting, various factors have to be considered, such as compatibility with biological products as well as the printing process being utilised [137]. With more biomaterials being engineered specifically for 3D bioprinting, the criteria for suitable characteristics have become more detailed and precise. Therefore, some of the more essential qualities that are now expected in 3D bioprinting biomaterials will be discussed.

*Printability:* Printability is an important factor in determining the suitability of biomaterials for 3D bioprinting, as it affects the printer's ability to accurately deposit biomaterials when producing the desired structure [137]. When determining the printability of a biomaterial, the type of printer being used must first be taken into consideration as the processing parameters and components will vary [138]. For example, continuous inkjet (CIJ) printing involves forcing a liquid through a small diameter orifice so that it produces a stream of smaller droplets that can be guided accurately to print a precise structure [141]. Therefore, bioinks are often used in CIJ printing, as they are predominantly liquid/gel solutions [142]. Another example is fused deposition modelling (FDM), which involves the

extrusion of thermoplastic polymer filaments through a nozzle onto a platform in a layer-by-layer process [142]. Thus, in FMD, thermoplastic polymers such as poly ( $\epsilon$ -caprolactone) are usually used for printing. Other factors affecting printability such as viscosity, gelling methods and melting temperature, also need to be considered to allow for optimal manipulation of the biomaterial during printing [137]. Bioinks must be gelled almost immediately after printing by polymer crosslinkers, photoactivation or thermal activation [143]. Thus, since this limitation does not allow the production of self-supporting structures, bioinks are usually more viscous to prevent the structure from collapsing as the gel is polymerised [144]. However, in FDM, it is more appropriate to consider the thermal properties of the biomaterial such as melting temperature or glass transition temperature as they determine the viscosity of the extruded biomaterial [145]. This is because viscosity decreases as temperature increases, and this will most likely affect the ability to control the deposition of the biomaterial.

*Mechanical and structural properties:* The mechanical and structural properties of the biomaterial are dependent on the tissue type it is mimicking such as skin, bone and cardiac tissue [137]. For example, elasticity is one of the major mechanical characteristics of soft tissues such as skin, blood vessels, cardiac and skeletal muscle, so elastomeric biomaterials such as  $\alpha$ -elastin hydrogels have been developed to mimic this property [146]. However, it has become increasingly difficult to engineer biomaterials that possess the desired mechanical and structural properties without compromising its other characteristics such as cell viability [144]. More recently, methods have been devised to modify biomaterials to attain particular properties while maintaining other important characteristics. For example, a recent study by Rutz and colleagues (2015) has attempted to devise a bioink method that produces bioinks from a variety of synthetic and natural biomaterials [144]. This has allowed them to modify the composition, degree of cross linking and polymer concentration to optimise the mechanical and structural properties of the bioink, while maintaining printability.

*Degradability:* In tissue engineering, it is necessary to use biomaterials that degrade at a rate that is slower or equal to the cells ability to produce its own extracellular matrix (ECM) [147]. This is particularly important as 3D bioprinted structures are intended to be temporary and only used to guide the proliferation



and differentiation of cells that will eventually replace damaged tissue. As such, hydrogels are often used because along with other biological, structural and mechanical properties, they are biodegradable [143]. However, when comparing naturally derived hydrogels (e.g. alginate, gelatin and elastin) and synthetic hydrogels (e.g. poly (ethylene glycol) (PEG) and poly (vinyl alcohol) (PVA)), both types of hydrogels are biodegradable but vary in their ability to control their rate of degradation [146]. Thus, it may be more suitable to use a combination of both depending on the application. Furthermore, linear aliphatic polyesters such as poly(lactic acid) (PLA), poly (glycolic acid) (PGA), and their copolymers poly(lactic acid-co-glycolic acid) (PLGA) are also used in printing scaffolds because they are both biodegradable and biocompatible [148]. When considering the degradability of the biomaterial, the products must be non-toxic so that they can be readily metabolised and cleared from the body [137]. Li and colleagues (2015) demonstrated that the DNA-based combination hydrogel utilised was biodegradable as it could be degraded by proteases (endoproteinase Glu-C) and nucleases (*EcoRI* and *BamHI*) [157].

*Biocompatibility:* The selected biomaterials should not be immunogenic and be able to coexist within the host since 3D-bioprinted structures are intended to be alternative transplant options for patients [149]. Generally, natural biomaterials such as alginate, collagen and fibrin are biocompatible due to their naturally derived origin [136]. However, synthetic polymers such as poly(lactic-co-glycolic acid) (PGA) and hydroxyapatite can also be made biocompatible by modifying particular properties such as composition, morphology and degradation [150].

*Cell viability:* Cell viability should also be considered when selecting biomaterials, especially those that incorporate cells before printing such as hydrogels [151]. Certain properties are desired when maximising cell viability in 3D-printed scaffolds. Lower-viscosity biomaterials are generally preferred as they provide a suitable environment for maintaining cell viability and function [137]. This is in contrast with high-viscosity biomaterials as they have been shown to decrease cell viability due to the increased shear stresses experienced during printing. Furthermore, biomaterials with low thermal conductivity and the ability to protect cells during printing may also increase viability and function after printing [152].

*Biomimicry*: The selected biomaterial should be able to support the proliferation, differentiation and function of cells by providing the appropriate signals *via* cell-material interactions or soluble factors [153]. As such, growth factors can be added to scaffolds *via* various methods to promote the differentiation of cells into tissue-specific cell lineages [148]. This will be discussed in greater detail in the next section. Alternatively, modifying the architecture of the scaffold can also enhance cellular signalling and interaction [154]. Due to advances in engineering and material science, modifications can now be achieved at the macro (*e.g.* shape), micro (*e.g.* porosity) and nano (*e.g.* surface modifications for cellular adhesion) levels [138]. For example, changing the porosity of the scaffold has been shown to enhance the biomimetic properties of scaffolds as it increases oxygenation throughout the scaffold to promote the viability and differentiation of multipotent stromal cells [155]. Porosity also enhances the delivery of osteogenic and angiogenic agents in bone tissue-engineered scaffolds [156]. However, porosity reduces mechanical properties such as compressive strength and increases the complexity of printing [156], so the degree of porosity that can be achieved is often limited.

Surface nanoarchitecture such as ridges, steps and grooves can also be included to increase biomolecule attachment for cellular adhesion, proliferation, and differentiation [154]. This is because the components of tissues and organs that cells interact with (*e.g.* extracellular matrices (ECM)) are nanometres in dimension so mimicking this characteristic in scaffolds will enhance and guide tissue growth [157]. For example, Elias and colleagues demonstrated that osteoblast function was increased in alumina and carbon fibre biomaterials possessing nanometre surface dimensions that approximated those of hydroxyapatite found in bone [148]. More recently, there have been attempts to develop biomaterials with enhanced biomimetic qualities through an understanding of the composition and arrangement of extracellular matrices (ECM) in the targeted tissues [137]. This has been achieved through tissue decellularisation protocols, which produce intact ECM scaffolds for structural and physiological analysis. Tissue decellularisation involves the lysis of cells in tissues and organs using decellularisation agents as well as the removal of cell remnants by rinsing [158]. However, there are certain limitations to consider when using this method including possible toxicity from

retention of decellularisation agents and difficulties in maintaining vascular structures [137]. Despite this, the possibility of incorporating ECM components into scaffolds using 3D bioprinting technology would be immensely beneficial to tissue engineering and regenerative medicine, as it would optimise biodegradability, biocompatibility and biomimicry.

*Scaffolding and 3D-Bioprinting:* 3D printing may currently be incorporated into tissue engineering in two different ways, both of which will be outlined in the section that follows. The first of these is the use of 3D printed scaffolds, which enable the fabrication of an extracellular architecture into which stem cells may be seeded, or the cells surrounding an implant may migrate into [159]. This approach has been particularly successful in the engineering of bone and tracheal tissues [160]. The second method of incorporating 3D printing into tissue engineering has been through 3D bioprinting. Bioprinting refers to the fabrication of 3D structures which incorporate living cells and bioactive moieties in a defined spatial distribution [161]. This technique also lends itself to stem cell research, where differentiation processes under different cellular architectures can be explored. An example of such research operating in a lab at the University of Sydney is given later in this section. The following sections will explore and discuss the current standing and the ongoing research with regard to 3D printing approaches in the engineering of various mesendodermal tissues.

Once the desired biomaterial has been selected, cells then need to be combined with the biomaterial to ultimately produce scaffolds that could potentially be used as replacements for disease or damaged tissues [136]. When determining which cell types to use for printing, it is firstly important to choose a cell type that is able to rapidly expand into the required numbers for printing [137]. If there are too little cells, this may result in reduced cell viability, but if there are too many cells, this may lead to hyperplasia or apoptosis [137]. Tissues and organs are complex structures composed of multiple cell types with specific biological functions. In tissue engineering, the aim is to replicate the structures of certain tissues or organs, so it is important that the engineered scaffolds contain cells that mimic the physiological properties of the targeted tissues. Thus, multiple cell types or stem cells (which can differentiate and proliferate into the required cell types) should be used [162].

Since the 3D bioprinted structure will ultimately be transplanted into patients, the structure must be biocompatible and resist rejection by the host immune system. This can be achieved by using an autologous cell source or tolerance-induction strategies [163, 164]. Furthermore, the cells must be robust enough to survive the bioprinting processes such as shear stress and pressure, and physiological stresses after transplantation such as enzymes and toxins [137]. Stem cells are the preferred choice of cells for 3D bioprinting as they are able to proliferate (*via* self-renewal) to generate large numbers of undifferentiated and multipotent cells that are able to transform into multiple functional tissue-specific cell types [137]. Stem cells can be produced autologously and therefore should not be rejected after transplantation [163]. Since ES cells and iPS cells clearly demonstrate these properties along with other cell-specific advantages, they are now being used for 3D bioprinting [151]. More recently, mesenchymal stromal cells have also been successfully isolated, expanded and differentiated for clinical trials [137]. This highlights that research into advancing cell-culture techniques could make more stem cell populations viable as cell sources, thus increasing the possible applications of 3D bioprinting. Cells can either be suspended in the biomaterial for printing or adhered to the printed scaffold. This depends on the biomaterial and printing processes being utilised [136]. When using softer biomaterials such as hydrogels, the cells can be suspended in the biomaterial before printing [140]. Cells are able to retain cell viability and function when suspended in a polymerised gel. However, when using more rigid biomaterials such as thermoplastic polymers, the polymerisation conditions are often too harsh for cells to survive printing [165]. Therefore, cells are often cultured separately and adhered to the surface instead, allowing them to proliferate and differentiate to ultimately produce an extracellular matrix and functional proteins and saccharides that compose the tissue [141].

*Biomimetic products:* Biomaterial scaffolds often require the delivery of soluble factors to provide additional signals for cellular proliferation, differentiation and function as cell-cell and cell-material interactions may not be sufficient enough to achieve this [153, 148]. Thus, various methods have been developed to deliver biological factors such as growth factors to aid in the development of tissue-engineered scaffolds. Growth factors can also be directly added to printing

solutions before constructing scaffolds [166]. TGF- $\beta$ , BMP and VEGF integrated into scaffolds promote the recruitment and differentiation of osteoprogenitor cells leading to regulation of osteogenesis, tissue regeneration and ECM production [156, 167].

Gelatin methacrylate microspheres have been used to delivery various biological factors for tissue engineering applications including stem cell differentiation within scaffolds [168, 169]. However, when using microspheres, the movement and amalgamation of spheres often results in the inconsistent diffusion of growth factors throughout the scaffold. Therefore, microspheres should be used in conjunction with macro-porous and nano-fibrous scaffolds that enhance the ability to spatially control the release of biological factors [148]. Coating techniques can also be used to enhance biomimicry as growth factors can be added to the surface of scaffolds [170]. This was highlighted by Bose and colleagues, where a layer of hydroxyl carbonate apatite (HCA) on the surface of a 3D bioglass scaffold was able to adsorb proteins and growth factors promoting new bone formation *in vivo*.

3D-printed scaffolds can be tested for cell viability, differentiation and growth as well as structural, mechanical and degradative properties to provide important information towards optimising scaffold design [171]. The biomaterial can be chosen to maximise cell viability in tissue-engineered scaffolds. However, the printing process may stress the cells, and cause injury or apoptosis [137]. In syringe-based printing, the nozzle diameter as well as the dispensing pressure have been found to affect the cell viability immediately after printing which can result in apoptosis and necrosis [172, 173]. An increase in dispensing pressure and decreasing nozzle diameter was found to decrease cell viability. Inkjet bioprinting usually records cell viabilities greater than 85%, whereas microextrusion printing reports viabilities range from 40–80% and laser-assisted bioprinting reports viabilities in excess of 90% [174, 175]. Cell viability should be monitored after printing to ensure that sufficient number of cells remain in the 3D printed scaffolds for proliferation and differentiation into the specific tissues or organs. Live/dead assays involve the use of different stains for both live and dead cells (e.g. Calcein acetoxymethylester stains live cells bright green and ethidiumhomodimer-2 stains dead cells red) and are often conducted at different

periods throughout the experiment to observe changes in cell viability over time [176].

3D-bioprinted stem cells must proliferate and differentiate into the appropriate lineages. It is predominantly the 3D environment (which consists of the selected biomaterial with or without biomimetic products) that affects cell differentiation in tissue-engineered scaffolds [153]. Therefore, to determine if the 3D environment is promoting or inhibiting the proliferation and differentiation of cells, gene or protein expression that are characteristic to specific cell types should be assessed [177]. Differentiation of human satellite cells into multinucleated myotubes was assessed by qRT-PCR to analyse the expression of myogenic transcription factors as well as immunocytochemistry using monoclonal antibodies that targeted muscle-specific proteins [177]. Tissue-engineered scaffolds may interfere with these analytical methods [176]. Structural, mechanical and degradative properties are often tested to determine the quality of the scaffold design in mimicking specific tissues [178]. Jeong & Hollister demonstrated that the porosity of scaffolds could affect its mechanical and degradative properties. Therefore, similar tests can be conducted on the 3D-printed scaffolds to assess its mechanical and degradative properties [179].

*Scaffolding:* Scaffolding results in a 3D structure that can mimic the extracellular matrix in which cells migrate or are seeded into the structure after printing. The scaffold then provides support and encourages the proliferation and differentiation of tissue specific cells [139]. More traditional techniques exist for the fabrication of scaffolds, however these are limited by a lack of control over the structure's shape and porosity [159]. 3D printing overcomes these limitations by custom manufacturing the scaffold in a layer by layer manner to optimise both the shape and porosity for potential implantation [180]. The manufacture of 3D printed scaffolds has been incorporated into the tissue engineering of a number of different mesendodermal-derived tissues and organs. The following sections will describe how this has been achieved in bone and tracheal tissues.

## **Applications of Scaffolding in Mesendodermal Tissues**

### ***Stem Cells, 3D Printing and Bone Healing***

The tissue engineering of bone structures is perhaps the area in which 3D printing has had the greatest tangible impact to date. Bone, as a tissue, possesses unique properties that have been harnessed in tissue engineering approaches. Bone tissue consists of cancellous and cortical bone. Together, these produce complex structures which have porosities from less than 10% in cortical bone, to 50-90% porosity in cancellous bone [156]. At a cellular level, bone is a dynamic structure. Osteoblast cells continuously deposit new bone matrix while old bone is resorbed by osteoclasts. The collection of these processes is known as bone remodelling and gives bone tissue self-healing properties. Despite this self-healing, severe fractures often require external intervention [156]. Amongst these interventions to heal the bone, tissue engineering approaches are now becoming more common. Some earlier approaches include bone autografts and allografts, both of which seek to incorporate an exogenous structure into the bone in an attempt to strengthen and improve healing *in vivo*. These grafting solutions present problems including graft availability, infection, donor site morbidity and the need for additional operations [140]. Biocompatible scaffolds have become viable alternatives to these approaches. The scaffolds attempt to mimic properties of the extracellular matrix and have traditionally been produced by methods which are limited in their ability to specify scaffold shape and pore size [156]. The incorporation of 3D printing into the bone tissue engineering approach has enabled the fabrication of scaffolds without these shortcomings [159].

A number of techniques have now been used to produce high precision, custom defined, 3D scaffolds. The power of this approach lies in the ability to tailor the 3D structure to the patient, as well as the ability to produce interconnected porous structures that become vascularised and populated by osteoblasts and parenchymal cells. Of the available scaffold printing techniques, Drop on Demand 3D Inkjet Printing (described above) has been most commonly adopted for the manufacture of scaffolds [156]. A number of powder and binding liquid combinations have been used in this approach, but the availability of a strong biocompatible complex remains an issue and a limitation. VEGF, FGFs and

BMPs are examples of growth factors that may have the effect of encouraging and accelerating the incorporation of desirable cells and subsequent healing of bone. These growth factors may be used together with stem cells to engineer a tissue that comes closer in structure and function to the implantation site *in vivo*. Muscle-derived stem cells have been cultured and bioprinted onto a printed scaffold containing BMP-2 resulting in more functional bone tissue [156]. Current limitations to this approach include the viability of the cells after bioprinting as well as that of the incorporated growth factor [156].

### ***Stem Cells and 3D Bioprinting of the Trachea***

The trachea is an organ in which 3D scaffold engineering by 3D printers has already had a major impact. The application of 3D printed tracheas has already been demonstrated in animal models clinically to correct tracheal stenosis [181, 182]. As scaffolding techniques become elaborated, the tissues printed match those of the native tissues more closely. Park and colleagues have produced a tissue-engineered trachea that has mechanical properties very similar to those of the native organ by adapting a cylindrical scaffold to the shape of a bellow [183]. A sacrificial scaffold was engineered using a micro-stereolithography technique with an alkali soluble photopolymer [183]. Each layer is printed to form a negative mold of the trachea, with the uncured photopolymer dissolved with isopropyl alcohol. Sustained release of TGF $\beta$ 1, through a functionalised gelatin sponge, induces the growth of tracheal cartilage [183]. Alternating layers of the gelatin sponge, one with TGF $\beta$ 1 and one seeded with the chondrocytes, were laid into the sacrificial scaffold. These structures were implanted subcutaneously into nude mice and the results show that the bellow structure were less resistant to three-point bending and more resistant to radial compression than the cylindrical structure [183]. This mechanical outcome is comparable to that of the biological trachea and can be further developed as an engineered substitute in the case of tracheal stenosis or other diseases affecting the airways. In 2014, Zopf and colleagues successfully produced and implanted a custom, 3D printed airway splint into a critical, paediatric tracheobronchomalacia patient under FDA emergency-use exemption [184]. The procedure restored patency of the bronchus and essentially reversed the respiratory distress of the patient. This case demonstrates the potential which tissue engineering holds and paves the way for



more extensive applications in the future.

### ***3D Bioprinting of Stem Cells for the Treatment of Cardiac Disease***

Cardiovascular structures are an obvious candidate for tissue engineering approaches with cardiovascular disease (CVD) accounting for approximately 30% of all deaths globally [185]. As treatment of myocardial infarction improves, increasing numbers of CVD patients now survive cardiovascular events and live with partially damaged heart muscle [186]. Bioprinting offers an avenue to manufacture tissues to replace damaged myocardium as well as other structures such as the heart valves and vessels. Currently engineered cardiovascular tissues are limited in their ability to support live cells, meaning that tissues have been limited to thicknesses of  $\sim 100\ \mu\text{m}$ , mainly as a result of the diffusion limitation for oxygen [187]. 3D printing may be promising way to overcome this, as it is able to print thick tissues with uniformly dispensed cells, which are also porous enough to sustain nutrient and gaseous exchange by cells. Promising research by Gaetani and colleagues have used pressure base extrusion methods to print human cardiac-derived cardiomyocyte progenitor cells (hCMPCs) in a sodium alginate hydrogel [188]. The group successfully maintained viability after printing, and demonstrated promising differentiation of cells. hCMPCs have proved to be a promising substrate for cardiovascular bioprinting as these cells are committed to the cardiac lineage, can differentiate into cardiomyocytes and can successfully proliferate *in vitro*. When these cells were printed into a 3D construct, they responded positively in comparison to 2D cultures with increased expression of cardiomyocyte transcription factors [188]. While the sodium alginate supported the hCMPCs in this experiment, the use of a decellularised extracellular matrix in a heart-derived bioink has shown great promise. Experiments by Pati and colleagues show that it is able to increase the expression of cardiac-specific genes *Myh6* and *Actn1* when printed with human inferior turbinate-tissue derived mesenchymal stromal cells (hTSMCs) [189].

Valvular heart disease is expected to triple by 2050. Developing countries struggle with the medical needs of those afflicted with rheumatic fever and its implications on heart valves; 30% of those born with congenital heart defects do not survive [190]. Heart valve malfunction as seen in stenosis or regurgitation cannot self-heal

and must be replaced [190, 191]. The successful engineering of functional bioprinted heart valves would have a similarly revolutionary impact for many patients requiring heart valve replacement. Patients currently seeking a heart valve replacement are limited to choosing an artificial valve which requires ongoing anticoagulant therapy, or a xenograft or allograft which requires replacement 25 years at most [192]. Specifically, children and younger adults require aortic valve replacements that can grow, regenerate, and remodel with their still growing bodies. Therefore, an option for a fully compatible and biological heart valve replacement would be vital to the improvement of quality of life of the patients and to avoid future replacement surgeries.

With 3D printing, significant progress has been made on the bioengineering of heart valves. Duan and colleagues have successfully cultured encapsulated root sinus smooth muscle cells (SMCs) (81.4  $\pm$  3.4% viability) and aortic valve leaflet interstitial cells (VICs) (83.2  $\pm$  4.0% viability) in the valve root and leaflets respectively, of alginate/gelatin valve conduits [191]. SMCs added to stiff matrix resulted in increased expression of alpha-smooth muscle actin while VICs in soft matrix resulted in increased vimentin expression. These results suggest that complex aortic valve hydrogel conduits are possible to construct, especially with further advances in 3D printing technology. Although the prospect of being able to custom print a heart valve is exciting, there are still limitations such as an unfit construct, long-term malformation, and loss of anisotropic function. A badly constructed structure would result in mechanical stress on the construct and ultimately, calcification, regurgitation and hemodynamic inefficiency of the heart. A long-term transplant malformation such as a uniform reduction or increase in thickness or remodelling could result in reduced function, regurgitation and calcification and will require further repair. Over time, anisotropic function may also cease and become isotropic, which may cause calcification [190].

### ***Bioengineering Blood Vessels***

Previous attempts have been made to produce vasculature by seeding 3D printed scaffolds. However this technique is limited by the fact that due to the printing conditions, cells cannot be printed into the scaffold directly, and the seeding of the scaffold at a later time poses a problem. Scaffold-free bioprinting methods have

been investigated. Norotte and colleagues bioprinted blood vessels through the layering of various vascular cell types around agarose rods [193]. Layers of smooth muscle cells and fibroblasts formed vasculature of 0.9-2.5mm in diameter. The agarose rods were then pulled out of the construct leaving a cylindrical structure however this method possessed some limitations. Structurally, only open-ended vasculature may be constructed using this method and more complex structures may be harder to achieve. Further research into the use of thermoreversible or photosensitive gels could improve the final steps of this process. Photolithography, a descendant of the stereolithography technique, has been investigated as another method of scaffold free bioprinting. This technique involves the exposure of photosensitive hydrogel to light through a photomask. The areas of the hydrogel exposed to the light polymerise and form a cross-linked material. Then, the rest of the uncrosslinked gel can be washed away leaving a polymerised structure designed by the shape of the light shown onto the photosensitive gel. This method is promising as the photosensitive hydrogel can be prepared to have specific porosity and mechanical properties, which affect the growth of the stem cells [194]. Bioprinted vascular structure made from GelMA hydrogel with endothelial progenitor cells (EPCs) and mesenchymal stem cells (MSCs) have been subcutaneously transplanted into immunodeficient mice. GelMA is a unique hydrogel in that it is a functionalised gelatin hydrogel with control over the degree of porosity and degradability for optimal cell viability post-printing. The results show that 7 days post-transplantation, lumen was present throughout the structure with murine erythrocytes flowing through the vasculature. This purports that the transplanted vessels had successfully fused with the host vasculature [195]. Using laser beams, the photolithography technique selectively polymerises the hydrogel used creating 3D structures.

### ***3D Stem Cell Bioprinting in an Undergraduate Research Laboratory***

To provide an example of a 3D Bioprinter in a research laboratory, the setup of an operational pressure based extrusion printer (PBE) has been described below. The printer is used for the purpose of stem cell research at the University of Sydney Charles Perkins Centre. This section will outline the general setup, operation and uses of this printer. The printer described above is a Fab@Home Model 3.0 PBE printer that is manufactured at Cornell University and is commercially available.

The chassis of the printer is produced from 3D printed acrylic panes. Five motors are then positioned within the chassis to drive either a belt, to manipulate the location of the printer head, or to drive one of two plungers that generate the pressure required for the extrusion of the syringe contents (Fig. 6).

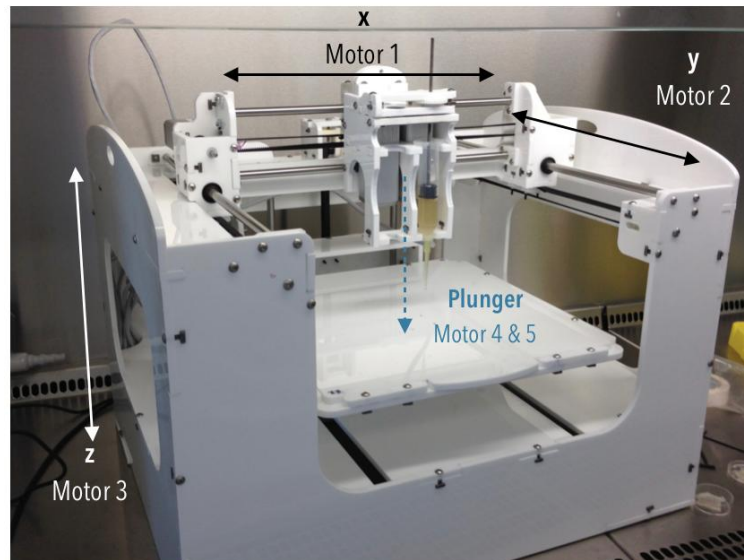


**Fig. (6).** Annotated set-up of the Fab@Home Model 3.0 Bioprinter in the X-lab undergraduate teaching facility of the Charles Perkins Centre. The printer is located in a biosafety cabinet (BSC) where it can be sterilized by UV light and used to print under cell culturing conditions. The annotations depict the printer axes of movement in 3D space.

The printer can be operated by software in one of two ways. Firstly, the motors may be driven by a basic programming language that sends movement trajectories directly to each motor. This gives the operator a high degree of control over the exact print path and extrusion speed but is limited to producing straight-line structures. Secondly, the printer may be driven by ‘Fab Studio’ and ‘Fab Interpreter’ software that allows the printing of objects from CAD (computer aided design) files. In this mode, the virtual 3D CAD object is converted automatically into a printer path that can then be executed.

The undergraduate research team operating this printer has been investigating differentiation of the cardiac lineage from embryonic stem cells (ESCs) in the context of bioprinted hydrogels. The group has successfully produced alginate

bioinks containing ESCs, which can be printed into a calcium chloride ( $\text{CaCl}_2$ ) bath to produce a dimerised hydrogel with precise architecture. Based on our own practical experience, we observed that the different viscosities of non-autoclaved and autoclaved alginate affected our ability to produce accurate and consistent structures using the Fab@Home printer. More specifically, the autoclaved alginate was considerably less viscous than the non-autoclaved alginate. Upon further analysis, we observed that this appeared to increase the time taken to polymerise autoclaved alginate with calcium chloride ( $\text{CaCl}_2$ ) compared to non-autoclaved alginate. We believe that this was most likely due to the autoclaving process decreasing the degree of polymerisation in the alginate [196]. Therefore, this highlights how the factors affecting printability also need to be considered when selecting biomaterials for 3D bioprinting.

This hydrogel has successfully produced viable structures *in vitro*, including a sheet of communicating contractile cardiomyocytes. The hydrogel has also been used to produce a number of printed 3D architectures including sheets of hydrogel (Fig. 7). The pictured sheets can be combined with different growth factors with the rationale of differentiating different morphologies at different levels within the gel.

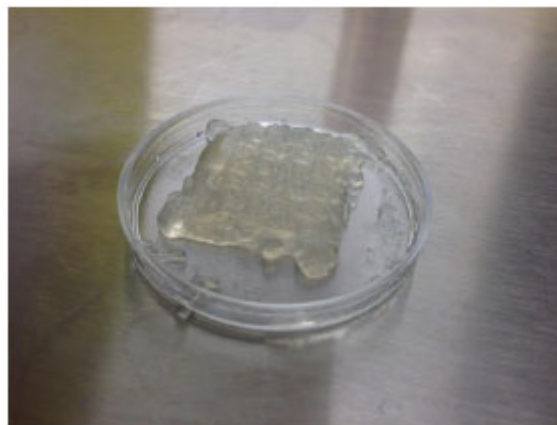


**Fig. (7).** This image shows an alginate- $\text{CaCl}_2$  hydrogel, which has been bioprinted in 2 layers which are combined with different growth factors for differentiation of mouse embryonic stem cells into cardiovascular lineages.

### ***Future Directions in Tissue Engineering***

3D bioprinting is the new frontier of clinical care, especially in the case of transplantation and cell therapy. It mitigates the risk of tissue rejection and the need for immunosuppressants. Organs and tissues can be customised to each patient and would eliminate the shortage of organ donors. At the moment, seeding the required stem cells onto a decellularised scaffold has been the closest to developing a whole functioning organ; however, the development of 3D printing technology allows control over the finer aspects of the process such as cell placement, cell concentration, and diameter of printed cells. 3D printing layers cells, growth factors, and the scaffold matrix (usually hydrogels), selectively to create tissue or whole organs [197]. These processes are outlined above. The clinical application of 3D bioprinted organs and tissues are still a couple of decades away, but there are a multitude of applications in the field emerging such as live implants of organs or parts of organs, *in situ* printing, and replacement of animal testing commercially and in drug discovery [137, 197].

3D bioprinting and tissue engineering have been used to successfully culture bone, vasculature, trachea, and heart tissue with ability to be transplanted. However, there are still issues with 3D bioprinting. Many of the whole organ bioengineering have only been produced in small scale and must be translated to human-sized organs. Specifically, the diffusion of oxygen between the host and transplanted tissue limits the engineered tissue width to under 200µm [197]. However, cutting edge vascular bed tissue engineering could solve this problem as new studies have shown successful perfusion of transplanted vasculature in murine models [198]. The integration of vasculature into current organ and tissue bioengineering would be vital, as thicker tissues will need a circulatory system to maintain cellular metabolic functions, mature, and fuse together. Tissues will grow in width as studies will continue to add various layers of multiple cell types to form a complete structure. A vascular network embedded onto the organ or tissue engineered would provide the cells with the oxygen, gas, nutrient, and waste exchange required by normal healthy living tissue [197].

Unfortunately, bifurcated and branched vessels have been challenging to grow with only a few studies investigating this area. A protocol for developing complex

vascular network still needs to be engineered before integration with whole organs [199]. Kusuma and colleagues have successfully implanted a vascular network that fused with the host vasculature and established blood flow [200]. Their method involved the culturing of a bicellular vascular population from human pluripotent stem cells (hPSCs) in a synthetic matrix. These mature to early vascular cells (EVCs) and then to endothelial cells and pericytes, which are vital for stable vasculature. The use of 3D printing technology could hopefully further this research in that the development of the vascular bed could move out of the synthetic matrix and into an engineered whole organ.

*In situ* printing, the direct printing of live organs or tissue during open surgery is a leading procedure following the progress in 3D bioprinting technology. It has already been done with a skin lesion filled with keratinocytes and fibroblasts, but its full potential is to be able to print an organ straight onto the patient [199]. The development of whole organs from our skin to the bone means that we can test drugs and collect accurate results with respect to reaction, side effects, and benefits. Currently, the results of animal testing for anything from cosmetics to cutting edge cancer treatments must be translated to accurate human body responses. Although it is expensive and labour intensive, the results normally are unable to predict that of a normal human body response as animals and humans would have differences such as variable immunogenic make up and gene regulation [201]. Furthermore, human clinical trials must be thoroughly conducted before deciding whether the drug is effective, ineffective or too toxic [202]. Therefore, advances in 3D bioprinting of tissues and whole organs would greatly benefit research of how various drugs affect the corresponding organs. Parameters such as immunogenicity, effect of environmental factors, and pre-existing diseases can be strictly set to best observe the effect of the drug on the patient. For example, in the study to find a drug against Duchenne Muscular Dystrophy (DMD), an mdx murine model is being used. DMD is a genetic X-linked disorder where the dystrophin protein is absent causing skeletal muscle deterioration [203]. Instead of the murine model, skeletal muscle with DMD can be 3D printed, cultured and tested against the drug in question with the results already in context to a human response. Although human clinical trials should still be required, these results from the 3D printed tissue could be a more accurate prediction of the

human outcome than would the results from an animal model.

## **CONCLUDING REMARKS**

Revolutions in both biology and engineering have taken place in the past decade. The ability to induce pluripotent stem cells from adult cells has opened the field of regenerative medicine enormously as it may alleviate the difficulties associated with transplantation such as immune rejection. Advances in 3D bioprinting have expanded our possibilities of printing functional tissues and organs for tailor-made regenerative medical interventions. As many of the diseases currently afflicting patients worldwide involve either tissues or organs originating from the mesendoderm, understanding the underlying biological processes leading to the formation of these tissues is crucial. Combining our biological understanding of mesendoderm formation with patient-specific iPS cell generation and 3D bioprinting technologies holds great promise for the future of regenerative medicine.

## **CONFLICT OF INTEREST**

The authors confirm that they have no conflict of interest to declare for this publication.

## **ACKNOWLEDGEMENTS**

We apologise for the many hard working researchers whose work we have not included in this chapter. We also acknowledge the members of the Laboratory of Blood Cell Development and the Andrology Research Group, School of Medical Science, Faculty of Medicine, University of Sydney. The Laboratory of Blood Cell Development gratefully acknowledges past support from the Sydney Medical School, the NWG Macintosh Award, the National Breast Cancer Foundation and the Feline Health Research Fund. MPT was supported by the University of Sydney Outstanding Achievement Scholarship, James Aitken Scholarship, and the Fairfax prize (2013). DTML was supported by the University of Sydney Outstanding Achievement Scholarship, James Aitken Scholarship (2013) and the University of Sydney Academic Merit Prize (2013). CH, MPT and DTML were engaged in an undergraduate research group run by STF in senior Physiology



units of study at the University of Sydney. We are grateful for the support of the Charles Perkins Centre in purchasing the 3D bioprinter described in this chapter. We also wish to acknowledge the help of Renee Barber, Denise McDonell, Virginia Klomp and Dr Soma Vignarajan from the Charles Perkins Centre in the purchase, establishment and operation of the 3D bioprinter described here. STF is the University of Sydney Sesquicentennial Senior Lecturer in Molecular Embryology. Finally, our thanks to Prof. Richard N. Mortie for all his wit and intelligence throughout this writing process-it has been a long time coming.

## REFERENCES

- [1] Lammert E, Cleaver O, Melton D. Induction of pancreatic differentiation by signals from blood vessels. *Science* 2001; 294(5542): 564-7.  
[<http://dx.doi.org/10.1126/science.1064344>] [PMID: 11577200]
- [2] Goldman O, Han S, Hamou W, *et al.* *Stem Cell Reports*. Authors 2014; 3(4): 556-65.
- [3] Rodaway A, Patient R. Mesendoderm. an ancient germ layer? *Cell* 2001; 105(2): 169-72.  
[[http://dx.doi.org/10.1016/S0092-8674\(01\)00307-5](http://dx.doi.org/10.1016/S0092-8674(01)00307-5)] [PMID: 11336666]
- [4] Maduro MF, Meneghini MD, Bowerman B, Broitman-Maduro G, Rothman JH. Restriction of mesendoderm to a single blastomere by the combined action of SKN-1 and a GSK-3beta homolog is mediated by MED-1 and -2 in *C. elegans*. *Mol Cell* 2001; 7(3): 475-85.  
[[http://dx.doi.org/10.1016/S1097-2765\(01\)00195-2](http://dx.doi.org/10.1016/S1097-2765(01)00195-2)] [PMID: 11463373]
- [5] Nieuwkoop PD. Short historical survey of pattern formation in the endo-mesoderm and the neural anlage in the vertebrates: the role of vertical and planar inductive actions. *Cell Mol Life Sci* 1997; 53(4): 305-18.  
[<http://dx.doi.org/10.1007/PL00000608>] [PMID: 9137623]
- [6] Agius E, Oelgeschläger M, Wessely O, Kemp C, De Robertis EM. Endodermal Nodal-related signals and mesoderm induction in *Xenopus*. *Development* 2000; 127(6): 1173-83.  
[PMID: 10683171]
- [7] Ryan K, Garrett N, Mitchell A, Gurdon JB. Eomesodermin, a key early gene in *Xenopus* mesoderm differentiation. *Cell* 1996; 87(6): 989-1000.  
[[http://dx.doi.org/10.1016/S0092-8674\(00\)81794-8](http://dx.doi.org/10.1016/S0092-8674(00)81794-8)] [PMID: 8978604]
- [8] Nelson AC, Cutty SJ, Niini M, *et al.* Global identification of Smad2 and Eomesodermin targets in zebrafish identifies a conserved transcriptional network in mesendoderm and a novel role for Eomesodermin in repression of ectodermal gene expression. *BMC Biol* 2014; 12(81): 81.  
[<http://dx.doi.org/10.1186/s12915-014-0081-5>] [PMID: 25277163]
- [9] Costello I, Nowotschin S, Sun X, *et al.* Lhx1 functions together with Otx2, Foxa2, and Ldb1 to govern anterior mesendoderm, node, and midline development. *Genes Dev* 2015; 29(20): 2108-22.  
[<http://dx.doi.org/10.1101/gad.268979.115>] [PMID: 26494787]
- [10] Costello I, Pimeisl I-M, Dräger S, Bikoff EK, Robertson EJ, Arnold SJ. The T-box transcription factor

- Eomesodermin acts upstream of *Mesp1* to specify cardiac mesoderm during mouse gastrulation. *Nat Cell Biol* 2011; 13(9): 1084-91.  
[<http://dx.doi.org/10.1038/ncb2304>] [PMID: 21822279]
- [11] Nikaido M, Tada M, Saji T, Ueno N. Conservation of BMP signaling in zebrafish mesoderm patterning. *Mech Dev* 1997; 61(1-2): 75-88.  
[[http://dx.doi.org/10.1016/S0925-4773\(96\)00625-9](http://dx.doi.org/10.1016/S0925-4773(96)00625-9)] [PMID: 9076679]
- [12] Winnier G, Blessing M, Labosky PA, Hogan BL. Bone morphogenetic protein-4 is required for mesoderm formation and patterning in the mouse. *Genes Dev* 1995; 9(17): 2105-16.  
[<http://dx.doi.org/10.1101/gad.9.17.2105>] [PMID: 7657163]
- [13] Grapin-Botton A. Endoderm specification. *StemBook*. The Stem Cell Research Community 2008.  
[<http://dx.doi.org/10.3824/stembook.1.30.1>]
- [14] Fukui A, Goto T, Kitamoto J, Homma M, Asashima M. SDF-1  $\alpha$  regulates mesendodermal cell migration during frog gastrulation. *Biochem Biophys Res Commun* 2007; 354(2): 472-7.  
[<http://dx.doi.org/10.1016/j.bbrc.2007.01.007>] [PMID: 17239342]
- [15] Clements D, Woodland HR. Changes in embryonic cell fate produced by expression of an endodermal transcription factor, *Xsox17*. *Mech Dev* 2000; 99(1-2): 65-70.  
[[http://dx.doi.org/10.1016/S0925-4773\(00\)00476-7](http://dx.doi.org/10.1016/S0925-4773(00)00476-7)] [PMID: 11091074]
- [16] Henry GL, Brivanlou IH, Kessler DS, Hemmati-Brivanlou A, Melton DA. TGF-beta signals and a pattern in *Xenopus laevis* endodermal development. *Development* 1996; 122(3): 1007-15.  
[PMID: 8631246]
- [17] Dougan ST, Warga RM, Kane DA, Schier AF, Talbot WS. The role of the zebrafish nodal-related genes *squint* and *cyclops* in patterning of mesendoderm. *Development* 2003; 130(9): 1837-51.  
[<http://dx.doi.org/10.1242/dev.00400>] [PMID: 12642489]
- [18] Liu Y, Festing M, Thompson JC, *et al.* *Smad2* and *Smad3* coordinately regulate craniofacial and endodermal development. *Dev Biol* 2004; 270(2): 411-26.  
[<http://dx.doi.org/10.1016/j.ydbio.2004.03.017>] [PMID: 15183723]
- [19] Thisse B, Wright CV, Thisse C. Activin- and Nodal-related factors control antero-posterior patterning of the zebrafish embryo. *Nature* 2000; 403(6768): 425-8.  
[<http://dx.doi.org/10.1038/35000200>] [PMID: 10667793]
- [20] Shen MM. Nodal signaling: developmental roles and regulation. *Development* 2007; 134(6): 1023-34.  
[<http://dx.doi.org/10.1242/dev.000166>] [PMID: 17287255]
- [21] Dubrulle J, Jordan BM, Akhmetova L, *et al.* Response to Nodal morphogen gradient is determined by the kinetics of target gene induction. *eLife* 2015; 4(4)  
[<http://dx.doi.org/10.7554/eLife.05042>] [PMID: 25869585]
- [22] Conlon FL, Lyons KM, Takaesu N, *et al.* A primary requirement for nodal in the formation and maintenance of the primitive streak in the mouse. *Development* 1994; 120(7): 1919-28.  
[PMID: 7924997]
- [23] Liu P, Wakamiya M, Shea MJ, Albrecht U, Behringer RR, Bradley A. Requirement for *Wnt3* in vertebrate axis formation. *Nat Genet* 1999; 22(4): 361-5.  
[<http://dx.doi.org/10.1038/11932>] [PMID: 10431240]

- [24] Brennan J, Lu CC, Norris DP, Rodriguez TA, Beddington RS, Robertson EJ. Nodal signalling in the epiblast patterns the early mouse embryo. *Nature* 2001; 411(6840): 965-9.  
[<http://dx.doi.org/10.1038/35082103>] [PMID: 11418863]
- [25] Aronson BE, Stapleton KA, Krasinski SD. Role of GATA factors in development, differentiation, and homeostasis of the small intestinal epithelium. *Am J Physiol Gastrointest Liver Physiol* 2014; 306(6): G474-90.  
[<http://dx.doi.org/10.1152/ajpgi.00119.2013>] [PMID: 24436352]
- [26] Jacobsen CM, Narita N, Bielinska M, Syder AJ, Gordon JI, Wilson DB. Genetic mosaic analysis reveals that GATA-4 is required for proper differentiation of mouse gastric epithelium. *Dev Biol* 2002; 241(1): 34-46.  
[<http://dx.doi.org/10.1006/dbio.2001.0424>] [PMID: 11784093]
- [27] Koutsourakis M, Langeveld A, Patient R, Beddington R, Grosveld F. The transcription factor GATA6 is essential for early extraembryonic development. *Development* 1999; 126(9): 723-32.  
[PMID: 10383242]
- [28] Molkentin JD, Tymitz KM, Richardson JA, Olson EN. Abnormalities of the genitourinary tract in female mice lacking GATA5. *Mol Cell Biol* 2000; 20(14): 5256-60.  
[<http://dx.doi.org/10.1128/MCB.20.14.5256-5260.2000>] [PMID: 10866681]
- [29] Ang SL, Wierda A, Wong D, *et al.* The formation and maintenance of the definitive endoderm lineage in the mouse: involvement of HNF3/forkhead proteins. *Development* 1993; 119(4): 1301-15.  
[PMID: 8306889]
- [30] McKnight KD, Hou J, Hoodless PA. Foxh1 and Foxa2 are not required for formation of the midgut and hindgut definitive endoderm. *Developmental Biology* 2010; 337(2): 471-81.
- [31] Bossard P, Zaret KS. GATA transcription factors as potentiators of gut endoderm differentiation. *Development* 1998; 125(24): 4909-17.  
[PMID: 9811575]
- [32] Cirillo LA, Lin FR, Cuesta I, Friedman D, Jarnik M, Zaret KS. Opening of compacted chromatin by early developmental transcription factors HNF3 (FoxA) and GATA-4. *Mol Cell* 2002; 9(2): 279-89.  
[[http://dx.doi.org/10.1016/S1097-2765\(02\)00459-8](http://dx.doi.org/10.1016/S1097-2765(02)00459-8)] [PMID: 11864602]
- [33] Sakaguchi T, Kuroiwa A, Takeda H. A novel sox gene, 226D7, acts downstream of Nodal signaling to specify endoderm precursors in zebrafish. *Mech Dev* 2001; 107(1-2): 25-38.  
[[http://dx.doi.org/10.1016/S0925-4773\(01\)00453-1](http://dx.doi.org/10.1016/S0925-4773(01)00453-1)] [PMID: 11520661]
- [34] Kanai-Azuma M, Kanai Y, Gad JM, *et al.* Depletion of definitive gut endoderm in Sox17-null mutant mice. *Development* 2002; 129(10): 2367-79.  
[PMID: 11973269]
- [35] Sinner D, Kirilenko P, Rankin S, *et al.* Global analysis of the transcriptional network controlling *Xenopus* endoderm formation. *Development* 2006; 133(10): 1955-66.  
[<http://dx.doi.org/10.1242/dev.02358>] [PMID: 16651540]
- [36] Tam PP, Khoo PL, Lewis SL, *et al.* Sequential allocation and global pattern of movement of the definitive endoderm in the mouse embryo during gastrulation. *Development* 2007; 134(2): 251-60.  
[<http://dx.doi.org/10.1242/dev.02724>] [PMID: 17151016]

- [37] Howell M, Itoh F, Pierreux CE, *et al.* *Xenopus* Smad4beta is the co-Smad component of developmentally regulated transcription factor complexes responsible for induction of early mesodermal genes. *Dev Biol* 1999; 214(2): 354-69.  
[<http://dx.doi.org/10.1006/dbio.1999.9430>] [PMID: 10525340]
- [38] Murry CE, Keller G. Differentiation of embryonic stem cells to clinically relevant populations: lessons from embryonic development. *Cell* 2008; 132(4): 661-80.  
[<http://dx.doi.org/10.1016/j.cell.2008.02.008>] [PMID: 18295582]
- [39] Engler AJ, Sen S, Sweeney HL, Discher DE. Matrix elasticity directs stem cell lineage specification. *Cell* 2006; 126(4): 677-89.  
[<http://dx.doi.org/10.1016/j.cell.2006.06.044>] [PMID: 16923388]
- [40] Warmflash A, Sorre B, Etoc F, Siggia ED, Brivanlou AH. A method to recapitulate early embryonic spatial patterning in human embryonic stem cells. *Nat Methods* 2014; 11(8): 847-54.  
[<http://dx.doi.org/10.1038/nmeth.3016>] [PMID: 24973948]
- [41] Tada S, Era T, Furusawa C, *et al.* Characterization of mesendoderm: a diverging point of the definitive endoderm and mesoderm in embryonic stem cell differentiation culture. *Development* 2005; 132(19): 4363-74.  
[<http://dx.doi.org/10.1242/dev.02005>] [PMID: 16141227]
- [42] Gadue P, Huber TL, Nostro MC, Kattman S, Keller GM. Germ layer induction from embryonic stem cells. *Exp Hematol* 2005; 33(9): 955-64.  
[<http://dx.doi.org/10.1016/j.exphem.2005.06.009>] [PMID: 16140142]
- [43] Fehling HJ, Lacaud G, Kubo A, *et al.* Tracking mesoderm induction and its specification to the hemangioblast during embryonic stem cell differentiation. *Development* 2003; 130(17): 4217-27.  
[<http://dx.doi.org/10.1242/dev.00589>] [PMID: 12874139]
- [44] Nostro MC, Cheng X, Keller GM, Gadue P. Wnt, activin, and BMP signaling regulate distinct stages in the developmental pathway from embryonic stem cells to blood. *Cell Stem Cell* 2008; 2(1): 60-71.  
[<http://dx.doi.org/10.1016/j.stem.2007.10.011>] [PMID: 18371422]
- [45] Kubo A, Shinozaki K, Shannon JM, *et al.* Development of definitive endoderm from embryonic stem cells in culture. *Development* 2004; 131(7): 1651-62.  
[<http://dx.doi.org/10.1242/dev.01044>] [PMID: 14998924]
- [46] Willey S, Ayuso-Sacido A, Zhang H, *et al.* Acceleration of mesoderm development and expansion of hematopoietic progenitors in differentiating ES cells by the mouse Mix-like homeodomain transcription factor. *Blood* 2006; 107(8): 3122-30.  
[<http://dx.doi.org/10.1182/blood-2005-10-4120>] [PMID: 16403910]
- [47] Nishikawa SI, Nishikawa S, Kawamoto H, *et al.* *In vitro* generation of lymphohematopoietic cells from endothelial cells purified from murine embryos. *Immunity* 1998; 8(6): 761-9.  
[[http://dx.doi.org/10.1016/S1074-7613\(00\)80581-6](http://dx.doi.org/10.1016/S1074-7613(00)80581-6)] [PMID: 9655490]
- [48] Ogawa M, Kizumoto M, Nishikawa S, Fujimoto T, Kodama H, Nishikawa SI. Expression of  $\alpha 4$ -integrin defines the earliest precursor of hematopoietic cell lineage diverged from endothelial cells. *Blood* 1999; 93(4): 1168-77.  
[PMID: 9949159]

- [49] Zhang H, Nieves JL, Fraser ST, *et al.* Expression of podocalyxin separates the hematopoietic and vascular potentials of mouse embryonic stem cell-derived mesoderm. *Stem Cells* 2014; 32(1): 191-203.  
[<http://dx.doi.org/10.1002/stem.1536>] [PMID: 24022884]
- [50] Takahashi K, Yamanaka S. Induction of pluripotent stem cells from mouse embryonic and adult fibroblast cultures by defined factors. *Cell* 2006; 126(4): 663-76.  
[<http://dx.doi.org/10.1016/j.cell.2006.07.024>] [PMID: 16904174]
- [51] Phillips MJ, Perez ET, Martin JM, *et al.* Modeling human retinal development with patient-specific induced pluripotent stem cells reveals multiple roles for visual system homeobox 2. *Stem Cells* 2014; 32(6): 1480-92.  
[<http://dx.doi.org/10.1002/stem.1667>] [PMID: 24532057]
- [52] Menon T, Firth AL, Scripture-Adams DD, *et al.* Lymphoid regeneration from gene-corrected SCID-X1 subject-derived iPSCs. *Cell Stem Cell* 2015; 16(4): 367-72.  
[<http://dx.doi.org/10.1016/j.stem.2015.02.005>] [PMID: 25772073]
- [53] Hanna J, Wernig M, Markoulaki S, *et al.* Treatment of sickle cell anemia mouse model with iPS cells generated from autologous skin. *Science* 2007; 318(5858): 1920-3.  
[<http://dx.doi.org/10.1126/science.1152092>] [PMID: 18063756]
- [54] L Charles Murtaugh and Daniel Kopinke. Pancreatic stem cells. *StemBook*
- [55] Madsen OD. Stem cells and diabetes treatment. *APMIS* 2005; 113(11-12): 858-75.  
[[http://dx.doi.org/10.1111/j.1600-0463.2005.apm\\_418.x](http://dx.doi.org/10.1111/j.1600-0463.2005.apm_418.x)] [PMID: 16480455]
- [56] Pagliuca FW, Millman JR, Gürtler M, *et al.* Generation of functional human pancreatic  $\beta$  cells in vitro. *Cell* 2014; 159(2): 428-39.  
[<http://dx.doi.org/10.1016/j.cell.2014.09.040>] [PMID: 25303535]
- [57] Murtaugh LC. Pancreas and beta-cell development: from the actual to the possible. *Development* 2007; 134(3): 427-38.  
[<http://dx.doi.org/10.1242/dev.02770>] [PMID: 17185316]
- [58] Ohlsson H, Karlsson K, Edlund T. IPF1, a homeodomain-containing transactivator of the insulin gene. *EMBO J* 1993; 12(11): 4251-9.  
[PMID: 7901001]
- [59] Kawaguchi Y, Cooper B, Gannon M, Ray M, MacDonald RJ, Wright CV. The role of the transcriptional regulator Ptf1a in converting intestinal to pancreatic progenitors. *Nat Genet* 2002; 32(1): 128-34.  
[<http://dx.doi.org/10.1038/ng959>] [PMID: 12185368]
- [60] Gu G, Dubauskaite J, Melton DA. Direct evidence for the pancreatic lineage: NGN3+ cells are islet progenitors and are distinct from duct progenitors. *Development* 2002; 129(10): 2447-57.  
[PMID: 11973276]
- [61] Piper K, Brickwood S, Turnpenny LW, *et al.* Beta cell differentiation during early human pancreas development. *J Endocrinol* 2004; 181(1): 11-23.  
[<http://dx.doi.org/10.1677/joe.0.1810011>] [PMID: 15072563]

- [62] Shi Y, Hou L, Tang F, *et al.* Inducing embryonic stem cells to differentiate into pancreatic  $\beta$  cells by a novel three-step approach with activin A and all-trans retinoic acid. *Stem Cells* 2005; 23(5): 656-62. [http://dx.doi.org/10.1634/stemcells.2004-0241] [PMID: 15849173]
- [63] Jiang J, Au M, Lu K, *et al.* Generation of insulin-producing islet-like clusters from human embryonic stem cells. *Stem Cells* 2007; 25(8): 1940-53. [http://dx.doi.org/10.1634/stemcells.2006-0761] [PMID: 17510217]
- [64] Zorn. Liver Development. *StemBook*. The Stem Cell Research Community 2008.
- [65] Zhao R, Duncan SA. Embryonic development of the liver. *Hepatology* 2005; 41(5): 956-67. [http://dx.doi.org/10.1002/hep.20691] [PMID: 15841465]
- [66] Tremblay KD, Zaret KS. Distinct populations of endoderm cells converge to generate the embryonic liver bud and ventral foregut tissues. *Dev Biol* 2005; 280(1): 87-99. [http://dx.doi.org/10.1016/j.ydbio.2005.01.003] [PMID: 15766750]
- [67] Asahina K, Zhou B, Pu WT, Tsukamoto H. Septum transversum-derived mesothelium gives rise to hepatic stellate cells and perivascular mesenchymal cells in developing mouse liver. *Hepatology* 2011; 53(3): 983-95. [http://dx.doi.org/10.1002/hep.24119] [PMID: 21294146]
- [68] Al-Drees MA, Yeo JH, Boumelhem BB, *et al.* Making Blood: The Haematopoietic Niche throughout Ontogeny. *Stem Cells Int* 2015; 2015(10): 571893. [PMID: 26113865]
- [69] Medlock ES, Haar JL. The liver hemopoietic environment: I. Developing hepatocytes and their role in fetal hemopoiesis. *Anat Rec* 1983; 207(1): 31-41. [http://dx.doi.org/10.1002/ar.1092070105] [PMID: 6638531]
- [70] Goldman O, Han S, Sourisseau M, *et al.* KDR identifies a conserved human and murine hepatic progenitor and instructs early liver development. *Cell Stem Cell* 2013; 12(6): 748-60. [http://dx.doi.org/10.1016/j.stem.2013.04.026] [PMID: 23746980]
- [71] Han S, Dziedzic N, Gadue P, Keller GM, Gouon-Evans V. An endothelial cell niche induces hepatic specification through dual repression of Wnt and Notch signaling. *Stem Cells* 2011; 29(2): 217-28. [http://dx.doi.org/10.1002/stem.576] [PMID: 21732480]
- [72] D'Amour KA, Agulnick AD, Eliazer S, Kelly OG, Kroon E, Baetge EE. Efficient differentiation of human embryonic stem cells to definitive endoderm. *Nat Biotechnol* 2005; 23(12): 1534-41. [http://dx.doi.org/10.1038/nbt1163] [PMID: 16258519]
- [73] Gouon-Evans V, Boussemart L, Gadue P, *et al.* BMP-4 is required for hepatic specification of mouse embryonic stem cell-derived definitive endoderm. *Nat Biotechnol* 2006; 24(11): 1402-11. [http://dx.doi.org/10.1038/nbt1258] [PMID: 17086172]
- [74] Shiraki N, Umeda K, Sakashita N, Takeya M, Kume K, Kume S. Differentiation of mouse and human embryonic stem cells into hepatic lineages. *Genes Cells* 2008; 13(7): 731-46. [http://dx.doi.org/10.1111/j.1365-2443.2008.01201.x] [PMID: 18513331]
- [75] Schuppan D, Afdhal NH. Liver cirrhosis. *Lancet* 2008; 371(9615): 838-51. [http://dx.doi.org/10.1016/S0140-6736(08)60383-9] [PMID: 18328931]

- [76] Agarwal S, Holton KL, Lanza R. Efficient differentiation of functional hepatocytes from human embryonic stem cells. *Stem Cells* 2008; 26(5): 1117-27.  
[<http://dx.doi.org/10.1634/stemcells.2007-1102>] [PMID: 18292207]
- [77] Soto-Gutiérrez A, Kobayashi N, Rivas-Carrillo JD, *et al.* Reversal of mouse hepatic failure using an implanted liver-assist device containing ES cell-derived hepatocytes. *Nat Biotechnol* 2006; 24(11): 1412-9.  
[<http://dx.doi.org/10.1038/nbt1257>] [PMID: 17086173]
- [78] Rasouly HM, Lu W. Lower urinary tract development and disease. *Wiley Interdiscip Rev Syst Biol Med* 2013; 5(3): 307-42.  
[<http://dx.doi.org/10.1002/wsbm.1212>] [PMID: 23408557]
- [79] Tripathi P, Guo Q, Wang Y, *et al.* Midline signaling regulates kidney positioning but not nephrogenesis through Shh. *Dev Biol* 2010; 340(2): 518-27.  
[<http://dx.doi.org/10.1016/j.ydbio.2010.02.007>] [PMID: 20152829]
- [80] Santos dos JRP, Piscione TD Development of the kidney and lower urinary tract. Berlin, Heidelberg: Springer Berlin Heidelberg 2013; pp. 1-58.
- [81] Rao PK, Burnett AL. Development of the male reproductive system. London: Springer London 2012; pp. 11-24.
- [82] Healey A. Embryology of the female reproductive tract medical radiology. Berlin, Heidelberg: Springer Berlin Heidelberg 2012; pp. 21-30.
- [83] De Felici M. Primordial germ cell biology at the beginning of the XXI century. *Int J Dev Biol* 2009; 53(7): 891-4.  
[<http://dx.doi.org/10.1387/ijdb.082815mf>] [PMID: 19598110]
- [84] Sajjad Y. Development of the genital ducts and external genitalia in the early human embryo. *J Obstet Gynaecol Res* 2010; 36(5): 929-37.  
[<http://dx.doi.org/10.1111/j.1447-0756.2010.01272.x>] [PMID: 20846260]
- [85] Tanaka SS, Nishinakamura R, Nishinakamura R, Nishinakamura R. Regulation of male sex determination: genital ridge formation and Sry activation in mice. *Cell Mol Life Sci* 2014; 71(24): 4781-802.  
[<http://dx.doi.org/10.1007/s00018-014-1703-3>] [PMID: 25139092]
- [86] Mae S, Shono A, Shiota F, *et al.* Monitoring and robust induction of nephrogenic intermediate mesoderm from human pluripotent stem cells. *Nat Commun* 2013; 4: 1367-7.  
[<http://dx.doi.org/10.1038/ncomms2378>] [PMID: 23340407]
- [87] Kang M, Han Y-M. Differentiation of human pluripotent stem cells into nephron progenitor cells in a serum and feeder free system. *PLoS One* 2014; 9(4): e94888.  
[<http://dx.doi.org/10.1371/journal.pone.0094888>] [PMID: 24728509]
- [88] Taguchi A, Kaku Y, Ohmori T, *et al.* Redefining the *in vivo* origin of metanephric nephron progenitors enables generation of complex kidney structures from pluripotent stem cells. *Cell Stem Cell* 2014; 14(1): 53-67.  
[<http://dx.doi.org/10.1016/j.stem.2013.11.010>] [PMID: 24332837]

- [89] Lam AQ, Freedman BS, Morizane R, Lerou PH, Valerius MT, Bonventre JV. Rapid and efficient differentiation of human pluripotent stem cells into intermediate mesoderm that forms tubules expressing kidney proximal tubular markers. *J Am Soc Nephrol* 2014; 25(6): 1211-25. [http://dx.doi.org/10.1681/ASN.2013080831] [PMID: 24357672]
- [90] Vigneau C, Polgar K, Striker G, *et al.* Mouse embryonic stem cell-derived embryoid bodies generate progenitors that integrate long term into renal proximal tubules *in vivo*. *J Am Soc Nephrol* 2007; 18(6): 1709-20. [http://dx.doi.org/10.1681/ASN.2006101078] [PMID: 17475814]
- [91] Takasato M, Er PX, Chiu HS, *et al.* Kidney organoids from human iPS cells contain multiple lineages and model human nephrogenesis. *Nature* 2015; 526(7574): 564-8. [http://dx.doi.org/10.1038/nature15695] [PMID: 26444236]
- [92] Gupta A, Bischoff A, Peña A, Runck LA, Guasch G. The great divide: septation and malformation of the cloaca, and its implications for surgeons. *Pediatr Surg Int* 2014; 30(11): 1089-95. [http://dx.doi.org/10.1007/s00383-014-3593-8] [PMID: 25217828]
- [93] Hall JE. Control of blood pressure by the renin-angiotensin-aldosterone system. *Clin Cardiol* 1991; 14(8) (Suppl. 4): IV6-IV21. [http://dx.doi.org/10.1002/clc.4960141802] [PMID: 1893644]
- [94] Roberts CS. An overview of the genitourinary system. In: Walker HK, Hall WD, Hurst JW, White JM, Eds. *Clinical Methods: The history, physical and laboratory examinations*. 3<sup>rd</sup> ed., Boston: Butterworths 1990.
- [95] Becker C, Jakse G. Stem cells for regeneration of urological structures. *Eur Urol* 2007; 51(5): 1217-28. [http://dx.doi.org/10.1016/j.eururo.2007.01.029] [PMID: 17254699]
- [96] Adamowicz J, Kowalczyk T, Drewa T. Tissue engineering of urinary bladder – current state of art and future perspectives. 2013; 66(2): 202-6.
- [97] Basile DP, Anderson MD, Sutton TA. Pathophysiology of acute kidney injury. *Compr Physiol* 2012; 2(2): 1303-53. [PMID: 23798302]
- [98] Osborn SL, Thangappan R, Luria A, Lee JH, Nolta J, Kurzrock EA. Induction of human embryonic and induced pluripotent stem cells into urothelium. *Stem Cells Transl Med* 2014; 3(5): 610-9. [http://dx.doi.org/10.5966/sctm.2013-0131] [PMID: 24657961]
- [99] Wu X-R, Kong X-P, Pellicer A, Kreibich G, Sun T-T. Uroplakins in urothelial biology, function, and disease. *Kidney Int* 2009; 75(11): 1153-65. [http://dx.doi.org/10.1038/ki.2009.73] [PMID: 19340092]
- [100] Oottamasathien S, Wang Y, Williams K, *et al.* Directed differentiation of embryonic stem cells into bladder tissue. *Dev Biol* 2007; 304(2): 556-66. [http://dx.doi.org/10.1016/j.ydbio.2007.01.010] [PMID: 17289017]
- [101] Mauney JR, Ramachandran A, Yu RN, Daley GQ, Adam RM, Estrada CR. All-trans retinoic acid directs urothelial specification of murine embryonic stem cells *via* GATA4/6 signaling mechanisms. *PLoS One* 2010; 5(7): e11513. [http://dx.doi.org/10.1371/journal.pone.0011513] [PMID: 20644631]



- [102] De Felici M. Origin, Migration, and Proliferation of Human Primordial Germ Cells. London: Springer London 2012; pp. 19-37.
- [103] Ginsburg M, Snow MH, McLaren A. Primordial germ cells in the mouse embryo during gastrulation. *Development* 1990; 110(2): 521-8. [PMID: 2133553]
- [104] Lawson KA, Hage WJ. Clonal analysis of the origin of primordial germ cells in the mouse. *Ciba Found Symp* 1994; 182: 68-84.
- [105] Ying Y, Zhao G-Q. Cooperation of endoderm-derived BMP2 and extraembryonic ectoderm-derived BMP4 in primordial germ cell generation in the mouse. *Dev Biol* 2001; 232(2): 484-92. [<http://dx.doi.org/10.1006/dbio.2001.0173>] [PMID: 11401407]
- [106] Tremblay KD, Dunn NR, Robertson EJ. Mouse embryos lacking Smad1 signals display defects in extra-embryonic tissues and germ cell formation. 2001; 128(18): 3609-21.
- [107] Lawson KA, Dunn NR, Roelen BA, *et al.* Bmp4 is required for the generation of primordial germ cells in the mouse embryo. *Genes Dev* 1999; 13(4): 424-36. [<http://dx.doi.org/10.1101/gad.13.4.424>] [PMID: 10049358]
- [108] Dudley BM, Runyan C, Takeuchi Y, Schaible K, Molyneaux K. BMP signaling regulates PGC numbers and motility in organ culture. *Mech Dev* 2007; 124(1): 68-77. [<http://dx.doi.org/10.1016/j.mod.2006.09.005>] [PMID: 17112707]
- [109] Magnúsdóttir E, Surani MA. How to make a primordial germ cell. *Development* 2014; 141(2): 245-52. [<http://dx.doi.org/10.1242/dev.098269>] [PMID: 24381195]
- [110] Kurimoto K, Yabuta Y, Ohinata Y, Shigeta M, Yamanaka K, Saitou M. Complex genome-wide transcription dynamics orchestrated by Blimp1 for the specification of the germ cell lineage in mice. *Genes Dev* 2008; 22(12): 1617-35. [<http://dx.doi.org/10.1101/gad.1649908>] [PMID: 18559478]
- [111] Ohinata Y, Payer B, O'Carroll D, *et al.* Blimp1 is a critical determinant of the germ cell lineage in mice. *Nature* 2005; 436(7048): 207-13. [<http://dx.doi.org/10.1038/nature03813>] [PMID: 15937476]
- [112] Durcova-Hills G, Tang F, Doody G, Tooze R, Surani MA. Reprogramming primordial germ cells into pluripotent stem cells. *PLoS One* 2008; 3(10): e3531. [<http://dx.doi.org/10.1371/journal.pone.0003531>] [PMID: 18953407]
- [113] Leitch HG, Blair K, Mansfield W, *et al.* Embryonic germ cells from mice and rats exhibit properties consistent with a generic pluripotent ground state. *Development* 2010; 137(14): 2279-87. [<http://dx.doi.org/10.1242/dev.050427>] [PMID: 20519324]
- [114] Ohinata Y, Ohta H, Shigeta M, Yamanaka K, Wakayama T, Saitou M. A signaling principle for the specification of the germ cell lineage in mice. *Cell* 2009; 137(3): 571-84. [<http://dx.doi.org/10.1016/j.cell.2009.03.014>] [PMID: 19410550]
- [115] Hayashi K, Ohta H, Kurimoto K, Aramaki S, Saitou M. Reconstitution of the mouse germ cell specification pathway in culture by pluripotent stem cells. *Cell* 2011; 146(4): 519-32. [<http://dx.doi.org/10.1016/j.cell.2011.06.052>] [PMID: 21820164]

- [116] Schover LR. Patient attitudes toward fertility preservation. *Pediatr Blood Cancer* 2009; 53(2): 281-4.  
[<http://dx.doi.org/10.1002/pbc.22001>] [PMID: 19301387]
- [117] Lee SJ, Schover LR, Partridge AH, *et al.* American Society of Clinical Oncology recommendations on fertility preservation in cancer patients. *J Clin Oncol* 2006; 24(18): 2917-31.  
[<http://dx.doi.org/10.1200/JCO.2006.06.5888>] [PMID: 16651642]
- [118] Radford J, Shalet S, Lieberman B. Fertility after treatment for cancer. Questions remain over ways of preserving ovarian and testicular tissue. *BMJ* 1999; 319(7215): 935-6.  
[<http://dx.doi.org/10.1136/bmj.319.7215.935>] [PMID: 10514140]
- [119] Radford J. Restoration of fertility after treatment for cancer. *Horm Res* 2003; 59 (Suppl. 1): 21-3.  
[<http://dx.doi.org/10.1159/000067840>] [PMID: 12566716]
- [120] Hermann BP, Sukhwani M, Winkler F, *et al.* Spermatogonial stem cell transplantation into rhesus testes regenerates spermatogenesis producing functional sperm. *Cell Stem Cell* 2012; 11(5): 715-26.  
[<http://dx.doi.org/10.1016/j.stem.2012.07.017>] [PMID: 23122294]
- [121] Shetty G, Uthamantil RK, Zhou W, *et al.* Hormone suppression with GnRH antagonist promotes spermatogenic recovery from transplanted spermatogonial stem cells in irradiated cynomolgus monkeys. *Andrology* 2013; 1(6): 886-98.  
[<http://dx.doi.org/10.1111/j.2047-2927.2013.00126.x>] [PMID: 24124124]
- [122] Berry DC, Stenesen D, Zeve D, Graff JM. The developmental origins of adipose tissue. *Development* 2013; 140(19): 3939-49.  
[<http://dx.doi.org/10.1242/dev.080549>] [PMID: 24046315]
- [123] Shan T, Liang X, Bi P, Zhang P, Liu W, Kuang S. Distinct populations of adipogenic and myogenic Myf5-lineage progenitors in white adipose tissues. *J Lipid Res* 2013; 54(8): 2214-24.  
[<http://dx.doi.org/10.1194/jlr.M038711>] [PMID: 23740968]
- [124] Ibrahim MM. Subcutaneous and visceral adipose tissue: structural and functional differences. *Obes Rev* 2010; 11(1): 11-8.  
[<http://dx.doi.org/10.1111/j.1467-789X.2009.00623.x>] [PMID: 19656312]
- [125] Moreno-Navarrete JM, Fernández-Real JM. *Adipocyte Differentiation*. New York, NY: Springer New York 2011; pp. 17-38.
- [126] Cuaranta-Monroy I, Simandi Z, Kolostyak Z, *et al.* Highly efficient differentiation of embryonic stem cells into adipocytes by ascorbic acid. *Stem Cell Research*. 2014; 13(1): 88-97.
- [127] Han J, Lee JE, Jin J, *et al.* The spatiotemporal development of adipose tissue. *Development* 2011; 138(22): 5027-37.  
[<http://dx.doi.org/10.1242/dev.067686>] [PMID: 22028034]
- [128] Lee Y-K, Cowan CA. Differentiation of white and brown adipocytes from human pluripotent stem cells. *Methods in Enzymology*. 2014; 533: pp. 35-47.  
[<http://dx.doi.org/10.1016/B978-0-12-800280-3.00003-7>]
- [129] Dani C, Smith AG, Dessolin S, *et al.* Differentiation of embryonic stem cells into adipocytes *in vitro*. *J Cell Sci* 1997; 110(Pt 11): 1279-85.  
[PMID: 9202388]

- [130] Mohsen-Kanson T, Hafner A-L, Wdziekonski B, *et al.* Differentiation of human induced pluripotent stem cells into brown and white adipocytes: role of Pax3. *Stem Cells* 2014; 32(6): 1459-67. [http://dx.doi.org/10.1002/stem.1607] [PMID: 24302443]
- [131] Nishio M, Saeki K. Differentiation of Human Pluripotent Stem Cells into Highly Functional Classical Brown Adipocytes. *Methods in Enzymology*. 2014; 537: pp. 177-97. [http://dx.doi.org/10.1016/B978-0-12-411619-1.00010-0]
- [132] Nishio M, Yoneshiro T, Nakahara M, *et al.* Production of functional classical brown adipocytes from human pluripotent stem cells using specific hemopoietin cocktail without gene transfer. *Cell Metabolism* 2012; 16(3): 394-406.
- [133] Tseng Y-H, Kokkotou E, Schulz TJ, *et al.* New role of bone morphogenetic protein 7 in brown adipogenesis and energy expenditure. *Nature* 2008; 454(7207): 1000-4. [http://dx.doi.org/10.1038/nature07221] [PMID: 18719589]
- [134] Hull CW. The birth of 3D printing: IRI achievement award address. *Res Technol Manage* 2015; 58(6): 25-9.
- [135] Gross BC, Erkal JL, Lockwood SY, Chen C, Spence DM. Evaluation of 3D printing and its potential impact on biotechnology and the chemical sciences. *Anal Chem* 2014; 86(7): 3240-53. [http://dx.doi.org/10.1021/ac403397r] [PMID: 24432804]
- [136] Willerth SM, Sakiyama-Elbert SE. Combining stem cells and biomaterial scaffolds for constructing tissues and cell delivery. Cambridge, MA: Harvard Stem Cell Institute 2008.
- [137] Murphy SV, Atala A. 3D bioprinting of tissues and organs. *Nat Biotechnol* 2014; 32(8): 773-85. [http://dx.doi.org/10.1038/nbt.2958] [PMID: 25093879]
- [138] Chia HN, Wu BM. Recent advances in 3D printing of biomaterials 2015; 9(1): 4-18.
- [139] Richards DJ, Tan Y, Jia J, Yao H, Mei Y. 3D printing for tissue engineering. *Isr J Chem* 2013; 53(9-10): 805-14. [PMID: 26869728]
- [140] Li J, He L, Zhou C, Zhou Y, *et al.* 3D printing for regenerative medicine: From bench to bedside. *MRS Bull* 2015; 40(2): 145-54. [http://dx.doi.org/10.1557/mrs.2015.5]
- [141] Derby B. Inkjet printing of functional and structural materials: fluid property requirements, feature stability, and resolution. *Annu Rev Mater Res* 2010; 40(1): 395-414. [http://dx.doi.org/10.1146/annurev-matsci-070909-104502]
- [142] Zein I, Huttmacher DW, Tan KC, Teoh SH. Fused deposition modeling of novel scaffold architectures for tissue engineering applications. *Biomaterials* 2002; 23(4): 1169-85. [http://dx.doi.org/10.1016/S0142-9612(01)00232-0] [PMID: 11791921]
- [143] Stanton MM, Samitier J, Sánchez S. Bioprinting of 3D hydrogels. *Lab Chip* 2015; 15(15): 3111-5. [http://dx.doi.org/10.1039/C5LC90069G] [PMID: 26066320]
- [144] Rutz AL, Hyland KE, Jakus AE, Burghardt WR, Shah RN. A multimaterial bioink method for 3D printing tunable, cell-compatible hydrogels. *Adv Mater* 2015; 27(9): 1607-14. [http://dx.doi.org/10.1002/adma.201405076] [PMID: 25641220]

- [145] Hwang S, Reyes EI, Moon K-S, Rumpf RC, Kim NS. Thermo-mechanical characterization of metal/polymer composite filaments and printing parameter study for fused deposition modeling in the 3D printing process. *Journal of Elec Materi* 2014; 44(3): 771-7.  
[<http://dx.doi.org/10.1007/s11664-014-3425-6>]
- [146] Annabi N, Tamayol A, Uquillas JA, *et al.* 25<sup>th</sup> anniversary article: Rational design and applications of hydrogels in regenerative medicine. *Adv Mater* 2014; 26(1): 85-123.  
[<http://dx.doi.org/10.1002/adma.201303233>] [PMID: 24741694]
- [147] West JL, Hubbell JA. Polymeric biomaterials with degradation sites for proteases involved in cell migration. *Macromolecules* 1999; 32(1): 241-4.  
[<http://dx.doi.org/10.1021/ma981296k>]
- [148] Ma PX. Biomimetic materials for tissue engineering. *Adv Drug Deliv Rev* 2008; 60(2): 184-98.  
[<http://dx.doi.org/10.1016/j.addr.2007.08.041>] [PMID: 18045729]
- [149] Williams DF. On the mechanisms of biocompatibility. *Biomaterials* 2008; 29(20): 2941-53.  
[<http://dx.doi.org/10.1016/j.biomaterials.2008.04.023>] [PMID: 18440630]
- [150] Fournier E, Passirani C, Montero-Menei CN, Benoit JP. Biocompatibility of implantable synthetic polymeric drug carriers: focus on brain biocompatibility. *Biomaterials* 2003; 24(19): 3311-31.  
[[http://dx.doi.org/10.1016/S0142-9612\(03\)00161-3](http://dx.doi.org/10.1016/S0142-9612(03)00161-3)] [PMID: 12763459]
- [151] Lutolf MP, Gilbert PM, Blau HM. Designing materials to direct stem-cell fate. *Nature* 2009; 462(7272): 433-41.  
[<http://dx.doi.org/10.1038/nature08602>] [PMID: 19940913]
- [152] Talbot EL, Berson A, Brown PS, Bain CD. Evaporation of picoliter droplets on surfaces with a range of wettabilities and thermal conductivities. *Phys Rev E Stat Nonlin Soft Matter Phys* 2012; 85(6 Pt 1): 061604.  
[<http://dx.doi.org/10.1103/PhysRevE.85.061604>] [PMID: 23005106]
- [153] Yao P, Fox PL. Aminoacyl-tRNA synthetases in medicine and disease. *EMBO Mol Med* 2013; 5(3): 332-43.  
[<http://dx.doi.org/10.1002/emmm.201100626>] [PMID: 23427196]
- [154] Skorb EV, Andreeva DV. Surface Nanoarchitecture for bio-applications: self-regulating intelligent interfaces. *Adv Funct Mater* 2013; 23(36): 4483-506.  
[<http://dx.doi.org/10.1002/adfm.201203884>]
- [155] Fedorovich NE, Alblas J, Hennink WE, Oner FC, Dhert WJ. Organ printing: the future of bone regeneration? *Trends Biotechnol* 2011; 29(12): 601-6.  
[<http://dx.doi.org/10.1016/j.tibtech.2011.07.001>] [PMID: 21831463]
- [156] Bose S, Vahabzadeh S, Bandyopadhyay A. Bone tissue engineering using 3D printing. *Mater Today* 2013; 16(12): 496-504.  
[<http://dx.doi.org/10.1016/j.mattod.2013.11.017>]
- [157] Li X, Akasaka T, Dunne N. Polymeric scaffolds for tissue engineering. *Int J Polym Sci* 2014; (Aug): 2014.
- [158] Crapo PM, Gilbert TW, Badylak SF. An overview of tissue and whole organ decellularization processes. *Biomaterials* 2011; 32(12): 3233-43.

- [http://dx.doi.org/10.1016/j.biomaterials.2011.01.057] [PMID: 21296410]
- [159] Lee M, Wu BM. Recent advances in 3D printing of tissue engineering scaffolds. Computer-Aided Tissue Engineering. Humana Press 2012.  
[http://dx.doi.org/10.1007/978-1-61779-764-4\_15]
- [160] Leukers B, Gulkan H, Irsen SH, Milz S, *et al.* Biocompatibility of ceramic scaffolds for bone replacement made by 3D printing. Materialwiss Werkstofftech 2005; 36(12): 781-7.  
[http://dx.doi.org/10.1002/mawe.200500968]
- [161] Gu Q, Hao J, Lu Y, Wang L, Wallace GG, Zhou Q. Three-dimensional bio-printing. Sci China Life Sci 2015; 58(5): 411-9.  
[http://dx.doi.org/10.1007/s11427-015-4850-3] [PMID: 25921944]
- [162] Tekin H, Sanchez JG, Landeros C, Dubbin K, Langer R, Khademhosseini A. Controlling spatial organization of multiple cell types in defined 3D geometries. Adv Mater Weinheim 2012; 24(41): 5543-7.
- [163] Howard D, Buttery LD, Shakesheff KM, Roberts SJ. Tissue engineering: strategies, stem cells and scaffolds. J Anat 2008; 213(1): 66-72.  
[http://dx.doi.org/10.1111/j.1469-7580.2008.00878.x] [PMID: 18422523]
- [164] Fändrich F, Schulze M, Zehle G, Lange H, Ungefroren H. Stem cell-mediated tolerance inducing strategies in organ transplantation. Kidney Int 2004; 65(5): 1548-50.  
[http://dx.doi.org/10.1111/j.1523-1755.2004.05408.x] [PMID: 15086889]
- [165] Olabisi RM. Cell microencapsulation with synthetic polymers. J Biomed Mater Res A 2015; 103(2): 846-59.  
[http://dx.doi.org/10.1002/jbm.a.35205] [PMID: 24771675]
- [166] Turksen K. Bioprinting in Regenerative Medicine. Springer 2015.  
[http://dx.doi.org/10.1007/978-3-319-21386-6]
- [167] Cao H, Kuboyama N. A biodegradable porous composite scaffold of PGA/beta-TCP for bone tissue engineering. Bone 2010; 46(2): 386-95.  
[http://dx.doi.org/10.1016/j.bone.2009.09.031] [PMID: 19800045]
- [168] Ogawa T, Akazawa T, Tabata Y. *In vitro* proliferation and chondrogenic differentiation of rat bone marrow stem cells cultured with gelatin hydrogel microspheres for TGF-beta1 release. J Biomater Sci Polym Ed 2010; 21(5): 609-21.  
[http://dx.doi.org/10.1163/156856209X434638] [PMID: 20338095]
- [169] Nguyen TB, Min YK, Lee B-T. Nanoparticle biphasic calcium phosphate loading on gelatin-pectin scaffold for improved bone regeneration. Tissue Eng Part A 2015; 21(7-8): 1376-87.  
[http://dx.doi.org/10.1089/ten.tea.2014.0313] [PMID: 25602709]
- [170] Kanematsu A, Yamamoto S, Ozeki M, *et al.* Collagenous matrices as release carriers of exogenous growth factors. Biomaterials 2004; 25(18): 4513-20.  
[http://dx.doi.org/10.1016/j.biomaterials.2003.11.035] [PMID: 15046942]
- [171] Rosenzweig DH, Carelli E, Steffen T, Jarzem P, Haglund L. 3D-Printed ABS and PLA scaffolds for cartilage and nucleus pulposus tissue regeneration. Int J Mol Sci 2015; 16(7): 15118-35.  
[http://dx.doi.org/10.3390/ijms160715118] [PMID: 26151846]

- [172] Chang M-Y, Shiau A-L, Chen Y-H, Chang C-J, Chen HH, Wu C-L. Increased apoptotic potential and dose-enhancing effect of gold nanoparticles in combination with single-dose clinical electron beams on tumor-bearing mice. *Cancer Sci* 2008; 99(7): 1479-84.  
[<http://dx.doi.org/10.1111/j.1349-7006.2008.00827.x>] [PMID: 18410403]
- [173] Nair K, Gandhi M, Khalil S, *et al.* Characterization of cell viability during bioprinting processes. *Biotechnol J* 2009; 4(8): 1168-77.  
[<http://dx.doi.org/10.1002/biot.200900004>] [PMID: 19507149]
- [174] Xu T, Jin J, Gregory C, Hickman JJ, Boland T. Inkjet printing of viable mammalian cells. *Biomaterials* 2005; 26(1): 93-9.  
[<http://dx.doi.org/10.1016/j.biomaterials.2004.04.011>] [PMID: 15193884]
- [175] Chang R, Nam J, Sun W. Direct cell writing of 3D microorgan for *in vitro* pharmacokinetic model. *Tissue Eng Part C Methods* 2008; 14(2): 157-66.  
[<http://dx.doi.org/10.1089/ten.tec.2007.0392>] [PMID: 18544030]
- [176] Yu Y, Zhang Y, Martin JA, Ozbolat IT. Evaluation of cell viability and functionality in vessel-like bioprintable cell-laden tubular channels. *J Biomech Eng* 2013; 135(9): 91011.  
[<http://dx.doi.org/10.1115/1.4024575>] [PMID: 23719889]
- [177] Stern-Straeter J, Bonaterra GA, Kassner SS, *et al.* Characterization of human myoblast differentiation for tissue-engineering purposes by quantitative gene expression analysis. *J Tissue Eng Regen Med* 2011; 5(8): e197-206.  
[<http://dx.doi.org/10.1002/term.417>] [PMID: 21370490]
- [178] Li JP, de Wijn JR, van Blitterswijk CA, de Groot K. The effect of scaffold architecture on properties of direct 3D fiber deposition of porous Ti6Al4V for orthopedic implants. *J Biomed Mater Res A* 2010; 92(1): 33-42.  
[<http://dx.doi.org/10.1002/jbm.a.32330>] [PMID: 19165798]
- [179] Jeong CG, Hollister SJ. Mechanical, permeability, and degradation properties of 3D designed poly(1,8 octanediol-co-citrate) scaffolds for soft tissue engineering. *J Biomed Mater Res B Appl Biomater* 2010; 93(1): 141-9.  
[PMID: 20091910]
- [180] Do AV, Khorsand B, Geary SM, Salem AK. 3D Printing of Scaffolds for Tissue Regeneration Applications. *Adv Healthc Mater* 2015; 4(12): 1742-62.  
[<http://dx.doi.org/10.1002/adhm.201500168>] [PMID: 26097108]
- [181] Chang JW, Park SA, Park JK, *et al.* Tissue-engineered tracheal reconstruction using three-dimensionally printed artificial tracheal graft: preliminary report. *Artif Organs* 2014; 38(6): E95-E105.  
[<http://dx.doi.org/10.1111/aor.12310>] [PMID: 24750044]
- [182] Zopf DA, Hollister SJ, Nelson ME, Ohye RG, Green GE. Bioresorbable airway splint created with a three-dimensional printer. *N Engl J Med* 2013; 368(21): 2043-5.  
[<http://dx.doi.org/10.1056/NEJMc1206319>] [PMID: 23697530]
- [183] Park JH, Hong JM, Ju YM, *et al.* A novel tissue-engineered trachea with a mechanical behavior similar to native trachea. *Biomaterials* 2015; 62: 106-15.  
[<http://dx.doi.org/10.1016/j.biomaterials.2015.05.008>] [PMID: 26041482]

- [184] Zopf DA, Flanagan CL, Wheeler M, Hollister SJ, Green GE. Treatment of severe porcine tracheomalacia with a 3-dimensionally printed, bioresorbable, external airway splint. *JAMA Otolaryngol Head Neck Surg* 2014; 140(1): 66-71.  
[<http://dx.doi.org/10.1001/jamaoto.2013.5644>] [PMID: 24232078]
- [185] Mozaffarian D, Benjamin EJ, Go AS, *et al.* Heart disease and stroke statistics--2015 update: a report from the American Heart Association. *Circulation* 2015; 131(4): e29-e322.  
[<http://dx.doi.org/10.1161/CIR.0000000000000152>] [PMID: 25520374]
- [186] Koch MB, Davidsen M, Andersen LV, Juel K, Jensen GB, Galinier A, *et al.* Increasing prevalence despite decreasing incidence of ischaemic heart disease and myocardial infarction. A national register based perspective in Denmark, 1980-2009. *Eur J Prev Cardiol* 2015; 22(2): 189-95.  
[<http://dx.doi.org/10.1177/2047487313509495>] [PMID: 24165474]
- [187] Lee VK, Lanzi AM, Haygan N, Yoo SS, Vincent PA, Dai G. Generation of multi-scale vascular network system within 3D hydrogel using 3D bio-printing technology. *Cell Mol Bioeng* 2014; 7(3): 460-72.  
[<http://dx.doi.org/10.1007/s12195-014-0340-0>] [PMID: 25484989]
- [188] Gaetani R, Doevendans PA, Metz CH, *et al.* Cardiac tissue engineering using tissue printing technology and human cardiac progenitor cells. *Biomaterials* 2012; 33(6): 1782-90.  
[<http://dx.doi.org/10.1016/j.biomaterials.2011.11.003>] [PMID: 22136718]
- [189] Pati F, Jang J, Ha DH, *et al.* Printing three-dimensional tissue analogues with decellularized extracellular matrix bioink. *Nat Commun* 2014; 5: 3935.  
[<http://dx.doi.org/10.1038/ncomms4935>] [PMID: 24887553]
- [190] Jana S, Tranquillo RT, Lerman A. Cells for tissue engineering of cardiac valves. *J Tissue Eng Regen Med* 2015; 10(10): 804-24.  
[<http://dx.doi.org/10.1002/term.2010>] [PMID: 25712485]
- [191] Duan B, Hockaday LA, Kang KH, Butcher JT. 3D bioprinting of heterogeneous aortic valve conduits with alginate/gelatin hydrogels. *J Biomed Mater Res A* 2013; 101(5): 1255-64.  
[<http://dx.doi.org/10.1002/jbm.a.34420>] [PMID: 23015540]
- [192] Lund O, Chandrasekaran V, Grocott-Mason R, *et al.* Primary aortic valve replacement with allografts over twenty-five years: valve-related and procedure-related determinants of outcome. *J Thorac Cardiovasc Surg* 1999; 117(1): 77-90.  
[[http://dx.doi.org/10.1016/S0022-5223\(99\)70471-X](http://dx.doi.org/10.1016/S0022-5223(99)70471-X)] [PMID: 9869760]
- [193] Norotte C, Marga FS, Niklason LE, Forgacs G. Scaffold-free vascular tissue engineering using bioprinting. *Biomaterials* 2009; 30(30): 5910-7.  
[<http://dx.doi.org/10.1016/j.biomaterials.2009.06.034>] [PMID: 19664819]
- [194] Hasan A, Khattab A, Islam MA, *et al.* Injectable Hydrogels for Cardiac Tissue Repair after Myocardial Infarction. *Adv Sci* 2015; 2(11)  
[<http://dx.doi.org/10.1002/advs.201500122>]
- [195] Chen Y-C, Lin R-Z, Qi H, *et al.* Functional human vascular network generated in photocrosslinkable gelatin methacrylate hydrogels. *Adv Funct Mater* 2012; 22(10): 2027-39.  
[<http://dx.doi.org/10.1002/adfm.201101662>] [PMID: 22907987]

- [196] Leo WJ, McLoughlin AJ, Malone DM. Effects of sterilization treatments on some properties of alginate solutions and gels. *Biotechnol Prog* 1990; 6(1): 51-3.  
[<http://dx.doi.org/10.1021/bp00001a008>] [PMID: 1366434]
- [197] Ventola CL. Medical applications for 3D printing: current and projected uses. *P&T* 2014; 39(10): 704-11.  
[PMID: 25336867]
- [198] Komae H, Sekine H, Dobashi I, *et al.* Three-dimensional functional human myocardial tissues fabricated from induced pluripotent stem cells. *J Tissue Eng Regen Med* 2015.  
[<http://dx.doi.org/10.1002/term.1995>] [PMID: 25628251]
- [199] Ozbolat IT, Yu Y. Bioprinting toward organ fabrication: challenges and future trends. *IEEE Trans Biomed Eng* 2013; 60(3): 691-9.  
[<http://dx.doi.org/10.1109/TBME.2013.2243912>] [PMID: 23372076]
- [200] Kusuma S, Shen Y-I, Hanjaya-Putra D, Mali P, Cheng L, Gerecht S. Self-organized vascular networks from human pluripotent stem cells in a synthetic matrix. *Proc Natl Acad Sci USA* 2013; 110(31): 12601-6.  
[<http://dx.doi.org/10.1073/pnas.1306562110>] [PMID: 23858432]
- [201] Shanks N, Greek R, Greek J. Are animal models predictive for humans? *Philos Ethics Humanit Med* 2009; 4(2): 2.  
[<http://dx.doi.org/10.1186/1747-5341-4-2>] [PMID: 19146696]
- [202] Mak IW, Evaniew N, Ghert M. Lost in translation: animal models and clinical trials in cancer treatment. *Am J Transl Res* 2014; 6(2): 114-8.  
[PMID: 24489990]
- [203] McGreevy JW, Hakim CH, McIntosh MA, Duan D. Animal models of Duchenne muscular dystrophy: from basic mechanisms to gene therapy. *Dis Model Mech* 2015; 8(3): 195-213.  
[<http://dx.doi.org/10.1242/dmm.018424>] [PMID: 25740330]



## Appendix II: Macrophage colony stimulating factor receptor: A potential cell surface marker for prostate oncogenesis.

Poster Presentation Abstracts

29

defined by AO staining, along with light microscopy and immunofluorescence morphological study. Other markers such as LC3B, SQSTM1/p62, Beclin-1 and mTOR pathway related proteins were assessed by confocal microscopy, western blotting and ELISA analysis.

**Results:** MPL induced accumulation of acidic vesicular organelles (AVO) which was found to be associated with autophagy and inhibition of phosphorylation of mTOR together with its downstream target proteins namely p70S6K and 4E-BP1.

**Conclusion:** MPL suppression of ovarian cancer growth may be associated with its capacity to block mTOR activation and induction of autophagy.

### P05: STUDIES ON COMBINATIONS OF TARGETED DRUGS WITH TUMOUR ACTIVE PLANT COMPOUNDS IN CANCER

Hana Faisal Bali, Jun Qing Yu, Philip Beale, Charles Chan, Fazlul Huq

Discipline of Biomedical Science, School of Medical Sciences, Sydney Medical School, University of Sydney, Australia

**Introduction:** Colorectal cancer is the second most common cancer affecting people in Australia for which the intrinsic drug resistance present as a major problem. Tumour active phytochemicals in combination with targeted therapy offer a means of overcoming drug resistance. This study aims to investigate synergism in activity from combinations of platinum with selected tumour active phytochemicals in colorectal tumour models.

**Methods:** Cytotoxic activities of the compounds (cisplatin, curcumin and indol-3-carbinol) alone and in combination against colorectal cancer cell lines H29/129 and Caco-2 are determined using MTT reduction assay. Combination indices are used as a quantitative measure of the nature of combined drug action.

**Results:** The IC<sub>50</sub> values of curcumin, indol-3-carbinol and cisplatin for H29/129 and Caco-2 were found to be cisplatin: 5 µM ± 0.65 and 26.02 µM ± 0.96; Curcumin: 17.25 µM ± 0.92 and 29.20 µM ± 1.38; and indol-3-carbinol: 89.38 µM ± 3.37 and 96.830 µM ± 5.71. Combination studies are in progress.

**Discussion:** Although the study in the initial stage, the large IC<sub>50</sub> values can be seen to indicate the presence of large resistance. Since the mechanisms of action of cisplatin and the phytochemicals are likely to be different, appropriately sequenced combinations of cisplatin with the phytochemicals may bring about pronounced cell death.

### P06: DEVELOPMENT AND TESTING THE ACCEPTABILITY OF REKINDLE, A WEB-BASED PSYCHOSEXUAL RESOURCE FOR ALL CANCER SURVIVORS AND THEIR PARTNERS

Catalina Lawsin<sup>1</sup>, Amelia Beaumont<sup>1</sup>, Phyllis Butow<sup>1</sup>, Annie Miller<sup>2</sup>, Judy Kay<sup>1</sup>, Kevin McGeechan<sup>1</sup>, Ilona Juraskova<sup>1</sup>, Fran Boyle<sup>1</sup>, Lee Ritterband<sup>3</sup>, Haryana Dhillon<sup>1</sup>, Kim Hobbs<sup>4</sup>, Zac Seidler<sup>1</sup>, Katherine Dobinson<sup>1</sup>, Gillian Batt<sup>2</sup>, Lori Brotto<sup>5</sup>

<sup>1</sup>University of Sydney, NSW, Australia, <sup>2</sup>Cancer Counsel NSW, Sydney, <sup>3</sup>BeHealth Solution, Virginia, USA, <sup>4</sup>Westmead Hospital, Sydney, <sup>5</sup>University of British Columbia, Vancouver, Canada

**Introduction:** Changes in sexual wellbeing after cancer treatment can lead to psychological distress for cancer survivors, impacting long-term quality of life for both cancer survivors and their partners. Psychosocial and pharmaceutical interventions have proven beneficial in reducing this burden, but are not accessed by most cancer survivors and their partners. This project aims to develop and test the acceptability of *Rekindle* as a theoretically guided, tailored and adaptive web-based psycho-educational resource to address sexual concerns for cancer survivors and their partners and demonstrate its acceptability.

**Methods:** The *Rekindle* design and construction was based on: i) empirical evidence gathered from a literature review; ii) qualitative interviews with cancer survivors and partners; iii) an online survey of psychosexual support intervention preferences; and iv) consultation with sexuality experts.

**Results:** Interviews with 20 survivors and 4 partners (ongoing) highlighted the importance of communication and the need for self-guided communication skills training. The online survey completed by 324 cancer survivors offered a clear preference for online delivery (27%) and interest in participating in interventions with their partner (32%). Embarrassment (28%) and lack of privacy (22%) were the most commonly cited barriers to uptake of psychosexual support, which provided further direction for *Rekindle*'s design and structure. These findings together with the literature review led to the development of seven modules for *Rekindle* addressing the reported sexual concerns and unmet needs. This presentation will describe and demonstrate how *Rekindle* works.

**Conclusions:** *Rekindle* has been designed to address significant sexual concerns amongst cancer survivors and their partners by offering accessible, private and cost-effective support. *Rekindle* uses information technology to create a tailored supportive care service to patients and their partners. Moreover, *Rekindle* may serve as a model for service delivery and integration of support services into standard care.

### P07: MACROPHAGE COLONY STIMULATING FACTOR RECEPTOR: A POTENTIAL CELL SURFACE MARKER FOR PROSTATE ONCOGENESIS

Badwi (Bobby) Boumelhem, Stephen Assinder, Stuart Fraser

Discipline of Physiology, School of Medical Science, Bosch Institute, University of Sydney, Australia

Prostate cancer is the most Common male malignancy and is the second most common cause of male cancer – Related deaths. The prostate is a male sex accessory gland and functions to provide constituents of seminal fluid. *In vitro* models of prostate development and prostate cancer are poor. Mouse embryonic stem (mES) cells are pluripotent, undifferentiated cells that have the capability to generate any cell type in the body and can be employed as useful *in vitro* models of early embryonic development. His feature is particularly useful since many processes of embryogenesis are reactivated during oncogenesis. Transient expression of macrophage Colony Stimulating Factor Receptor (CSF-1R) has been reported in the development of the prostate. In addition, CSF-1R as seen shown to be an important regulator in a range of human cancers. CSF-1R re-expression is suggested to be a prognostic actor able to predict the development of prostatic cancer metastases. Thus we aimed to explore CSF-1R as a potential surface marker for the identification of precursor prostatic cells during prostate development. Tissues that originate from the urogenital sinus, including the prostate, bladder and seminiferous tubules were dissected from prenatal and postnatal male mice and single cell suspensions were generated. Cells were stained with a combination of CSF-1R, epithelial marker EpCAM and macrophage marker F4/80. mES cells were also stained to assess whether CSF-1R has any involvement in the generation of the endoderm lineage, a precursor to the urogenital sinus. Flow cytometric analysis revealed CSF-1R is not expressed in the epithelium of urogenital tissues in newborn and young mice. However, it is expressed in fetal mice. also, CSF-1R is not expressed on either undifferentiated or differentiated mES cells. Future studies will aim to generate prostatic epithelium from wild-type and oncogenic mES cells and assess the role of CSF-1R in prostate organogenesis and oncogenesis.

### P08: COPPER AND CHEMOTHERAPY TRANSPORTER CTR1, INFLUENCES EMBRYONIC AND TUMOUR DEVELOPMENT

Kurt Brigden<sup>1,3</sup>, Heather Main<sup>4</sup> and Stuart Fraser<sup>1,2,3</sup>

<sup>1</sup>Disciplines of Physiology, <sup>2</sup>Anatomy & Histology and <sup>3</sup>Bosch Institute, <sup>4</sup>School of Physics, University of Sydney

Copper is an essential trace element, serving as a cofactor for many important enzymes and proteins. Copper uptake occurs through two highly conserved copper transporters, Copper transporter 1 (Ctr1) and Copper transporter 2 (Ctr2). These transporters are also responsible for the uptake of platinum-based chemotherapies such as cisplatin, oxaliplatin and carboplatin. Copper transporter expression correlates with outcome, with higher CTR1 expression associated with greater cisplatin uptake. As *Ctr1*

### **Appendix III: A new carborane-containing fluorophore as a stain of cellular lipid droplets.**

## Cellular Markers

# A Carborane-Containing Fluorophore as a Stain of Cellular Lipid Droplets

Andrew Wu<sup>+, [a]</sup>, Jacek L. Kolanowski<sup>+, [a]</sup>, Badwi B. Boumelhem,<sup>[b]</sup> Kylie Yang,<sup>[a]</sup> Rebecca Lee,<sup>[a]</sup> Amandeep Kaur,<sup>[a]</sup> Stuart T. Fraser,<sup>[b]</sup> Elizabeth J. New,<sup>\*, [a]</sup> and Louis M. Rendina<sup>\*, [a]</sup>

**Abstract:** The use of fluorescent markers and probes greatly enhances biological investigations but relies on the provision of an array of fluorophores with diverse properties. Herein we report a novel carborane-containing coumarin, **5**, which is sufficiently lipophilic to localise in cellular lipid droplets. In non-polar solvents which show comparable polarities to those of a lipid environment, compound **5** exhibits a fluorescence quantum yield two orders of magnitude greater than found in aqueous solvents, adding a further degree of selectivity to lipid droplet imaging. Compound **5** can stain lipid droplets in ex vivo adipocytes as well as in cultured cells, and can be utilised in flow cytometry as well as confocal microscopy.

Fluorescence techniques, such as confocal microscopy and flow cytometry, enable the imaging of biological systems with high sensitivity and resolution.<sup>[1]</sup> These methods usually employ fluorophores, whether synthetic or genetically encoded, that may stain organelles or macromolecules, or may respond to chemical conditions and environments.<sup>[2]</sup> Amongst the important classes of small-molecule fluorophores are the coumarins, which are commonly employed for imaging applications due to their good stability, water solubility and facile synthesis.<sup>[3]</sup> The structure–photophysical relationships of coumarins have been extensively studied, enabling the design of new analogues with superior properties for biological application.

The presence of electron-donating groups at the 7-position of coumarin or electron-withdrawing groups at the 3-position

can significantly shift the fluorescence band to longer wavelengths, including the NIR.<sup>[3,4]</sup> This bathochromic shift is advantageous for fluorescence applications, as longer emission wavelengths are distinct from cellular autofluorescence, exhibit greater tissue penetration, and typically require the use of lower energy, less damaging excitation wavelengths. 7-Dialkylaminocoumarins can undergo an efficient intramolecular charge transfer (ICT) from the electron-donating amino group to the carbonyl group of the coumarin ring, which results in a large excited-state dipole moment, and a large Stokes-shifted fluorescence emission, usually sensitive to the polarity of the environment. The incorporation of electron-withdrawing substituents such as phenyl at the 3-position of coumarin facilitates the ICT process by stabilising the excited state, and can therefore increase the quantum yield as well as inducing a bathochromic shift.<sup>[5]</sup> When C-bonded, the bioisosteric *closo*-carborane cage is also electron-withdrawing and highly lipophilic,<sup>[6]</sup> which could be advantageous in the visualisation of lipid structures within cells, for example.<sup>[7]</sup> Carboranes have been incorporated into a variety of organic molecules,<sup>[8]</sup> metal complexes,<sup>[9]</sup> and polymers,<sup>[10]</sup> or C-functionalised with bulky electron-deficient moieties such as dimesitylboryl, to afford new luminescent materials with exquisite emission properties.<sup>[11]</sup> However, very few examples exist of carborane-containing fluorophores being used as cellular probes.<sup>[12]</sup>

To the best of our knowledge, there exists only one single report of carborane-containing coumarins. In 2007, Justus et al. reported the synthesis and structural characterisation of a series of 4-substituted *closo*-1,2- and *closo*-1,7-carborane (and [B<sub>12</sub>H<sub>12</sub>]<sup>2−</sup>) derivatives of the parent coumarin and 6,7-benzocoumarin.<sup>[13]</sup> However, the authors did not report the fluorescence properties of any of these molecules. Herein we report the first example of a new carborane-containing coumarin which selectively stains lipid droplets in live adipocytes and provides a valuable, blue-emitting alternative for the commonly used lipid stain Nile Red.<sup>[14]</sup>

Given the sensitivity of coumarin fluorescence to the electronics of substituents at the 3-position, our probe design involved incorporation of *closo*-carborane at this position of 7-diethylaminocoumarin, to give the boronated derivative **5**. *Nido*-carboranes, in which one BH vertex is selectively removed from the *closo*-carborane cage, typically exhibit markedly different electronic and physical properties to those of the parent, and so the *nido*-carborane analogue **6** was also prepared. Finally, since carboranes are typically incorporated into

[a] A. Wu,<sup>+</sup> Dr. J. L. Kolanowski,<sup>+</sup> K. Yang, R. Lee, A. Kaur, Dr. E. J. New, Prof. L. M. Rendina  
School of Chemistry  
The University of Sydney  
Sydney, NSW 2006 (Australia)  
E-mail: elizabeth.new@sydney.edu.au  
louis.rendina@sydney.edu.au

[b] B. B. Boumelhem, Dr. S. T. Fraser  
Discipline of Physiology, School of Medical Sciences  
The University of Sydney  
Sydney, NSW 2006 (Australia)

[†] These authors contributed equally to this work.

Supporting information for this article can be found under:  
<https://doi.org/10.1002/asia.201700423>.

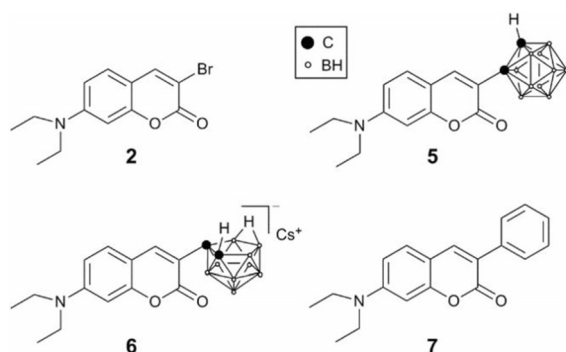


Figure 1. Coumarin derivatives prepared in this study.

bioactive molecules in place of phenyl rings,<sup>[6]</sup> we prepared 7-diethylamino-3-phenylcoumarin **7** for comparison (Figure 1).

The parent 4-(diethylamino)coumarin **1** was prepared by reacting 4-(diethylamino)salicylaldehyde and diethylmalonate with piperidine by following a well-established literature method.<sup>[15]</sup> Halogenation of the alkenyl functionality in **1** to give the 3-bromo derivative **2** did not proceed cleanly when Br<sub>2</sub> or dioxane dibromide was used, with polybrominated products being formed in addition to the desired **2**. However, when *N*-bromosuccinimide (NBS) was employed as the bromination reagent, the reaction proceeded cleanly to afford **2** in high yield (81%). Installation of the TMS-ethyne proceeded smoothly by using standard Sonogashira conditions to give **3** in 65% yield.<sup>[15]</sup> Deprotection of the TMS group in **3** using TBAF in THF/MeOH solution afforded the terminal 3-alkynyl derivative **4**.<sup>[15]</sup> Treatment of **4** with *nido*-decaborane in the presence of the Lewis base CH<sub>3</sub>CN gave the target *closo*-1,2-carboranyl derivative **5** as a bright orange solid (56%). The *closo*-carborane cage was then selectively deboronated by the use of CsF in EtOH under reflux conditions to afford the *nido*-7,8-carboranyl salt Cs-**6** in good yield.

Spectroscopic properties of the coumarin derivatives were assessed in both aqueous solution (phosphate-buffered saline; PBS; pH 7.4) and organic (dichloromethane) solvent (Table 1), and revealed that both the absorption (Figure S1) and emission (Figure S2) profiles of the two carborane-containing compounds were very similar to those of the phenylcoumarin derivative, **7**. However, a marked difference in the quantum yields was observed, with the *closo*- and *nido*-carborane derivatives **5** and **6**, respectively, exhibiting very low quantum yields in PBS, when compared to the phenyl derivative **7**. Interestingly, all three coumarin derivatives showed good quantum yields in dichloromethane. In particular, compound **5** showed the highest

relative increase in brightness when moving from aqueous solution to a hydrophobic environment (Table 1). This result indicates that, of the three compounds assessed, **5** showed the greatest discrimination between aqueous and organic solvents in terms of its brightness. All compounds showed no significant changes within at least the pH range of 5–8 (Figure S3).

Given the promising photophysical properties of our three compounds **5–7**, we investigated their interactions with cultured cells. 3T3-L1 mouse pre-adipocytes were treated with **5–7** (0.1–0.2 μM, 0.1% aqueous DMSO) for 10 min prior to washing and imaging by confocal microscopy. Negligible fluorescence could be observed in cells treated with **6**. In contrast, cells treated with **5** and **7** exhibited very bright, punctate patterns (Figures 2a,b). Co-staining with Nile Red, a commonly used marker of lipid droplets, confirmed that fluorescence from **5** and **7** was localised in these regions. This lipid droplet localisation could also be observed in other cell lines assessed in this study: A549 adenocarcinoma cells, DLD-1 colorectal cancer cells, and RAW 264.7 macrophages (Figures S4–S6). Co-staining experiments with LysoTracker and MitoTracker demonstrated no significant localisation of **5** and **7** in these organelles (Figure S7).

The sub-cellular localisations observed are consistent with the lipophilicities of each compound, as estimated by the partitioning between 1-octanol and water ( $\log P_{\text{oct}}$ ) using the shake-flask method (Table 2). These  $\log P_{\text{oct}}$  values confirm that

Table 2.  $\log P_{\text{oct}}$  values for the coumarin derivatives, as determined by the shake-flask method.

Derivative	$\log P_{\text{oct}}$
<b>5</b>	3.1 ± 0.4
<b>6</b>	1.1 ± 0.1
<b>7</b>	3.4 ± 0.2

*closo*-carboranyl coumarin **5** possesses identical lipophilicity to the phenyl coumarin **7** (within experimental error), in line with previous observations that *closo*-carboranes impart very similar lipophilicity to phenyl derivatives.<sup>[6]</sup> These values are also consistent with the high lipophilicity required for lipid droplet compartmentalisation.<sup>[16]</sup> In contrast, compound **6** was less lipophilic by 2 orders of magnitude, as expected, due to its charged, hydrophilic nature.<sup>[17]</sup>

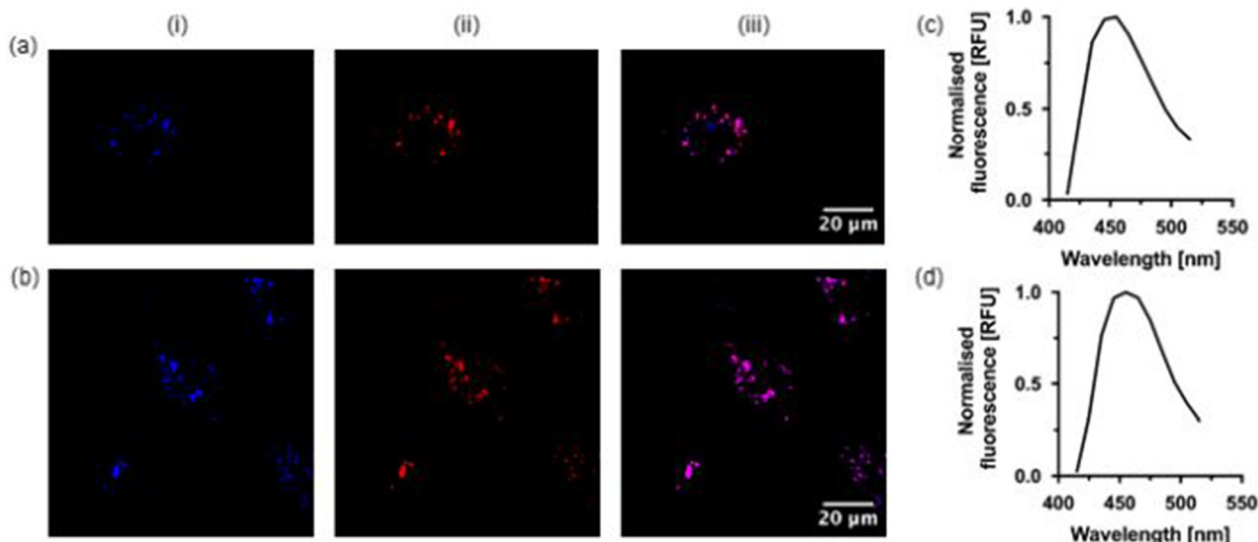
The weak intracellular fluorescence of **6** compared to **5** and **7** is likely to be due to both the lower lipophilicity, which is expected to lead to poorer cellular uptake, as well as the weaker

Table 1. Spectroscopic properties of coumarin derivatives in phosphate-buffered saline (PBS, pH 7.4) and dichloromethane (DCM).

Compound	$\lambda_{\text{max}}$ (abs.) [nm]		$\epsilon$ (at 400 nm) [M <sup>-1</sup> cm <sup>-1</sup> ]		$\lambda_{\text{max}}$ (em.) [nm]		$\Phi$ (400 nm excitation)		Brightness <sup>[a]</sup> [M <sup>-1</sup> cm <sup>-1</sup> ]		
	PBS	DCM	PBS	DCM	PBS	DCM	PBS	DCM	PBS	DCM	Ratio (DCM/PBS)
<b>5</b>	406	402	2.0 × 10 <sup>4</sup>	3.1 × 10 <sup>4</sup>	484	452	4.8 × 10 <sup>-12</sup>	4.0 × 10 <sup>-1</sup>	9.5 × 10 <sup>2</sup>	1.3 × 10 <sup>4</sup>	13.4
<b>6</b>	396	393	5.4 × 10 <sup>3</sup>	9.8 × 10 <sup>3</sup>	476	460	3.9 × 10 <sup>-2</sup>	1.4 × 10 <sup>-1</sup>	2.1 × 10 <sup>2</sup>	1.4 × 10 <sup>3</sup>	6.5
<b>7</b>	406	406	3.2 × 10 <sup>4</sup>	6.5 × 10 <sup>4</sup>	496	460	1.8 × 10 <sup>-1</sup>	6.6 × 10 <sup>-1</sup>	5.9 × 10 <sup>3</sup>	4.3 × 10 <sup>4</sup>	7.2

[a] Brightness was calculated according to the equation:  $B(\lambda) = \phi\epsilon(\lambda)$ .





**Figure 2.** Confocal microscope images of 3T3-L1 cells treated with both Nile Red (0.5 μM) and (a) **5** (0.1 μM) or (b) **7** (0.1 μM), showing (i) coumarin fluorescence (405 nm excitation, λ<sub>em</sub> = 415 nm – 455 nm), (ii) Nile Red fluorescence (405 nm excitation, λ<sub>em</sub> = 540 nm – 580 nm), and (iii) overlay. Confocal microscope spectroscopic scans of coumarin emission (c) **5** and (d) **7**.

fluorescence observed in both organic and aqueous solvents. As a result, the *nido*-carborane derivative **6** was not studied any further. Photostability studies of **5** and **7** confirmed good stability over multiple scans, with less than a 30% decrease in intensity after more than 200 scans (Figure S8). Intracellular spectra of **5** and **7** in 3T3-L1 cells (Figures 2c and d) were compared to the *in vitro* emission spectra of **5** and **7** in a range of solvents of varying polarity (Figure S9, Table S1). This analysis revealed that the emission profile of both compounds in cellulo most closely matched that of dichloromethane. This result is consistent with the estimated dielectric constant of lipid droplets of ca. 7,<sup>[18]</sup> which most closely matches the dielectric constant of dichloromethane (8.9 at 298 K).

To study the suitability of the compounds for single cell analysis by flow cytometry, live adipocytes were obtained from different adipose deposits (brown adipose, BAT; inguinal white adipose: WAT:ING and gonadal white adipose, WAT:GON) from adult wild-type mice. Single cell suspensions were prepared by collagenase digestion, gated according to size and granularity and stained with the dead-cell probe propidium iodide (Figure S10), the lipophilic probe Nile Red, and **5** or **7**. Following this protocol, bright fluorescence could be observed in both the 450 nm and 550 nm channels after excitation at 405 nm (Figure 3a,b). Cells treated with either **5** or **7** showed fluorescence markedly higher than in untreated cells at all concentrations tested, down to 0.1 μM. Cells were also stained with Nile Red, revealing a strong correlation between the two fluorescent signals, and showing, on a single-cell level, that cells positive for **5** were equally positive for Nile Red (Figure 3c,d). To study the sub-cellular co-localisation in *ex vivo* adipocytes, live-cell confocal imaging on single brown adipose or gonadal white adipocytes from wild-type adult mice was performed (Figure S11). While good co-localisation of Nile Red and **5** and **7** was evident, it was observed that the co-localisation across the range of samples tested was better for **5** than **7**. This result

was confirmed by co-localisation analysis (ImageJ). Pearson's coefficient gives an indication of the extent to which the fluorescence outputs of each molecule correlate, with a value of 1 indicating complete positive correlation.<sup>[19]</sup> Manders' overlap coefficient indicates the proportion of coumarin fluorescence which overlaps with Nile Red fluorescence, with a value of 1 again indicating 100% co-localisation.<sup>[20]</sup> The results of this analysis confirmed in both tests that **5** showed a statistically significantly higher correlation with Nile Red than **7** (Figure 3e).

Taken together, the observed compartmentalisation of **5** and **7**, and their photophysical properties in buffer and dichloromethane tell of the distinct advantages of the *closo*-carboranyl **5**, and provide an explanation for these observations. Since **7** is highly fluorescent in both aqueous and organic solvents, its ability to stain the lipid droplets relies solely upon its lipophilicity. However, small molecules, particularly those without targeting moieties, rarely localise exclusively to a single organelle,<sup>[21]</sup> so it is likely that the fluorescence of **7** will be observed elsewhere in the cell. By contrast, **5** is sufficiently dim in aqueous solvents that fluorescence will only be observed in the lipophilic environment of the lipid droplet.

There is much interest in the study of the lipid droplets for their importance in a variety of biological processes including autophagy,<sup>[22]</sup> metabolic signalling<sup>[23]</sup> and immune response.<sup>[24]</sup> To this end, a number of synthetic fluorescent dyes with selectivity for lipid droplets have been reported, including those based on small organic molecules,<sup>[25]</sup> metal complexes,<sup>[26]</sup> and aggregation-induced luminogens.<sup>[27]</sup>

In summary, we have reported a novel carborane coumarin derivative **5** that selectively stains cellular lipid droplets due to its solvent-dependent photophysical properties and lipophilic nature. The combination of these properties ensures its superior selectivity to lipid droplets over its phenyl-containing analogue **7**. Furthermore, **5** exhibits a blue-emitting alternative of

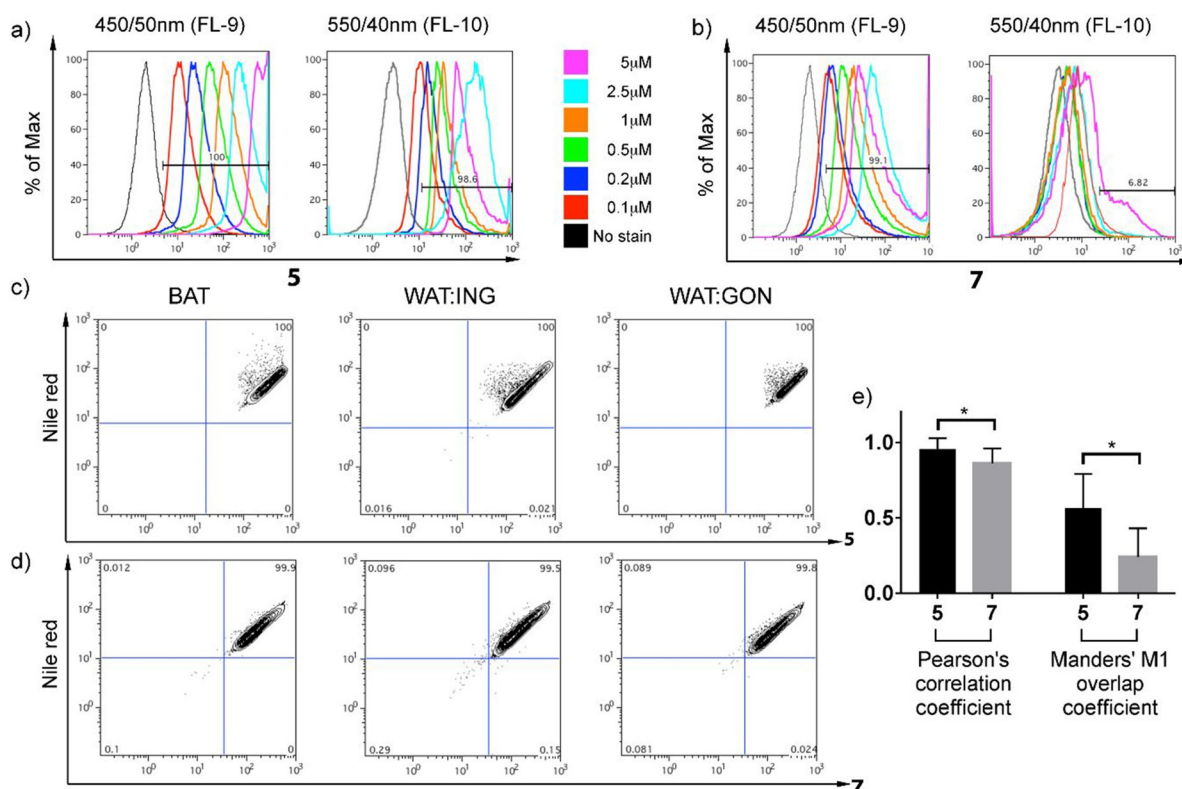


**Figure 3.** Compounds **5** and **7** are taken up by brown and white adipocytes. Single cell suspensions of adipocytes analysed by flow cytometry with increasing concentrations of (a) **5** and (b) **7**, as measured between 425–475 nm (FL-9) and 530–570 nm (FL-10). Representative flow cytometry plots of brown (BAT), white inguinal (WAT:ING) and gonadal (WAT:GON) adipocytes co-stained with Nile red and (c) **5** or (d) **7**. (e) Pearson's correlation coefficient and Manders' M1 overlap coefficients derived from co-localisation analysis of confocal images of adipocytes co-stained with Nile Red and **5** or **7**. Data represent mean  $\pm$  S.D., \* $p < 0.05$ .

the state-of-the-art Nile Red stain, with similar efficiency in lipid localisation, and which may facilitate the simultaneous use of multi-responsive sensors. Having demonstrated the promise of incorporating carborane derivatives into fluorophore scaffolds, we are now able to explore further applications of such molecules in fluorescent sensing applications.

## Acknowledgements

We acknowledge the University of Sydney for a World Scholars Scholarship and the John A. Lamberton Research Scholarship (AK), an Australian Postgraduate Award (KY), and the Westpac Bicentennial Foundation (EJN). We also acknowledge the support of the Bosch Institute Live Cell Analysis Facility and the facilities and the scientific and technical assistance of the Australian Microscopy and Microanalysis Research Facility at the Australian Centre for Microscopy and Microanalysis (ACMM) at the University of Sydney.

**Keywords:** carboranes • cellular markers • coumarins • fluorophores • lipid droplets

[1] E. J. New, *ACS Sens.* **2016**, *1*, 328–333.

[2] L. D. Lavis, R. T. Raines, *ACS Chem. Biol.* **2008**, *3*, 142–155.

[3] E. Kim, S. B. Park in *Advanced Fluorescence Reporters in Chemistry and Biology I: Fundamentals and Molecular Design* (Ed.: A. P. Demchenko), Springer, Berlin, **2010**, pp. 149–186.

[4] R. L. Atkins, D. E. Bliss, *J. Org. Chem.* **1978**, *43*, 1975–1980.

[5] A. Takadate, T. Masuda, C. Murata, T. Tanaka, M. Irikura, S. Goya, *Anal. Sci.* **1995**, *11*, 97–101.

[6] F. Issa, M. Kassiou, L. M. Rendina, *Chem. Rev.* **2011**, *111*, 5701–5722.

[7] A. Walter, J. Gutknecht, *J. Membr. Biol.* **1986**, *90*, 207–217.

[8] a) C. J. D. Austin, J. Kahlert, F. Issa, J. H. Reed, J. R. Smith, J. A. Ioppolo, J. A. Ong, J. F. Jamie, D. Hibbs, L. M. Rendina, *Dalton Trans.* **2014**, *43*, 10719–10724; b) S. M. Wilkinson, H. Gunosewoyo, M. L. Barron, A. Boucher, M. McDonnell, P. Turner, D. E. Morrison, M. R. Bennett, I. S. McGregor, L. M. Rendina, M. Kassiou, *ACS Chem. Neurosci.* **2014**, *5*, 335–339.

[9] a) E. L. Crossley, D. Caiazza, L. M. Rendina, *Dalton Trans.* **2005**, 2825–2826; b) J. A. Ioppolo, C. J. Kepert, D. J. Price, L. M. Rendina, *Aust. J. Chem.* **2007**, *60*, 816–820.

[10] R. Núñez, I. Romero, F. Teixidor, C. Vinas, *Chem. Soc. Rev.* **2016**, *45*, 5147–5173.

[11] a) J. Kahlert, L. Böhling, A. Brockhinke, H. G. Stämmler, B. Neumann, L. M. Rendina, P. J. Low, L. Weber, M. A. Fox, *Dalton Trans.* **2015**, *44*, 9766–9781; b) S. Y. Kim, A. R. Lee, Y. J. Cho, H. J. Son, W. S. Han, S. O. Kang, *J. Organomet. Chem.* **2015**, *798*, 245–251.

[12] a) J.-F. Nicoud, F. Bolze, X.-H. Sun, A. Hayek, P. Baldeck, *Inorg. Chem.* **2011**, *50*, 4272–4278; b) L. Zhu, W. Lv, S. Liu, H. Yan, Q. Zhao, W. Huang, *Chem. Commun.* **2013**, *49*, 10638–10640; c) A. Ferrer-Ugalde, A. González-Campo, C. Viñas, J. Rodríguez-Romero, R. Santillan, N. Farfán, R. Sillanpää, A. Sousa-Pedraes, R. Núñez, F. Teixidor, *Chem. Eur. J.* **2014**, *20*, 9940–9951.

[13] E. Justus, D. T. Iztelevova, A. V. Kasantsev, M. M. Axartov, E. Lork, D. Gabel, *Coll. Czech. Chem. Commun.* **2007**, *72*, 1740–1754.

[14] P. Greenspan, E. P. Mayer, S. D. Fowler, *J. Cell Biol.* **1985**, *100*, 965–973.

- [15] H. Sun, H. Guo, W. Wu, X. Liu, J. Zhao, *Dalton Trans.* **2011**, 40, 7834–7841.
- [16] R. W. Horobin, F. Rashid, *Histochemistry* **1990**, 94, 205–209.
- [17] H. Nakamura, M. Kirihaata in *Neutron Capture Therapy: Principles and Applications* (Eds.: W. Sauerwein, A. Wittig, R. Moss, Y. Nakagawa), Springer, Berlin, **2012**, pp. 99–116.
- [18] S. Ghosh, S. Chattoraj, T. Mondal, K. Bhattacharyya, *Langmuir* **2013**, 29, 7975–7982.
- [19] E. M. Manders, J. Stap, G. J. Brakenhoff, R. van Driel, J. A. Aten, *J. Cell Sci.* **1992**, 103, 857–862.
- [20] E. M. M. Manders, F. J. Verbeek, J. A. Aten, *J. Microsc.* **1993**, 169, 375–382.
- [21] N. Zheng, H. N. Tsai, X. Zhang, G. R. Rosania, *Mol. Pharm.* **2011**, 8, 1619–1628.
- [22] R. Singh, S. Kaushik, Y. Wang, Y. Xiang, I. Novak, M. Komatsu, K. Tanaka, A. M. Cuervo, M. J. Czaja, *Nature* **2009**, 458, 1131–1135.
- [23] E. L. Arrese, F. Z. Saudale, J. L. Soulages, *Lipid Insights* **2014**, 7, 7–16.
- [24] H. A. Saka, R. Valdivia, *Annu. Rev. Cell Dev. Biol.* **2012**, 28, 411–437.
- [25] a) E. Kim, S. Lee, S. B. Park, *Chem. Commun.* **2012**, 48, 2331–2333; b) A. Goel, A. Sharma, M. Kathuria, A. Bhattacharjee, A. Verma, P. R. Mishra, A. Nazir, K. Mitra, *Org. Lett.* **2014**, 16, 756–759; c) A. Sharma, S. Umar, P. Kar, K. Singh, M. Sachdev, A. Goel, *Analyst* **2016**, 141, 137–143.
- [26] C. A. Bader, R. D. Brooks, Y. S. Ng, A. Sorvina, M. V. Werrett, P. J. Wright, A. G. Anwer, D. A. Brooks, S. Stagni, S. Muzzioli, M. Silberstein, B. W. Skelton, E. M. Goldys, S. E. Plush, T. Shandala, M. Massi, *RSC Adv.* **2014**, 4, 16345–16351.
- [27] a) Z. Wang, C. Gui, E. Zhao, J. Wang, X. Li, A. Qin, Z. Zhao, Z. Yu, B. Z. Tang, *ACS Appl. Mater. Interfaces* **2016**, 8, 10193–10200; b) M. Gao, H. Su, S. Li, Y. Lin, X. Ling, A. Qin, B. Z. Tang, *Chem. Commun.* **2017**, 53, 921–924.

Manuscript received: March 19, 2017

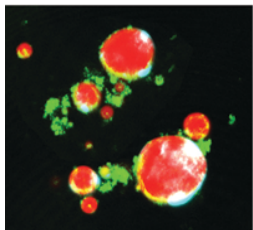
Revised manuscript received: May 31, 2017

Accepted manuscript online: May 31, 2017

Version of record online: June 22, 2017

#### **Appendix IV: Flow cytometric single cell analysis reveals heterogeneity between adipose depots.**





# Adipocyte



ISSN: 2162-3945 (Print) 2162-397X (Online) Journal homepage: <http://www.tandfonline.com/loi/kadi20>

## Flow cytometric single cell analysis reveals heterogeneity between adipose depots

Badwi B. Boumelhem, Stephen J. Assinder, Kim S. Bell-Anderson & Stuart T. Fraser

To cite this article: Badwi B. Boumelhem, Stephen J. Assinder, Kim S. Bell-Anderson & Stuart T. Fraser (2017) Flow cytometric single cell analysis reveals heterogeneity between adipose depots, *Adipocyte*, 6:2, 112-123, DOI: [10.1080/21623945.2017.1319536](https://doi.org/10.1080/21623945.2017.1319536)

To link to this article: <http://dx.doi.org/10.1080/21623945.2017.1319536>



Accepted author version posted online: 14 Apr 2017.  
Published online: 14 Apr 2017.



Submit your article to this journal [↗](#)



Article views: 213



View related articles [↗](#)



View Crossmark data [↗](#)



Citing articles: 1 View citing articles [↗](#)

RESEARCH PAPER



## Flow cytometric single cell analysis reveals heterogeneity between adipose depots

Badwi B. Boumelhem<sup>a,b</sup>, Stephen J. Assinder<sup>a,b</sup>, Kim S. Bell-Anderson<sup>b,c,d</sup>, and Stuart T. Fraser<sup>a,b,c</sup>

<sup>a</sup>Discipline of Physiology, University of Sydney, Sydney, Australia; <sup>b</sup>Bosch Institute, University of Sydney, Sydney, Australia; <sup>c</sup>Discipline of Anatomy and Histology, University of Sydney, Sydney, Australia; <sup>d</sup>Charles Perkins Centre, School of Life and Environmental Sciences, University of Sydney, Sydney, Australia

### ABSTRACT

Understanding adipose tissue heterogeneity is hindered by the paucity of methods to analyze mature adipocytes at the single cell level. Here, we report a system for analyzing live adipocytes from different adipose depots in the adult mouse. Single cell suspensions of buoyant adipocytes were separated from the stromal vascular fraction and analyzed by flow cytometry. Compared to other lipophilic dyes, Nile Red uptake effectively distinguished adipocyte populations. Nile Red fluorescence increased with adipocyte size and granularity and could be combined with MitoTracker<sup>®</sup> Deep Red or fluorescent antibody labeling to further dissect adipose populations. Epicardial adipocytes exhibited the least mitochondrial membrane depolarization and highest fatty-acid translocase CD36 surface expression. In contrast, brown adipocytes showed low surface CD36 expression. Pregnancy resulted in reduced mitochondrial membrane depolarisation and increased CD36 surface expression in brown and epicardial adipocyte populations respectively. Our protocol revealed unreported heterogeneity between adipose depots and highlights the utility of flow cytometry for screening adipocytes at the single cell level.

### ARTICLE HISTORY

Received 7 April 2017  
Accepted 10 April 2017

### KEYWORDS

adipocytes; adipose heterogeneity; flow cytometry; fatty acid translocase; lipophilic dye; lipid metabolism; mitochondria

### Introduction

The growing rates of obesity, diabetes and other metabolic diseases have led to an increased interest in the cell biology and physiology of adipocytes. Adipocytes play central roles in energy storage, body temperature control, blood glucose levels and insulin sensitivity.<sup>1</sup> The primary function of white adipose tissue (WAT) is energy storage in the form of the neutral lipid triglyceride in unilocular cytoplasmic lipid droplets.<sup>2,3</sup> Brown adipocytes regulate non-shivering thermogenesis and energy expenditure via mitochondrial uncoupling-protein 1.<sup>3</sup> Brown adipose tissue (BAT) is primarily restricted to the intrascapular region in adult mice. WAT is found in a range of distinct anatomic locations including; subcutaneous depots such as the inguinal adipose tissue; and visceral depots located in the thorax and abdominal cavity such as the gonadal, peri-renal, mesenteric and epicardial adipose tissues.

The anatomic and functional differences between adipose depots may be due to different developmental pathways.<sup>4</sup> Brown adipocytes and skeletal muscle cells arise from *Myf5*-expressing mesodermal progenitors.<sup>5</sup> *Wtl*-expressing mesothelial progenitors give rise to visceral but not subcutaneous WAT depots.<sup>6</sup> Heterogeneity

between depots is controlled at the genetic level with distinct genetic loci influencing local adipose behavior.<sup>7</sup> Proteomics analysis comparing different white adipose depots in inbred mice revealed significant differences in: the amount of protein expressed; expression profiles of proteins involved in glucose and lipid metabolism; endocrine function and insulin sensitivity.<sup>8</sup> Apolipoprotein E expression, as well as responsiveness to metabolic and inflammatory signals, differ across adipose tissue depots.<sup>9,10</sup> Adipose depot heterogeneity is also observed in human metabolic disorders and diseases. For example, increased visceral WAT is associated with the development of obesity and type 2 diabetes.<sup>11</sup>

Adipose tissue consists of developing and mature adipocytes as well as the stromal vascular fraction (SVF) which comprises fibroblasts, immune cells, endothelial cells and pre-adipocytes (adipocyte progenitors).<sup>12</sup> Flow cytometry can analyze complex cellular heterogeneity in mixed populations at the single cell level. While flow cytometry has been used extensively to identify pre-adipocytes and to characterize the SVF, flow cytometric analysis of mature adipocytes is not routinely used.<sup>6,12</sup> Previous reports of

flow cytometric analyses of adipocytes focus on adipocytes derived *in vitro* from myeloid cells or bone marrow progenitors, or on adipocytes isolated from a single depot.<sup>13–17</sup> Recently, Durandt and colleagues identified various subpopulations of adipocytes derived from mesenchymal stromal cells using fatty-acid translocase CD36 and lipophilic dyes Nile Red and BODIPY.<sup>18</sup> To improve our understanding of adipose cell biology, a robust flow cytometric protocol was developed to identify and characterize adipocytes according to nuclear content, lipid content, mitochondrial membrane depolarization and adipocyte surface protein phenotype of live cells. In contrast to previous reports, this protocol does not require fixation or permeabilization. We have used this system to assess differences in adipocyte biology during changes in whole-body physiology such as pregnancy. This system allows the robust quantification of live adipocyte phenotype and frequency at the single cell level and could be adapted for use in diagnostic settings in the future.

## Results

### Flow cytometric analysis of the buoyant adipose fraction

To develop a flow cytometric protocol to analyze adipocyte heterogeneity, adipose tissues were dissected from the regions outlined (Fig. 1A–F) in wild type, young adult (6–12 weeks) male outbred mice fed a standard chow diet *ad libitum*. Depots included; intrascapular BAT; subcutaneous inguinal WAT (lymph nodes removed); and 4 distinct visceral WAT depots namely the gonadal, peri-renal, mesenteric and epicardial. Each tissue was then digested with collagenase type II to obtain single cell suspensions as outlined in Experimental Procedures (Fig. 1G) and pictured beneath their respective depots in Figure 1A–F. The white arrows indicate multilocular adipocytes dissociated from BAT. Following centrifugation, the buoyant adipose fraction (adipocytes) and pelleted SVF were easily separated and analyzed by flow cytometry.

The buoyant fraction consistently showed a forward scatter (size) and side scatter (granularity) profile distinct from the pelleted SVF (Fig. 1H and I). Cell viability was consistently high as shown in Figure 1H 'live cells' panel. Propidium iodide<sup>neg</sup> live cells were gated and analyzed for the presence of contaminating blood cells. The SVF contained CD45<sup>+</sup> haematopoietic cells, F4/80<sup>+</sup> macrophages and Ter119<sup>+</sup> erythrocytes (Fig. 1H). The buoyant adipocyte fraction showed no binding to antibodies against blood cell surface proteins (Fig. 1I).

### Nile Red staining can separate buoyant adipocyte populations by flow cytometry

To confirm the buoyant fraction contained adipocytes, single cell suspensions (Fig. 2A) were stained with a range of fluorescent lipophilic dyes. These included Nile Red, Oil Red O, LipidTox<sup>®</sup> Red and LipidTox<sup>®</sup> Green. Oil Red O is not cell permeable and did not penetrate the live cells (Fig. 2B). In contrast, buoyant cells incubated with the neutral lipid dyes LipidTox<sup>®</sup> Red, LipidTox<sup>®</sup> Green and Nile Red all emitted a fluorescent signal. Nile Red consistently exhibited a higher fluorescent signal compared with LipidTox<sup>®</sup> Red and LipidTox<sup>®</sup> Green. Nile Red is also considerably more cost-effective and hence was chosen as the optimal fluorescent lipophilic dye for this study.

We hypothesized that Nile Red staining would correlate to size and granularity of the buoyant cells. The forward and side scatter profile of the buoyant fraction was subsequently divided into 3 regions. Nile Red uptake for each population revealed highest fluorescence in the largest, most granular cells (Fig. 2D, blue). The mean fluorescence intensity (MFI) was significantly different between each population (Fig. 2Di). Irrespective of the adipose depot assayed, MFI of Nile Red uptake was always greatest in the largest, most granular cells (Nile Red<sup>High</sup>) compared with Nile Red<sup>Mid</sup> and Nile Red<sup>Low</sup> populations. Dead cells were excluded in all studies using PI. Viability, as determined by lack of PI uptake, was greater than 95% in all Nile Red populations (Fig. 2Dii). DRAQ5, a cell permeable DNA-binding dye, and wheat germ agglutinin (WGA), a probe for cell surface glycosylated structures on the cell membrane, were included to demonstrate the presence of a nucleus and intact cell membranes. More than 90% of Nile Red<sup>High</sup> and Nile Red<sup>Mid</sup> cells were DRAQ5<sup>+</sup> and WGA<sup>+</sup> while the Nile Red<sup>Low</sup> population, which may include some cell debris as well as intact cells, showed reduced levels of DRAQ5 uptake and WGA binding (Fig. 2Diii–iv). Nile Red<sup>High</sup> and Nile Red<sup>Mid</sup> cells were not detected in the SVF fraction (data not shown). This demonstrates that the buoyant fraction contains intact, highly viable adipocytes with a high lipid and nuclei content as indicated by the absence of PI and by strong Nile Red, DRAQ5 and WGA staining.

### Mitochondrial membrane potential varies among adipose depots

Adipose tissues vary in mitochondrial number and membrane potential.<sup>21</sup> As the buoyant fraction can be segregated by Nile Red, it was hypothesized that analysis of combined Nile Red and mitochondrial probe MitoTracker<sup>®</sup> Deep Red may further differentiate

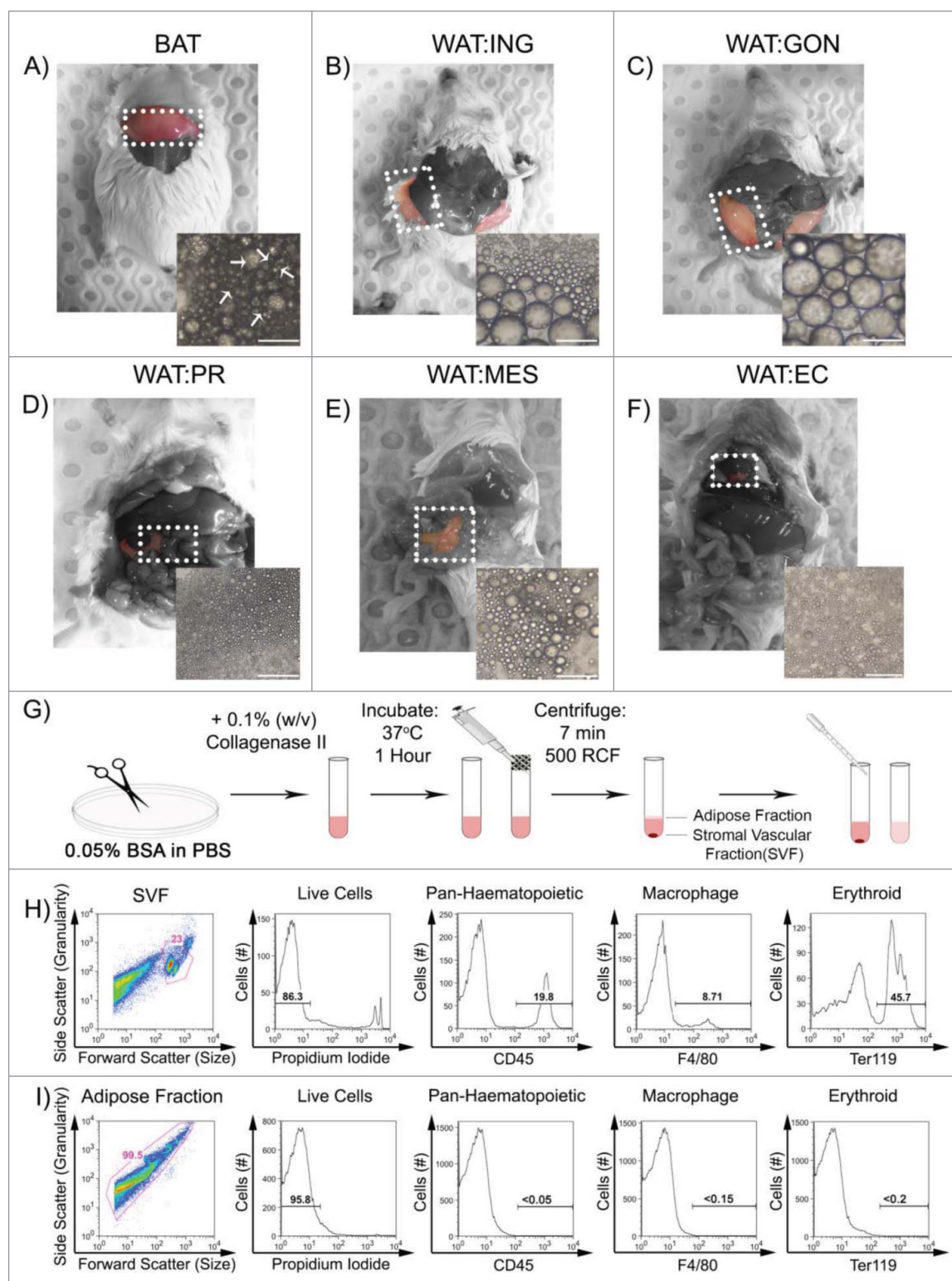


**Figure 1.** Single cell suspensions of buoyant adipocytes show distinct flow cytometric profiles to stromal vascular fraction cells. A – F. Adipose tissue was excised from intrascapular brown (BAT), subcutaneous inguinal (WAT:ING), visceral gonadal (WAT:GON), peri-renal (WAT:PR), mesenteric (WAT:MES), and epicardial (WAT:EC). G. The adipose tissue was minced in FACS buffer (PBS + 0.05% BSA) and then digested with 0.1% (w/v) collagenase II for one hour at 37°C. The mixture was pipetted multiple times and passed through a nylon filter. The solution was then centrifuged for 7min at 500 RCF. The buoyant, mature adipocytes were separated from the pelleted SVF using a transfer pipette. Phase contrast images of buoyant adipocytes are placed in the corner of each respective depot in A-F. Arrow-heads indicate multi-locular adipocytes. Scale bar represents 50  $\mu$ m. H and I. Cells from the SVF and buoyant adipocytes were analyzed according to their forward scatter (size) and side scatter (granularity) profile. Cells from both fractions were then stained for propidium iodide (PI) to gate live cells, CD45 for hematopoietic cells, F4/80 for macrophages, and Ter119 for erythroid cells.



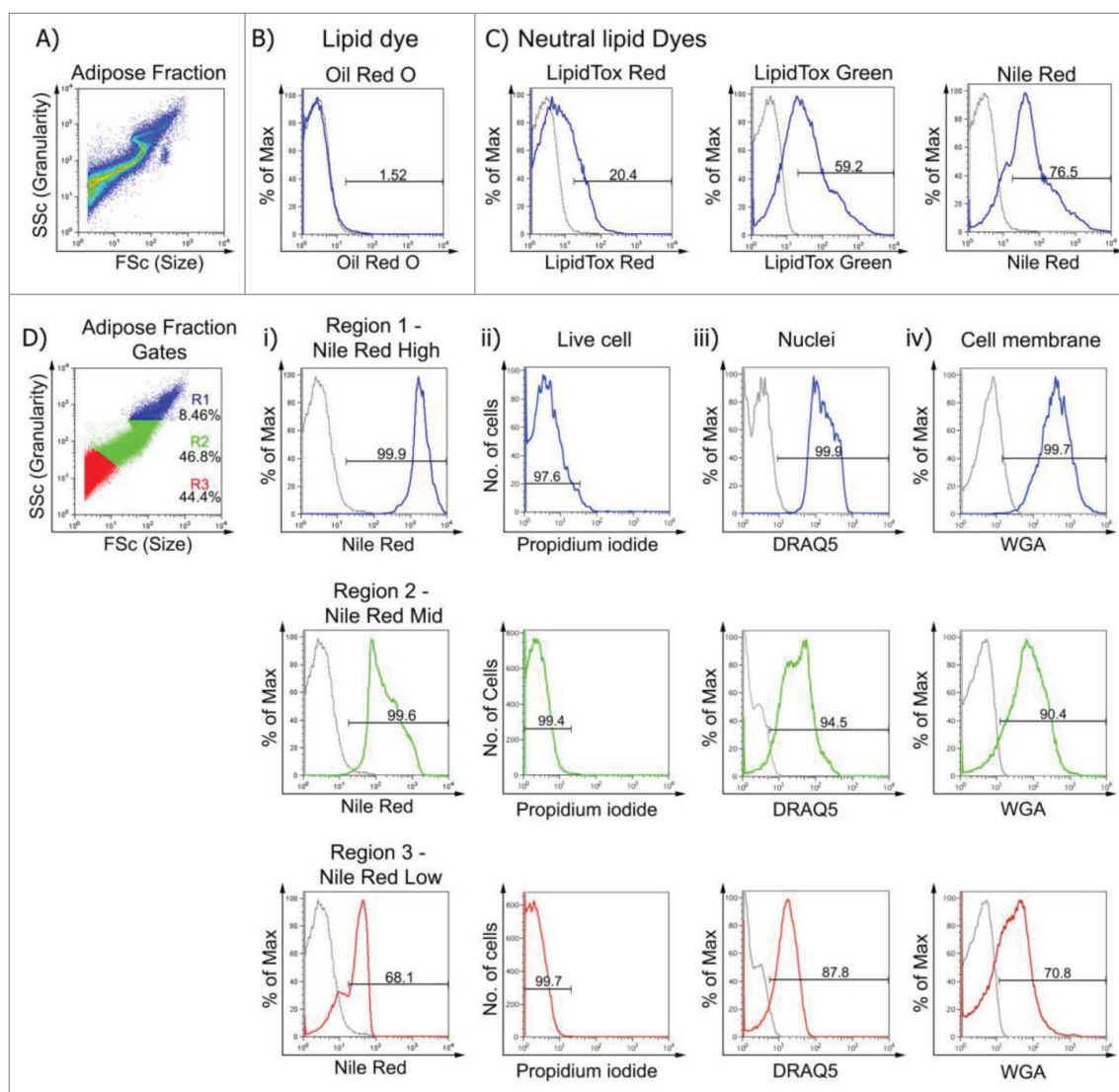


**Figure 2.** Nile Red is a cell-permeable lipophilic sensor of intracellular lipid droplets useful for flow cytometry. A. Buoyant mature adipocytes were analyzed according to their size and granularity. Buoyant mature adipocytes were stained with: B. Classic lipid dye Oil Red O, C. Neutral lipid dyes; LipidTox<sup>®</sup> Red; LipidTox<sup>®</sup> Green and Nile Red. D. Buoyant mature adipocytes were gated according to their size and granularity (R1, R2, and R3) and Nile Red, PI, DRAQ5 and WGA fluorescence measured. Di. Mean fluorescence intensity (MFI  $\pm$  SEM;  $n = 6$ ) of Nile Red<sup>High</sup> was  $2053 \pm 152$ , Nile Red<sup>Mid</sup> was  $234 \pm 32$  and Nile Red<sup>Low</sup> was  $41 \pm 6.1$ . Dii. Cells from all 3 populations were PI negative ( $> 97.5\%$  viable). Diii-iv. DRAQ5 and WGA fluorescence was greatest in Nile Red<sup>High</sup> cells ( $> 99\%$ ), while Nile Red<sup>Mid</sup> and Nile Red<sup>Low</sup> exhibited DRAQ5 ( $> 87\%$ ) and WGA ( $> 70\%$ ) uptake.

adipose depots. MitoTracker<sup>®</sup> Deep Red detect changes in mitochondrial membrane potential and measures mitochondrial respiration. To visualize uptake of Nile Red and MitoTracker<sup>®</sup> Deep Red in live adipocytes, confocal microscopic imaging of buoyant brown, inguinal and gonadal adipocytes was performed (Fig. 3a).

Prior to using Mitotracker Deep Red for flow cytometry of adipocytes, we confirmed uptake in live adipocytes by confocal microscopy (Fig. 3a). Adipocytes were dispersed as described previously and the buoyant fraction stained with Nile Red for lipid droplets; FITC-conjugated

WGA for cell membrane and Mitotracker<sup>®</sup> Deep Red for mitochondrial membrane depolarisation. Live cell confocal imaging of adipocytes posed a challenge as the buoyant lipid compartment typically hid the nucleus. Nile Red clearly stained the multilocular lipid droplets of brown adipocytes and the unilocular droplets of white adipocytes. WGA was found to bind to the cell membrane of brown and white adipocytes, however WGA signal rapidly became clustered on the surface of living adipocytes. To our knowledge this has not been reported before as WGA staining is typically performed on fixed

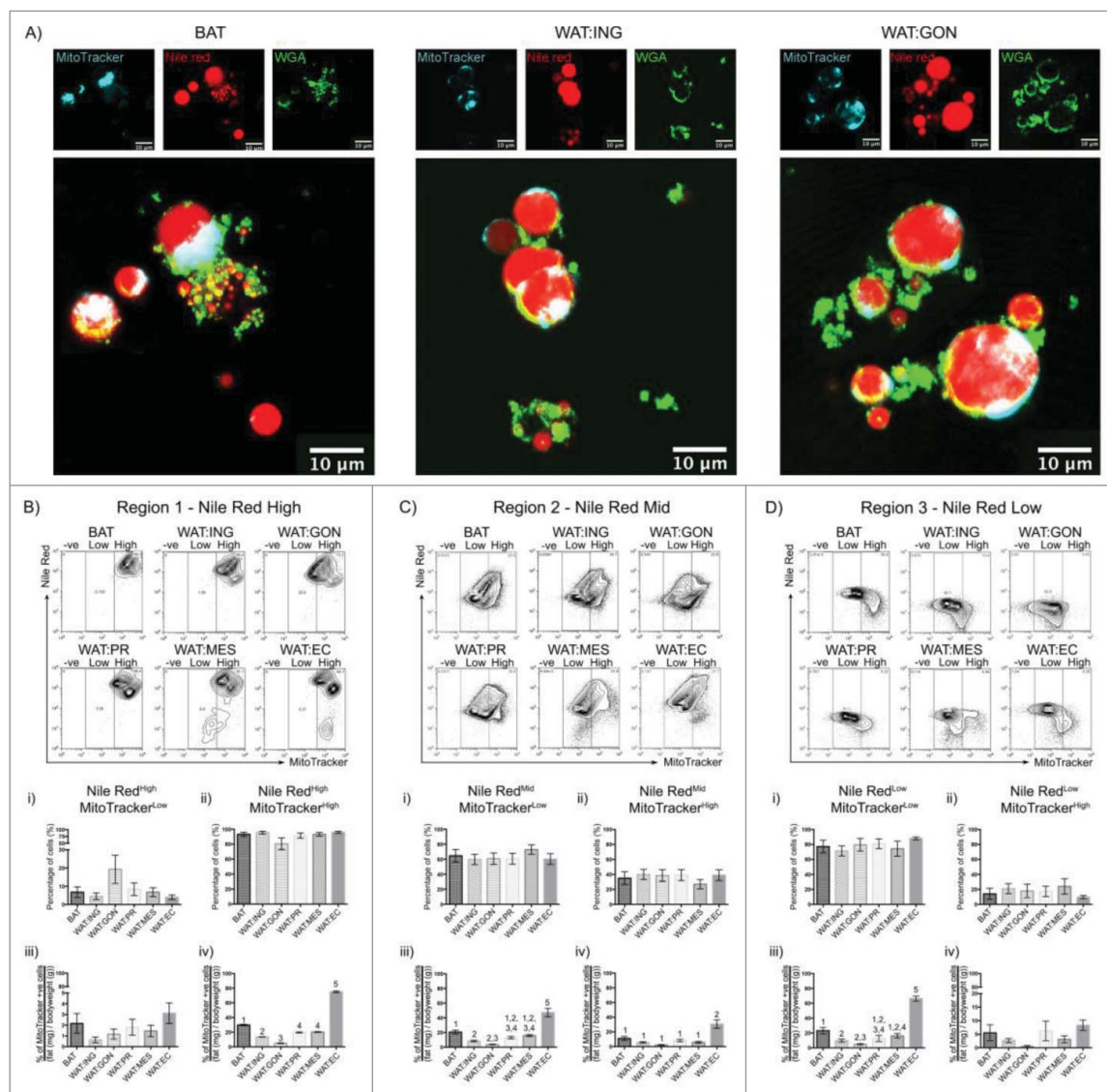


**Figure 3.** Mitochondrial membrane potential as assessed by Mitotracker® Deep Red fluorescence reveals heterogeneity in adipocytes from different depots. A. Confocal images of buoyant brown (left), white inguinal (middle) and gonadal (right) adipocytes stained with Nile Red (red), WGA (green) and Mitotracker® Deep Red (cyan). Scale bar represents 20  $\mu$ m. B – D. Representative flow cytometric plot of Mitotracker® Deep Red uptake in BAT, WAT:ING, WAT:GON, WAT:PR, WAT:MES and WAT:EC depots according to Nile Red fluorescence (High, Mid and Low). Gating of Mitotracker® Deep Red was defined as Mitotracker<sup>Low</sup>, Mitotracker<sup>Mid</sup> and Mitotracker<sup>High</sup>. Bi,ii – Di,ii. Adipocytes from the Nile Red<sup>High</sup>, Nile Red<sup>Mid</sup> and Nile Red<sup>Low</sup> gate of the 6 adipose depots were compared according to Mitotracker<sup>Low</sup> and Mitotracker<sup>High</sup> uptake in male mice (n = 6). Biii–iv – Diiv. Frequency of Mitotracker<sup>Low</sup> and Mitotracker<sup>High</sup> positive cells expressed as a proportion of adipose mass in the Nile Red<sup>High</sup>, Nile Red<sup>Mid</sup> and Nile Red<sup>Low</sup> adipocyte populations. Data presented as mean  $\pm$  SEM. Differences between adipose depots were determined by 2-tailed, one way ANOVA and pairwise post-hoc comparison by Tukey's HSD test. Groups sharing a numeral are not significantly different from each other.

or frozen adipose tissue rather than dissociated adipocytes.<sup>22</sup> Mitotracker® Deep Red uptake was readily observed by confocal imaging with an intense signal localized eccentrically within the cytoplasm. Together, these data, and those from the previous flow cytometric analyses (Fig. 2Dii–iv, PI and DRAQ5), demonstrate that the cells obtained through the dissociation technique described are indeed live, intact, metabolically active cells.

We were therefore confident to analyze adipocyte populations by flow cytometry according to size, granularity, Nile Red uptake and Mitotracker® Deep Red fluorescence (Fig. 3B–D). No significant differences were observed in mitochondrial membrane potential between adipose depots for the Nile Red<sup>High</sup>, Nile Red<sup>Mid</sup> and Nile Red<sup>Low</sup> population of cells (Fig. 3Ai,ii–Ci,ii). However, when frequency was expressed for each adipose depot as a proportion of body mass (fat (mg)/body

weight (g)), epicardial adipocytes exhibited less mitochondrial membrane depolarization compared with all other depots. This was observed in all 3 populations of adipose cells (Nile Red<sup>High</sup>, Nile Red<sup>Mid</sup> and Nile Red<sup>Low</sup>; Fig. 3Aiv, Biii-iv and Ciii respectively). Mitochondrial membrane depolarization in Nile Red<sup>High</sup> brown adipocytes was less than the similar population found in the inguinal, gonadal, peri-renal and mesenteric depots (Fig. 3Aiv). In contrast, gonadal Nile Red<sup>High</sup> adipocytes had the greatest mitochondrial membrane depolarization (Fig. 3Aiv).

### Multiparametric flow cytometry reveals heterogeneity of CD36 surface protein expression between adipose depots

Initial flow cytometric characterization of adipocytes centered upon surface proteins reported to be present on SVF cells, adipose stem cells or pre-adipocytes such as CD31, CD34, Flk1 and c-Kit.<sup>23</sup> No expression of these surface markers was detected on buoyant cells from any depot. The “self-antigen” CD47 and the transferrin receptor CD71 were also not expressed by buoyant cells. A range of adhesion molecules were examined for expression but were not detected including; integrins  $\alpha 2$ ,  $\alpha 4$ ,  $\alpha 5$ ,  $\beta 3$ ,  $\beta 4$ ,  $\beta 7$  and CD41; Intercellular Adhesion

Molecule 1, CD133 and the epithelial markers E-Cadherin and Epithelial Cell Adhesion Molecule (data not shown).

In contrast, monoclonal antibody against the surface fatty-acid translocase FAT/CD36 bound strongly to buoyant adipocytes. CD36 is a multi-ligand receptor that facilitates the movement of fatty acids into the cell.<sup>24</sup> Nile Red staining was combined with anti-CD36 antibody immunoreactivity to determine whether heterogeneity existed between adipose depots (Fig. 4A-C). Buoyant adipocytes showed a broad range of surface CD36 expression from CD36<sup>neg</sup> through to CD36<sup>High</sup> levels. In contrast to the other depots, all brown adipocytes exhibited low levels of CD36 surface expression (Fig. 4Aii- 4Cii). Surface CD36 expression was greater in the inguinal, gonadal and epicardial adipocytes compared with brown adipocytes (Fig. 4A-C). As each adipose depot varies significantly in mass (Fig. 5), and the body mass of any individual animal varies, surface expression of CD36 was standardized to ensure that variation of fat mass due to body size is normalized. Epicardial adipocytes showed the highest levels of CD36 expression whereas gonadal adipocytes showed the lowest levels of CD36 among adipose depots examined (Fig. 4Aiii-iv, Biii, Ciii). CD36 antibody binding can therefore be used with Nile Red uptake to distinguish

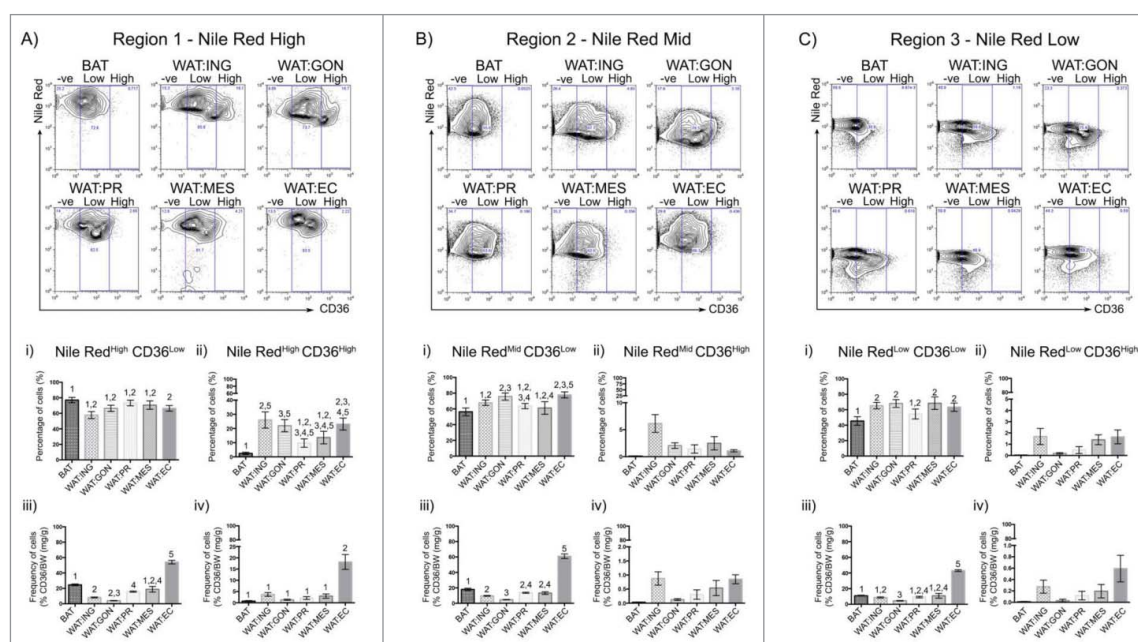


**Figure 4.** CD36 surface expression profiles vary across adipose depots. A – C. Representative flow cytometric plot of CD36 uptake in BAT, WAT:ING, WAT:GON, WAT:PR, WAT:MES and WAT:EC depots according to Nile Red fluorescence (High, Mid and Low). Gating of CD36 was defined as CD36<sup>-ve</sup>, CD36<sup>Low</sup> and CD36<sup>High</sup>. Ai,ii – Ci,ii. Adipocytes from the Nile Red<sup>High</sup>, Nile Red<sup>Mid</sup> and Nile Red<sup>Low</sup> gate of the 6 adipose depots were compared according to CD36<sup>Low</sup> and CD36<sup>High</sup> uptake in male mice (n = 6). Aiii-iv – Ciii-iv. Frequency of CD36<sup>Low</sup> and CD36<sup>High</sup> positive cells expressed as a proportion of adipose mass in the Nile Red<sup>High</sup>, Nile Red<sup>Mid</sup> and Nile Red<sup>Low</sup> adipocyte populations. Data presented as mean  $\pm$  SEM. Differences between adipose depots were determined by 2-tailed, one way ANOVA and pairwise post-hoc comparison by Tukey's HSD test. Groups sharing a numeral are not significantly different from each other.



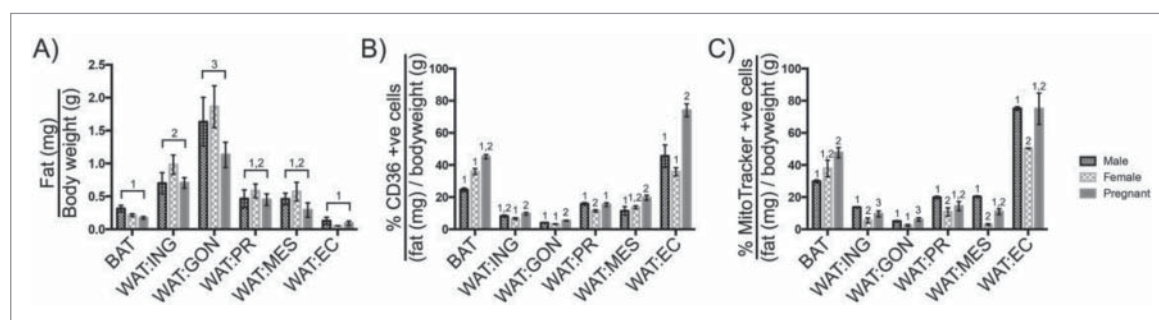


**Figure 5.** Changes in adipocyte surface phenotype and mitochondrial membrane potential during pregnancy. A. Comparing the mass of BAT, WAT:ING, WAT:GON, WAT:PR, WAT:MES and WAT:EC adipose tissue relative to bodyweight in male (n = 6), virgin (n = 6) and pregnant (n = 6) female mice. B. Expression of CD36 as a proportion of tissue mass in mature adipocytes. BAT, WAT:ING, WAT:GON, WAT:PR, WAT:MES and WAT:EC from male (n = 6), virgin (n = 6) and pregnant (n = 6) female mice were compared. C. Comparing uptake of MitoTracker® Deep Red as a proportion of tissue mass in mature adipocytes. BAT, WAT:ING, WAT:GON, WAT:PR, WAT:MES and WAT:EC from male (n = 6), virgin (n = 6) and pregnant (n = 6) female mice were compared. Data presented as mean  $\pm$  SEM. Differences between adipose depots were determined by 2-tailed, 2-way ANOVA and pairwise post-hoc comparison by Tukey's multiple comparison test. Groups sharing a numeral are not significantly different from each other.

adipose populations. We next asked whether there were distinctions between the depots according to physiologic state with particular reference to sex and pregnancy.

#### **Adipose tissue from pregnant mice have elevated surface CD36 and reduced mitochondrial membrane potential compared with male and virgin female mice**

The surface expression of CD36 and mitochondrial membrane potential of adipocytes was compared between different adipose depots from male, virgin female or pregnant female mice as a proportion of body weight (Fig. 5). The adipose mass varied according to sex and pregnancy status of the mice. Interestingly, in healthy adult mice, when adipose mass was expressed as a percentage of body weight, the relative proportions of adipose tissues were not significantly different (Fig. 5A). CD36 surface expression was elevated during pregnancy. The frequency of CD36<sup>High</sup> adipocytes increased in the BAT and epicardial WAT depots of pregnant mice compared with virgin female or male mice (Fig. 5B). Brown adipocytes from female mice showed less mitochondrial membrane depolarization compared with equivalent cell types from male mice (Fig. 5C). In contrast, virgin female epicardial adipocytes showed greater mitochondrial membrane depolarization than male or pregnant female epicardial adipocytes (Fig. 5C).

#### **Discussion**

Deeper understanding of adipocyte biology is needed as obesity and related metabolic disorders such as diabetes and metabolic syndrome are rapidly becoming major health burdens throughout the world. It is, therefore,

imperative that we develop assay systems to allow for rapid and cost-effective analysis of adipose tissues to monitor human health. Flow cytometry has proven to be very effective in the diagnosis of hematological and oncological diseases.<sup>25–28</sup> Flow cytometry has also been used to examine adipocytes derived from myeloid cells *in vitro* or from single depots.<sup>13–17</sup> Recently, Xiao and colleagues used flow cytometry of buoyant gonadal adipocytes to examine adipocyte size in relation to adipose tissue inflammation.<sup>29</sup> In contrast, our protocol categorizes adipocyte populations in accordance to lipophilic dye uptake. Irrespective of the depot assayed, all adipocyte populations were strongly fluorescent for DRAQ5 and WGA. DRAQ5 stains nuclei while WGA is a lectin that binds to oligosaccharides containing N-acetyl-D-glucosamine found on the membrane of cells.<sup>30</sup> Furthermore all adipocyte suspensions assayed had minimal propidium iodide uptake. Together, these parameters confirmed that the adipocytes are viable and intact with nuclei. These steps were taken to highlight the rigor and robustness of our approach.

In comparing a range of lipophilic dyes to label and quantify adipocytes, we found that Nile Red was the most cost-effective and the most effective at segregating distinct size populations. Nile Red is a lipophilic dye that stains neutral lipids.<sup>31,32</sup> Flow cytometric analyses using Nile Red have been conducted on macrophages, smooth muscle cells and Leydig cells.<sup>32,33</sup> Adipocytes differentiated from mouse embryonic stem cells *in vitro* have also been analyzed by flow cytometry using Nile Red.<sup>20</sup> More recently, Durandt and colleagues used Nile Red in *ex vivo* cultures to identify subpopulations of adipocytes derived from mesenchymal stromal cells.<sup>18</sup> This is the first study however, that expands upon these protocols by combining Nile Red staining with surface antigen



expression and mitochondrial membrane depolarisation to compare primary mature adipocytes from multiple adipose depots at the single cell level. Nile Red staining can be performed rapidly (~5 minutes) on live cells and does not require fixation or treatment with detergents as used previously.<sup>34</sup>

Nile Red can be combined with other fluorescent probes to obtain a more complete analysis of adipose cell biology. MitoTracker® Deep Red is a far-red fluorescent probe reported to represent mitochondrial membrane potential, with increasing signal indicating a reduction in mitochondrial membrane depolarization.<sup>35</sup> Brown and epicardial adipocytes exhibited less membrane depolarization compared with adipocytes from other adipose depots. The role of mitochondria in BAT is most prevalent in cold temperatures when BAT is activated to stimulate thermogenesis through uncoupling protein-1.<sup>36</sup> In humans, epicardial adipose tissue has higher expression of uncoupling protein-1 compared with other WAT depots.<sup>37</sup> This is supportive of increasing evidence which suggests epicardial adipocytes may have a similar function to BAT.<sup>37</sup> Our findings in the mouse support the similarities between BAT and epicardial adipose tissue in humans.

Fatty acid translocase CD36 facilitates the uptake of fatty acids and lipoproteins by accelerating intracellular esterification into triglycerides.<sup>38</sup> Surprisingly, brown adipocytes expressed less surface CD36 than their WAT counterparts. Mice exposed to cold temperatures have enhanced uptake of lipoproteins in BAT.<sup>39</sup> Mice that lack both alleles for *CD36* have impaired fatty acid, lipoprotein and glucose uptake in BAT.<sup>39</sup>

As the animals examined here were maintained at thermoneutrality, it is possible that the lower levels of CD36 surface protein expression may change upon exposure to lower temperatures and activation of BAT non-shivering thermogenesis. Epicardial adipocytes exhibited the highest levels of surface protein expression of CD36. This is the first report of CD36 expression in epicardial adipose tissue. Epicardial adipose tissue has been proposed to play roles distinct to those of BAT, subcutaneous WAT and other visceral WAT.<sup>37</sup> Reservoirs of adipose tissue surrounding the heart are scarce and largely serve to fuel myocardial contraction through the storage and supply of fatty acids for mitochondrial oxidation.<sup>40</sup> Disturbances in this balance results in an accumulation of triglycerides leading to cardiac lipotoxicity.<sup>41</sup> However, a specific role of CD36 in cardiac lipotoxicity is yet to be identified.

Evidence is increasing that adipose tissues exhibit sexual dimorphism.<sup>42</sup> For example, women have a higher prevalence of BAT compared with men.<sup>43</sup> In mice, BAT from pregnant and virgin female mice had greater surface CD36 expression and elevated mitochondrial

membrane potential compared with male mice. Pregnancy induced significant changes in adipocyte cell biology. Surface expression of CD36 was elevated in adipose tissue of pregnant mice compared with virgin female mice. This suggests a distinct role for fatty acid translocase during gestation. Ogunyemi and colleagues found a downregulation of CD36 expression in subcutaneous WAT during pregnancy.<sup>44</sup> Conversely, populations of inguinal adipocytes from pregnant mice had a minor but significant increase in CD36 surface expression compared with virgin female and male mice. More strikingly however, epicardial adipocytes showed a profound increase in CD36 surface expression. The changes observed may be due to the increased nutrient requirements of the mother during pregnancy, which is supplemented by the mobilization of lipid reserves.<sup>45</sup> Further, the changes in circulating hormones during pregnancy may alter the cellular physiology of epicardial adipocytes. For instance, circulating leptin is elevated during pregnancy.<sup>46</sup> Enhanced expression of CD36 in epicardial adipose tissue may serve to regulate leptin levels during gestation.<sup>47</sup> Additionally, elevated expression of CD36 has been reported in obese pregnant women with gestational diabetes mellitus.<sup>48</sup> Gestational diabetes occurs during pregnancy due to the increased load on the mother by the fetus and may lead to type II diabetes postpartum.<sup>49</sup> This often causes a larger accumulation of fat in the fetus as well as excess fetal growth.<sup>50</sup>

Our approach highlights the utility of flow cytometry in assessing adipocyte phenotype and behavior at the single cell level and relating this information to whole body physiology. This tool could be applied for bench-top diagnostics in adipose-related metabolism disorders such as obesity and type 2 diabetes, 2 of the most pressing health concerns for modern society.

## Materials and methods

### Mice

Young adult, wild type, outbred quackenbush Swiss mice (Animal Resource Center, Perth, Western Australia) were housed in filter top cages. Mice were kept under a 12-hour day-night cycle at constant temperature (21–22°C) and provided food and water *ad libitum*. The welfare of the animals in the housing area and experiments conducted were in accordance with the Australian Code of Practice for the use of animals in research.

### Adipose tissue excision

Mice were killed by cervical dislocation according to University of Sydney Animal Ethics Committee

approval. BAT was dissected from the intrascapular region. WAT was dissected from the subcutaneous inguinal (WAT:ING), visceral gonadal (WAT:GON), perirenal (WAT:PR), mesenteric (WAT:MES) and epicardial (WAT:EC) regions. Tissue was minced thoroughly ( $\sim 1\text{--}3\text{ mm}^3$  in diameter) in fluorescence-activated cell sorting (FACS) buffer (PBS + 0.05% bovine serum albumin) and digested in 0.1% (w/v) Collagenase II (Worthington) for 1 hour at 37°C with occasional shaking. Bovine serum albumin was used to maintain cell integrity of the adipocytes.<sup>17,19</sup>

### Isolation of mature adipocytes

Digested adipose tissue was dispersed further with repeated pipetting before filtering through a  $\sim 350\text{ }\mu\text{M}$  polystyrene mesh to remove cell clusters. The filtered single cell suspension was washed with 3 mL of FACS buffer to inactivate collagenase and centrifuged at 500 RCF for 7 minutes to pellet the SVF. The buoyant adipocytes were separated from the SVF using a plastic transfer pipette into individual tubes. The SVF was resuspended in FACS buffer and ready for antibody/dye labeling.

### Reconstitution of Nile Red

Nile Red (Sigma) was reconstituted as described previously in DMSO to a concentration of 10 mg/mL.<sup>20</sup> This was diluted to a working solution 100  $\mu\text{g/mL}$  in DMSO. The final concentration used to stain the buoyant adipocytes and SVF was 100 ng/mL in FACS buffer.

### Flow cytometry

Buoyant adipocytes and cells from the SVF were incubated with fluorescently-conjugated antibodies (Table 1) for 30 minutes on ice in the dark. Lipophilic dyes (Table 2) were subsequently added and incubated for 10 minutes on ice. Cells were then washed with FACS buffer and centrifuged at 500 RCF. Cells from the buoyant fraction were taken and stained with propidium iodide (PI) to exclude dead cells from analysis. Buoyant adipocytes were also stained with the lectin WGA conjugated to FITC (L4895, Sigma) and nuclear probe DRAQ5 (62251, ThermoFisher) to confirm the presence of intact adipocytes with nuclei. For cells from the SVF, the supernatant was removed before being resuspended in FACS buffer containing PI. For single color controls, CD45 (APC and PE, eBioscience, 17-0451-82 and 12-0451-81 respectively) and Ter119 (FITC, eBioscience, 11-5921-81) were used on flushed femoral bone marrow. The single color controls were then used to correct compensation. Isotype matched control was Rat IgG2b (APC,

**Table 1.** Antibodies used in this study.

Antigen-conjugate	Clone	Source
$\alpha 2$ -integrin	DX5	BioLegend
$\alpha 4$ -integrin	R1-2	eBioscience
$\alpha 5$ -integrin	eBioHMa5-1	eBioscience
$\beta 3$ -integrin	2C9.G3	eBioscience
$\beta 4$ -integrin	346-11A	AbD Serotec
$\beta 7$ -integrin	FIB504	eBioscience
c-Kit	2B8	BioLegend
CD31	390	eBioscience
CD34	RAM34	eBioscience
CD36	72-1	eBioscience
CD41	MWReg30	BD Bioscience
CD47	miap301	eBioscience
CD45	30-F11	eBioscience
CD71	R17217	eBioscience
CD133	315-2C11	BioLegend
E-Cadherin	DECMA-1	BioLegend
EpCAM	G8.8	BioLegend
F4/80	BM8	eBioscience
Flk-1	Avas12a1	eBioscience
Rat IgG2b K Isotype Control	eB149/10H5	eBioscience
ICAM1	YN1/1.7.4	eBioscience
Ter119	TER-119	BioLegend

eBioscience, 17-4031-81) and fluorescence minus one controls were Nile Red alone (Fig. 2C, D), CD36 alone and MitoTracker<sup>®</sup> Deep Red alone (data not shown). Cells were gently shaken before analyses to keep them in suspension and to avoid clumping.

### Flow cytometer parameters

A Becton Dickinson FACSCalibur 4 Color Benchtop Analytical Flow Cytometer (Becton Dickinson, San Jose, CA, USA) was used for flow cytometric analysis. The sheath pressure was 4.5 psi and the pressure differential sufficient to establish a sample flow of 60  $\mu\text{L/min}$  on a high flow rate. The flow cell internal dimensions are 180  $\mu\text{M}$  x 430  $\mu\text{M}$  with the flow cell optically coupled to the right angle objective lens for improved sensitivity. The laser used was a 15 mW Argon Ion with laser wavelength of 488 nm. The Sample Injection Port has a diameter of 1 mm. Cells were run at a max sample flow rate of 3000 events/second. Data was acquired using CellQuest Pro<sup>®</sup> 6.0. Data was analyzed using the FlowJo software package (TreeStar, Ashland, OR, USA).

**Table 2.** Probes used in this study.

Probe	Clone/Catalog Number	Source
DRAQ5	62251	ThermoFisher
LipidTox <sup>®</sup> Green	H34475	Life Technologies
LipidTox <sup>®</sup> Red	H34476	Life Technologies
MitoTracker <sup>®</sup> Deep Red	M22426	Life Technologies
Nile Red	N3013	Sigma
Oil Red O	OREDO	POCD Scientific
Wheat Germ Agglutinin	L4895	Sigma

## Phase contrast microscopy

Adipocytes were dissociated into single cells as described above. Buoyant adipocytes were transferred onto a 12-well plate and viewed on an Axiovert35 (Zeiss) microscope under 32x magnification (ACROSTIMA 32x objective, NA: 0.40) and imaged using ZEN 2011 imaging software (Zeiss). Scale bars represent 50  $\mu\text{m}$ .

## Confocal microscopy

Adipocytes were prepared and stained as above though PI was not added. Stained adipocytes were pipetted onto a glass slide and a coverslip placed on top. The coverslip was sealed with nail polish and the slide kept in the dark until imaging. Confocal images were taken with a Leica SPEII (Leica, Germany) equipped with the solid-state laser (405 nm, 488 nm, 532 nm and 625 nm). Images were taken using an oil-immersed Leica ACS Apochromat 63x objective coupled to the Leica Application Suite – Advanced Fluorescence software. WGA was excited by the 488 nm laser while Nile Red and MitoTracker® Deep Red were excited by the 532 nm and 625 nm lasers respectively. Scale bars represent 20  $\mu\text{m}$ .

## Statistical analysis

All data represented as mean  $\pm$  SEM. Statistical analyses were performed on GraphPad Prism®. Comparison of One-way ANOVA was used with Tukey's post-hoc analysis to determine differences among lipophilic dye uptake or surface expression of antibodies between adipose depots. Two-way ANOVA with Tukey's multiple comparison test was used to determine significant differences between male, virgin female and pregnant mice. To account for differences in body size between individual mice, raw data are expressed as a proportion of fat mass (as a percentage of body mass) where relevant.

## Abbreviations

BAT	brown adipose tissue
PI	propidium iodide
SVF	stromal vascular fraction
WGA	wheat germ agglutinin
WAT	white adipose tissue
WAT:EC	epicardial adipose tissue
WAT:GON	gonadal adipose tissue
WAT:ING	inguinal adipose tissue
WAT:MES	mesenteric adipose tissue
WAT:PR	peri-renal adipose tissue

## Disclosure of potential conflicts of interest

No conflicts of interest relevant for this study.

## Acknowledgments

The authors would like to acknowledge the support of the Disciplines of Physiology, Anatomy and Histology at the University of Sydney and the Bosch Institute Live Cell Analysis Facility (Dr Angeles Sanchez-Perez). We also acknowledge the Advanced Microscopy Facility at the University of Sydney. We thank Dr Andrew Hoy (Physiology, University of Sydney) for constructive feedback and suggestions. The authors would also like to acknowledge the laboratory members of the Blood Cell Development laboratory and the Andrology Research Group laboratory.

## Funding

No funding sources relevant for this study.

## References

- [1] Berry DC, Stenesen D, Zeve D, Graff JM. The developmental origins of adipose tissue. *Development* 2013; 140 (19):3939–49; PMID:24046315; <https://doi.org/10.1242/dev.080549>
- [2] Ahmadian M, E Duncan R, Jaworski K, Sarkadi-Nagy E, Sul HS. Triacylglycerol metabolism in adipose tissue. *Future Lipidol* 2007; 2(2):229–37; PMID:19194515; <https://doi.org/10.2217/17460875.2.2.229>
- [3] Harms M, Seale P. Brown and beige fat: development, function and therapeutic potential. *Nat Med* 2013; 19 (10):1252–63; PMID:24100998; <https://doi.org/10.1038/nm.3361>
- [4] Gesta S, Tseng Y-H, Kahn CR. Developmental origin of fat: Tracking obesity to its source. *Cell* 2007; 131(2):242–56; PMID:17956727; <https://doi.org/10.1016/j.cell.2007.10.004>
- [5] Lee MJ, Wu Y, Fried SK. Adipose tissue heterogeneity: Implication of depot differences in adipose tissue for obesity complications. *Mol Aspects Med* 2013; 34 (1):1–11; PMID:23068073; <https://doi.org/10.1016/j.mam.2012.10.001>
- [6] Chau YY, Hastie N. Wt1, the mesothelium and the origins and heterogeneity of visceral fat progenitors. *Adipocyte* 2014; 4(3):217–21; <https://doi.org/10.4161/21623945.2014.985009>
- [7] Shungin D, Winkler TW, Croteau-Chonka DC, Ferreira T, Locke AE, Mägi R, Strawbridge J, Pers TH, Fischer K, Justice AE, et al. New genetic loci link adipose and insulin biology to body fat distribution. *Nature* 2015; 518 (7538):187–96; PMID:25673412; <https://doi.org/10.1038/nature14132>
- [8] Sackmann-Sala L, Berryman DE, Munn RD, Lubbers ER, Kopchick JJ. Heterogeneity among white adipose tissue depots in male C57BL/6J mice. *Obesity* 2011; 20(1):101–11; PMID:21779095; <https://doi.org/10.1038/oby.2011.235>
- [9] Huang ZH, Espiritu DJ, Uy A, Holterman AX, Vitello J, Mazzone T. Adipose tissue depot-specific differences in

- adipocyte apolipoprotein E expression. *Metabolism* 2011; 60(12):1692–701; PMID:21664633; <https://doi.org/10.1016/j.metabol.2011.04.012>
- [10] White UA, Tchoukalova YD. Sex dimorphism and depot differences in adipose tissue function. *Biochim Biophys Acta* 2014; 1842(3):377–92; PMID:23684841; <https://doi.org/10.1016/j.bbadis.2013.05.006>
  - [11] Jeffery E, Church CD, Holtrup B, Colman L, Rodeheffer MS. Rapid depot-specific activation of adipocyte precursor cells at the onset of obesity. *Nat Cell Biol* 2015; 17(4):376–85; PMID:25730471; <https://doi.org/10.1038/ncb3122>
  - [12] Brake DK, Smith CW. Flow cytometry on the stromal-vascular fraction of white adipose tissue. *Methods Mol Biol* 2008; 456:221–29; PMID:18516564
  - [13] Majka SM, Miller HL, Sullivan T, Erickson PF, Kong R, Weiser-Evans M, Nemenoff R, Moldovan R, Morandi RSA, Davis JA, et al. Adipose lineage specification of bone marrow-derived myeloid cells. *Adipocyte* 2014; 1(4):215–29; <https://doi.org/10.4161/adip.21496>
  - [14] Majka SM, Fox KE, Psilas JC, Helm KM, Childs CR, Acosta AS, Janssen RC, Friedman JE, Woessner BT, Shade TR, et al. De novo generation of white adipocytes from the myeloid lineage via mesenchymal intermediates is age, adipose depot, and gender specific. *Proc Natl Acad Sci U S A* 2010; 107(22):14781–86; PMID:20679227; <https://doi.org/10.1073/pnas.1003512107>
  - [15] Crossno JT, Majka SM, Grazia T, Gill RG, Klemm DJ. Rosiglitazone promotes development of a novel adipocyte population from bone marrow-derived circulating progenitor cells. *J Clin Invest* 2006; 116(12):3220–28; PMID:17143331; <https://doi.org/10.1172/JCI28510>
  - [16] Gavin KM, Gutman JA, Kohrt WM, Wei Q, Shea KL, Miller HL, Sullivan TM, Erickson PD, Helm KM, Acosta AS, et al. De novo generation of adipocytes from circulating progenitor cells in mouse and human adipose tissue. *FASEB J* 2016; 30(3):1096–1108; PMID:26581599
  - [17] Majka SM, Miller HL, Helm KM, Acosta AS, Childs CR, Kong R, Klemm DJ. Analysis and isolation of Adipocytes by flow cytometry. *Methods Enzymol* 2014; 537:281–96; PMID:24480352
  - [18] Durandt C, van Vollenstee FA, Dessels C, Kallmeyer K, de Villiers D, Murdoch C, et al. Novel flow cytometric approach for the detection of adipocyte sub-populations during adipogenesis. *J Lipid Res* 2016; 57:729–42
  - [19] Carswell KA, Lee M-J, Fried SK. Culture of isolated human adipocytes and isolated adipose tissue. *Methods Mol Biol* 2012; 806:203–214; PMID:22057454
  - [20] Schaedlich K, Knelangen JM, Navarrete Santos A, Fischer B, Navarrete Santos A. A simple method to sort ESC-derived adipocytes. *Cytometry* 2010; 77A(10):990–5
  - [21] Bjørndal B, Burri L, Staalesen V, Skorve J, Berge RK. Different Adipose Depots: Their role in the development of metabolic syndrome and mitochondrial response to Hypolipidemic Agents. *J Obes* 2011; 2011(1):1–15
  - [22] Varlamov O, Somwar R, Cornea A, Kievit P, Grove KL, Roberts CT, Jr. Single-cell analysis of insulin-regulated fatty acid uptake in adipocytes. *Am J Physiol Endocrinol Metab* 2010; 299(3):E486–E496; PMID:20570821
  - [23] Cawthorn WP, Scheller EL, MacDougald OA. Adipose tissue stem cells meet preadipocyte commitment: going back to the future. *J Lipid Res* 2012; 53(2):227–46; PMID:22140268
  - [24] Qiao L, Zou C, Shao P, Schaack J, Johnson PF, Shao J. Transcriptional regulation of fatty acid translocase/CD36 expression by CCAAT/enhancer-binding protein alpha. *J Biol Chem* 2008; 283(14):8788–95; PMID:18263877
  - [25] Liu Q, Wang M, Hu Y, Xing H, Chen X, Zhang Y, Zhu P. Significance of CD71 expression by flow cytometry in diagnosis of acute leukemia. *Leuk Lymphoma* 2015; 55(4):892–8
  - [26] Adachi Y, Hino T, Ohsawa M, Ueki K, Murao T, Li M, Cui Y, Okigaki M, Ito M, Ikehara S. A case of CD10-negative angioimmunoblastic T cell lymphoma with leukemic change and increased plasma cells mimicking plasma cell leukemia: A case report. *Oncol Lett* 2015; 10:1555–60; PMID:26622708
  - [27] Rawstron AC, Fazi C, Agathangelidis A, Villamor N, Letestu R, Nomdedeu J, Palacio C, Stehlikova O, Kreuzer KA, Liptrot S, et al. A complementary role of Multiparameter flow cytometry and high-throughput sequencing for minimal residual disease detection in chronic lymphocyte leukemia: an European Research Initiative on CLL study. *Leukemia* 2015; 30:1–27; PMID:26108693
  - [28] Weir EG, Borowitz MJ. Flow cytometry in the diagnosis of acute leukemia. *Semin Hematol* 2001; 38(2):124–38; PMID:11309694
  - [29] Xiao L, Yang X, Lin Y, Li S, Jiang J, Qian S, Tang Q, He R, Li X. Large adipocytes function as antigen-presenting cells to activate CD4(+) T cells via upregulating MHCII in obesity. *Int J Obes (Lond)* 2016; 40(1):112–20; PMID:26248660
  - [30] Yoshida M, Stadler J, Bertholdt G, Gerisch G. Wheat germ agglutinin binds to the contact site A glycoprotein of *Dictyostelium discoideum* and inhibits EDTA-stable cell adhesion. *EMBO J* 1984; 3(11):2663–70
  - [31] Smith JL. The staining of fat by Nile-blue sulphate. *J Pathol Bacteriol* 1911; 15:53–5; <https://doi.org/10.1002/path.1700150107>
  - [32] Greenspan P, Mayer EP, Fowler SD. Nile red: a selective fluorescent stain for intracellular lipid droplets. *J Cell Biol* 1985; 100(3):965–73; PMID:3972906; <https://doi.org/10.1083/jcb.100.3.965>
  - [33] Gocze PM, Freeman DA. Factors underlying the variability of lipid droplet fluorescence in MA-10 Leydig tumor cells. *Cytometry* 1994; 17(2):151–8; PMID:7835165; <https://doi.org/10.1002/cyto.990170207>
  - [34] Chau YY, Bandiera R, Serrels A, Martínez-Estrada OM, Qing W, Lee M, Slight J, Thornburn A, Berry R, McHaffie S, et al. Visceral and subcutaneous fat have different origins and evidence supports a mesothelial source. *Nat Cell Biol* 2014; 16(4):367–75; PMID:24609269; <https://doi.org/10.1038/ncb2922>
  - [35] Poot M, Zhang YZ, Krämer JA, Wells KS, Jones LJ, Hanzel DK, Lugade AG, Singer VL, Haugland RP. Analysis of mitochondrial morphology and function with novel fixable fluorescent stains. *J Histochem Cytochem* 1996; 44(12):1363–72; PMID:8985128; <https://doi.org/10.1177/44.12.8985128>
  - [36] Virtanen KA, Lidell ME, Orava J, Heglin M, Westergren R, Niemi T, Taittonen M, Laine J, Savisto NJ, Enerbäck S, et al. Functional Brown Adipose Tissue in Healthy Adults. *N Engl J Med* 2009; 360(15):1518–25; PMID:19357407; <https://doi.org/10.1056/NEJMoa0808949>
  - [37] Sacks HS, Fain JN, Bahouth SW, Ojha S, Frontini A, Budge H, Cinti S, Symonds ME. Adult epicardial fat



- exhibits beige features. *J Clin Endocrinol Metab* 2013; 98(9):E1448–55; PMID:23824424; <https://doi.org/10.1210/jc.2013-1265>
- [38] Xu S, Jay A, Brunaldi K, Huang N, Hamilton JA. CD36 enhances fatty acid uptake by increasing the rate of intracellular Esterification but not transport across the plasma membrane. *Biochemistry* 2013; 52(41):7254–61; PMID:24090054; <https://doi.org/10.1021/bi400914c>
- [39] Putri M, Syamsunarno MRAA, Iso T, Yamaguchi A, Hanaoka H, Sunaga H, Koitabashi N, Matsui H, Yamazaki C, Kameo S, et al. CD36 is indispensable for thermogenesis under conditions of fasting and cold stress. *Biochem Biophys Res Commun* 2015; 457(4):520–5; PMID:25596128; <https://doi.org/10.1016/j.bbrc.2014.12.124>
- [40] Cherian S, Lopaschuk GD, Carvalho E. Cellular cross-talk between epicardial adipose tissue and myocardium in relation to the pathogenesis of cardiovascular disease. *AJP: Endocrinol Metab* 2012; 303(8):E937–49
- [41] Glatz JFC, Angin Y, Steinbusch LKM, Schwenk RW, Luiken JJFP. CD36 as a target to prevent cardiac lipotoxicity and insulin resistance. *Prostaglandins Leukot essent Fatty Acids* 2013; 88(1):71–7; PMID:22580174; <https://doi.org/10.1016/j.plefa.2012.04.009>
- [42] Fuente-Martín E, Argente-Arizón P, Ros P, Argente J, Chowen JA. Sex differences in adipose tissue. *Adipocyte* 2014; 2(3):128–34; <https://doi.org/10.4161/adip.24075>
- [43] Cypess AM, Lehman S, Williams G, Tal I, Rodman D, Goldfine AB, Kuo FC, Palmer EL, Tseng YH, Doria A, et al. Identification and importance of brown adipose tissue in adult humans. *N Engl J Med* 2009; 360(15):1509–17; PMID:19357406; <https://doi.org/10.1056/NEJMoa0810780>
- [44] Ogunyemi D, Xu J, Mahesan AM, Rad S, Kim E, Yano J, Alexander C, Rotter JI, Chen Y-DI. Differentially expressed genes in adipocytokine signaling pathway of adipose tissue in pregnancy. *J Diabetes Mellitus* 2013; 03(2):86–95; <https://doi.org/10.4236/jdm.2013.32013>
- [45] Millican PE, Vernon RG, Pain VM. Protein-Metabolism in the mouse during pregnancy and lactation. *Biochem J* 1987; 248(1):251–7; PMID:3435442; <https://doi.org/10.1042/bj2480251>
- [46] Jones HN, Woollett LA, Barbour N, Prasad PD, Powell TL, Jansson T. High-fat diet before and during pregnancy causes marked up-regulation of placental nutrient transport and fetal overgrowth in C57/BL6 mice. *FASEB J* 2008; 23(1):271–8; PMID:18827021; <https://doi.org/10.1096/fj.08-116889>
- [47] Hajri T, Hall AM, Jensen DR, Pietka TA, Drover VA, Tao H, Eckel R, Abumrad NA. CD36-facilitated fatty acid uptake inhibits leptin production and signaling in adipose tissue. *Diabetes* 2007; 56(7):1872–80; PMID:17440173; <https://doi.org/10.2337/db06-1699>
- [48] Boyle KE, Hwang H, Janssen RC, DeVente JM, Barbour LA, Hernandez TL, Mandarino LJ, Friedman JE. Gestational diabetes is characterized by reduced mitochondrial protein expression and altered calcium signaling proteins in skeletal muscle. *PLoS One* 2014; 9(9):e106872; PMID:25216282; <https://doi.org/10.1371/journal.pone.0106872>
- [49] Nar G, Inci S, Aksan G, Unal OK, Nar R, Soylu K. The relationship between epicardial fat thickness and gestational diabetes mellitus. *Diabetol Metab Syndr* 2014; 6(1):120; PMID:25400702; <https://doi.org/10.1186/1758-5996-6-120>
- [50] Friedman JE. Obesity and Gestational Diabetes Mellitus pathways for programming in mouse, monkey, and man—Where do we go next? The 2014 Norbert Freinkel award lecture. *Diabetes Care* 2015; 38(8):1402–11; PMID:26207051; <https://doi.org/10.2337/dc15-0628>

## Appendix V:

**Table 8.1: Comparisons in Nile Blue fluorescence between ethanol, palmitate, linoleate and oleate treated mouse ES cells starved of serum over 12 hours.**

<b>&lt;1 min</b>	EtOH	Palmitate	Linoleate	Oleate
EtOH		NS	NS	< 0.0001
Palmitate			NS	< 0.05
Linoleate				NS
Oleate				

<b>30 min</b>	EtOH	Palmitate	Linoleate	Oleate
EtOH		NS	NS	< 0.001
Palmitate			NS	< 0.05
Linoleate				NS
Oleate				

<b>1 hr</b>	EtOH	Palmitate	Linoleate	Oleate
EtOH		NS	NS	< 0.01
Palmitate			NS	< 0.05
Linoleate				NS
Oleate				

<b>2 hr</b>	EtOH	Palmitate	Linoleate	Oleate
EtOH		NS	NS	< 0.0001
Palmitate			NS	< 0.005
Linoleate				< 0.05
Oleate				

<b>6 hr</b>	EtOH	Palmitate	Linoleate	Oleate
EtOH		NS	< 0.05	< 0.0001
Palmitate			NS	< 0.0001
Linoleate				< 0.05
Oleate				

<b>12 hr</b>	EtOH	Palmitate	Linoleate	Oleate
EtOH		NS	NS	< 0.0001
Palmitate			NS	< 0.0001
Linoleate				< 0.0005
Oleate				

**Table 8.2: Comparisons in Nile Red fluorescence between ethanol, palmitate, linoleate and oleate treated mouse ES cells starved of serum over 12 hours.**

<b>&lt;1 min</b>	EtOH	Palmitate	Linoleate	Oleate
EtOH		NS	NS	NS
Palmitate			NS	NS
Linoleate				< 0.01
Oleate				

<b>30 min</b>	EtOH	Palmitate	Linoleate	Oleate
EtOH		NS	NS	< 0.05
Palmitate			NS	NS
Linoleate				< 0.01
Oleate				

<b>1 hr</b>	EtOH	Palmitate	Linoleate	Oleate
EtOH		NS	0.0002	0.0161
Palmitate			0.0147	0.0003
Linoleate				<0.0001
Oleate				

<b>2 hr</b>	EtOH	Palmitate	Linoleate	Oleate
EtOH		< 0.0001	< 0.005	< 0.005
Palmitate			NS	NS
Linoleate				NS
Oleate				

<b>6 hr</b>	EtOH	Palmitate	Linoleate	Oleate
EtOH		NS	NS	NS
Palmitate			NS	< 0.05
Linoleate				NS
Oleate				

<b>12 hr</b>	EtOH	Palmitate	Linoleate	Oleate
EtOH		< 0.01	< 0.005	< 0.05
Palmitate			NS	NS
Linoleate				NS
Oleate				

## **Appendix VI: Making blood: The haematopoietic niche throughout ontogeny**



## Review Article

# Making Blood: The Haematopoietic Niche throughout Ontogeny

Mohammad A. Al-Drees,<sup>1,2</sup> Jia Hao Yeo,<sup>3</sup> Badwi B. Boumelhem,<sup>1</sup> Veronica I. Antas,<sup>1</sup>  
Kurt W. L. Brigden,<sup>1</sup> Chanukya K. Colonne,<sup>1</sup> and Stuart T. Fraser<sup>1,3</sup>

<sup>1</sup>Discipline of Physiology, School of Medical Sciences, Bosch Institute, University of Sydney, Camperdown, NSW 2050, Australia

<sup>2</sup>Laboratory of Bone Marrow and Stem Cell Processing, Department of Medical Oncology, Medical Oncology and Stem Cell Transplant Center, Al-Sabah Medical Area, Kuwait

<sup>3</sup>Discipline of Anatomy & Histology, School of Medical Sciences, Bosch Institute, University of Sydney, Camperdown, NSW 2050, Australia

Correspondence should be addressed to Stuart T. Fraser; [stuart.fraser@sydney.edu.au](mailto:stuart.fraser@sydney.edu.au)

Received 24 March 2015; Accepted 10 May 2015

Academic Editor: Valerie Kouskoff

Copyright © 2015 Mohammad A. Al-Drees et al. This is an open access article distributed under the Creative Commons Attribution License, which permits unrestricted use, distribution, and reproduction in any medium, provided the original work is properly cited.

Approximately one-quarter of all cells in the adult human body are blood cells. The haematopoietic system is therefore massive in scale and requires exquisite regulation to be maintained under homeostatic conditions. It must also be able to respond when needed, such as during infection or following blood loss, to produce more blood cells. Supporting cells serve to maintain haematopoietic stem and progenitor cells during homeostatic and pathological conditions. This coalition of supportive cell types, organised in specific tissues, is termed the haematopoietic niche. Haematopoietic stem and progenitor cells are generated in a number of distinct locations during mammalian embryogenesis. These stem and progenitor cells migrate to a variety of anatomical locations through the conceptus until finally homing to the bone marrow shortly before birth. Under stress, extramedullary haematopoiesis can take place in regions that are typically lacking in blood-producing activity. Our aim in this review is to examine blood production throughout the embryo and adult, under normal and pathological conditions, to identify commonalities and distinctions between each niche. A clearer understanding of the mechanism underlying each haematopoietic niche can be applied to improving *ex vivo* cultures of haematopoietic stem cells and potentially lead to new directions for transplantation medicine.

## 1. Introduction

Haematopoietic stem and progenitor cells (HSPC) require signals from neighbouring cell types to maintain their self-renewing potential. The microenvironment that is responsible for maintaining this unique property of stem and progenitor cells is termed the niche. HSPC originate and expand in a number of very distinct niches in the mammalian conceptus. Shortly before birth, HSPC home to the bone marrow (BM) to reside there for the remainder of the mammal's life. The haematopoietic niche plays roles in supporting the initial production of HSPC, the expansion of HSPC to allow the embryo to survive, and the maintenance of HSPC in the BM maintaining homeostasis and may be activated in peripheral anatomical sites to respond to stress [1]. The role of the niche may therefore vary widely according to the developmental stage of the embryo or the stress the adult is placed under.

In contrast to embryonic stem cells and similar induced pluripotent stem cells, we are still unable to maintain HSPC indefinitely. Initial studies focused on stromal populations, often fibroblastic in nature, isolated from haematopoietic tissues such as the yolk sac, foetal liver, and BM. These stromal cells offered signals such as soluble factors and cell-cell interactions which supported the *ex vivo* or *in vitro* expansion of HSPC. Defining the mechanisms that niche cells orchestrate to maintain or expand HSPC under stress will improve the current therapeutic uses of blood stem and progenitor cells.

## 2. Blood Production or Haematopoiesis

No discussion of the haematopoietic niche can take place without discussing the haematopoietic cells themselves. However, we are focusing primarily on the niche rather than

describing the blood lineages in detail. Numerous reviews specifically discuss different blood lineage production [2–5]. The haematopoietic system in the adult is responsible for the production of a broad range of different cell types from oxygen-transporting erythrocytes, the blood-clotting platelets, to the numerous forms of granulocytes through to the lymphoid branch with different T, B, NK, and innate lymphocytes. Dendritic cells, of various forms, as well as mast cells are also generated by the haematopoietic system. The haematopoietic system is therefore a complex array of different blood cell types performing a broad range of tasks to maintain homeostasis [5].

In the developing embryo, blood cells are the first cell type to become functionally mature highlighting the critical requirement for this lineage. A range of different blood cell types are also generated during embryogenesis which either are unique to the conceptus (e.g., primitive erythroid cells, foetal liver erythroid cells) or contribute to haematopoietic lineages with low turnover in the adult (microglia, Kupffer cells, and other tissue macrophages) [6, 7]. The first blood cells to appear have limited progenitor activity and it is not for several more days of embryonic development that cells with multilineage haematopoietic stem cell (HSC) activity arise. However, once adult-type (definitive) HSCs are generated, a clear hierarchy appears in which rare HSCs give rise to more frequent, lineage-committed progenitors. These progenitors in turn become more lineage-restricted, eventually giving rise to the massive numbers of mature blood cells needed. This hierarchy is critical in maintaining life in the adult mammal. An expansion of any stage or a blockade in differentiation can lead to pathological conditions ranging from leukaemia to anaemia.

In this review, we will discuss the cellular constituents of the microenvironments that help to establish, maintain, or reactivate this haematopoietic hierarchy from the first appearance of blood cells in the extraembryonic yolk sac through to the cells inhibiting blood production in the diseased and aged BM. We will primarily focus on the processes in the mouse as this is the best characterised model system for investigating mammalian haematopoiesis.

### 3. Prenatal Haematopoietic Niches

The generation of blood cells during embryogenesis is complicated by the fact that an increasing number of anatomical sites have been proposed to give rise to blood. Figure 1 shows the complex changes in anatomical location of blood production from the appearance of the first blood through to aged animals. For a thorough explanation therefore, we will be using the term conceptus, which includes the developing embryo or foetus as well as the placenta and the extraembryonic yolk sac. Mouse embryogenesis takes approximately 21 days from fertilisation to birth. Embryonic day of development will be abbreviated to E.

**3.1. Initiation of Blood Production.** The first site of blood production in mouse conceptus is the yolk sac (YS) which is a bilayered membrane that surrounds the developing embryo (see Figure 2). Haematopoietic activity occurs in the

mesodermal layer of the vascularised visceral yolk sac (VYS), which contains blood vessels and haematopoietic cells. In addition to the extraembryonic mesoderm, the VYS is also composed of an outer epithelial layer of extraembryonic visceral endoderm (VE) made of columnar epithelial cells with a brush border [8]. The VE layer of the YS has a large absorptive surface and is involved in embryonic nutrition [9]. In addition to its role in transporting substances between the maternal and foetal environments, VE cells also contribute to haematopoiesis by secreting factors that induce commitment of mesodermal progenitors to the hematovascular fate [10, 11]. The developing endothelium and haematopoietic cells are in very close proximity to the visceral endodermal cells [8]. The VE itself is derived from an extraembryonic endodermal progenitor. The specification of VE identity is dependent upon the extraembryonic endodermal cells being exposed to bone morphogenetic protein-4 (Bmp4), leading to gene expression changes resulting in haematopoietic supportive activity [12]. Coculture of haematopoietic progenitors with YS-derived endodermal cell lines results in expansion of haematopoietic cells *in vitro* [13]. The transcription factor GATA4 is critical to VE formation [9]. Embryonic stem (ES) cells lacking GATA4 are unable to form blood islands demonstrating the role of the VE in haematopoietic cell induction [9]. Factors secreted by the VE can induce the primitive ectoderm (which is fated to become brain) to be respecified to become haematopoietic leading to epsilon ( $\epsilon$ )-haemoglobin expression [10]. Indian Hedgehog (Ihh) produced by the VE activates expression of bone morphogenic protein-4 (Bmp4) in neighbouring mesodermal cells leading to haematopoietic initiation and patterning [10, 11]. Ihh also regulates vascular endothelial growth factor receptor 1 and 2 (VEGFR-1 and VEGFR-2) expression [14]. While both layers of the YS produce VEGF, mesodermal VEGF is unable to induce blood cell formation [15]. VEGF produced by the VE however is critical in blood and endothelial cell development in the YS demonstrating a clear role for the VE in the first haematopoietic niche [15, 16].

**3.2. Primitive Haematopoiesis.** The onset of YS haematopoiesis occurs from E7.5 in the mouse conceptus [19, 20]. This initial phase of blood production is termed primitive haematopoiesis [20–22]. During this phase, bands of primitive blood cells loosely associated with endothelial cells (the so-called blood islands) can be identified in the YS [23]. Primitive erythroid cells enter the circulation at approximately E9.0 [24]. Primitive erythroid progenitors (EryP-CFC) are maintained in the YS for close to 48 hours in close proximity to vascular endothelial cells and the VE described above. EryP-CFC express receptors for soluble growth factors such as c-Kit (receptor for stem cell factor, SCF), transforming growth factor- $\beta$  (TGF $\beta$ ) receptor, erythropoietin receptor (EpoR), angiopoietin (Ang) receptors, and VEGFR-2 [20]. YS endothelial cells purified according to expression of VEGFR-2 express SCF, TGF $\beta$ 1, and Ang1 mRNA [20]. VE cells, isolated by virtue of GFP expression driven of the  $\alpha$ -fetoprotein protein (AFP) promoter, express Ang1 mRNA [20]. VCAM-1<sup>+</sup> mesenchymal cells in the YS have also been implicated as a niche cell controlling primitive erythroid cell maturation

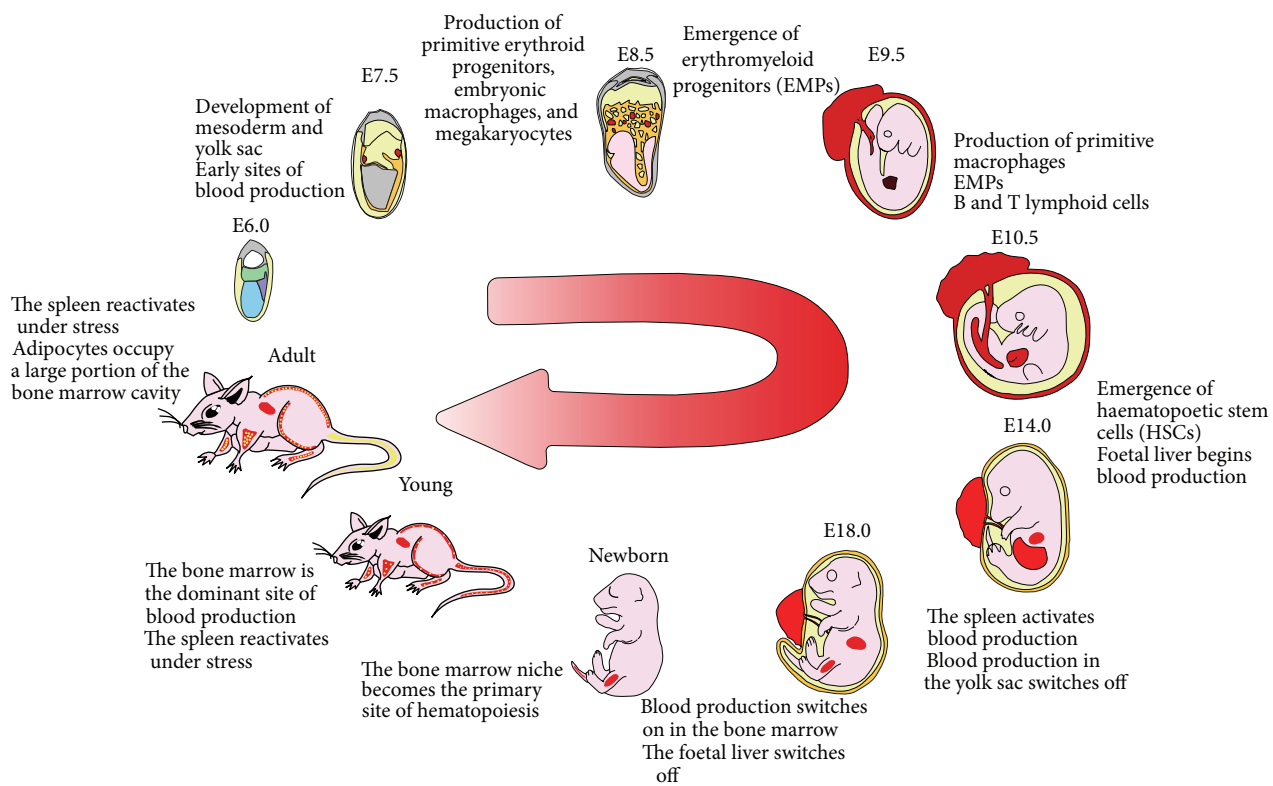


FIGURE 1: Timeline of haematopoiesis from early development to postnatal development in mice. This figure depicts the anatomical locations of haematopoiesis and the trafficking of haematopoietic stem cells (HSCs) and progenitor cells essential for maintaining haematopoiesis for life. Blood production begins at the mesoderm (blue, E6.0) and yolk sac (orange, all stages). From here, the first wave is initiated at the yolk sac blood islands (red, E7.0 and E8.5). Blood production is then shifted to the yolk sac and placenta (red, E9.5), with the latter providing blood to the foetus (pink) until birth. At E10.5, blood production initiates at the foetal liver and aorta-gonad-mesonephros (AGM) (red). The spleen initiates blood production at E14.0 (red) and continues to be a site of haematopoiesis after birth at time of stress. At E18.0, blood production shifts to the bone marrow (red), which remains the dominant site of haematopoiesis for life. After birth, adipocytes (yellow) begin to accumulate within the bone marrow and progressively increase as the mouse ages. Early development pictures modified from [17, 18].

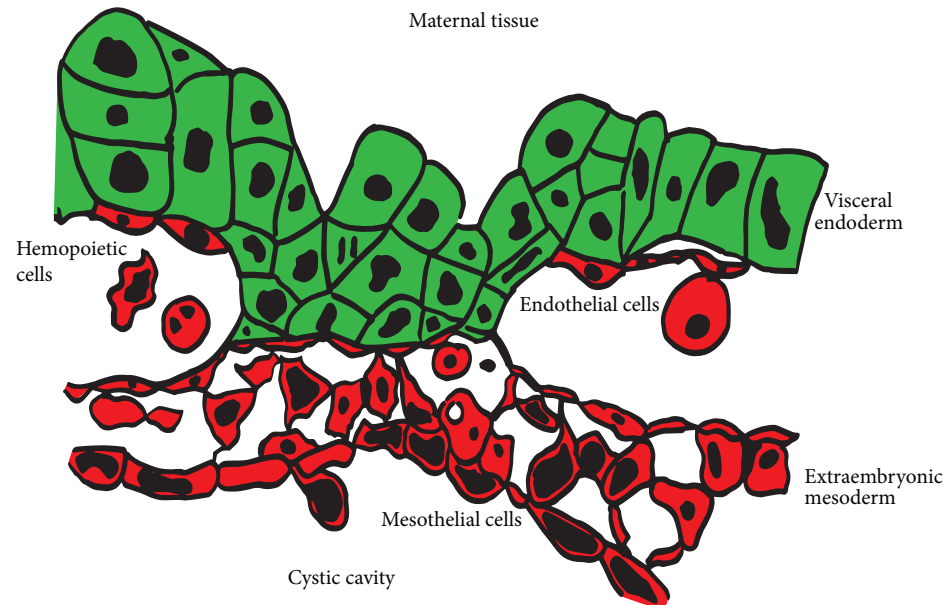


FIGURE 2: Histology of the yolk sac. The visceral endodermal cells form an epithelial sheet facing the maternal tissue (green). The mesoderm-derived tissue (red) includes vascular endothelial cells, haematopoietic cells, and a thin mesothelial layer facing the embryo proper.

[25]. These cells have not been histologically identified as yet though it is likely that they represent the thin mesothelial layer of the YS [25]. VCAM-1 is a receptor for  $\alpha 4 \beta 1$ -integrin present on EryP-CFC at this stage of development in the YS [20, 26]. Collectively, primitive erythropoiesis is supported by signals from the neighbouring YS endothelial cells, signals diffusing from the visceral endoderm and possibly through direct cell-cell interactions with the mesothelium.

**3.3. Definitive Haematopoietic Niches.** The first wave of definitive (adult-type) haematopoiesis starts at E8.25 in the YS with erythromyeloid progenitors [22, 27]. Embryonic definitive erythrocytes are smaller than their primitive counterparts but larger than adult erythrocytes [28]. The second wave of definitive haematopoiesis is characterised by the production of definitive progenitor and stem cell populations including lymphoid progenitors and HSCs capable of long-term multilineage reconstitution of newborn and foetal recipients [29–31]. Despite the rapid changes in haematopoietic potential in this narrow developmental window, the impact of the other YS compartments is not well defined. It is currently unclear which signals from the YS niche are activating the definitive haematopoietic programme within the developing blood cells. However, we have recently observed that the secreted peptide gastrin-2 is upregulated, transiently, in the YS VE cells close to the time at which haematopoietic activity diminishes in this tissue [32]. Gastrin-2 protein was localised at the basal end of the VE cell facing the neighbouring endothelial cell, suggesting that this may be a signal from the VE influencing endothelial and possibly haematopoietic cell behaviour [32].

**3.4. The Placental Haematopoietic Niche.** *In vitro* culture studies showed that the embryonic component of mouse placenta forms a niche supporting haematopoietic progenitors [33]. HSPC are present in the mouse and human placenta [34–37]. Clusters of haematopoietic progenitor cells can be observed attached to placental vascular endothelial cells [38]. Similar to the early YS, endothelial cells in the placenta produce SCF whilst the haematopoietic progenitors expressed the SCF receptor c-Kit [38]. Three regions are clearly defined in the placenta: the outer maternal decidua; the middle spongiotrophoblast layer; and the vascularized labyrinth. Placental trophoblasts produce platelet-derived growth factor- $\beta$  (PDGF $\beta$ ) to prevent the premature differentiation of HSPC, particularly erythroid progenitors [39]. The human placenta was identified as a niche supporting the terminal differentiation of primitive erythroid cells through interactions with macrophages [40].

## 4. Embryonic Haematopoietic Niches

**4.1. Aorta-Gonad-Mesonephros (AGM).** The dorsal aorta, at the level of the developing gonadal and mesonephros (AGM), exhibits clusters of haematopoietic cells attached to the endothelial wall [21, 41, 42]. These haematopoietic clusters contain definitive HSC activity [43–45]. Explant studies confirmed that tissues located ventrally relative to the dorsal

aorta induce HSPC activity [46]. In contrast, tissues located dorsal to the aorta lack HSPC supportive activity [46]. When liver or BM HSPC are cultured with AGM stromal cells, HSPC repopulating- and colony-forming potentials are preserved [47]. However, not all AGM endothelial populations have the same supportive abilities. Endothelial cells derived from the ventral region of the dorsal aorta support both HSC maintenance and differentiation. Meanwhile, cells from the urogenital subregion of the AGM support HSC maintenance but fail to induce HSC activity [47, 48]. Cytokines, soluble factors, and physical anchorage are part of the AGM microenvironment that play a role in supporting HSCs [48, 49]. Growth factors that enhance HSPC activity such as SCF, Flt3-ligand, interleukin-3 (IL-3), and Bmp4 are all expressed in the AGM [44, 50, 51]. Hedgehog signalling also plays a role in regulating HSC activity in the AGM [46]. Signalling from the nervous system also influences intraembryonic haematopoiesis [52]. Sympathetic nervous system mediators (catecholamines) regulate HSC emergence independent of blood flow [52]. Furthermore, catecholamine receptors are present on nascent HSCs, reinforcing the interplay between nervous system and haematopoiesis [52]. Other factors, such as retinoic acid signalling and blood shear stress, are also key regulators of embryonic blood production [53–55].

**4.2. Foetal Liver Haematopoietic Niche.** By E10.5–11.0, haematopoietic progenitors are migrating from the YS, AGM, and placenta to the foetal liver (FL). HSPC activity increases rapidly in this endoderm-derived tissue as the embryo matures. The FL haematopoietic niche consists of a variety of cell types including maturing haematopoietic cells themselves, sinusoidal endothelial cells, macrophages, stromal fibroblasts, and hepatoblasts (progenitors of hepatocytes). Hepatoblasts produce a broad range of haematopoietic growth factors including SCF, erythropoietin (Epo), thrombopoietin (TPO), and IL-6 which all support erythroid cell development [56]. The role of hepatoblasts in supporting haematopoiesis is best exemplified by mice lacking the tyrosine kinase Map2k4. These mice fail to form hepatoblasts, showing a significant reduction in Epo and SCF expression and a concomitant impairment in blood cell production, in particular erythropoiesis. HSPC express  $\beta 1$ -integrin which interacts with vitronectin and fibronectin in the extracellular matrix produced by hepatoblasts [57]. This deposition of extracellular matrix by hepatoblasts is regulated by autocrine production of TGF $\beta$  [57]. Hepatoblasts also produce IL-7 to support lymphoid cell development [58]. A series of reports detailed the surprising use of an anti-CD3e antibody to purify a FL population which supported HSC maintenance. This population expresses a range of soluble factors including insulin-like growth factor-2 (IGF-2) and angiopoietin-like proteins 2 and 3 (Angptl2 and Angptl3). These cells have since been shown to express the hepatoblast markers albumin and Dlk, GFP-driven by the AFP promoter, and surface SCF. These cells also produce the chemokine CXCL12, also known as stromal-derived factor (SDF) [59]. Collectively, this data suggests these cells are likely to be hepatoblastic in origin. The FL niche was modeled *in vitro* following the generation of AFT024, a mouse FL stromal cell line. This cell line is



highly supportive of HSPC and has been characterised at the transcriptome level to identify regulators of HSPC activity [60].

HSPC, expressing the surface marker Endothelial Protein C Receptor (EPCR), interact with sinusoidal endothelial cells [61]. These HSPC were observed in both the luminal and parenchymal aspects of the Lyve-1<sup>+</sup> sinusoidal endothelial cells extracellular matrix made up of laminin and fibronectin [61]. Very recent findings in the zebrafish show that the arrival of blood progenitors in the perivascular niche leads to profound changes in the niche itself. Endothelial cells actively surround HSCs once they have entered the perivascular space [62]. A similar process was observed in the mouse FL. When transgenic labelled HSPC entered the FL parenchyma, vascular endothelial cells congregated around the HSPC. The HSPC then anchor to perivascular cells and orient their mitotic division planes according to the perivascular cell body they have adhered to [62]. These intriguing findings show that the niche is responsive to the behaviour of HSPC.

FL macrophages form a supportive microenvironment termed the erythroblastic island (EBI). Although the role of EBI is better defined in the BM (will be described later), FL EBI macrophages support the terminal differentiation of primitive erythroid cells [63, 64]. This interaction is dependent upon  $\alpha 4 \beta 1$ -integrin present on the primitive erythroid cells binding to VCAM-1 expressed by the FL EBI macrophage [63]. The precise role is unclear; however one important element is the engulfment and destruction of millions of expelled erythroid nuclei. FL macrophages lacking DNase II, the primary DNA-degrading enzyme, show a massive uptake of erythroid nuclei which they are unable to digest. This leads to the macrophage rupturing releasing inflammatory mediators and killing the embryo [65].

## 5. The Bone Marrow Haematopoietic Niche

The bone marrow (BM) is the predominant blood-producing site of adult mammals. The migration of the haematopoietic activity from the embryonic and foetal tissues, described above, to the foetal BM is only now being defined at the molecular level. Investigating foetal BM niche formation will help us to define the essential elements of the niche as it maintains blood production in the newborn, juvenile, and adult mammals.

### 5.1. Foetal Bone Marrow Haematopoietic Niche Formation.

The long bones of the mouse foetus begin to develop at approximately E14.5 and arise from mesodermal progenitors. At E15.5, the mouse long bones are cartilaginous bone templates lacking blood vessels. One day later in development, vessels can be detected in the periosteum (the layer surrounding the developing bone) and the epiphyseal plates found at each end of the long bones [66]. Calcification and vascularisation of BM cavity then begin, primarily in the middle region of the long bone. At this stage, collagen type 1,  $\alpha 1$ - (Coll $\alpha 1$ -) expressing osteoblasts emerge in the periosteum [66]. The middle cavity region is dominated by CD31<sup>+</sup> endothelial cells forming blood vessels and c-Kit<sup>+</sup> Sca-1<sup>+</sup> Lineage<sup>neg</sup> (KSL) HSC can be detected. By E17.5,

Coll $\alpha 1$ <sup>+</sup> osteoblasts occupy the middle BM cavity and expand alongside CD31 expressing vascular endothelial cells, both proliferating toward the epiphyseal plate [66]. The BM will eventually fill the medullary cavities of bones throughout the skeleton. The BM cavity can be subdivided into four regions: endosteal, subendosteal, central, and perisinusoidal regions. The endosteum is tissue lining the bone surface and facing the marrow cavity or the trabeculae of the spongy bone within the cavity and is mostly composed of osteoblasts though osteoclasts are also important components of this microenvironment [67]. Mice lacking the transcription factor Osterix (*Osx*) fail to form mature osteoblasts and mineralised bone matrix [68]. *Osx*<sup>-/-</sup> foetal BM is vascularised normally but lacks functional HSPC [66]. *Osx*<sup>-/-</sup> mice are therefore a useful model for assessing the role of osteoblasts in establishing the foetal BM niche.

Homing, adhesion, and retention of HSPC in the haematopoietic BM niche and their migration to corresponding microenvironments are controlled by chemotactic factors. Inactivation of the genes encoding the chemokine CXCL12 or its receptor CXCR4 led to significant decrease of HSC frequency in E17.5 foetal BM [69]. Foetal liver HSC frequency was not affected by *Cxcr4*-deficiency [69]. *Cxcr4*-deficient foetal BM is hypocellular with a severe reduction in myeloid cell frequency [70]. Mice lacking the genes encoding serum response factor (*Srf*) or myocardin-related transcription factor (*Mrtf*), which is regulated by *Srf*, also show normal FL HSPC frequency and exhibit a failure of HSPC to migrate to the foetal BM [71]. *Srf*-deficient HSPC fail to respond to the chemotactic cues of CXCL12. This foetal BM colonisation defect is phenocopied in mice lacking either *Mrtfa* or *Mrtfb* which show defective cell motility and actin remodelling [71]. CXCL12 and *Scf* gene expression was upregulated in *Osx*<sup>-/-</sup> mutant E17.5 BM [66]. Collectively, these findings suggest a BM-specific mechanism of niche formation dependent upon the CXCL12-CXCR4 axis and associated molecules.

### 5.2. The Neonatal and Juvenile Bone Marrow Haematopoietic Niche.

Profound physiological changes take place at birth. The newborn must breathe and digest food for the first time; the connection to the maternal circulation via the placenta and YS has ceased and, perhaps most importantly, the newborn is exposed to the external environment resulting in the activation of both the innate and adaptive immune systems. Haematopoiesis needs to accommodate these changes in oxygen transport and immune response. Surprisingly, very little is known about the immediate changes in the neonatal niche in spite of the profound shift in physiological activity. However, calcium ions originating from the bone matrix are clearly important. Mice lacking the calcium receptor (*CaR*) have hypocellular marrow just after birth [72]. *CaR*<sup>-/-</sup> HSPC fail to migrate to the endosteal niche as they cannot detect the increase in free calcium ions released from the bone surface [72]. *CaR*<sup>-/-</sup> HSPC show defects in binding to the extracellular matrix proteins fibronectin and collagen type 1 [72]. As the juvenile mouse matures, the bone matrix becomes more heavily ossified (mineralised). This complex process is critical

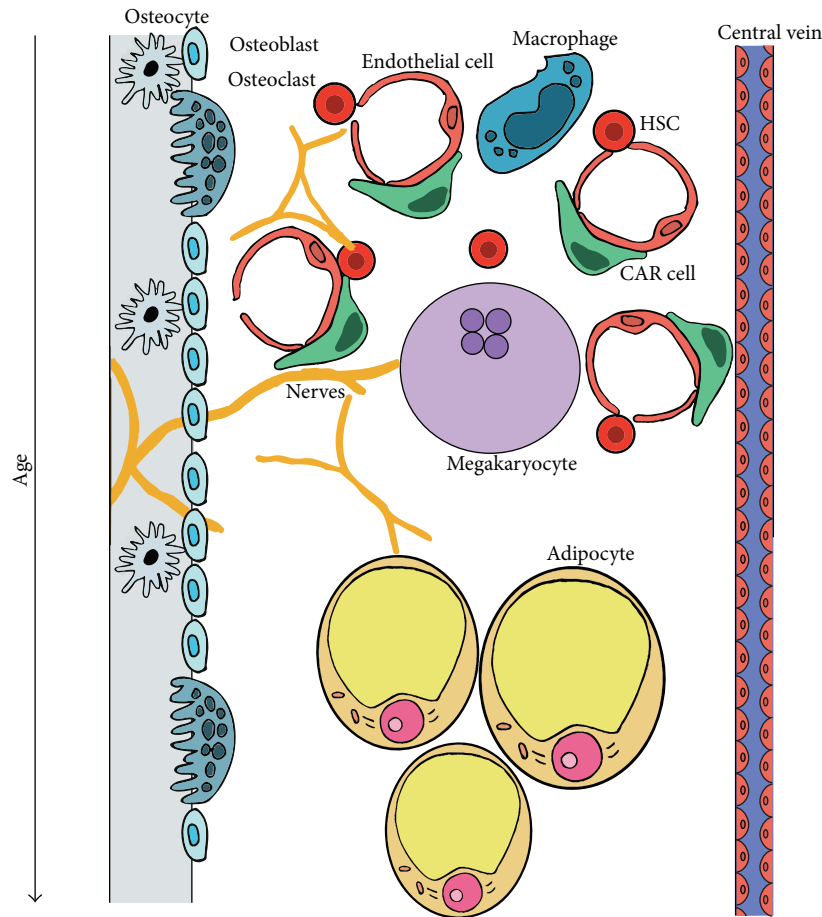


FIGURE 3: Cellular interactions within the adult bone marrow niche. The bone marrow niche is home to a variety of cell types that promote or inhibit the maintenance of HSCs and haematopoietic progenitors. The endosteal niche and perivascular niche can be clearly discerned. Adipocytes fill the marrow with age, inhibiting blood cell production.

in establishing a stable haematopoietic niche and relies on a broad range of regulators from transcription factors such as Runx2, phosphoproteins such as bone sialoprotein (Bsp), and osteocyte proteins such as Saa3. Deletion of genes encoding these proteins leads to abnormal mineralisation of the bone matrix potentially compromising the BM.

## 6. The Adult Bone Marrow Haematopoietic Niches

The BM serves as the main HSPC niche for adult eutherian mammals though the bones do not appear to vary in their HSC frequency [73]. The concept that there are specific cell types that can orchestrate a BM niche was strengthened by the discovery of a transplantable CD146-expressing cell in the human BM which, when transplanted into mice, could give rise to an entirely new BM niche which could support mouse HSC activity [74]. HSC can be found in most regions of the long bone; the trabeculated regions of the metaphysis are the preferred site of homing compared to the epiphysis (the endplates) or the diaphysis (the shaft of the long bone) [75, 76]. However, it is now clear that there

are at least two anatomically distinct niches: the endosteal niche close to the bone surface and the perivascular niche associated with arterioles. Figure 3 simplifies the complex cellular compartments in the adult BM niche.

**6.1. The Endosteal Niche of the Adult Bone Marrow.** High-resolution cytometric analysis of the adult BM has shown that HSCs preferentially localise to two distinct niches, the perivascular niche and the endosteal niche [77]. Mouse and human osteoblasts support HSPC [78]. The endosteal niche exhibits unique physiological properties including hypoxia and a greater concentration of free calcium ions coming from the bone surface [72, 77]. HSCs adhere to the osteoblasts [77, 79, 80]. Mice expressing a constitutively active form of parathyroid hormone led to an expansion in osteoblast number and HSC frequency [81]. Mice with conditional deletion of BMPRIa possess increased numbers of N-cadherin<sup>+</sup> osteoblastic cells. These in turn interact directly with HSC. This leads to an increased HSC frequency [82]. Conversely, transgenic ablation of osteoblasts led to a severe reduction in HSC frequency [83]. Inhibition of osteoclast function has been associated with reduced HSPC frequency [84]. However, osteopetrotic mice, which lack functional

osteoclasts, show overgrowth of mineralised bone matrix and increased levels of HSPC [85]. This report challenged previous reports suggesting that osteoclasts may play a role in the BM haematopoietic niche.

Cooperative regulation among cytokine signals and cell adhesion molecules is required for HSCs maintenance or activation. Many factors including cytokines, chemokines, adhesion molecules, and transcription factors regulate the HSC quiescence in the endosteal niche. Some of the molecules defined in this process include Tie2 and angiopoietin-1 [86]; SCF and its receptor c-Kit [87]; CXCL12 [88]; thrombopoietin [89], Jagged1 interactions with Notch receptors [81]; osteopontin [90]; and N-cadherin which became a lightning rod of controversy in the field. N-cadherin expression was reported in the endosteal HSC niche [81, 82, 86] though its role remained unclear. However, N-cadherin is not required for HSCs maintenance though it may play a role in osteoblastic homophilic interactions [91, 92].

**6.2. The Perivascular Niche.** A niche supporting HSC activity has been identified in close proximity to the blood vessels of the adult BM and has been termed the perivascular niche [79]. HSCs interact with a perivascular mesenchymal cell type which has become the focus of many research groups. Imaging of the adult mouse BM revealed that the majority of quiescent HSCs are situated close to arterioles [93]. Cells expressing GFP under the control of the Nestin promoter (Nes-GFP) localise in the perivascular region. Although they constitute only a small fraction of BM cells, once purified these cells were shown to contain essentially all of the mesenchymal stem cell (MSC) activity of the marrow [94]. Even more striking, these Nes-GFP<sup>+</sup> MSC were found to sit adjacent to HSC. Nes-GFP<sup>+</sup> MSC produce soluble factors that support HSC maintenance such as CXCL12 and SCF. This led to the proposal that MSC form a niche with HSC directly and maintain HSC activity [94].

Two distinct populations could be detected according to GFP transgene expression in the BM. Cells expressing high levels of the Nestin-GFP transgene (Nes-GFP<sup>bright</sup>) localise to the perivascular region, exhibit pericyte-like morphology, and express the pericyte marker NG2 and  $\alpha$ -smooth muscle actin. These are found exclusively around arterioles [93]. Dormant HSCs are found in close proximity to these Nes-GFP<sup>bright</sup> cells. Genetic ablation of the NG2-expressing Nes-GFP<sup>bright</sup> population resulted in HSC migrating away from the arterioles. In contrast, the more abundant cells expressing low levels of the Nestin-GFP transgene (Nes-GFP<sup>dim</sup> cells) are reticular in shape and associate with sinusoids [93].

Recently, much attention has been given to the role of the sympathetic nervous system forming the adult BM niche. Circadian noradrenalin secretion by the sympathetic nerves negatively regulates CXCL12 expression in the BM. This in turn reduces mobilisation of HSC from the BM niche [95]. Denervation of sympathetic nerves resulted in loss of HSC; however other BM components such as endothelial cells, MSC, and osteoblasts remained intact [96]. These sympathetic nerves were also found to be ensheathed by autonomous, nonmyelinating Schwann cells which are in

direct contact with HSCs and lie parallel to blood vessels [96]. These glial cells regulate activation of TGF $\beta$  and HSC quiescence via TGF $\beta$ /Smad signalling [96]. The sympathetic nerve regulation of HSC maintenance is mediated indirectly by Nestin<sup>+</sup> MSC expressing the  $\beta$ 3-adrenergic receptor [94]. Both adrenergic receptors  $\beta$ 3 and  $\beta$ 2 were reported to regulate HSC mobilisation [94].

Similar haematopoietic defects were seen in transgenic mice with neurological abnormalities. UDP-galactose ceramide galactosyltransferase (CGT) is required for the synthesis of galactocerebroside and sulfatide required for myelin [97]. CGT<sup>-/-</sup> mice exhibit altered fibronectin network in the BM and a pronounced reduction in CD45<sup>+</sup> VCAM-1<sup>+</sup> stromal cells numbers [97]. Diminished HSC mobilisation from the BM was also observed in these CGT<sup>-/-</sup> mice after following granulocyte colony-stimulating factor (G-CSF) or fucoidan administration [98].

The molecular mechanisms regulating this niche are becoming more clearly defined. SCF is clearly a critical factor in regulating the adult BM niche. Ding and colleagues performed an exhaustive analysis of the cell types expressing SCF in the marrow using the *Scf*<sup>gfp/+</sup> mouse [99]. Endothelial cells and perivascular cells express GFP in this transgenic model. Conditional deletion of *Scf* in osteoblasts or Nestin-expressing cells had no effect on HSC frequency. However, specific loss of *Scf* in endothelial cells expressing Tie2-Cre led to significant loss of HSC frequency. The role of perivascular cell-derived SCF was confirmed by conditional deletion in leptin-receptor (LepR)-Cre-expressing cells. Intriguingly, this led to a reduction in BM HSC frequency with a concomitant increase in splenic HSC numbers. No change was observed during developmental stages demonstrating that SCF originating from the perivascular mesenchymal cells regulates the BM niche specifically. A similar phenotype was observed in vitamin D receptor (VDR) null mutant mice which show reduced BM HSC frequency and enhanced splenic HSC numbers [100].

CXCL12 is crucial to HSC homing to the BM. A population of CXCL12-abundant reticular (CAR) cells was observed in the vascular niche [88, 101–103]. Conditional deletion of CXCR4 results in profound reduction in HSC frequency [88]. Conditional deletion of CXCL12 from *Osx*-expressing BM CAR cells and osteoblasts resulted in HPC mobilization and decline in B lymphoid progenitors [102]. Therefore, signalling between CXCL12 from CAR cells and CXCR4 on HSC maintains HSC self-renewal, proliferation, and migration. CAR cells are bipotent and are able to give rise to both osteoblasts and adipocytes as will be discussed later in this review [103].

**6.3. Other Cells of the Marrow Which Support Haematopoiesis.** HSCs reside in close proximity to megakaryocytes [104, 105]. Ablation of megakaryocytes reduces HSC proliferation and engraftment [105, 106]. Thrombopoietin (TPO) administration of megakaryocyte-ablated mice restores HSC function [105]. Cxcl4, which megakaryocytes produce, inhibits HSC proliferation, reduces HSC numbers, and decreases engraftment [104]. An increase in HSC number, proliferation, and repopulating activity was observed in *Cxcl4*-deficient

mice [104]. Megakaryocytes also maintain HSC quiescence through  $TGF\beta$  signalling under homeostatic conditions and promote HSC expansion via FGF-1 production under stress conditions [107]. High-resolution imaging *in vivo* revealed the colocalisation of HSCs with FoxP3<sup>+</sup> regulatory T (Treg) cells on the endosteal surface [108]. However, whether this interaction is biologically relevant in homeostatic HSPC maintenance is unclear.

## 7. Haematopoietic Progenitor Niches

The expansion and maturation of committed haematopoietic progenitors require specific microenvironments. Here, we describe several critical niches regulating haematopoietic progenitor development into functionally mature cells.

**7.1. Erythroblastic Islands Are Essential Niches for Erythropoiesis.** Erythroblastic islands (EBI) are a specialised niche found where mammalian erythroblasts proliferate and differentiate and are described in Figure 4. Discovered by Marcel Bessis in the 1950s, EBI were first described as multicellular structures with developing erythroblasts at various stages of differentiation surrounding a central macrophage [109–111]. EBI have also been isolated from the foetal liver [63, 112] and spleen [113, 114]. The clinical significance of this niche was demonstrated in animal models of human haemoglobinopathies [115, 116]. The central macrophage of the EBI was proposed to be a “nurse” cell for erythroid development with macrophages providing iron to developing erythroblasts for heme synthesis [109]. However, there is still no direct evidence that the central macrophage is providing iron to the surrounding erythroblasts. Cytokines such as RCAS [117], TRAIL [118], and IGF-2 [119] are produced by EBI central macrophages. Another proposed function of the EBI central macrophage is to engulf and destroy extruded erythroid nuclei. Phosphatidylserine (PS) is exposed on the outer leaflet of the plasma membrane of the extruded erythroid nuclei [120]. EBI macrophages actively phagocytose extruded erythroid nuclei via the PS receptor, Tim-4 [63, 121]. After phagocytosis, the macrophages degrade the nuclei. DNaseII and its regulator, erythroid Kruppel-like factor-1 (Klf1), are essential in this process [65, 120, 122]. Embryos with targeted deletions of retinoblastoma tumour suppressor (Rb) protein, *c-Maf*, or the cytoskeletal protein paladin die *in utero* with defects in EBI function [112, 123, 124].

**7.2. B Lymphoid Niche.** B lymphoid progenitors reside in close proximity to the endosteum and migrate towards the central blood vessels in the BM as they mature [125]. VCAM-1<sup>+</sup> CXCL12<sup>+</sup> expressing reticular cells were among the first B-cell-specific niche to be identified [101]. These cells lack endothelial and endosteal markers and are distant from the endosteal surface. Other cell types thought to play a role include CXCL-12-expressing osteoblasts and IL-7-expressing cells [83]. B-cell progenitors attach to CXCL-12-expressing cells and then relocate and attach to IL-7-expressing cells as they mature into pro-B-cells progenitors [101]. After naive B-cells are sensitized by antigens in the peripheral lymphoid

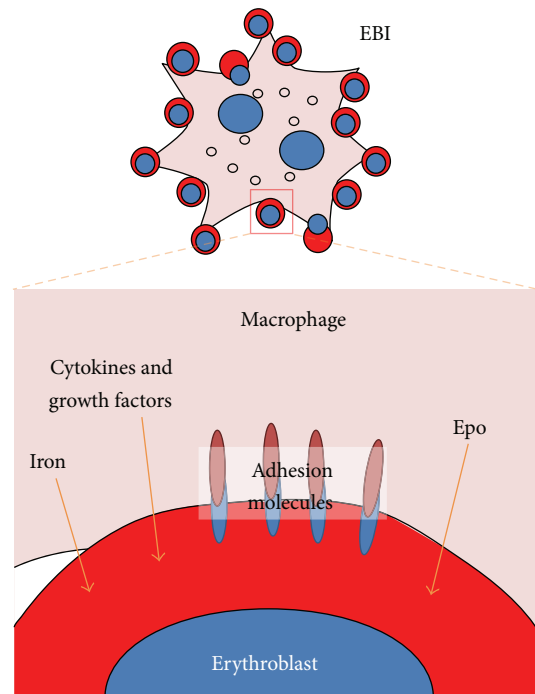


FIGURE 4: The erythroblastic island provides a niche for erythroid development. Central macrophage anchors erythroblasts in the erythroid niche via adhesion molecules. Within the EBI, the central macrophage supports erythropoiesis in several ways, such as providing iron for haemoglobin synthesis, cytokine, and growth factors as well as engulfing expelled erythroid nuclei.

organs, resultant plasma cells migrate to the marrow which then serves as a specific niche for these mature cells [101]. This niche offers prerequisite soluble factors (Blimp-1, CXCL12, APRIL, IL-5, IL-6, and  $TNF-\alpha$ ) as well as necessary cell-cell contacts through CD44 and CD28. In the absence of  $IgE^{+}$   $DX5^{+}$  basophils, isolated plasma cells rapidly die. Addition of basophils enabled plasma cells survival [126].  $F4/80^{+}$   $Gr-1^{low}$  Siglec-F<sup>+</sup> eosinophils associate with plasma cells and supply IL-6 and APRIL for plasma cell survival [127]. Depletion of eosinophils in mice results in apoptosis of plasma cells [127]. Plasma cells also interact with megakaryocytes, which secrete APRIL and IL-6. Mice deficient in the thrombopoietin receptor, c-Mpl, have impaired megakaryopoiesis and show reduced numbers of plasma cells [128].

## 8. Normal versus Stressed Splenic Microenvironments

Red blood cells, or erythrocytes, are normally generated from erythrocyte progenitor cells residing inside the BM in a process termed medullary erythropoiesis. The erythrocyte production rate increases dramatically during anaemia [129]. To recover from anaemic stress, erythroid progenitors migrate from the BM to extramedullary sites such as the spleen, which act as secondary sites for erythrocyte production. This process is termed stress erythropoiesis and is a critical phase in the recovery from haemorrhage or



diseases causing anaemia [130]. Stress erythropoiesis often manifests as a dramatic increase in spleen size (termed splenomegaly) and is most notable in chronic haemolytic conditions such as thalassaemia and sickle cell anaemia but is also observed in many haematological diseases such as myelofibrosis, leukaemia, and lymphoma [129]. Bmp4 and Hedgehog signalling act together with Epo, SCF, and hypoxia to encourage extramedullary haematopoiesis in the spleen during stress [131, 132]. Hedgehog signalling is also required for the recovery from anaemia [133]. The splenic stroma consists of vascular and lymphatic endothelial cells, marginal zone macrophages, follicular dendritic cells, fibroblastic reticular cells, marginal reticular cells, and red pulp fibroblasts. The erythroblastic island is the only known splenic stromal cell which has been examined during anaemic stress. Forssman antigen<sup>+</sup> F4/80<sup>+</sup> macrophages extend their cytoplasmic processes around erythroblasts in the spleen after irradiation and transplantation [113]. MSS31 endothelial-like cell lines isolated from newborn mouse spleen selectively supported the maturation and enucleation of the erythroid progenitor cells by direct cell-cell contact [134]. Fibroblast-like SPY3-2 cell line expresses high levels of SCF and low levels of granulocyte macrophage colony-stimulating factor and IL-3 and can support erythroid differentiation *in vitro* [135].

## 9. Inhibition of the Haematopoietic Niches

As mammals age, fatty marrow predominantly takes over the BM compartment [136]. BM adipocytes, or yellow adipose tissue (YAT), are often dismissed as simple “space-fillers” that lay dormant in the marrow [137]. YAT may also serve as an emergency energy reservoir [138]. However, it has been recently shown that YAT plays an active role within the haematopoietic microenvironment influencing haematopoiesis and osteogenesis [139]. YAT originates from BM MSC, the same precursors that give rise to osteoblasts and haematopoietic cell types. YAT responds to systemic changes in energy metabolism. This is most evident in ageing where there are large changes in YAT volume. As ageing individuals show increased BM YAT and anaemia, it was proposed that BM adipocytes may inhibit blood production. By comparing the haematopoietic recovery of wild-type and fatless A-ZIP/F1 mice after lethal irradiation, it was observed that the lack of adipogenesis in the fatless mice enhanced haematopoietic recovery [139]. This was due to the enhanced engraftment of short-term progenitors in the BM compartment. Ablation of YAT also improved osteogenesis [139]. *In vitro* cultures of BM-derived adipocytes yielded a reduced expansion of haematopoietic cells, indicating that adipocytes release diffusible inhibitors of haematopoiesis. Secretion of neuropilin-1, lipocalin 2, adiponectin, and TNF- $\alpha$  from adipose tissue can inhibit proliferation of haematopoietic cells [139]. However, adiponectin can support HSC proliferation [140]. Transgenic ablation of CAR cells revealed their essential role in the niche and demonstrated the potential of these cells to form both osteoblasts and adipocytes [103]. The transcriptional regulator Foxc1 is highly expressed by CAR cells. Conditional deletion of *Foxc1* led to a profound change in CAR cell fate. Rather than giving rise to both osteoblasts

and adipocytes, a lineage bias was observed with a far greater number of mature adipocytes forming in the BM [141]. This in turn led to a pronounced decrease in HSPC activity. CAR cells also expressed the adipogenesis markers leptin receptor and peroxisome proliferator-activated-receptor- $\gamma$ . Enforced expression of Foxc1 in the preadipocytic cell stromal cell line OP9 led to enhanced haematopoietic supporting activity and loss of adipogenic activity [141]. Collectively, these findings demonstrate that Foxc1 is acting as a rheostat within critical niche cells, specifying whether the marrow will support or inhibit haematopoiesis.

## 10. Commonalities and Distinctions between the Different Haematopoietic Niches

Assessing the cellular and signalling components of all of the critical haematopoietic niches throughout ontogeny was a revealing exercise. Commonalities between these profoundly distinct niches become obvious. Not surprisingly, SCF and its receptor c-Kit were observed to play critical roles in extraembryonic, embryonic, foetal, and adult blood production as well as during recovery from stress. SCF and Hedgehog signalling are significant players in haematopoiesis ranging from the first primitive erythroid cells through to extramedullary haematopoiesis in the spleen during anaemia. Likewise, Bmp4 signalling was highlighted as being important in numerous niches including the YS, AGM, BM, and anaemic spleen. Hypoxia is also clearly important in a number of niches. The role of blood flow is critical in the AGM for HSPC development. It may also play a role in shutting down primitive erythroid progenitor activity in the YS. Similar rheological signals are less likely to be important in the parenchyma of the FL or BM. The distinction between foetal and perinatal niches was highlighted by the importance of CXCL12 and its receptor CXCR4 in the BM. This signalling system plays a far less significant role in the early embryonic stages of haematopoiesis though it is critical in numerous elements of adult haematopoietic production.

## 11. Application of Our Understanding of the Haematopoietic Niche

How can we apply our understanding of the different haematopoietic niches to medical technology and practice? The deconstructionist approach has been flipped recently with the development of “bone marrow-on-a-chip.” Microfluidic cultures of marrow maintained HSPC *in vitro* for at least 1 week demonstrating that the critical microenvironment for controlling HSC activity can be engineered [142]. This could improve current models for drug development and screening. Animal experimentation could be reduced or replaced as human “bone marrow-on-a-chip” systems could be used to assess the toxicity or efficacy of novel compounds on the human haematopoietic system. This system can be scaled up allowing for high throughput screening of new therapeutical compounds.

Perhaps the most medically relevant utility of the niche is as a system for the *ex vivo* expansion of HSPC for

transplantation. Currently, we cannot maintain HSPC indefinitely *in vitro* or *ex vivo* in the same way we can maintain embryonic stem or induced pluripotent stem cells. One of the “holy grails” of haematology is therefore identifying the factor or combination of factors that can maintain HSPC indefinitely in an *ex vivo* setting. This would have massive repercussions for transplantation and transfusion medicine, as it could allow for the correction of genetic lesions in HSPC, thus allowing for effective engraftment after transplantation. This could be applied to a broad range of haematological disorders affecting millions of people such as sickle cell anaemia,  $\beta$ -thalassaemia, immunodeficiencies, and blood-clotting disorders.

## Disclosure

Stuart T. Fraser is the Sesquicentennial Senior Lecturer in Molecular Embryology.

## Conflict of Interests

The authors declare that there is no conflict of interests regarding the publication of this paper.

## Acknowledgments

The authors would like to acknowledge all the members of the Laboratory of Blood Cell Development, University of Sydney. They gratefully acknowledge the support of the Disciplines of Physiology and Anatomy and Histology, University of Sydney. They also acknowledge the encouragement and support of Dr. Stephen Assinder (University of Sydney) and Dr. Oliver K. Watt. The Laboratory of Blood Cell Development has been funded by the Sydney Medical School, the Bosch Institute Translational Grant-in-Aid, and the National Breast Cancer Foundation. Jia Hao Yeo is supported by a NWG Macintosh Award. Chanukya K. Colonne was supported by a Sydney Medical School Postgraduate Scholarship.

## References

- [1] L. D. Wang and A. J. Wagers, “Dynamic niches in the origination and differentiation of haematopoietic stem cells,” *Nature Reviews Molecular Cell Biology*, vol. 12, no. 10, pp. 643–655, 2011.
- [2] S. H. Orkin and L. I. Zon, “SnapShot: hematopoiesis,” *Cell*, vol. 132, no. 4, pp. 712.e1–712.e2, 2008.
- [3] S. T. Fraser, “The modern primitives: applying new technological approaches to explore the biology of the earliest red blood cells,” *ISRN Hematology*, vol. 2013, Article ID 568928, 21 pages, 2013.
- [4] M. H. Baron, J. Isern, and S. T. Fraser, “The embryonic origins of erythropoiesis in mammals,” *Blood*, vol. 119, no. 21, pp. 4828–4837, 2012.
- [5] M. A. Rieger and T. Schroeder, “Hematopoiesis,” *Cold Spring Harbor Perspectives in Biology*, vol. 4, no. 12, 2012.
- [6] F. Ginhoux, M. Greter, M. Leboeuf et al., “Fate mapping analysis reveals that adult microglia derive from primitive macrophages,” *Science*, vol. 330, no. 6005, pp. 841–845, 2010.
- [7] E. G. Perdiguero, K. Klapproth, C. Schulz et al., “Tissue-resident macrophages originate from yolk-sac-derived erythro-myeloid progenitors,” *Nature*, vol. 518, no. 7540, pp. 547–551, 2015.
- [8] J. L. Haar and G. A. Ackerman, “Ultrastructural changes in mouse yolk sac associated with the initiation of vitelline circulation,” *Anatomical Record*, vol. 170, no. 4, pp. 437–455, 1971.
- [9] M. Bielinska, N. Narita, M. Heikinheimo, S. B. Porter, and D. B. Wilson, “Erythropoiesis and vasculogenesis in embryoid bodies lacking visceral yolk sac endoderm,” *Blood*, vol. 88, no. 10, pp. 3720–3730, 1996.
- [10] M. Belaousoff, S. M. Farrington, and M. H. Baron, “Hematopoietic induction and respecification of A-P identity by visceral endoderm signaling in the mouse embryo,” *Development*, vol. 125, no. 24, pp. 5009–5018, 1998.
- [11] M. A. Dyer, S. M. Farrington, D. Mohn, J. R. Munday, and M. H. Baron, “Indian hedgehog activates hematopoiesis and vasculogenesis and can respecify prospective neurectodermal cell fate in the mouse embryo,” *Development*, vol. 128, no. 10, pp. 1717–1730, 2001.
- [12] J. Artus, P. Douvaras, A. Piliszek, J. Isern, M. H. Baron, and A.-K. Hadjantonakis, “BMP4 signaling directs primitive endoderm-derived XEN cells to an extraembryonic visceral endoderm identity,” *Developmental Biology*, vol. 361, no. 2, pp. 245–262, 2012.
- [13] M. C. Yoder, V. E. Papaioannou, P. P. Breitfeld, and D. A. Williams, “Murine yolk sac endoderm- and mesoderm-derived cell lines support *in vitro* growth and differentiation of hematopoietic cells,” *Blood*, vol. 83, no. 9, pp. 2436–2443, 1994.
- [14] N. Byrd, S. Becker, P. Maye et al., “Hedgehog is required for murine yolk sac angiogenesis,” *Development*, vol. 129, no. 2, pp. 361–372, 2002.
- [15] A. Damert, L. Miquerol, M. Gertsenstein, W. Risau, and A. Nagy, “Insufficient VEGFA activity in yolk sac endoderm compromises haematopoietic and endothelial differentiation,” *Development*, vol. 129, no. 8, pp. 1881–1892, 2002.
- [16] L. Miquerol, M. Gertsenstein, K. Harpal, J. Rossant, and A. Nagy, “Multiple developmental roles of VEGF suggested by a LacZ-tagged allele,” *Developmental Biology*, vol. 212, no. 2, pp. 307–322, 1999.
- [17] M. C. Yoder, “Inducing definitive hematopoiesis in a dish,” *Nature Biotechnology*, vol. 32, no. 6, pp. 539–541, 2014.
- [18] F. Ginhoux, S. Lim, G. Hoeffel, D. Low, and T. Huber, “Origin and differentiation of microglia,” *Frontiers in Cellular Neuroscience*, vol. 7, article 45, 2013.
- [19] J. Palis, S. Robertson, M. Kennedy, C. Wall, and G. Keller, “Development of erythroid and myeloid progenitors in the yolk sac and embryo proper of the mouse,” *Development*, vol. 126, no. 22, pp. 5073–5084, 1999.
- [20] J. Isern, Z. He, S. T. Fraser et al., “Single-lineage transcriptome analysis reveals key regulatory pathways in primitive erythroid progenitors in the mouse embryo,” *Blood*, vol. 117, no. 18, pp. 4924–4934, 2011.
- [21] F. R. Sabin, “Preliminary note on the differentiation of angioblasts and the method by which they produce blood-vessels, blood-plasma and red blood-cells as seen in the living chick,” *Anatomical Record*, vol. 13, no. 4, pp. 199–204, 1917.
- [22] J. Palis, K. E. McGrath, and P. D. Kingsley, “Initiation of hematopoiesis and vasculogenesis in murine yolk sac explants,” *Blood*, vol. 86, no. 1, pp. 156–163, 1995.

- [23] M. J. Ferkowicz, M. Starr, X. Xie et al., "CD41 expression defines the onset of primitive and definitive hematopoiesis in the murine embryo," *Development*, vol. 130, no. 18, pp. 4393–4403, 2003.
- [24] K. E. McGrath, A. D. Koniski, J. Malik, and J. Palis, "Circulation is established in a stepwise pattern in the mammalian embryo," *Blood*, vol. 101, no. 5, pp. 1669–1676, 2003.
- [25] G. Keller, L. Chicha, A. Ditadi et al., "Primitive erythropoiesis is regulated by miR-126 via nonhematopoietic Vcam-1+ cells," *Developmental Cell*, vol. 23, no. 1, pp. 45–57, 2012.
- [26] S. T. Fraser, J. Isern, and M. H. Baron, "Maturation and enucleation of primitive erythroblasts during mouse embryogenesis is accompanied by changes in cell-surface antigen expression," *Blood*, vol. 109, no. 1, pp. 343–352, 2007.
- [27] K. E. McGrath, J. M. Frame, G. J. Fromm et al., "A transient definitive erythroid lineage with unique regulation of the  $\beta$ -globin locus in the mammalian embryo," *Blood*, vol. 117, no. 17, pp. 4600–4608, 2011.
- [28] P. D. Kingsley, J. Malik, R. L. Emerson et al., "Maturation of globin switching in primary primitive erythroid cells," *Blood*, vol. 107, no. 4, pp. 1665–1672, 2006.
- [29] M. C. Yoder, K. Hiatt, P. Dutt, P. Mukherjee, D. M. Bodine, and D. Orlic, "Characterization of definitive lymphohematopoietic stem cells in the day 9 murine yolk sac," *Immunity*, vol. 7, no. 3, pp. 335–344, 1997.
- [30] M. C. Yoder, K. Hiatt, and P. Mukherjee, "In vivo repopulating hematopoietic stem cells are present in the murine yolk sac at day 9.0 postcoitus," *Proceedings of the National Academy of Sciences of the United States of America*, vol. 94, no. 13, pp. 6776–6780, 1997.
- [31] S. T. Fraser, M. Ogawa, R. T. Yu, S. Nishikawa, M. C. Yoder, and S.-I. Nishikawa, "Definitive hematopoietic commitment within the embryonic vascular endothelial-cadherin(+) population," *Experimental Hematology*, vol. 30, no. 9, pp. 1070–1078, 2002.
- [32] V. I. Antas, K. W. Brigden, A. J. Prudence, and S. T. Fraser, "Gastrokine-2 is transiently expressed in the endodermal and endothelial cells of the maturing mouse yolk sac," *Gene Expression Patterns*, vol. 16, no. 2, pp. 69–74, 2014.
- [33] C. Gekas, F. Dieterlen-Lièvre, S. H. Orkin, and H. K. Mikkola, "The placenta is a niche for hematopoietic stem cells," *Developmental Cell*, vol. 8, no. 3, pp. 365–375, 2005.
- [34] C. Gekas, F. Dieterlen-Lièvre, S. H. Orkin, and H. K. A. Mikkola, "The placenta is a niche for hematopoietic stem cells," *Developmental Cell*, vol. 8, no. 3, pp. 365–375, 2005.
- [35] K. Ottersbach and E. Dzierzak, "The murine placenta contains hematopoietic stem cells within the vascular labyrinth region," *Developmental Cell*, vol. 8, no. 3, pp. 377–387, 2005.
- [36] C. Robin, K. Bollerot, S. Mendes et al., "Human placenta is a potent hematopoietic niche containing hematopoietic stem and progenitor cells throughout development," *Cell Stem Cell*, vol. 5, no. 4, pp. 385–395, 2009.
- [37] A. Ivanovs, S. Rybtsov, L. Welch, R. A. Anderson, M. L. Turner, and A. Medvinsky, "Highly potent human hematopoietic stem cells first emerge in the intraembryonic aorta-gonad-mesonephros region," *Journal of Experimental Medicine*, vol. 208, no. 12, pp. 2417–2427, 2011.
- [38] T. Sasaki, C. Mizuochi, Y. Horio, K. Nakao, K. Akashi, and D. Sugiyama, "Regulation of hematopoietic cell clusters in the placental niche through SCF/Kit signaling in embryonic mouse," *Development*, vol. 137, no. 23, pp. 3941–3952, 2010.
- [39] A. Chhabra, A. J. Lechner, M. Ueno et al., "Trophoblasts regulate the placental hematopoietic niche through PDGF-B signaling," *Developmental Cell*, vol. 22, no. 3, pp. 651–659, 2012.
- [40] B. van Handel, S. L. Prasad, N. Hassanzadeh-Kiabi et al., "The first trimester human placenta is a site for terminal maturation of primitive erythroid cells," *Blood*, vol. 116, no. 17, pp. 3321–3330, 2010.
- [41] T. North, T.-L. Gu, T. Stacy et al., "Cbfa2 is required for the formation of intra-aortic hematopoietic clusters," *Development*, vol. 126, no. 11, pp. 2563–2575, 1999.
- [42] T. Yokomizo, C. E. Ng, M. Osato, and E. Dzierzak, "Three-dimensional imaging of whole midgestation murine embryos shows an intravascular localization for all hematopoietic clusters," *Blood*, vol. 117, no. 23, pp. 6132–6134, 2011.
- [43] T. Yokomizo and E. Dzierzak, "Three-dimensional cartography of hematopoietic clusters in the vasculature of whole mouse embryos," *Development*, vol. 137, no. 21, pp. 3651–3661, 2010.
- [44] S. Taoudi, C. Gonneau, K. Moore et al., "Extensive hematopoietic stem cell generation in the AGM region via maturation of VE-Cadherin + CD45 + pre-definitive HSCs," *Cell Stem Cell*, vol. 3, no. 1, pp. 99–108, 2008.
- [45] J.-C. Boisset, W. van Cappellen, C. Andrieu-Soler, N. Galjart, E. Dzierzak, and C. Robin, "In vivo imaging of haematopoietic cells emerging from the mouse aortic endothelium," *Nature*, vol. 464, no. 7285, pp. 116–120, 2010.
- [46] M. Peeters, K. Ottersbach, K. Bollerot et al., "Ventral embryonic tissues and Hedgehog proteins induce early AGM hematopoietic stem cell development," *Development*, vol. 136, no. 15, pp. 2613–2621, 2009.
- [47] R. A. J. Oostendorp, K. N. Harvey, N. Kusadasi et al., "Stromal cell lines from mouse aorta-gonads-mesonephros subregions are potent supporters of hematopoietic stem cell activity," *Blood*, vol. 99, no. 4, pp. 1183–1189, 2002.
- [48] O. Ohneda, C. Fennie, Z. Zheng et al., "Hematopoietic stem cell maintenance and differentiation are supported by embryonic aorta-gonad-mesonephros region-derived endothelium," *Blood*, vol. 92, no. 3, pp. 908–919, 1998.
- [49] R. A. J. Oostendorp, C. Robin, C. Steinhoff et al., "Long-term maintenance of hematopoietic stem cells does not require contact with embryo-derived stromal cells in cocultures," *Stem Cells*, vol. 23, no. 6, pp. 842–851, 2005.
- [50] C. Robin, K. Ottersbach, C. Durand et al., "An unexpected role for IL-3 in the embryonic development of hematopoietic stem cells," *Developmental Cell*, vol. 11, no. 2, pp. 171–180, 2006.
- [51] C. J. Marshall, J. C. Sinclair, A. J. Thrasher, and C. Kinnon, "Bone morphogenetic protein 4 modulates c-Kit expression and differentiation potential in murine embryonic aorta-gonad-mesonephros haematopoiesis in vitro," *British Journal of Haematology*, vol. 139, no. 2, pp. 321–330, 2007.
- [52] S. R. Fitch, G. M. Kimber, N. K. Wilson et al., "Signaling from the sympathetic nervous system regulates hematopoietic stem cell emergence during embryogenesis," *Cell Stem Cell*, vol. 11, no. 4, pp. 554–566, 2012.
- [53] B. Chanda, A. Ditadi, N. N. Iscove, and G. Keller, "XRetinoic acid signaling is essential for embryonic hematopoietic stem cell development," *Cell*, vol. 155, no. 1, pp. 215–227, 2013.
- [54] L. Adamo, O. Naveiras, P. L. Wenzel et al., "Biomechanical forces promote embryonic haematopoiesis," *Nature*, vol. 459, no. 7250, pp. 1131–1135, 2009.
- [55] T. E. North, W. Goessling, M. Peeters et al., "Hematopoietic stem cell development is dependent on blood flow," *Cell*, vol. 137, no. 4, pp. 736–748, 2009.



- [56] D. Sugiyama, K. Kulkeaw, C. Mizuochi, Y. Horio, and S. Okayama, "Hepatoblasts comprise a niche for fetal liver erythropoiesis through cytokine production," *Biochemical and Biophysical Research Communications*, vol. 410, no. 2, pp. 301–306, 2011.
- [57] D. Sugiyama, K. Kulkeaw, and C. Mizuochi, "TGF-beta-1 up-regulates extra-cellular matrix production in mouse hepatoblasts," *Mechanisms of Development*, vol. 130, no. 2-3, pp. 195–206, 2013.
- [58] B. Liang, T. Hara, K. Wagatsuma et al., "Role of hepatocyte-derived IL-7 in maintenance of intrahepatic NKT cells and T cells and development of B cells in fetal liver," *Journal of Immunology*, vol. 189, no. 9, pp. 4444–4450, 2012.
- [59] S. Chou and H. F. Lodish, "Fetal liver hepatic progenitors are supportive stromal cells for hematopoietic stem cells," *Proceedings of the National Academy of Sciences of the United States of America*, vol. 107, no. 17, pp. 7799–7804, 2010.
- [60] J. A. Hackney, P. Charbord, B. P. Brunk, C. J. Stoeckert, I. R. Lemischka, and K. A. Moore, "A molecular profile of a hematopoietic stem cell niche," *Proceedings of the National Academy of Sciences of the United States of America*, vol. 99, no. 20, pp. 13061–13066, 2002.
- [61] H. Iwasaki, F. Arai, Y. Kubota, M. Dahl, and T. Suda, "Endothelial protein C receptor-expressing hematopoietic stem cells reside in the perisinusoidal niche in fetal liver," *Blood*, vol. 116, no. 4, pp. 544–553, 2010.
- [62] O. J. Tamplin, E. M. Durand, L. A. Carr et al., "Hematopoietic stem cell arrival triggers dynamic remodeling of the perivascular Niche," *Cell*, vol. 160, no. 1-2, pp. 241–252, 2015.
- [63] J. Isern, S. T. Fraser, Z. He, and M. H. Baron, "The fetal liver is a niche for maturation of primitive erythroid cells," *Proceedings of the National Academy of Sciences of the United States of America*, vol. 105, no. 18, pp. 6662–6667, 2008.
- [64] J. Isern, S. T. Fraser, Z. He, and M. H. Baron, "Developmental niches for embryonic erythroid cells," *Blood Cells, Molecules, and Diseases*, vol. 44, no. 4, pp. 207–208, 2010.
- [65] K. Kawane, H. Fukuyama, G. Kondoh et al., "Requirement of DNase II for definitive erythropoiesis in the mouse fetal liver," *Science*, vol. 292, no. 5521, pp. 1546–1549, 2001.
- [66] S. Coşkun, H. Chao, H. Vasavada et al., "Development of the fetal bone marrow niche and regulation of HSC quiescence and homing ability by emerging osteolineage cells," *Cell Reports*, vol. 9, no. 2, pp. 581–590, 2014.
- [67] A. Balduino, S. P. Hurtado, P. Frazão et al., "Bone marrow subendosteal microenvironment harbours functionally distinct haemosupportive stromal cell populations," *Cell and Tissue Research*, vol. 319, no. 2, pp. 255–266, 2005.
- [68] K. Nakashima, X. Zhou, G. Kunkel et al., "The novel zinc finger-containing transcription factor Osterix is required for osteoblast differentiation and bone formation," *Cell*, vol. 108, no. 1, pp. 17–29, 2002.
- [69] Y.-R. Zou, A. H. Kottman, M. Kuroda, I. Taniuchi, and D. R. Littman, "Function of the chemokine receptor CXCR4 in haematopoiesis and in cerebellar development," *Nature*, vol. 393, no. 6685, pp. 595–599, 1998.
- [70] Q. Ma, D. Jones, P. R. Borghesani et al., "Impaired B-lymphopoiesis, myelopoiesis, and derailed cerebellar neuron migration in CXCR4- and SDF-1-deficient mice," *Proceedings of the National Academy of Sciences of the United States of America*, vol. 95, no. 16, pp. 9448–9453, 1998.
- [71] P. Costello, M. Sargent, D. Maurice et al., "MRTF-SRF signaling is required for seeding of HSC/PS in bone marrow during development," *Blood*, vol. 125, no. 8, pp. 1244–1255, 2015.
- [72] G. B. Adams, K. T. Chabner, I. R. Alley et al., "Stem cell engraftment at the endosteal niche is specified by the calcium-sensing receptor," *Nature*, vol. 439, no. 7076, pp. 599–603, 2006.
- [73] M. J. Kiel, T. Iwashita, Ö. H. Yilmaz, and S. J. Morrison, "Spatial differences in hematopoiesis but not in stem cells indicate a lack of regional patterning in definitive hematopoietic stem cells," *Developmental Biology*, vol. 283, no. 1, pp. 29–39, 2005.
- [74] B. Sacchetti, A. Funari, S. Michienzi et al., "Self-renewing osteoprogenitors in bone marrow sinusoids can organize a hematopoietic microenvironment," *Cell*, vol. 131, no. 2, pp. 324–336, 2007.
- [75] Y. Jiang, H. Bonig, T. Ulyanova, K. Chang, and T. Papayannopoulou, "On the adaptation of endosteal stem cell niche function in response to stress," *Blood*, vol. 114, no. 18, pp. 3773–3782, 2009.
- [76] S. L. Ellis, J. Grassinger, A. Jones et al., "The relationship between bone, hemopoietic stem cells, and vasculature," *Blood*, vol. 118, no. 6, pp. 1516–1524, 2011.
- [77] C. Nombela-Arrieta, G. Pivarnik, B. Winkel et al., "Quantitative imaging of haematopoietic stem and progenitor cell localization and hypoxic status in the bone marrow microenvironment," *Nature Cell Biology*, vol. 15, no. 5, pp. 533–543, 2013.
- [78] R. S. Taichman and S. G. Emerson, "Human osteoblasts support hematopoiesis through the production of granulocyte colony-stimulating factor," *Journal of Experimental Medicine*, vol. 179, no. 5, pp. 1677–1682, 1994.
- [79] M. J. Kiel, Ö. H. Yilmaz, T. Iwashita, O. H. Yilmaz, C. Terhorst, and S. J. Morrison, "SLAM family receptors distinguish hematopoietic stem and progenitor cells and reveal endothelial niches for stem cells," *Cell*, vol. 121, no. 7, pp. 1109–1121, 2005.
- [80] C. Celso Lo, H. E. Fleming, J. W. Wu, C. X. Zhao, S. Miake-Lye, and J. Fujisaki, "Live-animal tracking of individual haematopoietic stem/progenitor cells in their niche," *Nature*, vol. 457, no. 7225, pp. 92–96, 2008.
- [81] L. M. Calvi, G. B. Adams, K. W. Weibrecht et al., "Osteoblastic cells regulate the haematopoietic stem cell niche," *Nature*, vol. 425, no. 6960, pp. 841–846, 2003.
- [82] J. Zhang, C. Niu, L. Ye et al., "Identification of the haematopoietic stem cell niche and control of the niche size," *Nature*, vol. 425, no. 6960, pp. 836–841, 2003.
- [83] D. Visnjic, Z. Kalajic, D. W. Rowe, V. Katavic, J. Lorenzo, and H. L. Aguila, "Hematopoiesis is severely altered in mice with an induced osteoblast deficiency," *Blood*, vol. 103, no. 9, pp. 3258–3264, 2004.
- [84] S. Lymperi, A. Ersek, F. Ferraro, F. Dazzi, and N. J. Horwood, "Inhibition of osteoclast function reduces hematopoietic stem cell numbers in vivo," *Blood*, vol. 117, no. 5, pp. 1540–1549, 2011.
- [85] K. Miyamoto, S. Yoshida, M. Kawasumi et al., "Osteoclasts are dispensable for hematopoietic stem cell maintenance and mobilization," *Journal of Experimental Medicine*, vol. 208, no. 11, pp. 2175–2181, 2011.
- [86] F. Arai, A. Hirao, M. Ohmura et al., "Tie2/angiopoietin-1 signaling regulates hematopoietic stem cell quiescence in the bone marrow niche," *Cell*, vol. 118, no. 2, pp. 149–161, 2004.
- [87] L. A. Thorén, K. Liuba, D. Bryder et al., "Kit regulates maintenance of quiescent hematopoietic stem cells," *Journal of Immunology*, vol. 180, no. 4, pp. 2045–2053, 2008.

- [88] T. Sugiyama, H. Kohara, M. Noda, and T. Nagasawa, "Maintenance of the hematopoietic stem cell pool by CXCL12-CXCR4 chemokine signaling in bone marrow stromal cell niches," *Immunity*, vol. 25, no. 6, pp. 977–988, 2006.
- [89] H. Qian, N. Buza-Vidas, C. D. Hyland et al., "Critical role of thrombopoietin in maintaining adult quiescent hematopoietic stem cells," *Cell Stem Cell*, vol. 1, no. 6, pp. 671–684, 2007.
- [90] S. K. Nilsson, H. M. Johnston, G. A. Whitty et al., "Osteopontin, a key component of the hematopoietic stem cell niche and regulator of primitive hematopoietic progenitor cells," *Blood*, vol. 106, no. 4, pp. 1232–1239, 2005.
- [91] M. J. Kiel, G. L. Radice, and S. J. Morrison, "Lack of evidence that hematopoietic stem cells depend on N-cadherin-mediated adhesion to osteoblasts for their maintenance," *Cell Stem Cell*, vol. 1, no. 2, pp. 204–217, 2007.
- [92] A. M. Greenbaum, L. D. Revollo, J. R. Woloszynek, R. Civitelli, and D. C. Link, "N-cadherin in osteolineage cells is not required for maintenance of hematopoietic stem cells," *Blood*, vol. 120, no. 2, pp. 295–302, 2012.
- [93] Y. Kunisaki, I. Bruns, C. Scheiermann et al., "Arteriolar niches maintain haematopoietic stem cell quiescence," *Nature*, vol. 502, no. 7473, pp. 637–643, 2013.
- [94] S. Méndez-Ferrer, T. V. Michurina, F. Ferraro et al., "Mesenchymal and haematopoietic stem cells form a unique bone marrow niche," *Nature*, vol. 466, no. 7308, pp. 829–834, 2010.
- [95] S. Méndez-Ferrer, D. Lucas, M. Battista, and P. S. Frenette, "Haematopoietic stem cell release is regulated by circadian oscillations," *Nature*, vol. 452, no. 7186, pp. 442–447, 2008.
- [96] S. Yamazaki, H. Ema, G. Karlsson et al., "Nonmyelinating schwann cells maintain hematopoietic stem cell hibernation in the bone marrow niche," *Cell*, vol. 147, no. 5, pp. 1146–1158, 2011.
- [97] Y. Katayama and P. S. Frenette, "Galactocerebrosides are required postnatally for stromal-dependent bone marrow lymphopoiesis," *Immunity*, vol. 18, no. 6, pp. 789–800, 2003.
- [98] Y. Katayama, M. Battista, W.-M. Kao et al., "Signals from the sympathetic nervous system regulate hematopoietic stem cell egress from bone marrow," *Cell*, vol. 124, no. 2, pp. 407–421, 2006.
- [99] L. Ding, T. L. Saunders, G. Enikolopov, and S. J. Morrison, "Endothelial and perivascular cells maintain haematopoietic stem cells," *Nature*, vol. 481, no. 7382, pp. 457–462, 2012.
- [100] M. Jeansson, A. Gawlik, G. Anderson et al., "Angiopoietin-1 is essential in mouse vasculature during development and in response to injury," *The Journal of Clinical Investigation*, vol. 121, no. 6, pp. 2278–2289, 2011.
- [101] K. Tokoyoda, T. Egawa, T. Sugiyama, B.-I. Choi, and T. Nagasawa, "Cellular niches controlling B lymphocyte behavior within bone marrow during development," *Immunity*, vol. 20, no. 6, pp. 707–718, 2004.
- [102] A. Greenbaum, Y.-M. S. Hsu, R. B. Day et al., "CXCL12 in early mesenchymal progenitors is required for haematopoietic stem-cell maintenance," *Nature*, vol. 495, no. 7440, pp. 227–230, 2013.
- [103] Y. Omatsu, T. Sugiyama, H. Kohara et al., "The essential functions of adipo-osteogenic progenitors as the hematopoietic stem and progenitor cell niche," *Immunity*, vol. 33, no. 3, pp. 387–399, 2010.
- [104] I. Bruns, D. Lucas, S. Pinho et al., "Megakaryocytes regulate hematopoietic stem cell quiescence through CXCL4 secretion," *Nature Medicine*, vol. 20, no. 11, pp. 1315–1320, 2014.
- [105] A. Nakamura-Ishizu, K. Takubo, M. Fujioka, and T. Suda, "Megakaryocytes are essential for HSC quiescence through the production of thrombopoietin," *Biochemical and Biophysical Research Communications*, vol. 454, no. 2, pp. 353–357, 2014.
- [106] T. S. Olson, A. Caselli, S. Otsuru et al., "Megakaryocytes promote murine osteoblastic HSC niche expansion and stem cell engraftment after radioablative conditioning," *Blood*, vol. 121, no. 26, pp. 5238–5249, 2013.
- [107] M. Zhao, J. M. Perry, H. Marshall et al., "Megakaryocytes maintain homeostatic quiescence and promote post-injury regeneration of hematopoietic stem cells," *Nature Medicine*, vol. 20, no. 11, pp. 1321–1326, 2014.
- [108] J. Fujisaki, J. Wu, A. L. Carlson et al., "In vivo imaging of T<sub>reg</sub> cells providing immune privilege to the haematopoietic stem-cell niche," *Nature*, vol. 474, no. 7350, pp. 216–219, 2011.
- [109] M. C. Bessis and J. Breton-Gorius, "Iron metabolism in the bone marrow as seen by electron microscopy: a critical review," *Blood*, vol. 19, pp. 635–663, 1962.
- [110] J. A. Chasis and N. Mohandas, "Erythroblastic islands: niches for erythropoiesis," *Blood*, vol. 112, no. 3, pp. 470–478, 2008.
- [111] N. Mohandas and M. Prenant, "Three-dimensional model of bone marrow," *Blood*, vol. 51, no. 4, pp. 633–643, 1978.
- [112] M. Kusakabe, K. Hasegawa, M. Hamada et al., "c-Maf plays a crucial role for the definitive erythropoiesis that accompanies erythroblastic island formation in the fetal liver," *Blood*, vol. 118, no. 5, pp. 1374–1385, 2011.
- [113] Y. Sadahira, T. Yasuda, and T. Kimoto, "Regulation of Forssman antigen expression during maturation of mouse stromal macrophages in haematopoietic foci," *Immunology*, vol. 73, no. 4, pp. 498–504, 1991.
- [114] M. M. Rhodes, P. Kopsombut, M. C. Bondurant, J. O. Price, and M. J. Koury, "Adherence to macrophages in erythroblastic islands enhances erythroblast proliferation and increases erythrocyte production by a different mechanism than erythropoietin," *Blood*, vol. 111, no. 3, pp. 1700–1708, 2008.
- [115] A. Chow, M. Huggins, J. Ahmed et al., "CD169+ macrophages provide a niche promoting erythropoiesis under homeostasis and stress," *Nature Medicine*, vol. 19, no. 4, pp. 429–436, 2013.
- [116] P. Ramos, C. Casu, S. Gardenghi et al., "Macrophages support pathological erythropoiesis in polycythemia vera and  $\beta$ -thalassemia," *Nature Medicine*, vol. 19, no. 4, pp. 437–445, 2013.
- [117] T. Matsushima, M. Nakashima, K. Oshima et al., "Receptor binding cancer antigen expressed on SiSo cells, a novel regulator of apoptosis of erythroid progenitor cells," *Blood*, vol. 98, no. 2, pp. 313–321, 2001.
- [118] L. Zamai, P. Secchiero, S. Pierpaoli et al., "TNF-related apoptosis-inducing ligand (TRAIL) as a negative regulator of normal human erythropoiesis," *Blood*, vol. 95, no. 12, pp. 3716–3724, 2000.
- [119] K. Sawada, S. B. Krantz, E. N. Dessypris, S. T. Koury, and S. T. Sawyer, "Human colony-forming units-erythroid do not require accessory cells, but do require direct interaction with insulin-like growth factor I and/or insulin for erythroid development," *Journal of Clinical Investigation*, vol. 83, no. 5, pp. 1701–1709, 1989.
- [120] H. Yoshida, K. Kawane, M. Koike, Y. Mori, Y. Uchiyama, and S. Nagata, "Phosphatidylserine-dependent engulfment by macrophages of nuclei from erythroid precursor cells," *Nature*, vol. 437, no. 7059, pp. 754–758, 2005.
- [121] M. Miyanishi, K. Tada, M. Koike, Y. Uchiyama, T. Kitamura, and S. Nagata, "Identification of Tim4 as a phosphatidylserine receptor," *Nature*, vol. 450, no. 7168, pp. 435–439, 2007.

- [122] S. Porcu, M. F. Manchinu, M. F. Marongiu et al., "Klf1 Affects dnase II-Alpha Expression in the central macrophage of a fetal liver erythroblastic Island: a non-cell-autonomous role in definitive erythropoiesis," *Molecular and Cellular Biology*, vol. 31, no. 19, pp. 4144–4154, 2011.
- [123] B. T. Spike, B. C. Dibling, and K. F. Macleod, "Hypoxic stress underlies defects in erythroblast islands in the Rb-null mouse," *Blood*, vol. 110, no. 6, pp. 2173–2181, 2007.
- [124] X.-S. Liu, X.-H. Li, Y. Wang et al., "Disruption of palladin leads to defects in definitive erythropoiesis by interfering with erythroblastic island formation in mouse fetal liver," *Blood*, vol. 110, no. 3, pp. 870–876, 2007.
- [125] K. Jacobsen and D. G. Osmond, "Microenvironmental organization and stromal cell associations of B lymphocyte precursor cells in mouse bone marrow," *European Journal of Immunology*, vol. 20, no. 11, pp. 2395–2404, 1990.
- [126] M. R. Gomez, Y. Talke, N. Goebel, F. Hermann, B. Reich, and M. Mack, "Basophils support the survival of plasma cells in mice," *Journal of Immunology*, vol. 185, no. 12, pp. 7180–7185, 2010.
- [127] V. T. Chu, A. Fröhlich, G. Steinhauser et al., "Eosinophils are required for the maintenance of plasma cells in the bone marrow," *Nature Immunology*, vol. 12, no. 2, pp. 151–159, 2011.
- [128] O. Winter, K. Moser, E. Mohr et al., "Megakaryocytes constitute a functional component of a plasma cell niche in the bone marrow," *Blood*, vol. 116, no. 11, pp. 1867–1875, 2010.
- [129] M. Socolovsky, "Molecular insights into stress erythropoiesis," *Current Opinion in Hematology*, vol. 14, no. 3, pp. 215–224, 2007.
- [130] R. F. Paulson, L. Shi, and D.-C. Wu, "Stress erythropoiesis: new signals and new stress progenitor cells," *Current Opinion in Hematology*, vol. 18, no. 3, pp. 139–145, 2011.
- [131] L. E. Lenox, J. M. Perry, and R. F. Paulson, "BMP4 and Madh5 regulate the erythroid response to acute anemia," *Blood*, vol. 105, no. 7, pp. 2741–2748, 2005.
- [132] J. M. Perry, O. F. Harandi, and R. F. Paulson, "BMP4, SCF, and hypoxia cooperatively regulate the expansion of murine stress erythroid progenitors," *Blood*, vol. 109, no. 10, pp. 4494–4502, 2007.
- [133] J. M. Perry, O. F. Harandi, P. Porayette, S. Hegde, A. K. Kannan, and R. F. Paulson, "Maintenance of the BMP4-dependent stress erythropoiesis pathway in the murine spleen requires hedgehog signaling," *Blood*, vol. 113, no. 4, pp. 911–918, 2009.
- [134] N. Yanai, T. Satoh, and M. Obinata, "Endothelial cells create a hematopoietic inductive microenvironment preferential to erythropoiesis in the mouse spleen," *Cell Structure and Function*, vol. 16, no. 1, pp. 87–93, 1991.
- [135] J. Tsuchiyama, M. Mori, and S. Okada, "Murine spleen stromal cell line SPY3-2 maintains long-term hematopoiesis in vitro," *Blood*, vol. 85, no. 11, pp. 3107–3116, 1995.
- [136] J. Justesen, K. Stenderup, E. N. Ebbesen, L. Mosekilde, T. Steiniche, and M. Kassem, "Adipocyte tissue volume in bone marrow is increased with aging and in patients with osteoporosis," *Biogerontology*, vol. 2, no. 3, pp. 165–171, 2001.
- [137] R. Sugimura and L. Li, "Shifting in balance between osteogenesis and adipogenesis substantially influences hematopoiesis," *Journal of Molecular Cell Biology*, vol. 2, no. 2, pp. 61–62, 2010.
- [138] J. M. Gimble, C. E. Robinson, X. Wu, and K. A. Kelly, "The function of adipocytes in the bone marrow stroma: an update," *Bone*, vol. 19, no. 5, pp. 421–428, 1996.
- [139] O. Naveiras, V. Nardi, P. L. Wenzel, P. V. Hauschka, F. Fahey, and G. Q. Daley, "Bone-marrow adipocytes as negative regulators of the haematopoietic microenvironment," *Nature*, vol. 460, no. 7252, pp. 259–263, 2009.
- [140] L. DiMascio, C. Voermans, M. Ugoezwa et al., "Identification of adiponectin as a novel hemopoietic stem cell growth factor," *The Journal of Immunology*, vol. 178, no. 6, pp. 3511–3520, 2007.
- [141] Y. Omatsu, M. Seike, T. Sugiyama, T. Kume, and T. Nagasawa, "Foxcl is a critical regulator of haematopoietic stem/progenitor cell niche formation," *Nature*, vol. 508, no. 7497, pp. 536–540, 2014.
- [142] Y.-S. Torisawa, C. S. Spina, T. Mammoto et al., "Bone marrow-on-a-chip replicates hematopoietic niche physiology in vitro," *Nature Methods*, vol. 11, no. 6, pp. 663–669, 2014.



